Université de Montréal

Modélisation des effets de haute densité à la photosphère des naines blanches froides

par
Simon Blouin

Département de physique
Faculté des arts et des sciences

Thèse présentée à la Faculté des études supérieures
en vue de l'obtention du grade de Philosophiæ Doctor (Ph.D.)
en physique

Avril, 2019

Université de Montréal
Faculté des études supérieures

Cette thèse intitulée:

Modélisation des effets de haute densité à la photosphère des naines blanches froides

présentée par:

Simon Blouin

a été évaluée par un jury composé des personnes suivantes:

Paul Charbonneau,	président-rapporteur
Patrick Dufour,	directeur de recherche
René Doyon,	membre du jury
Didier Saumon,	examinateur externe
Liliana Perez,	représentante du doyen de la FES

Thèse acceptée le: .....

RÉSUMÉ

Cette thèse présente une nouvelle génération de modèles d'atmosphère d'étoiles naines blanches froides. Ces étoiles, étant parmi les plus vieilles de la Voie lactée, sont particulièrement utiles pour dater des populations stellaires et ainsi mieux comprendre l'évolution de notre Galaxie. La datation de ces objets repose toutefois sur la détermination de leurs paramètres atmosphériques, lesquels sont incertains étant donné les difficultés inhérentes à la modélisation de leur atmosphère. En effet, les atmosphères de naines blanches froides ont la particularité d'être denses, ce qui complique sérieusement leur modélisation en raison de l'importance des interactions entre particules.

Nous nous servons de techniques de simulation modernes (théorie de la fonctionnelle de la densité, dynamique moléculaire et méthodes ab initio de chimie quantique) pour améliorer la physique constitutive des modèles d'atmosphère. En particulier, nous mettons en évidence l'existence de la distorsion des profils d'absorption induite par les collisions entre l'hydrogène moléculaire et l'hélium, nous quantifions l'ionisation par pression des éléments lourds dans un milieu dense et riche en hélium et nous calculons des profils de raies métalliques au-delà de l'approximation d'impact. En intégrant ces nouveaux calculs à un code d'atmosphère existant (et en y ajoutant également une nouvelle équation d'état et des opacités du continu appropriées pour les hautes densités), nous avons mis au point le code d'atmosphère de naines blanches froides le plus précis à ce jour.

Pour tester l'exactitude de nos modèles, nous avons évalué leur capacité à reproduire le spectre de naines blanches froides dont l'atmosphère est polluée par des métaux. Ces naines blanches froides sont les seules à présenter des raies atomiques et représentent donc des cas idéaux pour valider observationnellement nos modèles. Notre code de modèles d'atmosphère passe le test : il parvient à reproduire le spectre d'étoiles que les codes précédents peinaient à expliquer, démontrant sa supériorité et validant la physique constitutive qui y est implantée.

Dans cette thèse, ce nouvel outil trouve plusieurs applications. En particulier, il permet de révéler la composition atmosphérique inusitée de la naine blanche WD J2356−209. Notre analyse montre que cette étoile aurait accrété un planétésimal riche en sodium, pour lequel aucun analogue n'est connu dans le Système solaire. Par ailleurs, en combinant nos

modèles avec les récentes observations du relevé Pan-STARRS et de la mission *Gaia*, nous dressons un portrait précis et complet de l'évolution spectrale des naines blanches froides. Plus spécifiquement, nous identifions un déclin de la fraction d'étoiles riches en hydrogène entre 7500 et 6250 K que nous interprétons comme étant dû au brassage convectif. Entre 6250 et 5000 K, nous trouvons que cette même fraction augmente, phénomène pour lequel aucune explication physique n'est connue. À plus basses températures, nous démontrons que la fraction d'objets riches en hydrogène cesse de croître, ce qui discrédite le scénario selon lequel l'accrétion d'hydrogène du milieu interstellaire domine l'évolution spectrale des naines blanches froides.

Mots clés: équation d'état — étoiles : abondances — étoiles : atmosphères — étoiles : évolution — matière dense — naines blanches — opacité — raies : profils — systèmes planétaires

ABSTRACT

This thesis presents a new generation of cool white dwarf atmosphere models. Those stars, being among the oldest in the Milky Way, are especially useful for age dating stellar populations and improving our understanding of the evolutionary history of our galaxy. Age dating of those objects however, relies on the determination of their atmospheric parameters, which are uncertain given the difficulties inherent in modeling their atmospheres. Indeed, the atmospheres of cool white dwarfs are particularly dense, which seriously complicates their modeling because of the importance of interactions between particles.

We use modern simulation techniques (density functional theory, molecular dynamics and ab initio methods of quantum chemistry) to improve the constitutive physics of atmosphere models. In particular, we show that the collision-induced absorption profiles are distorted under the physical conditions found in cool white dwarf atmospheres, we quantify the pressure ionization of heavy elements in a dense helium medium and we compute spectral line profiles beyond the impact approximation. By integrating these new calculations into an existing atmosphere code (and also by adding a new equation of state and continuum opacities suitable for high densities), we have developed the most accurate cool white dwarf atmosphere code to date.

To test the accuracy of our models, we have evaluated their ability to reproduce the spectra of cool, metal-polluted white dwarfs. Those cool white dwarfs are the only ones to show atomic spectral lines and thus represent ideal benchmarks to observationally validate our models. Our model atmosphere code passes the test: it manages to reproduce the spectra of stars that previous codes were struggling to model, which demonstrates its superiority and validates its constitutive physics.

In this thesis, this new tool finds several applications. In particular, it allows to reveal the strange atmospheric composition of white dwarf WD J2356−209. Our analysis shows that this star has accreted a sodium-rich planetesimal, for which no Solar System analogue is known. Moreover, by combining our models with recent observations from the Pan-STARRS survey and the *Gaia* mission, we paint the most accurate picture to date of the spectral evolution of cool white dwarfs. More specifically, we identify a decrease of the fraction of stars that are hydrogen-rich between 7500 and 6250 K, which we interpret

as being due to convective mixing. Between 6250 and 5000 K, we find that this fraction increases, a phenomenon for which no physical explanation exists at the moment. At lower temperatures, we show that the fraction of hydrogen-rich objects does not increase, thus ruling out the scenario according to which accretion of hydrogen from the interstellar medium dominates the spectral evolution of cool white dwarfs.

Key words: dense matter — equation of state — line: profiles — opacity — planetary systems — stars: abundances — stars: atmospheres — stars: evolution — white dwarfs

TABLE DES MATIÈRES

LISTE DES TABLEAUX

LISTE DES FIGURES

LISTE DES ABBRÉVIATIONS

2MASS	*Two Micron All-Sky Survey*
AIC	Critère d'information d'Akaike
CASSCF	Méthode du champ auto-cohérent de l'espace actif complet
CCSD(T)	Méthode des clusters couplés avec excitations simples et doubles, et triples traitées comme perturbations
CIA	Opacité induite par les collisions
DA	Naine blanche montrant des raies spectrales d'hydrogène
DB	Naine blanche montrant des raies spectrales d'hélium neutre
DC	Naine blanche ne montrant aucune raie spectrale
DFT	Théorie de la fonctionnelle de la densité
DQ	Naine blanche montrant des raies de carbone atomique ou des bandes de carbone moléculaire
DZ	Naine blanche montrant des raies spectrales d'éléments lourds
ETL	Équilibre thermodynamique local
FOS	*Faint Object Spectrograph*
GGA	Approximation des gradients généralisée
HNC	Approximation de l'*hypernetted chain*
HST	Télescope spatial Hubble
IDS	Surface de moment dipolaire induit
IR	Infrarouge
IUE	*International Ultraviolet Explorer*
LDA	Approximation de la densité locale
LRS	*Marcario Low-Resolution Spectrograph*
LRIS	*Low Resolution Imaging Spectrometer*
MD	Dynamique moléculaire

MRCI	Méthode d'interaction de configuration multi-référence
MWDD	*Montreal White Dwarf Database*
OZ	Équation d'Ornstein–Zernike
Pan-STARRS	*Panoramic Survey Telescope And Rapid Response System*
PBE	Fonctionnelle d'échange-corrélation de Perdew–Burke–Ernzerhof
PEC	Courbe d'énergie potentielle (1D)
PES	Surface d'énergie potentielle (2D)
PY	Approximation de Percus–Yevick
SDSS	*Sloan Digital Sky Survey*
SED	Distribution spectrale d'énergie
SIMBAD	*Set of Identifications, Measurements and Bibliography for Astronomical Data*
UKIDSS	*UKIRT Infrared Deep Sky Survey*
UV	Ultraviolet
VLT	*Very Large Telescope*
WISE	*Wide-field Infrared Survey Explorer*

NOTATION

a_0	Rayon de Bohr
A	Poids atomique
au	Unité atomique
α	Coefficient d'absorption
β	$\equiv 1/k_B T$
c	Vitesse de la lumière
$c(r)$	Fonction de corrélation directe
D	Debye (10^{-10} esu Å)
D	Distance entre la Terre et une étoile
e	Charge élémentaire
ϵ_0	Permittivité du vide
$\epsilon(\omega)$	Fonction diélectrique
f_ν	Flux monochromatique
F	Énergie libre de Helmholtz
$\mathcal{F}$	Transformée de Fourier
ϕ	Potentiel d'interaction
φ_ν	Profil normalisé d'une raie spectrale
$\log g$	Logarithme de la gravité de surface ($\mathrm{cm\,s^{-2}}$)
$g(r)$	Fonction de distribution radiale
G	Constante gravitationnelle
h	Constante de Planck
$\hbar$	Constante de Planck réduite
$h(r)$	Fonction de corrélation totale
H_ν	Flux d'Eddington

I	Potentiel d'ionisation
J_ν	Intensité radiative moyenne
k_B	Constante de Boltzmann
κ_ν	Opacité radiative
L	Luminosité
λ	Longueur d'onde
$\mathbf{M}$	Moment dipolaire électrique
m_e	Masse de l'électron
M	Masse d'une étoile
$M_\odot$	Masse solaire
μ	Potentiel chimique
n_i	Densité de l'espèce i en cm^{-3}
$n(\omega)$	Indice de réfraction
N	Nombre de particules
N_A	Nombre d'Avogadro
ν	Fréquence
ω	Fréquence en cm^{-1} $(= 1/\lambda)$
p	Pression
π	Parallaxe trigonométrique
Q	Fonction de partition
R	Rayon d'une étoile
$R_\odot$	Rayon solaire
$S(k)$	Facteur de structure
S/N	Rapport signal sur bruit
S_ν	Fonction source
σ	Section efficace d'absorption

σ_S	Constante de Stefan–Boltzmann
T	Température
T_{eff}	Température effective
τ_{cool}	Temps de refroidissement
τ_R	Profondeur optique de Rosseland
τ_Z	Temps de diffusion de l'élément Z
u	Densité d'énergie
X	Fraction de masse d'hydrogène
Y	Fraction de masse d'hélium
Z	Numéro atomique d'un noyau

REMERCIEMENTS

Je tiens tout d'abord à remercier mon directeur de recherche, Patrick Dufour. D'une grande disponibilité, il était toujours prêt à m'ouvrir sa porte—souvent plusieurs fois par jour—pour que je lui partage mes résultats et je quittais toujours son bureau avec une motivation renouvelée. À mon sens, il a su trouver le parfait équilibre entre m'offrir un bon encadrement et me laisser assez de liberté pour me permettre d'explorer à ma guise différentes avenues. Je le remercie pour le merveilleux projet de doctorat qu'il ma proposé : c'était vraiment le défi idéal pour moi. Enfin, je lui serai toujours reconnaissant d'avoir eu la patience de me soutenir et de m'encourager dans mes moments de doute.

Je tiens à remercier Piotr M. Kowalski pour m'avoir permis de passer quatre mois avec lui au Forschungszentrum Jülich afin d'apprendre à maîtriser l'art des simulations de dynamique moléculaire ab initio.

Je remercie Pierre Bergeron pour m'avoir aidé avec le problème très délicat de la convergence des modèles d'atmosphère et pour avoir partagé avec moi ses idées sur l'évolution spectrale des naines blanches froides.

J'exprime aussi ma gratitude envers Didier Saumon, qui m'a donné l'occasion à deux reprises de présenter ma recherche à une grande diversité de physiciens et d'astrophysiciens. Ma présentation à la conférence *Current Challenges in the Physics of White Dwarf Stars* et mon séminaire à Los Alamos en décembre 2018 constituent des événements phares de mon parcours.

Je tiens à remercier Nicole F. Allard pour tous ses calculs de profils de raies spectrales qui ont été si utiles pour mes modèles de naines blanches DZ. Sans elle, mes fits seraient pas mal moins convaincants !

J'ai une pensée spéciale pour Gilles Fontaine. Il est le premier à m'avoir introduit à la théorie des modèles d'atmosphères stellaires et il a su me communiquer sa grande passion pour le sujet.

Mes remerciements vont aussi à mes collègues du D–433 (Cynthia, François et Benoît) et à mes collègues des ailes B et F (Maude, Simon et Antoine). Je garderai toujours de vifs souvenirs de nos interminables parties de *Avalon* à Warwick, Santa Fe et Austin. Sans eux, mon doctorat n'aurait pas été aussi divertissant.

Ces remerciements seraient incomplets sans mentionner Josée-Anne, Joëlle, Camille, papa et maman. Grâce à vous (et à votre intérêt limité pour les simulations de dynamique moléculaire et les atmosphères stellaires), j'ai pu me maintenir à une saine distance de ma recherche dans mes temps libres, me permettant ainsi d'apprécier toutes les bonnes choses de la vie.

Enfin, je remercie le Conseil de recherches en sciences naturelles et en génie du Canada, la Faculté des études supérieures et postdoctorales de l'Université de Montréal, les Fonds québécois de la recherche sur la nature et les technologies et le Deutscher Akademischer Austauschdienst pour leur généreux soutien financier.

CHAPITRE 1

Introduction

Astronomy, as nothing else can do, teaches men humility.

—Arthur C. Clarke (1917−2008), écrivain et inventeur britannique

L'objectif de ce chapitre est d'introduire les notions astrophysiques sur lesquelles repose le corps de cette thèse. La Section 1.1 discute de quelques notions générales sur les naines blanches. Il y sera question de leur structure (Section 1.1.1) et de leur évolution (Section 1.1.2), de même que d'observations (Section 1.1.3) et de modèles d'atmosphère (Section 1.1.4). Ensuite, la Section 1.2 se penche plus spécifiquement sur notre compréhension des naines blanches froides, objets constituant le centre d'intérêt de cette thèse. Enfin, le but et la structure de ce travail sont donnés à la Section 1.3.

1.1 Notions fondamentales

Dans quelques milliards d'années, après avoir épuisé ses réserves de carburant nucléaire et englouti la Terre lors de sa phase de géante rouge (Schröder & Smith, 2008), le Soleil perdra ses couches externes pour former une nébuleuse planétaire. Cette coquille de gaz ionisé disparaîtra en moins de $\sim 10^4$ années (Kwok, 2000). En revanche, le cœur stellaire dénudé d'environ $0.53\,M_\odot$ (Catalan et al., 2008) qui se trouve au centre de la nébuleuse planétaire, lui, ne fait qu'entamer une longue évolution qui s'étendra sur des milliards d'années. Ce cadavre stellaire, c'est une étoile naine blanche. Le sort du Soleil n'a rien d'exceptionnel, puisqu'on estime qu'environ 97% des étoiles de notre Galaxie—c'est-à-dire toutes les étoiles dont la masse initiale est comprise entre ≈ 0.07 et $8\,M_\odot$—termineront leur évolution sous forme de naines blanches (Fontaine et al., 2001).

1.1.1 Structure

Une naine blanche est un objet compact soumis à une gravité intense : l'accélération gravitationnelle à la surface d'une naine blanche typique est de $10^8\,\mathrm{cm\,s^{-2}}$ ($\log g = 8$). Par conséquent, un tri gravitationnel efficace des éléments s'effectue (Schatzman, 1945), les plus lourds demeurant au centre de l'étoile (formant ainsi le cœur) et les plus légers flottant à la surface (formant ainsi une enveloppe dont la partie externe constitue l'atmosphère). Le cœur d'une naine blanche est extrêmement dense—la densité y est de l'ordre de $10^6\,\mathrm{g\,cm^{-3}}$ (Koester & Chanmugam, 1990; Fontaine et al., 2001)—et généralement constitué de carbone et d'oxygène issus de la fusion de l'hélium lors de la phase de géante rouge. À l'inverse, l'atmosphère est beaucoup plus ténue et dominée par l'hydrogène et l'hélium. Bien que l'atmosphère ne représente qu'une infime fraction de la masse totale d'une naine blanche, toute l'information que nous recevons de l'étoile provient de cette mince couche : l'atmosphère est trop opaque pour nous permettre de voir plus loin.[1]

Étant donné l'extrême densité que l'on retrouve au cœur d'une naine blanche, la séparation moyenne entre les particules est beaucoup plus petite que la longueur d'onde de de Broglie des électrons. Ainsi, les électrons y sont complètement dégénérés et il en résulte une pression de dégénérescence donnée par

$$p = \frac{(3\pi^2)^{2/3}}{5}\frac{\hbar^2}{m_e}n_e^{5/3}\ \text{(cas non relativiste)}, \tag{1.1}$$

où $\hbar$ est la constante de Planck réduite, m_e est la masse de l'électron et n_e est la densité électronique. C'est cette pression de dégénérescence qui s'oppose à la gravité et permet ainsi de maintenir l'équilibre hydrostatique de la naine blanche (Fowler, 1926). On peut montrer que les naines blanches doivent obéir à une relation masse-rayon bien précise pour que l'équilibre hydrostatique soit maintenu (Chandrasekhar, 1935). Ainsi, pour une composition de noyau donnée, lorsque la masse M d'une naine blanche est connue, son rayon R l'est automatiquement, et vice-versa. Étant donné la dépendance en densité de la pression de dégénérescence, la relation masse-rayon implique que les naines blanches les

[1] Bien que l'on ne voit que l'atmosphère des naines blanches, précisons que l'astérosismologie nous permet d'accéder à énormément d'information sur les couches internes des naines blanches (Fontaine & Brassard, 2008; Winget & Kepler, 2008). Par exemple, l'astérosismologie a été utilisée pour caractériser le profil de rotation interne (Charpinet et al., 2009) et pour cartographier la structure chimique interne (Giammichele et al., 2018) de naines blanches.

plus massives sont aussi les plus petites. En effet, une plus grande densité est nécessaire pour produire une pression de dégénérescence suffisamment élevée pour contrecarrer la plus grande force gravitationnelle associée à une étoile plus massive. Remarquons qu'une fois une certaine densité atteinte, les électrons peuplent des niveaux d'énergie très élevés, de sorte qu'ils deviennent relativistes. La pression de dégénérescence perd alors sa dépendance en $n_e^{5/3}$ au profit d'une dépendance en $n_e^{4/3}$. Ainsi, une fois le régime relativiste atteint, la pression de dégénérescence devient moins efficace à maintenir l'équilibre hydrostatique, jusqu'à atteindre une masse limite (Chandrasekhar, 1931)—d'environ $1.4\,M_\odot$—au-delà de laquelle l'équilibre hydrostatique est tout simplement impossible. La Figure 1.1 illustre la relation masse-rayon dans le cas simple d'un gaz de Fermi froid.

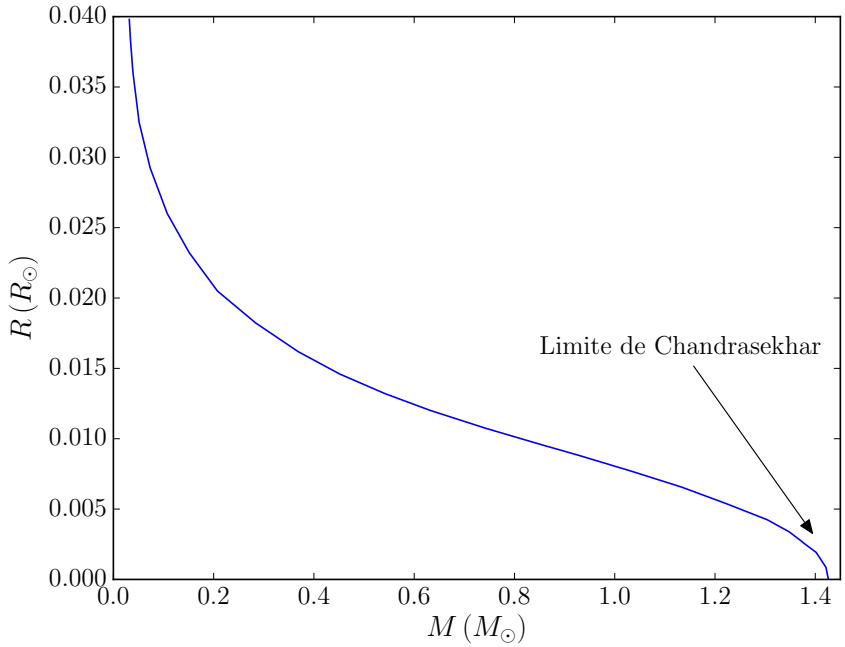

Figure 1.1 – Relation masse-rayon pour une étoile constituée d'un gaz de Fermi froid ($T = 0$) relativiste. Le poids moléculaire par électron a été fixé à 2 pour tracer cette figure.

1.1.2 Évolution

À leur formation, les naines blanches sont extrêmement chaudes. Or, comme elles sont dépourvues de source d'énergie interne, toute la radiation qu'elles émettent provient de

l'énergie thermique emmagasinée[2] et elles ne peuvent que se refroidir (Mestel, 1952). Étant donné leur petite surface et la grande opacité de leur atmosphère, ce refroidissement s'effectue très lentement. Éventuellement, les naines blanches devraient devenir assez froides pour ne plus émettre une quantité significative de radiation et ainsi atteindre un état d'équilibre avec le fond diffus cosmologique. L'Univers est encore trop jeune pour qu'une naine blanche ait atteint ce stade : les naines blanches les plus froides connues ont une température effective[3] de l'ordre de 3500 K (Gianninas et al., 2015).

En utilisant un certain nombre d'approximations, Mestel (1952) a dérivé le temps de refroidissement $\tau_{\rm cool}$ d'une naine blanche sous forme d'une équation analytique simple (Fontaine et al., 2001),

$$\tau_{\rm cool} \propto \bar{A}^{-1}\bar{\mu}^{-2/7}M^{5/7}L^{-5/7}, \tag{1.2}$$

où $\bar{A}$ est le poids atomique moyen des atomes constituant le cœur de la naine blanche, $\bar{\mu}$ est le poids moléculaire moyen, M est la masse de l'étoile et L est sa luminosité. Trois conséquences importantes découlent de cette relation :

1. Une grande luminosité est associée à un refroidissement rapide.

2. La composition chimique du cœur d'une naine blanche affecte son taux de refroidissement. Par exemple, un cœur de carbone se refroidit plus lentement qu'un cœur d'oxygène, puisque la capacité thermique massique de ce dernier est plus faible (il y a plus d'ions dans un gramme de carbone que dans un gramme d'oxygène).

3. Les étoiles les plus massives se refroidissent plus lentement : d'une part, elles ont davantage d'énergie thermique emmagasinée et, d'autre part, elles ont un plus petit rayon et donc une plus faible luminosité.

Depuis les travaux pionniers de Mestel, plusieurs générations de modèles d'évolution de naines blanches ont vu le jour pour décrire de manière de plus en plus détaillée le refroidissement des naines blanches (Lamb & Van Horn, 1975; Wood, 1990; Hansen, 1999; Fontaine et al., 2001; Renedo et al., 2010). Le jeu en vaut la chandelle, puisque ces modèles

[2]Notons toutefois que la contraction résiduelle de la naine blanche fournit une petite quantité d'énergie additionnelle (Wood, 1995; Fontaine et al., 2001).

[3]La température effective $T_{\rm eff}$ d'un objet est définie comme la température que devrait avoir un corps noir pour émettre la même quantité de radiation électromagnétique que l'objet en question.

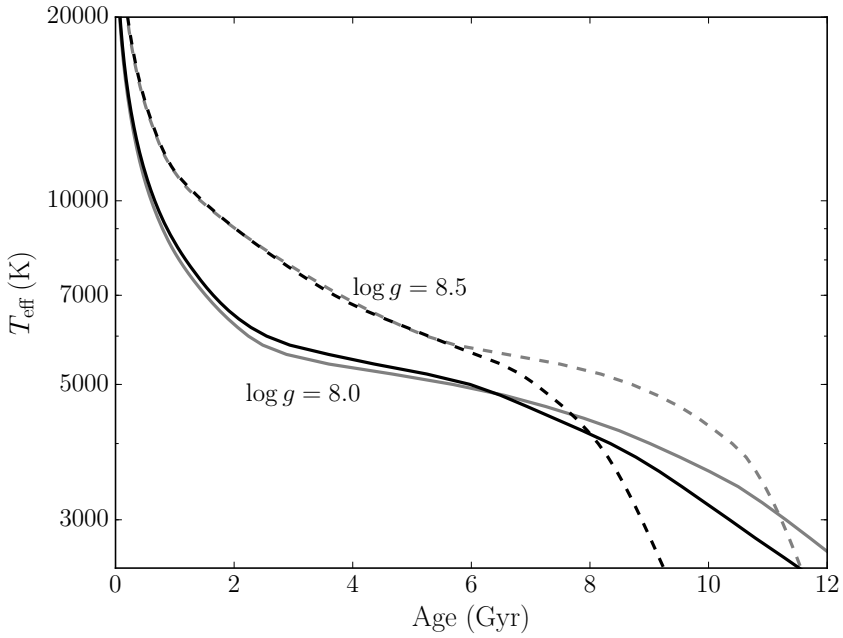

Figure 1.2 – Refroidissement de naines blanches à atmosphère d'hydrogène (lignes grises) et à atmosphère d'hélium (lignes noires). Les traits pleins montrent le cas d'une naine blanche avec une gravité de surface $\log g = 8.0$ et les traits discontinus correspondent au cas où $\log g = 8.5$. Les données utilisées pour tracer cette figure proviennent des modèles de Fontaine et al. (2001).

permettent de déterminer l'âge des naines blanches de manière semi-empirique. En effet, comme l'illustre la Figure 1.2, le refroidissement monotone des naines blanches implique que si l'on détermine leurs paramètres atmosphériques (température effective, gravité de surface et composition chimique), on peut se servir des modèles évolutifs pour calculer leur temps de refroidissement. En additionnant cette quantité au temps de vie de l'étoile sur la séquence principale[4], on obtient l'âge total de l'étoile. Non seulement cette mesure est-elle intéressante du point de vue de l'étude des naines blanches en soi, mais surtout, elle permet de dater les populations stellaires auxquelles ces naines blanches appartiennent. Ainsi, cette technique a été appliquée à la mesure de l'âge du disque galactique (Winget et al., 1987; Oswalt et al., 1996; Leggett et al., 1998; Gianninas et al., 2015), d'amas

[4]Le temps de vie de l'étoile sur la séquence principale est déterminé de façon semi-empirique (Catalan et al., 2008; Cummings et al., 2018). En mesurant l'âge d'un amas stellaire (en identifiant la point de sortie de la séquence principale) et en déterminant le temps de refroidissement des naines blanches comprises dans l'amas, on peut identifier la relation qui relie la masse d'une naine blanche au temps de vie de son progéniteur (âge de l'amas − temps de refroidissement de la naine blanche = temps de vie du progéniteur).

globulaires (Hansen et al., 2002, 2004, 2007; Bedin et al., 2009), d'amas ouverts (Richer et al., 1998; von Hippel & Gilmore, 2000; Bedin et al., 2005; García-Berro et al., 2010) et d'étoiles du halo (Kilic et al., 2010a, 2012; Kalirai, 2012).

1.1.3 Observations

Trois catégories d'observations sont pertinentes à l'étude de l'atmosphère des naines blanches : les mesures astrométriques, les données photométriques et les observations spectroscopiques. Cette section explique quelle information nous pouvons retirer de chacune de ces catégories.

1.1.3.1 Parallaxe

La mesure d'une parallaxe trigonométrique constitue le seul moyen disponible pour mesurer directement la distance D d'une naine blanche. Jusqu'à récemment, nous ne disposions de mesures de parallaxe que pour quelques centaines de naines blanches (Bédard et al., 2017). Grâce à l'arrivée du satellite *Gaia*, les choses ont complètement changé et nous disposons aujourd'hui de parallaxes pour environ 260 000 naines blanches (Fusillo et al., 2018). Les choses ne s'arrêteront pas là puisqu'on estime qu'à terme la mission *Gaia* devrait permettre de découvrir quelque 400 000 naines blanches (Jordan, 2007).

La mesure de la distance d'une naine blanche, combinée à une mesure de flux incident, permet de déterminer son rayon et sa masse. En effet, si l'on connaît le flux émis par l'étoile H_ν[5] et le flux f_ν reçu sur Terre, on peut se servir de la relation

$$f_\nu = 4\pi \left(\frac{R}{D}\right)^2 H_\nu \tag{1.3}$$

pour isoler le rayon stellaire R. Ensuite, la relation masse-rayon permet de calculer directement la masse de la naine blanche.

1.1.3.2 Photométrie

La photométrie consiste à mesurer le flux f_ν^m émis par l'étoile et reçu sur Terre à l'intérieur d'une bande passante m donnée. En mesurant le flux à l'intérieur de plusieurs

[5]Le flux émis par l'étoile est a priori inconnu. On le trouve en calculant un modèle d'atmosphère qui reproduit la distribution spectrale d'énergie observée.

bandes passantes, on obtient la distribution spectrale d'énergie (SED) de l'étoile. À elle seule, la SED permet de mesurer plusieurs paramètres atmosphériques.

D'une part, la SED permet de contraindre la température effective de l'étoile. En première approximation, la SED est donnée par la loi de Planck,

$$B_\nu(\nu, T) = \frac{2h\nu^3}{c^2} \frac{1}{e^{\frac{h\nu}{k_\mathrm{B}T}} - 1}. \tag{1.4}$$

Étant donné la dépendance en température de la loi de Planck, la forme générale—et en particulier la position du maximum—de la SED est fortement influencée par la température effective. Cette dépendance est évidente pour les SED synthétiques tracées à la Figure 1.3.

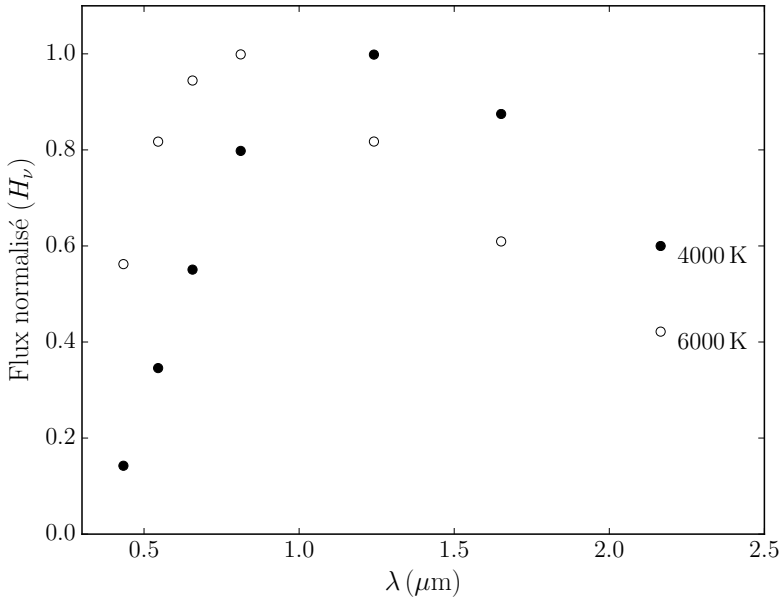

Figure 1.3 – Photométrie $BVRI$ et JHK calculée pour deux naines blanches avec des températures effectives différentes. Ces modèles ont été calculés en supposant une atmosphère d'hélium et une gravité de surface $\log g = 8$. Les SED ont été normalisées à leur maximum.

D'autre part, les écarts de la SED par rapport à la loi de Planck permettent souvent d'établir la composition chimique de l'atmosphère. C'est en particulier possible dans le cas des naines blanches froides avec une composition mixte H/He. Chez ces étoiles, on observe une puissante source d'opacité dans l'infrarouge due au phénomène d'absorption induite par les collisions (CIA, *collision-induced absorption*) entre les atomes d'hélium

et l'hydrogène moléculaire. Comme l'intensité de cette source d'absorption dépend de l'abondance de H_2 à la photosphère, la portion infrarouge de la SED varie fortement selon l'abondance d'hydrogène (Figure 1.4). On peut donc se servir de cette signature pour contraindre le rapport H/He à la surface de l'étoile (Bergeron et al., 2001; Kilic et al., 2010b; Gianninas et al., 2015).

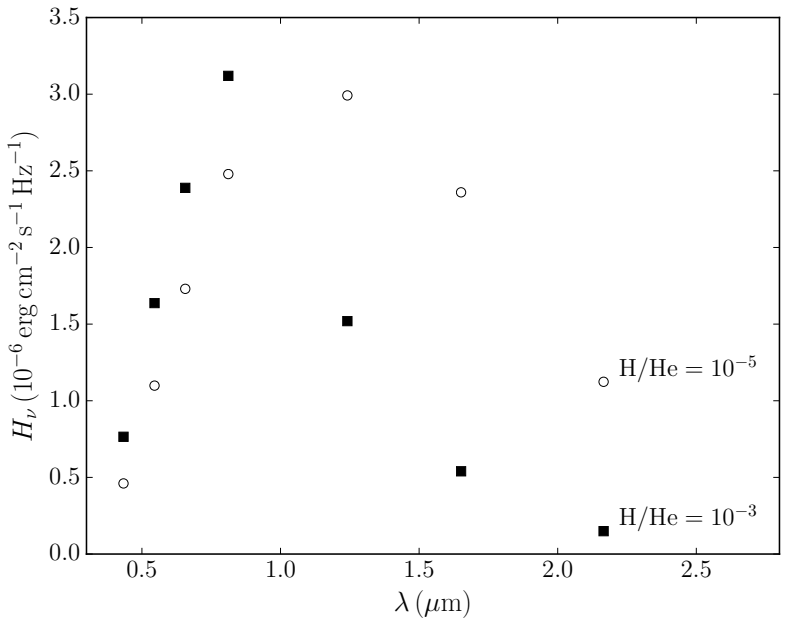

Figure 1.4 – Photométrie $BVRI$ et JHK calculée pour deux naines blanches avec différentes abondances d'hydrogène. Ces modèles ont été calculés en supposant une température effective $T_{\mathrm{eff}} = 4000\,\mathrm{K}$ et une gravité de surface $\log g = 8$.

Même en l'absence de fortes sources de CIA, il demeure souvent possible d'établir la composition chimique de l'atmosphère sur la base de mesures photométriques. En effet, pour une même température effective, la SED d'une étoile riche en hélium diffère de celle d'une étoile riche en hydrogène (Figure 1.5). Ces différences sont dues aux sources d'opacité différentes qui affectent ces deux types d'étoiles, notamment l'aile rouge de la raie Lyman α (voir par exemple Kowalski & Saumon, 2006). Toutefois, il n'est pas rare que la meilleure solution obtenue en supposant une atmosphère d'hélium pur soit très proche de la meilleure solution obtenue en supposant une atmosphère d'hydrogène pur, rendant l'identification de la composition chimique plutôt délicate (Bergeron et al., 1997, 2001).

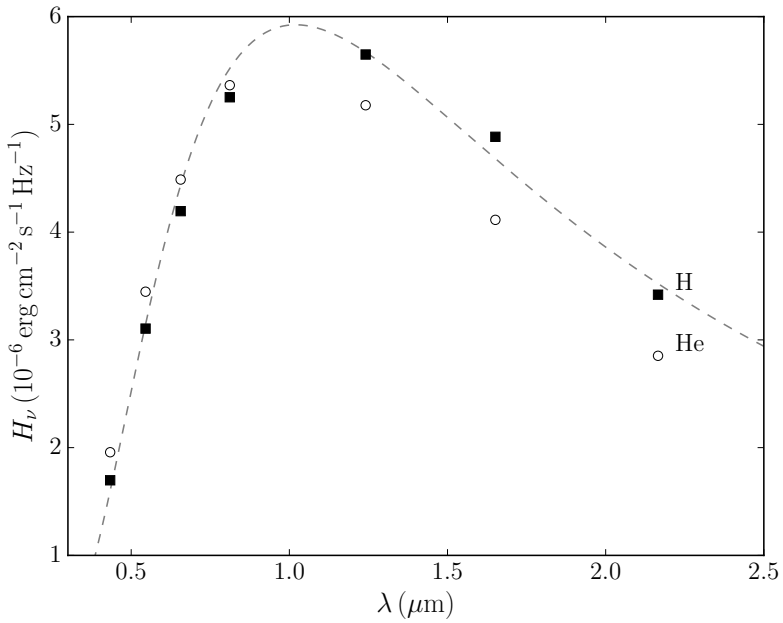

Figure 1.5 – Photométrie $BVRI$ et JHK calculée pour deux naines blanches avec des compositions chimiques différentes. Ces modèles ont été calculés en supposant une température effective de 5000 K et une gravité de surface $\log g = 8$. La courbe en trait discontinu correspond à un spectre de corps noir à la même température.

1.1.3.3 Spectroscopie

En spectroscopie, on mesure le flux émis par l'étoile en fonction de la longueur d'onde. Contrairement aux mesures photométriques, il est alors possible de résoudre les raies spectrales et les bandes moléculaires, permettant généralement une caractérisation plus précise de la composition chimique de l'étoile. Étant donné leur grande diversité de températures et de compositions chimiques, les naines blanches présentent une grande variété de spectres. Pour classer ces spectres, on utilise un système de classification où chaque étoile se voit attribuer une classe représentée par deux lettres ou plus. La première lettre est systématiquement un D—rappelant qu'il s'agit d'étoiles dégénérées—et la deuxième lettre indique la signature spectrale dominante dans la portion visible du spectre. Ainsi, on retrouve les classes spectrales suivantes, dont un exemple de chacune est donné à la Figure 1.6.

DA Ces étoiles montrent des raies d'hydrogène (les raies de Balmer dans la portion visible du spectre).

DB Les naines blanches DB ont un spectre qui contient des raies d'absorption d'hélium neutre.

DC En bas d'une température effective d'environ 12 000 K pour l'hélium et de 5000 K pour l'hydrogène, plus aucune raie spectrale n'est détectable dans la portion visible du spectre. Le spectre est alors continu (sans aucune raie d'absorption) et on parle d'une naine blanche de type DC. Les données spectroscopiques ne sont d'aucune utilité pour l'étude des naines blanches DC en bas de 5000 K : on doit alors se replier sur les mesures photométriques pour établir la composition chimique de l'étoile.

DO L'hélium neutre a un potentiel d'ionisation très élevé (24.6 eV), ce qui implique que l'ion He II n'est spectroscopiquement visible qu'à la photosphère des naines blanches les plus chaudes. Si des raies de He II sont visibles, on parle d'une naine blanche DO.

DQ Certaines naines blanches ont une atmosphère dominée par l'hélium, mais polluée par le carbone. L'origine du carbone—qui, normalement, est confiné aux régions internes—dans l'atmosphère de ces étoiles s'explique par le dragage convectif de l'hélium qui fait remonter à la surface le carbone diffusé à l'extérieur du noyau de la naine blanche (Pelletier et al., 1986). En haut de $T_{\text{eff}} \approx 10\,000$ K, la composition chimique de ces atmosphères est trahie par la présence de raies atomiques de carbone dans le spectre. À plus basses températures, la présence de carbone se manifeste plutôt par l'absorption causée par les bandes moléculaires de C_2—en particulier les bandes Swan, entre 4500 et 6000 Å. En dessous d'une température effective d'environ 6000 K, les bandes Swan sont déformées et décalées vers le bleu en raison d'effets de haute pression (Hall & Maxwell, 2008; Kowalski, 2010). On parle alors de naines blanches DQpec.

DZ Le spectre de naines blanches DZ comporte des raies atomiques associées à des métaux autres que le carbone (par exemple, le fer, le sodium, le magnésium ou le calcium). Tel que mentionné plus haut, le tri gravitationnel est extrêmement efficace chez les naines blanches. On s'attend donc à ce qu'une petite quantité de métaux saupoudrée à la surface d'une naine blanche coule rapidement au-delà de la photosphère (Pelletier et al., 1986; Koester, 2009), la rendant ainsi impossible à détecter. Par conséquent, la présence de mé-

taux à la photosphère de certaines naines blanches implique l'existence d'un mécanisme qui injecte (ou qui a récemment injecté) des métaux dans leur atmosphère. Aujourd'hui, il est bien accepté que ce flot d'éléments lourds a pour origine l'accrétion par les naines blanches DZ de corps rocheux (astéroïdes, comètes, planètes naines ; Debes & Sigurdsson, 2002; Jura, 2003, 2008). L'étude de la composition chimique des atmosphères de naines blanches DZ nous donne donc la chance de pouvoir inférer la composition des corps rocheux de systèmes exoplanétaires (Zuckerman et al., 2007; Dufour et al., 2010; Klein et al., 2010; Jura et al., 2012; Farihi et al., 2013; Hollands et al., 2018a). Il s'agit là d'une opportunité unique et essentiellement inaccessible aux méthodes conventionnelles d'étude des exoplanètes (Dorn et al., 2015). Il a ainsi été possible de montrer que les planétésimaux appartenant à des systèmes exoplanétaires ont des compositions chimiques très similaires à celles d'objets du Système solaire, suggérant des processus de formation et d'évolution similaires à ceux ayant lieu dans le Système solaire (Jura & Young, 2014).

Il est fréquent de trouver dans la littérature des étoiles dont la classe spectrale contient trois lettres ou plus. Ces lettres supplémentaires permettent d'indiquer la présence de signatures spectrales de moindre importance dans n'importe quelle portion du spectre électromagnétique. Ainsi, une naine blanche avec des raies de Balmer dans le visible et des raies métalliques dans l'UV sera désignée comme DAZ. Tous les détails concernant ce système de classification sont donnés dans Sion et al. (1983). Soulignons enfin que la classe spectrale d'une étoile ne correspond pas nécessairement à l'espèce chimique la plus abondante dans son atmosphère. Par exemple, une étoile de type DAZ peut avoir une atmosphère dominée par l'hélium (Zuckerman et al., 2007).

Comme cette thèse porte sur les naines blanches froides, il y sera uniquement question des étoiles de types DC, DZ et DQ/DQpec : les classes DA, DB et DO n'existent que chez les naines blanches plus chaudes. Par ailleurs, on s'intéressera aussi aux naines blanches ultra-froides (*ultracool*). Il s'agit d'étoiles dont l'atmosphère a une composition mixte H/He et dont la température effective est sous la barre des 4000 K. Sous ces conditions, la CIA devient une source importante d'absorption dans l'infrarouge et engendre ainsi un déficit de flux aux grandes longueurs d'onde. Il en résulte un phénomène inusité selon lequel les

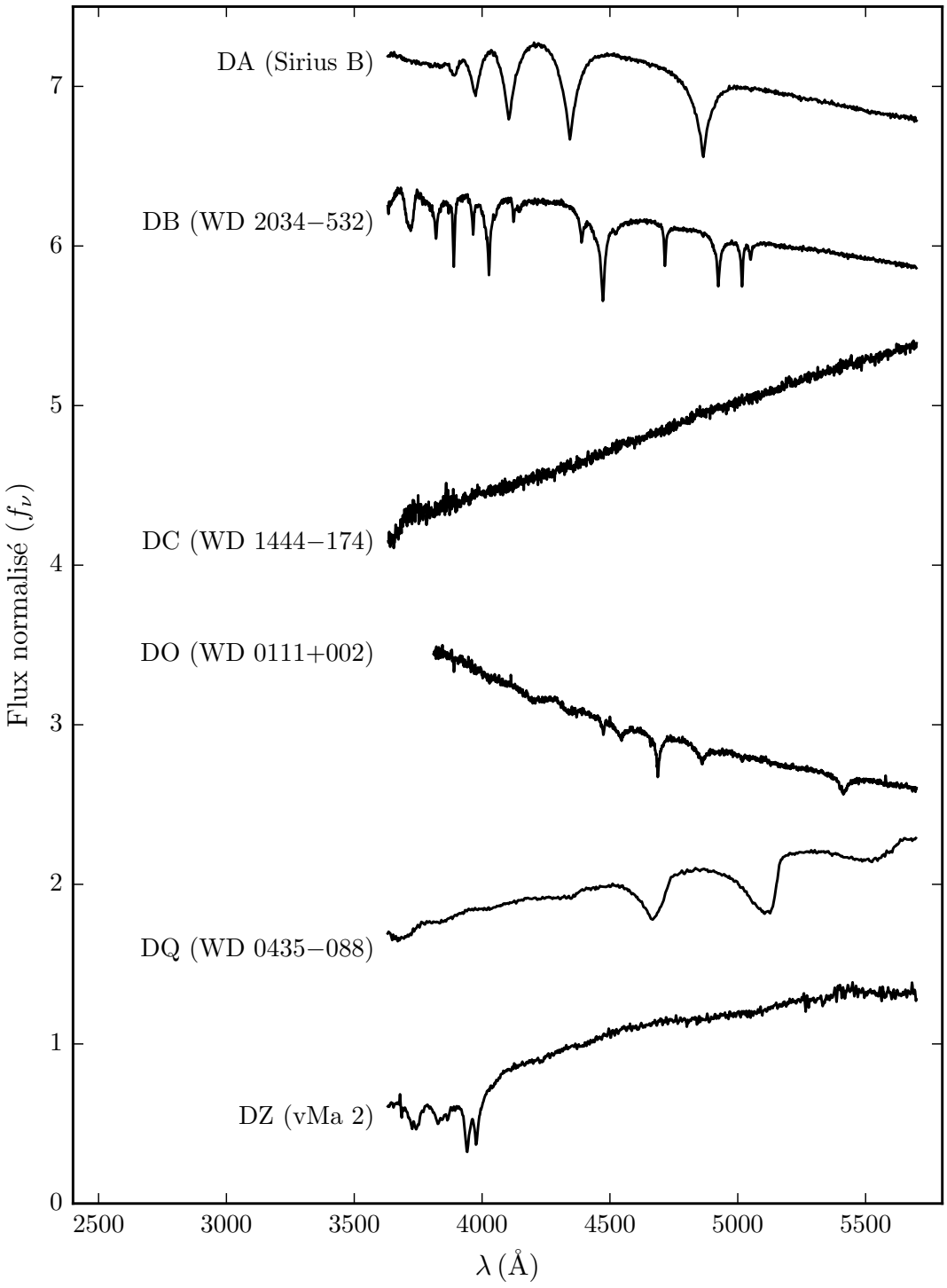

Figure 1.6 – Spectres typiques de naines blanches de types DA, DB, DC, DO, DQ et DZ. Les spectres ont été normalisés à 5000 Å et sont décalés verticalement de manière arbitraire. Les données utilisées pour tracer cette figure sont tirées de Bergeron et al. (2011), Gianninas et al. (2011), Giammichele et al. (2012), Alam et al. (2015) et Limoges et al. (2015).

naines blanches ultra-froides deviennent de plus en plus bleues en se refroidissant (plutôt que plus rouges, comme dans le cas d'un corps noir).

1.1.4 Modèles d'atmosphère

Pour déterminer avec précision les paramètres fondamentaux d'une naine blanche, on recourt à des codes de modèles d'atmosphère. Ces codes sophistiqués permettent de prédire le flux monochromatique émergeant à la surface d'une naine blanche pour des paramètres atmosphériques donnés (température effective, gravité de surface et composition chimique). La théorie qui supporte ces modèles est présentée dans le Chapitre 2 de cette thèse.

En calculant des modèles pour des centaines de combinaisons de paramètres atmosphériques, on peut bâtir une grille de modèles. Il suffit ensuite d'interpoler dans cette grille pour trouver les paramètres atmosphériques qui permettent d'obtenir le meilleur accord possible—en terme de χ^2—aux observations photométriques et spectroscopiques de l'étoile étudiée. Dans le cadre de cette thèse, des dizaines de grilles (soit plus de 100 000 modèles) ont été calculées grâce à la grappe d'ordinateurs CALYS qui comporte 320 processeurs permettant de calculer simultanément plusieurs modèles (Brassard et al., 2010; Latour et al., 2015).

1.2 L'étude des naines blanches froides

Les naines blanches froides—en particulier celles dont l'atmosphère est dominée par l'hélium—ont la particularité de posséder une atmosphère dense. Cette caractéristique complique grandement leur analyse, comme l'atteste la difficulté qu'éprouvent les modèles d'atmosphère à reproduire le spectre de ces étoiles (Section 1.2.1). En revanche, tel qu'expliqué dans la Section 1.2.2, la grande quantité d'information que l'on peut soutirer de ces étoiles justifie que l'on s'y attarde malgré les difficultés inhérentes à leur modélisation.

1.2.1 Défis

La densité à la photosphère d'une naine blanche froide riche en hélium peut atteindre $1\,\mathrm{g\,cm^{-3}}$ (Bergeron et al., 1995; Kowalski, 2010). Ce phénomène s'explique par le fait qu'à basse température la matière demeure peu ionisée. Ainsi, l'atmosphère des naines blanches froides contient peu d'électrons libres. Comme la source d'opacité dominante des naines

blanches froides riches en hélium est le He^- libre-libre, cette diminution de l'abondance d'électrons entraîne une réduction de l'opacité de l'atmosphère. Les photons que nous captons proviennent alors de régions plus profondes dans l'étoile, où la densité est élevée. Pour les naines blanches riches en hélium les plus froides, la photosphère se trouve alors dans une région de l'étoile qui correspond davantage à un fluide qu'à un gaz (Figure 1.7).

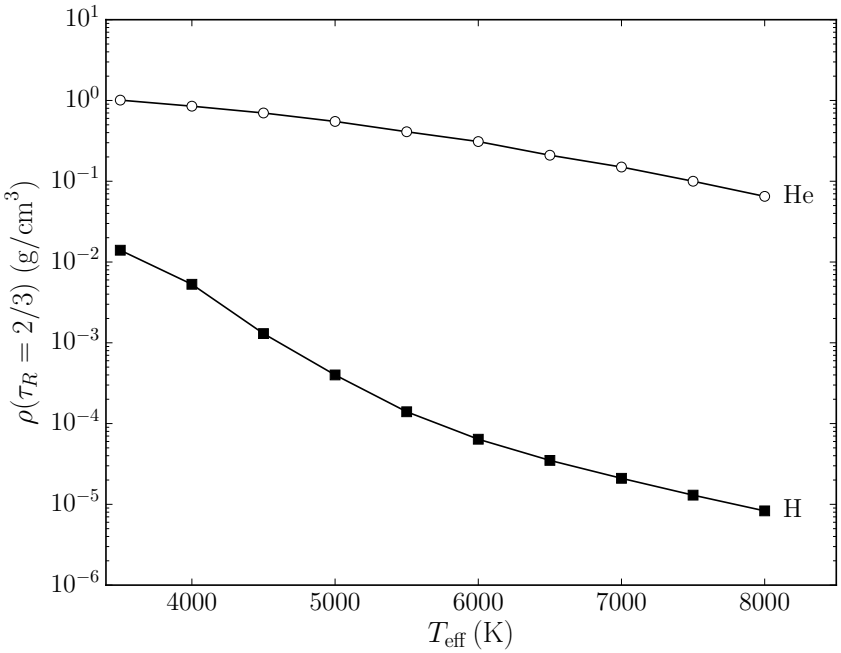

Figure 1.7 – Densité à la photosphère ($\tau_R = 2/3$) de modèles d'atmosphère riches en hélium et riches en hydrogène en fonction de la température effective en supposant une gravité de surface $\log g = 8$.

Cette situation est problématique pour les modèles d'atmosphère. D'une part, comme nous le verrons au Chapitre 2, les modèles d'atmosphère sont classiquement basés sur une série d'approximations valides seulement dans un régime de basse densité. D'autre part, les conditions physiques caractérisant la photosphère des naines blanches froides riches en hélium sont difficilement atteignables en laboratoire, de sorte que les données expérimentales qui permettraient une meilleure compréhension de la physique de tels milieux sont souvent fragmentaires ou incertaines (Nellis et al., 1984; Fortov et al., 2003; Eggert et al., 2008; Celliers et al., 2010; Soubiran et al., 2012). Cela implique que les modèles d'atmosphère peinent à décrire correctement le comportement de la matière dans le régime physique pertinent à la modélisation de ces étoiles.

Ces lacunes sont particulièrement visibles dans l'échec des modèles disponibles jusqu'ici à reproduire correctement le spectre de la majorité des naines blanches ultra-froides, DQpec et DZ froides. La Figure 1.8 montre un exemple tiré de la littérature pour chacune de ces trois classes spectrales. Avec d'aussi pauvres accords entre les modèles et les observations, les paramètres atmosphériques qu'on en déduit sont forcément entachés d'erreurs importantes.

Les problèmes éprouvés par les codes de modèles d'atmosphère sont également manifestes, quoique plus subtilement, dans le cas des naines blanches DC. Comme nous l'avons vu, il s'agit de naines blanches froides avec un spectre continu. Ainsi, il est relativement aisé pour un modèle d'atmosphère de reproduire le spectre de ces étoiles : il n'y a pas de raie spectrale ou de bande moléculaire pour donner un véritable défi aux modèles. Or, le fait de reproduire leur SED ne signifie pas nécessairement que l'on obtient les bons paramètres atmosphériques. Pour preuve, différents codes de modèles d'atmosphère donnent des solutions différentes pour une même naine blanche. Les modèles de Kowalski (2006a) et de Bergeron et al. (1995) sont tous deux capables de reproduire la distribution spectrale d'énergie de la grande majorité des naines blanches DC, mais ils sont en désaccord sur la composition chimique de ces étoiles. L'origine de ce désaccord provient du traitement différent des effets de haute densité dans le calcul des opacités et de l'équation d'état. Le fait que les choix effectués par ces auteurs sur la physique constitutive de leurs modèles influencent les résultats obtenus montre à quel point notre compréhension du comportement de la matière sous ces conditions est limitée.

1.2.2 Motivation

Il est de première importance que les lacunes des modèles d'atmosphère de naines blanches froides soient corrigées. Non seulement ces lacunes entachent-elles d'erreur toute caractérisation des naines blanches ultra-froides, DZ froides, DQpec et DC, mais surtout, elles remettent en doute les analyses astrophysiques qui sont basées sur ces caractérisations. C'est entre autres le cas des études cosmochronologiques, où l'on date une population stellaire grâce au temps de refroidissement des étoiles naines blanches. Comme expliqué plus haut (Section 1.1.2), pour déterminer le temps de refroidissement d'une naine blanche, il faut mesurer sa température effective, sa gravité de surface et la composition chimique

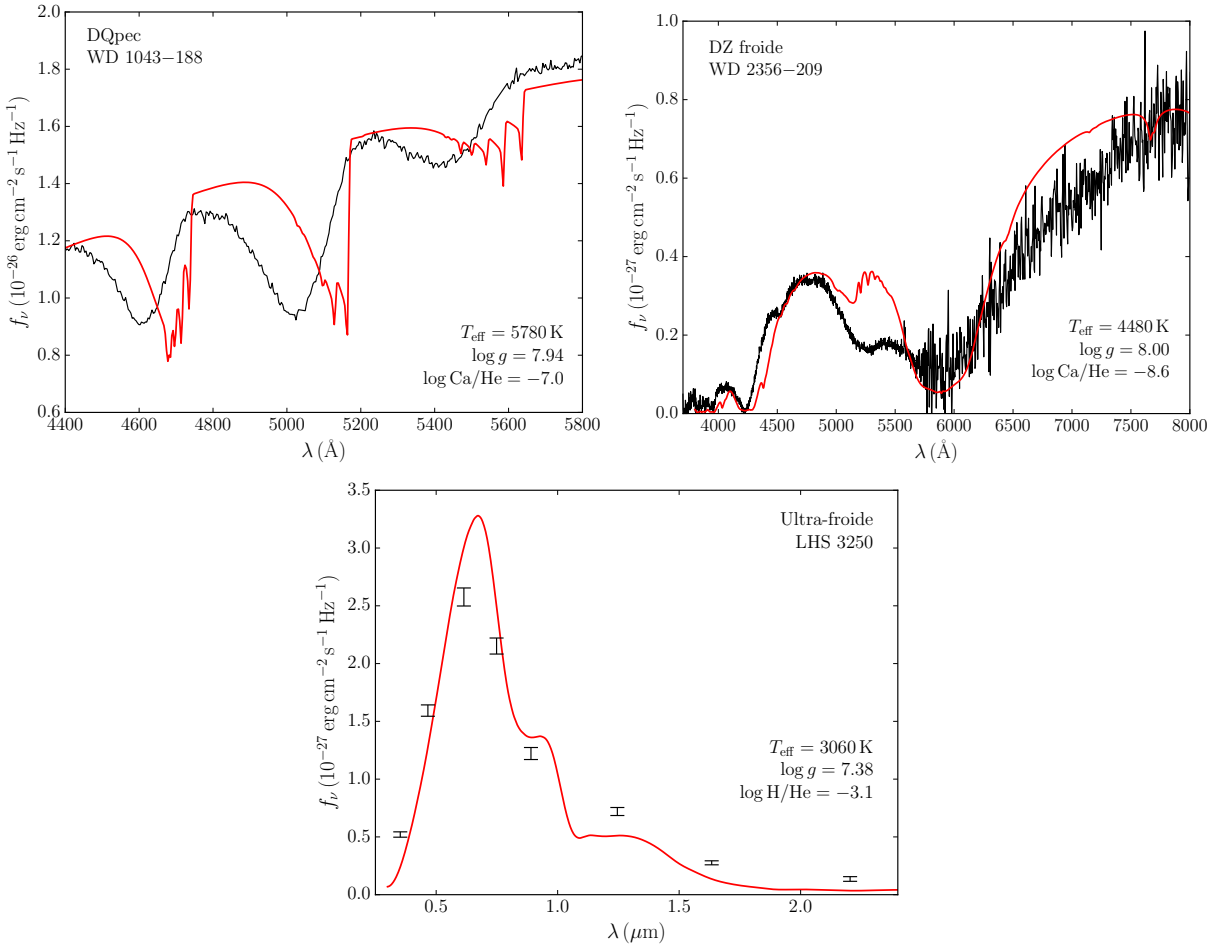

Figure 1.8 – Meilleures solutions obtenues au moyen des modèles d'atmosphère disponibles avant les travaux de cette thèse pour trois naines blanches froides problématiques. Les deux figures du haut montrent les solutions spectroscopiques trouvées pour une DQpec et une DZ froide avec les modèles de Dufour et al. (2005) et de Dufour et al. (2007). La figure du bas compare les mesures photométriques de la naine blanche ultra-froide LHS 3250 (barres d'erreur) à la meilleure solution de Gianninas et al. (2015, trait plein).

de son atmosphère. Bien sûr, la précision de l'âge déterminé dépend directement de la précision avec laquelle ces paramètres atmosphériques sont contraints. Or, on a de bonnes raisons de croire que ces paramètres sont incorrects pour une bonne partie des naines blanches froides.

Premièrement, comme nous l'avons vu, la détermination de la composition chimique d'une naine blanche de type DC est délicate et le résultat dépend bien souvent du code de modèles d'atmosphère utilisé. Ainsi, il est fort probable que la composition chimique de l'atmosphère de nombreuses étoiles DC soit incorrectement déterminée. Cette situation est problématique dans la mesure où la composition de l'atmosphère influence grandement le temps de refroidissement d'une naine blanche. Comme une atmosphère dominée par l'hydrogène est plus opaque qu'une atmosphère dominée par l'hélium, la première conduit à un refroidissement plus lent. À titre d'exemple, pour une naine blanche possédant une température effective de 4000 K, une mauvaise détermination de la composition chimique peut entraîner une erreur d'un milliard d'années sur son âge (Bergeron et al., 2001).

Deuxièmement, la SED des naines blanches ultra-froides est systématiquement mal reproduite par les modèles actuels (voir par exemple la Figure 1.8), ce qui implique fort probablement que les paramètres atmosphériques de ces étoiles sont erronés. Or, une simple différence de 300 K sur la température effective d'une naine blanche ultra-froide à 3500 K implique une erreur de plus d'un demi-milliard d'années sur son temps de refroidissement. Cette situation est d'autant plus troublante que les naines blanches ultra-froides sont les plus vieilles naines blanches et ce sont donc elles qui apportent les meilleures contraintes dans toute étude cosmochronologique.

Un autre type d'analyse touché par les lacunes des modèles de naines blanches froides est l'étude de l'évolution spectrale. En examinant comment la composition de l'atmosphère des naines blanches varie au cours de leur évolution, des tendances peuvent être identifiées. On sait notamment que la fraction d'étoiles riches en hydrogène diminue lorsque l'on passe de $T_{\rm eff} = 12\,000$ K à $T_{\rm eff} = 6000$ K (Bergeron et al., 1997, 2001). Cette transition s'explique par le brassage convectif qui peut mixer la couche mince d'hydrogène qui flotte à la surface de l'étoile avec l'épaisse couche d'hélium qui se trouve en dessous (Vauclair & Reisse, 1977; Rolland et al., 2018), transformant ainsi une atmosphère dominée par l'hydrogène en une atmosphère dominée par l'hélium. Par contre, les choses se compliquent

lorsque l'on passe sous la barre des 6000 K : deux scénarios distincts, résumés par la Figure 1.9, ont été proposés. D'une part, plusieurs auteurs (Bergeron et al., 1997, 2001; Kilic et al., 2006, 2010b) trouvent un important déficit d'étoiles riches en hélium entre 6000 K et 5000 K—connu sous le nom de *non-DA gap*—et une proportion similaire d'étoiles riches en hydrogène et riches en hélium en bas de 5000 K. Ces conclusions impliquent que la majorité des étoiles riches en hélium se transforment en étoiles riches en hydrogène lorsqu'elles atteignent $T_{\rm eff} \approx 6000$ K, puis qu'une bonne partie d'entre elles retrouvent une composition riche en hélium en bas de 5000 K. À ce jour, aucune explication complète quant au mécanisme physique causant cette transition n'a été fournie (Hansen, 1999; Malo et al., 1999; Bergeron et al., 2001). D'autre part, certains auteurs (Kowalski, 2006a; Kilic et al., 2009a,b) arrivent à la conclusion qu'il n'existe aucune naine blanche riche en hélium en dessous de 5000 K (mis à part les étoiles dont l'atmosphère est polluée par des métaux) et que le déficit observé entre 6000 K et 5000 K fait partie d'un processus continu selon lequel les naines blanches accrètent de l'hydrogène du milieu interstellaire (Kowalski, 2006a). Toutefois, ce scénario a été remis en question en raison du taux d'accrétion trop élevé nécessaire à un tel phénomène.

Le fait que certaines études concluent à l'existence du *non-DA gap* et que d'autres concluent à son inexistence a pour origine le choix des modèles d'atmosphère utilisés dans l'analyse des SED. Toutes les études qui concluent à l'existence du *non-DA gap* utilisent les modèles de Bergeron et al. (1995), tandis que ceux qui concluent à son inexistence utilisent ceux de Kowalski (2006a). En fait, ce problème est directement lié au désaccord mentionné plus haut quant à la détermination de la composition chimique de l'atmosphère des naines blanches DC. Tant et aussi longtemps qu'un code de modèles d'atmosphère ne sera pas prouvé supérieur aux autres, l'évolution spectrale des naines blanches froides demeurera sujette à débat.

Enfin, notons que l'atmosphère des naines blanches froides représente une opportunité unique d'étudier la matière sous des conditions extrêmes. De telles conditions—c'est-à-dire une température de quelques milliers de degrés et une densité de l'ordre du $\mathrm{g\,cm^{-3}}$—sont difficilement atteignables en laboratoire et sont rarement rencontrées dans la nature. En fait, comme l'illustre la Figure 1.10, les conditions physiques à la photosphère des naines blanches froides riches en hélium sont comparables à celles caractérisant les couches

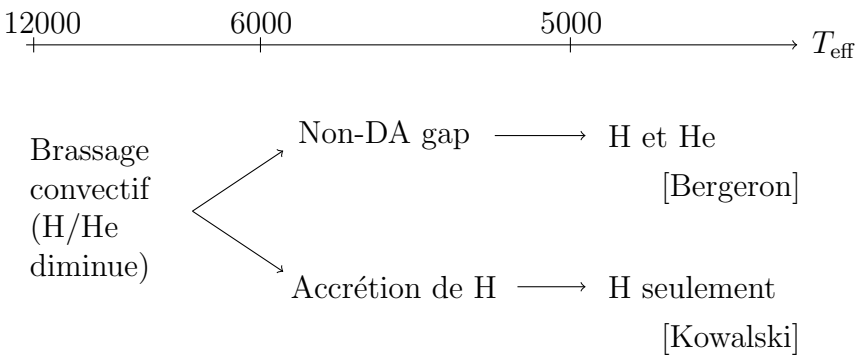

Figure 1.9 – Représentation schématique des deux scénarios concurrents pour l'évolution spectrale des naines blanches froides. Le scénario du haut correspond à celui trouvé en utilisant les modèles de Bergeron et al. (1995) et le scénario du bas à celui obtenu avec les modèles de Kowalski (2006a).

profondes des planètes géantes. La grande différence, c'est que dans le cas des naines blanches cette région de haute densité est visible alors que chez les planètes géantes elle est enfouie bien au-delà de la photosphère. L'étude de l'atmosphère des naines blanches froides peut donc aider à contraindre le comportement de la matière dans un régime physique qui est d'intérêt pour d'autres champs d'études.

1.3 Structure de cette thèse

Le but de cette thèse est de mettre au point un code permettant une modélisation adéquate de l'atmosphère de toutes les naines blanches froides. Pour ce faire, plusieurs améliorations doivent être apportées à la physique constitutive des modèles développés par Dufour (2006). Par le passé, les effets de haute densité présents à la photosphère des naines blanches froides devaient être inclus au moyen d'ingénieuses approximations (formalisme de la probabilité d'occupation, Hummer & Mihalas 1988 ; interpolation entre l'approximation quasi statique et l'approximation d'impact pour l'élargissement des raies spectrales, Walkup et al. 1984 ; etc.). Aujourd'hui, avec la puissance de calcul numérique à laquelle nous avons accès, ces approximations ne sont plus nécessaires. Nous pouvons désormais avoir recours aux techniques ab initio pour calculer le comportement de la matière à partir des principes premiers de la mécanique quantique (Chapitre 3).

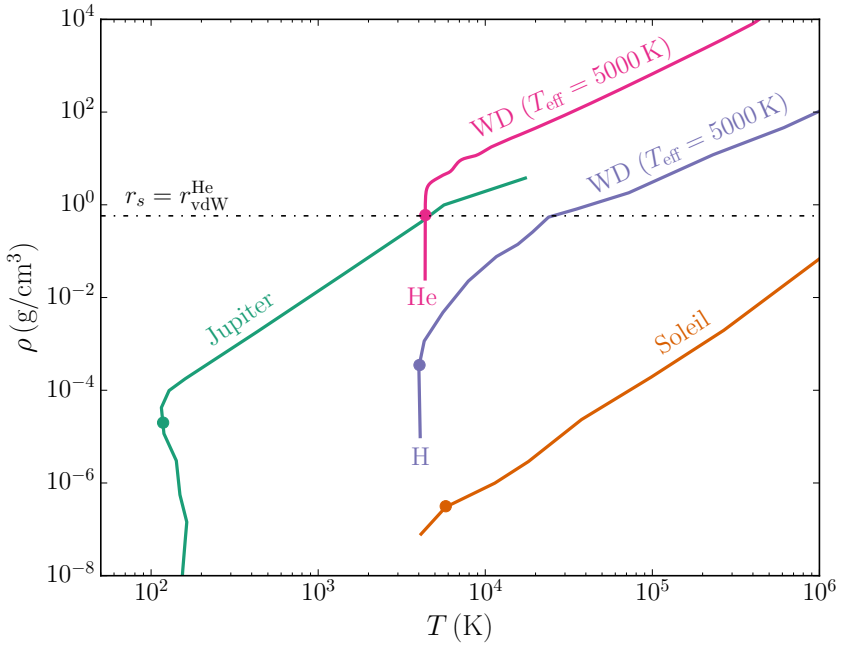

Figure 1.10 – Profils densité−température de Jupiter, du Soleil et de naines blanches à atmosphère riche en hélium et riche en hydrogène avec une température effective de 5000 K. Les cercles indiquent la position de la photosphère de chacun des quatre objets et la ligne pointillée marque la densité où la séparation moyenne entre deux atomes est égale au rayon de van der Waals de l'hélium neutre. Les données utilisées pour tracer cette figure sont tirées de Seiff et al. (1998), Fontaine et al. (2001), Fortney et al. (2010) et Cox (2015).

Récemment, Kowalski (2006a) a utilisé cette approche pour tenter de mettre au point de meilleurs modèles. Toutefois, il demeure à ce jour difficile de vérifier si ces modèles sont véritablement meilleurs que les précédents, puisqu'ils sont seulement valides pour des atmosphères ne contenant aucun métaux. Comme nous l'avons vu, chez les naines blanches froides, les atmosphères ne contenant que de l'hydrogène ou de l'hélium ne produisent aucune raie atomique ni aucune bande moléculaire dans la portion visible du spectre. Normalement, ce sont ces caractéristiques spectrales qui permettent de diagnostiquer la précision des modèles. En effet, il faut que les conditions physiques (pression, température, abondances) dans les régions de formation des raies soient bien représentées par le modèle d'atmosphère pour parvenir à bien reproduire les raies atomiques et les bandes moléculaires. Ainsi, en ignorant les naines blanches polluées par des métaux, Kowalski (2006a) s'est privé du moyen le plus puissant dont nous disposons pour tester observationnellement les modèles de naines blanches froides.

Pour solutionner ce problème, cette thèse élargit le travail de Kowalski (2006a) en l'étendant à toutes les naines blanches froides, rendant ainsi possible une comparaison directe entre les modèles et les observations astronomiques. Ce travail vise donc non seulement à améliorer les modèles d'atmosphère de naines blanches froides, mais aussi à les valider au moyen d'observations. Une fois mis au point, ces modèles permettront de

1. Rafiner les résultats des études cosmochronologiques en obtenant des paramètres atmosphériques plus justes ;

2. Accéder à la composition de planétésimaux accrétés par les plus vieilles naines blanches ;

3. Dissiper l'incertitude entourant l'évolution spectrale des naines blanches.

Les Chapitres 2 et 3 mettent la table en introduisant quelques notions théoriques de base concernant la modélisation d'atmosphères stellaires et la modélisation des milieux denses. Ces chapitres seront particulièrement utiles à un lecteur non expert, puisqu'une certaine compréhension du fonctionnement de ces outils est présupposée dans les chapitres subséquents.

Le Chapitre 4 présente les résultats de calculs ab initio qui montrent que les profils de CIA H_2-He sont décalés et déformésss à la photosphère des naines blanches froides riches en hélium. Cet effet, jusqu'ici inconnu, pourrait être l'élément-clé nous permettant de comprendre la SED des naines blanches ultra-foides.

Le Chapitre 5 décrit le nouveau code de modèles d'atmosphère mis au point dans le cadre de cette thèse. On y détaille les améliorations apportées à la physique constitutive (en particulier l'équilibre d'ionisation des métaux dans les conditions physiques rencontrées à la photosphère des naines blanches froides) et on y présente l'analyse de deux DZ froides qui montre comment ces améliorations se traduisent en termes de la capacité des modèles à mieux reproduire les observations.

Le Chapitre 6 est consacré à l'analyse de SDSS J080440.63+223948.6, la première naine blanche DZ connue à montrer de la CIA. Il s'agit d'une étoile importante pour la validation de notre code d'atmosphère, puisqu'elle montre à la fois des raies spectrales et de la CIA, deux caractéristiques spectrales indépendantes nous permettant de tester nos modèles. Grâce aux améliorations apportées à la physique constitutive de nos modèles, nous

parvenons à obtenir une solution en bon accord avec toutes les données observationnelles—résultat auquel les précédentes versions du code d'atmosphère étaient incapables de parvenir.

Le Chapitre 7 présente l'analyse d'une des plus vieilles naines blanches DZ connues, WD J2356−209. Bien qu'identifiée il y a près de 20 ans, c'est la première fois qu'une analyse détaillée et réaliste de cet objet est présentée. En effet, il a fallu attendre le développement des modèles décrits dans cette thèse pour qu'une analyse rigoureuse soit possible. Nous trouvons que l'atmosphère de cet objet contient 10 fois plus de sodium que de calcium, ce qui n'a encore jamais été observé. Ces résultats suggèrent que WD J2356−209 a accrété un objet riche en sodium, ce qui soulève de nombreuses questions étant donné que nous ne connaissons aucun objet équivalent dans le Système solaire.

Dans le Chapitre 8 nous présentons des calculs détaillés (au-delà de l'approximation d'impact) des profils d'absorption de la raie de résonance du calcium. Nous présentons plusieurs exemples d'applications qui montrent comment ces nouveaux profils permettent d'obtenir une description adéquate du spectre des étoiles DZ les plus froides.

Le Chapitre 9 est consacré à l'analyse du plus grand échantillon homogène de naines blanches froides jamais étudié. On y présente un nouveau regard critique sur les analyses pionnières de Bergeron et al. (1997, 2001) grâce aux nouveaux modèles développés dans cette thèse et à l'ensemble des données observationnelles qui ont été obtenues depuis. Nous y peignons un portrait plutôt complexe de l'évolution spectrale des naines blanches froides. Entre $T_{\rm eff} \approx 7500\,{\rm K}$ et $6250\,{\rm K}$, nous identifions un déclin de la fraction d'étoiles riches en hydrogène que nous interprétons comme étant dû au brassage convectif. Ensuite, entre $6250\,{\rm K}$ et $5000\,{\rm K}$, nous trouvons que cette même fraction augmente, phénomène pour lequel aucune explication physique n'est présentement connue. À plus basses températures ($T_{\rm eff} \lesssim 5000\,{\rm K}$), nous démontrons que la fraction d'objets riches en hydrogène cesse de croître. Ces résultats discréditent le scénario selon lequel l'évolution spectrale des naines blanches froides est dominée par l'accrétion d'hydrogène du milieu interstellaire. Par ailleurs, le Chapitre 9 contient aussi une discussion approfondie sur plusieurs objets individuels d'intérêt, dont les naines blanches DQpec.

Enfin, les conclusions de cette thèse sont données au Chapitre 10. On y résume les avancées rendues possibles grâce à ce travail, mais aussi les défis qui restent à relever.

1.4 Déclaration de l'étudiant

C'est moi qui ai rédigé la totalité des chapitres constituant cette thèse, à l'exception de l'Annexe A. De même, j'ai créé chacune des figures présentées dans ces pages (lorsque les données utilisées pour tracer une figure proviennent d'autres sources, la légende en fait mention). C'est également moi qui ai mis au point les scripts Python utilisés pour ajuster les modèles d'atmosphère aux données spectroscopiques et photométriques. Le code de modèles d'atmosphère que j'utilise m'a initialement été fourni par Patrick Dufour, mais tel qu'expliqué plus loin (voir en particulier le Chapitre 5), je l'ai modifié de fond en comble (j'ai réécrit ou ajouté plus de 17 000 lignes de Fortran à ce programme). À l'exception des calculs de profils de quelques raies spectrales, j'ai personnellement réalisé tous les calculs sur lesquels repose cette thèse (calculs de modèles d'atmosphère, calculs ab initio et détermination des paramètres atmosphériques). C'est aussi moi qui ai effectué toute l'analyse scientifique présentée dans ce travail (en particulier les calculs statistiques et l'interprétation physique et astrophysique des résultats).

Concernant la *Montreal White Dwarf Database* (Annexe A), c'est moi qui ai développé les scripts Python qui permettent d'assembler dans une seule et même base de données les résultats provenant de l'ensemble de la littérature. Avec Simon Coutu, j'ai développé une bonne partie de l'interface HTML et des codes JavaScript qui permettent de visualiser les données sous forme de tableaux et de figures interactives.

Je dois l'idée du projet à la base de cette thèse à Patrick Dufour, la méthode du calcul de la CIA à haute densité à Piotr M. Kowalski (Chapitre 4) et les calculs de profils de raies spectrales au-delà de l'approximation d'impact à Nicole F. Allard (Chapitres 5 et 8). Les analyses d'étoiles reposent sur des données spectroscopiques et photométriques qui sont publiquement accessibles (notamment les relevés 2MASS, *Gaia*, Pan-STARRS et SDSS) ou qui m'ont été fournies par des collaborateurs (Pierre Bergeron, Patrick Dufour, Mukremin Kilic, Samir Salim, Michael Rich, Léon Koopmans, Stéphane Vennes et Adela Kawka).

CHAPITRE 2

Modèles d'atmosphère

In the good old days physicists repeated each other's experiments, just to be sure. Today they stick to FORTRAN, so that they can share each other's programs, bugs included.

—Edsger W. Dijkstra (1930−2002), informaticien néerlandais

Dans le chapitre précédent, les modèles d'atmosphère ont été introduits comme outils de choix pour déterminer les paramètres atmosphériques des étoiles naines blanches. Ce chapitre a pour but de décrire le fonctionnement du code de modèles d'atmosphère utilisé dans cette thèse (Chapitres 4, 5, 6, 7, 8 et 9). La première section (Section 2.1) discute de son fonctionnement général et la seconde (Section 2.2) aborde la physique constitutive qui y est implantée ainsi que ses limitations.

2.1 Structure du code

Notre code de modèles d'atmosphère est basé sur plusieurs hypothèses usuelles (voir par exemple Mihalas, 1978). L'atmosphère est divisée en 70 couches, s'étendant de $\tau_R = 10^{-7}$ à $\tau_R = 10^2$, où τ_R est la profondeur optique de Rosseland. Ces couches sont traitées dans le cadre de l'approximation des plans parallèles et la structure est dictée par l'équilibre hydrostatique,

$$\frac{\mathrm{d}p}{\mathrm{d}r} = -\rho(r)g. \tag{2.1}$$

De plus, l'atmosphère est supposée en équilibre thermodynamique local (ETL), ce qui implique que chaque couche de l'atmosphère est individuellement considérée comme étant en équilibre.

Plusieurs étapes sont requises pour calculer un modèle à partir des paramètres stellaires d'entrée (température effective, gravité de surface et composition chimique) : celles-ci sont résumées par la Figure 2.1.

1. Tout d'abord, une structure initiale $(p(\tau), T(\tau))$ qui respecte l'équilibre hydrostatique est posée comme premier essai.

2. Pour chacune des couches de ce modèle d'essai, on résout l'équation d'état pour obtenir la densité et les abondances de chacune des espèces comprises dans le modèle (le Tableau 2.1 indique quelles espèces sont incluses).

3. Ensuite, ces abondances sont utilisées pour calculer l'opacité monochromatique à chaque couche et pour chaque point de fréquence (les opacités incluses sont énumérées dans le Tableau 2.2).

4. Le flux radiatif $F_{\rm rad}$ et les différents moments du champ de radiation sont calculés pour chaque couche au moyen de la méthode de Feautrier (1964). Le flux convectif $F_{\rm conv}$ est quant à lui estimé au moyen de la théorie de la longueur de mélange.

5. Si le flux est conservé pour chaque couche de la zone convective,

$$\frac{F_{\rm rad} + F_{\rm conv} - \sigma_S T_{\rm eff}^4}{\sigma_S T_{\rm eff}^4} \approx 0, \tag{2.2}$$

   et que l'équilibre radiatif est atteint pour chaque couche de la zone radiative,

$$\int_0^\infty \chi_\nu (J_\nu - S_\nu) {\rm d}\nu \approx 0, \tag{2.3}$$

   alors le modèle est convergé et il s'agit de la solution recherchée. Sinon, il faut appliquer une correction au profil en température et recommencer le processus avec ce nouveau profil $T(\tau)$ à partir de l'étape 2. Pour la plupart des modèles, cette correction est calculée au moyen de la méthode de Rybicki (1971). Par contre, pour certains modèles où la convergence est plus difficile à atteindre (en particulier les modèles froids contenant de l'hydrogène) la méthode proposée par Saumon et al. (1994, Équation 5) est utilisée pour calculer la correction en température à appliquer dans les couches radiatives du modèle.

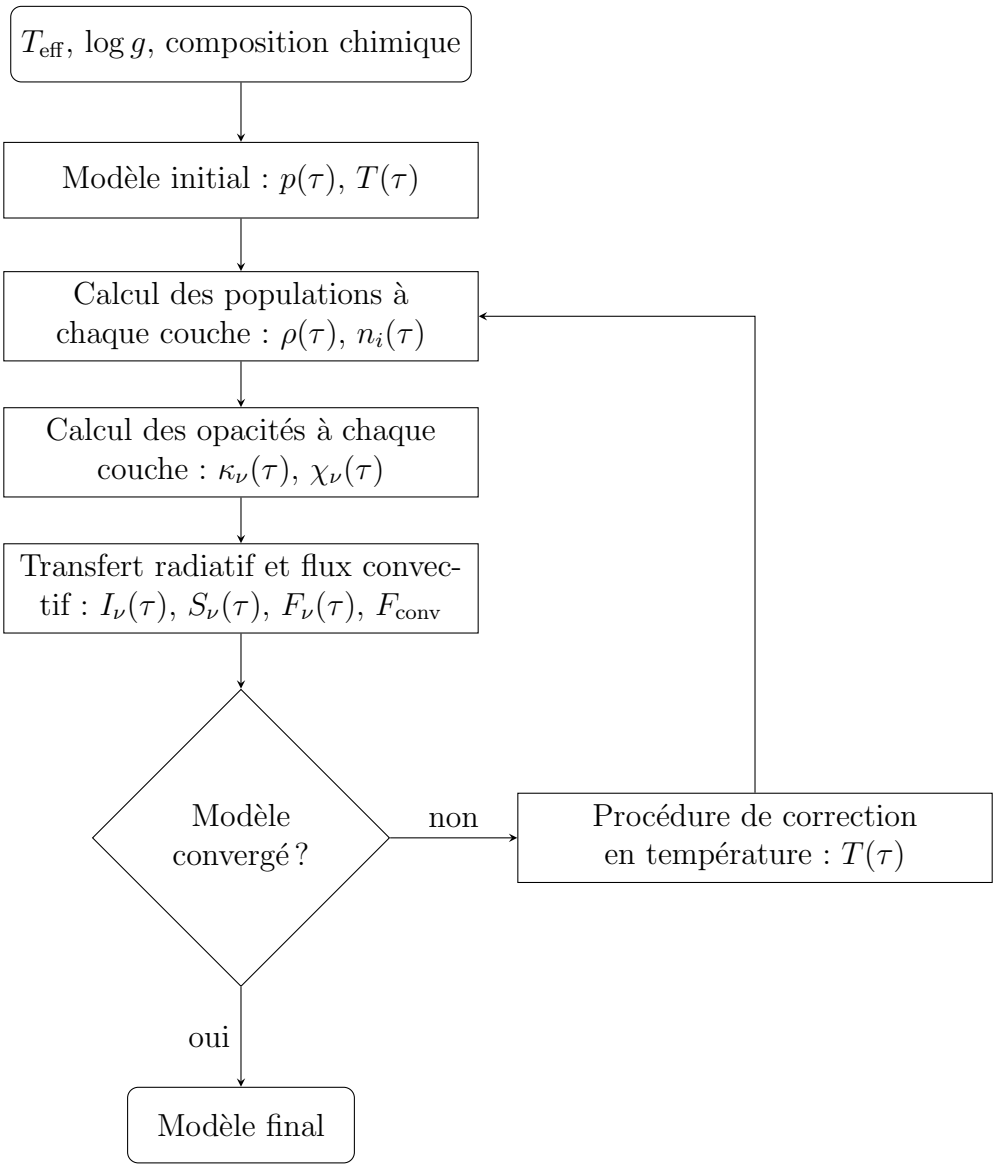

Figure 2.1 – Représentation schématique du calcul d'un modèle d'atmosphère.

2.2 Physique constitutive

Maintenant que la structure globale d'un code de modèle d'atmosphère a été présentée, attardons-nous au calcul de l'équation d'état et au calcul des opacités radiatives. Il s'agit de deux composantes critiques de tout modèle d'atmosphère et il s'agit aussi des deux modules du code qui nécessitent d'être révisés de fond en comble pour que le code soit en mesure de correctement modéliser l'atmosphère des naines blanches froides.

2.2.1 Équation d'état

La tâche du module d'équation d'état est de calculer la densité de chacune des espèces (Tableau 2.1) à chaque couche du modèle d'atmosphère à partir des structures en pression et en température. Dans le code d'atmosphère de Dufour et al. (2007), la première étape de ce calcul est de trouver la densité totale au moyen de la loi des gaz parfaits,

$$p = nk_BT, \tag{2.4}$$

où p est la pression de la couche, n la densité totale de particules, k_B la constante de Boltzmann et T la température. De là, on peut calculer les populations des différents ions au moyen de l'équation de Saha,

$$\frac{n_{k+1}n_e}{n_k} = \frac{2Q_{k+1}}{Q_k}\left(\frac{2\pi m_e k_B T}{h^2}\right)^{3/2} e^{-I/k_BT}, \tag{2.5}$$

où les indices k et $k+1$ représentent deux états d'ionisation consécutifs, Q_k est la fonction de partition de l'espèce k et I est le potentiel d'ionisation associé à l'ionisation de k vers $k+1$. Enfin, l'occupation de chaque niveau électronique est calculée grâce à la distribution de Boltzmann,

$$\frac{n_{jk}}{n_k} = \frac{g_{jk}}{Q_k}\exp\left(-\frac{e_{jk}}{k_BT}\right), \tag{2.6}$$

où n_{jk}/n_k est la fraction de l'espèce k dans le niveau j, g_{jk} est le poids statistique de ce niveau et e_{jk} est l'énergie du niveau j par rapport au fondamental.

Comme nous l'avons vu (Section 1.2.1), l'approximation du gaz parfait n'est pas valide dans l'atmosphère dense des naines blanches froides, où les interactions entre particules doivent être considérées. Les améliorations apportées à ce module du code—notamment

Catégorie	Espèce(s)
Hydrogène	H, H^-, H^+, H_2, H_2^+, H_3^+
Hélium	He, He^+, He_2^+
Métaux	Tous les éléments de C jusqu'à Cu (pour des états d'ionisation allant de I à V)
Molécules	C_2, C_3, CH, CH_2, CH_3, CH_4, C_2H, C_2H_2, CN, CO, CaH, HCN, MgH, N_2, NH, NO, O_2, OH, SiH, TiO
Autres	Électrons libres

Tableau 2.1 – Espèces incluses dans les modèles d'atmosphère

en ce qui concerne l'équation d'état et le calcul de l'équilibre d'ionisation—sont détaillées au Chapitre 5.

2.2.2 Opacités radiatives

Une liste exhaustive des opacités incluses dans le code d'atmosphère est donnée dans le Tableau 2.2. Premièrement, il faut inclure les opacités du continu. Cela inclut la diffusion de Thomson par les électrons, la diffusion de Rayleigh par les atomes et les molécules, les transitions lié-libre et les transitions libre-libre. Tel que détaillé dans le Chapitre 5, dans le cas particulier des naines blanches froides, il faut appliquer des corrections aux valeurs classiques des opacités du continu afin de prendre en compte les interactions collectives entre les particules.

Deuxièmement, on doit calculer l'opacité des raies spectrales résultant des transitions lié-lié. Une des composantes essentielles du calcul de l'opacité des raies est le profil utilisé. Le profil φ_ν d'une raie spectrale est donné par la contribution de trois types d'élargissement : l'élargissement naturel, l'élargissement Doppler et l'élargissement par collisions. Chez les naines blanches froides, c'est l'élargissement causé par les collisions (engendrées par des particules neutres) qui domine. Dans la plupart des cas, le profil des raies peut alors être approximé par un simple profil de Lorentz,

$$\varphi_\nu = \frac{\Gamma/(4\pi^2)}{(\Delta\nu)^2 + (\Gamma/(4\pi))^2}, \tag{2.7}$$

Source	Espèce(s) impliquée(s)
Diffusion de Thomson	Électrons libres
Diffusion de Rayleigh	H, H_2, He
Transition lié-libre	H, H^-, H_2^+, He, He_2^+, C, O
Transition libre-libre	H^+−e, H_2^+−e, H_3^+−e, H−e, H−H^+, H_2−e, He−He^+, He^+−e, He−e, C^+−e, O^+−e
Raies spectrales (transition lié-lié)	H, He, C, O, Na, Mg, Al, Si, K, Ca, Ti, Cr, Mn, Fe, Co, Ni (neutres et ionisés)
Bandes moléculaires	C_2, CH, MgH
CIA	H_2−H, H_2−H_2, H_2−He, He−He−He

Tableau 2.2 – Sources d'opacité incluses dans les modèles d'atmosphère

où $\Delta\nu$ est l'écart par rapport au centre de la raie et la largeur à mi-hauteur Γ est un paramètre d'élargissement qui peut être trouvé dans différentes compilations (VALD par exemple, Piskunov et al., 1995). À la photosphère dense des naines blanches froides, un simple profil lorentzien symétrique peine à reproduire les raies observées et des calculs plus détaillés—au-delà de l'approximation d'impact—sont requis (voir Chapitres 5, 6, 7 et 8).

Troisièmement, étant donné la présence de C_2, de CH et de MgH dans l'atmosphère de certaines naines blanches froides, il faut également inclure les bandes moléculaires au calcul des opacités. Dans le cas général, une bande moléculaire est le résultat d'une combinaison de trois types de transitions : une transition électronique, une transition vibrationnelle et une transition rotationnelle. Pour inclure cette source d'opacité dans les modèles, il faut prendre en compte les milliers de transitions possibles. Encore une fois, les choses se compliquent à haute densité. Les niveaux d'énergie des molécules peuvent être décalés, ce qui engendre une déformation des bandes moléculaires (voir Chapitre 9 et Kowalski 2010).

Quatrièmement, pour les objets les plus froids, il faut inclure la CIA. Chez les naines blanches, cette source d'opacité est principalement due à l'induction d'un moment dipolaire électrique lors d'une collision H_2–He ou d'une collision H_2–H_2. Comme nous le verrons au Chapitre 4, le calcul de la CIA se corse dans le cas des atmosphères les plus denses, lorsque les collisions à plus de deux particules deviennent fréquentes.

CHAPITRE 3

Modélisation des milieux denses

The fundamental laws necessary for the mathematical treatment of a large part of physics and the whole of chemistry are thus completely known, and the difficulty lies only in the fact that application of these laws leads to equations that are too complex to be solved.

—Paul Dirac (1902−1984), physicien et mathématicien britannique

Dans cette thèse, une variété d'outils théoriques sont utilisés pour sonder le comportement de la matière à la photosphère des naines blanches froides (voir les Chapitres 4, 5, 8 et 9). Chacune de ces méthodes possède ses propres forces, ses lacunes et son contexte d'application. Ce chapitre présente brièvement la théorie sous-jacente à ces outils. Le but ici n'est pas de détailler rigoureusement les bases théoriques de ces méthodes, mais bien de donner juste assez de contexte pour qu'un lecteur non expert ne les voie pas comme de simples boîtes noires lorsqu'elles seront employées dans les chapitres suivants. Dans un premier temps, la Section 3.1 présente la théorie classique des fluides. Les deux sections suivantes introduisent les deux grandes approches utilisées en chimique numérique pour calculer l'état quantique d'un système d'atomes, soit les méthodes basées sur les fonctions d'ondes (Section 3.2) et la théorie de la fonctionnelle de la densité (Section 3.3). Finalement, la Section 3.4 discute de simulations de dynamique moléculaire, où l'on s'intéresse aux fluctuations spatiales et temporelles d'un système.

3.1 Théorie classique des fluides

Comme la densité photosphérique des naines blanches les plus froides atteint $\sim$1 g cm^{-3}, il est plus approprié d'y traiter la matière comme un liquide plutôt que comme un gaz. En

effet, l'interaction entre les composantes du milieu fait en sorte que, contrairement à un gaz ténu, le fluide montre une importante corrélation (c'est-à-dire que la position d'une particule donnée dépend de la position des autres particules). Cette section introduit les outils théoriques permettant de caractériser cette corrélation et de quantifier ses effets sur l'équation d'état du milieu.

3.1.1 Fonction de distribution radiale

La fonction de distribution radiale $g(r)$ décrit la variation de la densité en fonction de la distance r d'une particule de référence. Pour un milieu homogène et isotrope de densité $n = N/V$, la densité locale à un point situé à une distance r d'une particule donnée correspond à $ng(r)$. Par exemple, dans le cas limite d'un gaz parfait, les particules n'interagissent pas entre elles, donc $g(r) = 1$ et la densité demeure constante. À l'inverse, dans un fluide dense, les particules interagissent entre elles, ce qui donne lieu à des zones de plus haute et de plus basse densité locale. À titre d'exemple, la Figure 3.1 montre $g(r)$ pour un fluide composé de particules interagissant selon un potentiel de Lennard–Jones,

$$\phi(r) = 4\epsilon \left[\left(\frac{\sigma}{r}\right)^{12} + \left(\frac{\sigma}{r}\right)^{6} \right]. \tag{3.1}$$

Remarquons que la forme de $\phi(r)$ influence directement celle de $g(r)$. En particulier, la région où le potentiel est répulsif (c'est-à-dire la région telle que $\phi(r) > 0$) donne lieu à une région où $g(r)$ est quasiment nulle, donc une région qu'à peu près aucune particule ne parvient à atteindre.

3.1.2 Équation d'Ornstein–Zernike

Plusieurs approches existent pour déterminer $g(r)$ pour un fluide donné. On peut par exemple avoir recours à des simulations de dynamique moléculaire (Section 3.4). Une autre approche consiste à obtenir $h(r) = g(r) - 1$ au moyen de l'équation d'Ornstein–Zernike (Hansen & McDonald, 2013),

$$h(r) = c(r) + n \int c(|\mathbf{r} - \mathbf{r}'|) h(r') \mathrm{d}\mathbf{r}', \tag{3.2}$$

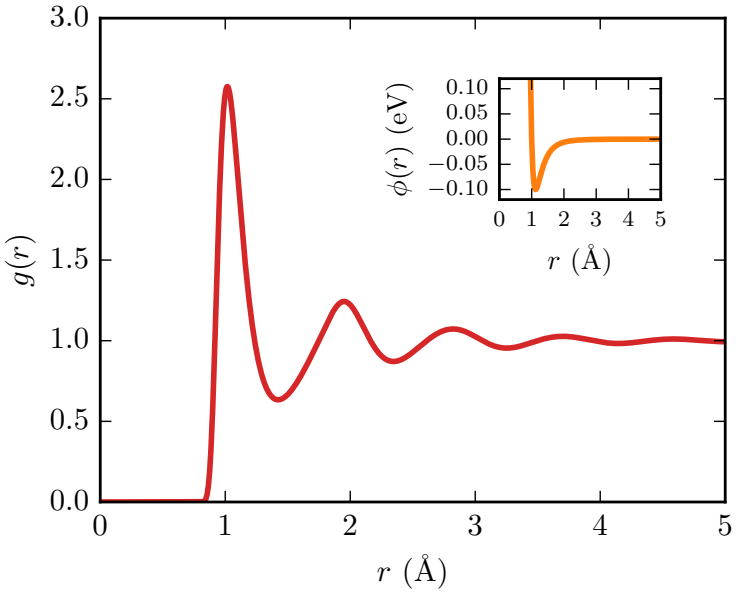

Figure 3.1 – La courbe rouge montre $g(r)$ pour un fluide à $T = 4000\,\mathrm{K}$ et $n = 10^{24}\,\mathrm{cm}^{-3}$ composé de particules interagissant selon un potentiel de Lennard–Jones avec $\sigma = 1\,\text{Å}$ et $\epsilon = 0.1\,\mathrm{eV}$. La courbe orangée, dans le coin supérieur droit, montre le potentiel $\phi(r)$ utilisé pour obtenir la fonction de distribution radiale.

où $c(r)$ est la fonction de corrélation directe. Qualitativement, l'équation d'Ornstein–Zernike nous dit que la corrélation totale $h(r)$ entre deux particules est due à la corrélation directe $c(r)$ entre elles, mais aussi aux corrélations indirectes découlant de corrélations directes entre de tierces particules (Nägele, 2008).

A priori, $c(r)$ est inconnue. On doit donc utiliser une relation de fermeture pour approximer $c(r)$ en l'exprimant comme une fonction de $h(r)$ et de $\phi(r)$. Les deux relations de fermeture les plus communes sont celles de Percus–Yevick (PY) et de l'*hypernetted chain* (HNC). Les caractéristiques de ces relations de fermeture sont résumées dans le Tableau 3.1. Remarquons que la relation de fermeture de PY est plus appropriée que la HNC pour décrire des interactions entre particules neutres. Étant donné que les atmosphères des naines blanches froides sont pratiquement neutres, c'est cette relation de fermeture qui sera utilisée dans cette thèse. Une fois la relation de fermeture choisie, l'équation d'Ornstein–Zernike peut être résolue de manière itérative. Pour ce faire, nous utilisons une version modifiée du code pyOZ[1] (Chapitre 5).

[1] http://pyoz.vrbka.net

Nom	$c(r)$	Potentiel approprié
PY	$c(r) = g(r)\left(1 - e^{\beta\phi(r)}\right)$	Courte portée (p. ex., interatomique)
HNC	$c(r) = \beta\phi(r) + h(r) - \ln\left(g(r)\right)$	Longue portée (p. ex., coulombique)

Tableau 3.1 – Propriétés des principales relations de fermeture de l'équation d'Ornstein–Zernike

3.1.3 Propriétés thermodynamiques d'un fluide classique

Pour un potentiel $\phi(r)$ donné, une fois que $g(r)$ est connue, le calcul de n'importe quelle quantité thermodynamique devient aisé. L'énergie E du fluide est donnée par la somme de l'énergie cinétique translationnelle $\frac{3}{2}Nk_BT$ et de l'énergie d'interaction entre toutes les paires de particules (Nägele, 2008),

$$E = \frac{3}{2}Nk_BT + \frac{1}{2}Nn\int_0^\infty g(r)\phi(r)4\pi r^2\mathrm{d}r. \tag{3.3}$$

Similairement, la pression p est calculée en additionnant la pression nk_BT d'un gaz parfait classique à la pression résultant de l'interaction entre les particules,

$$p = nk_BT - \frac{2\pi}{3}n^2\int_0^\infty g(r)\frac{\mathrm{d}\phi}{\mathrm{d}r}r^3\mathrm{d}r. \tag{3.4}$$

Dans le même ordre d'idées, le potentiel chimique μ peut être calculé en ajoutant une contribution non idéale μ^{nid} au potentiel chimique d'un gaz parfait μ^{id}. En utilisant l'approximation de PY, on peut montrer que (Kiselyov & Martynov, 1990)

$$\beta\mu^{\mathrm{nid}} = -n\int_0^\infty \left[h(r) - \omega(r) - \frac{1}{6}h(r)\left(4\omega(r) + 1 - e^{\omega(r)}\right)\right]4\pi r^2\mathrm{d}r, \tag{3.5}$$

où $\omega(r) = \ln\left[g(r)\right] + \beta\phi(r)$. L'équation 3.5 jouera un rôle central dans le calcul de l'équilibre d'ionisation des métaux à la photosphère des naines blanches froides (Section 5.5).

3.2 Méthodes ab initio basées sur les fonctions d'onde

Nous venons de voir comment les propriétés thermodynamiques d'un système non idéal peuvent être déterminées à partir de la théorie classique des fluides. Remarquons que toutes les équations issues de ce cadre théorique reposent ultimement sur le potentiel d'interaction $\phi(r)$. A priori, cette quantité est inconnue. $\phi(r)$ peut parfois être obtenu à partir de mesures expérimentales, mais—à quelques exceptions près—nous ne disposons pas de données fiables pour les interactions nécessaires aux calculs effectués dans cette thèse. Pour pallier ce manque, on peut faire appel aux méthodes ab initio pour calculer $\phi(r)$ à partir des principes premiers de la mécanique quantique. Cette section présente la théorie derrière ces méthodes.

3.2.1 Définition du problème

L'équation de Schrödinger constitue la relation fondamentale qui décrit l'état de n'importe quel système quantique (non relativiste). Sous sa forme indépendante du temps, elle s'écrit

$$\hat{H}\Psi = E\Psi. \tag{3.6}$$

Il s'agit d'une équation aux valeurs propres, où $\hat{H}$ est l'hamiltonien, E l'énergie totale du système et $\Psi = \Psi(\mathbf{r}_i, \sigma_i)$ la fonction d'onde qui dépend des positions $\mathbf{r}_i$ et des spins σ_i des particules constituant le système. Pour un système composé de N électrons et de M noyaux, l'hamiltonien s'exprime comme une somme de cinq termes (Kedziera & Kaczmarek-Kedziera, 2016),

$$\hat{H} = \hat{T}_e + \hat{T}_n + \hat{V}_{ee} + \hat{V}_{nn} + \hat{V}_{ne}, \tag{3.7}$$

où $\hat{T}_e$ représente l'énergie cinétique des électrons, $\hat{T}_n$ l'énergie cinétique des noyaux, $\hat{V}_{ee}$ l'énergie d'interaction électron-électron, $\hat{V}_{nn}$ l'énergie d'interaction noyau-noyau et $\hat{V}_{ne}$ l'énergie d'interaction électron-noyau. En définissant m_i comme étant la masse du noyau i, Z_i la charge du noyau i, $r_{ij} = |\mathbf{r}_i - \mathbf{r}_j|$ la distance entre les électrons i et j et $R_{ij} = |\mathbf{R}_i - \mathbf{R}_j|$ la distance séparant le noyau i du noyau j, ces cinq opérateurs peuvent s'expri-

mer comme[2]

$$\hat{T}_e = -\frac{1}{2}\sum_{i=1}^{N} \nabla^2{}_{r_i}, \tag{3.8}$$

$$\hat{T}_n = -\sum_{i=1}^{M} \frac{1}{2m_i} \nabla^2{}_{R_i}, \tag{3.9}$$

$$\hat{V}_{ee} = \sum_{i=1}^{N}\sum_{j>i}^{N} \frac{1}{r_{ij}}, \tag{3.10}$$

$$\hat{V}_{nn} = \sum_{i=1}^{M}\sum_{j>i}^{M} \frac{Z_i Z_j}{R_{ij}}, \tag{3.11}$$

$$\hat{V}_{ne} = -\sum_{i=1}^{N}\sum_{j=1}^{M} \frac{Z_j}{|\mathbf{r}_i - \mathbf{R}_j|}. \tag{3.12}$$

La présence dans ces expressions de termes faisant intervenir la position relative d'une particule i par rapport à une particule j complique sérieusement le problème posé par l'équation de Schrödinger. En fait, sa résolution analytique exacte est possible seulement pour le cas simple d'un atome hydrogénoïde isolé. Pour les autres atomes et molécules, une approche approximative doit être utilisée.

Reconnaissons d'abord que les noyaux étant plusieurs milliers de fois plus massifs que les électrons, leur mouvement est très lent par rapport à celui de ces derniers. Par conséquent, en très bonne approximation, on peut considérer les noyaux comme étant fixes lors du calcul du mouvement des électrons. Il s'agit là de l'approximation de Born & Oppenheimer (1927). Grâce à elle, le calcul des niveaux d'énergie et des fonctions d'onde est grandement simplifié, puisque *le mouvement des électrons s'exprime désormais paramétriquement en fonction des positions fixes des noyaux*. Le problème qui nous intéresse devient donc (Kedziera & Kaczmarek-Kedziera, 2016)

$$\left(\hat{T}_e + \hat{V}_{ee} + \hat{V}_{ne}\right)\Psi = \hat{H}_e(\mathbf{r};\mathbf{R})\Psi(\mathbf{r};\mathbf{R}) = E_e(\mathbf{R})\Psi(\mathbf{r};\mathbf{R}). \tag{3.13}$$

[2]On utilise ici le système d'unités atomiques, qui prévaut dans ce domaine. Dans le cadre de ce système, $\hbar$, m_e, la charge électronique e et la constante de Coulomb $1/4\pi\epsilon_0$ valent 1 par définition.

3.2.2 Méthode de Hartree–Fock

Historiquement, la théorie proposée par Fock (1930), connue sous le nom de méthode de Hartree–Fock, constitue un jalon important dans l'élaboration de théories permettant de résoudre l'Équation 3.13. Comme première approximation pour résoudre cette équation, on remplace les interactions individuelles entre chaque paire d'électrons par un potentiel effectif $\hat{V}_{\text{eff}}$ qui modélise le champ moyen ressenti par un électron et causé par tous les autres électrons du système. On obtient alors un ensemble de N équations d'onde à un électron,

$$\hat{H}_{\text{eff}}\phi_i(\mathbf{r}_i,\sigma_i) = \left(-\frac{1}{2}\nabla_{r_i}^2 - \sum_{j=1}^{M}\frac{Z_j}{|\mathbf{r}_i-\mathbf{R}_j|} + \hat{V}_{\text{eff}}(\mathbf{r}_i)\right)\phi_i(\mathbf{r}_i,\sigma_i) = \epsilon_i\phi_i(\mathbf{r}_i,\sigma_i), \tag{3.14}$$

où $\phi_i(\mathbf{r}_i,\sigma_i)$ est la fonction d'onde de l'électron i (Kedziera & Kaczmarek-Kedziera, 2016). L'opérateur de potentiel effectif comprend deux termes : l'interaction de Coulomb et l'interaction d'échange (découlant du principe d'exclusion de Pauli) avec les autres électrons (Jahn & Kowalski, 2014),

$$\hat{V}_{\text{eff}}(\mathbf{r}_i) = \sum_{j=1}^{N}\int \mathrm{d}\mathbf{r}'\frac{|\phi_j(\mathbf{r}',\sigma_j)|^2}{|\mathbf{r}_i-\mathbf{r}'|} - \sum_{j=1}^{N}\delta_{\sigma_i\sigma_j}\int \mathrm{d}\mathbf{r}'\frac{\phi_j^*(\mathbf{r}',\sigma_j)\phi_i(\mathrm{r}_i,\sigma_i)}{|\mathbf{r}_i-\mathbf{r}'|}\phi_j(\mathbf{r}',\sigma_j), \tag{3.15}$$

où δ_{ij} est le delta de Kronecker. Dans l'approche de Hartree–Fock, la fonction d'onde du système est calculée sous la forme d'un déterminant de Slater,

$$\Psi = \frac{1}{\sqrt{N!}}\begin{vmatrix} \phi_1(\mathbf{r}_1,\sigma_1) & \phi_2(\mathbf{r}_1,\sigma_1) & \dots & \phi_N(\mathbf{r}_1,\sigma_1) \\ \phi_1(\mathbf{r}_2,\sigma_2) & \phi_2(\mathbf{r}_2,\sigma_2) & \dots & \phi_N(\mathbf{r}_2,\sigma_2) \\ \vdots & \vdots & \ddots & \vdots \\ \phi_1(\mathbf{r}_N,\sigma_N) & \phi_2(\mathbf{r}_N,\sigma_N) & \dots & \phi_N(\mathbf{r}_N,\sigma_N) \end{vmatrix}. \tag{3.16}$$

Numériquement, pour obtenir la fonction d'onde totale du système via les Équations 3.14 et 3.16, on exprime les fonctions d'onde individuelles ϕ_i en termes d'une base de fonctions $\{\xi_k\}$,

$$\phi_i = \sum_k c_{ik}\xi_k. \tag{3.17}$$

Plusieurs types de bases peuvent être utilisés pour réaliser ce genre de calcul (Tsuneda, 2014). Pour des raisons pratiques, les ξ_k sont typiquement des orbitales atomiques centrées sur les noyaux des atomes, mais plusieurs autres possibilités existent.[3] Évidemment, plus la base utilisée est complète, plus les résultats seront précis, mais plus le temps de calcul sera élevé.[4] On a donc avantage à utiliser une base aussi efficace que possible, c'est-à-dire une base qui permet de décrire précisément le système tout en contenant aussi peu de fonctions que possible.

3.2.3 Méthodes post-Hartree–Fock

La théorie de Hartree–Fock prédit des énergies totales qui sont à environ 1% des valeurs exactes. Cette différence peut paraître petite, mais il s'agit en fait d'une erreur beaucoup trop grande, même pour décrire les comportements chimiques les plus simples (Tsuneda, 2014). Le problème, c'est qu'en modélisant les interactions électron-électron au moyen d'un champ moyen, on se trouve à ignorer la *corrélation électronique*. Pour corriger la méthode de Hartree–Fock, il faut donc pouvoir évaluer l'énergie de corrélation électronique E_{corr},

$$E_{\text{corr}} = E_{\text{HF}} - E_{\text{exact}}. \tag{3.18}$$

Pour ce faire, on emploie des méthodes dites post-Hartree–Fock. Ces méthodes sont nombreuses (théorie de la perturbation de Møller–Plesset, Møller & Plesset 1934 ; interaction de configuration, Slater 1929 ; méthode du cluster couplé, Čížek 1966), mais elles ont toutes pour but de corriger la méthode de Hartree–Fock en y ajoutant un traitement de la corrélation électronique.

Au Chapitre 5 de cette thèse, la méthode CCSD(T)[5] est utilisée pour obtenir les potentiels d'interaction nécessaires au calcul de l'équilibre d'ionisation des métaux à la

[3] Par exemple, lorsque l'on s'intéresse à des interactions de type van der Waals (comme c'est le cas à quelques reprises dans cette thèse), il est avisé de complémenter la base utilisée par des fonctions diffuses.

[4] En principe, la méthode de Hartree–Fock demande le calcul d'un nombre d'intégrales proportionnel à P^4 (où P est le nombre total de fonctions de base utilisées dans le calcul), donc le temps de calcul augmente lui aussi comme P^4. En pratique, on obtient toutefois un temps de calcul bien plus efficace, notamment en ignorant les intégrales qui sont négligeables (Strout & Scuseria, 1995).

[5] Abréviation pour « méthode des clusters couplés avec excitations simples et doubles, et excitations triples traitées comme perturbations » (*Coupled-Cluster with Single and Double and Perturbative Triple excitations*). Nous nous servons du programme ORCA pour effectuer ces calculs (`https://orcaforum.kofo.mpg.de`).

photosphère des naines blanches froides. Cette méthode est largement utilisée en chimie numérique et donne en général des résultats qui sont en excellent accord avec les mesures expérimentales. Elle est à ce titre considérée comme la méthode étalon de la chimie numérique (Ramabhadran & Raghavachari, 2013; Tsuneda, 2014). Cette grande précision a toutefois un coût : la méthode CCSD(T) demande un temps de calcul qui augmente comme la septième puissance de la taille du système. Son utilisation est donc restreinte à des systèmes qui ne contiennent qu'un très petit nombre d'atomes.

3.3 Théorie de la fonctionnelle de la densité

Dans la section précédente, nous avons vu que les méthodes ab initio basées sur les fonctions d'onde peuvent donner des résultats précis, mais qu'elles sont en revanche très coûteuses pour un système contenant plusieurs atomes. Ainsi, si la méthode CCSD(T) est la méthode de choix pour calculer le potentiel d'interaction $\phi(r)$ entre deux atomes, elle devient inapplicable si l'on souhaite calculer l'état de plusieurs dizaines d'atomes interagissant collectivement. Or, dans le contexte de l'absorption induite par les collisions (Chapitre 4), nous nous intéresserons à des systèmes où les interactions multiples doivent être prises en considération. À cette fin, nous ferons appel à la théorie de la fonctionnelle de la densité (DFT).

La DFT est aujourd'hui la méthode la plus utilisée en chimie numérique et en physique de la matière condensée. En fait, la DFT est utilisée dans 80% des articles publiés en chimie numérique (Tsuneda, 2014). Sa grande popularité est essentiellement due au faible temps de calcul qu'elle requiert (comparativement aux méthodes post-Hartree–Fock).

3.3.1 Fondations théoriques

L'idée-clé de la DFT, c'est de décrire un système à plusieurs électrons en *représentant le potentiel comme une fonctionnelle de la densité électronique* $\rho_e(\mathbf{r})$ *et non comme une fonctionnelle des orbitales électroniques*. Ce faisant, on parvient à exprimer le potentiel comme une fonction de seulement 3 variables spatiales (plutôt que $3N$), ce qui ouvre la porte à des temps de calcul beaucoup plus intéressants.

Historiquement, c'est le modèle de Thomas–Fermi (Thomas, 1927; Fermi, 1927) qui fut le premier à proposer l'utilisation de la densité électronique pour déterminer l'état d'un

système comportant plusieurs électrons. Dans ce modèle, l'énergie d'un gaz d'électrons dans un potentiel nucléaire $V_N(\mathrm{r})$ est donnée par (Lundqvist & March, 2013)

$$E_e = \frac{3}{10}(3\pi^2)^{2/3}\int \rho_e(\mathbf{r})^{5/3}\mathrm{d}\mathbf{r} + \int \rho_e(\mathbf{r})V_N(\mathbf{r})\mathrm{d}\mathbf{r} + \frac{1}{2}\iint \frac{\rho_e(\mathbf{r})\rho_e(\mathbf{r}')}{|\mathbf{r}-\mathbf{r}'|}\mathrm{d}\mathbf{r}\mathrm{d}\mathbf{r}'. \tag{3.19}$$

Le premier terme de l'Équation 3.19 correspond à l'énergie cinétique d'un gaz d'électrons libres, le deuxième terme à l'interaction de Coulomb entre les noyaux et les électrons et le dernier terme à l'interaction de Coulomb entre les électrons. Bien qu'intéressant par son approche, le modèle de Thomas–Fermi ne parvient pas à décrire correctement les orbitales électroniques. Deux lacunes expliquent cet échec : (1) le modèle de Thomas–Fermi ignore complètement les termes d'échange et de corrélation électroniques et (2) l'énergie cinétique est calculée comme celle d'un gaz d'électrons libres.

Après avoir été mise de côté pendant trois décennies, l'idée de Thomas et Fermi renaît grâce au travail de Hohenberg & Kohn (1964). Ces auteurs ont prouvé que pour un système à plusieurs électrons *la densité électronique* $\rho_e(\mathbf{r})$ *détermine uniquement l'hamiltonien et donc toutes les propriétés du système.*

Le théorème de Hohenberg et Kohn pose les bases de la DFT, mais ne permet pas en soi de calculer l'état électronique d'un système. C'est là qu'intervient la méthode de Kohn & Sham (1965). Cette méthode consiste à transformer un système où N électrons interagissent ensemble en un système équivalent de N électrons qui n'interagissent pas ensemble. Ainsi, comme dans la méthode de Hartree–Fock, on obtient N équations d'onde à un électron,

$$\hat{F}_{\mathrm{KS}}\phi_i = \epsilon_i\phi_i, \tag{3.20}$$

où $\hat{F}_{\mathrm{KS}}$ est l'opérateur de Kohn–Sham,

$$\hat{F}_{\mathrm{KS}} = -\frac{1}{2}\nabla^2_{r_i} + \int \frac{\rho_e(\mathbf{r})}{|\mathbf{r}_i-\mathbf{r}|}\mathrm{d}\mathbf{r} + V_{xc}(\mathbf{r}_i) - \sum_{j=1}^{M}\frac{Z_j}{|\mathbf{r}_i-\mathbf{R}_j|}. \tag{3.21}$$

Les quatre termes du membre de droite de l'Équation 3.21 correspondent respectivement à l'énergie cinétique de l'électron i, à l'énergie d'interaction avec les autres électrons, à $\frac{\delta E_{xc}}{\delta \rho_e}$ (où E_{xc} est l'énergie d'échange et de corrélation avec les autres électrons) et à l'énergie d'interaction avec les noyaux. Pour faire le pont entre les fonctions d'onde ϕ_i et la densité

$\rho_e(\mathbf{r})$, on calcule simplement

$$\rho_e(\mathbf{r}) = \sum_{i=1}^{N} \sum_{\sigma} |\phi_i(\mathbf{r}, \sigma)|^2 . \tag{3.22}$$

Pour trouver $\rho_e(\mathbf{r})$, il suffit de trouver une solution cohérente au système d'équations constitué des Équations 3.20 à 3.22. Si l'on connaissait exactement la fonctionnelle V_{xc} pour le terme d'échange-corrélation, l'approche de Kohn–Sham conduirait à une solution exacte de l'équation de Schrödinger. Or, ce n'est pas le cas : V_{xc} doit être approximée, ce qui introduit une erreur dans les calculs.

3.3.2 Fonctionnelles d'échange-corrélation

Comme l'énergie d'échange-corrélation constitue la seule approximation inhérente à la méthode de Kohn–Sham, la qualité des résultats obtenus avec la DFT dépend fortement de la justesse de la fonctionnelle d'échange-corrélation choisie. La fonctionnelle d'échange-corrélation doit à la fois satisfaire à des conditions physiques de base (par exemple, l'énergie d'échange et l'énergie de corrélation ne peuvent être positives) et permettre de reproduire des résultats expérimentaux aussi précisément que possible. En se basant sur différents modèles physiques, plusieurs auteurs ont proposé des fonctionnelles d'échange-corrélation, de sorte qu'au fil des ans un véritable zoo de fonctionnelles s'est formé (voir par exemple Perdew et al., 2005).

La fonctionnelle la plus simple est celle résultant de l'approximation de la densité locale (LDA). Dans le cadre de cette approximation, l'énergie d'échange-corrélation E_{xc} est celle d'un gaz uniforme d'électrons et ne dépend donc que de la densité ρ_e. La contribution d'échange à E_{xc} possède alors une forme analytique exacte et la contribution de la corrélation est obtenue à partir de calculs Monte-Carlo quantiques (voir par exemple Ceperley & Alder, 1980).

Au-delà de la LDA, on utilise l'approximation des gradients généralisée (GGA). Cette approximation est plus sophistiquée que la LDA, puisque E_{xc} dépend alors du gradient de la densité $\nabla\rho_e$ en plus de la densité ρ_e elle-même. Ainsi, une certaine information sur les variations spatiales de la densité électronique est incluse dans le calcul de l'énergie d'échange-corrélation. Plusieurs fonctionnelles GGA existent : la fonctionnelle PBE (Per-

dew et al., 1996) sera fréquemment utilisée dans ce travail (Chapitres 4, 5 et 9).[6] Notons qu'il existe aussi des fonctionnelles plus complexes que la GGA, c'est-à-dire des fonctionnelles qui dépendent d'autres variables que ρ_e et $\nabla\rho_e$. Nous n'en ferons toutefois pas usage dans cette thèse.

3.4 Simulations de dynamique moléculaire

Toutes les méthodes présentées jusqu'ici ne permettent d'accéder à aucune information sur l'évolution temporelle d'un système d'atomes. Or, la dépendance temporelle de certaines quantités physiques constitue une information cruciale pour plusieurs calculs nécessaires à la modélisation de l'atmosphère des naines blanches froides (notamment le calcul de l'absorption induite pas les collisions au Chapitre 4). Cette section présente la théorie sous-jacente aux simulations de dynamique moléculaire, qui permettent de calculer, pas à pas, l'évolution d'un système de particules en interaction.

3.4.1 Dynamique moléculaire conventionnelle

Dans toutes les situations considérées dans cette thèse, la séparation entre les atomes est beaucoup plus grande que leur longueur d'onde de de Broglie. Par conséquent, on peut les traiter comme des particules classiques qui obéissent aux équations newtoniennes du mouvement. Comme l'illustre la Figure 3.2, calculer l'évolution d'un tel système est plutôt simple. On commence par placer les atomes dans une configuration initiale, puis, à chaque pas de temps de la simulation, on calcule leur déplacement. Pour ce faire, un évalue d'abord la force ressentie par chacune des particules au moyen d'un potentiel d'interaction spécifié au préalable. Ce potentiel peut être obtenu à partir de mesures expérimentales ou à l'aide de méthodes ab initio basées sur les fonctions d'onde (Section 3.2). En un sens, toute la physique du système est contenue dans ce potentiel d'interaction. Une fois que les forces qui s'appliquent sur chacun des atomes sont connues, on peut intégrer les équations du mouvement de Newton, ce qui se fait habituellement au moyen de l'intégration de Verlet (1967). Cette méthode offre une excellente stabilité numérique tout en étant à peine plus

[6] Ces calculs sont réalisés avec le code QUANTUM ESPRESSO (https://www.quantum-espresso.org/).

coûteuse en temps de calcul que la simple méthode d'Euler.[7] On laisse ainsi rouler la simulation pendant un certain nombre de pas de temps jusqu'à ce qu'un état d'équilibre soit atteint. Ensuite, la simulation est prolongée et on sauvegarde à intervalle régulier les quantités physiques d'intérêt (par exemple la position des atomes et leur vitesse).

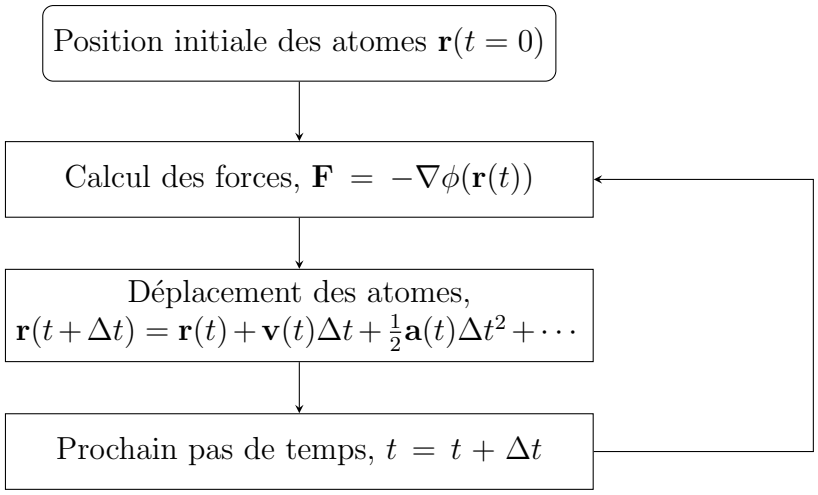

Figure 3.2 – Représentation simplifiée d'un algorithme de dynamique moléculaire

Évidemment, à cause de limitations numériques, on ne peut modéliser un système macroscopique de 10^{23} particules au moyen de la dynamique moléculaire : il faut se contenter d'un plus petit nombre de particules. Pour qu'un tel système soit représentatif d'un système macroscopique, on modélise les particules à l'intérieur d'une cellule de simulation qui a un volume permettant d'obtenir la même densité que le système macroscopique. Aux frontières de cette cellule de simulation, on applique des conditions périodiques. Autrement dit, la cellule de simulation est entourée de cellules identiques contenant des atomes ayant les mêmes positions et les mêmes vitesses. Ces conditions périodiques aux limites permettent d'éviter des problèmes liés à la taille finie du système et d'émuler le comportement d'un système macroscopique (qui, à cette échelle, est en pratique infini).[8]

[7] Notons toutefois que l'intégration de Verlet ne permet pas de prendre en compte des forces qui dépendent de la vitesse des particules.

[8] Concrètement, les calculs de dynamique moléculaire conventionnelle présentés dans cette thèse ont été réalisés avec le code LAMMPS (https://lammps.sandia.gov/).

3.4.2 Dynamique moléculaire ab initio

Le potentiel total d'un système constitué de N particules en interaction peut s'écrire comme une série de potentiels à N corps,

$$V(\mathbf{r}_1, \mathbf{r}_2, \ldots, \mathbf{r}_N) = \sum_{i<j}^{N} \phi_2(\mathbf{r}_i, \mathbf{r}_j) + \sum_{i<j<k}^{N} \phi_3(\mathbf{r}_i, \mathbf{r}_j, \mathbf{r}_k) + \cdots + \sum_{i<j<k<,\ldots,n}^{N} \phi_n(\mathbf{r}_i, \mathbf{r}_j, \mathbf{r}_k, \mathbf{r}_n). \tag{3.23}$$

Très fréquemment, dans une simulation de dynamique moléculaire, cette série est tronquée après le premier terme, de sorte que seules les interactions à deux corps sont considérées. On parle alors de la *pairwise additive approximation*. Il s'agit d'une approximation pratique puisqu'elle ne requiert que la connaissance du potentiel à deux corps $\phi_2(\mathbf{r}_i, \mathbf{r}_j)$. Or, il n'est pas toujours suffisant de se limiter au premier terme de l'expansion de $V(\mathbf{r}_1, \mathbf{r}_2, \ldots, \mathbf{r}_N)$. En particulier, dans un milieu dense, on s'attend à ce que les termes d'ordres supérieurs jouent un rôle non négligeable.

Si les termes d'interaction pour $n > 2$ sont importants mais que leur forme est inconnue, on peut se tourner vers la dynamique moléculaire ab initio pour obtenir une évaluation de $V(\mathbf{r}_1, \mathbf{r}_2, \ldots, \mathbf{r}_N)$ qui ne repose pas sur la *pairwise additive approximation*. La différence entre une simulation de dynamique moléculaire conventionnelle et ab initio, c'est que dans le dernier cas les forces ne sont pas calculées à partir de potentiels prédéfinis. La densité électronique est calculée à chaque pas de temps au moyen de méthodes ab initio (en particulier la DFT), ce qui permet de calculer l'énergie potentielle pour la configuration atomique du système sans supposer au préalable aucune forme de potentiel d'interaction. Cette approche rend les simulations de dynamique moléculaire ab initio généralement plus appropriées que les simulations conventionnelles pour les systèmes denses où les interactions à plusieurs particules sont importantes. En revanche, ces simulations sont beaucoup plus coûteuses en temps de calcul, puisqu'il faut recalculer la densité électronique à chaque pas de temps de la simulation. Ce type de simulation est utilisé aux Chapitres 4, 5 et 9 pour le calcul de l'absorption induite par les collisions et l'équilibre d'ionisation des éléments lourds à la photosphère des naines blanches froides. Nous utilisons le code CPMD[9] pour réaliser ces calculs.

[9] http://cpmd.org

CHAPITRE 4

Pressure Distortion of the H_2-He Collision-Induced Absorption at the Photosphere of Cool White Dwarf Stars

Physics is really nothing more than a search for ultimate simplicity, but so far all we have is a kind of elegant messiness.

—Bill Bryson (1951−), écrivain anglo-américain

Ce chapitre est une adaptation de «Pressure Distortion of the H_2-He Collision-Induced Absorption at the Photosphere of Cool White Dwarf Stars», par Simon Blouin, Piotr M. Kowalski et Patrick Dufour. Cet article a été publié en octobre 2017 dans *The Astrophysical Journal*.[1]

4.1 Abstract

Collision-induced absorption (CIA) from molecular hydrogen is a dominant opacity source in the atmosphere of cool white dwarfs. It results in a significant flux depletion in the near-IR and IR parts of their spectra. Because of the extreme conditions of helium-rich atmospheres (where the density can be as high as a few $\mathrm{g\,cm^{-3}}$), this opacity source is expected to undergo strong pressure distortion and the currently used opacities have not been validated at such extreme conditions. To check the distortion of the CIA opacity we applied state-of-the-art ab initio methods of computational quantum chemistry to simulate the CIA opacity at high densities. The results show that the CIA profiles are significantly

[1] Blouin, S., Kowalski, P. M., & Dufour, P. 2017, ApJ, 848, 36.

distorted above densities of $0.1\,\mathrm{g\,cm^{-3}}$ in a way that is not captured by the existing models. The roto-translational band is enhanced and shifted to higher frequencies as an effect of the decrease of the interatomic separation of the H_2 molecule. The vibrational band is blueward shifted and split into Q_R and Q_P branches, separated by a pronounced interference dip. Its intensity is also substantially reduced. The distortions result in a shift of the maximum of the absorption from $2.3\,\mu$m to $3-7\,\mu$m, which could potentially explain the spectra of some very cool, helium-rich white dwarfs.

4.2 Introduction

White dwarf stars represent the last stage in the evolution of most stars. Deprived of any internal energy source, they slowly cool down during billions of years. Since their cooling rate and cooling time can be accurately calculated, these stars are excellent cosmochronometers (Winget et al., 1987; Fontaine et al., 2001). The analysis of a large sample of white dwarf stars can reveal the age and the historical stellar formation rate of various stellar populations (Bergeron et al., 1997, 2001; Hansen et al., 2002; Tremblay et al., 2014).

To extract the cooling time of a white dwarf star from its spectrum, it is necessary to accurately estimate its atmospheric parameters, namely the effective temperature $T_{\rm eff}$, the surface gravity $\log g$ and the chemical composition. To do so, detailed atmosphere models are used to fit the observed spectral energy distribution (SED) (e.g., Bergeron et al., 1997, 2001). While current atmosphere models are able to successfully reproduce the spectra of most white dwarf stars, cool ($T_{\rm eff} < 6000\,\mathrm{K}$) helium-rich objects represent a challenge. This is because at low temperatures helium becomes increasingly transparent, allowing the photosphere of cool helium-rich white dwarfs to reach fluid-like densities (up to a few $\mathrm{g\,cm^{-3}}$, Bergeron et al., 1995; Kowalski, 2010). Under such conditions, the average interatomic distance is very short ($\sim 2\,$Å) and the collective interactions between particles are strong, affecting the chemistry and physics. Various studies have proposed nonideal corrections to the equation of state (Fontaine et al., 1977; Saumon & Jacobson, 1998; Bergeron et al., 1995), the chemical abundances of species (Kowalski, 2006b; Kowalski et al., 2007), the opacities (Iglesias et al., 2002; Kowalski & Saumon, 2006; Kowalski, 2014), and the radiative transfer (Kowalski & Saumon, 2004) in dense helium-rich media. Despite these improvements, atmosphere models have problems to correctly reproduce the

spectra of cool, helium-rich stars, and thus fail to deliver reliable atmospheric parameters for many of them. The reproduction of the near-IR and IR parts of the spectra is especially problematic (Bergeron & Leggett, 2002; Gianninas et al., 2015). This points to a problem with the current description of the CIA opacity from molecular hydrogen as a trace species in a dense helium-rich medium (see the case of LHS 3250, Kilic et al., 2009a; Kowalski et al., 2013).

The importance of CIA opacity from molecular hydrogen in the atmospheres of cool white dwarfs was discussed for the first time by Mould & Liebert (1978). This absorption results from collisions of H_2, which alone is IR inactive, with other particles (H, H_2, He, Frommhold, 1993), leading to the induction of an electric dipole moment through the formation of a super-molecular complex (e.g., H_2He, Lenzuni et al., 1991). This absorption mechanism has been observed experimentally (Crawford et al., 1950; Chisholm et al., 1952; Chisholm & Welsh, 1954; Hare & Welsh, 1958; Birnbaum, 1978; Birnbaum et al., 1987; Bouanich et al., 1990; Brodbeck et al., 1995) and computed by various authors (Borysow et al., 1985, 1989, 1997, 2001; Lenzuni et al., 1991; Borysow, 1992, 2002; Frommhold, 1993; Jørgensen et al., 2000; Gustafsson & Frommhold, 2001; Abel et al., 2012; Abel & Frommhold, 2013). Its importance in the modeling of stellar atmospheres, including white dwarfs, was highlighted by Lenzuni et al. (1991) and its implementation in the context of white dwarf atmosphere modeling was discussed in follow-up studies (e.g., Bergeron et al., 1995; Saumon & Jacobson, 1998). We note however that most of these studies focus on modeling binary H_2-perturber collisions. The density correction that accounts for the three-body collisions is applied on top of these calculations (e.g., Lenzuni et al., 1991; Saumon & Jacobson, 1998) and comes from the experimental measurements of Hare & Welsh (1958). Because of the limitations of these static-like calculations, the pressure-induced distortion of the roto-translational and vibrational bands, which arises from the kinetics of the collision, have not been considered.

In this study we applied a state-of-the-art ab initio molecular dynamics method to directly simulate the H_2-He CIA absorption in a density regime where many-body collisions are important ($\rho > 0.1\,\mathrm{g\,cm^{-3}}$, $T > 1000\,\mathrm{K}$). This allows us for the first time to observe the pressure distortion of the absorption profiles at such extreme and previously

unexplored conditions. Moreover, we constructed a model for this distortion, which can be easily implemented in existing white dwarf atmosphere codes.

In Section 4.3, we provide a brief description of the physics of CIA and the details of our simulation strategy. The discussion of the results of our virtual experiments are presented in Section 4.4, where we compare the obtained data with previous calculations and the available experimental data. Here we also provide a detailed analysis of the simulated H_2-He CIA distortion that arises at densities above $0.1\,g\,cm^{-3}$ and an analytical model of the distortion is given in Section 4.5. In Section 4.6, we discuss the resulting atmosphere models and their implications for our understanding of white dwarf spectra. Our conclusions and future directions are provided in Section 4.7.

4.3 Theoretical framework

4.3.1 Collision-induced absorption

Due to symmetry, an isolated H_2 molecule in its electronic ground state has no electric dipole moment. Hence, it can only absorb photons through less probable electric quadrupole transitions, which makes it effectively IR inactive. However, in a dense medium, the interaction of H_2 molecule with surrounding particles (binary collisions at low densities) leads to a distortion of its charge distribution and induction of a (small) electric dipole moment. This induced dipole allows the absorption of photons via electric dipole transitions, which are more probable than the aforementioned quadrupole transitions. This phenomenon is known as collision-induced absorption (Frommhold, 1993).

The CIA spectrum of a molecule can be viewed as the sum of two contributions : one from the collisional complex and one from the unperturbed molecule (Frommhold, 1993). As shown in Figure 4.1, for the H_2-He CIA spectrum, the dominant contribution to the spectrum comes from the rovibrational transitions of the unperturbed H_2 molecule (which are dipole-forbidden for an isolated H_2 molecule). The energy of an absorbed photon, $\hbar\omega$, satisfies the relationship (Abel & Frommhold, 2013)

$$E_{\nu,J} + E_r + \hbar\omega = E_{\nu',J'} + E'_r, \tag{4.1}$$

where $E_{\nu,J}$ and $E_{\nu',J'}$ are the rovibrational energies of the H_2 molecule (ν and J are the vibrational and rotational quantum numbers, respectively) and E_r and E'_r are the energies of relative motion before and after the interaction. Figure 4.1 also shows that the bands arising from rovibrational transitions are broadened at high temperature. This is a consequence of faster collisions (shorter interaction times) at higher temperatures (Lenzuni et al., 1991; Abel & Frommhold, 2013).

To compute CIA spectra, previous investigators (e.g., Birnbaum et al., 1984; Meyer & Frommhold, 1986; Borysow, 1992; Hammer et al., 1999; Abel et al., 2012) have relied on an approach combining quantum chemical computations with molecular scattering theory. In such calculations ab initio methods (e.g., Møller–Plesset calculations, coupled-cluster calculations) are used to obtain accurate potential energy (PES) and induced dipole (IDS) surfaces for the H_2-perturber super-molecular complex in the infinite-dilution limit. Then, the PES and IDS are used as inputs in the molecular scattering theory to compute the resulting spectrum. This approach has been very successful in predicting the measured H_2-H_2 (Borysow, 1992; Borysow et al., 2000) and H_2-He (Borysow et al., 1988; Borysow, 1992) CIA in the dilute limit.

The three-body collision effects at higher densities are modeled with a $1 + \beta\rho$ scaling factor (assuming that binary collisions are proportional to ρ^2 and triple collisions to ρ^3). We note that this approach has not been validated for densities larger than $\rho = 0.26\,\mathrm{g\,cm^{-3}}$—the highest density measured by Hare & Welsh (1958)—and temperatures higher than room temperature. It is also expected to break down for the much higher, fluid-like densities encountered at the photosphere of cool white dwarf stars with helium-rich atmospheres. This is because PES and IDS obtained in the infinite-dilution limit are not expected to correctly capture the distortion of the charge distribution resulting from simultaneous, multi-atomic interactions. In order to check how these interactions affect the CIA spectrum, here we applied the ab initio molecular dynamics method to simulate the H_2-He CIA at these extreme helium densities. These simulations can be seen as a virtual experiment that intrinsically accounts for all the many-body effects.

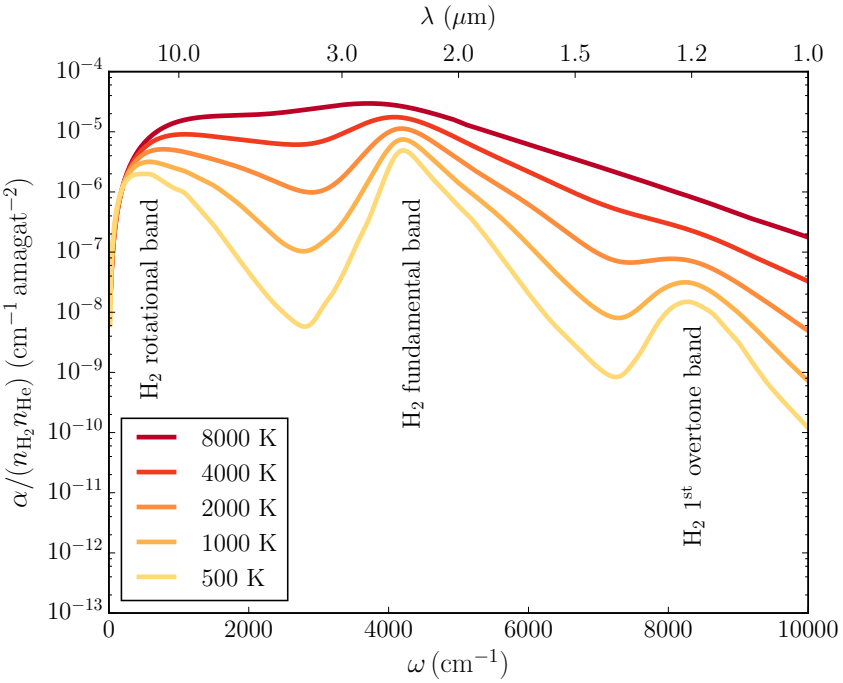

Figure 4.1 – H_2-He CIA spectra for different temperatures, as computed by Abel et al. (2012). All spectra are divided by the number density of H_2 and He.

4.3.2 Ab initio molecular dynamics simulations

We simulated the interactions between H_2 and He atoms and the resulting IR absorption spectrum using the same procedure and computational setup as Kowalski (2014) in his simulations of He−He−He CIA. We used ab initio Born–Oppenheimer molecular dynamics (MD) method with density functional theory (DFT) to calculate the structure of the H_2-He atomic fluid. In this simulation framework, the electronic charge density is recomputed at each simulated time point applying DFT, and the atomic dynamics is driven by the resulting forces and classical dynamics. Hence, contrarily to the static molecular scattering approach, PES and IDS are computed on the fly for the atomic configurations representing real atomic arrangements and dynamics in a dense fluid. This is what makes this approach very suitable for the high-density regime, where multi-particles interactions become important.

Simulations were performed using the CPMD[2] plane-wave DFT code (Marx & Hutter, 2000) with the PBE exchange-correlation functional (Perdew et al., 1996) and ultrasoft

[2] http://cpmd.org

pseudopotentials (Vanderbilt, 1990). To assure the convergence of the electronic charge density we applied a plane-wave energy cut-off of 340 eV. In each simulation, the cubic supercell that represents the simulation box contained one H_2 molecule and either 31, 63 or 127 He atoms. The simulation box length was adjusted to obtain the desired density. Numerous simulations were performed for different (T, ρ) conditions.

At each simulation time step, with a time interval of 0.5 fs, the total dipole moment $\mathbf{M}$ of the simulation supercell (i.e., the dipole moment resulting from the total electronic charge density and the distribution of all nuclei in the simulation supercell) was computed using the localized Wannier function approach (Silvestrelli et al., 1998; Berghold et al., 2000). The IR absorption coefficient $\alpha(\omega)$ was then obtained through the Fourier transform of the dipole moment time autocorrelation function as (Silvestrelli et al., 1997)

$$\alpha(\omega) = \frac{2\pi\omega^2}{3ck_BTV} \int_{-\infty}^{\infty} \mathrm{d}t \exp(-i\omega t) \langle \mathbf{M}(t) \cdot \mathbf{M}(0) \rangle, \tag{4.2}$$

where ω is the wavenumber, c is the speed of light in the fluid, k_B is the Boltzmann constant, T is the temperature, V is the supercell volume and the angle brackets denote the time-autocorrelation function, i.e. $\langle \mathbf{M}(\tau) \cdot \mathbf{M}(0) \rangle = \frac{1}{t_{\mathrm{sim}}} \int_0^{t_{\mathrm{sim}}} \mathbf{M}(t) \cdot \mathbf{M}(t+\tau) \mathrm{d}t$, with t_{sim} being the total simulation time. For the physical conditions considered in this work, the dipole moment induced on the hydrogen molecule is larger by a factor of ≈ 100 than the total dipole moment induced on helium atoms. Therefore, the interactions between helium atoms have a negligible contribution to the simulated infrared absorption spectrum (it is about four orders of magnitude smaller than H_2-He CIA, see Kowalski 2014). Since in cool, helium-rich white dwarf stars the index of refraction $n(\omega)$ departs significantly from unity (Kowalski & Saumon, 2004), the actual absorption coefficient that has to be implemented in atmosphere codes is not $\alpha(\omega)$, but $\alpha(\omega)/n(\omega)$. For helium in the atmosphere of white dwarf stars, $n(\omega)$ can be approximated using for instance the semiempirical virial expansion given by Kowalski et al. (2007), which accounts for binary and triple interatomic collisions and is consistent with quantum molecular dynamics data for helium densities up to $2\,\mathrm{g\,cm^{-3}}$. However, we note that its applicability at higher densities may be inappropriate due to the expected contributions from quadruple and higher-order collisions.

The outlined procedure for the simulation of IR absorption spectra using a molecular dynamics approach and the time evolution of the dipole moment is a well-established method that has been successfully applied in various previous studies. For instance, this technique was used to simulate the IR spectrum of water (Guillot, 1991; Silvestrelli et al., 1997; Iftimie & Tuckerman, 2005), the absorption spectra of minerals (Pagliai et al., 2008, 2011) and the He−He−He CIA in dense helium for the conditions of white dwarf atmospheres (Kowalski, 2014).

4.3.3 Quality of the computed dipole moments

It is well known that due to intrinsic approximations, DFT methods do not result in precise values of dipole moments. Since accurate dipole moments are essential to a correct determination of CIA opacities, we validated the dipole moments of the H_2−He supermolecular complex computed with our DFT approach against those computed by Li et al. (2012). The latter study was performed using the couple-cluster method with large basis sets and thus represents the most accurate estimate of dipole moments for this complex. As shown in Figure 4.2, the agreement between both calculations is satisfactory, as the relative difference is not larger than 15%. Figure 4.2 also indicates that the DFT dipole moments are systematically slightly overestimated. Interestingly, previous studies obtained similar trends for liquid water. Using DFT and maximally-localized Wannier functions to compute the dipole moment per molecule in liquid water, Silvestrelli & Parrinello (1999) found an average value of 3.0 D (1.2 au), which is slightly larger than the coupled-cluster result ($\approx$ 2.7 D, Kongsted et al., 2002). Nevertheless, the reasonably good match of the results of our simulations of H_2−He CIA in the dilute limit to those obtained by more accurate techniques (as will be discussed in Section 4.4) shows that these differences do not significantly affect the results of our study.

4.3.4 Simulation box size effect

As our simulations employ periodic boundary conditions to mimic the continuity of the fluid, the simulation box must be large enough to eliminate any side effects resulting from artificial periodicity. Thus, for a given helium density we performed simulations with different numbers of helium atoms per simulation box and different box sizes. We then

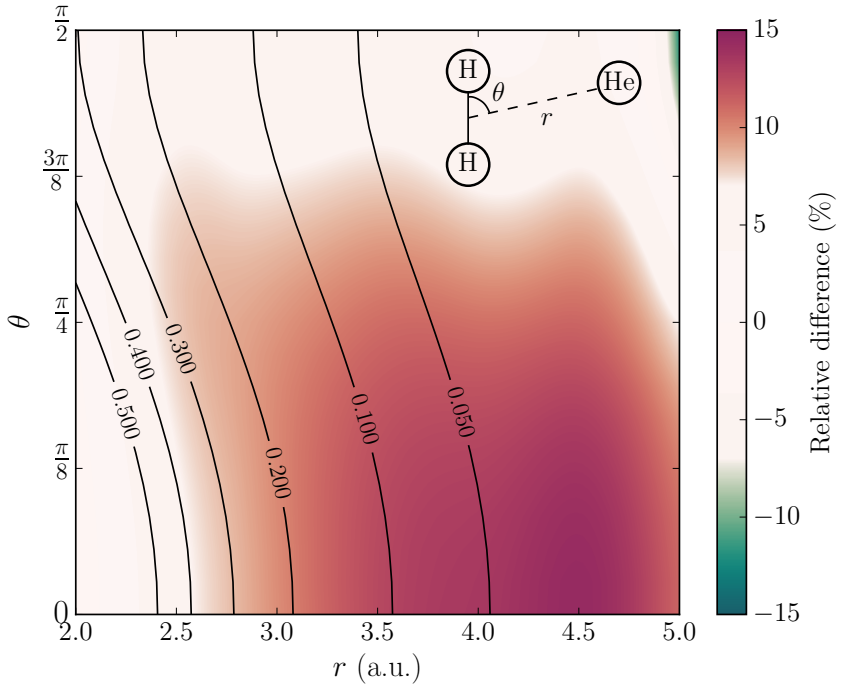

Figure 4.2 – Colors indicate the relative difference between the dipole moments of the H_2−He complex computed using DFT and those reported by Li et al. (2012) and contour lines show the amplitude of the dipole moment in atomic units. As shown in the upper-right corner, θ is the angle between the H_2 bond and the line connecting the center of the H_2 molecule to the He atom (the length of this line being r). The separation between the two H atoms is fixed at 1.449 au to allow comparison with the data provided in Li et al. (2012).

compared the resulting spectra and found that as long as the cubic simulation box has a dimension of at least $a = 10\,\text{au}$ (5.3 Å) and contains at least $N = 32$ atoms, the resulting spectra are virtually identical. All the results reported here are therefore obtained from simulations that satisfy these criteria.

4.3.5 Simulation convergence

To test the convergence of our simulations in regard to the molecular dynamics simulation time, we computed IR spectra for different trajectory lengths. We found that a 64 ps trajectory is long enough to attain a satisfactorily good convergence. This is shown in Figure 4.3, where it can be seen that the 64 ps and 128 ps trajectories yield almost identical spectra. Therefore, for all simulations reported here, we use a simulation time of 64 ps.

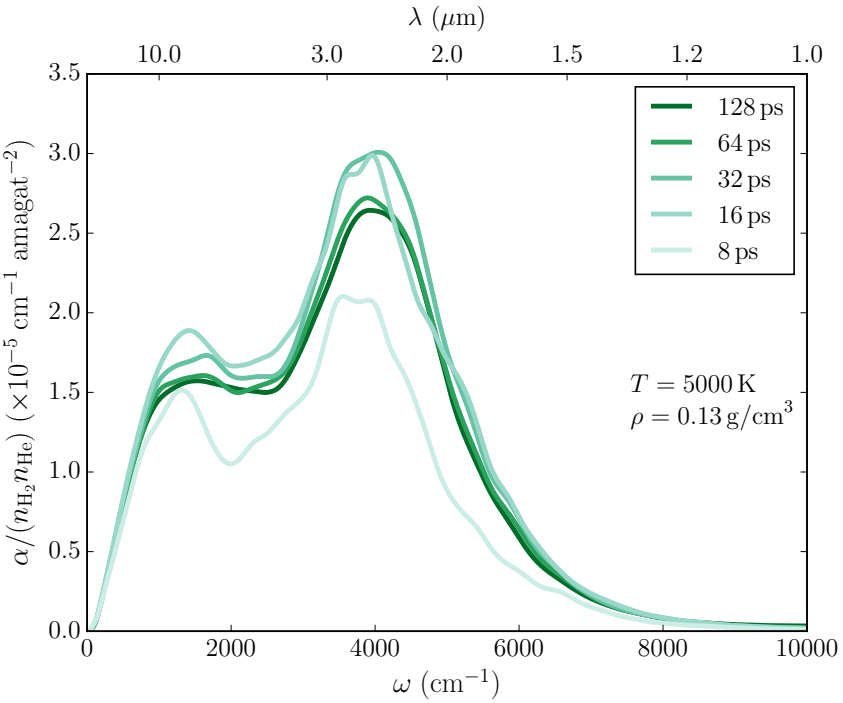

Figure 4.3 – H_2−He CIA spectra computed with our DFT-MD simulations for $T = 5000\,\text{K}$ and $\rho = 0.13\,\text{g}\,\text{cm}^{-3}$. The spectra shown here were obtained using various trajectory lengths, as indicated in the upper-right corner.

4.3.6 Quantum effects on the motion of nuclei

Ions in ab initio Born–Oppenheimer molecular dynamics simulations obey the classical laws of motion. Hence, the simulated time evolution of dipole moments follows the classical motion of nuclei. A priori, this is a problematic situation. Our simulations include light atoms, and for $\omega \gtrsim kT/\hbar$, quantum effects are expected to become important. Contrarily to what is done in classical molecular dynamics, one should ideally treat nuclei quantum-mechanically (for instance by applying path integral molecular dynamics). However, when combined with ab initio force determination, this approach becomes computationally very costly. As an alternative, quantum correction factors are applied a posteriori to the simulated "*classical*" IR spectrum, $\alpha_{\rm cl}$. Several different quantum correction factors are discussed in the literature. Ramírez et al. (2004) compared many of them and found that the harmonic approximation,

$$\alpha_{\rm corr} = \alpha_{\rm cl} \cdot \frac{\beta\hbar\omega}{1 - \exp(-\beta\hbar\omega)}, \tag{4.3}$$

performs generally better than the other corrections. Hence, we use this approach to correct our IR spectra for quantum effects. This correction factor is already included in Equation 4.2.

4.4 Results and discussion

4.4.1 H_2−He CIA at low density : comparison to previous studies

As a first step, we discuss the simulation results at low density ($\rho = 0.13\,\mathrm{g\,cm^{-3}}$) to verify that they are consistent with previous calculations. We note that $\rho = 0.13\,\mathrm{g\,cm^{-3}}$ is the lowest density we consider, since simulations at $\rho \ll 0.1\,\mathrm{g\,cm^{-3}}$ require much larger simulation cells that are prohibitively computationally intensive. In Figure 4.4 we compare the simulated H_2−He CIA opacity with the absorption profiles computed for $T = 5000\,\mathrm{K}$ by Abel et al. (2012) and Jørgensen et al. (2000), and commonly used in white dwarf atmosphere codes (see respectively Kowalski, 2014; Bergeron & Leggett, 2002). We consider the most recent calculations of Abel et al. (2012) as the best reference, since these calculations rely on PES and IDS that are more accurate than the ones used by Jørgensen et al. 2000 (the latter study used a smaller basis set for their first-principles calculations). We also note that the absorption profiles of Abel et al. (2012) are in excellent agreement

with room-temperature measurements (Birnbaum, 1978; Birnbaum et al., 1987; Brodbeck et al., 1995).

The direct comparison indicates that our simulations overestimate the CIA absorption by $\approx 30\%$. However, at $0.13\,\mathrm{g\,cm^{-3}}$, many-body interactions are already important and the three-body interaction correction (i.e., the ρ^3 term) should be taken into account (van Kranendonk, 1957; Lenzuni & Saumon, 1992). In other words, the absorption profiles of Abel et al. (2012) and Jørgensen et al. (2000) should be scaled by $(1+\beta\rho)$, where $\beta = 2.79\,\mathrm{cm^3/g}$ is a coefficient fitted to the experimental data of Hare & Welsh (1958). As indicated in Figure 4.4 our simulation profile matches the rescaled profiles of Abel et al. (2012) and Jørgensen et al. (2000). Some small differences can be noticed in the region between the roto-translational and the fundamental band, and at frequencies above $5000\,\mathrm{cm^{-1}}$. This could reflect the uncertainty level caused by the application of the DFT method (see discussion in Section 4.3.3). However, these effects are of minor importance and there is an overall satisfactorily good agreement between the simulated and the previously computed CIA profiles, which validates our simulation approach.

We note that Lenzuni et al. (1991) suggested that the strength of the three-body correction can be estimated by scaling the CIA spectrum as ρP instead of ρ^2. Using the tabulated equation of state of Becker et al. (2014) to get the pressure as a function of density and temperature, we found that the pressure was 33% higher than the pressure predicted by the ideal gas law for $T = 5000\,\mathrm{K}$ and $\rho = 0.13\,\mathrm{g\,cm^{-3}}$, which results in $\beta = 3.30\,\mathrm{cm^3/g}$. This value is similar to the $\beta = 2.79\,\mathrm{cm^3/g}$ value measured by Hare & Welsh (1958).

4.4.2 H_2-He CIA at high density

After demonstrating that our computational approach satisfactorily reproduces the low-density absorption profiles of Abel et al. (2012), we used it to explore how the H_2-He CIA profiles behave at higher densities. Figure 4.5 shows a density sequence of the simulated CIA profiles and the profiles of Abel et al. (2012) rescaled for three-body collisions (Section 4.4.1). When we compare the two sets of profiles, it is clear that for densities exceeding $0.1\,\mathrm{g\,cm^{-3}}$, the spectrum becomes significantly distorted. Three main effects are visible :

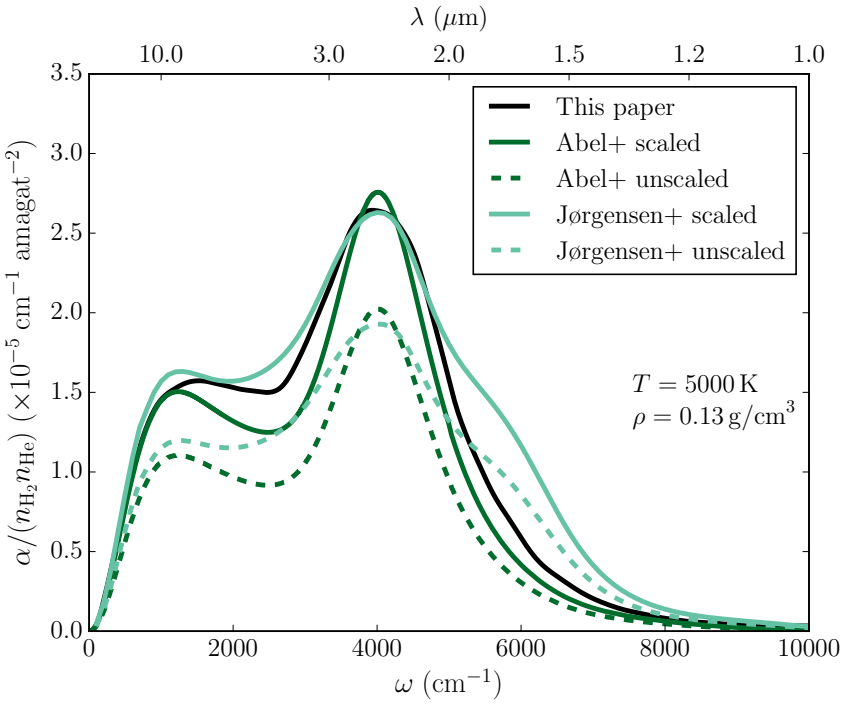

Figure 4.4 – The black line is the H_2-He CIA spectrum computed with our DFT-MD method. The colored spectra are from Abel et al. (2012) and Jørgensen et al. (2000). For these two references, the spectra are shown without a three-body correction (dashed lines) and with the density correction of Hare & Welsh 1958 (solid lines, see Section 4.4.1).

(a) The roto-translational band becomes stronger.

(b) The absorption is shifted towards higher frequencies.

(c) The fundamental vibrational band is gradually split into two branches with a pronounced, intermediate dip.

Below we discuss these effects in details and try to identify the physical phenomena that cause these distortions.

(a) Many-body collisions As already discussed, many-body collisions become increasingly important (compared to binary interactions) under high-density conditions (Hare & Welsh, 1958; Lenzuni & Saumon, 1992). This leads to a perturber density-induced scaling of the integrated CIA spectrum,

$$\int \alpha \mathrm{d}\omega = \kappa_2 n_{\mathrm{He}} n_{\mathrm{H_2}} + \kappa_3 n_{\mathrm{He}}^2 n_{\mathrm{H_2}} + \ldots, \tag{4.4}$$

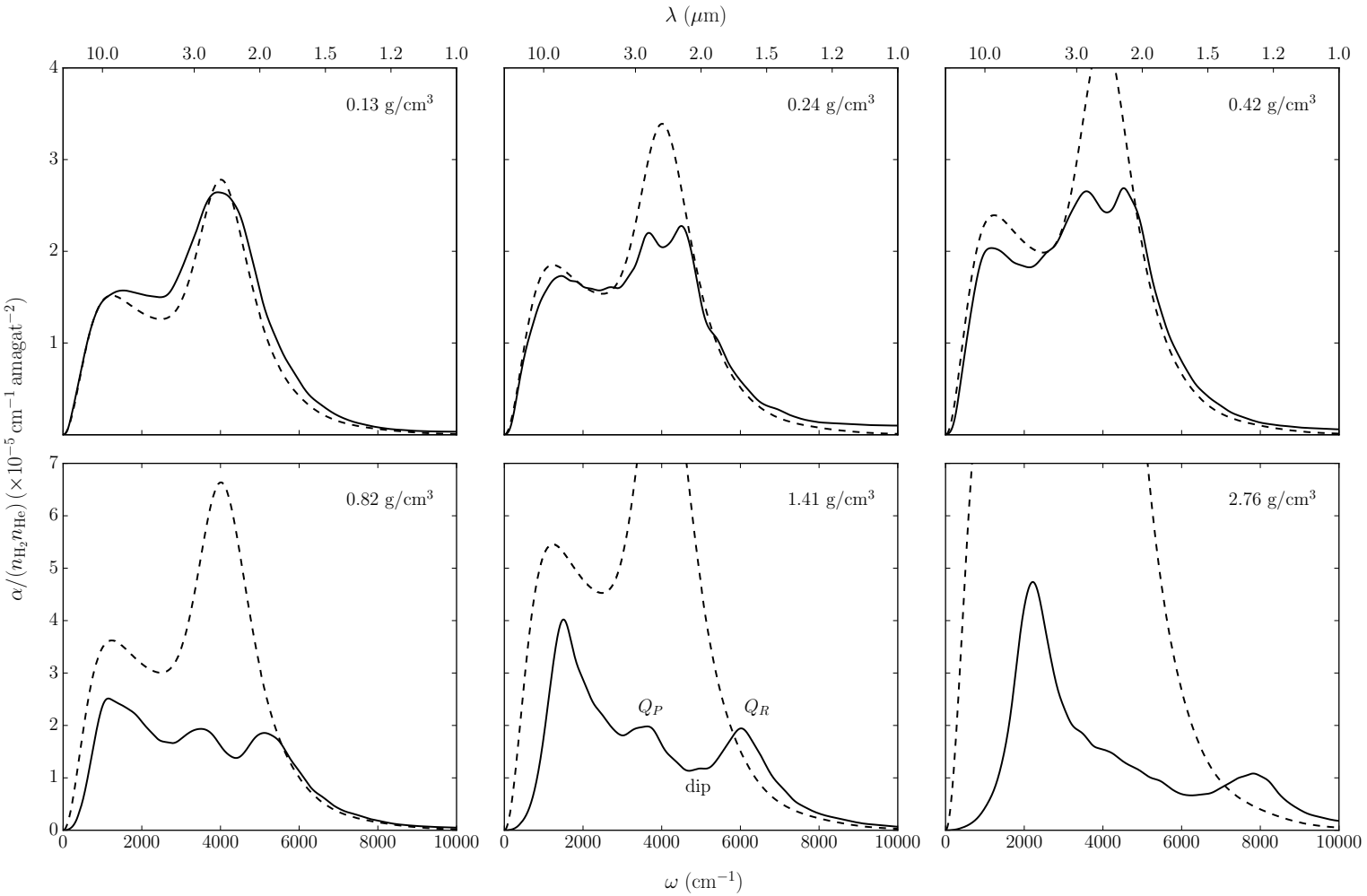

Figure 4.5 – The solid lines show the results of our simulations for the absorption coefficient of H_2-He CIA as a function of wavenumber, for various densities and $T = 5000\,\mathrm{K}$. The dashed lines are the spectra computed by Abel et al. (2012), scaled by the $1 + \beta\rho$ factor discussed in Section 4.4.1. The scale of the vertical axis is not the same for the top and the bottom plots.

and the related rescaling of the dilute-limit profiles ($1 + \beta\rho$, Section 4.4.1). As shown in Figure 4.5, the rescaled profiles of Abel et al. (2012) match nicely the strength of the simulated roto-translational band up to a density of $0.4\,\mathrm{g\,cm^{-3}}$. Therefore, we can confidently conclude that the increase of the roto-translational band occurs as a consequence of three-body collisions. Moreover, our simulation results validate the $1 + \beta\rho$ correction of Hare & Welsh (1958) and its implementation in white dwarf atmosphere codes (Lenzuni & Saumon, 1992) for densities up to $0.4\,\mathrm{g\,cm^{-3}}$.

Figure 4.6 shows how the integrated absorption spectrum changes as a function of density and temperature. It can be seen that the relation between the integrated profile and density is linear up to a density of $\approx 0.5\,\mathrm{g\,cm^{-3}}$ and thus that it follows Equation 4.4. These results are consistent with the measurements of Hare & Welsh (1958), who found a linear relation up to $\rho = 0.26\,\mathrm{g\,cm^{-3}}$.

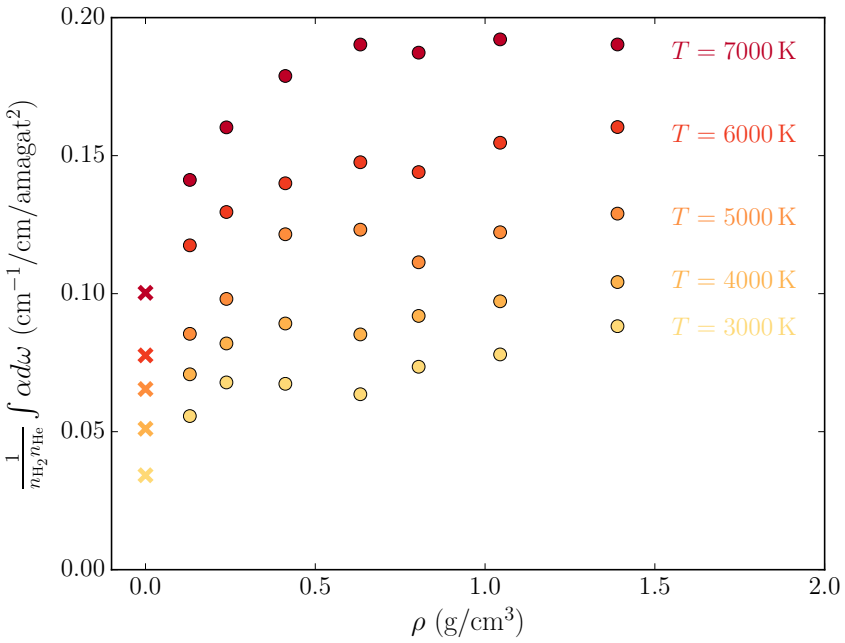

Figure 4.6 – Integrated absorption spectra with respect to density. Circles show the results extracted from our ab initio simulations and crosses indicate the values obtained from the low-density calculations of Abel et al. (2012).

(b) Frequency shift The density sequence illustrated in Figure 4.5 indicates a systematic shift of the absorption profile towards higher frequencies. This includes the shift of the position of the roto-translational band from $\approx 1000\,\mathrm{cm^{-1}}$ in the dilute limit to

$> 2000\,\mathrm{cm}^{-1}$ at $\rho = 2.8\,\mathrm{g\,cm}^{-3}$. In the case of rotational transitions, the absorption frequencies (energies) are determined by the rotational constant B, which for a H_2 molecule is given by

$$B = \frac{h}{8\pi^2 cI} = \frac{h}{4\pi^2 c m_{\mathrm{H}} d_{\mathrm{H_2}}^2}, \tag{4.5}$$

where h is the Planck constant, m_{H} is the mass of the hydrogen atom, $d_{\mathrm{H_2}}$ is the distance between the hydrogen atoms in H_2 and $I = 0.5 m_{\mathrm{H}} d_{\mathrm{H_2}}^2$ is the moment of inertia of H_2. In Figure 4.7 we show the average $d_{\mathrm{H_2}}$ values measured along the simulation trajectories at different densities. We note that the average separation plotted in Figure 4.7 is not equivalent to the equilibrium separation. This is because at high temperatures, the anharmonicity of the $\mathrm{H}-\mathrm{H}$ potential, which is softer for longer interatomic distances, results in an average separation that is larger than the equilibrium bond length (Kittel, 1996). The equilibrium $d_{\mathrm{H_2}}$ computed using our DFT setup is 0.74 Å and equals the experimental value (0.74 Å, Huber & Herzberg, 1979). At $\rho = 1.4\,\mathrm{g\,cm}^{-3}$, $d_{\mathrm{H_2}}$ decreases by $\approx 10\%$ with respect to the low-density values, which, according to Equation 4.5, should lead to the increase of the absorption frequency by ≈ 1.23. This is consistent with the shift of the roto-translational band observed in the simulated profiles. We thus attribute the observed frequency shift of the absorption profiles to the decrease of the $\mathrm{H}-\mathrm{H}$ bond length induced by dense helium. The frequency shift of the fundamental vibrational band requires a more detailed discussion because of the more complex distortion pattern.

(c) Distortion of the fundamental band The simulated profiles show a splitting of the fundamental vibrational band and appearance of an intermediate dip. Theses effects have not been considered in previous calculations, but such a density-induced split of the vibrational peak into Q_P and Q_R branches has been experimentally observed by Crawford et al. (1950); Chisholm & Welsh (1954); Hare & Welsh (1958); Bouanich et al. (1990). It is interpreted as an intercollisional interference effect resulting from a time correlation in the intermolecular forces (Lewis, 1976). The negative correlation resulting in the destructive interference and appearance of the dip results from the opposite direction of dipole moments induced in two successive collisions (van Kranendonk, 1968, 1980). Moreover, there are experimental indications of a density-induced shift of the dip position, which is estimated at $37\rho\,(\mathrm{g/cm}^3)\,\mathrm{cm}^{-1}$ (Lewis, 1976).

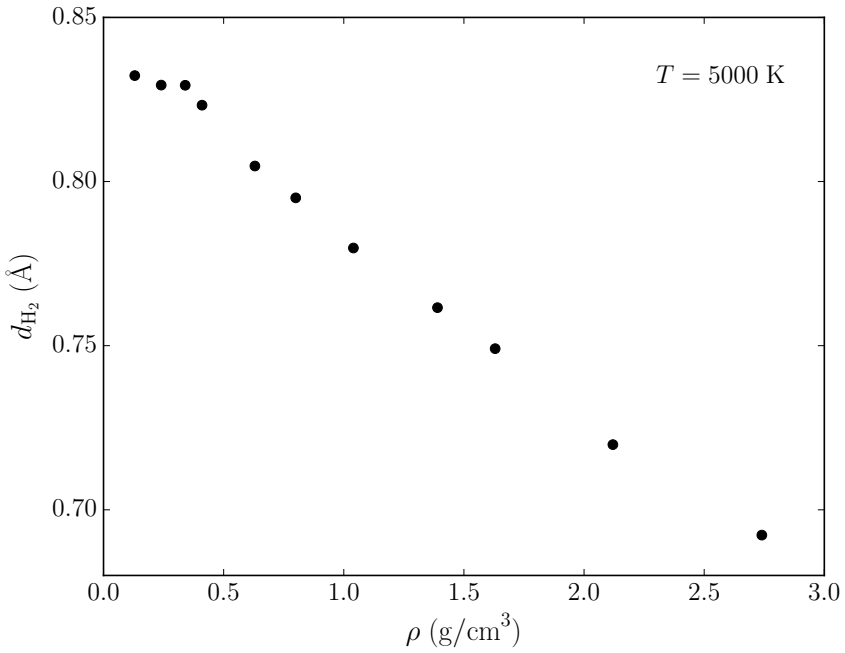

Figure 4.7 – Average separation between the two hydrogen atoms for simulations performed at different densities and at $T = 5000$ K.

The density dependence of the position of Q_P and Q_R branches and the dip are given in Figure 4.8. The positions of the Q_R branch and the dip show a linear dependence on density, while the Q_P component is almost fixed. We note that the shift of the Q_R branch is about twice as big as the shift of the dip. This is an interesting observation that requires further analysis.

We first discuss the size of the splitting into the Q_P and Q_R branches. Assuming that the splitting is caused by the interference effect, we compared the separation observed in our simulated spectra (measured as the distance between the peaks on either side of the dip) to the values reported in experimental studies (Chisholm & Welsh, 1954; Hare & Welsh, 1958). The comparison is shown in Figure 4.9. We observe that the separation increases with density (both for the simulated and experimental data) and that at a given density simulations yield a significantly higher peak separation.

The increase of the separation between the Q_P and Q_R peaks can be understood from previous theoretical considerations. Indeed, van Kranendonk (1968) demonstrated that the peak separation should be proportional to the frequency of H_2-He collisions, which increases with density. Moreover, this collision frequency dependence might explain

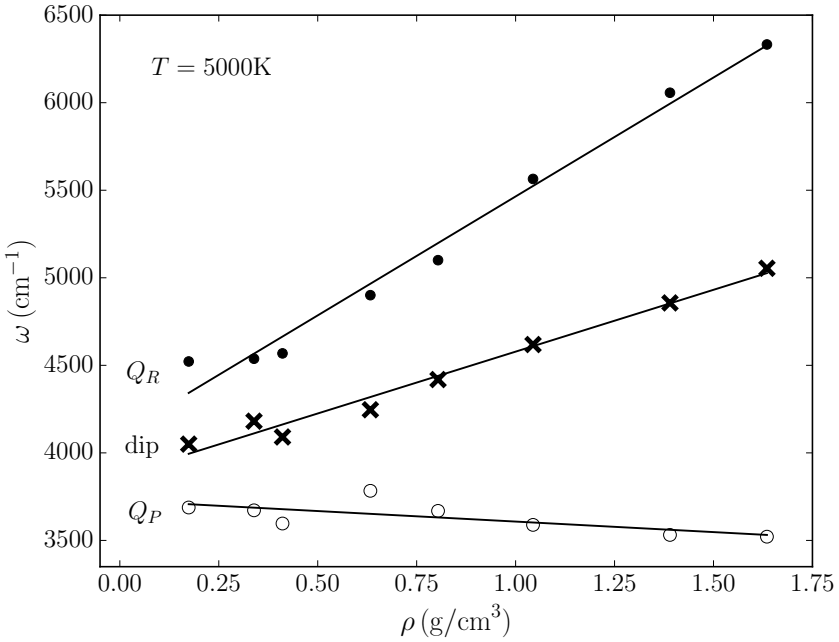

Figure 4.8 – Position of the fundamental band interference dip (crosses), Q_P branch (open circles) and Q_R branch (full circles) for various helium densities, at $T = 5000\,\mathrm{K}$. The data points were extracted from our simulation results and the lines are linear fits.

the mismatch between the experimental and simulated data as both sets of results were produced at significantly different temperature regimes. In the kinetic theory, the collision frequency is proportional to the mean particle speed $\bar{v}$, which depends on the temperature as

$$\bar{v} = \sqrt{\frac{8k_B T}{\pi m}}. \tag{4.6}$$

Since the discussed simulations were performed at 5000 K and the experimental data was collected at ambient conditions ($T = 300\,\mathrm{K}$), the collision frequency in the simulations is expected to be $(5000/300)^{1/2} \approx 4$ times higher than in the experiments. When we rescaled the simulation results by this factor, we found a good agreement with the experimental data, as shown by the open circles in Figure 4.9. This match with the experimental data further validates our simulation results.

We note that for a more straightforward comparison with the experimental data we should perform simulations assuming room temperature. Unfortunately, simulations performed at such low temperatures are problematic because of slower dynamics and of the quantum effects on atomic motions that become more pronounced. As discussed in Sec-

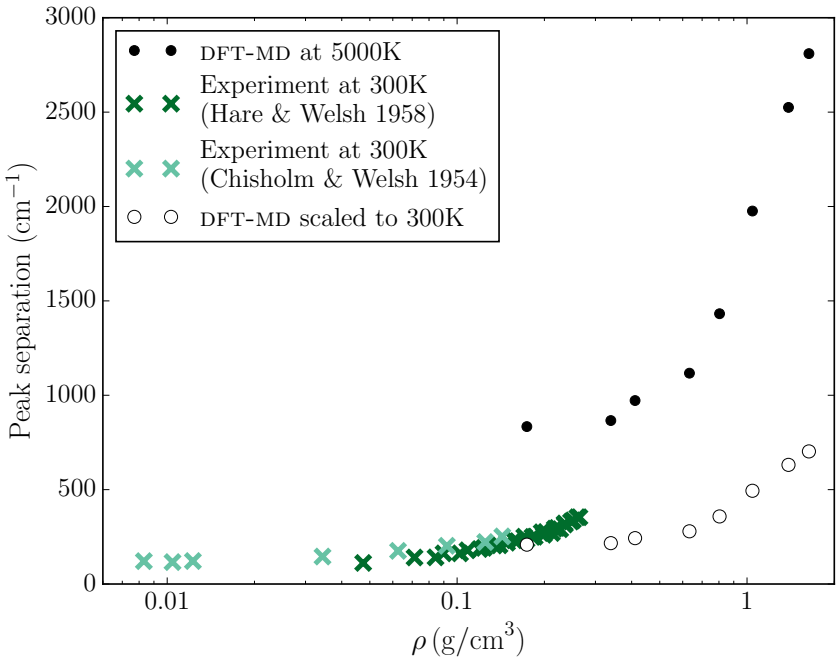

Figure 4.9 – Separation between the peaks on either sides of the fundamental band inter-collisional dip (distance between the Q_P and Q_R branches). Full circles show the results of our simulations at 5000 K, open circles are our results rescaled to 300 K (divided by a $\sqrt{5000/300}$ factor to account for the temperature difference between simulations and experiments), and crosses indicate the measurements of Chisholm & Welsh (1954) and Hare & Welsh (1958), performed at room temperature.

tion 4.3.6, these quantum effects are only approximately accounted by our simulation technique. Eventually, a more sophisticated simulation approach such as path integral molecular dynamics would give reliable results, but theses simulations are currently computationally too intensive.

Figure 4.8 indicates that the dip position is shifted linearly. Previous experimental studies have also found such a linear shift in density (Mactaggart, 1971; McKellar et al., 1975; Bouanich et al., 1990), but the experimental estimate of the shift ($37\rho\,\mathrm{g\,cm^{-3}\,cm^{-1}}$, Lewis, 1976) is smaller than the simulated value by a factor of 10. As in the case of the separation between the Q_R and Q_P branches, this could be the effect of the much higher simulated temperatures. The current theoretical explanation for this shift is that the H_2 dipole moment shifts during collisions (Lewis, 1976, 1980). These intracollisional shifts are produced in such a way that the destructive interference is maximal at a frequency that is a function of the perturber density. This also implies an asymmetry between the

low-frequency and the high-frequency wings of the dip (Lewis, 1985). This asymmetry is possibly visible in our simulations (Figure 4.5) and in experimental measurements (Kelley & Bragg, 1984).

We notice that for $\rho < 0.4\,\mathrm{g\,cm^{-3}}$ the shift of the dip visible in the simulated spectra is barely detectable. Therefore, we cannot exclude the possibility that up to these densities it is much smaller than at higher densities. Interestingly, the progress of the shift of the dip as a function of density resembles the shift of the roto-translational band. Since we explained the latter by the shortening of the separation of hydrogen atoms in H_2, it is likely that the change in the rotation of the H_2 molecule contributes to the shift of the dip. This is plausible since at large densities ($\rho > 0.4\,\mathrm{g\,cm^{-3}}$) the collisional frequency becomes comparable to the rotational frequency. The interplay of these high-density effects illustrates the complexity of the behavior of matter under fluid-like densities.

Both theoretical studies (van Kranendonk, 1968) and room-temperature experiments (Hare & Welsh, 1958) show that the fundamental band dip extends all the way down to $\alpha(\omega_{\mathrm{dip}}) = 0$. This is clearly not the case for our simulated spectra (see Figure 4.5). However, since previous studies were focusing on ambient or low-temperature conditions, little is known about the formation of intercollisional interference at high temperatures. It is highly probable that the simulated dip is shallower because of the important broadening arising under high-temperature conditions.

We note that the intercollisional interference could also explain the density-induced flux suppression of the roto-translational band at $\omega \approx 0\,\mathrm{cm^{-1}}$ observed in Figure 4.5. Theoretical arguments (van Kranendonk, 1968) suggest the presence of another intercollisional dip at $\omega = 0$. Just like the dip of the fundamental band, this dip should become wider with increasing density and gradually shift the maximum of the roto-translational band towards higher frequencies. This feature has been experimentally observed by Cunsolo & Gush (1972), who measured a $10\,\mathrm{cm^{-1}}$ wide dip for a pure H_2 gas at $\rho = 0.01\,\mathrm{g\,cm^{-3}}$ and $T = 300\,\mathrm{K}$. The simulated H_2−He CIA profiles indicate a $\approx 1000\,\mathrm{cm^{-1}}$ dip at $\rho \approx 1\,\mathrm{g\,cm^{-3}}$, which is thus consistent with the measurements for the H_2 gas. We note that very few measurements exist because of the experimental challenges associated with the low frequencies involved (Buontempo et al., 1975).

To conclude, the distortion of the fundamental band observed in the simulated absorption profiles is consistent with previous measurements and theoretical considerations. With this analysis of the three main distortion effects, we are able to proceed with the formulation of a general distortion model (Section 4.5). Before that, we briefly discuss the temperature dependence of the simulated absorption profiles.

4.4.3 Temperature dependence

So far, our analysis of the distortion effects was limited to the fixed temperature of $T = 5000\,\mathrm{K}$. To correctly set up the model of high-density distortion of CIA, we checked if the simulations correctly capture the temperature dependence of the absorption profiles. Figure 4.10 shows the temperature dependence of our simulated profiles for two different helium densities. It is clear that the simulated CIA becomes stronger with increasing temperature and the roto-translational and fundamental bands are more broadened. These two observations are consistent with previous studies (e.g., the same behavior can also be observed in Abel et al. 2012, see Figure 4.1). In addition to these two well-known effects, Figure 4.10 shows that the separation of the Q_P and Q_R branches also increases with temperature, which is also expected from the mechanism driving the intercollisional interference (see discussion in Section 4.4.2). We also note that at the highest reported temperatures the maximum of the roto-translational band is shifted towards higher frequencies, which is also visible in the results of Abel et al. 2012 (Figure 4.1). We took all these effects into account in the construction of the distortion model that is discussed in the next section.

4.5 Model of the high-density distortion of H_2−He CIA

Using our results, we designed an analytical model of the high-density distortion of the CIA profiles. The idea is that this model can be applied on top of the more accurate dilute-limit ($\rho \to 0$) calculations, and thus easily implemented in existing white dwarf atmosphere codes.

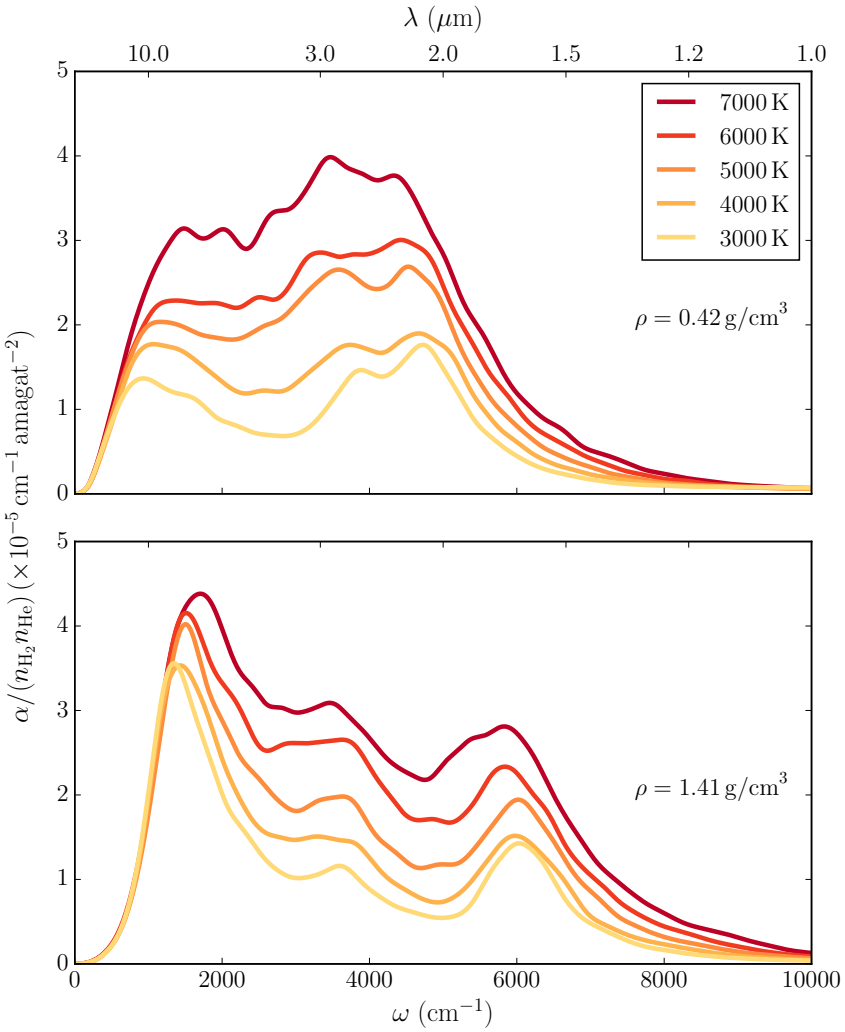

Figure 4.10 – DFT-MD H_2-He CIA profiles for 5 different temperatures (see legend) and for a density of $0.42\,\mathrm{g\,cm^{-3}}$ (top panel) and $1.41\,\mathrm{g\,cm^{-3}}$ (bottom panel).

Given a low-density limit absorption coefficient $\alpha(\omega, T)$ in $\mathrm{cm^{-1}amagat^{-2}}$ (e.g., Abel et al., 2012), ρ in $\mathrm{g\,cm^{-3}}$ and T in K, we model a distorted profile $\alpha'(\omega, T, \rho)$ as

$$\alpha'(\omega, T, \rho) = [\alpha(\omega', T)\,\mathrm{rot}(\omega', T, \rho) + \mathrm{fun}(\omega', T, \rho)] \times \mathrm{dip}(\omega', T, \rho). \tag{4.7}$$

The shifted frequency, ω', reproduces the shift of absorption profiles towards higher frequencies,

$$\omega' = (1 + 0.23\rho)\omega. \tag{4.8}$$

The linear fit found in Figure 4.8 was used to implement the density dependence of ω'. The function $\mathrm{rot}(\omega, T, \rho)$ accounts for the enhancement of the roto-translational band with increasing density,

$$\mathrm{rot}(\omega, T, \rho) = 1 + 3.15\, T_3 \rho g(\omega, 1500, 800), \tag{4.9}$$

where $T_3 = T/3000\,\mathrm{K}$ and $g(\omega, \mu, \sigma)$ is the Gaussian function,

$$g(\omega, \mu, \sigma) = \exp\left[-\frac{(\omega - \mu)^2}{2\sigma^2}\right]. \tag{4.10}$$

The density and temperature dependences of $\mathrm{rot}(\omega, T, \rho)$ were fitted to obtain the right intensity of the roto-translational band. The function $\mathrm{dip}(\omega, T, \rho)$ mimics the splitting of the fundamental band,

$$\mathrm{dip}(\omega, T, \rho) = 1 - \rho e^{-\rho} g(\omega, 4100 - 50T_3, 800\rho). \tag{4.11}$$

The temperature dependence of the center of the Gaussian function in Equation 4.11 takes into account the slight shift of the fundamental vibrational band intercollisional dip with respect to temperature (see lower panel of Figure 4.10). The density dependence of the width of the Gaussian function accounts for the increased peak separation at higher density (see Figure 4.9). Finally, the $\mathrm{fun}(\omega, T, \rho)$ function accounts for the shift of the fundamental band and the gradual disappearance of the minimum between the roto-translational and fundamental bands,

$$\begin{aligned}\mathrm{fun}(\omega, T, \rho) =& 5T_3^{0.5} g(\omega, 4000 - 200\rho T_3, 400T_3^{0.5}) \times 10^{-5} \rho e^{-1.2\rho} \\ &+ 2T_3 g(\omega, 2800, 500) \times 10^{-5} \rho e^{-2\rho}.\end{aligned} \tag{4.12}$$

Equation 4.12 was found by visually fitting the simulated spectra for all (T, ρ) conditions considered in this work. Figure 4.11 compares the simulated CIA profiles, the spectra of Abel et al. 2012 (scaled to account for three-body interactions, as discussed in Section 4.4.1) and the spectra given by our analytical model. Overall, the model reproduces well the main distortion effects described in the previous sections. We note that some arbitrary choices were made in the design of the distortion model, but our goal was to derive an analytical model that reproduces our simulated profiles and which can be applied on top

of the H_2-He CIA profiles used in white dwarf atmosphere codes. Certainly, a better understanding of the distortion—obtained either through future experimental studies or more accurate simulations—may result in a simpler and more physically grounded model.

4.6 Implications for the modeling of the atmosphere of cool white dwarf stars

Our simulations have revealed important high-density distortions of the strength and the shape of H_2-He CIA profiles. Using the model described in Section 4.5, we implemented these distortions in our atmosphere code to investigate how they affect the synthetic spectra of cool, helium-rich white dwarf stars.

4.6.1 Description of the atmosphere code

The local thermodynamic equilibrium (LTE) atmosphere model code we use is based on the one described in Bergeron et al. (1995), with the improvements discussed in Tremblay & Bergeron (2009) and Bergeron et al. (2011). It was further modified to include several nonideal effects required to properly describe the dense atmosphere of cool helium-rich white dwarf stars. In particular, it includes the nonideal H_2 dissociation equilibrium described by Kowalski (2006b), the nonideal chemical potentials of helium reported by Kowalski et al. (2007), the He−He−He CIA opacities found by Kowalski (2014), and high-density corrections to the free-free absorption of He^- and to Rayleigh scattering (Iglesias et al., 2002). Moreover, the energy density and the total number density of each atmospheric layer are computed using the H−REOS.3 and He−REOS.3 ab initio equations of state for hydrogen and helium (Becker et al., 2014). For mixed H/He compositions, we use the additive volume rule to compute the mass density $\rho(P,T)$ and the internal energy density $u(P,T)$,

$$\frac{1}{\rho_{\rm mix}(P,T)} = \frac{X}{\rho_{\rm H}(P,T)} + \frac{Y}{\rho_{\rm He}(P,T)}, \tag{4.13}$$

$$u_{\rm mix}(P,T) = X u_{\rm H}(P,T) + Y u_{\rm He}(P,T), \tag{4.14}$$

where X and Y are respectively the mass fractions of hydrogen and helium. Although it does not represent an exact treatment of H/He mixtures, Becker et al. (2014) showed

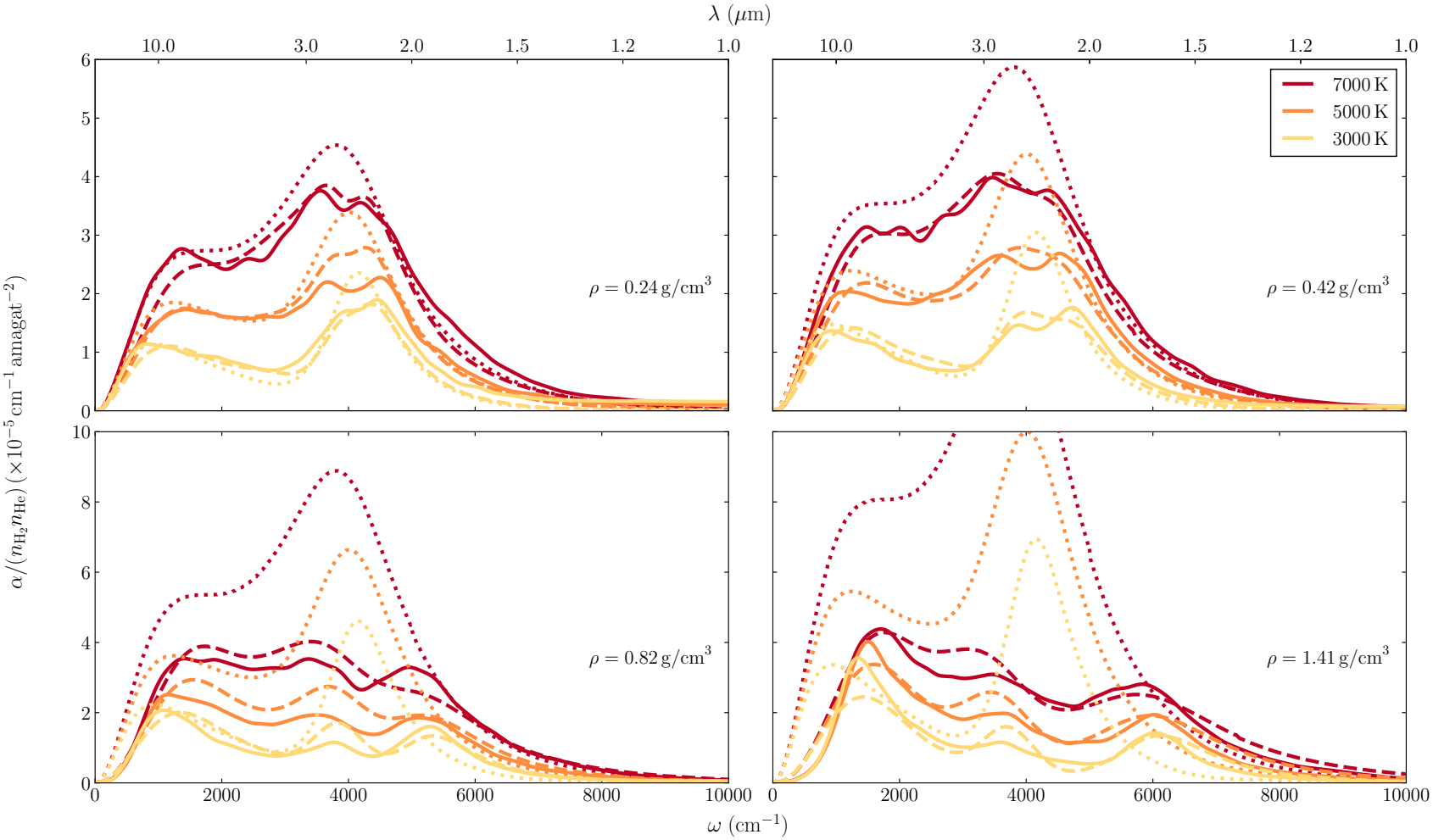

Figure 4.11 – Comparison between our absorption profiles (solid lines), the spectra obtained from our analytical distortion model (dashed lines, Section 4.5) and the spectra of Abel et al. (2012) scaled for many-body interactions following the method described in Section 4.4.1 (dotted lines). The scale of the vertical axis is not the same for the top and the bottom plots.

that using Equations 5.10 and 5.11 yields values that are in good agreement with the real mixture results of Militzer & Hubbard (2013), obtained through DFT-MD calculations.

4.6.2 Synthetic spectra

Figure 4.12 compares the synthetic spectra computed with the new H_2-He CIA profiles to those computed with the spectra of Abel et al. (2012), for various $T_{\rm eff}$ and hydrogen abundances. Accounting for high-density effects in the H_2-He CIA results in two important changes. First, a flux depletion redward of 2 μm is observed. This effect is a direct consequence of the many-body collisions that arise at high density and cause an important CIA intensity gain. Secondly, we notice a slight distortion of the absorption band at 2.3 μm. This distortion is the result of the fundamental H_2-He CIA band splitting and shifting. As the absorption bands observed in the synthetic spectra are the result of the sum of the contributions of different atmospheric layers (which have different temperatures and densities), the splitting of the fundamental band is not directly visible.

Figure 4.12 shows that high-pressure CIA distortion effects are more important in the cooler atmospheres. This trend is a direct consequence of the higher photospheric density of low-$T_{\rm eff}$ models. When the temperature is low, there are fewer electrons, which results in a reduction of He^- free-free absorption and an increased transparency of the atmosphere. This raises the density at the photosphere of the star (see Figure 4.13), which leads to a stronger distortion of CIA.

Figure 4.12 also shows that the discrepancies between the new and old synthetic spectra are mostly important at intermediate hydrogen abundances (around $\log {\rm H/He} = -3$). This is the result of the competition between two mechanisms. On one hand, a high hydrogen abundance results in stronger H_2-He CIA features, since there is more H_2 in the atmosphere. On the other hand, if the atmosphere contains too much molecular hydrogen, it is more opaque and the photosphere is less dense (see Figure 4.13). This explains why the distortion of CIA is stronger at $\log {\rm H/He} = -3$ than at $\log {\rm H/He} = -1$ (where the density is too low to produce significant distortion effects) or $\log {\rm H/He} = -5$ (where there is too little H_2 to produce significant H_2-He CIA features).

In general, the density-distorted CIA profiles can contribute to our understanding of the SED of some puzzling cool, helium-rich white dwarf stars. In particular, they might help

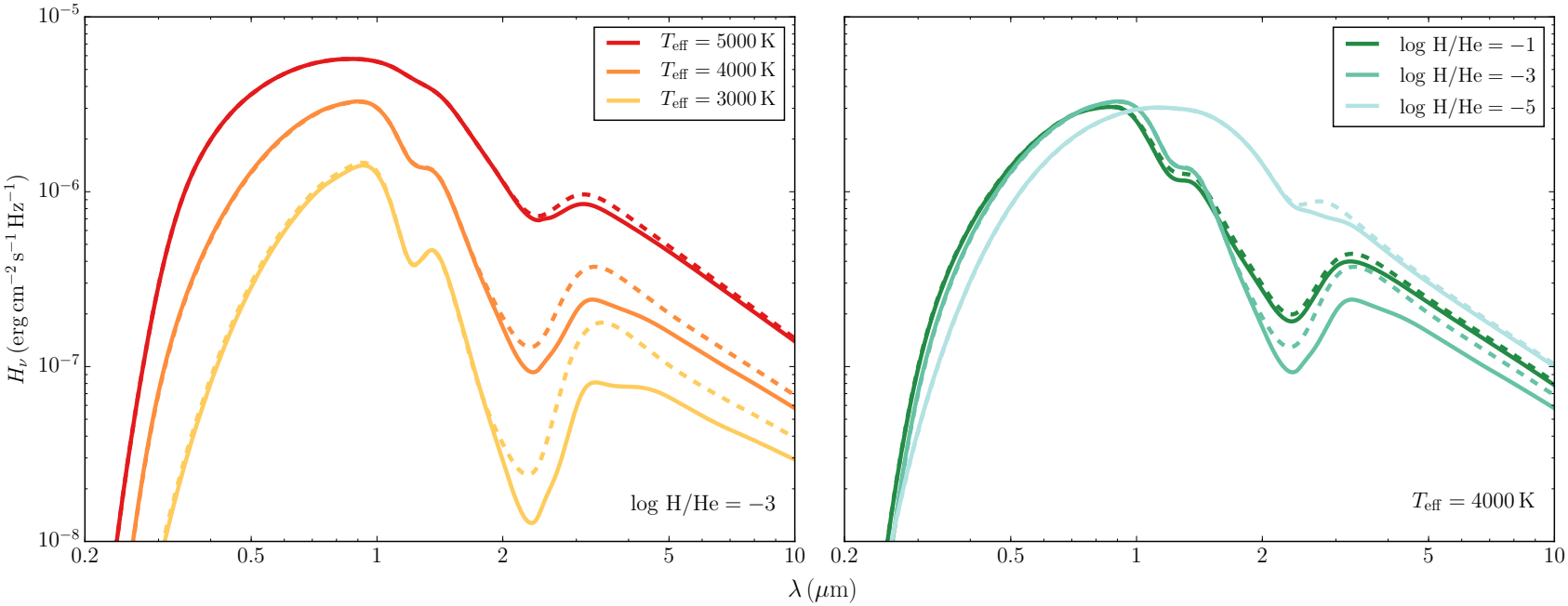

Figure 4.12 – Synthetic spectra computed with our distorted H_2−He CIA spectra (solid lines) and with the spectra of Abel et al. 2012 (dashed lines). The left plot shows spectra obtained with $\log \mathrm{H/He} = -3$ and various effective temperatures, while the right plot shows results obtained with various hydrogen abundances and a fix $T_{\rm eff} = 4000\,\mathrm{K}$ effective temperature. All spectra were computed assuming $\log g = 8$.

explain the flux minimum observed in the $3-7\,\mu$m region of the spectrum of LHS 3250, as opposite to the minimum at $2.3\,\mu$m predicted by the models (see the comparisons between *Spitzer* photometry and atmosphere models in Kilic et al., 2009a; Kowalski et al., 2013). In fact, our new CIA profiles at high densities lead to a significant decrease of the absorption at the position of the fundamental band and an enhancement of the roto-translational band ($3-10\,\mu$m). This could explain the spectrum of LHS 3250 if the photospheric density for this star is sufficiently high ($\rho > 1.5\,\mathrm{g\,cm^{-3}}$).

The spectra shown in Figure 4.12 indicate that the distortion effects are not strong enough (or the photospheric density is too low) to improve the fit of this particular star. However, we note that this discrepancy may be caused by a too strong pressure-induced ionization of helium by the chemical equilibrium model implemented in the code. Namely, a slightly reduced ionization would produce less free electrons and thus potentially increase the photospheric density so the CIA distortion could better match the observed spectra of cool, helium-rich stars. Indeed, when computing a model with $T_{\rm eff} = 4000\,\mathrm{K}$, $\log\,\mathrm{H/He} = -3$ and $\log g = 8$ using the nonideal helium ionization equilibrium of Kowalski et al. (2007), we find a photospheric density of $0.7\,\mathrm{g\,cm^{-3}}$. For the same atmospheric parameters, if we use the ideal Saha equation to compute the helium ionization equilibrium, the density at the photosphere reaches $1.5\,\mathrm{g\,cm^{-3}}$. Since the density at the photosphere depends strongly on helium ionization equilibrium, a slight change in it might result in major changes to the signature of H_2-He CIA in the synthetic spectra.

Furthermore, the ionization equilibrium of helium also depends on the applied EOS (Bergeron et al., 1995). This indicates that all problems related to the modeling of these extreme atmospheres must be solved to obtain a satisfactory and final fit to the entire SED of cool, helium-rich stars.

4.7 Conclusion

We applied the ab initio molecular dynamics method to simulate the distortion of H_2-He CIA at high densities and temperatures that resemble the physical conditions found at the photospheres of cool, helium-rich white dwarf stars. At low densities the obtained absorption profiles are consistent with previous calculations and experimental data. However, under high-density conditions ($\rho > 0.1\,\mathrm{g\,cm^{-3}}$), we found that the H_2-He CIA

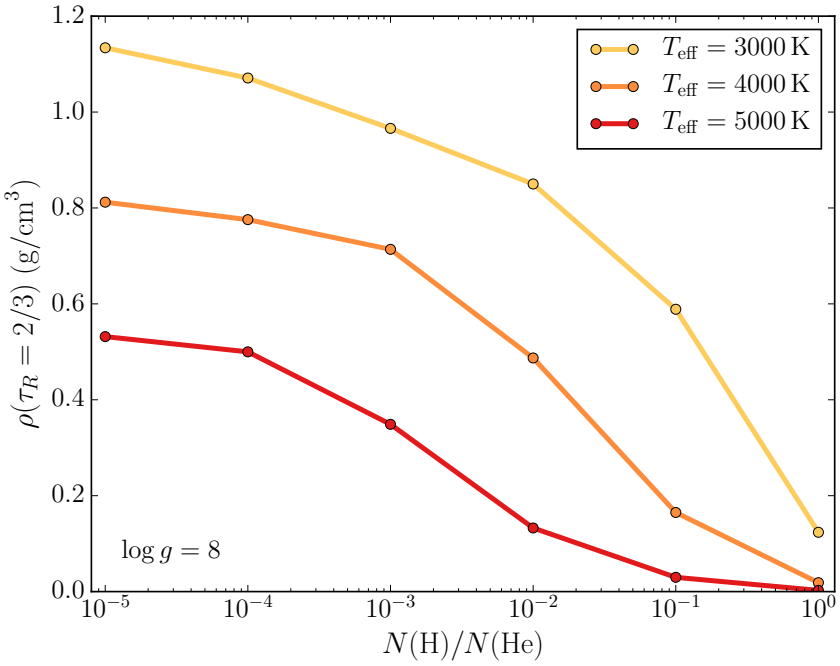

Figure 4.13 – Density of our atmosphere models at a Rosseland optical depth $\tau_R = 2/3$, as a function of $T_{\rm eff}$ and the hydrogen abundance. These calculations were made assuming $\log g = 8$.

absorption becomes significantly distorted in a way that is not accounted by current models, but that is consistent with experimental findings. For densities beyond $0.1\,{\rm g\,cm^{-3}}$, the integrated absorption profile increases because of multi-atomic collisions, the absorption is shifted towards higher frequencies and the fundamental vibrational band is split. We provided a detailed analysis of these phenomena and constructed an analytical model of the distortion that can be easily applied on top of any low-density H_2-He CIA absorption profiles used in current white dwarfs atmosphere codes.

The density-driven evolution of the distortion of H_2-He CIA changes the maximum of the absorption from $2.3\,\mu$m to $3-7\,\mu$m, through the enhancement of the roto-transitional absorption peak and the depletion of the vibrational band. This behavior seems to be consistent with the spectra of some cool, helium rich stars, including LHS 3250. The simulations of the representative white dwarf spectra indicate that these distortion effects can significantly affect their mid-IR spectra. They are particularly important for objects cooler than $T_{\rm eff} = 4000\,{\rm K}$ with mixed H/He atmospheres. However, the strength of the distor-

tion depends on the photospheric density, which is governed by the still highly uncertain ionization equilibrium of helium.

While the new high-density H_2-He CIA distorted spectra might be part of the solution to explain the peculiar SED of some cool white dwarf stars, further effort on the constitutive physics of cool, helium-rich white dwarf atmospheres is needed before we can obtain reliable spectral fits for these objects. In particular, the helium ionization equilibrium, which determines the photospheric density and thus the strength of the CIA profile distortion, must be revisited.

Acknowledgments This work was supported in part by NSERC (Canada). S.B. acknowledges financial support from DAAD (Germany) for his research stay at Forschungszentrum Jülich GmbH.

CHAPITRE 5

A New Generation of Cool White Dwarf Atmosphere Models. I. Theoretical Framework and Applications to DZ Stars

All models are wrong, but some are useful.

—George E. P. Box (1919−2013), statisticien britannique

Ce chapitre est une adaptation de «A New Generation of Cool White Dwarf Atmosphere Models. I. Theoretical Framework and Applications to DZ Stars», par Simon Blouin, Patrick Dufour et Nicole F. Allard. Cet article a été publié en août 2018 dans *The Astrophysical Journal*.[1]

5.1 Abstract

The photospheres of the coolest helium-atmosphere white dwarfs are characterized by fluidlike densities. Under those conditions, standard approximations used in model atmosphere codes are no longer appropriate. Unfortunately, the majority of cool He-rich white dwarfs show no spectral features, giving us no opportunities to put more elaborate models to the test. In the few cases where spectral features are observed (such as in cool DQ or DZ stars), current models completely fail to reproduce the spectroscopic data, signaling shortcomings in our theoretical framework. In order to fully trust parameters derived solely from the energy distribution, it is thus important to at least succeed in reproducing

[1]Blouin, S., Dufour, P., & Allard, N. F. 2018, ApJ, 863, 184.

the spectra of the few coolest stars exhibiting spectral features, especially since such stars possess even less extreme physical conditions due to the presence of heavy elements. In this paper, we revise every building block of our model atmosphere code in order to eliminate low-density approximations. Our updated white dwarf atmosphere code incorporates state-of-the-art constitutive physics suitable for the conditions found in cool helium-rich stars (DC and DZ white dwarfs). This includes new high-density metal-line profiles, non-ideal continuum opacities, an accurate equation of state and a detailed description of the ionization equilibrium. In particular, we present new ab initio calculations to assess the ionization equilibrium of heavy elements (C, Ca, Fe, Mg and Na) in a dense helium medium and show how our improved models allow us to achieve better spectral fits for two cool DZ stars, Ross 640 and LP 658−2.

5.2 Introduction

Pure helium-rich white dwarfs do not show any spectral lines when $T_{\rm eff} \lesssim 10\,000\,{\rm K}$. The same occurs for $T_{\rm eff} \lesssim 5000\,{\rm K}$ in the case of pure hydrogen-rich atmospheres. Together, these featureless white dwarfs are known as DC stars. One is thus forced to rely solely on the shape of the spectral energy distribution to deduce the chemical composition and effective temperature of these white dwarfs (Bergeron et al., 1997, 2001). Although most cool white dwarfs have featureless spectra, some cool helium-rich white dwarfs do show significant spectral features that can be exploited to retrieve additional information on the physical conditions encountered in their atmospheres. Some contain enough hydrogen to show strong H_2-He collision-induced absorption (CIA) features, some show C_2 Swan bands (DQ and DQpec stars) and others show metal lines (DZ stars). Interestingly, in all cases, models fail to reproduce these spectra. For instance, the CIA is inadequately modeled (e.g., LHS 3250, SDSS J123812.85+350249.1, SDSS J125106.11+440303.0, Giannas et al., 2015), the C_2 bands are distorted (e.g., LHS 290, Kowalski, 2010) and the metal absorption lines often do not have the right strength or the right shape (e.g., WD J2356−209, Bergeron et al. 2005; Homeier et al. 2005, 2007, LP 658−2, Dufour et al. 2007; Wolff et al. 2002).

For all these stars, the discrepancies between models and observations can be related to nonideal high-density effects arising at the photosphere since for cool ($T_{\rm eff} < 6000\,{\rm K}$)

helium-rich white dwarfs, densities reach fluidlike values. At a Rosseland optical depth $\tau_R = 2/3$, density can be as high as $1\,\mathrm{g\,cm^{-3}}$ (Bergeron et al., 1995; Kowalski, 2010), which corresponds to a fluid where the separation between atoms is roughly equivalent to the dimension of atoms themselves. Clearly, under such conditions, interactions between species are no longer negligible and the ideal gas approximation must be discarded.

The nonideal effects arising from this high density have remained mostly unnoticed for DC stars, since a featureless spectrum provides little opportunity to test the accuracy of atmosphere models. In contrast, cool helium-rich stars with spectral features (i.e., DQpec, DZ and those with CIA features) provide a real challenge to atmosphere models and an opportunity to test our understanding of the chemistry and physics of warm dense helium.

In this series of papers, we present and apply our new generation of atmosphere models for cool white dwarf stars. In the first paper of the series, we focus on improving our modeling of cool DZ stars. Note that obtaining better fits of these objects is far more than a mere aesthetic whim. Indeed, because they show spectral lines, cool DZ stars represent a unique opportunity to probe the physics and chemistry of cool helium-rich atmospheres. In a way, they allow us to test the models used for DC stars. Once we will have proven that our new models are able to reproduce the rich and complex spectra of cool DZ stars, we will be confident that the constitutive physics is accurate and that the models can reliably be used to measure the atmospheric parameters of all DC stars in general.

This paper describes our new model atmosphere code that includes all nonideal effects relevant for the modeling of the atmospheres of cool DZ and DC stars. This updated atmosphere code is based on the one described in Dufour et al. (2007). Building on other published works, as well as on our own new calculations, we have considerably improved the constitutive physics in our code. Section 5.3 describes the additions made to correctly calculate radiative opacities and, in Section 5.4, we discuss the improvements related to the equation of state and the chemical equilibrium. Among the new physics added to the chemical equilibrium calculations, we used ab initio techniques to implement a state-of-the-art description of the chemical equilibrium of heavy elements (C, Ca, Fe, Mg and Na) in the dense atmosphere of cool DZ stars. These calculations are detailed at length in Section 5.5. In Section 5.6, we present two applications that show how the improvements

included in our models translate in terms of spectroscopic fits. Finally, in Section 5.7, we summarize our results and outline the upcoming papers of this series.

5.3 Radiative opacities

In this section, we describe the additions brought to the code of Dufour et al. (2007) regarding the calculation of radiative opacities. This includes improved line profiles, high-density CIA distortion and continuum opacities corrected for collective interactions.

5.3.1 Line profiles

In the atmosphere of cool DZ stars, the wings of heavy-element absorption lines are severely broadened by interactions with neutral helium. Hence, Lorentzian profiles poorly reproduce observed spectral features. It is thus an absolute necessity to implement the unified line shape theory described in Allard et al. (1999) to treat such line profiles. We implemented this formalism for the strongest transitions found in cool DZ white dwarfs (see Table 5.1). In particular, the line profiles described in Allard & Alekseev (2014) and Allard et al. (2014, 2016a,b, 2018) are used to compute the wings and a conventional Lorentzian profile is assumed for the core of the spectral lines, where the density is low enough for this approximation to hold. To connect the two profiles, we use a hyperbolic tangent function, which allows a smooth transition. It should also be noted that our Ca I 4226 Å profile is still preliminary, as we do not yet have access to the high-quality ab initio potentials required for the computation of this particular line profile. To make up for this lack, we computed our own ab initio potentials through open-shell configuration-interaction singles calculations with the ROCIS module of the ORCA quantum chemistry package[2] (Neese, 2012).

For transitions not listed in Table 5.1, our code assumes a simple Lorentzian function or quasistatic van der Waals broadening (Walkup et al. 1984; D. Koester 2018, private communication). Note that the exact treatment of these secondary transitions has a limited impact on our atmospheric determinations.

We show in Figure 5.1 a comparison of line profiles calculated using the theory of Allard et al. (1999) to those found assuming a Lorentzian profile for temperature and

[2] https://orcaforum.cec.mpg.de

Lines	Source
Ca I 4226 Å	Allard (2018, private communication)
Ca II H & K	Allard & Alekseev (2014)
Mg I 2852 Å	Allard et al. (2018)
Mg II 2795/2802 Å	Allard et al. (2016a)
Mgb triplet	Allard et al. (2016b)
Na I D doublet	Allard et al. (2014)

Table 5.1 – Metal-line profiles computed using the unified line shape theory described in Allard et al. (1999)

density conditions representative of the photosphere of cool DZ stars. Clearly, under such conditions, the Lorentzian function fails to provide a satisfactory description of the line profiles. It underestimates the strong broadening observed in the more accurate line profiles and does not take into account the distortion and shift observed for many transitions.

5.3.2 Collision-induced absorption

The calculation of the H_2-He CIA includes the high-density distortion effects described in Blouin et al. (2017). This pressure distortion effect alters the infrared energy distribution of cool DZ stars with hydrogen in their atmosphere and a photospheric density greater than $\approx 0.1\,\mathrm{g\,cm^{-3}}$ ($n_{\mathrm{He}} = 1.5 \times 10^{22}\,\mathrm{cm^{-3}}$). Moreover, we have also included the He−He−He CIA using the analytical fits given in Kowalski (2014).

5.3.3 Rayleigh scattering

In a dense helium medium, collective interactions between atoms lead to a reduction of the Rayleigh scattering cross section (Iglesias et al., 2002). For the wavelength domain relevant for white dwarf modeling (i.e., in the low-frequency limit), the reduced cross section can be expressed as (Kowalski, 2006a; Rohrmann, 2018)

$$\sigma_{\mathrm{Rayleigh}}(\omega) = S(0)\sigma^0_{\mathrm{Rayleigh}}(\omega), \tag{5.1}$$

where $\sigma^0_{\rm Rayleigh}(\omega)$ is the ideal gas result (e.g., Dalgarno, 1962) and $S(0)$ is the structure factor of the fluid at a wavenumber $k = 0$. Therefore, to take into account the reduction of the Rayleigh scattering, we simply need to know $S(0)$, which is a function of the temperature and the density of the helium fluid. To compute $S(0)$, we use the analytical fit to the Monte Carlo results of Rohrmann (2018).

5.3.4 He^- free-free absorption

Iglesias et al. (2002) also showed that the free-free absorption cross section of the negative helium ion is reduced in a dense helium medium. Given that it is the dominant source of opacity in DZ stars, it is important to take this reduction into account. The corrected cross section for He^- free-free absorption is given by (Iglesias et al., 2002)

$$\sigma_{\rm ff}(\omega) = \delta_{\rm ff}(\omega)\sigma^0_{\rm ff}(\omega), \tag{5.2}$$

where $\sigma^0_{\rm ff}(\omega)$ is the ideal gas result (e.g., John, 1994). Here $\delta_{\rm ff}(\omega)$ can be computed as (Iglesias et al., 2002)

$$\delta_{\rm ff}(\omega) = \frac{\int_0^\infty I(k){\rm d}k}{\int_0^\infty I_0(k){\rm d}k}, \tag{5.3}$$

where

$$I(k) = I_0(k)\frac{S(k)}{|\epsilon(\omega)|^2} \tag{5.4}$$

and

$$I_0(k) = \frac{1}{k}\exp\left[-\frac{\hbar^2}{2m_e k_B T}\left(\frac{k}{2} - \frac{m_e\omega}{\hbar k}\right)^2\right] \times \left|\frac{k^2\mathcal{F}\left[\phi_{\rm e-He}(r)\right]}{4\pi e^2}\right|^2. \tag{5.5}$$

In the last expressions, $\epsilon(\omega)$ is the dielectric function, m_e and e are the electron mass and charge, k_B is the Boltzmann constant, $\hbar$ is the reduced Planck constant and $\mathcal{F}\left[\phi_{\rm e-He}(r)\right]$ is the Fourier transform of the electron-helium potential, for which we use the simple form given by Equations 3.5 and 3.6 of Iglesias et al. (2002). From these equations, it follows that two external inputs are needed to compute $\delta_{\rm ff}(\omega)$: (1) the structure factor $S(k)$, and (2) the index of refraction of helium $n(\omega) = \sqrt{\epsilon(\omega)}$. The details regarding the calculation of the structure factor are given below, while our evaluation of the index of refraction is described in Section 5.3.5.

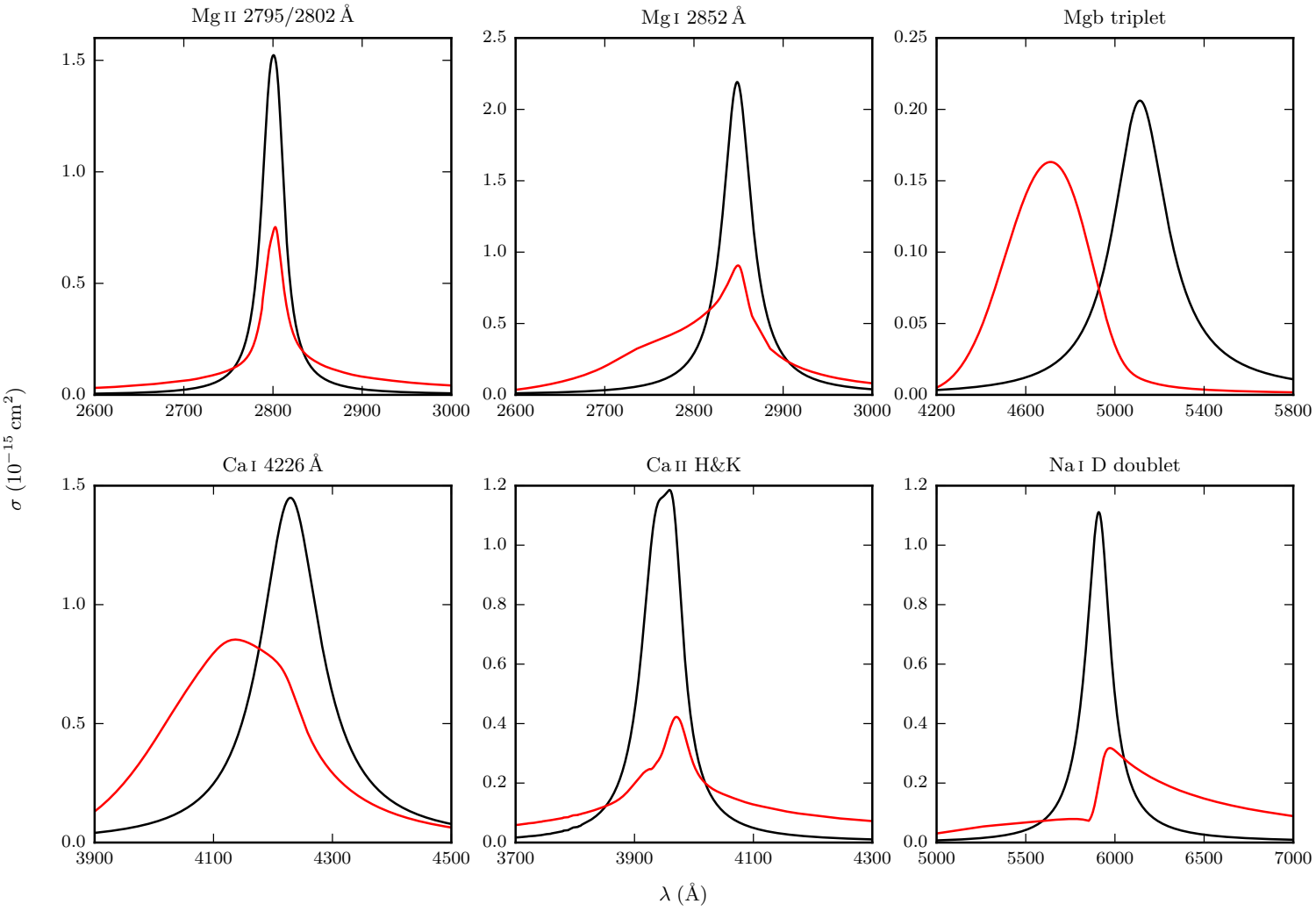

Figure 5.1 – Absorption cross section of metal spectral lines. The black lines correspond to the Lorentzian profiles and the red ones are the profiles obtained with the unified line shape theory of Allard et al. (1999). These line profiles were computed assuming $T = 6000\,\mathrm{K}$ and $n_{\mathrm{He}} = 10^{22}\,\mathrm{cm}^{-3}$. Note that the improved line profile for Ca I 4226 Å relies on approximate potentials (see text).

To compute $S(k)$, we rely on the classical fluid theory and the Ornstein–Zernike (OZ) equation. To solve the OZ equation, we use the Percus–Yevick closure relation (Percus & Yevick, 1958), since it is well-suited for fluids dominated by short-range interactions (i.e., non-Coulombic interactions ; Hansen & McDonald 2013). The calculations are performed using a modified version of pyOZ[3]. Figure 5.2 compares our $S(0)$ values to the $S(0)$ analytical fit given in Rohrmann (2018). The agreement between both datasets is satisfactory under $\rho = 1\,\mathrm{g\,cm^{-3}}$ ($n_{\mathrm{He}} = 1.5 \times 10^{23}\,\mathrm{cm^{-3}}$), but worsens at higher densities. This disagreement reflects the limitations of the Percus–Yevick closure relation at high densities in a regime where the Monte Carlo calculations of Rohrmann (2018) are more appropriate. Nevertheless, this small discrepancy is of limited importance in the context of the modeling of cool DZ stars, since the photospheric density of our models never exceeds $\approx 1\,\mathrm{g\,cm^{-3}}$.

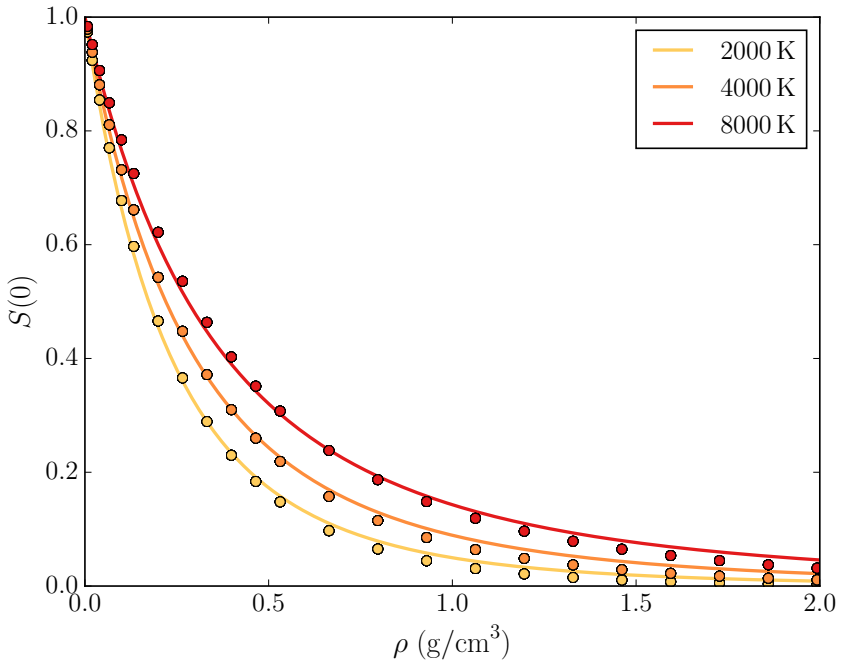

Figure 5.2 – Structure factor at $k = 0$ as a function of density and for different temperatures. The solid lines show the analytical fits obtained by Rohrmann (2018) from Monte Carlo calculations and the circles show the results we found by solving the OZ equation.

[3] http://pyoz.vrbka.net

5.3.5 Index of refraction

The index of refraction, which is needed to compute the correction to the He^- free-free cross section (Equations 5.3 and 5.4), is obtained from the Lorentz–Lorenz equation,

$$\frac{n^2-1}{n^2+2} = A_R\left(\frac{n_{\rm He}a_0^3}{N_A}\right) + B_R\left(\frac{n_{\rm He}a_0^3}{N_A}\right)^2 + \mathcal{O}(n_{\rm He}^3), \tag{5.6}$$

where A_R and B_R are the first and the second refractivity virial coefficients, $n_{\rm He}$ is the helium number density, a_o is the Bohr radius and N_A is the Avogadro constant. Here A_R is proportional to the atomic polarizability $\alpha(\omega)$ and is given by

$$A_R(\omega) = \frac{4\pi N_A \alpha(\omega)}{3}. \tag{5.7}$$

To compute A_R, we use the helium polarizability values reported in Masili & Starace (2003). For the second refractivity virial coefficient, we rely on the classical statistical mechanics expression (e.g., Fernández et al., 1999)

$$B_R(\omega, T) = \frac{8N_A^2\pi^2}{3}\int_0^\infty \Delta\alpha_{\rm ave}(\omega, r)\exp\left[-\frac{\phi(r)}{k_B T}\right] r^2 dr, \tag{5.8}$$

where $\Delta\alpha_{\rm ave}(\omega, r)$ is the interaction-induced isotropic polarizability and $\phi(r)$ is the helium-helium interatomic potential. To compute $\Delta\alpha_{\rm ave}(\omega, r)$, we turn to the expansion

$$\Delta\alpha_{\rm ave}(\omega, r) = \Delta\alpha_{\rm ave}(0, r) + \omega^2\Delta S(-4, r) + \mathcal{O}(\omega^4), \tag{5.9}$$

where $\Delta\alpha_{\rm ave}(0, r)$ is given in Hättig et al. (1999) and Maroulis (2000), and the Cauchy moment $\Delta S(-4, r)$ is given in Hättig et al. (1999). Finally, for the interaction potential $\phi(r)$ in Equation 5.8, we use the effective pair potential of Ross & Young (1986), which is calibrated to fit experimental data for high-density helium.

To validate our analytical model of the index of refraction, we compared its predicted values with the high-pressure experimental measurements of Dewaele et al. (2003). This comparison is shown in Figure 5.3 and reveals no significant deviation between our values and the laboratory measurements. Additionally, we checked that our index of refraction values are virtually identical to those obtained by Rohrmann (2018).

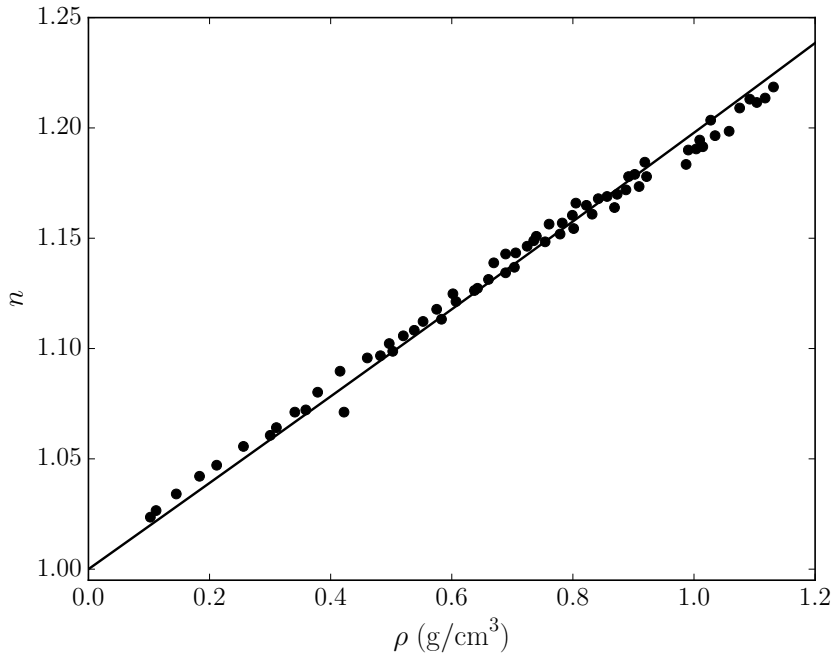

Figure 5.3 – Index of refraction of helium as a function of density. The line corresponds to the results of our calculations with Equations 5.6, 5.7 and 5.8, and the circles are the laboratory measurements extracted from Dewaele et al. (2003). For both datasets, $T = 300\,\mathrm{K}$ and $\lambda = 6328\,\mathrm{\AA}$.

5.4 Equation of state and chemical equilibrium

In this Section, we describe how the equation of state and the chemical equilibrium calculations were modified to take high-density nonideal effects into account.

5.4.1 Equation of state

The total number density and the internal energy density in each atmospheric layer are computed using the ab initio equations of state for hydrogen and helium published by Becker et al. (2014). As in Blouin et al. (2017), we resort to the additive volume rule for mixed H/He compositions. The mass density $\rho(P,T)$ and the internal energy density $u(P,T)$ are given by

$$\frac{1}{\rho_{\rm mix}(P,T)} = \frac{X}{\rho_{\rm H}(P,T)} + \frac{Y}{\rho_{\rm He}(P,T)}, \tag{5.10}$$

$$u_{\rm mix}(P,T) = X u_{\rm H}(P,T) + Y u_{\rm He}(P,T), \tag{5.11}$$

where X and Y are the mass fractions of hydrogen and helium, respectively.

For the densest cool DZ stars, the pressure at the photosphere exceeds $10^{11}\,\mathrm{dyn\,cm^{-2}}$. Under such conditions, using the ideal gas law can lead to an important overestimation of the density. In fact, as shown in Figure 5.4, the ideal gas density can be up to a factor of 5 greater than the value found when using the equation of state of Becker et al. (2014). Such a difference can have a significant effect on the computed atmosphere structure and the synthetic spectrum, since most nonideal effects included in the code (e.g., detailed line profiles, distorted CIA profiles, high-density continuum opacities, nonideal chemical equilibrium) are parameterized as functions of the density. For instance, using the ideal gas law would lead to an overestimation of the broadening of spectral lines due to an overestimation of the density of perturbing helium atoms.

5.4.2 Chemical equilibrium

To compute the ionization equilibrium of helium, we rely on the chemical model proposed by Kowalski et al. (2007). Since it does not rely on any free parameter, this ionization equilibrium model is a major improvement over the occupation probability formalism (Hummer & Mihalas, 1988; Mihalas et al., 1988) used in most white dwarf atmosphere codes. Compared to models where the ideal Saha equation is assumed, DZ models that include the helium ionization equilibrium of Kowalski et al. (2007) reach slightly lower densities in their deepest layers. This is the result of pressure ionization, which increases the electronic density and, in turn, the opacity. However, this effect is not as important as in metal-free atmospheres, since heavy elements provide the majority of free electrons and therefore govern the atmosphere structure. We have also included a detailed description of the ionization equilibrium of heavy elements, which is the subject of Section 5.5.

5.5 Ionization equilibrium of heavy elements

Properly characterizing the ionization equilibrium of heavy elements in the atmosphere of cool DZ stars is important from several perspectives. First, accurate ionization ratios are necessary to obtain the right spectral-line depths. For instance, in the case of a star that shows both Ca II H & K and Ca I 4226 Å in its spectrum, obtaining the right Ca II/Ca I ratio is a prerequisite for simultaneously reproducing all spectral lines. Moreover, in cool DZ

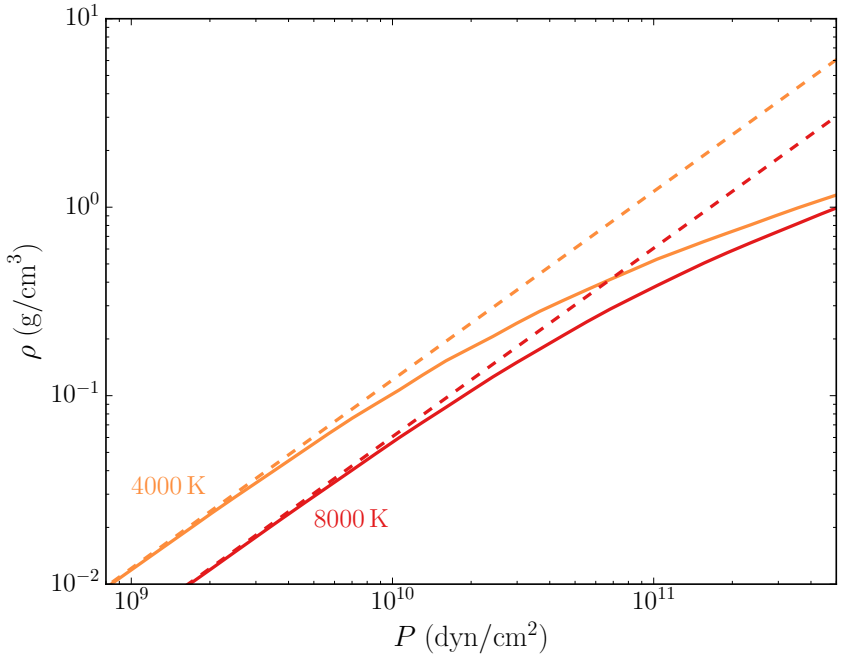

Figure 5.4 – Density of a helium medium as a function of pressure and temperature. The solid lines show the results found when using the equation of state of Becker et al. (2014) and the dashed lines correspond to the case where the ideal gas law is assumed.

stars, heavy elements provide most of the electrons. Therefore, a change in the ionization equilibrium of these trace species can influence other opacity sources (most importantly He^- free-free), and hence the whole structure of the atmosphere.

Unlike the rest of the nonideal effects added to our atmosphere code, the equilibrium of heavy elements in the dense atmosphere of cool DZ stars has not yet been explored by other investigators using state-of-the-art methods. Therefore, we had to perform our own calculations before implementing this improved constitutive physics in our code. In this section, we first give some theoretical background and describe our strategy to compute the ionization equilibrium (Section 5.5.1). Then, results from our ab initio calculations are presented in Section 5.5.2 and applied to white dwarf atmospheres in Section 5.5.3.

5.5.1 Theoretical framework

5.5.1.1 The chemical picture

To tackle the problem of the ionization equilibrium of heavy elements in the dense atmosphere of cool white dwarfs, we rely on the chemical picture. In this approach, atoms,

ions and electrons are considered as the basic particles and their interactions are modeled through interaction potentials. This is not as exact as the physical picture, where nuclei and electrons are the basic particles. However, using the chemical picture has several advantages. Since this approach is semi-analytical, the results derived from it are more easily applicable in stellar atmosphere codes (especially regarding opacity calculations, where thousands of bound states must be taken into account to include the multitude of observed spectral lines). Moreover, it is easier to identify the contribution of every physical effect and thus gain a better physical insight of the problem at hand (Winisdoerffer & Chabrier, 2005).

In the chemical picture, the ionization equilibrium problem is reduced to the minimization of the Helmholtz free energy $F(\{N_i\}, V, T)$ associated with a mixture made of species $\{N_i\}$ in a volume V maintained at temperature T (see, for instance, Fontaine et al., 1977; Magni & Mazzitelli, 1979; Hummer & Mihalas, 1988; Saumon & Chabrier, 1992). The total Helmholtz free energy of a mixture of atoms, ions and electrons can be expressed as the sum of the ideal free energy of the electron gas $F_{\rm e}^{\rm id}$, the ideal free energy of every ion from every species $F_{\rm j,k}^{\rm id}$, the contribution from the internal structure of bound species $F_{\rm j,k}^{\rm int}$ and the nonideal contribution related to the interaction between species $F^{\rm nid}$,

$$F = F_{\rm e}^{\rm id} + \sum_j \sum_k F_{\rm j,k}^{\rm id} + \sum_j \sum_k F_{\rm j,k}^{\rm int} + F^{\rm nid}, \tag{5.12}$$

where k is an ionization state and j is an atomic species.

Since F must be minimized, $dF = 0$ and the ionization equilibrium of species J between ionization states K and $K+1$ imposes

$$\begin{aligned} 0 = &\left(\frac{\partial F}{\partial N_e}\bigg|_{N_{j,k},V,T} \right) dN_e + \left(\frac{\partial F}{\partial N_K}\bigg|_{N_e,N_{j,k\neq K},V,T} \right) dN_K \\ &+ \left(\frac{\partial F}{\partial N_{K+1}}\bigg|_{N_e,N_{j,k\neq K+1},V,T} \right) dN_{K+1}, \end{aligned} \tag{5.13}$$

which, by definition of the chemical potential, is equivalent to the condition

$$\mu_{J,K} = \mu_{J,K+1} + \mu_e. \tag{5.14}$$

Neglecting the interaction term $F^{\rm nid}$ in Equation 5.12 and taking $F_{\rm e}^{\rm id}$ and $F_{\rm j,k}^{\rm id}$ to be the free energy of an ideal nonrelativistic, nondegenerate gas (Landau & Lifchitz, 1980), Equation 5.14 leads to the well-known Saha equation,

$$\frac{n_{K+1}n_e}{n_K} = \frac{2Q_{K+1}}{Q_K}\left(\frac{2\pi m_e k_B T}{h^2}\right)^{3/2} e^{-I/k_B T}, \tag{5.15}$$

where h is the Planck constant, n_i are number densities, Q_i are partition functions and I is the ionization potential.

Now, if we keep the nonideal terms in the free-energy equation, we find a result of the form of Equation 5.15, but with an *effective* ionization potential $I + \Delta I$ (Kowalski et al., 2007; Zaghloul, 2009),

$$\frac{n_{K+1}n_e}{n_K} = \frac{2Q_{K+1}}{Q_K}\left(\frac{2\pi m_e k_B T}{h^2}\right)^{3/2} e^{-(I+\Delta I)/k_B T}, \tag{5.16}$$

where

$$\Delta I = \mu_e^{\rm nid} + \mu_{K+1}^{\rm nid} - \mu_K^{\rm nid}. \tag{5.17}$$

Therefore, to compute the nonideal ionization equilibrium of heavy elements in dense helium-rich fluids, all that is needed is to compute the appropriate ΔI given by the above equation.

In Equation 5.17, it is the difference in free energy of many-body systems in thermodynamic equilibrium with different ionization states that is computed. This yields an effective ionization potential applicable to *thermodynamic* ionization equilibrium calculations. As emphasized by Crowley (2014), this ionization potential is not directly applicable to nonequilibrium processes (e.g., photoionization). These are fast (adiabatic) processes that occur before the surrounding plasma has any time to respond.

5.5.1.2 General strategy

To compute ΔI, we have to evaluate the nonideal chemical potential of every species involved in the ionization process. The electronic term $\mu_e^{\rm nid}$ is already available in the literature. Kowalski et al. (2007) performed density functional theory (DFT) calculations to evaluate the excess energy of an electron embedded in a dense helium medium and found

values that are in good agreement with existing laboratory measurements (Broomall et al., 1976). These calculations, published as polynomial expansions, were performed for a range of temperatures and densities suitable for our purpose.

While $\mu_{K+1}^{\rm nid}$ and $\mu_K^{\rm nid}$ were calculated by Kowalski et al. (2007) in the case of helium ionization, we are not aware of any study where the nonideal chemical potentials were computed for heavy elements surrounded by dense helium. The central task of this section is to compute these chemical potentials in order to obtain ΔI by virtue of Equation 5.17.

In the limit of strongly coupled systems, the role of entropy can be neglected for the calculation of thermodynamic equilibrium ionization potential, since the configuration of atoms remains the same before and after the ionization takes place. However, plasmas encountered in white dwarf atmospheres have a finite coupling strength. When an atom is ionized, the medium responds and additional energy is transferred between the atom and the surrounding particles (Crowley, 2014). Therefore, the nonideal chemical potential of a species in ionization state K can be expressed as the sum of two contributions,

$$\mu_K^{\rm nid} = E_K^{\rm exc} + \mu_K^{\rm nid,ent}, \tag{5.18}$$

where $E_K^{\rm exc}$ is the excess of internal energy per particle and $\mu_K^{\rm nid,ent}$ is the entropic contribution to the nonideal chemical potential. Note that this separation of $\mu_K^{\rm nid}$ into two distinct components directly follows from the definition of the Helmholtz free energy. As $F = E + TS$ and $\mu_K^{\rm nid} = (\partial F_K^{\rm nid}/\partial N_K)\big|_{N_{k\neq K},V,T}$, we can write

$$\mu_K^{\rm nid} = \left.\frac{\partial\left(E_K^{\rm nid} + TS_K^{\rm nid}\right)}{\partial N_K}\right|_{N_{k\neq K},V,T} = E_K^{\rm exc} + \mu_K^{\rm nid,ent}. \tag{5.19}$$

Our general strategy is summarized in Figure 5.5. To compute the $\mu_K^{\rm nid,ent}$ contribution, we follow the work of Kowalski (2006b) and Kowalski et al. (2007) and use the classical fluid theory and the OZ equation, as detailed in Section 5.5.2.1. To retrieve $E_K^{\rm exc}$, we turn to DFT to compute the excess energy of a metallic ion embedded in a dense helium medium. This approach has the advantage of naturally taking into account many-body interaction terms. Prior to using DFT to compute $E_K^{\rm exc}$, we use molecular dynamics (MD) simulations to obtain representative atomic configurations, as described in detail in Section 5.5.2.2.

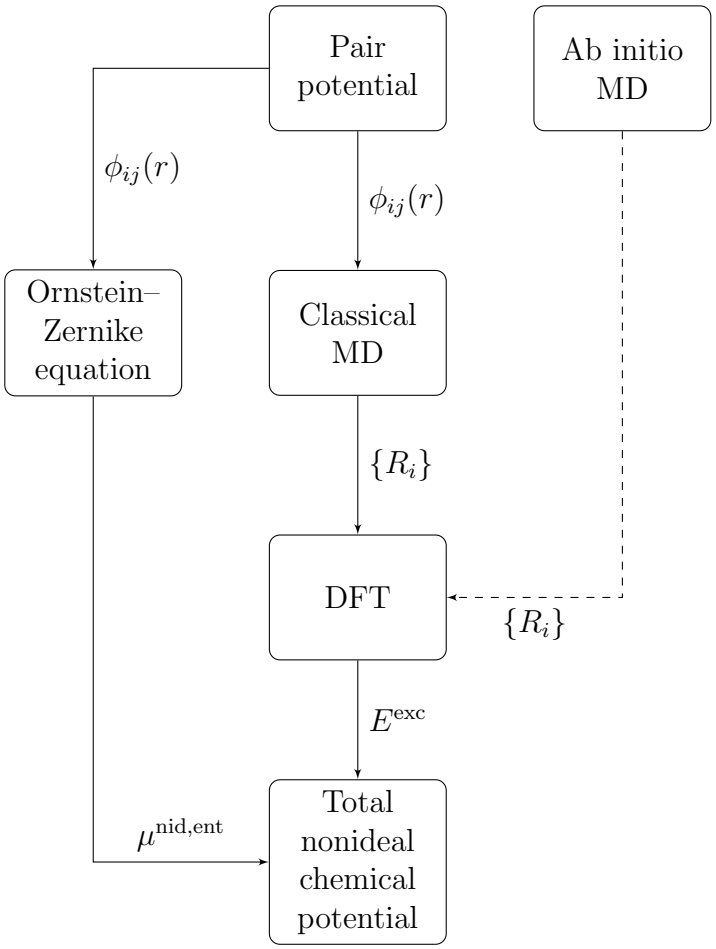

Figure 5.5 – Computational strategy used to retrieve the nonideal chemical potential of ionic species. The dashed arrow indicates a validation step described in Section 5.5.2.2.

5.5.1.3 Comparison with previous studies

To take into account the nonideal ionization of heavy elements, white dwarf atmosphere models (Koester & Wolff, 2000; Wolff et al., 2002; Dufour et al., 2007) typically rely on the Hummer–Mihalas occupation probability formalism (Hummer & Mihalas, 1988; Mihalas et al., 1988). In this framework, an occupation probability w_i is assigned to every electronic level of every ion. If the level is unperturbed, $w_i = 1$; if the level is completely destroyed by interparticle interactions, $w_i = 0$. This occupation probability appears in the Boltzmann distribution and it multiplies every term of the partition function,

$$Q_K = \sum_i w_{iK} g_{iK} \exp\left(-\frac{e_{iK}}{k_B T}\right), \tag{5.20}$$

where the sum is over all states i of species K, and g is a statistical weight. To compute w_i in the particular case of neutral interactions, Hummer & Mihalas (1988) used the second virial coefficient in the van der Waals equation of state to obtain

$$w_i = \exp\left[-\frac{4\pi}{3}\sum_{i'} n_{i'}(r_i + r_{i'})^3\right], \tag{5.21}$$

where n_i is the number density of the particles in state i and r_i is the radius of the particles in this state. The interpretation of Equation 5.21 is straightforward : when a state occupies a volume of the same order as the mean volume allowed per particle, it is gradually destroyed. Although simple and easy to implement in atmosphere models, we see three important drawbacks with this approach.

1. This formalism is expected to break down above $\approx 0.01\,\mathrm{g\,cm^{-3}}$ (Hummer & Mihalas, 1988), which is insufficient for many cool DZ white dwarfs.

2. The excluded volume effect is only a caricature of the real interaction potential between two neutral particles.

3. There is no theoretical prescription for the radii r_i. For instance, for a ground-state He I atom, should r be given by the hydrogenic approximation ($r = n^2 a_0/Z_{\mathrm{eff}} = 0.39\,\text{Å}$) or should it be given by the van der Waals radius (1.40 Å, Bondi, 1964) ? To address this problem, it is always possible to calibrate the radii to fit the spectral lines observed in white dwarf stars. This was successfully done by Bergeron et al. (1991) for hydrogen, but it would be impracticable for DZ stars, where many ions contribute to the total electronic density.

Our approach aims at answering these three concerns. First, by taking into account many-body interaction terms, it is designed to remain physically exact up to densities of the order of $1\,\mathrm{g\,cm^{-3}}$. Secondly, the interaction between species is modeled through ab initio calculations that accurately describe the complex behavior of electrons under these high-density conditions. Finally, since we rely only on first-principles physics, our method does not require any free parameters.

5.5.1.4 Approximations

Before moving to the calculation of the nonideal chemical potentials and ΔI in Section 5.5.2, we take time to justify three important approximations that we use throughout Section 5.5.

Electrons and heavy elements as trace species We are interested in helium-rich plasmas, where heavy elements and electrons can be considered as trace species. Hence, we completely neglect the interaction of metallic ions with other metallic ions and with electrons. This approximation is justified by the very low abundance of heavy elements in white dwarf atmospheres. Indeed, to our knowledge, the most metal-rich DZ star mentioned in the literature has an atmosphere with a number density ratio of $\log \mathrm{Ca/He} \approx -6$ (Ton 345, Wilson et al., 2015).

As a consequence of this approximation, we completely ignore the excess energy resulting from the interaction between charged species. Since electrostatic interactions occur at long range, this approximation deserves some additional justification. To show that electrostatic interactions are negligible, we computed the contribution of electrostatic interactions to the Helmholtz free energy. The latter can be broken down into three components (Chabrier & Potekhin, 1998),

$$F^{\mathrm{elec}} = F^{ee} + F^{ii} + F^{ie}, \tag{5.22}$$

where F_{ee} is the exchange-correlation contribution from the electron fluid, F^{ii} is the contribution from the one-component ion plasma and F^{ie} is the electron screening contribution. To evaluate F^{elec}, we used the equations reported in Ichimaru et al. (1987) for F^{ee} and those in Chabrier & Potekhin (1998) for F^{ii} and F^{ie}. If all electrons originate from singly ionized species, then F^{elec} is a function of only the electronic density n_e and the plasma temperature T. Figure 5.6 shows $\Delta I^{\mathrm{elec}} = \left(\frac{\partial}{\partial N_e} + \frac{\partial}{\partial N_{j,i+1}}\right) F^{\mathrm{elec}}$ for different n_e and T. The dashed line indicates the electronic density at the photosphere ($\tau_R = 2/3$) of vMa2, a typical cool DZ star. At these electronic densities and temperatures, the effect of electrostatic interactions on ΔI is of only a few meV and is therefore negligible compared to the total

ΔI reported later in this paper (which is of the order of a few eV). The charged-particles density is simply too low for electrostatic interactions to have any significant effect.

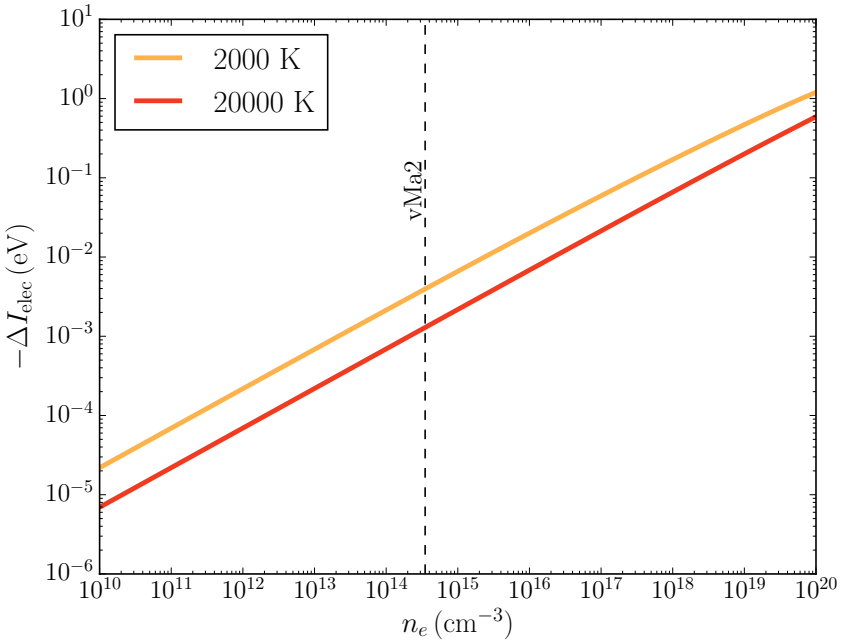

Figure 5.6 – Contribution of the electrostatic interaction to the effective ionization potential with respect to the electronic density and the temperature. The dashed line indicates the electronic density at $\tau_R = 2/3$ for vMa2, a typical cool DZ star.

Omission of the quantum behavior of ions We do not take into account the quantum behavior of ions and atoms. To justify this approximation, we can compute the first quantum correction of the Helmholtz free energy (Wigner, 1932), which can be seen as a correction for the overlapping wave functions of nearby particles. For an m-component mixture, it can be expressed as (Saumon & Chabrier, 1991)

$$F^{\mathrm{quant}} = \frac{\pi\hbar^2}{12kTV} \sum_{a,b}^{m} \frac{N_a N_b}{\mu_{ab}} \int \nabla^2 \phi_{ab}(r) g_{ab}(r) r^2 dr, \tag{5.23}$$

where $\phi_{ab}(r)$ and $g_{ab}(r)$ are, respectively, the pair potential and the pair distribution function between species a and b, and $\mu_{ab} = \frac{m_a m_b}{m_a + m_b}$ is the reduced mass of particles a and b. The contribution of this term to ΔI is computed as $\Delta I^{\mathrm{quant}} = \left(\frac{\partial}{\partial N_{j,k+1}} - \frac{\partial}{\partial N_{j,k}} \right) F^{\mathrm{quant}}$. Using the pair distribution functions and the pair potentials described in Section 5.5.2.1, we find that $\Delta I^{\mathrm{quant}}$ remains below 5 meV for all physical conditions relevant for the mo-

deling of the atmosphere of cool DZ stars. As this is well below $E^{\rm exc}$ and $\mu^{\rm nid,ent}$, we can safely ignore the quantum behavior of ions.

The ground-state approximation To compute the ionization equilibrium of heavy elements, we assume that every atom is in its electronic ground state. This solely means that we consider all species to be in their ground state *when computing the ionization equilibrium*. Once the ionization equilibrium is computed, the population of every electronic state can be obtained through the Boltzmann distribution. How good is this approximation ? For helium atoms, this approximation is excellent. The first excited state of He I lies at 19.8 eV, so almost all helium atoms are in their fundamental state for the temperature domain in which we are interested ($k_BT < 1\,\mathrm{eV}$).

For heavy elements, this approximation could be problematic. It is well known that excited states are typically more affected by nonideal effects than the fundamental state (e.g., Hummer & Mihalas, 1988). Therefore, since the ΔI term in Equation 5.16 only takes into account the destruction of the fundamental state, an error could be introduced in the ionization equilibrium if excited states are affected in a significantly different way *and* if they account for a large portion of the partition function Q.

To investigate the maximum error associated with this approximation, we computed the fundamental-state contribution to the partition function Q for C, Ca, Fe, Mg and Na. The results are shown in Figure 5.7 for $k_BT = 0.5\,\mathrm{eV}$. The worst possible error associated with this approximation will occur if all excited states are destroyed while the fundamental state remains unperturbed (see Equation 5.20). This scenario is highly unlikely but provides an easy way of assessing the maximum error. If it is the case, then, as shown in Figure 5.7, the maximum error on Q is $\approx 40\%$ (see Fe II). Therefore, in the worst case, the ionization fraction will be wrong by a factor of ≈ 2.

This maximum error is not a cause of concern for the modeling of the atmosphere of cool DZ stars. First, for all other atomic species (C, Ca, Mg and Na) Q is far more dominated by the fundamental-state contribution and the maximal error associated with this approximation is thus much smaller than the value derived for Fe. Secondly, for the coolest DZ stars, the relative contribution of the fundamental state to the partition function is higher than for their warmer counterparts. Therefore, the ground-state approximation becomes more accurate for the stars for which the departure for the ideal chemical equili-

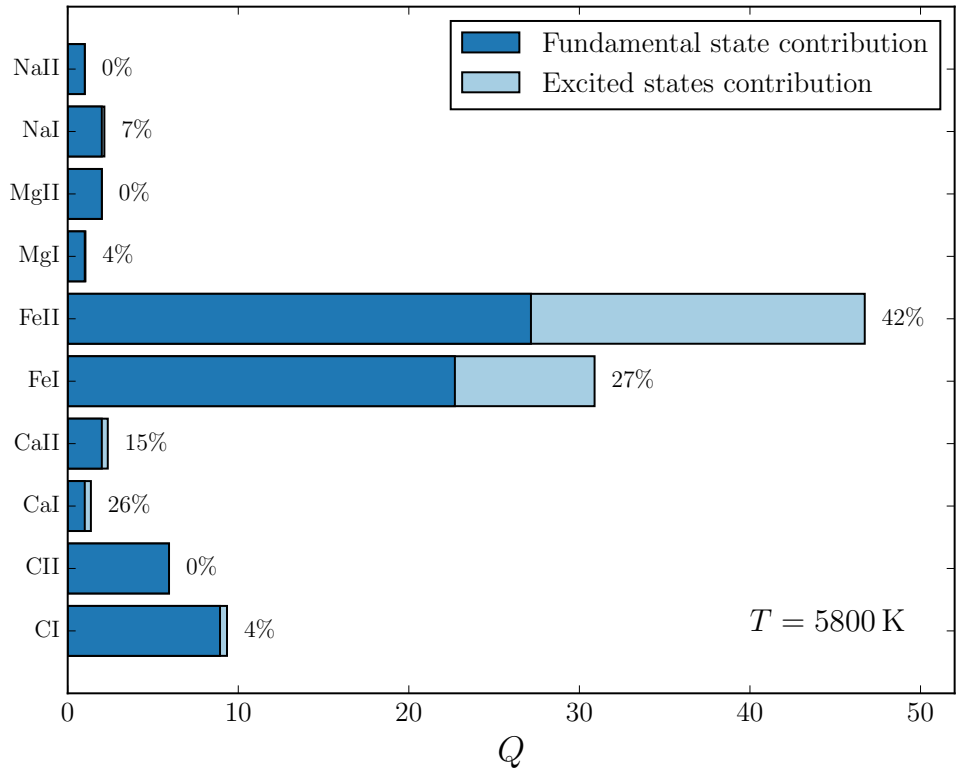

Figure 5.7 – Comparison of the contributions of the fundamental state and the excited states to the partition function Q at $k_B T = 0.5\,\mathrm{eV}$ for heavy ions found in cool DZ stars. The number at the end of each bar gives the fraction of Q resulting from excited states. This figure was made using the atomic data of the NIST Atomic Spectra Database (Kramida et al., 2015).

brium is expected to be the most important. Last but not least, for the conditions relevant for the modeling of cool DZ stars, both this work and the formalism of Hummer & Mihalas (1988) predict deviations for the ideal gas equilibrium that are much more important than the aforementioned factor of ≈ 2 (see, for instance, Figure 5.15).

5.5.2 Results

In this section, we detail the computations performed to obtain ΔI for C, Ca, Fe, Mg and Na. In Sections 5.5.2.1 and 5.5.2.2, we describe the computational setup and our intermediate results, and our final results are given in Section 5.5.2.3. For the sake of clarity, we only refer to Ca in the discussion of Sections 5.5.2.1 and 5.5.2.2, although all of the reported calculations were also performed for C, Fe, Mg and Na.

5.5.2.1 Entropic contribution

To compute the entropic contribution to the nonideal chemical potential, we first use the OZ equation (and the Percus–Yevick closure relation) to find the radial distribution function $g_{\mathrm{He-Ca}}(r)$ describing the spatial configuration of Ca relative to He atoms. Then, once the radial distribution function $g_{\mathrm{He-Ca}}(r)$ is obtained, $\mu_{\mathrm{Ca}}^{\mathrm{nid}}$ can be obtained through Equations 9 and 12 of Kiselyov & Martynov (1990). From there, we simply subtract the excess energy of Ca (as computed in the OZ framework) to obtain $\mu_{\mathrm{Ca}}^{\mathrm{nid,ent}}$ (Equation 5.18).

To compute $g_{\mathrm{He-Ca}}(r)$ with the OZ equation, the pair potentials $\phi_{\mathrm{He-He}}(r)$ and $\phi_{\mathrm{He-Ca}}(r)$ must be specified (in accordance with the approximation detailed in Section 5.5.1.4, $\phi_{\mathrm{Ca-Ca}}(r) = 0$ since the metal-metal interactions are neglected). For the helium-helium pair potential, we use the effective pair potential of Ross & Young (1986).

As metal-helium pair potentials are not available in the literature for every metallic ion considered in this work, we had to compute ab initio pair potentials between helium and metallic ions. To do so, we used the ORCA quantum chemistry package to obtain the potential energy $\phi_{\mathrm{Ca-He}}$ at various separations,

$$\phi_{\mathrm{Ca-He}}(r) = E_{\mathrm{Ca-He}}(r) - E_{\mathrm{He}} - E_{\mathrm{Ca}}, \tag{5.24}$$

where $E_{\mathrm{Ca-He}}(r)$ is the total energy for a separation r and E_{He} and E_{Ca} are the computed energies of isolated He and Ca atoms. We rely on the CCSD(T) method (Raghavachari et al., 1989) as implemented in ORCA (Neese et al., 2009; Kollmar & Neese, 2010) with the aug-cc-pCVQZ basis sets (Dunning, 1989; Kendall et al., 1992; Woon & Dunning, 1993). Using the counterpoise method (Boys & Bernardi, 1970), we verified that the basis set superposition error is small enough ($< 2\,\mathrm{meV}$) to be neglected for our purpose.

In the particular case of Ca, a few interaction potentials can be found in the literature for the Ca I–He I (Partridge et al., 2001; Lovallo & Klobukowski, 2004) and the Ca II–He I interactions (Czuchaj et al., 1996; Allard & Alekseev, 2014). We used the values reported by these authors to validate our computational setup. This comparison, which reveals no significant differences, is shown in Figure 5.8.

The main limitation of these pair potentials is that they were obtained in the infinite-dilution limit (i.e., Ca interacts with only one He atom). Therefore, when we use these

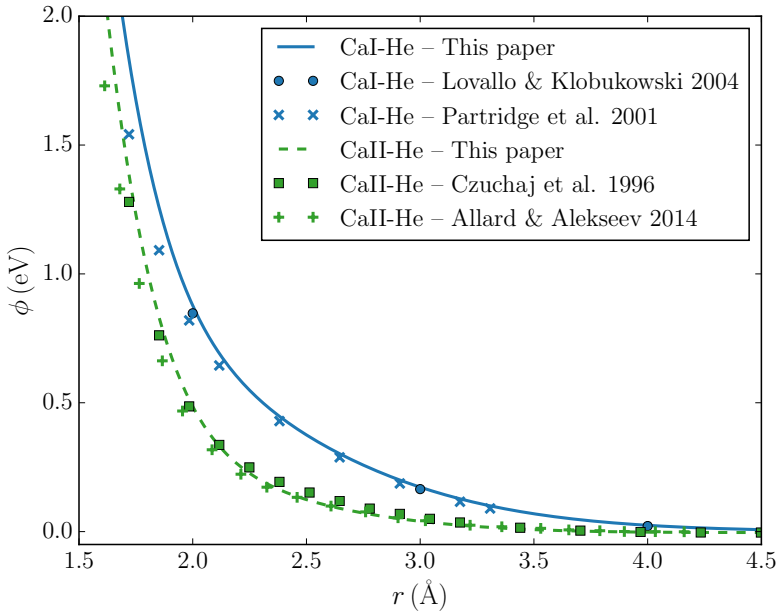

Figure 5.8 – Comparison between the pair potentials for the Ca I–He I and Ca II–He I interactions computed in this work and the values reported in Lovallo & Klobukowski (2004), Partridge et al. (2001), Czuchaj et al. (1996) and Allard & Alekseev (2014)

potentials, we implicitly assume that the total potential is pairwise additive, and an error may be introduced if many-body terms are important. This is the main reason why we resort to the OZ equation only to compute the entropic contribution and not to compute the excess energies. In fact, as described in Section 5.5.2.2, we turn to DFT to compute excess energies, which guarantees that many-body interaction terms are properly taken into account.

5.5.2.2 Excess energy contribution

The excess energy of Ca embedded in a dense helium medium made of N He atoms is given by

$$E^{\text{exc}}_{\text{Ca}-\text{He}} = E_{N\text{He}+\text{Ca}} - E_{N\text{He}} - E_{\text{Ca}}, \tag{5.25}$$

where $E_{N\text{Ca}+\text{He}}$ is the total energy of the system, $E_{N\text{He}}$ is the energy of the N He atoms and E_{Ca} is the computed energy of the isolated Ca atom. This calculation requires two steps. First, we need to find meaningful atomic configurations for the system (i.e., configurations that are representative of the thermodynamic fluctuations undergone by the real system). Then, we can use these configurations to compute the excess energy with Equation 5.25.

Molecular dynamics To obtain representative atomic configurations of a system consisting of one Ca atom surrounded by N He atoms at a given temperature and a given density, we turned to classical molecular dynamics simulations. More precisely, we used LAMMPS[4] (Plimpton, 1995) and the pair potentials described in Section 5.5.2.1. The simulations were performed in a cubic box with periodic boundary conditions. The box size and the number of He atoms included in the simulations were chosen to attain the desired density (additional considerations regarding finite-size effects are discussed in the next paragraph) and the temperature was kept near the target value using a Nosé–Hoover thermostat (Nosé, 1984; Hoover, 1985). The simulations were run for 5 ns using 0.2 fs time steps. At regular time intervals, the atomic positions were saved and it is these configurations that we use in the next section to compute the excess energies.

DFT calculations To compute the excess energy of Ca in the atomic configurations extracted from the MD simulations, we used the Quantum ESPRESSO[5] DFT package (Giannozzi et al., 2009), with the PBE exchange-correlation functional (Perdew et al., 1996) and norm-conserving pseudopotentials. For all DFT calculations, we chose a kinetic energy cutoff of 45 Ry (612 eV) and a charge density cutoff of 180 Ry. We checked that this cutoff is enough to achieve a < 0.05 eV convergence of the metal excess energy. To remove the electrostatic interaction associated with periodic boundary conditions, we used the Martyna–Tuckerman correction (Martyna & Tuckerman, 1999) as implemented in Quantum ESPRESSO, which allows us to correct both the total energy and the SCF potential.

Furthermore, to make sure that the finite size of the box does not result in undesired artifacts, we performed simulations using different numbers of helium atoms per simulation box and different box sizes (up to $N = 160$ helium atoms and up to $a = 30$ a.u.). We found that using at least $N = 50$ helium atoms and a simulation box of at least $a = 15$ a.u. (7.94 Å) allows a < 0.1 eV convergence of the excess energy compared to results obtained at the same density with higher N and a values. This indicates that finite-size artifacts are negligible when these two conditions are met. Hence, all DFT calculations reported in this work were performed with $a \geq 15$ a.u. and $N \geq 50$.

[4] http://lammps.sandia.gov
[5] http://quantum-espresso.org

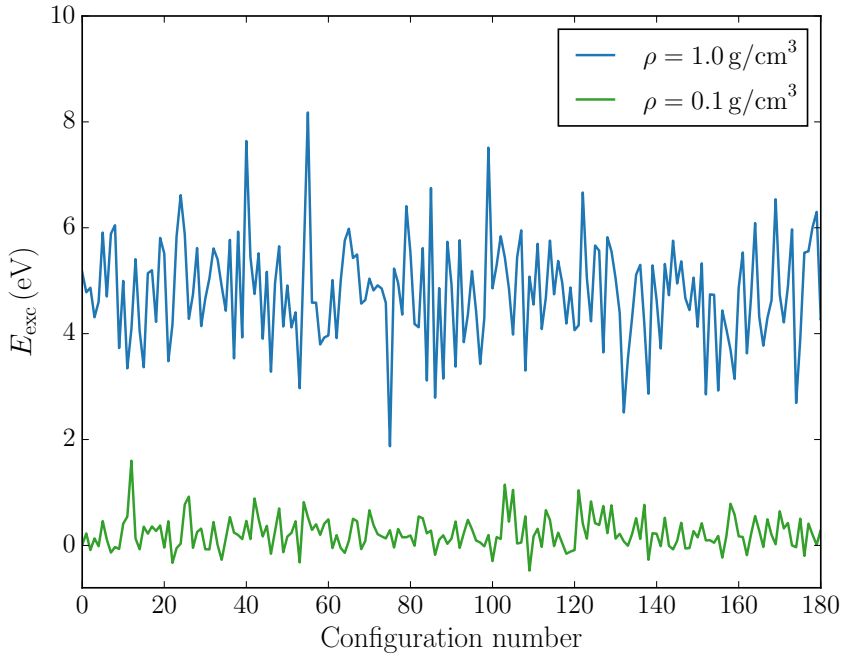

Figure 5.9 – Excess energy of Ca at $T = 4000\,\mathrm{K}$ for configurations taken at 25 ps intervals from MD trajectories for different helium densities.

When computing the excess energy E_{exc} using configuration snapshots extracted from MD simulations, the results can fluctuate drastically from one configuration to the other. This is shown in Figure 5.9, where the lines represent the evolution of E_{exc} from configuration to configuration. In Figure 5.10, we show the autocorrelation function of the E_{exc} time series,

$$r_k = \frac{\sum_{i=1}^{N-k} \left(E_{\mathrm{exc}}^{i} - \langle E_{\mathrm{exc}} \rangle\right)\left(E_{\mathrm{exc}}^{i+k} - \langle E_{\mathrm{exc}} \rangle\right)}{\sum_{i=1}^{N} \left(E_{\mathrm{exc}}^{i} - \langle E_{\mathrm{exc}} \rangle\right)^2}. \tag{5.26}$$

Since the autocorrelation function quickly decays to zero, we conclude that the time elapsed between each configuration snapshot is long enough for the E_{exc} time-series values to be statistically independent. Therefore, we can safely apply the central-limit theorem to compute the standard error of the mean,

$$\sigma_{\langle E_{\mathrm{exc}} \rangle} = \frac{\sigma_{E_{\mathrm{exc}}}}{\sqrt{N}}. \tag{5.27}$$

Figure 5.11 shows the evolution of $\sigma_{\langle E_{\mathrm{exc}} \rangle}$ with respect to the number of configurations used to compute the mean. For both $\rho = 0.1$ and $\rho = 1.0\,\mathrm{g\,cm^{-3}}$, we notice the $1/\sqrt{N}$ decay of $\sigma_{\langle E_{\mathrm{exc}} \rangle}$. This implies that to improve the error by a factor of two, the number of

configurations needs to be quadrupled. From this analysis, we chose to use 100 configurations for each (T, ρ) condition. This value is enough to obtain $\sigma_{\langle E_{\mathrm{exc}} \rangle} \lesssim 0.1\,\mathrm{eV}$ for most physical conditions considered in this work, which is an error that we consider acceptable for our purpose.

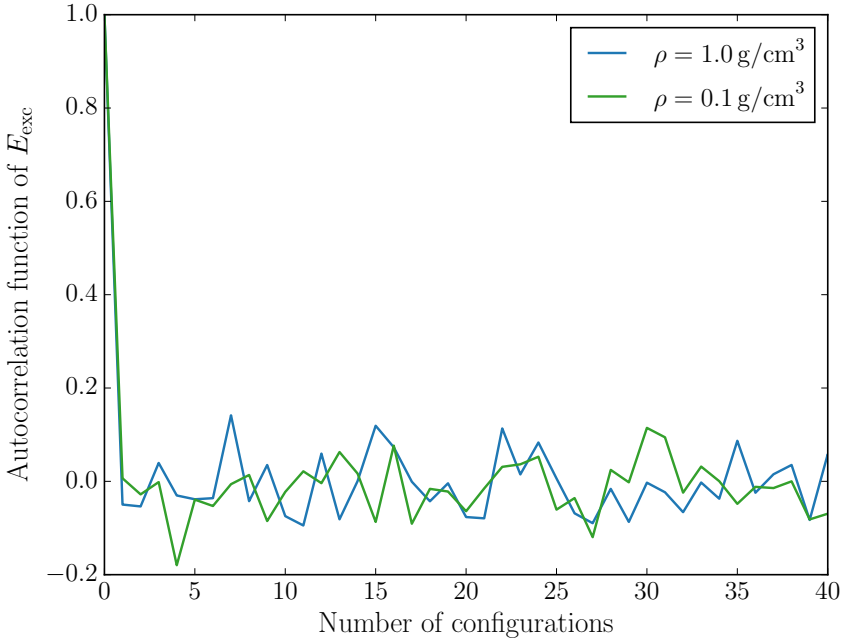

Figure 5.10 – Autocorrelation function of the excess energy time series shown in Figure 5.9.

Validation with ab initio molecular dynamics Since our $\phi_{\mathrm{Ca-He}}(r)$ potential was calculated in the infinite-dilution limit, one could be worried about the exactitude of the atomic configurations obtained through MD using this potential. To check this point, we computed the excess energy of Ca using configurations extracted from *ab initio* MD simulations. In this framework, no pair potential is assumed. The electronic density, energy and forces on ions are recomputed at every time step of the simulation using DFT. This approach is expected to be more exact than the classical MD approach, but its computational cost is larger by orders of magnitude. These calculations were performed using Born–Oppenheimer MD with the CPMD package[6] (Marx & Hutter, 2000; Hutter et al., 2008), with the PBE exchange-correlation functional and ultrasoft pseudopotentials (Vanderbilt, 1990). We employed 0.5 fs time steps and an energy cutoff of 35 Ry. As before, we

[6] http://cpmd.org

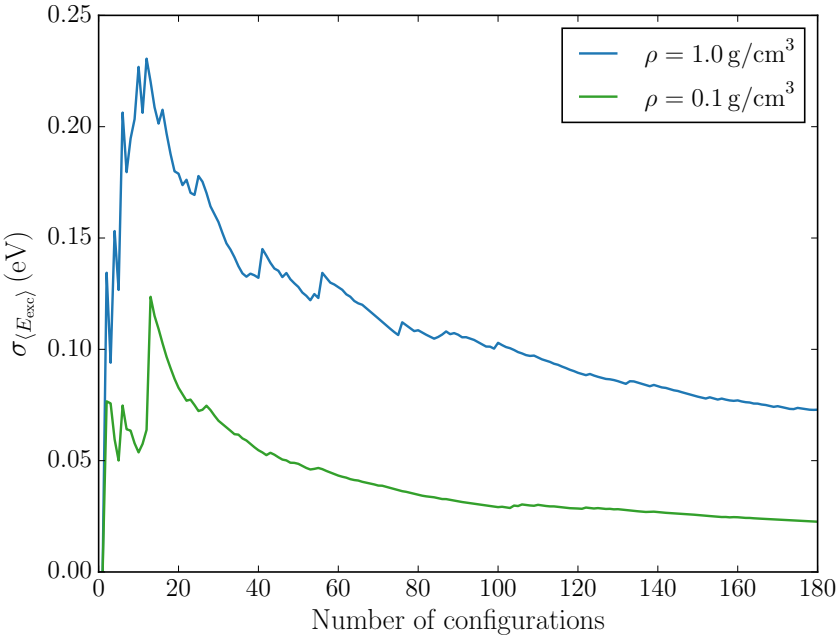

Figure 5.11 – Standard error of the mean of the Ca excess energy at $T = 4000\,\mathrm{K}$ with respect to the number of independent configurations used to compute the mean for different helium densities.

extracted atomic configurations from these simulations and used these configurations to compute the interaction energy of Ca with the surrounding medium through DFT calculations.

Figure 5.12 compares the results obtained to those found with the classical MD simulations. This comparison shows that there is only a negligible difference between the two approaches, at least below $\rho = 1\,\mathrm{g\,cm^{-3}}$. We did not perform any comparison at higher densities because of the prohibitive calculation time of such calculations. In any case, densities above $1\,\mathrm{g\,cm^{-3}}$ are never encountered at the photosphere of cool DZ white dwarfs (Section 5.5.3). Therefore, we conclude that our infinite-dilution limit potential $\phi_{\mathrm{Ca-He}}(r)$ is sufficient to generate the atomic configurations used to compute the excess energy (and it is much faster than resorting to ab initio MD simulations).

5.5.2.3 Ionization equilibrium

Following the methodology described in the previous sections, we computed $\mu_K^{\mathrm{nid,ent}}$ and E_K^{exc} for C I/C II, Ca I/Ca II, Fe I/Fe II, Mg I/Mg II and Na I/Na II. By adding these excess chemical potentials to the electron excess energy, we computed by how much

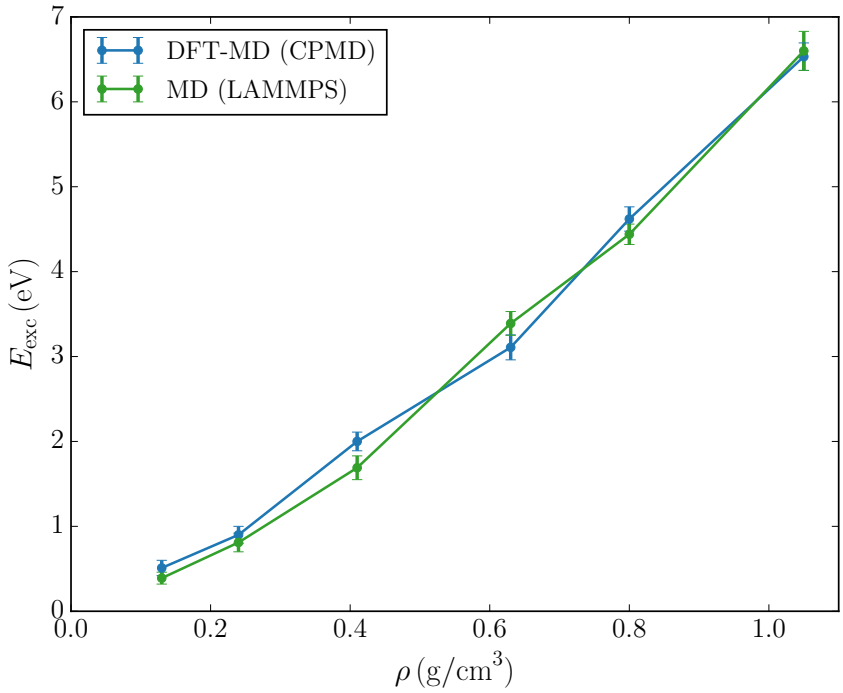

Figure 5.12 – Excess energy of Ca at $T = 5000\,\mathrm{K}$ for different helium densities, obtained from configurations extracted from ab initio molecular dynamics (DFT-MD) and from classical molecular dynamics (MD) using the pair potentials described in Section 5.5.2.1.

the ionization potential is altered at a given density and temperature (Equation 5.17). Figure 5.13, which shows the three contributions to ΔI (free electron excess energy, variation of E_K^{exc} and change in $\mu_K^{\mathrm{nid,ent}}$), illustrates this process in the case of Ca.

Figure 5.14 shows our final results. First, for every ion considered, we notice that $\Delta I \to 0$ when $\rho \to 0$. This is the expected behavior and it shows that our methodology is consistent with the ideal regime when we push it to low densities. Secondly, we note that ΔI is always negative and that its absolute value increases with density. This result means that ionization becomes easier with increasing density, which also corresponds to the expected behavior. Finally, for all elements except Fe, we notice that higher temperatures are associated with slightly larger ionization potential depressions. This result is consistent with the findings of Kowalski et al. (2007), who found a reduction of the band gap of warm dense helium with increasing temperature.

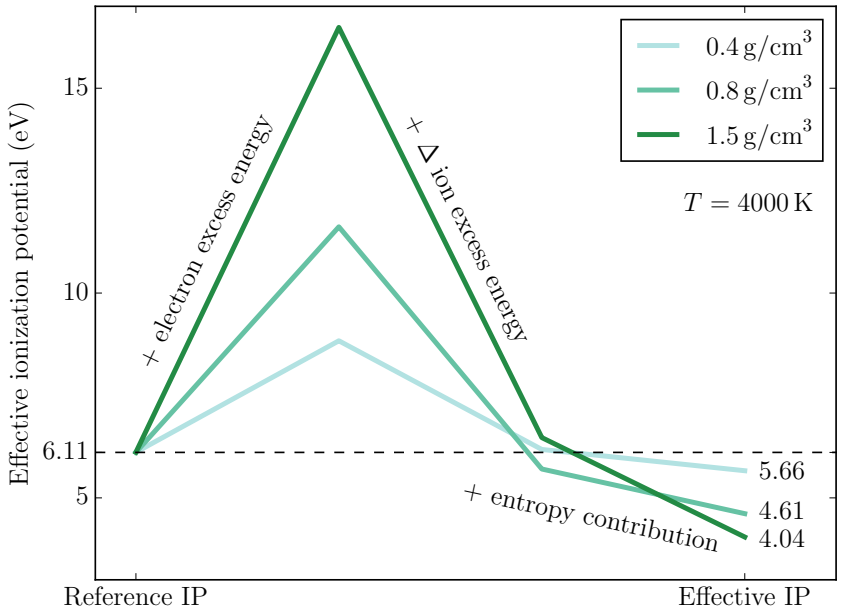

Figure 5.13 – Contributions added to the reference ionization potential of Ca to obtain its effective ionization potential at various densities (see legend). These results are for $T = 4000\,\mathrm{K}$.

To easily implement these nonideal ionization potentials in atmosphere models, we have fitted our results with a simple function of ρ and T,

$$\Delta I(\rho, T) = \min\left\{0, (a + bT)\rho + c\rho^2\right\}, \tag{5.28}$$

where a, b and c are parameters found using a chi-squared minimization algorithm, ρ is the helium density in $\mathrm{g\,cm^{-3}}$ and T is the temperature in K. This expression allows a satisfactory fit to the data and yields $\Delta I = 0$ at $\rho = 0$. The analytical fits are shown in Figure 5.14 and the fitting parameters are reported in Table 5.2. Formally, in order to stay within the limits of our calculations, the use of these analytical expressions should be limited to densities between 0 and $1.5\,\mathrm{g\,cm^{-3}}$ and to temperatures between 4000 and 8000 K. Nevertheless, we have verified that Equation 5.28 can safely be extrapolated to lower (down to 2000 K) or higher (at least up to 10 000 K) temperatures if needed.

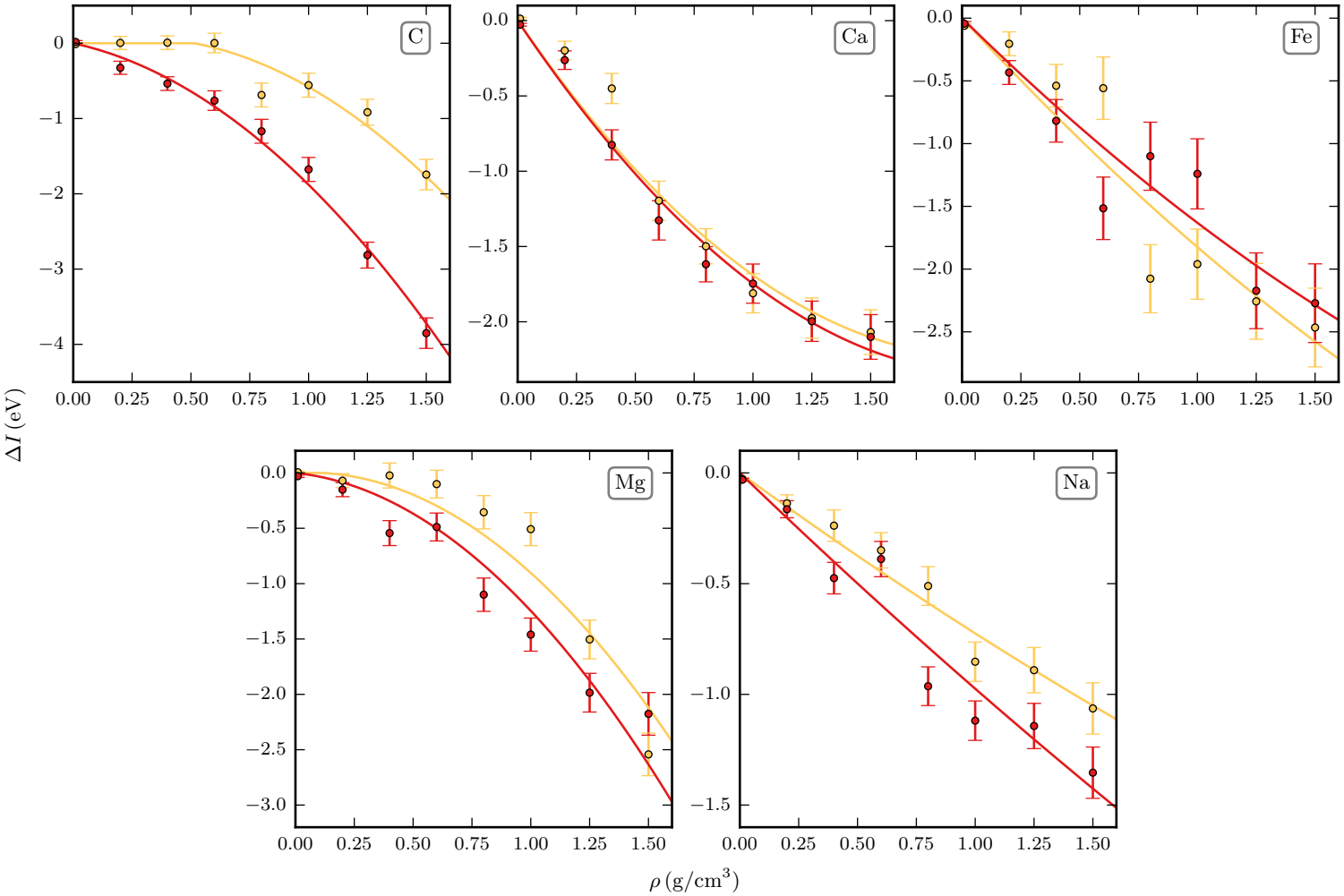

Figure 5.14 – Depression of the ionization potential of C, Ca, Fe, Mg and Na embedded in a dense helium fluid. Circles show the results of our ab initio calculations and error bars indicate the statistical errors associated with the configuration sampling. The solid lines show the analytical fits found through a χ^2 minimization of Equation 5.28. Data in red are for $T = 8000\,\mathrm{K}$ and data in yellow are for 4000 K.

Ion	$a\,(\mathrm{eV\,g^{-1}\,cm^3})$	$b\,(10^{-4}\,\mathrm{eV\,g^{-1}\,K^{-1}\,cm^3})$	$c\,(\mathrm{eV\,g^{-2}\,cm^6})$
C	1.91782	−3.24813	−1.19948
Ca	−2.20703	−0.14431	0.57494
Fe	−2.23142	0.48427	0.21301
Mg	0.45809	−0.85522	−1.01958
Na	−0.52305	−0.62471	0.04833

Table 5.2 – Fitting parameters for $\Delta I(\rho, T)$ (Equation 5.28)

5.5.2.4 Comparison with previous studies

It is instructive to compare these results with the ionization equilibrium predicted by the Hummer–Mihalas occupation probability formalism, which is widely used in atmosphere codes. Since there is no theoretical prescription for the values of the hard sphere radii used to compute the occupation probabilities (Equation 5.21), a somewhat arbitrary choice must be made to perform this comparison. We chose to compute the hard sphere radii with the hydrogenic approximation, as described by Beauchamp (1995). In this approximation, the radius of a species in state i is given by

$$r_i = \frac{n_i^2 a_0}{Z_i^{\mathrm{eff}}}, \tag{5.29}$$

where n_i is the principal quantum number of the uppermost electron, a_0 is the Bohr radius and the effective nuclei charge Z_i^{eff} is given by

$$Z_i^{\mathrm{eff}} = n_i \sqrt{\frac{I_i}{13.598\,\mathrm{eV}}}, \tag{5.30}$$

where I_i is the energy needed to ionize an electron from state i. In the Hummer–Mihalas formalism, every term in the partition function is multiplied by the occupation probability (Equation 5.20). If we stick to the ground-state approximation (Section 5.5.1.4), the occupation probability is the same for every level and it can be factored out of the partition-function sum. Hence, the net effect of the Hummer–Mihalas formalism is to mul-

tiply the right-hand side of the Saha equation (Equation 5.15) by the ratio of occupation probabilities, $w_{\rm ZII}/w_{\rm ZI}$.

Figure 5.15 compares the multiplicative factors that need to be applied to the right-hand side of the Saha equation for the Ca I/Ca II ionization equilibrium to account for nonideal effects (i.e., $w_{\rm CaII}/w_{\rm CaI}$ in the case of the Hummer–Mihalas formalism and $e^{-\Delta I/(k_B T)}$ for our ionization model). The most obvious aspect of Figure 5.15 is that we find a weaker pressure ionization than what is predicted using the Hummer–Mihalas formalism and hard sphere radii computed in the hydrogenic approximation. We checked that this result holds true for C, Fe, Mg and Na. This conclusion is consistent with the findings of Bergeron et al. (1991) for the ionization equilibrium of hydrogen in cool DA stars. Using the Hummer–Mihalas formalism and a hydrogen radius given by $r_n = n^2 a_0$, they found that the high Balmer lines are predicted to be too weak, indicating that pressure ionization in the Hummer–Mihalas formalism is too strong. They showed that using a smaller radius in the computation of the occupation probabilities, $r_n = 0.5 n^2 a_0$, allows better spectral fits.

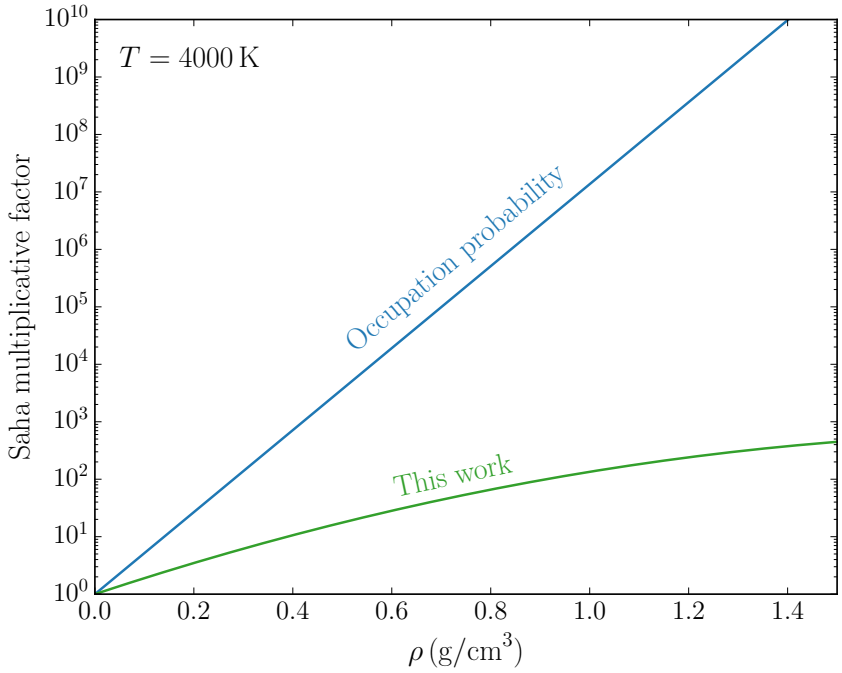

Figure 5.15 – Multiplicative factor applied to the right-hand side of the Ca I/Ca II Saha equation (Equation 5.15) to take nonideal effects into account. The blue line is $w_{\rm CaII}/w_{\rm CaI}$, the result obtained using the Hummer–Mihalas formalism, and the green curve is $e^{-\Delta I/(k_B T)}$, the result obtained with our ionization model.

Unfortunately, we cannot compute the ionization potential depression of H to directly confirm the conclusion of Bergeron et al. (1991). The problem is that the H II–He potential (e.g., Kołos & Peek, 1976; Pachucki, 2012) has a deep attractive well (since H^+ and He can form the HeH^+ molecule) that prevents proper convergence of the OZ equation solver. The same issue arises if we try to compute the ionization potential of H in an H-rich medium, since the H II–H I potential (e.g., Frost & Musulin, 1954) also has an important attractive well (H^+ and H can form the H_2^+ molecule).

5.5.3 Atmosphere models

Using the analytical model described in the previous section, we implemented the improved ionization equilibrium of heavy elements in our atmosphere code to investigate how it affects the synthetic spectra of cool DZ stars. Before even examining any spectrum, we can get an idea of the impact of the new nonideal ionization equilibrium by looking at the densities involved in the model atmospheres. Figure 5.16 shows the density at $\tau_\nu = 2/3$ as a function of λ for a few atmosphere models with different effective temperatures and calcium abundances.[7] This type of figure is useful to identify which densities are probed at different wavelengths. In the previous Section, we saw that no important deviation from the ideal ionization equilibrium is expected below $0.1\,\mathrm{g\,cm^{-3}}$ (see Figure 5.14). From Figure 5.16, it is clear that the probed densities are below this threshold for Ca/He $\gtrsim 10^{-10}$ and above this threshold for Ca/He $\lesssim 10^{-10}$. Therefore, it should become important to take into account the nonideal ionization equilibrium for cool DZ atmosphere models with Ca/He $\lesssim 10^{-10}$, but it is probably superfluous for models with Ca/He $\gtrsim 10^{-10}$ (note that nonideal effects on the opacities and the equation of state nevertheless remain important in this regime). For intermediate densities (Ca/He $\approx 10^{-10}$), using the nonideal ionization equilibrium should result in small changes in the spectral-line wings of the coolest models.

Figure 5.17 compares synthetic spectra computed with our ionization equilibrium model to spectra computed using the occupation probability formalism and the ideal Saha equilibrium (in each case, the atmosphere model structure and the synthetic spectrum were computed using the same ionization model). This figure focuses on the region between 3500 and 4500 Å, since it contains several Ca, Fe and Mg absorption lines susceptible of being

[7] In this paper, the abundance of all metallic species, from C to Cu, is scaled to the abundance of Ca to match the abundance ratios of chondrites reported in Lodders (2003).

affected by the choice of the ionization model. The first thing to note is that for the high-density models (i.e., those with a low metal abundance and a low effective temperature) there are important differences between spectra obtained using the ideal Saha equilibrium and our ionization model. These differences are mostly due to a shift in the continuum associated with the increased electronic density in models that take pressure ionization into account. Next, we notice that the spectra computed using the Hummer–Mihalas formalism are even further from the spectra obtained using the ideal Saha equilibrium than those computed with our ionization model. This is not surprising, since, as seen in Figure 5.15, the Hummer–Mihalas formalism predicts a very strong pressure ionization. Finally, for the low-density models (i.e., those with a high metal abundance and/or a high effective temperature), all three sets of spectra are virtually identical, which is consistent with our analysis of Figure 5.16.

The nonideal chemical equilibrium of heavy elements also has a small impact on the model atmosphere structure. The increased electronic density associated with pressure ionization leads to an increase of the Rosseland mean opacity and therefore to a reduction of the pressure at the photosphere. For instance, for $T_{\rm eff} = 4000\,{\rm K}$, $\log g = 8$ and ${\rm Ca/He} = 10^{-11}$, a model that assumes the ideal Saha equation has a photospheric density of $0.93\,{\rm g\,cm^{-3}}$, while an atmosphere structure based on our ionization model has a photospheric density of $0.89\,{\rm g\,cm^{-3}}$. Moreover, the occupation probability formalism predicts a density that is still lower ($0.84\,{\rm g\,cm^{-3}}$). Given Figure 5.15, this result is not surprising : compared to our calculations, the Hummer–Mihalas formalism overestimates the efficiency of pressure ionization.

Our results constitute a physically grounded answer to the question of the importance of pressure ionization in cool DZ stars, which will help to reduce the gap between solutions found with different atmosphere codes. A good example to illustrate this point is vMa2 (WD 0046+051). On one hand, using an ideal treatment of chemical equilibrium, Dufour et al. (2007) found a solution with $T_{\rm eff} = (6220 \pm 240)\,{\rm K}$. On the other hand, using the Hummer–Mihalas occupation probability formalism, Wolff et al. (2002) found $T_{\rm eff} = (5700 \pm 200)\,{\rm K}$. In their analysis, Dufour et al. (2007) showed that the difference between both solutions can largely be explained by the different chemical equilibrium models used

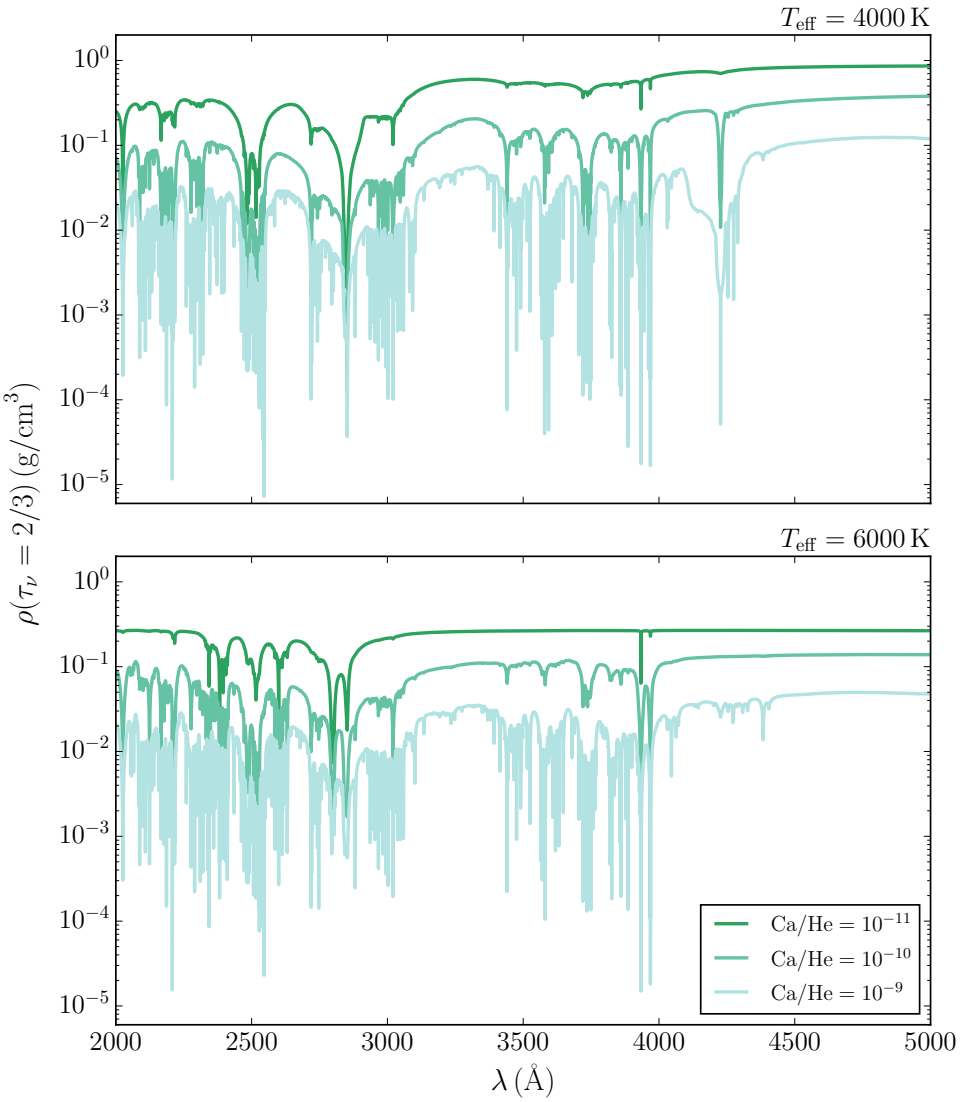

Figure 5.16 – Density at an optical depth $\tau_\nu = 2/3$ with respect to λ. The top panel shows the results for $T_{\rm eff} = 4000\,{\rm K}$ models and the bottom panel for $T_{\rm eff} = 6000\,{\rm K}$. The Ca abundance is given in the legend and a surface gravity $\log g = 8$ is assumed.

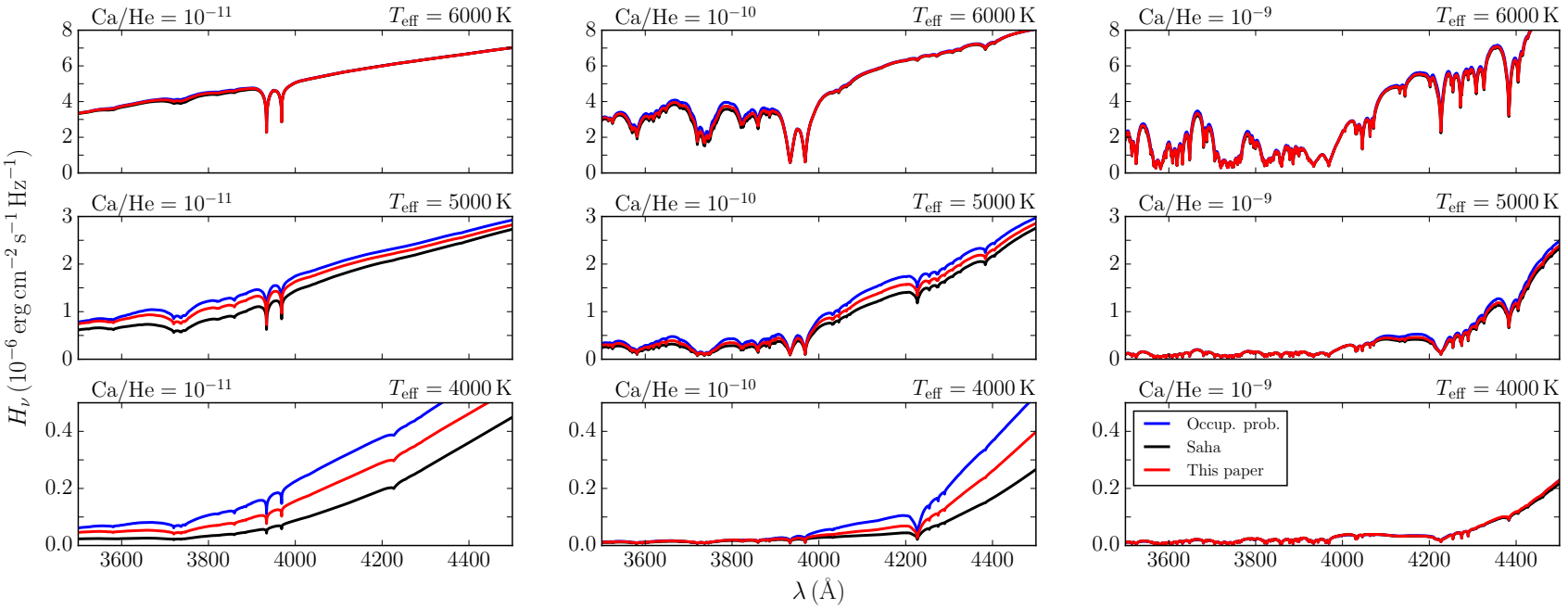

Figure 5.17 – Comparison between synthetic spectra computed using the Hummer & Mihalas (1988) formalism (in blue), the ionization equilibrium presented in this work (in red) and the ideal Saha equation (in black). All models were computed assuming $\log g = 8$ and H/He = 0. The effective temperature and the metal abundance are indicated above each panel.

in both studies. This uncertainty can be removed by relying on the accurate description of the chemical equilibrium described in the current work.

5.6 Applications

To show how the improved constitutive physics presented in this work translates in terms of better spectroscopic fits, this section presents the analysis of two well-known DZ stars : Ross 640 (WD 1626+368) and LP 658−2 (WD 0552−041). Applications to other objects will be presented in other papers of the series.

Our new analysis of these two objects makes use of *Gaia* DR2 parallaxes (Gaia Collaboration, 2016, 2018), $BVRI$ and JHK photometry published in (Bergeron et al. 2001, see Table 5.3), optical spectra published in Giammichele et al. (2012) and UV spectra obtained with HST and the Faint Object Spectrograph (FOS, Koester & Wolff 2000; Wolff et al. 2002)

	Ross 640	LP 658–2
Parallax (mas)	62.915 ± 0.022	155.250 ± 0.029
B[8]	14.02	15.49
V	13.83	14.45
R	13.75	13.99
I	13.66	13.54
J	13.58	13.05
H	13.57	12.86
K	13.58	12.78

Table 5.3 – Observational data

5.6.1 Ross 640

At $T_{\rm eff} \approx 8000\,{\rm K}$, Ross 640 is technically not a "cool" white dwarf. Since the density at its photosphere is $\approx 0.01\,{\rm g\,cm^{-3}}$ ($n_{\rm He} = 1.5 \times 10^{21}\,{\rm cm^{-3}}$), nonideal effects affecting the equation of state and the chemical equilibrium are minimal. However, this density is high enough to induce important differences between Lorentzian profiles and the improved line

[8]There is a 3% uncertainty on all photometric measurements.

profiles presented in Section 5.3.1. This object is therefore the perfect candidate to test our line profiles separately, without the interference of other nonideal effects.

To fit this star, we follow the procedure described in Dufour et al. (2007). In short, we first find $T_{\rm eff}$ and $\log g$ using the photometric technique described in Bergeron et al. (2001). The photometric measurements are first converted into fluxes using the constants reported in Holberg & Bergeron (2006). Then, these observed fluxes f_ν are compared to the model fluxes H_ν to obtain $T_{\rm eff}$ and the solid angle $\pi(R/D)^2$, where R is the radius of the star and D is its distance to the Earth. These parameters are found using a χ^2 minimization technique relying on the Levenberg–Marquardt algorithm. Since D is known from the parallax measurement, the radius R can be computed from the solid angle. The mass of the star and the corresponding surface gravity $g = GM/R^2$ are then found using the evolutionary models of Fontaine et al. (2001). This $\log g$ value being generally different from our initial guess, we repeat the fitting procedure until all fitting parameters are converged.

Once a consistent solution for $T_{\rm eff}$ and $\log g$ is obtained from the procedure described in the previous paragraph, we move to the determination of the abundances using spectroscopic observations. We keep $T_{\rm eff}$ and $\log g$ fixed to the values found using the photometric observations and then fit the Ca/He and H/He ratios by minimizing the χ^2 between our synthetic spectra and the observed spectrum. Since the abundances found with this technique are generally different from those initially used for the photometric fit, the whole fitting procedure is repeated until internal consistency is reached.

Although the abundance ratio between the different heavy elements is kept constant during the χ^2 minimization procedure, we manually adjust the abundance ratio of Mg, Fe and Si to fit the spectral lines labeled in Figure 5.18. All other heavy elements (from C to Cu) are included in the models, but since we could not use any spectral line to fit their abundances, we simply assume the same abundance ratio with respect to Ca as in chondrites (Lodders, 2003).

As shown in Figure 5.18, our solution is consistent with observations across all wavelengths. Our fitting parameters, given in Table 5.4, are roughly similar to those found by Dufour et al. (2007), Koester & Wolff (2000) and Zeidler-K.T. et al. (1986) , although they all found a higher effective temperature (8440 ± 320 K, 8500 ± 200 K and 8800 K, respecti-

vely). One major improvement compared to previous authors is our fit to the broad Mg II 2795/2802 Å lines. To obtain a good fit, Koester & Wolff (2000) arbitrarily multiplied the van der Waals broadening constant of these lines by 10. No arbitrary constants are needed using our new line profiles and a consistent abundance is found from both the optical and ultraviolet magnesium lines.

5.6.2 LP 658−2

LP 658−2 is a DZ star that exhibits a weak Ca II H & K doublet. During the last two decades, many authors have tried to fit this star, but none has reached a consistent solution across all wavelengths. Because they relied on different models and observations, the solutions they found are quite diverse (see Table 5.5).

First, Bergeron et al. (2001) found that LP 658−2 has a helium-rich atmosphere with $T_{\rm eff} = (5060 \pm 60)$ K. However, their analysis was based on atmosphere models that did not include heavy elements, which strongly influence UV opacities and the temperature profile.

Then, using HST data (FOS), Wolff et al. (2002) extended the analysis of Bergeron et al. (2001) with an investigation of the UV portion of the spectrum of LP 658−2. The large absorption feature observed in the UV was interpreted as strong broadening from the wing of Lyα. Keeping the effective temperature fixed at the $T_{\rm eff} = 5060$ K value found by Bergeron et al. (2001), they used this UV absorption feature to fit the hydrogen abundance and found that H/He $= 5 \times 10^{-4}$. However, contrary to other stars in their sample (e.g.,

	Ross 640	LP 658−2
$T_{\rm eff}$ (K)	8070 ± 140	4430 ± 40
$\log g$	7.923 ± 0.008	7.967 ± 0.022
$\log$ H/He	-3.5 ± 0.2	< -5
$\log$ Ca/He	-9.12 ± 0.05	-11.38 ± 0.05
$\log$ Fe/He	-8.44 ± 0.10	–
$\log$ Mg/He	-7.40 ± 0.10	-8.66 ± 0.20
$\log$ Si/He	-7.90 ± 0.20	–

Table 5.4 – Fitting parameters

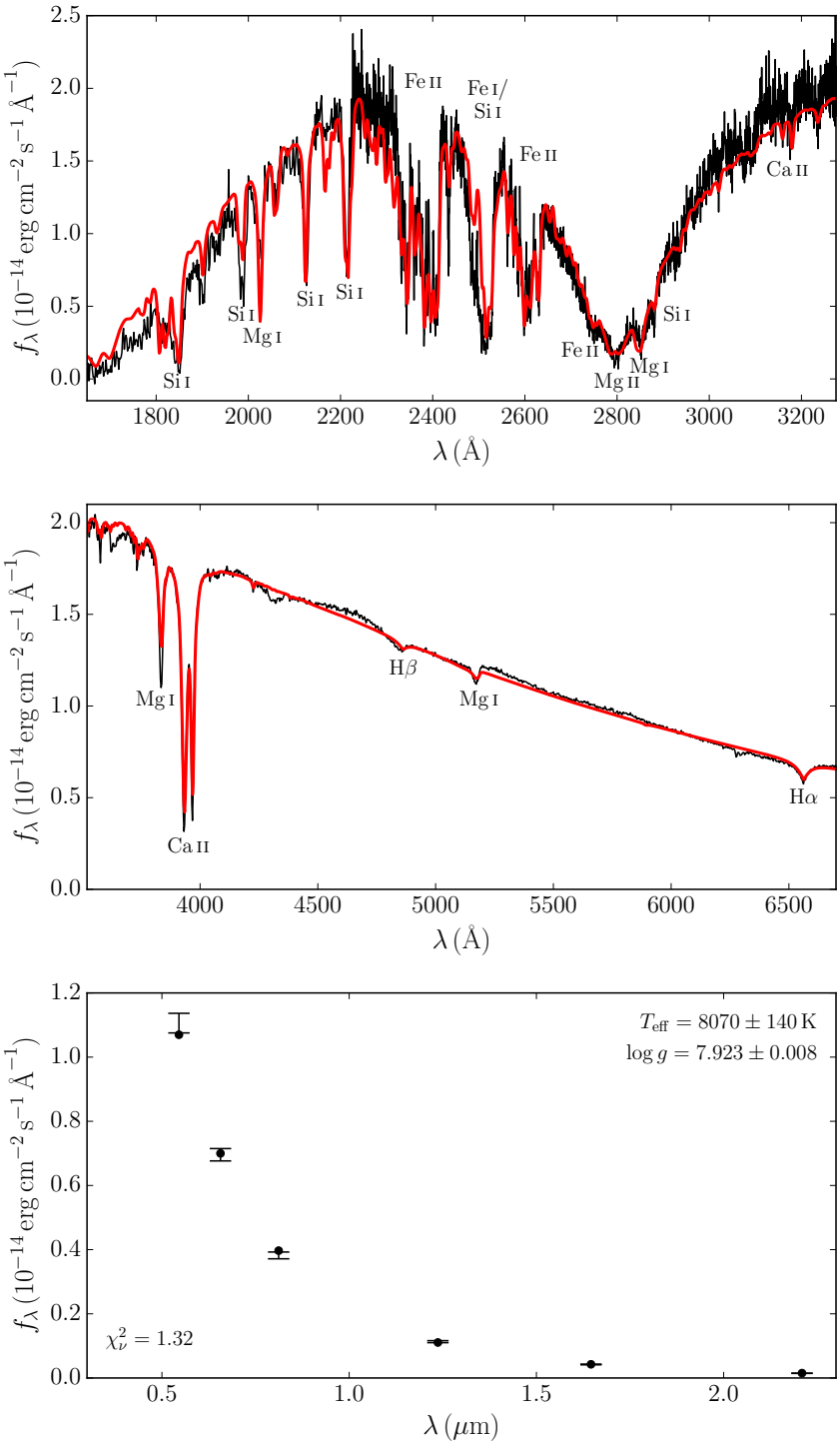

Figure 5.18 – Our best solution for Ross 640. The top panel shows our fit to the UV spectrum, the middle panel is our fit to the visible spectrum and the bottom panel shows our photometric fit to the $BVRI$ and JHK bands.

Authors	$T_{\rm eff}$ (K)	H/He
Bergeron et al. (2001)	5060 ± 60	He
Wolff et al. (2002)	5060 ± 60	H/He $= 5 \times 10^{-4}$
Dufour et al. (2007)	4270 ± 70	He
Giammichele et al. (2012)	5180 ± 80	H

Table 5.5 – Literature review of LP 658−2

LHS 1126 and BPM 4729), they were not able to properly reproduce the shape of this UV absorption feature.

Subsequently, using models that include heavy elements in the atmosphere structure, Dufour et al. (2007) determined a much cooler temperature for LP 658−2 ($T_{\rm eff} = 4270 \pm 70$ K). At this temperature, the photometric data can completely exclude the presence of traces of hydrogen at the level found by Wolff et al. (2002) since H_2−He CIA would cause a strong IR flux depletion that is not observed. However, the solution of Dufour et al. (2007) does not explain the UV absorption feature seen in the FOS data and their spectroscopic solution predicted a large Ca I 4226 Å line, which is completely absent from the observations.

More recently, Giammichele et al. (2012) argued that the narrow H & K lines observed in the spectra of LP 658−2 indicate that it is perhaps a hydrogen-rich star after all. However, although an H-rich composition allowed a better fit to the visible spectrum than that of Dufour et al. (2007), the photometric fit was not as good (and it cannot explain the shape of the UV spectrum).

Using our improved models, we can now obtain a solution that agrees perfectly with the observations across all wavelengths assuming a helium-rich atmosphere (Figure 5.19). We can also constrain the amount of hydrogen to H/He $< 10^{-5}$, as a higher hydrogen abundance would produce an IR flux depletion that is incompatible with the observations. Given this limit, the shape of the UV continuum can no longer be explained by the wing of Lyα (see the green dash-dotted line in Figure 5.19). Instead, we find that the absorption in the UV can naturally be explained by the presence of trace amounts of magnesium (absorption from the Mg II 2795/2802 Å and the Mg I 2852 Å lines). While there are no

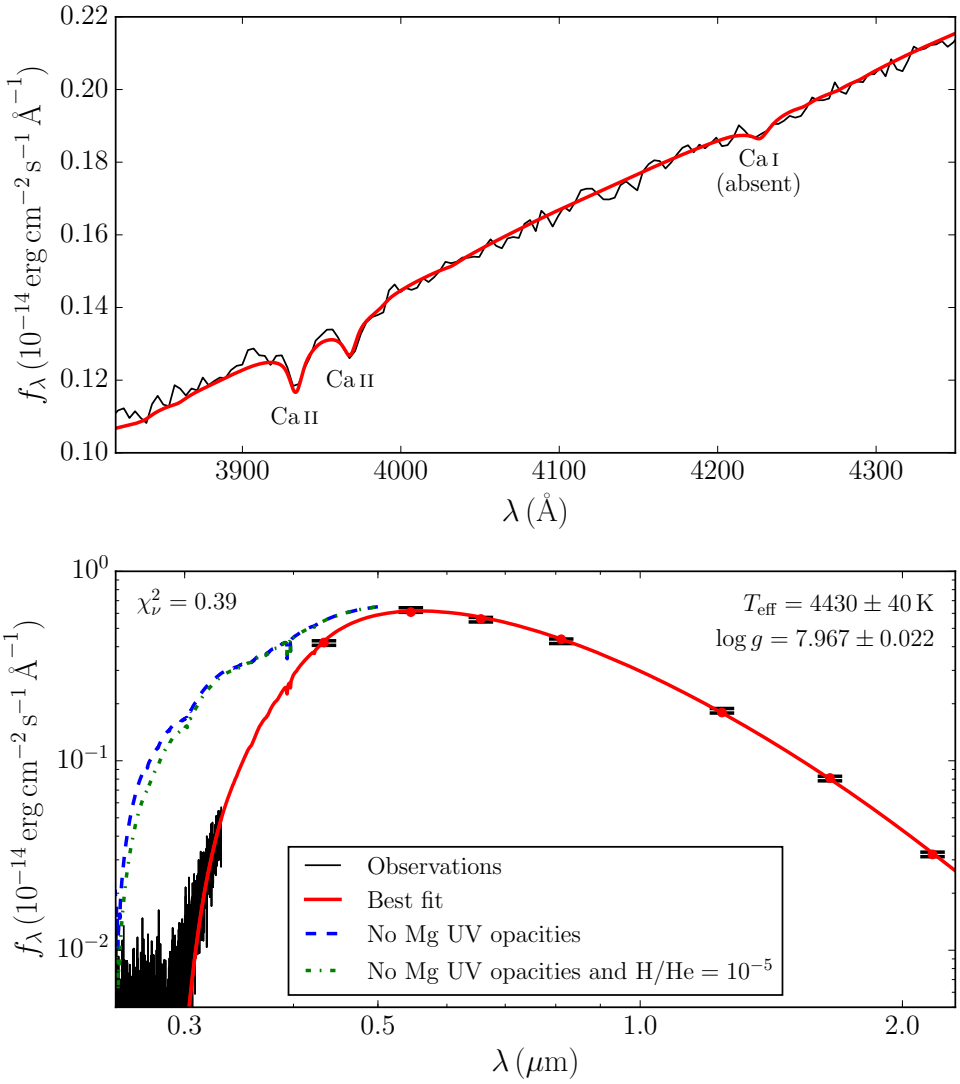

Figure 5.19 – Our best solution for LP 658−2. The top panel shows our fit to the visible spectrum and the bottom panel displays our fit to the photometric observations and to the FOS data. The bottom panel also shows two synthetic UV spectra computed without the Mg II 2795/2802 Å and the Mg I 2852 Å lines, one without hydrogen (in blue) and one with H/He = 10^{-5} (in green).

lines formally detected, the amount of magnesium needed to reproduce the UV continuum is small enough as to not produce features in the optical spectrum.

Finally, our new models do not predict the strong Ca I 4226 Å line that was predicted using the models of Dufour et al. (2007). This is mainly due to the use of our improved line profiles (Section 5.3.1) as well as our new nonideal Ca ionization equilibrium calculation (Section 5.5), the former effect being the most important. Our fitting parameters, given in Table 5.4, were found using the same fitting procedure as for Ross 640.

5.7 Conclusion

We have developed an updated atmosphere model code that incorporates all the necessary constitutive physics for an accurate description of cool DZ stars. This code includes

- The most important heavy-element line profiles computed using the unified line shape theory of Allard et al. (1999),
- CIA profiles suitable for fluids where the density exceeds $0.1\,\mathrm{g\,cm^{-3}}$,
- He Rayleigh scattering and $\mathrm{He^-}$ free-free absorption corrected for collective interactions between atoms,
- An ab initio equation of state for H and He,
- A nonideal chemical equilibrium model for He, C, Ca, Fe, Mg and Na.

While most of these nonideal effects were implemented using results previously published by various authors, we performed our own calculations to assess the chemical equilibrium of heavy elements.

More precisely, we used the classical theory of fluid and DFT calculations to characterize the ionization equilibrium of C, Ca, Fe, Mg and Na in a dense helium medium and under the temperature and density conditions found in the atmosphere of cool DZ stars. These calculations show that the effective ionization potential begins to decrease when the density exceeds $0.1\,\mathrm{g\,cm^{-3}}$, reaching a depression of $\approx 1 - 2\,\mathrm{eV}$ at $\rho = 1\,\mathrm{g\,cm^{-3}}$. We provided analytical fits to our data that can be implemented in atmosphere model codes to obtain the effective ionization potential for a given temperature and density.

We computed atmosphere models using this improved description of the ionization of heavy elements and found that under the right conditions (i.e., weakly polluted, low-$T_{\rm eff}$ objects) the synthetic spectrum can significantly differ from results obtained using the ideal Saha equation. Moreover, we found that the Hummer–Mihalas formalism—when used in conjunction with hydrogenic hard sphere radii—leads to a much stronger pressure ionization than our model, which indicates an overestimation of pressure ionization. This result is consistent with previous findings based on comparisons between atmosphere models and observed spectra (Bergeron et al., 1991). Finally, we showed how the improved constitutive physics included in our code translates into better spectral fits for Ross 640 and LP 658−2, two cool DZ stars that presented a challenge to previous atmosphere model codes.

In the next papers of this series, we will use our updated models to analyze in detail other cool white dwarfs, in particular WD J2356−209 (a peculiar cool DZ star showing an exceptionally strong Na D feature) and the first cool DZ star to show CIA absorption. We will also analyze the bulk of the known cool white dwarfs taking advantage of the *Gaia* data and revisit the spectral evolution of these objects.

Acknowledgments We wish to thank Piotr M. Kowalski for useful discussions regarding the DFT calculations presented in Section 5.5. This work was supported in part by NSERC (Canada).

This work has made use of data from the European Space Agency (ESA) mission *Gaia* (https://www.cosmos.esa.int/gaia), processed by the *Gaia* Data Processing and Analysis Consortium (DPAC, https://www.cosmos.esa.int/web/gaia/dpac/consortium). Funding for the DPAC has been provided by national institutions, in particular the institutions participating in the *Gaia* Multilateral Agreement.

This work has made use of the Montreal White Dwarf Database (Dufour et al., 2017).

This work used observations made with the NASA/ESA Hubble Space Telescope, and obtained from the Hubble Legacy Archive, which is a collaboration between the Space Telescope Science Institute (STScI/NASA), the Space Telescope European Coordinating Facility (ST-ECF/ESA) and the Canadian Astronomy Data Centre (CADC/NRC/CSA).

CHAPITRE 6

A New Generation of Cool White Dwarf Atmosphere Models. II. A DZ Star with Collision-Induced Absorption

If it disagrees with experiment, it's wrong.

—Richard P. Feynman (1918−1988), physicien américain

Ce chapitre est une adaptation de «A New Generation of Cool White Dwarf Atmosphere Models. II. A DZ Star with Collision-Induced Absorption», par Simon Blouin, Patrick Dufour, Nicole F. Allard et Mukremin Kilic. Cet article a été publié en novembre 2018 dans *The Astrophysical Journal*.[1]

6.1 Abstract

In the first paper of this series, we presented our upgraded cool white dwarf atmosphere code. In this second paper, we use our new models to analyze SDSS J080440.63+223948.6 (J0804+2239), the first DZ star to show collision-induced absorption (CIA). This object provides a crucial test for our models, since previous versions of our code were unable to simultaneously fit the metal absorption lines and the CIA. We find an excellent fit to both the spectroscopic and photometric data, which further validates the improved constitutive physics of our models. We also show that the presence of metal lines allows lift of the degeneracy between high and low hydrogen abundances that usually affects the fits of

[1]Blouin, S., Dufour, P., Allard, N. F., & Kilic, M. 2018, ApJ, 867, 161.

white dwarfs with CIA. Finally, we investigate the potential impact of spectroscopically undetected metals on the photometric solutions of DC stars.

6.2 Introduction

Most cool white dwarfs ($T_{\rm eff} \lesssim 5000\,{\rm K}$) are classified as DC stars, meaning that they have a featureless spectrum. At such temperatures, there is too little thermal energy to excite the transitions that are required to produce hydrogen or helium spectral lines in the optical and infrared (IR). Therefore, all the information we can get from these objects is limited to photometric observations and parallaxes. This is sufficient to obtain the effective temperature $T_{\rm eff}$ and the surface gravity $\log g$ by fitting the spectral energy distribution (SED) with atmosphere models (e.g., Bergeron et al., 1997, 2001). It is even possible to deduce the atmospheric composition of these objects through a detailed analysis of their SED. However, different atmosphere model codes often yield different results. For instance, Kowalski & Saumon (2006) and Kilic et al. (2009a,b) conclude that there are virtually no helium-rich DC stars below $T_{\rm eff} = 5000\,{\rm K}$, while the findings of Bergeron et al. (1997, 2001) and Kilic et al. (2006, 2010b) suggest that hydrogen and helium-rich stars are roughly equally abundant in this temperature range. These differences arise mainly because the pure helium atmosphere models of Kowalski & Saumon (2006) are similar to blackbodies, while those of the Montreal group (Bergeron et al., 1995, 2001) are not. Since cool white dwarfs do not have blackbody SEDs, using the models of Kowalski & Saumon (2006) leads to all cool DC stars being assigned a H-rich composition.

Since the featureless spectra of cool DC white dwarfs provide very few opportunities to test and compare different atmosphere models, problems with these models have not yet been identified. In the absence of any observational test, it is hard to say which atmosphere code should be trusted. Fortunately, cool metal-polluted white dwarfs (DZ stars) show atomic absorption lines that can be used to diagnose the accuracy of different atmosphere models. Properly fitting the spectral lines of DZ stars requires models that precisely map the temperature and density conditions of the line-forming regions of the atmosphere. This is particularly true for cool DZ stars, where spectral lines can significantly differ from conventional Lorentzian profiles (Allard et al., 2014, 2016a,b, 2018; Allard & Alekseev, 2014). Good examples of this deviation include the Mg II 2795/2802 Å lines of van Maanen

2 (Wolff et al., 2002) and Ross 640 (Blouin et al., 2018a; Koester & Wolff, 2000), as well as the Na I D doublet of WD J2356−209 (Bergeron et al., 2005; Homeier et al., 2005, 2007).

Another way of diagnosing atmosphere models is to examine cool white dwarfs that show collision-induced absorption (CIA) from molecular hydrogen in the IR. CIA arises due to collisions between H_2 and other particles (H, H_2 or He), which lead to the induction of an electric dipole that enables IR absorption (Lenzuni et al., 1991; Frommhold, 1993). The intensity of the IR flux depletion resulting from CIA depends mainly on the hydrogen abundance and the photospheric density, thus allowing one to constrain the physical conditions in these white dwarfs. Recent theoretical calculations (Blouin et al., 2017) also show that for white dwarfs with a mixed H/He atmosphere and an effective temperature below 4000 K, the H_2−He CIA profiles undergo a density-driven distortion, which could provide another way of assessing the physical conditions in the atmospheres of these objects.

In the first paper of this series (Blouin et al., 2018a), we presented an improved atmosphere model code that relies on ab initio calculations to properly model cool DZ stars. We showed how this upgraded code allows better spectroscopic fits for two cool DZ stars (LP 658–2 and Ross 640) that presented a challenge to previous atmosphere models. These improved fits suggest that our models properly capture the physics and chemistry of cool white dwarf atmospheres. To extend the validation of our code, we turn to SDSS J080440.63+223948.6 (J0804+2239), the first DZ star to show CIA. Originally identified by Kilic et al. (2010b), this star has not yet been the object of any published spectroscopic or photometric fit. Since it presents both metal absorption lines and CIA, this star provides a crucial test for our models. Our detailed analysis of J0804+2239 is presented in Section 6.3, we discuss of the possibility of parameter degeneracies in Section 6.4 and our conclusions are given in Section 6.5.

6.3 Analysis of J0804+2239

6.3.1 Observations

Kilic et al. (2010b) identified J0804+2239 as a DZ white dwarf based on a low-resolution spectrum from the Hobby–Eberly Telescope. These spectra were obtained with the Marcario Low Resolution Spectrograph (LRS ; Hill et al., 1998) on UT 2005 October 30 using the G1 grism with a 2.0″ slit and the GG385 blocking filter. This setup provided an $R = 300$

optical spectrum redward of 4100 Å, which revealed significant absorption features from Ca I and the Na D doublet. The discovery of both metal lines in its optical spectrum and a significant flux deficit in the IR prompted us to obtain a higher resolution and better quality spectrum.

We used the 6.5-m MMT with the Blue Channel Spectrograph to obtain additional spectroscopy of J0804+2239 on UT 2009 November 20. We operated the spectrograph with the 500 line mm^{-1} grating in first order, providing wavelength coverage from 3660 to 6800 Å and a resolving power of $R = 1200$ with the 1.25″ slit. We obtained four three-minute exposures and one two-minute exposure of the target. We obtained all spectra at the parallactic angle and acquired a He–Ar–Ne comparison lamp exposure for wavelength calibration. We used the observations of the spectrophotometric standard star G24–9, which is also a cool white dwarf, for flux calibration. Figure 6.1 shows the MMT spectrum of J0804+2239, which reveals additional lines from Ca II and Fe in the blue.

Our photometric analysis of J0804+2239 is based on the *ugriz* and *JHK* photometry reported in Kilic et al. (2010b) and the *Gaia* DR2 parallax (Gaia Collaboration, 2016, 2018), which are given in Table 6.1. Note that this object was also observed by the UKIDSS Large Area Survey (Lawrence et al., 2007) with photometric measurements that are consistent with those of Kilic et al. (2010b) within the errors.

Observation	Value
Parallax (mas)	25.28 ± 0.14
u	19.73 ± 0.03
g	18.30 ± 0.03
r	17.59 ± 0.03
i	17.39 ± 0.03
z	17.33 ± 0.03
J	16.71 ± 0.04
H	16.92 ± 0.04
K	17.29 ± 0.06

Table 6.1 – Observational data

6.3.2 Best fit

To analyze J0804+2239, we use a new grid of atmosphere models computed using the code described in the first paper of this series (Blouin et al., 2018a). This code takes into account numerous high-pressure effects relevant for the modeling of cool DZ stars. In particular, ab initio equations of state for helium and hydrogen are used (Becker et al., 2014), the most important spectral lines (Ca I 4226 Å, Ca II H & K, Mg I 2852 Å, Mg II 2795/2802 Å, the Mgb triplet and the Na I D doublet) are computed using the unified line shape theory of Allard et al. (1999), the nonideal ionization of helium and metals is taken into account using ab initio results (Kowalski et al., 2007; Blouin et al., 2018a), the high-density distortion of the H_2-He CIA profiles is included (Blouin et al., 2017), continuum opacities are corrected for collective interactions between atoms (Iglesias et al., 2002; Rohrmann, 2018) and the opacity of the far red wing of the Lyα line is included (Kowalski & Saumon, 2006). The model grid we use to fit J0804+2239 extends in four distinct dimensions : hydrogen abundance (helium only, hydrogen only and log H/He from -5 to 0 in steps of 0.5 dex), metal abundance (log Ca/He from -12 to -8 in steps of 0.5 dex), effective temperature (from 3500 to 7000 K in steps of 250 K) and surface gravity (from 7.0 to 9.0 in steps of 0.5 dex).

We use the photometric technique (Bergeron et al., 2001) to find $T_{\rm eff}$, $\log g$ and the hydrogen abundance of J0804+2239. In particular, the solid angle $\pi(R/D)^2$, $T_{\rm eff}$ and the abundance ratio H/He are found using a χ^2 minimization technique based on the Levenberg–Marquardt algorithm. The photometric observations are converted into fluxes using the constants reported in Holberg & Bergeron (2006) and the evolutionary models of Fontaine et al. (2001) are used to find the mass of the star from its solid angle and parallax. Once a consistent photometric solution is found, we use the spectroscopic observations to fit the abundance of Ca, Fe and Na. [2] More specifically, we use the Ca II H & K and Ca I 4226 Å lines to constrain the Ca/He ratio, the small spectroscopic features near $3700-3800$ Å for Fe/He and the Na D doublet for Na/He. The metal abundance ratios thus found being different from our initial guesses, the photometric loop is repeated until internal consistency is reached.

[2] All other heavy elements (from C to Cu) are included in the models, but since we could not use any spectral line to fit their abundance, we simply assumed the same abundance ratio with respect to Ca as in chondrites (Lodders, 2003).

The parameters of our best-fit solution are given in Table 6.2. The uncertainties were estimated by manually altering the solution parameters and visually inspecting the resulting fits. The corresponding spectroscopic and photometric solutions are shown in Figures 6.1 and 6.2. The spectroscopic fit is excellent ; in particular, the Ca II H & K lines, the Ca I 4226 Å line and the Na D doublet are all well reproduced by our model. However, we note that our fit to the weak Fe lines is not so good. This is not surprising insofar as these lines are still computed assuming Lorentzian profiles, which are known to poorly reproduce the spectral features of cool DZ stars (Allard et al., 2018). Nevertheless, since these Fe lines are weak, they have a very limited impact on the model atmosphere structure and they do not affect our solution. As shown in Figure 6.2, the photometric fit is satisfactory : all model fluxes are within (or very close to) the observational uncertainties and the reduced χ^2 is 2.0.

Parameter	Value
$T_{\rm eff}$	4970 ± 100 K
$\log g$	7.98 ± 0.05
$\log$ H/He	-1.6 ± 0.2
$\log$ Ca/He	-10.0 ± 0.1
$\log$ Fe/He	-9.8 ± 0.2
$\log$ Na/He	-11.0 ± 0.2
$\tau_{\rm cool}$	5.9 ± 0.6 Gyr

Table 6.2 – Fitting parameters

Also shown in Figure 6.2 is the best solution found when assuming a hydrogen-free atmosphere. To obtain this solution, we used the whole fitting procedure described above to find the best $T_{\rm eff}$, $\log g$ and metal abundances if a hydrogen-free atmosphere is assumed. This exercise clearly shows that there must be hydrogen in the atmosphere of this star, since there is no other way to generate the IR flux depletion observed in the photometric measurements.

Note that with the previous version of our atmosphere code (Dufour et al., 2007) we were unable to find a solution that simultaneously fit both the photometry and the spectroscopy. Moreover, the atmospheric parameters of the best solution found with those

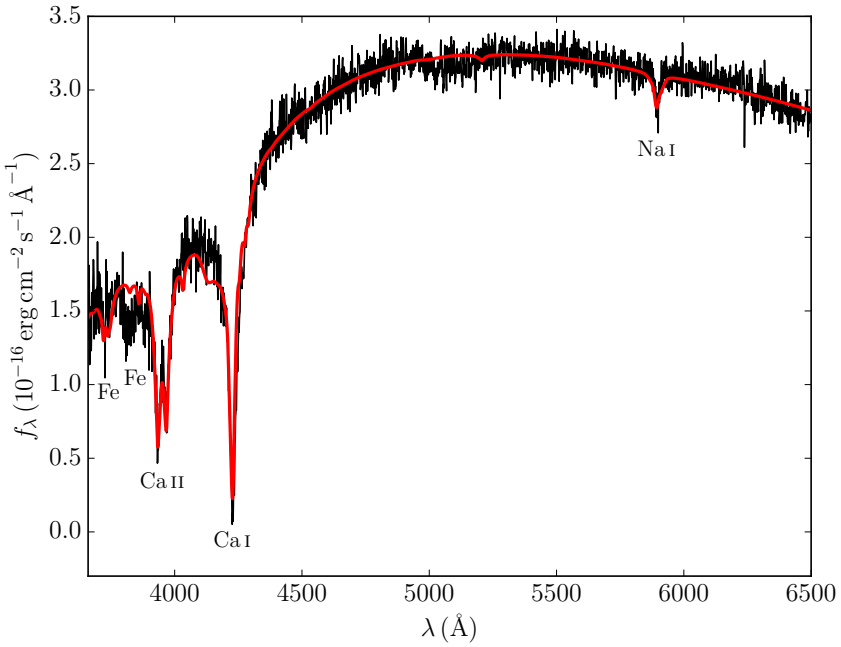

Figure 6.1 – Best spectroscopic solution. The corresponding fitting parameters are given in Table 6.2.

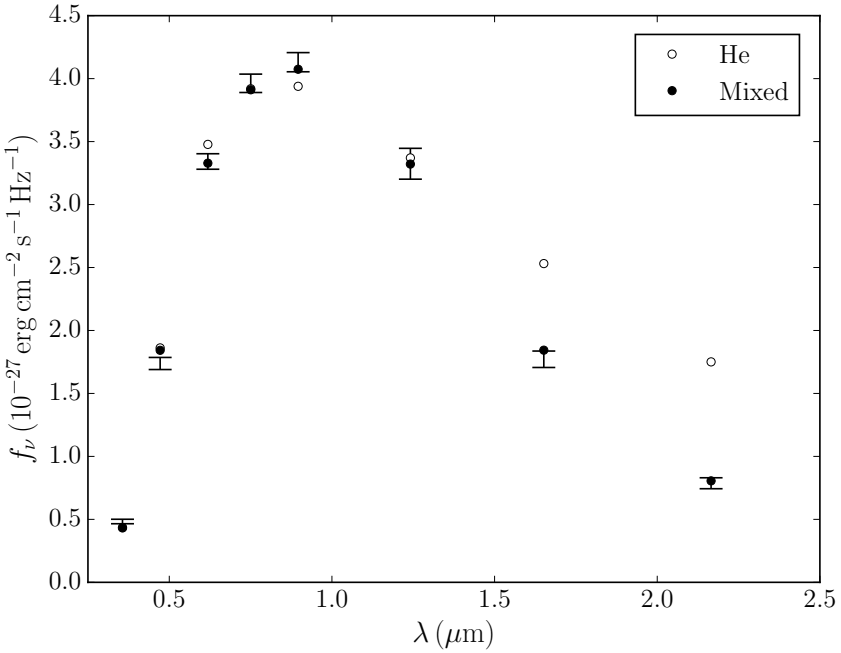

Figure 6.2 – Comparison between the best photometric solution found when assuming a hydrogen-free atmosphere (open circles) and the best solution found when the H/He ratio is fitted to the photometric observations (filled circles). The atmospheric parameters of the mixed model are given in Table 6.2 and the hydrogen-free model has $T_{\mathrm{eff}} = 4620\,\mathrm{K}$, $\log g = 7.93$ and $\log \mathrm{Ca/He} = -10.5$.

models were quite different ($T_{\rm eff} = 4780\,{\rm K}$, $\log g = 7.80$, $\log {\rm H/He} = -3$ and $\log {\rm Ca/He} = -10.9$), resulting in a cooling time of 4.2 Gyr, which is 1.7 Gyr shorter than the cooling time found with our improved models. The next section describes the improvements made to our model atmosphere code that explain the difference between both solutions.

6.3.3 On the importance of the improved constitutive physics

The density at the photosphere of our best-fitting model reaches $0.07\,{\rm g\,cm^{-3}}$ ($n_{\rm He} = 1.05 \times 10^{22}\,{\rm cm^{-3}}$). This density is low enough that many nonideal high-density effects (e.g., nonideal ionization equilibrium, Kowalski et al. 2007; Blouin et al. 2018a and nonideal dissociation equilibrium, Kowalski 2006b) are negligible. Nevertheless, the photospheric density is high enough to significantly affect spectral line profiles. Figure 6.3 compares the best spectroscopic solution found in the previous section to the best solution found from a model grid computed assuming Lorentzian profiles for all metal lines. Clearly, the improved profiles for Ca II H & K (Allard & Alekseev, 2014) and Ca I 4226 Å lead to a much better spectral fit. Still, our Ca I 4226 Å profile is not perfect, since it predicts an unobserved small opacity bump around 4140 Å. This could be due to the fact that our Ca I 4226 Å profile was derived from interaction potentials that are not as accurate as the ones used for the rest of our improved line profiles (the Ca−He potentials were found through open-shell configuration-interaction singles calculations, using the ROCIS module of the ORCA quantum chemistry package, Neese 2012). We expect that more accurate potentials will resolve this issue.

Another improvement to the atmosphere code which proved to be crucial to obtain a good fit to J0804+2239 is the use of improved CIA profiles. As mentioned above, we use the H_2−He CIA profiles given in Blouin et al. (2017). They consist of the profiles computed by Abel et al. (2012), but corrected for various high-density nonideal effects. Below a photospheric density of about $0.1\,{\rm g\,cm^{-3}}$ ($n_{\rm He} = 1.5 \times 10^{22}\,{\rm cm^{-3}}$) , these effects are almost nonexistent and the CIA profiles used to compute our best-fitting model are therefore virtually identical to those of Abel et al. (2012). Before the implementation of these profiles, our atmosphere models were relying on the CIA profiles of Jørgensen et al. (2000). Using these profiles, we found that it is impossible to obtain a photometric solution that is as good as the one found using the profiles of Abel et al. (2012). In fact, as shown

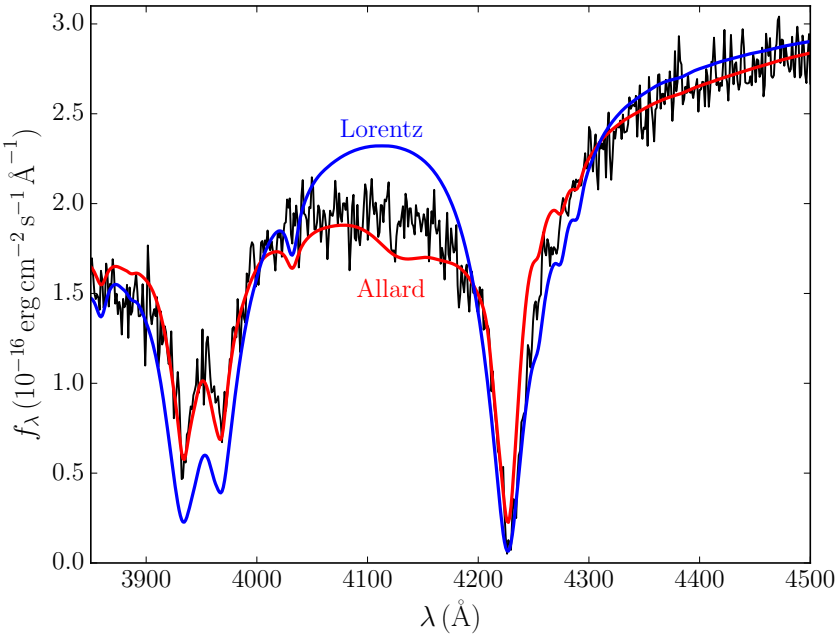

Figure 6.3 – Comparison between the best solutions found when line profiles are computed using the unified line shape theory of Allard et al. (1999) (in red) and when conventional Lorentzian profiles are assumed (in blue).

in Figure 6.4, the profiles of Jørgensen et al. (2000) lead to an SED that does not have enough flux in the J and H bands to fit the photometric observations. This is a direct consequence of the strong disagreement between the CIA profiles of Jørgensen et al. (2000) and Abel et al. (2012) in the $\approx 1.2 - 2\,\mu$m region (see Figure 6.5). We are confident that the profiles of Abel et al. (2012) are more accurate, since Jørgensen et al. (2000) computed their CIA profiles using potential energy and induced dipole surfaces that were obtained with a smaller basis set. Moreover, using an entirely independent method (i.e., molecular dynamics with density functional theory), Blouin et al. (2017) found absorption spectra that were in better agreement with Abel et al. (2012) than with Jørgensen et al. (2000) in the $\approx 1.2 - 2\,\mu$m interval.

6.4 Possible degeneracies

6.4.1 Hydrogen abundance in J0804+2239

In our atmosphere models, the intensity of the $H_2{-}He$ CIA reaches a maximum when $\log \mathrm{H/He} \approx -2.5$. This maximum is the result of two competing effects. On the one hand,

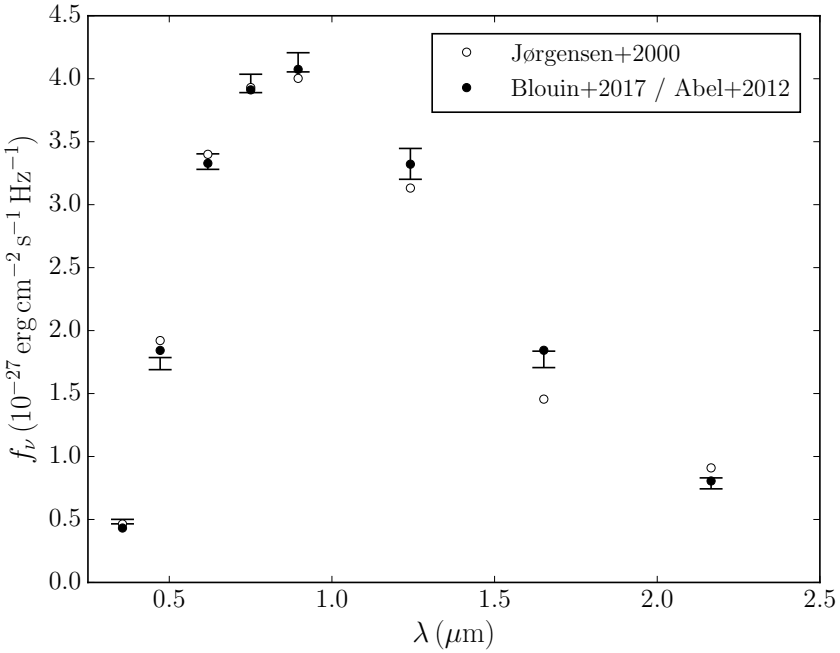

Figure 6.4 – Best photometric solutions for model grids with $\log \mathrm{H/He} = -1.6$ and different CIA implementations. The filled circles show the solution obtained using the CIA profiles of Abel et al. (2012) or Blouin et al. (2017) (which are virtually identical for the physical conditions encountered at the photosphere of J0804+2239) and the open circles illustrate the best fit found when using the CIA profiles of Jørgensen et al. (2000). T_{eff} and $\log g$ are adjusted to fit the photometry, while spectroscopy is used to fit the metal abundance.

if the H/He ratio is high, H_2 is more abundant and the H_2-He CIA intensity increases. On the other hand, if there is little hydrogen in the atmosphere, the density of the atmosphere is higher, which also leads to a stronger CIA. Because of this maximum, χ^2 minimization algorithms often find two solutions when fitting the photometric observations of white dwarfs with CIA in their spectrum : one above the $\log \mathrm{H/He} \approx -2.5$ maximum and one below. In the case of DC stars, the spectroscopic data is not helpful in deciding between the two solutions, so the usual approach is to simply keep the solution that has the smallest χ^2. However, the difference between the two solutions can be quite small and minute changes in the models or in the observations can make the difference between choosing a solution instead of the other. As an example, Kilic et al. (2010b) concluded that SDSS J030924.87+002525.3, SDSS J143718.15+415151.5 and SDSS J172257.78+575250.7 have, respectively, log H/He abundance ratios of -4.43, -4.26 and -4.21, while Gianninas et al. (2015) found that the same three stars have abundance ratios of -1.30, -1.97 and -1.49.

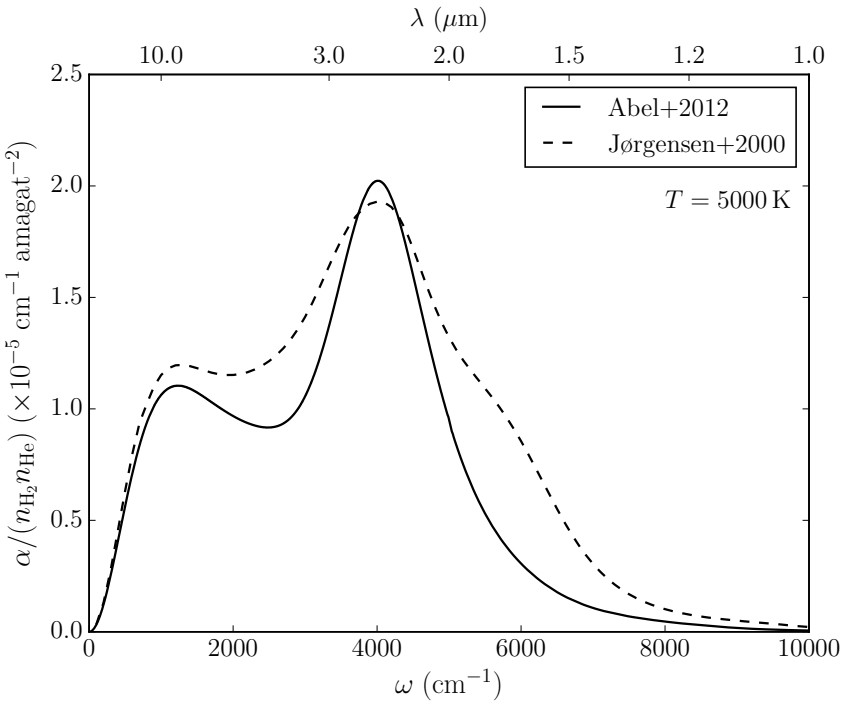

Figure 6.5 – H_2-He CIA profiles at 5000 K, as computed by Abel et al. (2012) and Jørgensen et al. (2000). The spectra are divided by the number density of H_2 and He.

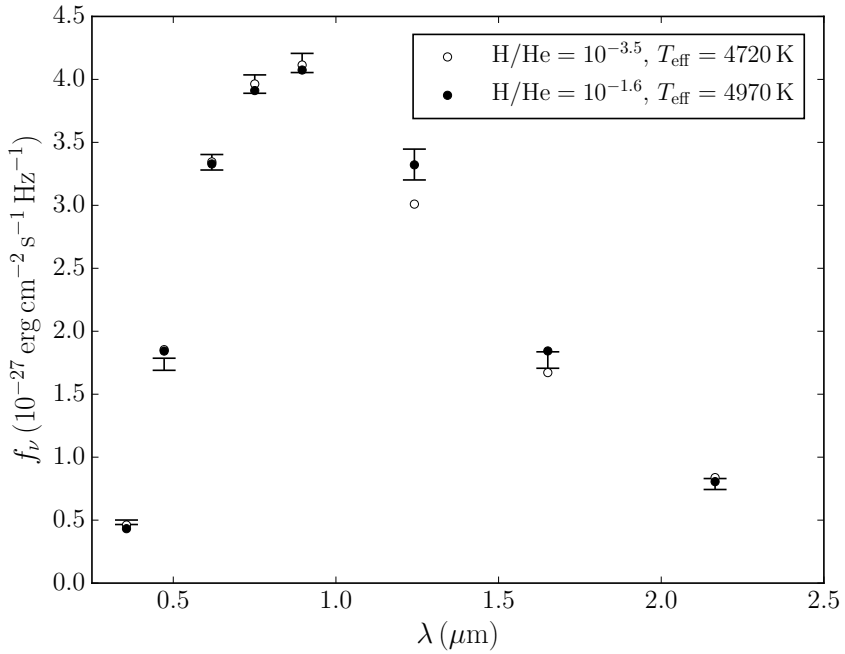

Figure 6.6 – Best photometric solutions for models with $\log \mathrm{H/He} = -1.6$ and $\log \mathrm{H/He} = -3.5$. The first solution has a metal abundance of $\log \mathrm{Ca/He} = -10.0$ and fits the spectroscopic data very well (Figure 6.1), while the second solution has a metal abundance of $\log \mathrm{Ca/He} = -11.0$ and is unable to reproduce the spectral lines observed in J0804+2239.

Can our analysis of J0804+2239 also be tainted by uncertainties associated with this degeneracy of the CIA intensity ? As in the examples given in the previous paragraph, we found that it is possible to obtain a second photometric solution for J0804+2239 using a hydrogen abundance below the CIA maximum at $\log \mathrm{H/He} \approx -2.5$. This solution, found at $\log \mathrm{H/He} = -3.5$, is shown in Figure 6.6. This second photometric solution is slightly better than our original solution at $\log \mathrm{H/He} = -1.6$: the reduced χ^2 is 1.9. However, in order to reach the right density conditions to obtain this second solution, we had to decrease the metal abundance down to $\log \mathrm{Ca/He} = -11.0$. Such a low metallicity is totally incompatible with the metal lines visible in the spectrum of J0804+2239. At $\log \mathrm{Ca/He} = -11.0$, the spectral lines are simply too shallow to reproduce the observed spectrum, and hence this second solution can safely be discarded. We can therefore be confident that our fit of J0804+2239 is not affected by any degeneracy related to the CIA intensity since the spectroscopic data enables us to lift this degeneracy. Note that if J0804+2239 had not shown any metal lines (as it is the case with DC stars), we could not have eliminated this degeneracy.

6.4.2 DC stars with undetected metals

In this section, we discuss of another type of degeneracy : undetectable metals in DC stars. It is well known that the inclusion of metals in atmosphere models can significantly affect the effective temperature derived from a photometric fit (compare for example the results found by Bergeron et al. 1997, 2001 to those of Dufour et al. 2005, 2007 for the same DQ and DZ samples). In this context, Figure 6.6 raises an interesting question. Can a spectroscopically undetectable amount of metals create a degeneracy in the photometric solution of DC stars that show CIA features ? If it is the case, the atmospheric parameters of many DC stars could be wrong due to the impossibility of lifting this degeneracy.

To investigate this point, we compared *ugriz* and *JHK* photometry of atmosphere models that have the same effective temperature and hydrogen abundance, but that have different metal abundances (note that a surface gravity $\log g = 8$ is assumed throughout this section). Figure 6.7 shows a sample of these comparisons for models without any heavy elements, with $\log \mathrm{Ca/He} = -12$ and with $\log \mathrm{Ca/He} = -11$. (For a typical spectrum with a signal-to-noise ratio of 50 and a spectral resolution of 1 Å, the spectroscopic detection

threshold of metals is $\log \mathrm{Ca/He} \approx -11.5$, assuming T_{eff} and H/He values similar to the models of Figure 6.7.) We notice that the SEDs of models with a relatively high hydrogen abundance ($\log \mathrm{H/He} = -2$) are barely affected by the addition of heavy elements, while the SEDs of models with a lower hydrogen abundance ($\log \mathrm{H/He} = -4$) are much more affected. There are two reasons for this difference. First, hydrogen is much less transparent than helium. As a result, for a model with little hydrogen, it does not take a lot of heavy elements before we start "seeing" metals in the SED. Secondly, the atmosphere model structure is less affected by the addition of metals for the $\log \mathrm{H/He} = -2$ models since hydrogen provides most of the free electrons, which largely control continuum opacities and the photospheric pressure. For the $T_{\mathrm{eff}} = 4500\,\mathrm{K}$, $\log \mathrm{H/He} = -2$ and $\log \mathrm{Ca/He} = -11$ model, hydrogen atoms provide 96.9% of the free electrons at the photosphere, while heavy elements account for a mere 3.1%. Since the addition of metals barely affects the free electron density, it is unsurprising that it hardly affects the SED. On the contrary, for the $T_{\mathrm{eff}} = 4500\,\mathrm{K}$, $\log \mathrm{H/He} = -4$ and $\log \mathrm{Ca/He} = -11$ model, heavy elements provide 23.4% of the free electrons at the photosphere and can therefore significantly influence the atmosphere model structure.

From our analysis of Figure 6.7, we can conclude that for stars with a relatively high hydrogen abundance there is no danger of solution degeneracies caused by a spectroscopically undetectable amount of metals. However, for DC stars with a smaller amount of hydrogen (e.g., $\log \mathrm{H/He} = -4$), the SED is changed even when a spectroscopically undetectable amount of metals is added to the atmosphere and there is therefore a risk of finding an erroneous photometric solution. In other words, it is a priori possible that fitting a white dwarf that has a small quantity of metals (e.g., $\log \mathrm{Ca/He} = -12$) using metal-free models yields an effective temperature and hydrogen abundance that are incorrect given that the influence of metals on the atmosphere structure of this hypothetical star was not taken into account.

If this scenario has a chance to come true, then it should be possible for a metal-free model to emulate the SED of a model with a small quantity of metals and a different T_{eff} and H/He abundance ratio. To test if it is the case, we tried to fit the SEDs of cool DZ stars using a grid of helium-rich DC models. For these fits, both the effective temperature and the H/He ratio were adjusted. We explored a parameter space extending

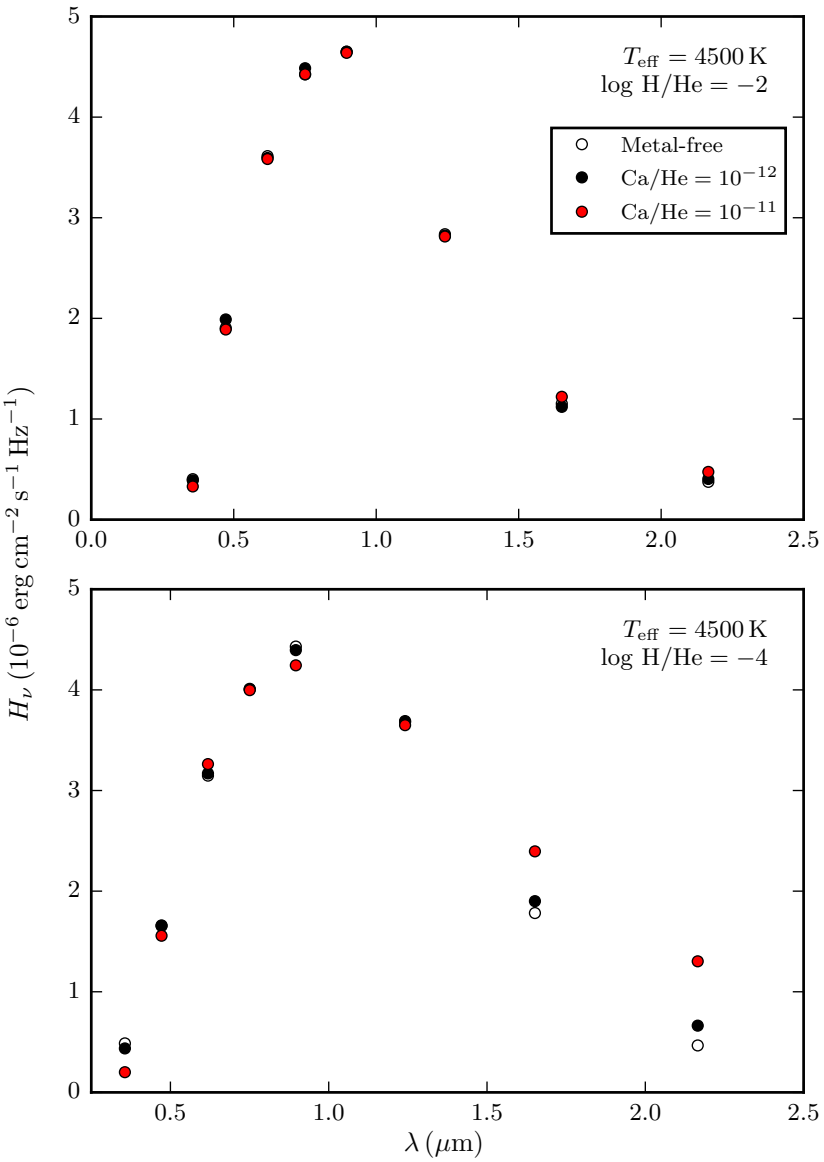

Figure 6.7 – *ugriz* and *JHK* photometry of atmosphere models with $T_{\rm eff} = 4500\,{\rm K}$ and $\log g = 8$. The top panel shows SEDs of models with $\log {\rm H/He} = -2$ and the bottom one those of $\log {\rm H/He} = -4$ models. On each panel, we compare the SEDs of models with different metal abundances, as indicated in the legend. For the top panel, note that the metal-free SED is virtually identical to the SED with $\log {\rm Ca/He} = -12$.

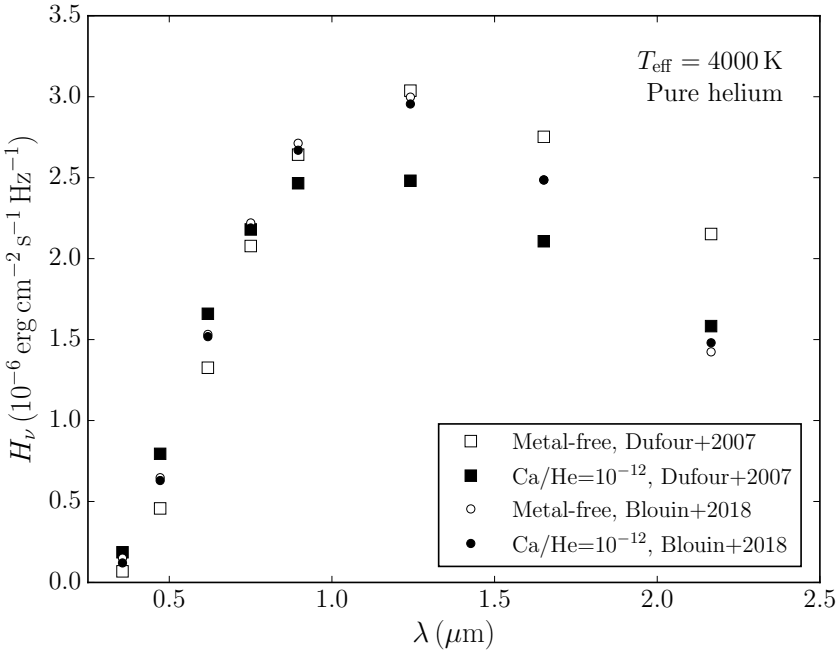

Figure 6.8 – SEDs of hydrogen-free atmosphere models with $T_{\rm eff} = 4000\,{\rm K}$ and $\log g = 8$. The circles correspond to the results obtained using the models of Blouin et al. (2018a) and the squares to those found with the models of Dufour et al. (2007). For the latter, note how the SED changes when a minute amount of metals is added to the atmosphere.

from $T_{\rm eff} = 4000$ to $5500\,{\rm K}$, from $\log {\rm H/He} = -6$ to -3, and from $\log {\rm Ca/He} = -13$ (well below the detection threshold) to -11 (slightly above the detection threshold). In the worst case, we find that the effective temperature obtained by the fitting procedure has a 250 K discrepancy with the actual temperature of the DZ model that is being fitted. More important are the discrepancies found on H/He (which can reach 3 dex), but this is simply a manifestation of the CIA degeneracy described in Section 6.4.1 and not an effect attributable to the presence of metals in the atmosphere. Therefore, we can conclude that the degeneracy due to the presence of undetected metals does not generate errors that go beyond the usual fitting uncertainties.

Note that these conclusions also extend to DC stars that do not show any CIA feature ($\log {\rm H/He} < -5$). This result is quite different than what was previously found using the models of Dufour et al. (2007). Figure 6.8 shows how the SED of those models are affected by the addition of a small amount of metals. At $T_{\rm eff} = 4000\,{\rm K}$, a metal abundance as low as $\log {\rm Ca/He} = -12$ leads to drastic differences in the shape of the SED. As shown in Figure 6.8, such a difference is not visible with our improved models. The

main explanation for the disagreement between both sets of models lies in the atmosphere model structure of pure helium models. In particular, as the pressure ionization of helium (Kowalski et al., 2007) was not implemented in the models of Dufour et al. (2007), their pure helium models are much more transparent than our new models. The photospheric pressure reaches $10^{13}\,\mathrm{dyn/cm^2}$ for $T_{\rm eff} = 4000\,\mathrm{K}$, more than 20 times the pressure of a model with $\log \mathrm{Ca/He} = -12$. On the contrary, with our improved models, the model atmosphere structure without metals and with $\log \mathrm{Ca/He} = -12$ are very similar. Because of the pressure ionization of helium, free electrons are still abundant when metals are absent. For that reason, the intensity of $\mathrm{He^-}$ free-free absorption does not fall dramatically as it is the case with the models of Dufour et al. (2007).

6.5 Conclusion

We presented the first spectroscopic and photometric fit of J0804+2239, a unique cool DZ star that shows CIA. The improvements recently made to our atmosphere code (in particular, the improved high-pressure Ca line profiles and the new $\mathrm{H_2}-\mathrm{He}$ CIA profiles) proved to be crucial to obtain a good fit. These results show that our upgraded code properly captures the physics of the moderately dense atmospheres of cool DZ stars.

Because its atmosphere contains metals, the hydrogen abundance of J0804+2239 could be determined with greater certainty than the hydrogen abundance of most white dwarfs with CIA features. In fact, the presence of metal absorption lines lifts the degeneracy between high and low hydrogen abundances. We also explored the possibility that spectroscopically undetected metals could affect the photometric solutions of DC stars. We found that, in the worst case, the errors induced on the atmospheric parameters are of the order of the usual fit uncertainties.

In the next paper of this series, we will continue the observational validation of our model atmosphere code with still cooler DZ stars. In particular, we will revisit WD J2356−209, a cool DZ with an atypically strong Na D doublet.

Acknowledgments This work was supported in part by NSERC (Canada). This work has made use of the Montreal White Dwarf Database (Dufour et al., 2017).

This work has made use of data from the European Space Agency (ESA) mission *Gaia* (https://www.cosmos.esa.int/gaia), processed by the *Gaia* Data Processing and Analysis Consortium (DPAC, https://www.cosmos.esa.int/web/gaia/dpac/consortium). Funding for the DPAC has been provided by national institutions, in particular the institutions participating in the *Gaia* Multilateral Agreement.

CHAPITRE 7

A New Generation of Cool White Dwarf Atmosphere Models. III. WD J2356−209 : Accretion of a Planetesimal with an Unusual Composition

It is just these exceptions that lead to an advance in our knowledge.
—Edward C. Pickering (1846−1919), astronome et physicien américain

Ce chapitre est une adaptation de l'article «A New Generation of Cool White Dwarf Atmosphere Models. III. WD J2356−209 : Accretion of a Planetesimal with an Unusual Composition», par Simon Blouin, Patrick Dufour, Nicole F. Allard, Samir Salim, Michael Rich et Léon Koopmans. Ce travail a été publié en février 2019 dans *The Astrophysical Journal*.[1]

7.1 Abstract

WD J2356−209 is a cool metal-polluted white dwarf whose visible spectrum is dominated by a strong and broad sodium feature. Although discovered nearly two decades ago, no detailed and realistic analysis of this star had yet been realized. In the absence of atmosphere models taking into account the nonideal high-density effects arising at the photosphere of WD J2356−209, the origin of its unique spectrum had remained nebulous.

[1]Blouin, S., Dufour, P., Allard, N. F., Salim, S., Rich, R. M., & Koopmans, L. V. E. 2019, ApJ, 872, 188.

We use the cool white dwarf atmosphere code presented in the first paper of this series to finally reveal the secrets of this peculiar object and details about the planetesimal that polluted its atmosphere. Thanks to the improved input physics of our models, we find a solution that is in excellent agreement with the photometric observations and the visible spectrum. Our solution reveals that the photosphere of WD J2356−209 has a number density ratio of $\log \mathrm{Na/Ca} = 1.0 \pm 0.2$, which is the highest ever found in a white dwarf. Since we do not know how long ago the accretion episode stopped (if it has), we cannot precisely determine the composition nor the mass of the accreted planetesimal. Nevertheless, all scenarios considered indicate that its composition is incompatible with that of chondrite-like material and that its mass was at least 10^{21} g.

7.2 Introduction

WD J2356−209[2], was discovered by Oppenheimer et al. (2001) as part of their search for cool white dwarfs in the galactic halo. Since its spectrum shows a broad asymmetric feature around 6000 Å, it was described as having a "bizarre spectrum, incomparable to any other known object".

Using only BRI photometry, Bergeron (2003) attempted the first atmospheric parameter determination of WD J2356−209. It was found that it must have an effective temperature of the order of 4000 K : the best photometric solution was at $T_{\rm eff} = 3400$ K if a hydrogen-rich atmosphere was assumed and at $T_{\rm eff} = 4610$ K in the case of a helium-rich composition. Note that because of the absence of Balmer lines at such low temperatures, the atmospheric composition of this object remained unknown.

Shortly after, Salim et al. (2004) reobserved WD J2356−209 and confirmed the measurements of Oppenheimer et al. (2001). In particular, in a color-color diagram, it appears as a strong outlier with an excessively blue $B - V$ and an extremely red $V - I$. Salim et al. (2004) suggested that these peculiar colors may be the result of a very broad Na I D doublet, implying that WD J2356−209 is a metal-polluted white dwarf (i.e., a DZ star).

Then, Bergeron et al. (2005) obtained new photometric observations of WD J2356−209 in the $BVRI$ and JH bands. They picked up the interpretation proposed by Salim et al.

[2]Also known as WD 2354−211 in the electronic version of of the Catalog of Spectroscopically Identified White Dwarfs (McCook & Sion, 1999)

(2004) and analyzed WD J2356−209 with atmosphere models that included Na. Their solution ($T_{\rm eff}$ = 4790 K and log Na/He = −5) yields a satisfactory fit both to their photometric measurements and to the spectrum of Oppenheimer et al. (2001) in the 5000–9000 Å region. However, in the absence of any spectrum below 5000 Å they could not detect any other metal than Na, and thus Na and He were the only atomic species included in their atmosphere model. In retrospective, this was an unrealistic assumption. With the discovery of dozens of circumstellar debris discs around metal-polluted white dwarfs (e.g., Zuckerman & Becklin, 1987; Gänsicke et al., 2006; Farihi et al., 2009; Melis et al., 2010; Rocchetto et al., 2015) and the detection of planetary transits in the light curve of WD 1145+017 (Vanderburg et al., 2015; Gänsicke et al., 2016; Croll et al., 2017) it is now clear that the presence of heavy elements in white dwarfs is the consequence of the accretion of tidally disrupted rocky bodies (Jura, 2003; Farihi et al., 2010; Jura & Young, 2014). Therefore, all elements representative of the composition of rocky planetesimals should be included in DZ atmosphere models.

Moreover, the analysis of Bergeron et al. (2005) was based on models that did not take into account the nonideal high-density effects that are known to arise under the physical conditions met in the atmospheres of cool white dwarfs. In particular, their models relied on the ideal gas law, which is inappropriate for the high pressures of cool white dwarfs (e.g., Saumon et al., 1995; Becker et al., 2014) ; nonideal effects affecting the chemical equilibrium (Kowalski et al., 2007; Blouin et al., 2018a) were neglected ; and simple Lorentzian line profiles, which poorly reproduce the spectral lines observed in cool DZ white dwarfs (Allard et al., 2016b, 2018; Hollands et al., 2017), were assumed.

An independent analysis of WD J2356−209 was performed by Homeier et al. (2005, 2007) using the PHOENIX general-purpose stellar atmosphere code (Hauschildt et al., 1997; Baron & Hauschildt, 1998; Hauschildt & Baron, 1999) and the spectrum obtained by Oppenheimer et al. (2001). The first results identified an apparent overabundance of Na relative to Ca and suggested that WD J2356−209 has a hydrogen-rich atmosphere (Homeier et al., 2005). An important limitation of this first analysis was that line profiles implemented in their atmosphere models were limited to perturber densities not exceeding 10^{19} cm^{-3} (Allard et al., 2003), which is about three orders of magnitude below the density at the photosphere of a $T_{\rm eff}$ = 4000 K helium-rich DZ white dwarf (Blouin et al., 2018a).

In a second analysis (Homeier et al., 2007), improved line profiles appropriate for larger densities were employed and a helium-rich composition was favored. Homeier et al. (2005, 2007) were also the first to point out that metal hydrides (namely, MgH and CaH) should form under the conditions encountered in the atmosphere of WD J2356−209. However, these preliminary analyses were exploratory in nature and no quantitative fit to the spectroscopic and photometric data was attempted. Furthermore, as in Bergeron et al. (2005), their models did not include the nonideal effects that are known to affect the chemical equilibrium and the equation of state.

In this paper, the third of a series, we present the most detailed analysis to date of WD J2356−209. Our models, which include an accurate description of the high-pressure physics relevant to the modeling of cool DZ stars (see Blouin et al. 2018a,b, hereafter Papers I and II), make it possible for the first time to obtain a satisfactory fit to the photometric data and to the entire visible spectrum. In Section 7.3, we present the observations on which our analysis of WD J2356−209 is based. A few new improvements brought to our model atmosphere code are detailed in Section 7.4. Section 7.5 contains our analysis of WD J2356−209, where we find that the sodium to calcium ratio is the highest ever encountered in a white dwarf photosphere. Finally, Section 7.6 provides a discussion on the origins of the peculiar abundances measured in WD J2356−209 and our conclusions are given in Section 7.7.

7.3 Observations

Our analysis of WD J2356−209 makes use of $BVRI$ and JH photometry from Bergeron et al. (2005), *grizy* photometry from Pan-STARRS (Chambers et al., 2016) and the *Gaia* DR2 parallax measurement (Gaia Collaboration, 2016, 2018). The parallax indicates that WD J2356−209 is located at a distance $D = (64.8 \pm 2.5)\,\mathrm{pc}$ from the Earth, which is in good agreement with the estimation obtained by Salim et al. (2004) using color-magnitude relations ($74 \pm 34\,\mathrm{pc}$).

For the spectroscopy, we rely on data obtained with LRIS (Oke et al., 1995) on Keck I telescope on 2002 September 14.[3] A 300/5000 grating was used for both the blue and

[3]Proposal "Spectroscopy of High-Velocity Cool White Dwarfs" by Léon Koopmans (PI), Roger Blandford, Brad Hansen, Ben Oppenheimer and Mike Rich

the red spectra, together with a 1 arcsec slit, giving an effective resolution of 10.3 Å. A D560 dichroic filter was used to split the beams, giving useful wavelength coverage of 5000−9000 Å on the red side and 3500−5800 Å on the blue side. Each of the blue and red spectra were obtained with a total exposure time of 45 minutes. Standard arc spectra were taken for wavelength calibration. Only one standard star was available for flux calibration, while there were no suitable observations for the removal of the telluric absorption. The observations of the standard star may have been affected by detector non-linearity. Therefore, we correct the flux calibration by scaling the spectrum so that the photometry extracted from the joined blue/red spectrum agrees with the broad-band photometry. As shown in Figure 7.1, the scaled LRIS spectrum agrees very well with the low-resolution shallow spectrum of Oppenheimer et al. (2001) in the region where they overlap (> 5000 Å).

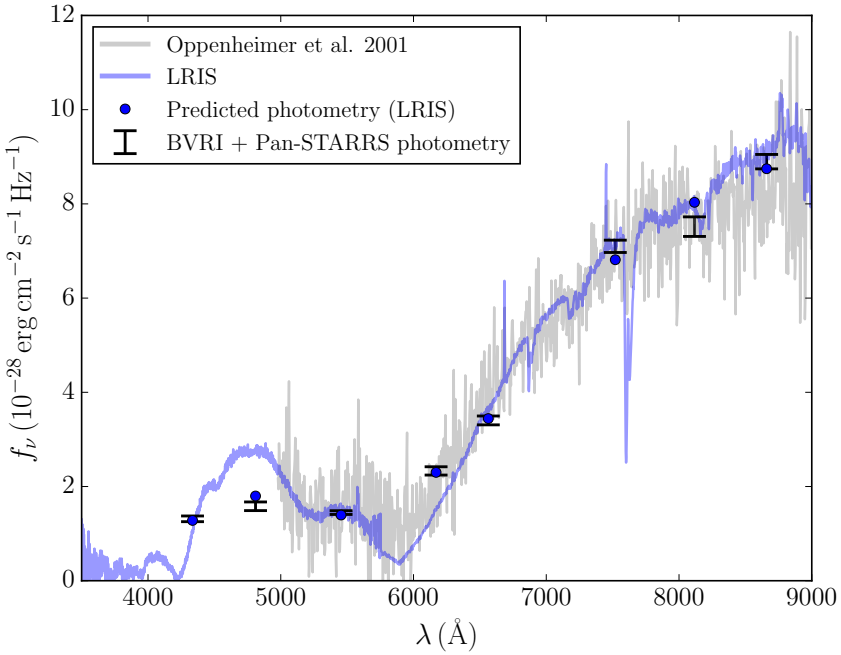

Figure 7.1 – Observed spectra and photometry of WD J2356−209. The spectrum of Oppenheimer et al. (2001) is in gray and the Keck LRIS spectrum is in blue. Note that the LRIS spectrum was scaled so that the predicted photometry (blue circles) match the observed photometry (black error bars).

7.4 Atmosphere models

The atmosphere models used in this work are described at length in Paper I. Our models are uniquely suited for the analysis of such a very cool DZ star, since they are the only ones to include both a state-of-the-art description of the ionization equilibrium of heavy elements (Paper I) and unified line profiles (Allard et al., 1999) for the strong Na and Ca spectral lines that characterize the spectrum of WD J2356−209.

Compared to the models used in Papers I and II, two changes were made to our code. First, we have improved our collisional profiles of the resonance line of neutral calcium perturbed by helium using the ab initio Ca−He potential energies of M. Krośnicki reported in Hernando et al. (2008). It is a significant improvement in the description of Ca−He singlet potential energies, but only at close range (i.e., only for radiator-perturber separations of ≈ 3.5 to 11 Å). To predict the impact core shift and width, the long-range part of the potential energies needs to be accurately determined. Moreover, our approach requires prior knowledge of the variation of the radiative dipole moments with atom-atom separation for each molecular state. As this variation is unknown at present, the dipole moments were assumed to remain constant throughout the collision. In order to obtain more accurate line profiles, intensive ab initio calculations are being performed to obtain both the ground and first excited potential energy curves (PECs) and the transition dipole moments for the Ca−He system (N. F. Allard et al., in preparation).

The second change made to our atmosphere model code was to add the opacity due to the rovibrational transitions of the MgH and CaH molecules. The MgH opacities are computed using the linelists of GharibNezhad et al. (2013) for the the $X^2\Sigma^+ \rightarrow A^2\Pi$ and $X^2\Sigma^+ \rightarrow B'^2\Sigma^+$ transitions, which are available on the ExoMol website[4] (Tennyson & Yurchenko, 2012; Tennyson et al., 2016). For CaH, the $X^2\Sigma^+ \rightarrow A^2\Pi$ and $X^2\Sigma^+ \rightarrow B^2\Sigma^+$ transitions are computed using the Kurucz linelists[5], which rely on molecular data from Weck et al. (2003) and Shayesteh et al. (2013).

[4] http://exomol.com
[5] http://kurucz.harvard.edu

7.5 Analysis of WD J2356−209

We rely on the *BVRIJH* and *grizy* photometry of WD J2356−209 to find its effective temperature, surface gravity and H/He abundance ratio. More specifically, the solid angle $\pi\,(R/D)^2$ and $T_{\rm eff}$ are found by fitting the model fluxes to the spectral energy distribution. Since the distance D is already known from the *Gaia* parallax, we can obtain the radius R from the solid angle. The mass of the white dwarf (and the corresponding surface gravity) are then found using the evolutionary models of Fontaine et al. (2001) with C/O cores, $\log(M_{\rm He}/M_\star) = -2$ and $\log(M_{\rm H}/M_\star) = -10$, which are representative of helium-atmosphere white dwarfs. The H/He abundance ratio is inferred from the infrared photometric measurements, which are affected by the presence of H_2−He collision-induced absorption (CIA, Jørgensen et al., 2000; Blouin et al., 2017). Once a photometric solution is found, we use the spectroscopic data to constrain the abundances of Na, Ca, Fe and Mg. In particular, the Na I D doublet is used to derive the Na/He ratio, the Ca I 4226 Å and Ca II H & K lines for Ca/He, Fe I and Fe II lines in the 3600–3800 Å region for Fe/He, and the MgH rovibrational bands between 5000 and 5300 Å for Mg/He. Once the heavy element abundance ratios are found, the whole fitting procedure—including the photometric fit—is repeated until internal consistency is reached.

Figure 7.2 compares our best solution to the photometric and spectroscopic data. Except for the core of the Na I D doublet and an unknown feature near 4500 Å, our fit is in excellent agreement with the observations across all wavelengths. In particular, our spectroscopic fit closely matches the Fe lines at small wavelengths, the Ca II H & K and Ca I 4226 Å lines, the blue and red wings of the Na I D doublet, and the flux depletion between 5000 and 5500 Å. Note that due to strong telluric absorption we could not use the Na I doublet at 8200 Å to validate the sodium abundance inferred from the Na I D doublet. Regarding the photometric fit, we found that a mixed H/He atmosphere has to be assumed to produce the H_2−He CIA that is required to properly match the J and H bands.

The atmospheric parameters of WD J2356−209 are given in Table 7.1. Its very cool temperature of $T_{\rm eff} = 4040 \pm 110$ K makes it—to our knowledge—the oldest known DZ

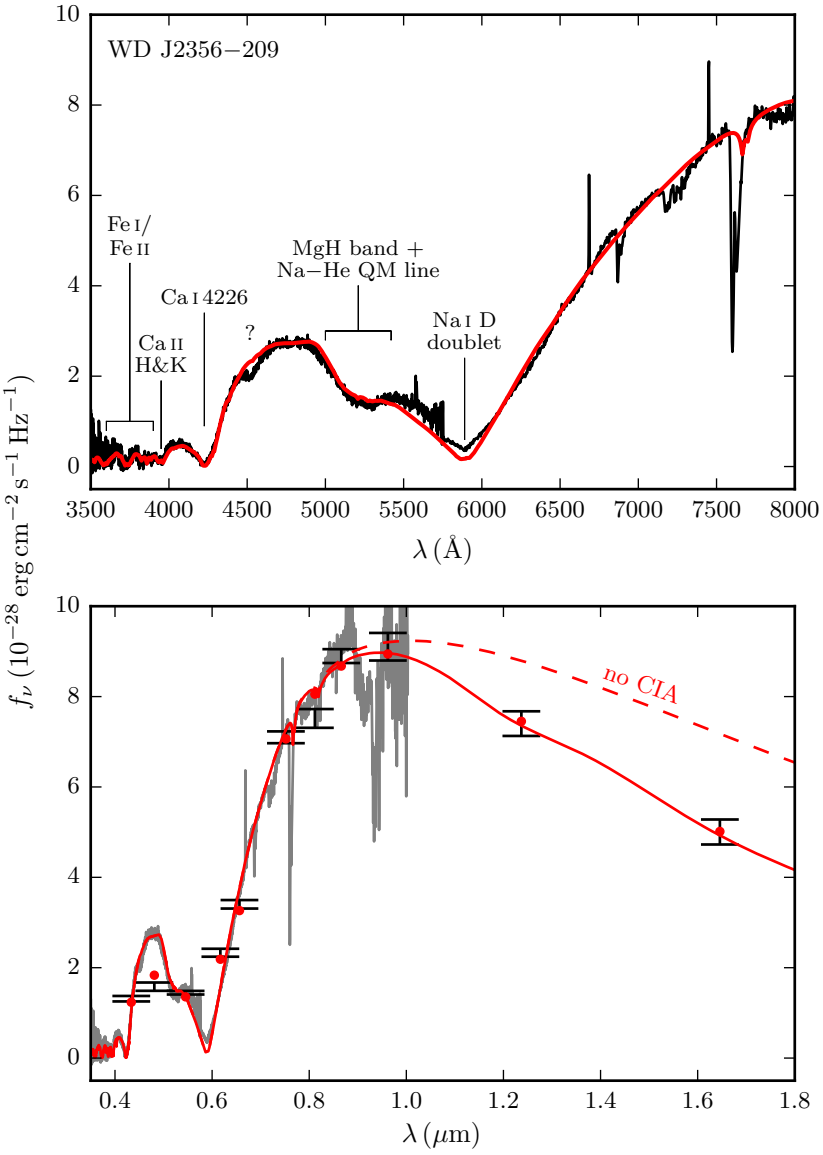

Figure 7.2 – Our best solution for WD J2356−209. The top panel shows our fit (in red) to the visible spectrum (in black) and the bottom panel shows our photometric fit to the *BVRI*, *JH* and *grizy* bands (the photometric observations are represented by the error bars). The dashed spectrum in the bottom panel was computed from our best-fitting model, but without including H_2−He CIA in the synthetic spectrum calculation. The strong absorption lines near 7600 Å are of telluric origin and were ignored in our analysis.

star, with a cooling age of 8.0 ± 0.8 Gyr.[6]

Parameter	Value	Parameter	Value
$T_{\rm eff}$	4040 ± 110 K	log Si/He	(< -6.8)
log g	7.98 ± 0.07	log K/He	< -10.0
log H/He[7]	-1.5 ± 0.2	log Ca/He	-9.3 ± 0.1
log C/He	< -6.0	log Ti/He	< -9.8
log O/He	(< -4)[8]	log Cr/He	< -9.9
log Na/He	-8.3 ± 0.2	log Mn/He	< -10.7
log Mg/He	-8.0 ± 0.2	log Fe/He	-8.6 ± 0.2
log Al/He	< -8.8	log Ni/He	< -8.0

Table 7.1 – WD J2356−209 atmospheric parameters

Table 7.1 also lists the constraints on metal abundance ratios in the atmosphere of WD J2356−209. Apart from the sodium abundance, which is further discussed in Section 7.6, all abundances are close to the average values measured in metal-polluted atmospheres. In particular, in a ternary diagram of Ca, Mg and Fe abundances (e.g., Hollands et al., 2018a, Figure 2), WD J2356−209 would be close to the bulk of DZ stars. The constraints on Al, K, Ti, Cr, Mn and Ni, for which no feature is observed in the spectrum of WD J2356−209, were found by raising their abundances up to the point where a spectral line should be visible. Note that the constraint on the K/He ratio was found using the spectrum of Oppenheimer et al. (2001) instead of the LRIS spectrum, since the latter shows strong telluric features near the K I 7665/7699 Å lines (see Figure 7.1). The constraint on C/He was established using the C_2 rovibrational bands instead of the atomic carbon lines, since the former require a smaller carbon abundance before being visible in the spectrum. Finally, no firm constraints could be found for the abundances of O and Si, since even the addition of a very large amount of these elements does not result in any visible spectral lines. The limits for O/He and Si/He given in Table 7.1 are therefore

[6]Note that Giammichele et al. (2012) found a greater cooling age (8.5 Gyr) for WD 2251−070. However, their analysis was based on a model atmosphere code (Dufour et al., 2007) that did not include a detailed description of the high-density effects arising at the photosphere of such a cool object. Our reanalysis of WD 2251−070 (Section 7.5.3) suggests that it has an effective temperature $T_{\rm eff} = 4050 \pm 60$ K and a surface gravity $\log g = 7.94 \pm 0.04$, which corresponds to a cooling age of 7.5 ± 0.5 Gyr.

[7]All abundances are reported as ratios of number densities.

[8]The abundances in parentheses are not firm limits (see text).

lower-bound estimates of the maximum abundance of these elements that is compatible with the spectroscopic observations of WD J2356−209.

Our excellent fit to the wings of the broad Ca and Na spectral lines of WD J2356−209 (Figure 7.2) was made possible thanks to the improved lines profiles implemented in our models (Allard & Alekseev, 2014; Allard et al., 2014). This good agreement indicates that our model predicts the right physical conditions in the line-forming regions of the atmosphere. In particular, it suggests that the total number density $n_{\rm tot}$ is accurate, since it is the parameter that governs the broadening of the spectral lines. At the photosphere of WD J2356−209, the pressure is high enough ($\log P = 10.0$) that deviations from the ideal gas law begin to be important (see Figure 4 of Paper I). If the ideal gas law was assumed, $n_{\rm tot}$ would be 20% higher and the line profiles would be slightly broader (particularly the Na I D doublet). Note though that WD J2356−209 cannot be used to validate our implementation of pressure ionization, since its photospheric density ($\rho = 0.1\,{\rm g\,cm^{-3}}$) is too small to induce significant deviations from the ideal Saha equation (Kowalski et al., 2007, Paper I).

7.5.1 Collision-induced absorption

Figure 7.3 compares the H_2−He CIA profiles obtained by different authors for physical conditions that are representative of the photosphere of WD J2356−209. Differences between the profiles imply that the H/He ratio derived from the photometry depends on the choice of the CIA profiles implemented in our models. In particular, if the profiles of Jørgensen et al. (2000) were assumed, a smaller hydrogen abundance would be found. In fact, as already noted in Paper II, the profiles of Jørgensen et al. (2000) predict a too strong absorption in the $\approx 1.2 - 2\,\mu$m region, possibly because the potential energy and induced dipole surfaces used to derive those profiles were computed with a smaller atomic orbital basis set.

Furthermore, Figure 7.3 shows that significant differences between the profiles of Abel et al. (2012) and Blouin et al. (2017) appear above $2\,\mu$m (particularly near the maximum of the fundamental band at $\approx 2.5\,\mu$m). Those differences are due to many-body collisions (which are only included in the profiles of Blouin et al.) that lead to an enhancement and a distortion of the absorption profile. The only photometric measurements available beyond

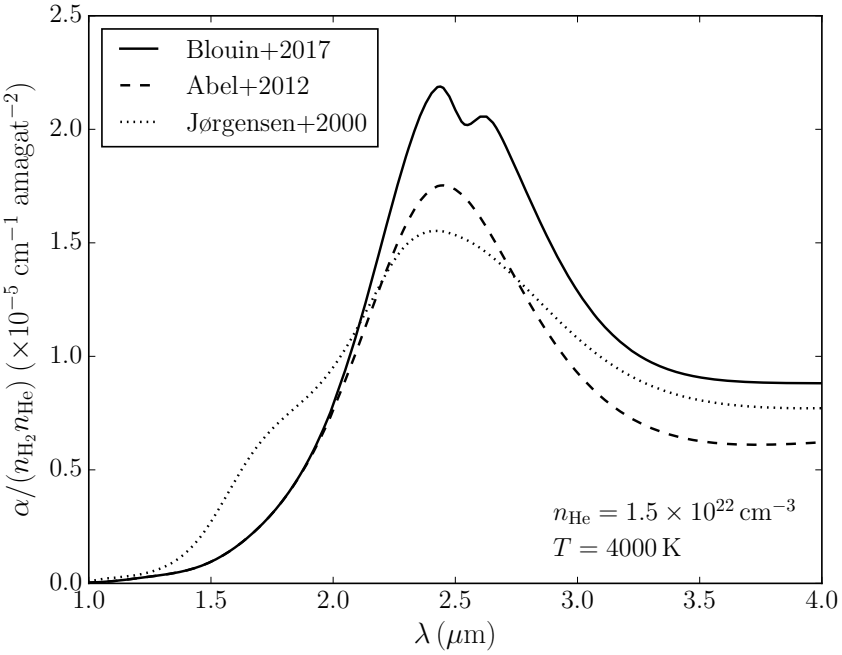

Figure 7.3 – H_2−He CIA profiles at 4000 K and $n_{\mathrm{He}} = 1.5 \times 10^{22}\,\mathrm{cm}^{-3}$, as computed by Blouin et al. (2017, Equation 7), Abel et al. (2012) and Jørgensen et al. (2000). The absorption profiles are divided by the number density of H_2 and He and are therefore constant with respect to density (with the exception of the Blouin et al. profile, which includes the effects of many-body collisions).

the H band are those from the Wide-field Infrared Survey Explorer (WISE, Wright et al., 2010) for the 3.4 and 4.6 μm bands. Our best fit is compatible with those measurements, but their large uncertainties do not allow us to explicitly confirm that the CIA is indeed enhanced by many-body effects.

7.5.2 The Na−He satellite and the MgH bands

The wide absorption feature in the blue wing of the Na I D doublet proved particularly challenging to model. Allard et al. (2014) suggested that it could be the result of the quasi-molecular satellite feature arising from the Na−He interaction. Our detailed analysis reveals that it is only part of the explanation and that MgH rovibrational bands must be included to fully explain this absorption feature. Figure 7.4 compares our best fit to the 5000–5500 Å absorption feature with and without the MgH bands. Clearly, the Na−He

satellite visible in the fit that omits the MgH bands (dashed line) is not sufficient to explain the whole absorption feature and MgH absorption bands must be invoked.

We emphasize that including MgH in our models is physically motivated. Given the temperature of WD J2356−209, its hydrogen abundance (independently constrained from the H_2−He CIA) and the presence of magnesium (which is given by a Mg/Ca ratio that is very close to the value expected for chondrite-type material), MgH has to be present at the photosphere of WD J2356−209. To our knowledge, this is the first detection of MgH molecular features in a white dwarf. MgH bands were proposed by Dufour et al. (2006) to explain the asymmetry of the Mg I 5175 Å line in G165−7, but it was later shown that improved line profiles—beyond the impact approximation—are enough to explain this asymmetry (Allard et al., 2016b). Finally, note that for our derived atmospheric parameters CaH is not sufficiently abundant to produce visible bands around 7000 Å.

7.5.3 The unknown absorption feature near 4500 Å

Our fit of WD J2356−209 does not reproduce the small asymmetric absorption feature near 4500 Å (Figure 7.4). Technically, boosting the Ti/Ca ratio by a factor of ≈ 10 with respect to chondritic abundances allows the Ti I $a^5F - y^5F^\circ$ multiplet (centered at 4535 Å) to be strong enough to reasonably match the absorption feature near 4500 Å. However, another cool DZ star, WD 2251−070, offers good reasons to be suspicious of this interpretation.

Indeed, WD 2251−070 also shows a strikingly similar absorption feature in that region (Figure 7.5). Using photometric and spectroscopic data reported in Bergeron et al. (1997) and Dufour et al. (2007), we analyzed WD 2251−070 with our cool DZ grid. Our preliminary fit yields $T_{\rm eff} = 4050 \pm 60$ K, $\log g = 7.94 \pm 0.04$, log H/He < -4.5, log Na/He < -10.3 and log Ca/He $= -10.0 \pm 0.1$ (an in-depth analysis of this object will be presented in N. F. Allard et al., in preparation). Given the strong similarities between WD 2251−070 and WD J2356−209 (i.e., same feature near 4500 Å, similar Ca abundances and virtually identical effective temperatures), it is very likely that the origins of the 4500 Å absorption feature are the same for both objects. If it is the case, then there is a good reason to reject Ti as the explanation for this feature. Boosting the Ti ratio to produce a sufficiently strong Ti I $a^5F - y^5F^\circ$ multiplet also implies that the similarly important $a^5F - y^5G^\circ$

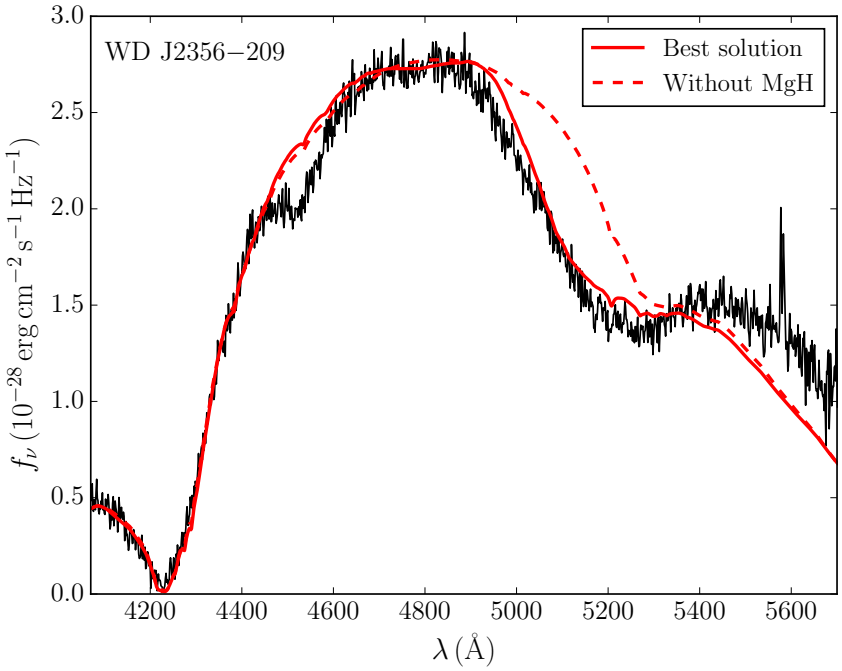

Figure 7.4 – Comparison between the best solutions found when including (solid line) and when omitting (dashed line) the MgH bands in our models.

multiplet (centered around 5020 Å) should be visible. By adjusting the Mg abundance, our fit of WD J2356−209 could accommodate the additional opacity resulting from the Ti I $a^5F - y^5G^\circ$ multiplet. However, the spectrum of WD 2251−070 clearly rules out the presence of any absorption feature around 5020 Å and thus suggests that Ti cannot be the explanation of the 4500 Å absorption feature.

Still, since we rely on Lorentzian line profiles for all Ti spectral lines, we need to be careful before completely ruling out Ti as the source of the 4500 Å feature. In principle, it is possible that accurate line profile calculations will show that the $a^5F - y^5G^\circ$ multiplet is flattened out under the density conditions encountered at the photosphere of WD 2251−070 ($n_{\rm He} \approx 6 \times 10^{22}\,{\rm cm}^{-3}$). However, there is a second argument against the Ti scenario. We constrained the Na abundance in WD 2251−070 to log Na/He < -10.3, implying that it has a log Na/Ca ratio smaller than -0.3. This ratio is vastly different from the log Na/Ca $= 1.0$ ratio found for WD J2356−209 and we therefore expect the abundance pattern of WD 2251−070 to be quite different from that of WD J2356−209. In particular, it would be surprising if WD 2251−070 and WD J2356−209 had similar Ti/Ca

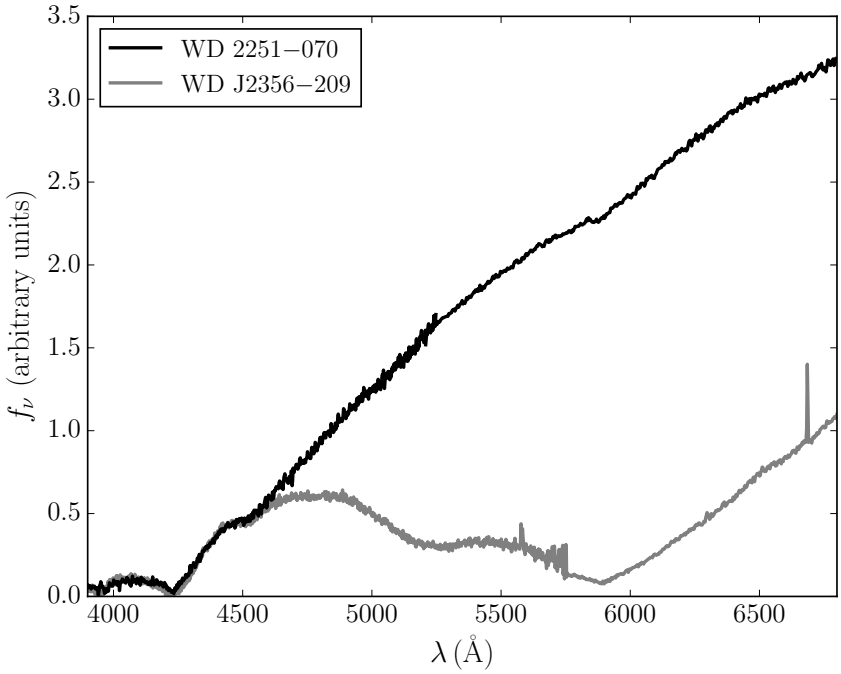

Figure 7.5 – Comparison of the spectrum of WD J2356−209 to that of WD 2251−070. The data for WD 2251−070 is from Bergeron et al. (1997) and Dufour et al. (2007). Note the resemblance between both spectra below 4600 Å and their strong dissimilarity at longer wavelengths.

ratios but significantly different Na/Ca ratios. All things considered, it is unlikely that the feature near 4500 Å is due to Ti.

Alternatively, since it is observed in two white dwarfs with similar Ca abundances, it is tempting to explain the 4500 Å feature as being due to Ca. In a dense helium medium, it turns out that the Ca II H & K profile can show a quasi-molecular feature near 4500 Å (Allard & Alekseev, 2014). However, for the physical conditions in the atmosphere of WD 2251−070 and WD J2356−209, this quasi-molecular line is predicted to be too weak to explain the shape of the spectrum around 4500 Å. We are therefore unable to identify the origin of this feature at the moment.

7.6 How to explain the high sodium abundance ?

As it is well above the chondritic value of $\log \mathrm{Na/Ca} = 0.0$ (Lodders, 2003), the $\log \mathrm{Na/Ca} = 1.0 \pm 0.2$ ratio measured in WD J2356−209 is surprising and needs to be

explained. Note that this extreme abundance ratio is not only supported by our excellent fit to the observations (Figure 7.2), but also by the direct comparison of WD J2356−209 to WD 2251−070. While both objects have a very similar calcium abundance and a virtually identical effective temperature, their spectra are drastically different in the region affected by the Na I D doublet (as seen in Figure 7.5).

7.6.1 Comparison to other sodium-rich stars

WD J2356−209 is not the only white dwarf to have a high Na/Ca abundance ratio. A few objects with log Na/Ca > 0 were identified by Hollands et al. (2017) and are shown in Figure 7.6. However, because of the very noisy spectra of many of those objects, the derived abundances are often highly uncertain. Using our own atmosphere model grid, we performed a reanalysis of this sample and we found that, within the uncertainties, most of those objects are compatible with a chondritic abundance ratio of log Na/Ca $= 0$ (a detailed analysis will be presented in S. Coutu et al., in preparation). In fact, we found compelling evidence of a high Na/Ca abundance ratio only for three objects (SDSS J095645.14+591240.6, SDSS J164939.23+223807.2 and SDSS J212312.20+001653.5). Another potentially sodium-rich white dwarf, G77−50, was analyzed by Farihi et al. (2011). They found a log Na/Ca $= 0.7$ abundance ratio, but this result should also be taken with a grain of salt as the magnetism of this object complicates its analysis and the authors explicitly noted that their sodium abundance measurement is uncertain.

Furthermore, Harris et al. (2003) identified a faint ($g = 21.4$) DZ star in the Sloan Digital Sky Survey (SDSS) that has a spectrum that also appears to show a broad Na line. As WD J2356−209, the visible spectrum of SDSS J133001.13+643523.7 (J1330+6435) is dominated by a strong and broad Na I D doublet. Figure 7.7 shows our best solution for this star and Table 7.2 lists its derived atmospheric parameters. Note that a hydrogen-free atmosphere was assumed, since we do not have any infrared photometry to fit the H/He ratio to an eventual infrared flux depletion.[9] The SDSS spectrum being noisy, the Ca/He and Na/He abundance ratios are subject to considerable uncertainties. Nonetheless, it is clear that the Na/Ca ratio of J1330+6435 is higher than average, but well below the extreme ratio found for WD J2356−209. While there are some objects with a Na/Ca

[9] In any case, the addition of a moderate amount of hydrogen (up to log H/He $= -1.5$) does not change our conclusions on the Na/Ca abundance ratio of this object.

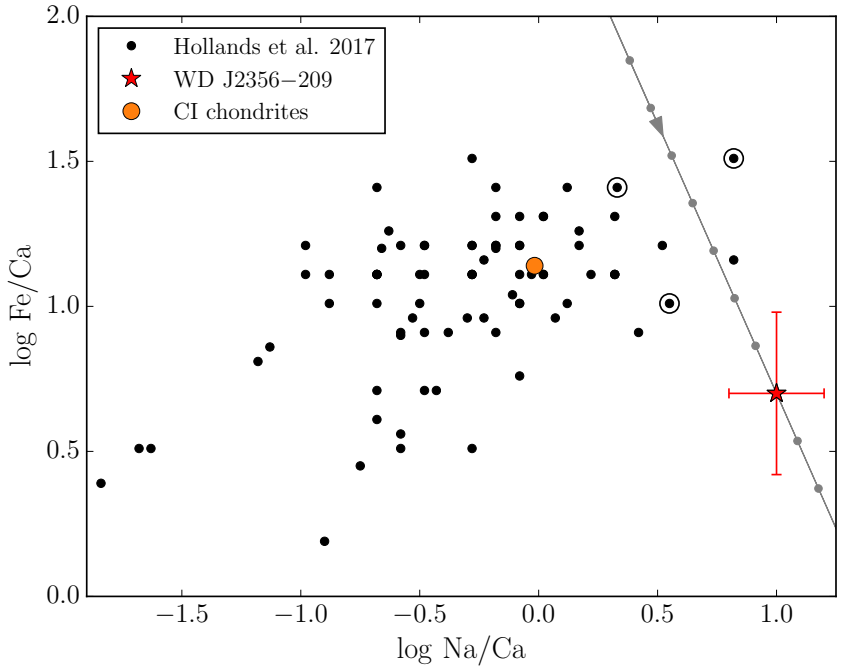

Figure 7.6 – Elemental abundances for CI chondrites (Lodders, 2003, filled orange circle), WD J2356−209 (red star) and the DZ stars analyzed by Hollands et al. (2017, filled black circles). The three encircled objects are those for which we found compelling evidence of a Na/Ca abundance ratio greater than 1. Note that magnetic objects in the Hollands et al. (2017) sample are not shown in this figure. The gray line indicates how the metal abundances in WD J2356−209 would have evolved, assuming the diffusion timescales mentioned in the text. The distance between two gray circles on the chemical evolution track corresponds to 1 Myr.

abundance ratio above the chondritic value, WD J2356−209 is the most extreme case ever encountered.

7.6.2 Constraints on the accreted planetesimal

The abundances of heavy elements in a DZ star are indicative of the nature of the accreted parent body and can be used to infer its composition (Zuckerman et al., 2007; Koester et al., 2011; Dufour et al., 2012; Hollands et al., 2018a; Harrison et al., 2018). Such studies have highlighted the existence of a great diversity of accreted bodies, ranging from Kuiper-Belt-Object analogs (Xu et al., 2017) to differentiated rocky bodies (Zuckerman et al., 2011; Melis & Dufour, 2017) and water-bearing planetesimals (Farihi et al., 2013;

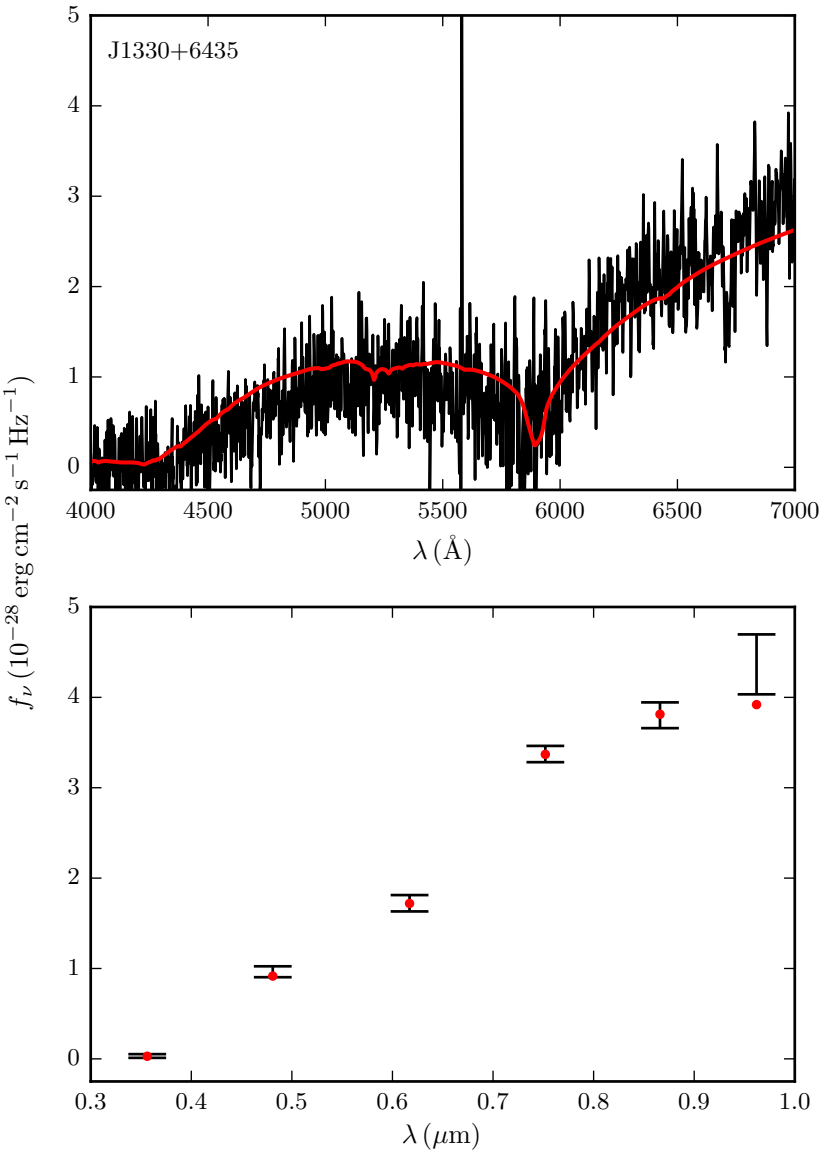

Figure 7.7 – Our best solution for J1330+6435. The top panel shows our fit to the visible spectrum and the bottom panel displays our photometric fit to the SDSS u band and Pan-STARRS *grizy* bands. Note that the SDSS spectrum was smoothed for clarity.

Parameter	Value
$T_{\rm eff}$	4310 ± 190 K
$\log g$	8.26 ± 0.15
H/He	0
log Na/He	-8.5 ± 0.3
log Ca/He	-8.8 ± 0.3

Table 7.2 – J1330+6435 atmospheric parameters

Raddi et al., 2015). Can we relate the high Na/Ca ratio of WD J2356−209 to any solar system counterpart ?

Table 7.3 lists the Na/Ca ratio of a few solar system objects. The only measurements compatible with the composition of WD J2356−209 are those obtained for the dust of the comet 67P/Churyumov–Gerasimenko (67P). Those measurements were obtained by the COmetary Secondary Ion Mass Analyzer (COSIMA, Kissel et al. 2007) onboard the *Rosetta* spacecraft while it followed comet 67P at close distances for two years. Additionally, with the exception of Mn and Fe, the abundances of the other heavy elements in WD J2356−209 are compatible with those measured in the dust of comet 67P (Figure 7.8).

Object	log Na/Ca[10]	Reference
WD J2356−209	1.0 ± 0.2	This paper
CI chondrites	-0.017 ± 0.002	Lodders (2003)
Bulk Earth	-0.64 ± 0.04	Wang et al. (2018)
Earth's mantle	-0.74 ± 0.04	Wang et al. (2018)
Earth's crust	0.00	Rumble (2018)
Halley	0.2 ± 0.3	Jessberger et al. (1988)
67P	1.2 ± 0.6	Bardyn et al. (2017)

Table 7.3 – Sodium abundances

That being said, the total mass accreted by WD J2356−209 is incompatible with the mass of a comet. By estimating the mass of metals currently in the convection zone, we can obtain a lower limit on the total accreted mass (it is a lower limit since diffusion might

[10]Ratio of number densities

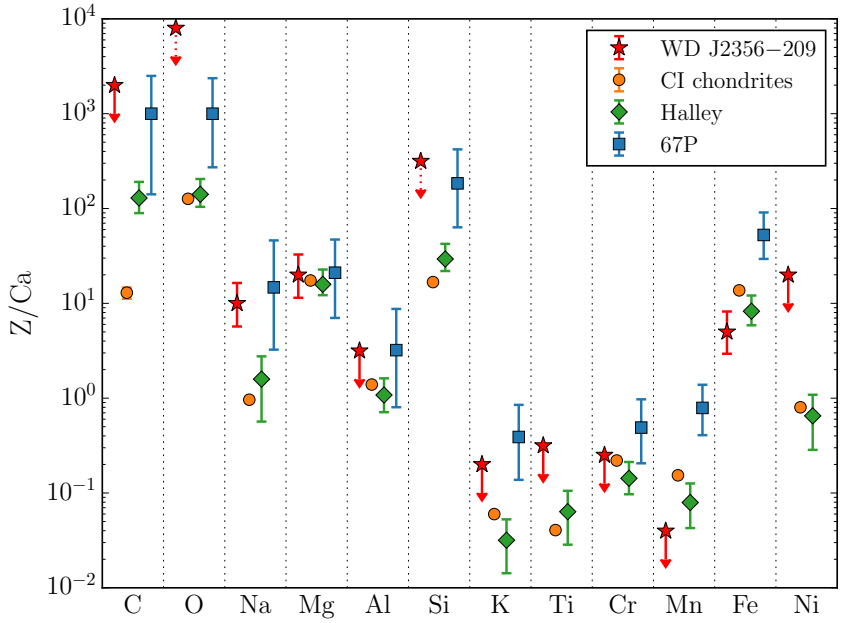

Figure 7.8 – Elemental abundances by number relative to Ca. The data for WD J2356−209 is from Table 7.1, chondritic abundances are taken from Lodders (2003) and the data for comets Halley and 67P are from Jessberger et al. (1988) and Bardyn et al. (2017), respectively. The upper limits represented by dotted arrows are those for which no firm constraint could be established. Note that the abundances for WD J2356−209 correspond to the abundance ratios of the accreted planetesimal only if accretion is in its early phase (i.e., the effects of relative diffusion are not included in this figure).

already have evacuated heavy elements from the convection zone). Using the envelope model code of Rolland et al. (2018), we find that the fractional mass of the convection zone is $\log q = -5.49$ for a $T_{\rm eff} = 4000\,{\rm K}$ white dwarf with $\log g = 8$ and $\log {\rm H/He} = -1.5$. With this value, we find that the total mass in the convection zone of the four heavy elements clearly detected in WD J2356−209 (Ca, Mg, Na and Fe) is $5 \times 10^{20}\,{\rm g}$. This value could significantly underestimate the total mass of metals currently in the convection zone, since it does not include C, O and Si, three elements that are expected to be particularly abundant (Figure 7.8). A higher estimate can be obtained by assuming that the accreted planetesimal had a chondritic composition relative to Ca and computing its total mass from the abundance of Ca detected in WD J2356−209. Using the values published in Lodders (2003), this yields a mass of $\sim 10^{21}\,{\rm g}$. This mass is significantly higher than the mass of comet 67P ($10^{16}\,{\rm g}$, Pätzold et al., 2016) and that of the most massive comets of the solar system (Hale–Bopp has a mass of $\sim 10^{19}\,{\rm g}$, Weissman, 2007), suggesting that a

single comet cannot be the cause of the pollution of the atmosphere of WD J2356−209. As the lower limit on the accreted mass is $\sim 10^2$ times higher than the mass of the largest comets, any scenario in which several comets were accreted can safely be rejected.

7.6.3 Relative diffusion

Alternatively, it is possible that the accreted planetesimal did not have an unusual composition and the extreme Na/Ca abundance ratio could simply be due to the different diffusion timescales of Na and Ca. In fact, for a cool helium-rich white dwarf like WD J2356−209, diffusion-accretion equilibrium cannot be assumed (Koester et al., 2011; Hollands et al., 2018a). This follows from the fact that the diffusion times are of the order of a few Myr (Paquette et al., 1986; Koester, 2009; Hollands et al., 2017), while the typical duration of an accretion episode is only of $10^4 - 10^6$ years (Jura, 2008; Kilic et al., 2008; Melis et al., 2011; Girven et al., 2012). It is therefore possible that WD J2356−209 has stopped accreting and that the difference between the diffusion timescales of Na and Ca has led to a composition that is not representative of the accreted planetesimal.

Once the accretion episode has stopped, relative diffusion implies that a variation $\Delta \log$ Ca/He will be accompanied by a change of the Na/Ca abundance ratio given by (Hollands et al., 2018a, Equation 3),

$$\frac{\Delta \log \text{ Na/Ca}}{\Delta \log \text{ Ca/He}} = \frac{\tau_{\text{Ca}}}{\tau_{\text{Na}}} - 1. \tag{7.1}$$

In WD J2356−209, the diffusion timescale of Na is longer by a factor of ≈ 1.7 than the diffusion timescale of Ca ($\log \tau_{\text{Ca}} \approx 6.32$ and $\log \tau_{\text{Na}} \approx 6.56$).[11] From Equation 7.1, it follows that every 1 dex decrease in log Ca/He is accompanied by a 0.4 increase in log Na/Ca. If we assume for a moment that the accreted planetesimal had a chondritic composition with log Na/Ca = 0, it implies that the Ca abundance in the atmosphere of WD J2356−209 was log Ca/He = −6.8 when the accretion episode stopped, some ≈ 10 Myr ago (Kawka & Vennes, 2016, Equation 4). This would raise our lower limit on the total accreted mass to $\sim 10^{23}$ g, which corresponds to the mass of a very large asteroid (Vesta has a mass of 2.6×10^{23} g, Russell et al., 2012). However, this scenario appears unlikely. Cool DZ

[11] To estimate the diffusion timescales, we use the values given by Hollands et al. (2017) for SDSS J163601.33+161907.1, as this star has similar atmospheric parameters to WD J2356−209.

stars are known to be much less polluted than hotter objects (Dufour et al., 2007; Koester et al., 2011; Hollands et al., 2017), possibly because the largest planetesimals are gradually scattered away from the planetary system (Veras et al., 2013, 2016; Hollands et al., 2018a). In fact, according to the Montreal White Dwarf Database (Dufour et al., 2017), no known DZ star cooler than $T_{\rm eff} = 5000\,{\rm K}$ has a calcium abundance higher than $\log\,{\rm Ca/He} = -9.3$.

More importantly, assuming that WD J2356−209 accreted a planetesimal with a chondritic composition might not be a realistic hypothesis. Figure 7.6 shows how the composition of WD J2356−209 is expected to have evolved given the diffusion timescales of Hollands et al. (2017). This evolution rules out the possibility that the accreted planetesimal had a chondrite-like composition. A more realistic hypothesis would probably be to assume that the accreted planetesimal had a sodium abundance ratio of $\log\,{\rm Na/Ca} \approx 0.6$, which corresponds to the region where the chemical evolution track of WD J2356−209 intersects the middle of the distribution of objects plotted in Figure 7.6. In that case, the Ca abundance in the atmosphere of WD J2356−209 when the accretion episode stopped $\approx 4\,{\rm Myr}$ ago (i.e., $1.9\tau_{\rm Ca}$ or $1.1\tau_{\rm Na}$) would have been a less extreme $\log\,{\rm Ca/He} \approx -8.3$ and the lower limit on the accreted mass is decreased to $\sim 10^{22}\,{\rm g}$. Assuming a typical asteroid density of $2\,{\rm g\,cm^{-3}}$, the accreted planetesimal had a radius of at least 100 km.

7.7 Conclusion

We presented a detailed analysis of WD J2356−209, a very cool DZ star whose spectrum is dominated by a strong sodium feature. Thanks to our improved atmosphere models (Papers I and II), we find an excellent fit to the photometry and the visible spectrum, allowing the first reliable atmospheric parameter determination of this object. We found that WD J2356−209 has a record sodium abundance with a number density ratio $\log\,{\rm Na/Ca} = 1.0 \pm 0.2$.

A possible explanation for this high sodium content is that WD J2356−209 has accreted a planetesimal with an abnormally high sodium abundance and a total mass $\gtrsim 10^{21}\,{\rm g}$. However, we were unable to identify a solar system analog to this hypothetical planetesimal, since none of the examined candidates simultaneously matched the constraints on the sodium abundance and the total mass. Alternatively, the high sodium abundance in the atmosphere of WD J2356−209 could be explained by the slower diffusion of Na with res-

pect to Ca. According to this scenario, the accreted object would have had a less extreme composition but a larger total mass ($\gtrsim 10^{22}$ g).

This paper concludes the observational validation of our improved cool white dwarf model atmosphere code. The excellent fit obtained for this extreme object is a clear demonstration of the capacity of our models to properly take into account the nonideal effects that prevail in the atmospheres of cool white dwarfs. In the next paper of this series, we will use our improved models to analyze a large sample of cool white dwarfs and revisit their spectral evolution.

Acknowledgments We would like to thank Manuel Barranco for sharing with us ab initio potentials for the Ca−He interaction. We are grateful to the anonymous reviewer for her or his valuable comments on our manuscript. We also thank Siyi Xu for useful discussions regarding the composition of WD J2356−209.

This work was supported in part by NSERC (Canada) and the Fund FRQNT (Québec). This work has made use of the Montreal White Dwarf Database (Dufour et al., 2017).

This work has made use of data from the European Space Agency (ESA) mission *Gaia* (https://www.cosmos.esa.int/gaia), processed by the *Gaia* Data Processing and Analysis Consortium (DPAC, https://www.cosmos.esa.int/web/gaia/dpac/consortium). Funding for the DPAC has been provided by national institutions, in particular the institutions participating in the *Gaia* Multilateral Agreement.

The Pan-STARRS1 Surveys (PS1) and the PS1 public science archive have been made possible through contributions by the Institute for Astronomy, the University of Hawaii, the Pan-STARRS Project Office, the Max-Planck Society and its participating institutes, the Max Planck Institute for Astronomy, Heidelberg and the Max Planck Institute for Extraterrestrial Physics, Garching, The Johns Hopkins University, Durham University, the University of Edinburgh, the Queen's University Belfast, the Harvard-Smithsonian Center for Astrophysics, the Las Cumbres Observatory Global Telescope Network Incorporated, the National Central University of Taiwan, the Space Telescope Science Institute, the National Aeronautics and Space Administration under Grant No. NNX08AR22G issued through the Planetary Science Division of the NASA Science Mission Directorate, the National Science Foundation Grant No. AST-1238877, the University of Maryland, Eotvos

Lorand University (ELTE), the Los Alamos National Laboratory, and the Gordon and Betty Moore Foundation.

This publication makes use of data products from the Wide-field Infrared Survey Explorer, which is a joint project of the University of California, Los Angeles, and the Jet Propulsion Laboratory/California Institute of Technology, funded by the National Aeronautics and Space Administration.

CHAPITRE 8

Line Profiles of the Calcium I Resonance Line in Cool Metal-polluted White Dwarfs

Le diable est dans les détails.

—Souvent attribué à Friedrich Nietzsche (1844−1900), philosophe allemand

Ce chapitre est une adaptation de l'article «Line Profiles of the Calcium I Resonance Line in Cool Metal-polluted White Dwarfs», par Simon Blouin, Nicole F. Allard, Thierry Leininger, Florent Xavier Gadéa et Patrick Dufour. Ce travail a été publié en avril 2019 dans *The Astrophysical Journal*.[1]

8.1 Abstract

Metal-polluted white dwarfs (DZ stars) are characterized by a helium-rich atmosphere contaminated by heavy elements traces originating from accreted rocky planetesimals. As a detailed spectroscopic analysis of those objects can reveal the composition of the accreted debris, there is a great interest in developing accurate DZ atmosphere models. However, the coolest DZ white dwarfs are challenging to model due to the fluidlike density of their atmospheres. Under such extreme conditions, spectral absorption lines are heavily broadened by interactions with neutral helium and it is no longer justified to use the conventional Lorentzian profiles. In this work, we determine the theoretical profiles of the Ca I resonance line (the most prominent spectral line for the coolest DZ white dwarfs) in the dense atmospheres of cool DZ white dwarfs. To do so, we use a unified theory

[1]Blouin, S., Allard, N. F., Leininger, T., Gadéa, F. X., & Dufour, P. 2019, ApJ, 875, 137.

of collisional line profiles and accurate ab initio potential energies and transition dipole moments for the CaHe molecule. We present the resulting profiles for the full range of temperatures and helium densities relevant for the modeling of cool, metal-polluted white dwarfs (from 3000 to 6000 K and from 10^{21} to $10^{23}\,\mathrm{cm}^{-3}$). We also implement these new profiles in our atmosphere models and show that they lead to improved fits to the Ca I resonance line of the coolest DZ white dwarfs.

8.2 Introduction

After exhausting their supplies of nuclear fuel, the vast majority of main-sequence stars will end their lives as white dwarfs. These stellar remnants are then condemned to a slow cooling that will extend over billions of years. White dwarfs are compact objects ($\approx 0.6\,M_{\odot}$ compressed into a volume similar to that of the Earth) and thus, they are characterized by a very intense surface gravity. Because of this strong gravitational field (typically, $\log g = 8$), atomic species stratify according to their weights. Hence, only the lightest elements—hydrogen and helium—are found in the atmospheres of most white dwarfs.

A particularly interesting exception to this rule is the existence of DZ stars, white dwarfs whose helium-rich atmospheres are contaminated by traces of heavy elements (e.g., Mg, Ca, Na, Fe, Si) that are detected thanks to their absorption lines. The existence of those objects is a priori incompatible with the very efficient gravitational settling at work in white dwarfs. In particular, these heavy elements are expected to sink below the photosphere within timescales that are much smaller than the age of the white dwarf (Paquette et al., 1986; Koester, 2009).

The accepted scenario for the existence of DZ white dwarfs is that heavy elements were recently (or are being) added to the atmospheres of those objects through the accretion of rocky planetesimals (e.g., see the reviews of Jura & Young, 2014; Farihi, 2016). This scenario is now supported by the detection of infrared excesses that signal the presence of circumstellar debris disks around dozens of white dwarfs (Melis et al., 2010; Brinkworth et al., 2012; Rocchetto et al., 2015) and the discovery of planetary transits in the light curve of WD 1145+017 (Vanderburg et al., 2015). Metal-polluted white dwarfs constitute a unique observational window into the bulk composition of planetesimals (comets,

asteroids, dwarf planets) outside our solar system. Using atmosphere models to fit the observed spectra of DZ white dwarfs, we can determine the chemical composition of their atmospheres and trace back the composition of the accreted planetesimals (Zuckerman et al., 2007; Farihi et al., 2013; Hollands et al., 2018a).

For the coolest ($T_{\rm eff} \approx 4000\,{\rm K}$)—and thus, oldest—white dwarfs, very few metal spectral lines remain visible. In this regime, one of the most prominent lines is the Ca I resonance line at 4226 Å (see for instance WD 2251−070 in Dufour et al., 2007). Properly modeling this absorption feature is of utmost importance if we want to precisely determine the composition of these old objects. For instance, one of the oldest DZ white dwarf known to date (WD J2356−209, with a cooling age of $\approx 8\,{\rm Gyr}$) has been shown to have an abnormally high Na/Ca abundance ratio, which raises a number of questions about the origin of the planetesimal that it accreted (Blouin et al., 2019b). The Ca abundance in the atmosphere of this object was inferred from a fit to its Ca I resonance line. Therefore, the determination of the atmospheric composition of this white dwarf and any conclusions about the nature of the accreted planetesimal are strongly influenced by the quality of our Ca I 4226 Å line profiles.

However, obtaining accurate absorption line profiles under the physical conditions found at the photosphere of those cool, helium-rich white dwarfs is challenging. Because of their very transparent atmospheres, cool DZ white dwarfs have photospheres where the density can reach $n_{\rm He} = 10^{23}\,{\rm cm}^{-3}$ (Blouin et al., 2018a). Under such fluidlike conditions, the wings of heavy-element spectral lines are strongly broadened by interactions with neutral helium and Lorentzian profiles do not allow a satisfactory fit to the observed spectra (e.g., Allard et al., 2016b). It is then necessary to implement a unified line shape theory (Allard et al., 1999) to obtain the right spectral line profiles. This approach requires prior knowledge, for each molecular state involved in the transition, of the potential energy and the variation of the dipole moment with respect to the atom–atom separation.

The accuracy of the line profiles is strongly affected by the quality of the atomic data from which they are computed. The study of SDSS J080440.63+223948.6 (SDSS J0804+2239) by Blouin et al. (2018b) offers a good example of the importance of using high-quality ab initio data for these calculations. As no accurate potential energies for the CaHe molecule were available, Blouin et al. (2018b) tried to model the Ca I resonance line

of SDSS J0804+2239 using approximate potential energy curves (PECs). The limitations of their approximate potentials were quite obvious, as they were unable to obtain a completely satisfactory fit to this absorption line.

For their analysis of WD J2356−209, Blouin et al. (2019b) relied on more accurate Ca I 4226 Å line profiles—thanks to improved PECs from Hernando et al. 2008 (M. Barranco 2018, private communication)—and achieved an excellent fit to the Ca I resonance line of this object. Still, Blouin et al. (2019b) did not have access to the transition dipole moments and to the long-range portion of the PECs, which are both needed to obtain the most accurate line profiles. In this paper, we use state-of-the-art ab initio data to fill these gaps and obtain more accurate Ca I resonance line profiles. The new ab initio data on which this work relies are described in Section 8.3. In Section 8.4, we present our new Ca I resonance line profiles. We apply these new profiles to three cool DZ white dwarfs in Section 8.5 and our conclusions are given in Section 8.6.

8.3 Ab initio data

Line profile intensities are functions of both excited and ground-state interactions. Therefore, a precise determination of the electronic energies and optical transition dipole moments is crucial to accurately compute the Ca I resonance line profiles for the whole wavelength range. To obtain the necessary atomic data, we performed ab initio calculations with the MOLPRO package (Werner et al., 2012). All singlet states up to the Ca ^{1}S (4s5s) + He ($1s^2$) asymptote have been involved (i.e., four Σ states, two Π states and one Δ state). A large core pseudopotential was used for Ca (Czuchaj et al., 1991) together with the usual Core Polarisation Potential approach (Müller et al., 1984). For Ca, the associated 8s8p7d basis set of Czuchaj et al. has been complemented by 7f and 3g gaussian functions, while for He, the spdfg aug-v5z-cc basis set has been used (Woon & Dunning, 1994). State-averaged CASSCF (complete active space self-consistent field) calculations with four active electrons in eleven orbitals (corresponding to the 4s, 4p, 3d, 5s orbitals for Ca and the 1s orbital for He) were performed, followed by MRCI (multireference configuration interaction) calculations for each symmetry. The transition dipole moments were then computed using the averaged natural orbitals from the bra wavefunction.

The resulting potentials are reported in Figure 8.1. The ground state (X $1\,^1\Sigma$) is mainly repulsive with a shallow van der Waals well, the $2\,^1\Sigma$ and $2\,^1\Pi$ (A) potentials are more attractive and similar to the ground-state potential of the Ca^+He ion, and the $3\,^1\Sigma$ (B) potential is very repulsive. From the generalized Fermi model (Dickinson & Gadéa, 2002), because the electron−He scattering length is positive, repulsive effects are expected. Moreover, since the ^{1}D (4s3d) and ^{1}P (4s4p) asymptotes are rather close in energy, it is not surprising that the highest B state ($3\,^1\Sigma$) cumulates the repulsive interactions with He, while the lower one does not and looks like the ground-state potential of the Ca^+He ion.

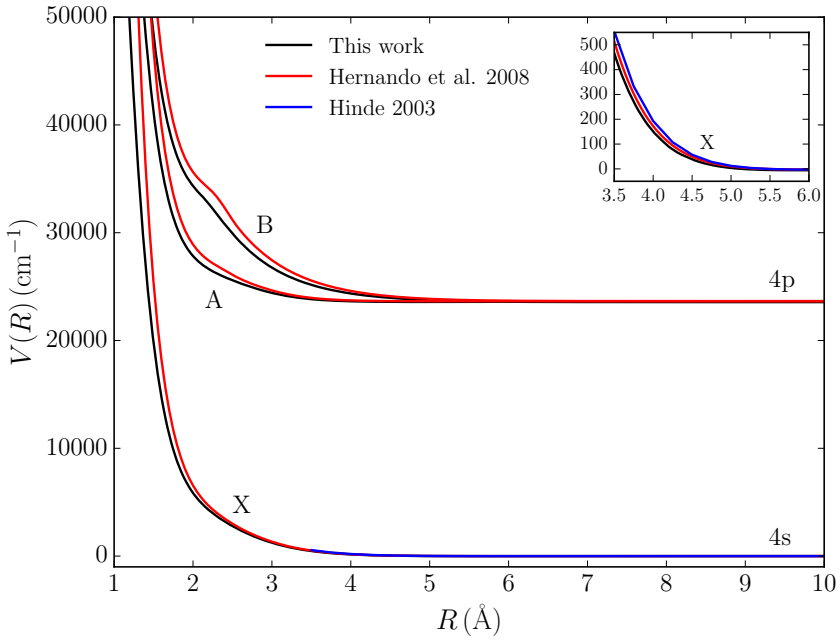

Figure 8.1 – PECs for the 4s and 4p states of the CaHe molecule. For comparison, the potentials computed by Hinde (2003) and Hernando et al. 2008 (which were used in Blouin et al. 2019b) are also shown.

8.4 Line profiles

To compute the pressure broadening of the Ca I resonance line, we rely on the classical path expression derived by Allard et al. (1999). In contrast with other more usual approximations (Anderson, 1952; Baranger, 1958a,b), the approach of Allard et al. takes into account the dependence of the electric dipole moment on the position of perturbers, which can significantly affect the spectral line shape (Allard et al., 1998a,b).

8.4.1 Low Densities

Under sufficiently low perturber densities, the center of the spectral line is expected to be symmetric and described by a Lorentzian profile. This profile is defined by two parameters, a width and a shift, which have a linear dependence on the density. We find that the core of the line is adequately described by a Lorentzian up to $n_{\mathrm{He}} = 10^{21}\,\mathrm{cm}^{-3}$ (Figure 8.2). Using the impact limit of the general calculation of the autocorrelation function (Allard et al., 1999), we computed the line parameters that characterize this Lorentzian core. As shown in Figure 8.3, the resulting theoretical broadening parameters are in reasonable agreement with laboratory measurements (Smith, 1972; Driver & Snider, 1976; Bowman & Lewis, 1978; Harris et al., 1986). Note that the error bars on the experimental data are probably underestimated, since the three points at low temperature appear to imply an improbable temperature dependence.

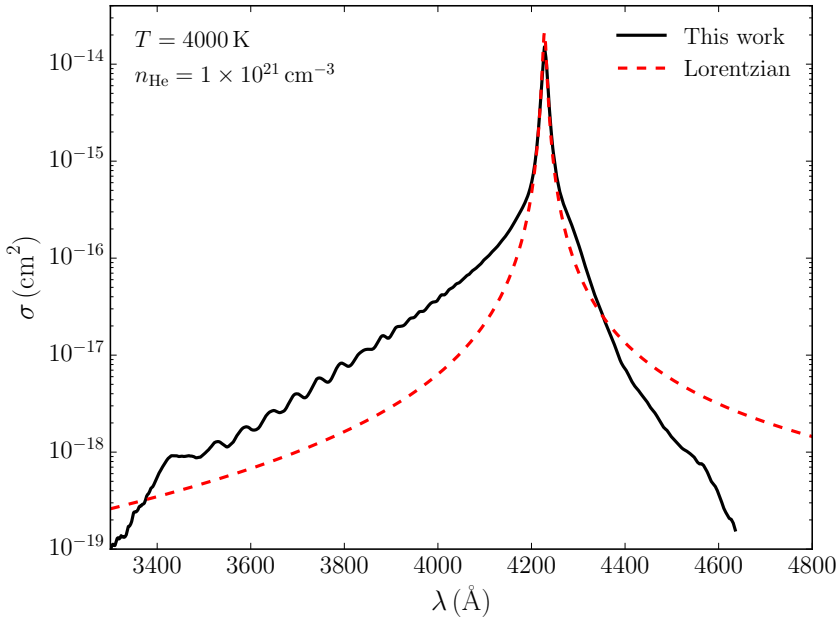

Figure 8.2 – Comparison of the unified profile (solid black line) with the corresponding Lorentzian profile (dashed red line).

While the core of the resonance line is adequately described by a Lorentzian profile at $n_{\mathrm{He}} = 10^{21}\,\mathrm{cm}^{-3}$, it is of course not the case for the wings (Figure 8.2). The X−B transition is responsible for the shape of the blue wing and the X−A transition affects the red side. The small maximum in the blue wing near 3400 Å is a direct consequence of the

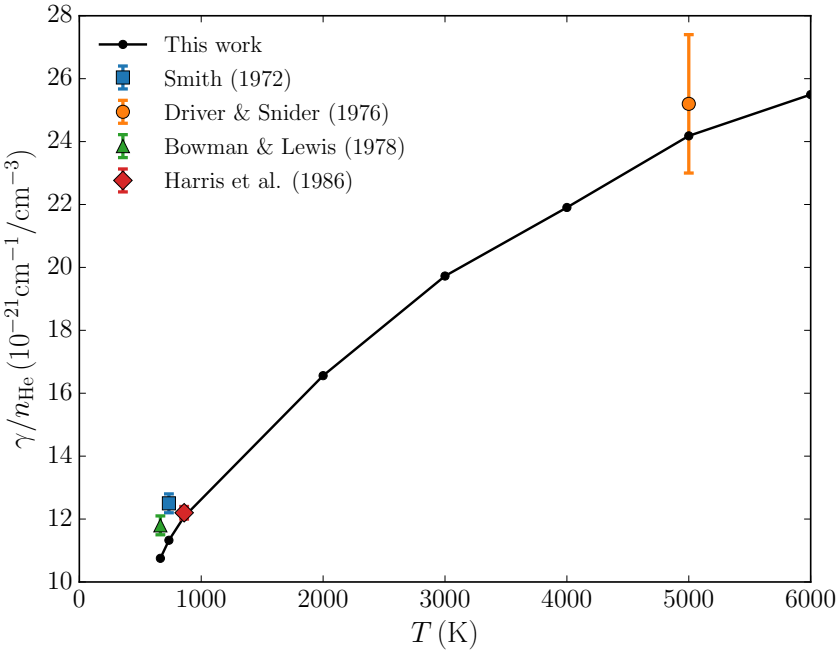

Figure 8.3 – Variation with temperature of the half width at half maximum of the Ca I resonance line perturbed by He collisions. Our results are shown in black and the error bars represent experimental measurements.

shoulder of the B state PEC at $R = 2.2\,\text{Å}$, which gives rise to a local maximum of $\Delta V(R)$ at $\Delta V = 5800\,\text{cm}^{-1}$. As satellite lines occur at frequencies corresponding to extrema of ΔV, a satellite feature appears at $\Delta\omega = 5800\,\text{cm}^{-1}$ (which corresponds to $\lambda \simeq 3400\,\text{Å}$).

8.4.2 High Densities

The coolest DZ white dwarfs are characterized by photospheric densities that can go up to $n_{\rm He} = 10^{23}\,\text{cm}^{-3}$, with much of their line-forming regions located at densities exceeding $10^{21}\,\text{cm}^{-3}$ (Figure 8.4). As those cool objects are precisely the ones that show a prominent Ca I resonance line, there is a strong astrophysical interest in properly modeling its line shape under such high-density conditions.

Given the high perturber densities involved, simultaneous collisions are very frequent. This implies that many-body collisions must be included in our calculation of the Ca I resonance line pressure broadening and this is why we rely on the autocorrelation formalism of Allard et al. (1999). This approach has already proved successful for the modeling of spectral lines in cool DZ white dwarfs (e.g., Allard et al., 2016b, 2018). Another proof of the

accuracy of the Allard et al. (1999) formalism has been provided by the study of He doped with alkali atoms, which has recently been a subject of active study (e.g., Hernando et al., 2010; Mateo et al., 2011). In such experiments, large He clusters produced in a supersonic jet are doped with alkali atoms and characterized by laser-induced fluorescence. In the case of Na atoms attached to He droplets (Stienkemeier et al., 1996), Allard et al. (2013) have shown that calculations performed within the autocorrelation framework can successfully explain the laboratory spectra. Moreover, it was also shown that the absorption spectra obtained by this approach are consistent with those obtained from path integral Monte Carlo simulations and the Franck–Condon approximation (Nakayama & Yamashita, 2001).

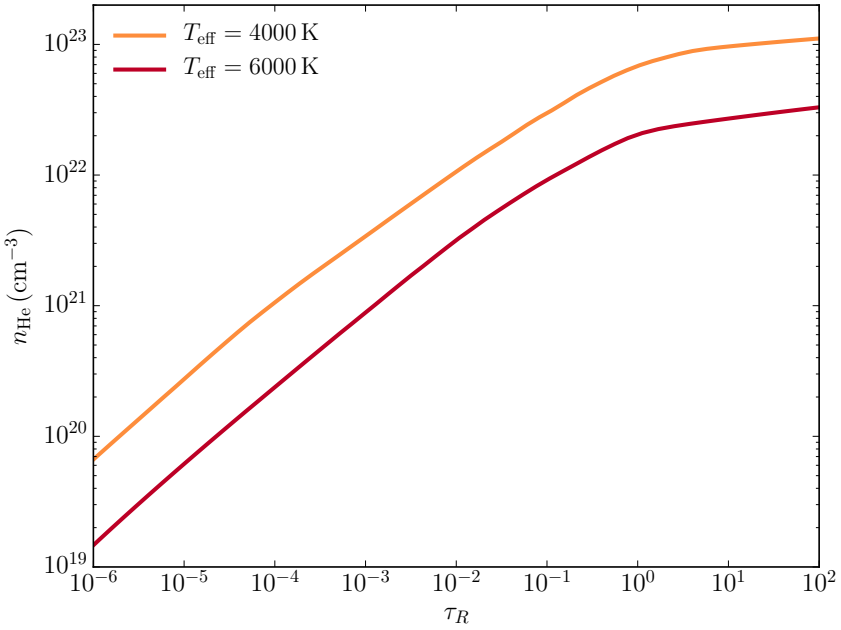

Figure 8.4 – He density as a function of the Rosseland mean optical depth for two models of cool DZ atmospheres. Note that a hydrogen-free atmosphere with a calcium abundance $\log {\rm Ca/He} = -10$ and a surface gravity $\log g = 8$ was assumed for both models. The abundance ratios of all other heavy elements were scaled to the abundance of Ca to match the abundance ratios measured in CI chondrites (Lodders, 2003).

Figure 8.5 shows the results of our calculations for the evolution of the Ca I resonance line profile with increasing He density. Clearly, above $10^{21}\,{\rm cm}^{-3}$, the profiles become strongly asymmetric and are shifted toward smaller wavelengths. Note that, as expected, the maximum of the line shifts toward the satellite line at 3400 Å. Apart from being strongly affected by the perturber density, line profiles can also be affected by the temperature

of the medium (Allard et al., 2004). However, for the temperature range relevant to cool DZ atmospheres, we find that the profiles are not very sensitive to the temperature (Figure 8.6).

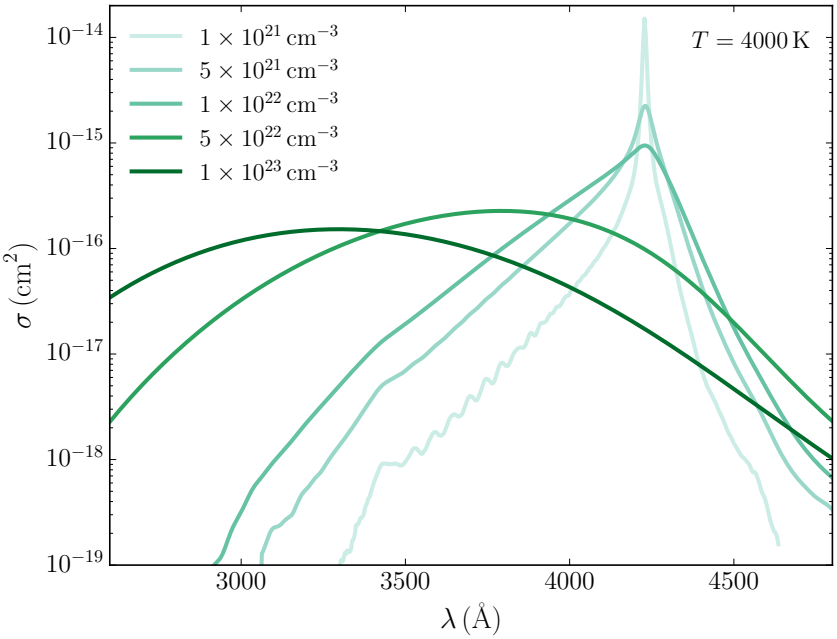

Figure 8.5 – Density dependence of the Ca I resonance line profiles. A constant temperature $T = 4000\,\mathrm{K}$ is assumed.

8.5 Astrophysical Applications

8.5.1 SDSS J0804+2239

A comprehensive analysis of the DZ white dwarf SDSS J0804+2239 was recently presented in Blouin et al. (2018b). Thanks to the improved constitutive physics of their atmosphere models, they were able to find a satisfactory fit to both its metal spectral lines and its spectral energy distribution, which is affected by H_2-He collision-induced absorption. They found an effective temperature of $T_{\mathrm{eff}} = 4970 \pm 100\,\mathrm{K}$, a surface gravity of $\log g = 7.98 \pm 0.05$ and number abundances of $\log \mathrm{H/He} = -1.6 \pm 0.2$ and $\log \mathrm{Ca/He} = -10.0 \pm 0.1$. However, their spectroscopic fit of SDSS J0804+2239 was tarnished by their inability to adequately fit the blue wing of the Ca I resonance line, which they attributed to the poor quality of the CaHe PECs used to compute the profiles of this spectral line. Using the same at-

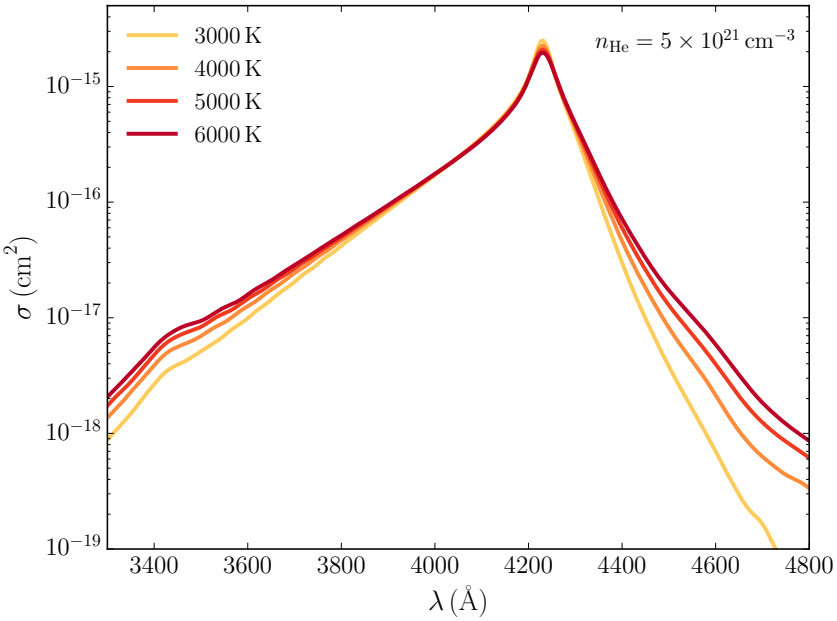

Figure 8.6 – Temperature dependence of the Ca I resonance line profiles. A constant density of $n_{\rm He} = 5 \times 10^{21}\,{\rm cm}^{-3}$ is assumed.

mospheric parameters as those found by Blouin et al. (2018b), we fitted the Ca lines of SDSS J0804+2239 with our improved Ca I 4226 Å profiles. As shown in Figure 8.7, these new profiles allow us to obtain an improved spectroscopic fit to the blue wing of the Ca I resonance, solving the problem identified by Blouin et al. (2018b).

8.5.2 WD J2356−209

WD J2356−209 is a very cool DZ white dwarf whose visible spectrum is dominated by a very broad sodium feature (Salim et al., 2004). Blouin et al. (2019b) have obtained a fit that is in very good agreement with observations across all wavelengths and they have shown that WD J2356−209 has a record Na/Ca abundance ratio. However, some uncertainty persisted as the Ca I resonance profiles were computed assuming constant transition dipole moments and as the long-range portion of the CaHe PECs was not available. Thanks to our new ab initio data on the CaHe molecule, the uncertainties that could potentially plague the Ca abundance determination are no longer present. Using our Ca I 4226 Å profiles, we performed a new spectroscopic fit of WD J2356−209 (Figure 8.8) and we found virtually the same abundances. In particular, we found a calcium abundance

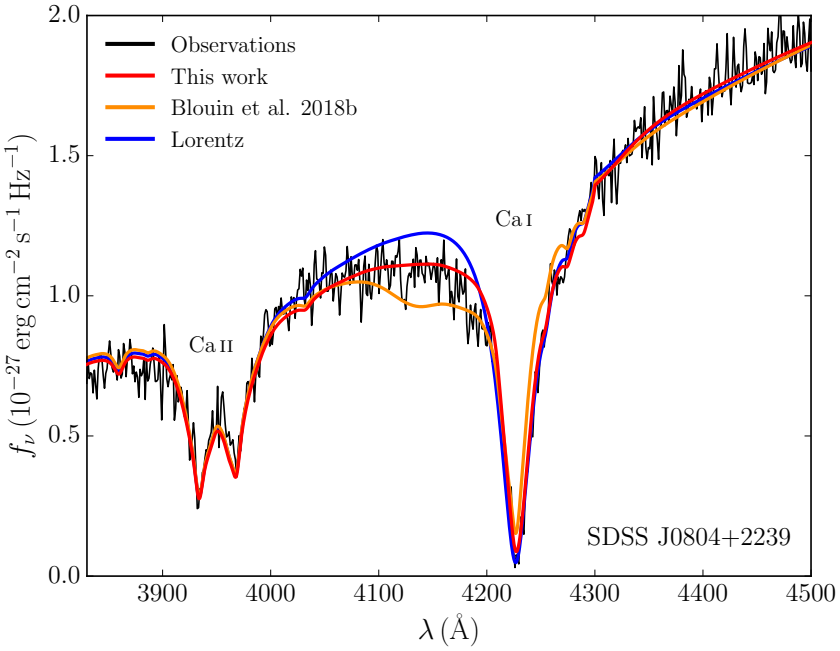

Figure 8.7 – Comparison of synthetic spectra computed with different line profiles for the Ca I 4226 Å transition. Observations of J0804+2239 are in black, results found when assuming a Lorentzian profile are in blue and synthetic spectra obtained with the unified line shape theory of Allard et al. (1999) are in orange for the case where approximate CaHe potentials were used (Blouin et al., 2018b) and in red for the case where the high-quality CaHe potentials presented in this work were used. All synthetic spectra were computed assuming the atmospheric parameters of SDSS J0804+2239 found in Blouin et al. (2018b, i.e., $T_{\rm eff} = 4970$ K, $\log g = 7.98$, $\log {\rm H/He} = -1.6$ and $\log {\rm Ca/He} = -10.0$). Note that in all cases the Ca II H & K lines are computed with the profiles described in Allard & Alekseev (2014).

of $\log {\rm Ca/He} = -9.4 \pm 0.1$, which is within the uncertainties of the -9.3 ± 0.1 value of Blouin et al. (2019b). Therefore, their conclusions are unchanged despite the addition of our new profiles : WD J2356−209 does have a uniquely high Na/Ca abundance ratio. We note, however, that our new profiles cannot account for the absorption feature near 4500 Å. The nature of this absorption feature remains unknown (see Section 4.3 of Blouin et al. 2019b for a comprehensive discussion on this issue).

8.5.3 WD 2251−070

After WD J2356−209, WD 2251−070 is the second coolest known DZ white dwarf. Its spectrum is quite different from that of WD J2356−209, as it has a prominent Ca I

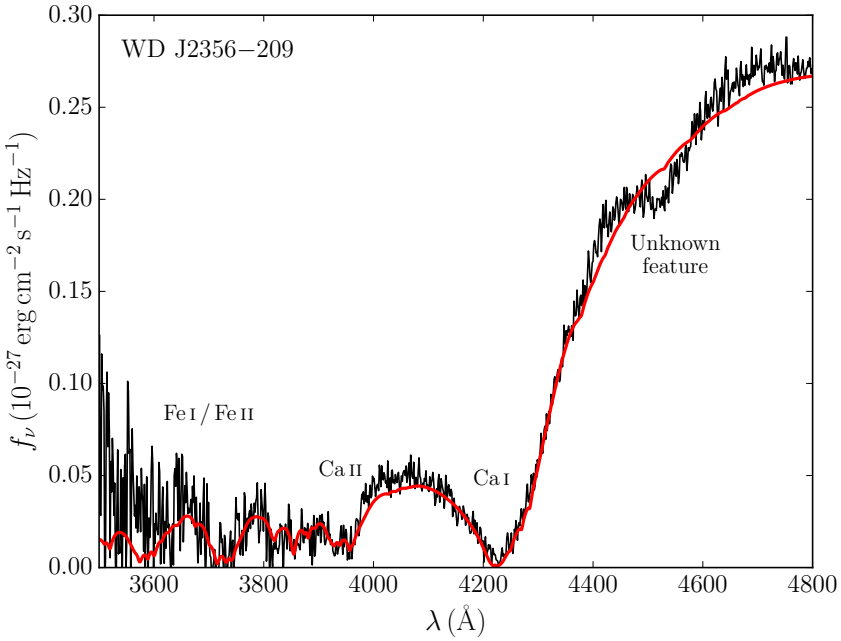

Figure 8.8 – Spectroscopic fit of the Ca I resonance line of WD J2356−209. As in Blouin et al. (2019b), $T_{\rm eff} = 4040\,{\rm K}$, $\log g = 7.98$ and $\log {\rm Na/He} = -8.3$. However, the calcium abundance is now $\log {\rm Ca/He} = -9.4 \pm 0.1$, which is slightly lower than the value reported by Blouin et al. (2019b).

resonance line but does not show a strong Na D doublet (Blouin et al., 2019b, Figure 5). While reasonable fits to its spectrum have been obtained in previous studies (Kapranidis & Liebert, 1986; Dufour et al., 2007), atmosphere model codes used to analyze this object relied on constitutive physics that is not totally appropriate for the dense atmosphere of this cool white dwarf.

In particular, the analysis of Kapranidis & Liebert (1986) relied on models that assumed a Thomas–Fermi equation of state (Kapranidis, 1983). Because of this assumption, they found that electron thermal conduction was an important energy transport mechanism, a conclusion that does not hold if we use more realistic equations of state (Bergeron et al., 1995; Kowalski et al., 2007). Also, Kapranidis & Liebert (1986) computed their synthetic spectra from pure helium atmosphere structures, thus ignoring the impact of heavy elements on the pressure and temperature stratification. Moreover, a simple Lorentzian profile was assumed for the Ca I resonance line. Despite all those simplifying assumptions, they managed to obtain an excellent fit to the resonance line (with $T_{\rm eff} = 4500\,{\rm K}$ and

log Ca/He = −6.3) and were even able to find a good agreement to the unknown feature at 4500 Å. Unfortunately, no detail regarding this puzzling structure was given so we cannot know how they were able to explain it.

Dufour et al. (2007) revisited WD 2251−070 using more realistic atmosphere models, where heavy elements are included in the calculation of the atmosphere structures. That being said, a number of unjustified approximations remained, such as the ideal gas law, the ideal Saha ionization equilibrium and Lorentzian profiles. Their best solution ($T_{\rm eff}$ = 4000 K and log Ca/He = −10.5) was in good agreement with the photometry and with the Ca I resonance line, but they were unable to explain the absorption feature near 4500 Å.

Here, we revisit this star using our improved models (Blouin et al., 2018a) and our new Ca I resonance line profiles. To do so, we use the spectroscopic observations of Dufour et al. (2007), the *Gaia* data release 2 (DR2) parallax measurement ($\pi = 117.15 \pm 0.05$ mas, Gaia Collaboration, 2016, 2018), and photometry from Bergeron et al. (1997), the Panoramic Survey Telescope And Rapid Response System (Pan-STARRS, Chambers et al., 2016), and the Two Micron All-Sky Survey (2MASS). Our best fit to the spectroscopic and photometric observations is shown in Figure 8.9 and the corresponding atmospheric parameters are given in Table 8.1.

Parameter	Value
$T_{\rm eff}$	4170 ± 90 K
$\log g$	8.06 ± 0.08
log H/He	< -4.5
log Ca/He	-9.8 ± 0.2

Table 8.1 – WD 2251−070 atmospheric parameters

To obtain this solution, we used the photometric technique (Bergeron et al., 1997) to determine $T_{\rm eff}$ and $\log g$. More precisely, the solid angle $\pi(R/D)^2$ and the effective temperature were found by adjusting the model fluxes to the photometric observations. From the solid angle, we computed the white dwarf radius R (D is given by the *Gaia* parallax) and, from there, we found the mass and the surface gravity using the evolutionary models of Fontaine et al. (2001). Using the parameters given by the photometric fit, we then adjusted the Ca abundance to the spectroscopy. As the abundance obtained from this spectroscopic

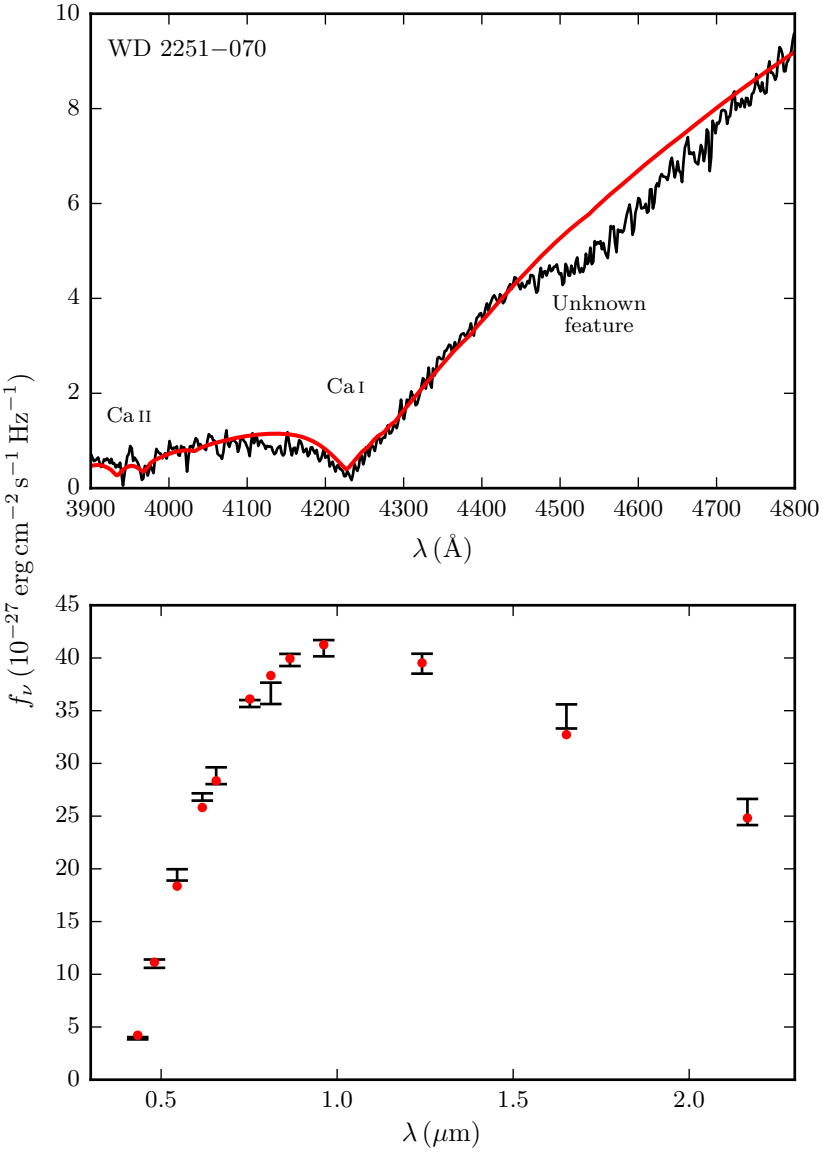

Figure 8.9 – Our best solution for WD 2251−070. The top panel shows our spectroscopic fit and the bottom panel shows our fit to the $BVRI$, $grizy$ and JHK photometry.

fit was different from that originally assumed, we repeated the whole fitting procedure (the photometric and the spectroscopic fits) until we reached a consistent solution. Additionally, as no collision-induced absorption is visible in the infrared photometry, we were able to constrain the hydrogen abundance to log H/He < -4.5.

As shown in Figure 8.9, we are able to find a good fit to most of the spectrum of WD 2251−070 (with the notable exception of the unknown absorption feature near 4500 Å). In particular, our best solution is in good agreement with the observations in the region located between the Ca II H & K doublet and the Ca I resonance line, whereas the best solution of Dufour et al. (2007) was significantly above the observed spectrum in this region. Moreover, unlike Kapranidis & Liebert (1986), we find a reasonable match to the weak Ca II H & K doublet.

8.6 Conclusion

Ca I resonance line profiles suitable for the extreme densities of the atmospheres of cool, metal-polluted white dwarfs were presented. These new profiles were computed using state-of-the-art ab initio data and a unified theory of collisional line profiles. At low densities, they are compatible with laboratory measurements and, at high densities, they are heavily broadened and shifted towards lower wavelengths. We implemented these new profiles in our model atmosphere code and showed how they lead to good spectroscopic fits for three cool DZ white dwarfs (SDSS J0804+2239, WD J2356−209 and WD 2251−070). However, in the case of WD J2356−209 and WD 2251−070, there remains a discrepancy between our models and the observations, as there seems to be missing an absorption source in our models near 4500 Å.

Acknowledgments This work was supported in part by NSERC (Canada) and the Fund FRQNT (Québec).

This work has made use of data from the European Space Agency (ESA) mission *Gaia* (https://www.cosmos.esa.int/gaia), processed by the *Gaia* Data Processing and Analysis Consortium (DPAC, https://www.cosmos.esa.int/web/gaia/dpac/consortium). Funding for the DPAC has been provided by national institutions, in particular the institutions participating in the *Gaia* Multilateral Agreement.

CHAPITRE 9

A New Generation of Cool White Dwarf Atmosphere Models. IV. Revisiting the Spectral Evolution of Cool White Dwarfs

In God we trust, all others must bring data.

—W. Edwards Deming (1900−1993), ingénieur et statisticien américain

Ce chapitre est une adaptation de «A New Generation of Cool White Dwarf Atmosphere Models. IV. Revisiting the Spectral Evolution of Cool White Dwarfs», par Simon Blouin, Patrick Dufour, Christian Thibeault et Nicole F. Allard. Cet article a été publié en juin 2019 dans *The Astrophysical Journal*.[1]

9.1 Abstract

As a result of competing physical mechanisms, the atmospheric composition of white dwarfs changes throughout their evolution, a process known as spectral evolution. Because of the ambiguity of their atmospheric compositions and the difficulties inherent to the modeling of their dense atmospheres, no consensus exists regarding the spectral evolution of cool white dwarfs ($T_{\rm eff} < 6000\,{\rm K}$). In the previous papers of this series, we presented and observationally validated a new generation of cool white dwarf atmosphere models that include all the necessary constitutive physics to accurately model those objects. Using these new models and a homogeneous sample of 501 cool white dwarfs, we revisit the spectral

[1]Blouin, S., Dufour, P., Thibeault, C., Allard, N. F. 2019, ApJ, 878, 63.

evolution of cool white dwarfs. Our sample includes all spectroscopically identified white dwarfs cooler than 8300 K for which a parallax is available in *Gaia* DR2 and photometric observations are available in Pan-STARRS1 and 2MASS. Except for a few cool carbon-polluted objects, our models allow an excellent fit to the spectroscopic and photometric observations of all objects included in our sample. We identify a decrease of the ratio of hydrogen- to helium-rich objects between 7500 and 6250 K, which we interpret as the signature of convective mixing. After this decrease, hydrogen-rich objects become more abundant up to 5000 K. This puzzling increase, reminiscent of the non-DA gap, has yet to be explained. At lower temperatures, below 5000 K, hydrogen-rich white dwarfs become rarer, which rules out the scenario in which the accretion of hydrogen from the interstellar medium dominates the spectral evolution of cool white dwarfs.

9.2 Introduction

White dwarf stars are compact stellar remnants condemned to a slow cooling that extends over billions of years. One of the fundamental properties of white dwarfs is their intense surface gravity ($\log g = 8$ on average). This strong gravitational field implies that heavy elements are expected to sink toward the core of the white dwarf and that light elements should float high up in the atmosphere (Schatzman, 1945). If gravitational settling were the only process influencing the chemical composition of white dwarf atmospheres, then all white dwarfs would show pure hydrogen atmospheres (i.e., only the DA and DC spectral types would exist).

However, we know that at least ∼20% of white dwarfs have helium-rich atmospheres (Giammichele et al., 2012; Kepler et al., 2015), that many have metal-polluted atmospheres (DQs and DZs) and that some even have carbon-dominated (Hot DQs, Dufour et al., 2007) or oxygen-dominated atmospheres (DS[2], Kepler et al., 2016a). These simple observational facts imply that additional mechanisms can alter the atmospheric composition of a white dwarf. For instance, a white dwarf atmosphere can undergo simple diffusion (Muchmore, 1984; Paquette et al., 1986; Koester, 2009), convective dilution (Fontaine & Wesemael, 1987; MacDonald & Vennes, 1991; Rolland et al., 2018), convective mixing (Koester, 1976; Vauclair & Reisse, 1977; Dantona & Mazzitelli, 1979; Rolland et al., 2018), convective

[2]DS is the proposed classification for oxygen-rich objects (see also Table 8 of Leggett et al., 2018).

dredge-up from the core (Pelletier et al., 1986), radiative levitation (Chayer et al., 1995), accretion from the interstellar medium (Dupuis et al., 1993; Koester & Wilken, 2006) and accretion of rocky planetesimals (Graham et al., 1990; Jura, 2003; Farihi et al., 2010). As those mechanisms change in importance during the evolution of white dwarfs, their surface compositions also change as a function of decreasing effective temperature. This phenomenon, known as spectral evolution, is one of the most studied aspects of white dwarf evolution.

The most spectacular feature of the spectral evolution of white dwarfs is probably the existence of a so-called DB gap between $T_{\rm eff} \approx 45\,000$ K and 30 000 K (Liebert, 1986; Liebert et al., 1986), where helium-rich white dwarfs are significantly less abundant than at higher or lower temperatures (Eisenstein et al., 2006a). This deficiency has been explained as the result of a hydrogen float-up process at the blue edge of the gap and a convective dilution process below the red edge (Fontaine & Wesemael, 1987; MacDonald & Vennes, 1991).

Going down the temperature scale, the next striking feature in the spectral evolution of white dwarfs is the increase of the ratio of non-DA to DA objects below $T_{\rm eff} \approx 12\,000$ K (Sion, 1984; Tremblay & Bergeron, 2008). This observation is the consequence of the convective mixing of a thin hydrogen layer with the thick helium envelope underneath that can transform a hydrogen-rich atmosphere into a helium-rich atmosphere (Koester, 1976; Vauclair & Reisse, 1977; Dantona & Mazzitelli, 1979; Rolland et al., 2018). The lower the temperature of the star, the deeper the convection zone extends into the white dwarf. Therefore, objects with a thicker hydrogen layer turn into helium-rich stars later in their evolution (Tassoul et al., 1990; Bergeron et al., 1997).

At lower temperatures, however, our understanding of the spectral evolution of white dwarfs is more limited. In fact, results obtained in the last two decades point in conflicting directions. One the one hand, analyses performed by Bergeron et al. (1997, 2001) and Kilic et al. (2006, 2010b) have revealed that the ratio of hydrogen-rich to helium-rich stars is greatly enhanced between 5000 and 6000 K. Due to its deficiency of helium-rich objects, this temperature range was termed the non-DA gap. The existence of this gap is usually understood as the consequence of processes that transform a significant fraction of helium-rich stars into hydrogen-rich stars (near 6000 K) and that later transform hydrogen-rich

objects into helium-rich objects (near 5000 K). So far, no consistent physical explanation for the existence of the non-DA gap has been proposed (Hansen, 1999; Malo et al., 1999; Bergeron et al., 2001).

On the other hand, results obtained by Kowalski & Saumon (2006) and Kilic et al. (2009a,b) suggest that the overabundance of hydrogen-rich objects is not limited to the 5000−6000 K range and that it extends all the way to the coolest objects at $T_{\rm eff} \approx 4000$ K. In fact, they find that almost every single object in their samples is hydrogen-rich for $T_{\rm eff} < 5000$ K. The overabundance of hydrogen-rich stars between 5000 and 6000 K would therefore not be a gap but rather a portion of a continuous process that irreversibly transforms helium-rich atmosphere into hydrogen-rich atmospheres. Kowalski (2006a) has tentatively suggested that this transformation could be due to the accretion of hydrogen from the interstellar medium.

The fact that the atmospheric composition of the coolest white dwarfs is still open to debate is concerning for white dwarf age dating. As white dwarfs cool down monotonically and as their cooling rate can be precisely modeled (Hansen, 1999; Fontaine et al., 2001; Renedo et al., 2010), they can be very accurate cosmic clocks (for applications to various stellar populations, see Oswalt et al., 1996; García-Berro et al., 2010; Kalirai, 2012; Tremblay et al., 2014). However, in order to use a white dwarf as a cosmochronometer, a precise determination of its atmospheric parameters is required. In particular, it is important to know its atmospheric composition, since helium-rich and hydrogen-rich atmospheres do not have the same opacities and therefore have different cooling rates. For instance, for a white dwarf with $T_{\rm eff} = 4000$ K and $\log g = 8$, a mistake on the atmospheric composition can lead to an error of ∼1 Gyr on its cooling age (Fontaine et al., 2001, assuming that the white dwarf evolves with a constant atmospheric composition). In this context, knowing the atmospheric composition of the coolest (and thus oldest) white dwarfs becomes an even more pressing problem.

There are two main reasons that explain the discrepancies between studies that conclude to the existence of the non-DA gap and those that suggest a continuous increase of the hydrogen-rich to helium-rich ratio. The first one is that the samples of Kowalski & Saumon (2006) and Kilic et al. (2009a,b) are limited to DA and DC white dwarfs. Therefore, they completely ignore the existence of DQs and DZs, which have helium-rich atmospheres (for

limits on the hydrogen abundance in the atmospheres of DQs and DZs, see Dufour et al., 2005, 2007). For this reason, their samples are strongly biased toward hydrogen-rich stars. In particular, we can be confident that helium-rich white dwarfs do exist below 5000 K, since DQs and DZs are found at those temperatures.

The second reason that explains the discrepancy between both sets of studies is related to the fact that both helium-rich and hydrogen-rich stars become DCs below ≈ 5000 K. In fact, the thermal energy becomes too small to excite the atomic states that are required to produce hydrogen or helium spectral lines in the visible and most white dwarfs with $T_{\rm eff} \lesssim 5000$ K thus show a flat, featureless spectrum. This implies that the chemical composition of the atmospheres of such stars must be derived solely from the photometric observations (since no useful information can be retrieved from the spectroscopy). Atmosphere models are used to fit the spectral energy distribution (SED) assuming both hydrogen-rich and helium-rich models and the best solution indicates the most likely composition of the atmosphere. As this process depends on a detailed fit of the SED, small differences between different sets of atmosphere models can lead to different solutions. The same star can be classified as having a hydrogen-rich atmosphere using one set of models and as having a helium-rich atmosphere using another set of models. This is precisely what happens here. Compared to the models of Bergeron et al. (1995, used in Bergeron et al. 1997, 2001; Kilic et al. 2006, 2010b), the models employed in Kowalski & Saumon (2006) and Kilic et al. (2009a,b) include numerous improvements for the treatment of nonideal effects in the dense atmospheres of cool white dwarfs. These improved models predict that cool helium-rich white dwarfs have SEDs that are very close to those of blackbodies. As this is not observed, cool white dwarfs are almost all classified as hydrogen-rich (Kowalski, 2006a).

This paper aims to fix the issues that tarnished previous analyses of the spectral evolution of cool white dwarfs. On the theoretical front, our analysis is based on state-of-the-art atmosphere models that take into account all high-density effects relevant for the modeling of the atmospheres of cool white dwarfs (Blouin et al., 2018a, hereafter Paper I). These new models have the advantage of also being applicable to metal-polluted white dwarfs. Not only is this useful for modeling all cool white dwarfs (and not only pure hydrogen and pure helium objects), but it is also an excellent way of observationally validating the input physics of our models. Indeed, as metal-polluted white dwarfs (DQs and DZs) are the only

ones to still show spectral features in the visible below $T_{\rm eff} \approx 5000\,{\rm K}$, they represent a unique opportunity to test our models against observations. In contrast, as there is no challenge in fitting the flat spectrum of DC white dwarfs, they cannot be used to discriminate between good and poor models. Using this insight, we tested our models against some of the most challenging cool metal-polluted white dwarfs (see Paper I and Blouin et al. 2018b, 2019b, hereafter Papers II and III). In every case, we showed that our models can accurately reproduce the complex spectral features observed in those objects, which validates their constitutive physics.

On the observational front, the analysis presented in this paper is based on the largest (501 objects) homogeneous sample of cool white dwarfs ever studied. The homogeneity of our sample is guaranteed by the fact that all our fits are based on data obtained from the same three surveys (Pan-STARRS1, 2MASS and *Gaia* DR2). Additionally, no discrimination on the spectral types was made during the selection of the sample, which ensures a good representation of the diversity of the chemical compositions of cool white dwarf atmospheres.

Section 9.3 details our methodology, including the selection of the sample, the model atmosphere code and the fitting procedures. In Section 9.4, we present the solutions of our fits and analyze in detail some interesting objects. In particular, we turn our attention to the so-called peculiar non-DAs—stars for which the photometric and spectroscopic observations suggest conflicting atmospheric compositions (Bergeron et al., 1997)—and to DQpec white dwarfs—carbon-polluted objects with distorted Swan bands (Hall & Maxwell, 2008). After a careful analysis of the biases that affect our sample, Section 9.5 presents our conclusions on the spectral evolution of cool white dwarfs. Finally, our main findings are summarized in Section 9.6.

9.3 Methodology

9.3.1 Sample selection

We defined the selection criteria of our sample so that the maximum number of white dwarfs could be included, while ensuring that the observations used for the photometric fits are homogeneous. Six criteria must be satisfied for an object to be part of our sample.

1. It must have a parallax measurement from the *Gaia* DR2 (Gaia Collaboration, 2016, 2018). The parallax is important not only for measuring the mass of the white dwarf, but also for identifying unresolved binary systems.

2. Each object must have *grizy* photometry from the Panoramic Survey Telescope and Rapid Response System (Pan-STARRS1, Chambers et al., 2016).

3. For each object, there must be at least J photometry (ideally H and K also) in the Two Micron All Sky Survey (2MASS).

4. A spectrum must be available for each object, so that the appropriate atmospheric composition can be assumed in our models. In particular, the presence of Hα is useful for identifying hydrogen-rich atmospheres and metal lines and C_2 Swan bands are used to fix the amount of heavy elements in the model atmospheres of DZ and DQ white dwarfs, respectively.

5. Stars that are part of a known unresolved binary system were rejected.

6. Only objects cooler than 8300 K were retained. This upper limit is motivated by our wish to verify the existence of the non-DA gap. To do so, we need to compare the abundance of hydrogen-rich stars above and below the blue edge of this gap at $T_{\rm eff} \approx 6000$ K. The 8300 K value was chosen as it allows to compute the fraction of hydrogen-rich stars as a function of effective temperature for 500 K bins up to a bin centered at 8000 K.

We relied on the Montreal White Dwarf Database (MWDD, Dufour et al., 2017) to identify objects that match these criteria. In total, we found 503 stars that satisfy all six criteria. The bulk of these objects are part of the Limoges et al. (2015) sample (292 objects) and the rest comes from a number of other studies (Bergeron et al., 1997, 2001; Bergeron et al., 2005; Putney, 1997; Kawka & Vennes, 2006, 2012; Subasavage et al., 2007, 2008, 2009, 2017; Kilic et al., 2010b; Giammichele et al., 2012; Sayres et al., 2012; Kleinman et al., 2013; Gianninas et al., 2015; Kepler et al., 2015, 2016b). Among the 503 objects initially selected, two of them (GJ 1221 and GJ 1228) were rejected because no appropriate models are available at the moment to properly model their atmospheres. These two white dwarfs, classified as DXP stars, are characterized by broad, unidentified

absorption features and a very large magnetic field ($B > 100$ MG, Putney & Jordan, 1995; Berdyugin & Piirola, 1999). Therefore, our final sample contains 501 objects, which are listed in Tables 9.1 (astrometric data) and 9.2 (photometric data).

Due to the relatively small limiting magnitude of 2MASS, requiring each object to be in 2MASS considerably reduces the size of our sample. Nevertheless, this constraint is important since observations in the infrared are necessary to detect collision-induced absorption (CIA) from molecular hydrogen, which is very useful to constrain the hydrogen abundance. This is a particularly important parameter to determine if we want to get an accurate picture of the spectral evolution of cool DC white dwarfs.

9.3.2 Atmosphere models

Our model atmosphere code is described at length in Paper I. It is based on the code described in Bergeron et al. (1995) and Dufour et al. (2005, 2007), but also includes a number of nonideal high-density effects that arise in the dense atmospheres of cool white dwarfs. In particular, continuum opacities are corrected for collective interactions (Iglesias et al., 2002; Rohrmann, 2018), an ab initio equation of state for hydrogen and helium is assumed (Becker et al., 2014), the pressure ionization of helium is modeled using the ab initio calculations of Kowalski et al. (2007), an accurate description of the pressure broadening of Lyα is included (Kowalski & Saumon, 2006), the H_2-He CIA profiles are corrected for many-body collisions (Blouin et al., 2017) and CIA from He−He−He interactions is included (Kowalski, 2014).

Moreover, our code includes significant improvements relevant for the accurate modeling of cool metal-polluted atmospheres, such as accurate line profiles for important heavy element lines (Paper III; Allard & Alekseev, 2014; Allard et al., 2014, 2016a,b, 2018; Blouin et al., 2019a), a state-of-the-art treatment of the nonideal ionization equilibrium of C, Ca, Fe, Mg and Na (Paper I), and the distortion of the C_2 Swan bands in DQpec stars (Kowalski, 2010). Note also that we now include the C_2 Swan bands opacity using a line-by-line approach with the line list of Hornkohl et al. (2005). This approach noticeably improves our fit to the shape of the Swan bands compared to the just overlapping line approximation (Zeidler-K.T. & Koester, 1982) implemented in the models of Dufour et al. (2005).

PSO[3]	MWDD object ID	Gaia object ID	R.A. (J2015.5)	Decl. (J2015.5)	π (mas)
J000224.474+635745.512	2MASS J00022257+6357443	431635455820288128	0.6033724	63.9627281	38.080(0.079)
J000410.478−034008.751	PHL 2595	2447889401738675072	1.0439384	−3.6691769	21.076(0.100)
J000720.831+123018.402	WD 0004+122	2766234439302571904	1.8371872	12.5048777	57.308(0.114)
J000728.917+340342.227	NLTT 301	2875903332533220992	1.8705266	34.0618834	29.336(0.099)
J000754.487+394731.294	LP 240−30	383108338321272448	1.9774884	39.7919426	29.038(0.064)
J000935.139+310840.332	EGGR 1	2861792754354276352	2.3959624	31.1440912	18.638(0.077)
J001122.399+424038.082	GD 5	384636109728592768	2.8432990	42.6770566	42.714(0.045)
J001214.188+502514.381	GJ 1004	395234439752169344	3.0583199	50.4200515	91.983(0.029)
J001412.352−131109.057	GJ 3016	2418116963320446720	3.5508822	−13.1867135	53.812(0.070)
J001737.914−051650.624	LP 644−81	2443826805441462656	4.4082578	−5.28121904	21.405(0.153)

Table 9.1 – Astrometry of objects included in our sample. This table is published in its entirety in the machine-readable format. (Voir aussi le Tableau B.1 de l'Annexe B.)

[3]Pan-STARRS object name

PSO	Spectral type	g	r	i	z	y	J	H	K
J000224.474+635745.512	DC	17.63	16.99	16.73	16.63	16.57	15.80	15.57	15.51
J000410.478−034008.751	DA	16.91	16.75	16.73	16.76	16.79	16.12	15.89	15.44
J000720.831+123018.402	DC	16.77	16.25	16.02	15.93	15.92	15.08	15.10	14.90
J000728.917+340342.227	DC	17.61	17.23	17.12	17.05	17.08	16.39	16.25	15.83
J000754.487+394731.294	DC	17.25	16.53	16.23	16.12	16.06	15.18	14.85	14.65
J000935.139+310840.332	DC	16.81	16.74	16.85	16.94	17.01	16.45	16.19	–
J001122.399+424038.082	DA	15.42	15.27	15.23	15.28	15.31	14.54	14.35	14.39
J001214.188+502514.381	DAH	14.52	14.27	14.20	14.21	14.22	13.49	13.25	13.19
J001412.352−131109.057	DAH	16.12	15.76	15.62	15.59	15.60	14.81	14.55	14.63
J001737.914−051650.624	DA	17.92	17.52	17.35	17.32	17.27	16.48	16.35	–

Table 9.2 – Spectral type and photometric data. This table is published in its entirety in the machine-readable format. (Voir aussi le Tableau B.2 de l'Annexe B.)

9.3.3 Fitting procedures

9.3.3.1 DAs

The fundamental parameters of DA white dwarfs are obtained with the photometric technique (Bergeron et al., 1997). The solid angle $\pi(R/D)^2$ and $T_{\rm eff}$ are found by fitting the model fluxes to the observed SED with the Levenberg–Marquardt algorithm. Since D is known from the *Gaia* parallax measurement, the white dwarf radius R can be computed from the solid angle. The mass and the surface gravity of the white dwarf are then found with the evolutionary models of Fontaine et al. (2001). Note that for all DA stars in our sample we assume a pure hydrogen atmosphere. This assumption is very common in the literature (e.g. Bergeron et al., 2001; Gianninas et al., 2011; Limoges et al., 2015) and is supported by the comparison between synthetic and observed Balmer lines profiles. For cool white dwarfs, Balmer lines become shallower and wider when the H/He ratio is decreased. While it is not possible to distinguish between Balmer lines created in a pure hydrogen atmosphere and an atmosphere with log H/He = 2, the differences between a pure hydrogen atmosphere and a helium-dominated atmosphere (log H/He < 0) are obvious. As our sample is largely based on the sample of Limoges et al. (2015) and as their spectroscopic analysis shows no evidence of helium-dominated DAs, we conclude that we can safely assume that all DAs in our sample are hydrogen-rich. There remains the question of whether they simply have a hydrogen-dominated atmosphere or a pure hydrogen atmosphere, but since we cannot distinguish between both possibilities we assume a pure hydrogen composition for simplicity. Note that this assumption does not interfere with the main purpose of this work, since we only need to know which stars are hydrogen-rich and which ones are helium-rich.

9.3.3.2 DCs

The fitting procedure for DC stars is identical to the procedure described above for DAs, except that the atmospheric composition is a priori unknown. If the effective temperature is high enough that we should see Balmer lines if the atmosphere was hydrogen-rich, then we assume a helium-rich composition. If the temperature is too low to produce detectable Balmer lines ($T_{\rm eff} \lesssim 5000\,{\rm K}$), then the atmospheric composition determination is based

on the photometry. Finding the atmospheric composition of a DC white dwarf solely from the photometry can be difficult. That being said, differences between SEDs produced by stars with different compositions (see Figure 9.1) can generally be exploited to confidently establish the atmospheric composition of such objects.

Three distinct photometric fits are performed for each cool DC white dwarf in our sample : one assuming a pure hydrogen atmosphere, one assuming a pure helium atmosphere and one assuming a mixed H/He atmosphere, where the H/He ratio is a free parameter that is adjusted to the observations. To identify the best of the three solutions, we do not simply pick the solution with the smallest χ^2. This approach is misguided when comparing solutions obtained with different numbers of free parameters. In fact, it is almost always possible to obtain a smaller χ^2 by adding one more free parameter to the fit (the H/He ratio), but the gain obtained with this additional parameter is not always statistically significant. Instead, we use the Akaike information criterion (AIC). This criterion penalizes a model according to the number of free parameters it contains, thus enforcing Occam's razor. The best model is the one with the smallest AIC, which is given by (Akaike, 1974; Burnham & Anderson, 2002)

$$\mathrm{AIC} = 2k - 2\ln L, \tag{9.1}$$

where k is the number of degrees of freedom in the model and L is the maximum value of the likelihood function. Note that for least-squares model fitting the likelihood function is simply given by $\ln L = C - \chi^2/2$, where C is a constant that is independent from the model and can be ignored. When we fit photometric data, we are only fitting a small number of data points. In such circumstances, it is necessary to use an AIC that is corrected for small data samples (Hurvich & Tsai, 1989),

$$\mathrm{AICc} = \mathrm{AIC} + \frac{2k(k+1)}{n-k-1}, \tag{9.2}$$

where n is the sample size (in our case the sample size corresponds to the number of bands included in our photometric fit).

To our knowledge, this is the first time that such a detailed statistical analysis is applied to the problem of the determination of the atmospheric composition of DC stars. Previous

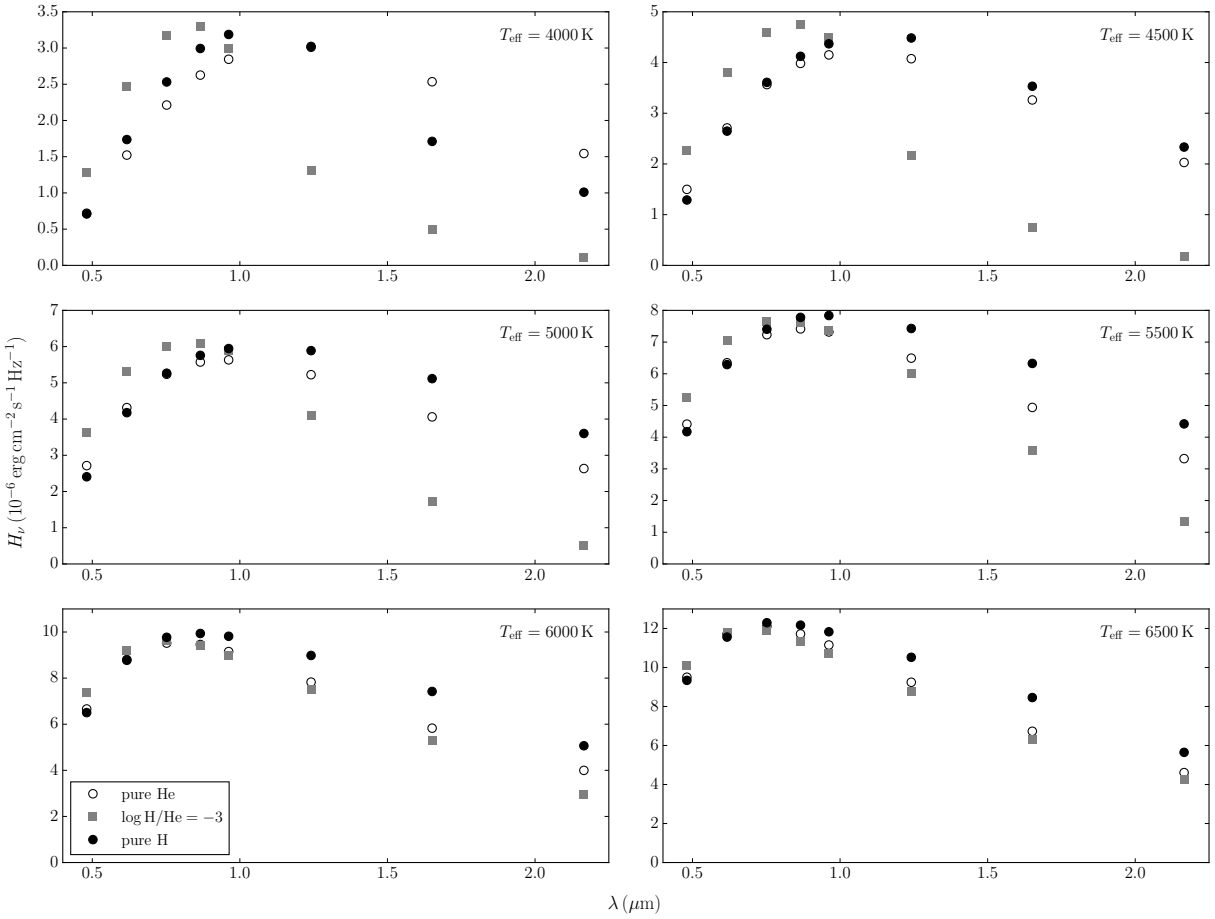

Figure 9.1 – Synthetic Pan-STARRS and 2MASS photometry obtained with our model atmosphere code. Each panel corresponds to a different effective temperature and each symbol represents a different atmospheric composition (see legend). In all cases, a surface gravity of $\log g = 8$ is assumed.

analyses either only used mixed H/He models when CIA was obviously present in the SED (Bergeron et al., 1997, 2001; Kilic et al., 2010b) or directly compared mixed and pure solutions without rigorously computing the significance of the χ^2 reduction following the addition of a third free parameter (Kowalski, 2006a; Kilic et al., 2009a).[4] Both approaches are problematic. The first one could miss mixed objects that do not show strong CIA and the second one is biased toward mixed solutions (e.g., $\approx$ 50% of DCs analyzed by Kilic et al. 2009a are classified as mixed objects). By accurately quantifying the weight of evidence in favor of each solution, our methodology should not be influenced by those biases.

We performed a small numerical experiment that clearly illustrates the danger of using an approach where the H/He ratio is directly considered as a free parameter (i.e., by fitting every DC star with a grid of mixed H/He compositions ranging from pure hydrogen to pure helium and adjusting the H/He ratio as a free parameter). We generated a set of 100 "synthetic" pure hydrogen stars with effective temperatures ranging from 4000 to 6000 K. To do so, we used the synthetic photometry obtained from our models to which we added a Gaussian noise to mimic the observational uncertainties (we assumed a typical 3% uncertainty for the visible photometry and 5% for the infrared). For 45% of these pure hydrogen objects, the fit obtained by adjusting the H/He ratio in order to obtain the smallest χ^2 corresponds to a mixed H/He solution (i.e., $-5 < \log \mathrm{H/He} < 0.5$).[5] This numerical experiment demonstrates that this approach is heavily biased toward finding mixed solutions, even for stars that actually have a pure composition. In contrast, if we use our AIC approach, we find the correct (pure hydrogen) solution in all cases.

We also performed an experiment to make sure that our AIC approach is not biased toward pure compositions. To do so, we fitted a set of 100 "synthetic" mixed H/He white dwarfs with effective temperatures ranging from 4000 to 6000 K and hydrogen abundances between $\log \mathrm{H/He} = -5$ and 0. As in our previous experiment, we injected a Gaussian noise to mimic the observational uncertainties. We find that our AIC approach retrieves a mixed

[4] A third approach, proposed by Saumon et al. (2014), consists of plotting χ^2 as a function of the H/He abundance ratio and checking if χ^2(H/He) has a significant minimum. Note, however, that no quantitative criterion was used to define what makes a χ^2(H/He) minimum statistically significant.

[5] Note that pure helium models are less susceptible to this bias, as the same experiment with pure helium models shows that 10% are (incorrectly) classified as mixed objects.

solution for 92% of these objects.[6] The cases where our AIC approach fails to retrieve a mixed solutions are all for objects with hydrogen abundances near $\log \mathrm{H/He} = 0$, where the SED becomes very similar to that of a pure hydrogen object. Therefore, the bias of the AIC approach against mixed objects is very weak compared to the bias against pure compositions exhibited by the method where the H/He ratio is directly considered as a free parameter, which justifies our methodology.

The AIC can also be used to estimate how likely it is that our atmospheric composition determinations are accurate (Burnham & Anderson, 2002). For each model i (i.e., for the pure hydrogen, the pure helium and the mixed H/He models) we can compute the difference in AIC with respect to the best model,

$$\Delta_i(\mathrm{AIC}) = \mathrm{AIC}_i - \min \mathrm{AIC}. \tag{9.3}$$

From there, the Akaike weights w_i are computed as,

$$w_i = \frac{\exp\left[-\frac{1}{2}\Delta_i(\mathrm{AIC})\right]}{\sum_j \exp\left[-\frac{1}{2}\Delta_j(\mathrm{AIC})\right]}. \tag{9.4}$$

Each weight w_i can be interpreted as the probability that model i is the best model. Therefore, we can now quantify the degree of confidence of our atmospheric composition determinations. In particular, given our hydrogen-rich and helium-rich fits, we can compute the odds that a DC star is hydrogen-rich versus helium-rich. Some examples of the usefulness of the Akaike weights are given in Section 9.4.1.

9.3.3.3 DQs and DZs

For metal-polluted objects, we still rely on a photometric fit (see Section 9.3.3.1) to determine T_{eff} and $\log g$, but we also use the observed spectrum to find the abundances of heavy elements. Our approach is identical to that of Dufour et al. (2005, 2007). Once a photometric solution is found, we adjust the metal abundances to obtain a good fit to the spectroscopy. As the abundances derived from this spectroscopic fit are usually different

[6] While we find a mixed solution in 92% of cases, we find the correct H/He ratio in 68% of cases. This difference is due to the degeneracy between the SEDs of mixed objects with a high H/He ratio and a low H/He ratio (see Section 3.1 of Paper II).

from our initial guess, we repeat the whole procedure (including the photometric fit) until a consistent solution is found. For DQ and DQpec objects, we use the C_2 Swan bands to constrain the C/He abundance ratio. For DZs, we use the Ca II H & K doublet and the Ca I resonance line to find Ca/He. The Fe/He, Mg/He and Na/He ratios are also adjusted when the relevant spectral lines are visible. Otherwise, the abundance ratios of all heavy elements are scaled to the abundance of Ca to match the abundance ratios of CI chondrites (Lodders, 2003).[7] Finally, unless there is direct evidence of the presence of hydrogen in the atmosphere (i.e., Balmer lines, CH bands or H_2-He CIA), a hydrogen-free atmosphere is assumed for all DQ and DZ white dwarfs.

9.4 Results

Following the fitting procedures described in Section 9.3.3, we obtained the atmospheric parameters of all 501 objects included in our sample. They are listed in Table 9.3, which is published in its entirety in the machine-readable format. Our statistical analysis of this sample and its implication on the spectral evolution of cool white dwarfs is presented in Section 9.5. The rest of this section is devoted to a more in-depth analysis of a number of noteworthy objects.

9.4.1 DAs and DCs

Figure 9.2 displays some examples of photometric fits to DA and DC white dwarfs (the complete set of photometric fits is available in the online journal). For DCs, both pure hydrogen and pure helium solutions are shown. The mixed H/He solution is only shown if the solution found when the H/He ratio was adjusted as a free parameter does not correspond to a pure hydrogen or a pure helium solution. For each object, the composition that leads to the smallest Akaike weight is designated as being the most likely composition (Section 9.3.3.2).

[7] There is an exception to this rule. For Fe, we set the default abundance to half that predicted by the chondritic Fe/Ca number ratio. This is a rough way of taking the faster diffusion of Fe (Paquette et al., 1986; Koester, 2009; Hollands et al., 2017) into account when Fe lines are not detected.

PSO	$T_{\rm eff}$ (K)	$\log g$	M ($M_\odot$)	$\tau_{\rm cool}$ (Gyr)[8]	log H/He	log C/He	log Ca/He
J000224.474+635745.512	4565(50)	7.758(0.024)	0.432(0.013)	4.45	He	–	–
J000410.478−034008.751	6955(60)	7.931(0.023)	0.551(0.013)	1.40	H	–	–
J000720.831+123018.402	4885(45)	8.090(0.021)	0.625(0.014)	6.45	He	–	–
J000728.917+340342.227	5545(50)	8.153(0.021)	0.666(0.013)	5.02	He	–	–
J000754.487+394731.294	4680(25)	6.768(0.039)	0.081(0.016)	1.40	H	–	–
J000935.139+310840.332	7960(290)	8.053(0.100)	0.609(0.062)	1.21	He	–	–
J001122.399+424038.082	6990(50)	7.975(0.017)	0.577(0.010)	1.47	H	–	–
J001214.188+502514.381	6445(40)	8.247(0.012)	0.746(0.008)	3.24	H	–	–
J001412.352−131109.057	5855(35)	8.217(0.016)	0.724(0.010)	4.10	H	–	–
J001737.914−051650.624	5630(40)	7.918(0.026)	0.537(0.015)	2.40	H	–	–

Table 9.3 – Atmospheric parameters. This table is published in its entirety in the machine-readable format. (Voir aussi le Tableau B.3 de l'Annexe B.)

[8]Cooling times are computed using the evolutionary models of Fontaine et al. (2001).

Note that the Akaike weights are particularly useful when trying to assess our degree of confidence in the determination of the atmospheric composition of DC stars. For instance, for a star like WD 1033+714 (Figure 9.2), the Akaike weights are $w_{\rm H} = 0.93$ for the pure hydrogen solution, $w_{\rm He} = 0.07$ for the pure helium solution and $w_{\rm mixed} = 0.00$ for the mixed H/He solution. This indicates that we can be quite confident that it is a hydrogen-rich object. Similarly, the Akaike weights strongly suggest that WD 1346+121 has a pure helium atmosphere ($w_{\rm He} = 0.94$, see Figure 9.2). Note that if we had simply used the χ^2 to identify the atmospheric composition of WD 1346+121, the mixed model would have been chosen since its χ^2 is smaller than that of the pure hydrogen and pure helium solutions. By adding a penalty for the additional free parameter, the Akaike weights reverse this verdict and assign a low probability to the mixed solution. Figure 9.3 shows an example where large observational errors lead to a much more uncertain composition. The Akaike weights for the mixed and pure hydrogen solutions are virtually equal, which reflects our inability to confidently identify the atmospheric composition of this object.

Another interesting aspect of Figure 9.2 is the presence of two $T_{\rm eff} < 5000\,{\rm K}$ DC white dwarfs for which we find a pure helium solution. Note that the Akaike weights for the pure helium solutions are ≥ 0.9 in both cases, which suggests that we can be quite confident in those solutions. In fact, out of the 74 DC stars cooler than 5000 K in our sample, we find pure helium solutions for 16 of them. We also find that 3 of those 74 DC stars have a mixed H/He atmosphere dominated by helium, which implies that $\approx 25\%$ of DCs cooler than 5000 K have helium-rich atmospheres. This result is in strong disagreement with the conclusions of Kowalski (2006a), Kowalski & Saumon (2006) and Kilic et al. (2009a,b), according to whom helium-rich DC white dwarfs cooler than 5000 K are nearly nonexistent. The implications of this finding on the spectral evolution of cool white dwarfs will be discussed in Section 9.5.

9.4.1.1 Peculiar non-DAs

In the $6200\,{\rm K} \leq T_{\rm eff} \leq 7600\,{\rm K}$ temperature range, Bergeron et al. (1997, 2001) have identified DC stars for which the photometric fit yields a pure hydrogen solution. Given their surface temperatures, those objects are expected to show Hα in their spectra if they have a hydrogen-rich atmosphere. The pure hydrogen photometric fits are therefore in

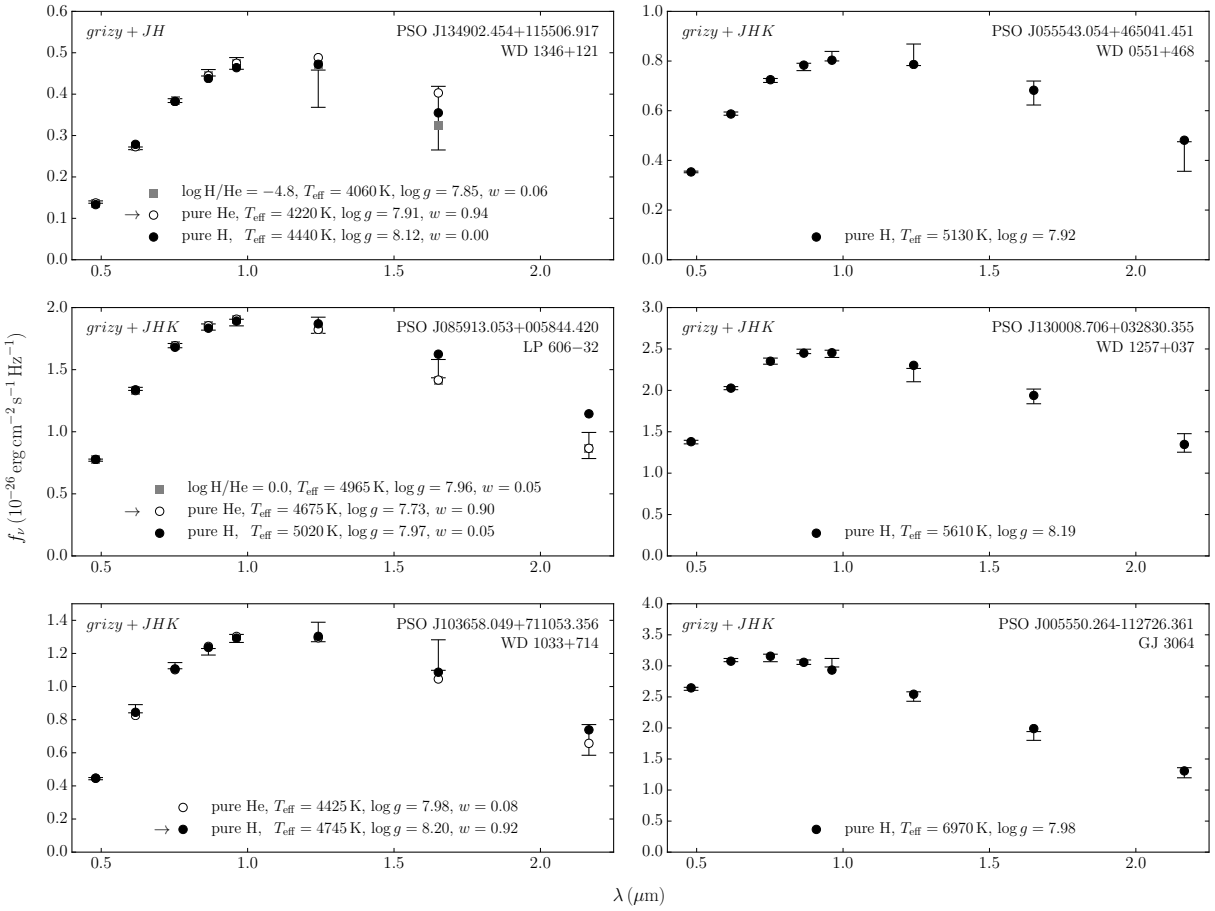

Figure 9.2 – Examples of photometric fits to DC (left column) and DA white dwarfs (right column). For DCs, pure hydrogen, pure helium and mixed solutions are shown (the best fit is indicated by the small arrow next to the legend). Note that the mixed H/He solution is only shown if it corresponds to a different solution than the pure hydrogen and pure helium solutions. The complete set of photometric fits (459 objects) is available in the online journal. (Voir aussi la Figure C.1 de l'Annexe C.)

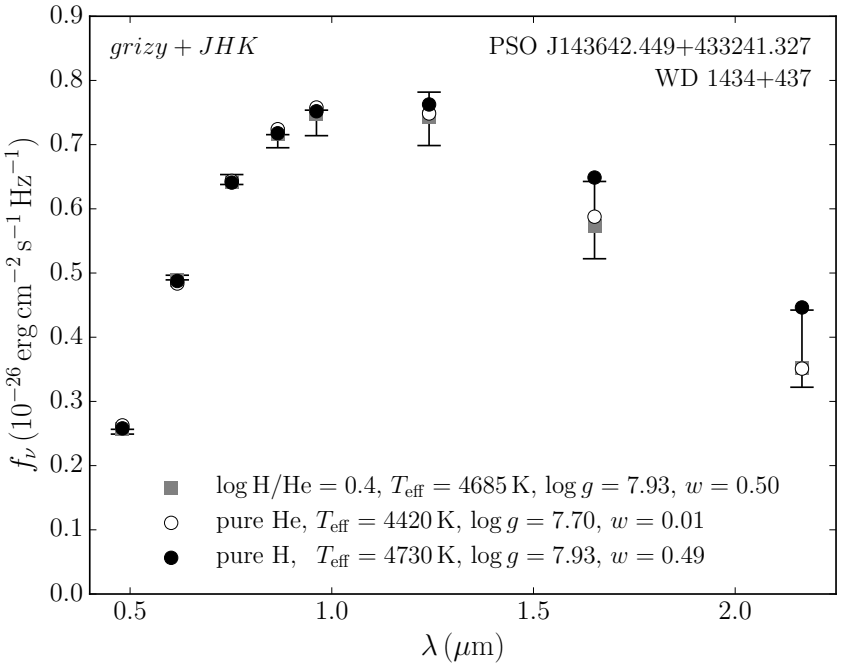

Figure 9.3 – Photometric fits to the DC white dwarf WD 1434+437. It is hard to tell the atmospheric composition of this object.

contradiction with the spectroscopic observations, which led Bergeron et al. (1997, 2001) to designate those stars as peculiar non-DAs. Furthermore, they interpreted these peculiar non-DAs as forming a distinct physical group and, because of their proximity to the blue edge of the non-DA gap, they speculated that they are objects whose atmospheres are about to become hydrogen-rich.

Our analysis also reveals the presence of 13 objects for which the pure hydrogen composition inferred from the photometry is incompatible with the absence of Hα (see Table 9.4).[9] Interestingly, out of the seven peculiar non-DAs in Bergeron et al. (1997, 2001) that are part of our sample, only two (PSO J091554.370+532508.067 and PSO J104153.917+141545.969) are found to have an SED that is better represented by a hydrogen-rich atmosphere. In principle, if peculiar non-DAs did form a physical group, we should find that objects identified as peculiar non-DAs by Bergeron et al. (1997, 2001) are also flagged as peculiar non-DAs in our analysis. These conflicting results could be due to the fact that we rely on different photometric systems. In particular, we note that

[9]Note that in all 13 cases the best mixed solution corresponds either to a pure hydrogen composition or to a mixed H/He composition that should give rise to a detectable Hα feature.

our 2MASS infrared photometry is of lesser quality than the JHK photometry used in Bergeron et al. (1997, 2001). To evaluate the impact of the photometric system, we performed photometric fits for the nine peculiar non-DAs identified in Bergeron et al. (1997, 2001) using their photometric data, but with our atmosphere model grid. We found that the photometric fits favor a pure hydrogen composition for five of those objects and a pure helium composition for the remaining four. Note that we reach the same conclusions if we use the trigonometric parallaxes reported in Bergeron et al. (1997, 2001) instead of the more accurate *Gaia* parallaxes.

PSO	MWDD object ID	$T_{\rm eff}$ (K)
J021148.605+711911.081	NLTT 7194	4790
J023759.111+163809.334	LP 410−67	5250
J095120.241+190009.463	WD 0948+192	5460
J084901.422+443934.262	2MASS J08490170+4439355	5810
J234612.394+115849.053	PM J23462+1158	5935
J081411.267+484526.630	WD 0810+489	6515
J142747.971+053230.563	WD 1425+057	6725
J141143.197+220644.803	WD 1409+223	6785
J104718.292+000717.423	WD 1044+003	6965
J104153.917+141545.969	V* CY Leo	7140
J105734.525−073122.157	LAWD 34	7155
J091554.370+532508.067	EGGR 250	7170
J122619.639+183634.295	WD 1223+188	7465

Table 9.4 – Peculiar non-DAs in our sample

The fact that the choice of the photometric system and small differences in model grids can tip the photometric solution to another atmospheric composition raises some doubt on the interpretation that peculiar non-DAs form a distinct physical group. Could the existence of those objects simply be explained by random errors in the observations? After all, the difference between a pure hydrogen and a pure helium solution is not always statistically significant (i.e., the Akaike weights can be close to each other), which inevitably leads to a number of misclassifications. Given the Akaike weights of our best solution for every DC with $T_{\rm eff} > 5000\,{\rm K}$ (that is, objects for which we should see Hα if they had

a hydrogen-rich atmosphere), we can actually compute how many peculiar non-DAs we expect due to the uncertainties of our photometric fits. For the 45 DCs in this temperature range, we find an average Akaike weight of 0.76 for the best solutions. This means that we expect that the composition inferred from the photometry will be incorrect for $(24\pm6)\%$ of those 45 DCs, which is perfectly consistent with our actual error rate in this temperature range of 27% (12 out of 45).[10]

While the number of peculiar non-DAs in our sample seems consistent with random errors, we note that Bergeron et al. (1997, 2001) identified systematic trends in the observed SEDs of peculiar non-DAs that supported the interpretation that they form a distinct physical group. In particular, they found that the pure helium models systematically fail to reproduce the observed B and I photometry by underestimating the B flux and overestimating the I flux. The four clearest examples of this behavior are given in Figure 17 of Bergeron et al. (1997) and Figure 11 of Bergeron et al. (2001). In Figure 9.4, we show our fits to those four objects. While we do observe that our pure helium models slightly underestimate the flux in the B band and overestimate the flux in the I band, the differences are smaller than $\approx 1\sigma$ (except for WD 2011+065) and might not be significant. Moreover, for WD 0000−345 and WD 1039+145, the Akaike weights of the pure helium solution are too high to confidently rule out this solution, and, in the case of WD 0423+120, we even find that the pure helium solution is a better fit to the data than the pure hydrogen solution.

As an additional test, we fitted the nine peculiar non-DAs of Bergeron et al. (1997, 2001)—all stars for which they found a better match to pure hydrogen than to pure helium models—using their observations and their atmosphere models. For the pure helium solutions, we find an average Akaike weight of 0.44, meaning that the quality of the pure hydrogen and pure helium solutions is very similar and that the chemical composition determination is quite uncertain. Moreover, for three of those objects, we actually find a smaller χ^2 (and a larger Akaike weight) for the pure helium solution than for the pure hydrogen solution, suggesting that they are not peculiar non-DAs after all.

Our analysis makes a strong case for a simple interpretation according to which the existence of peculiar non-DAs is the unavoidable consequence of the intrinsic uncertainty of

[10]For comparison, Bergeron et al. (2001) have a 33% error rate for DCs between 5000 K and 8300 K (i.e., the maximum surface temperature of stars included in our sample).

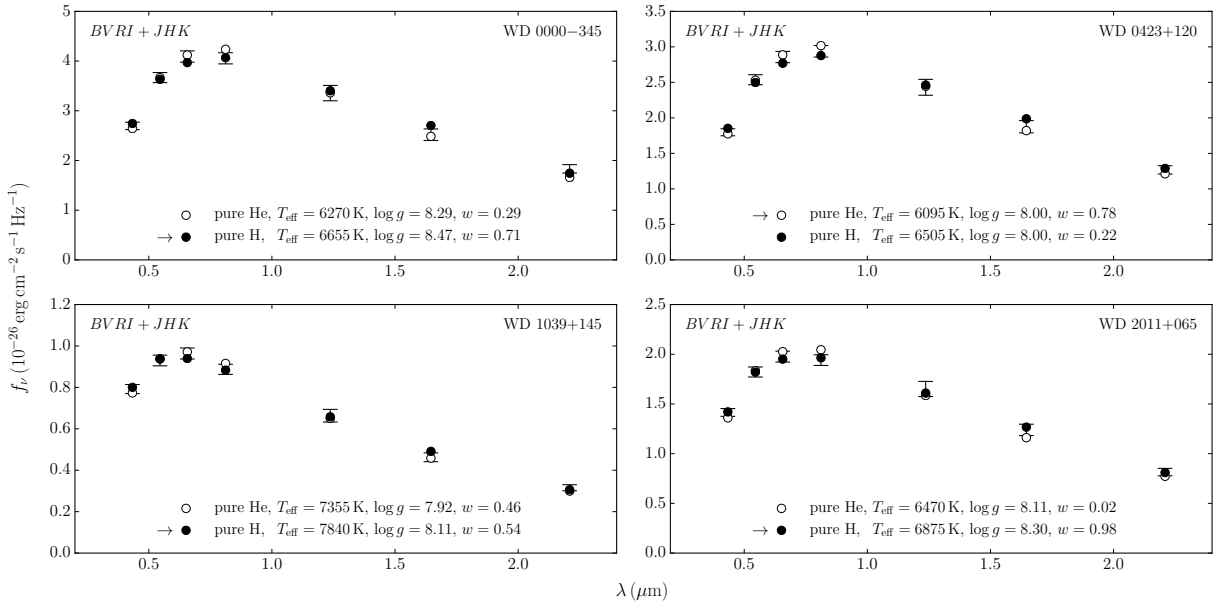

Figure 9.4 – Photometric fits to four peculiar non-DAs identified in Bergeron et al. (1997, 2001). These fits were obtained using their photometric data and trigonometric parallaxes (as they did not have any parallax measurement for WD 0423+120, we assumed $\log g = 8$ for this object).

the photometric technique. That being said, the fact that two objects—PSO J091554.370+532508.067 (WD 0912+536) and PSO J104153.917+141545.969 (WD 1039+145)—are flagged as peculiar non-DAs in both our analysis and the analysis of Bergeron et al. (1997, 2001) prevents us from ruling out the idea that *some* peculiar non-DAs are part of a distinct physical group. Given that the same conclusion is reached using both different models and different observations, it appears that those two objects are indeed peculiar. Interestingly, WD 0912+536 harbors a very strong magnetic field ($B \sim 100$ MG, Angel et al., 1972; Angel, 1978), possibly hinting to a connection between peculiar non-DAs and magnetism (however, no circular polarization was detected for WD 1039+145, Angel et al., 1981). In the same vein, we note that Bergeron et al. (1997) have suggested the existence of a relation between magnetic fields and the chemical evolution of cool white dwarfs.

9.4.1.2 Hydrogen traces in helium-rich DC white dwarfs

Based on a comprehensive analysis of white dwarfs discovered by the *Gaia* mission, Bergeron et al. (2019) recently claimed that pure helium white dwarfs below $T_{\rm eff} = 11\,000$ K are extremely rare. In a nutshell, additional electron donors (metals or hydrogen) have to

be included in the atmosphere models of helium-rich objects in order to obtain reasonable masses. Formally, only upper limits on the hydrogen abundance of DC stars can be determined. As the presence of hydrogen traces affects the atmospheric parameters obtained from a photometric fit, our inability to accurately measure the H/He abundance ratio of those objects implies that our $T_{\rm eff}$ and $\log g$ determinations are uncertain.

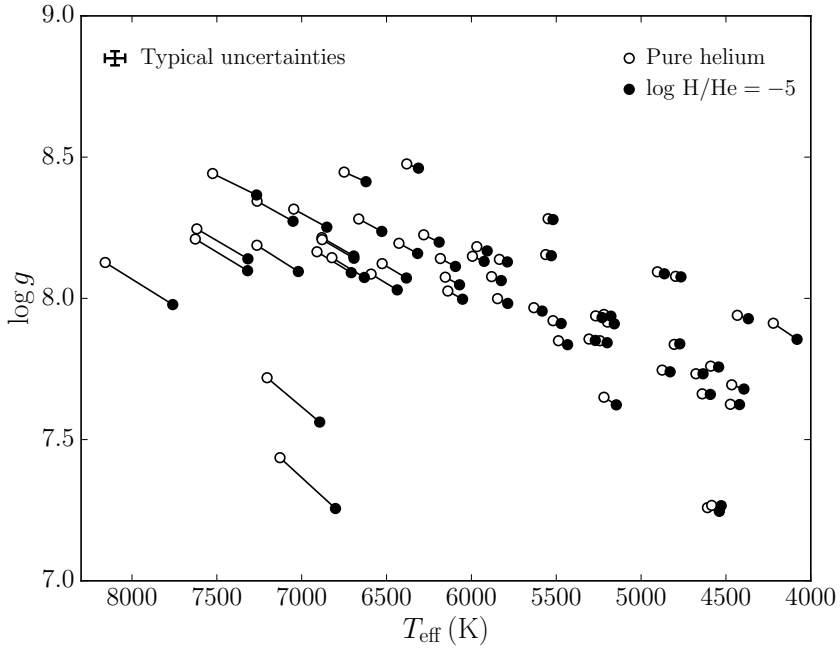

Figure 9.5 – Surface gravity of helium-rich DC white dwarfs in our sample as a function of their effective temperatures. The open circles correspond to our pure helium solutions and the filled circles represent the solutions found if log H/He = −5 is assumed. Typical uncertainties on $\log g$ and $T_{\rm eff}$ are shown in the top-left corner.

To see by how much $T_{\rm eff}$ and $\log g$ can be affected by trace amounts of hydrogen, we studied a subsample made up of all DC stars for which we found a pure helium composition. For each of those objects, we performed a second photometric fit assuming a hydrogen abundance of log H/He = −5. Note that this hydrogen abundance is too small to produce any detectable Hα feature or to give rise to significant H_2-He CIA. As shown in Figure 9.5, the addition of this trace amount of hydrogen has an important effect on $T_{\rm eff}$ and $\log g$, particularly at high temperatures. This implies significant uncertainties on the atmospheric parameters of helium-rich DC white dwarfs. By adding free electrons to the atmosphere, small amounts of hydrogen reduce the determined effective temperature (by 400 K at worst

and by 120 K on average) and the surface gravity (to keep the luminosity constant, the star has to be inflated to compensate the decrease of $T_{\rm eff}$). This behavior is analogous to the reduction of the photometric $T_{\rm eff}$ and $\log g$ following the addition of carbon—another electron donor—in DQ model atmospheres (see Figure 8 of Dufour et al., 2005). To account for this uncertainty, we shifted our helium-rich solutions for DC white dwarfs halfway between the pure helium and the log H/He = −5 solutions and we adjusted the uncertainties so that they now encompass both solutions. The $T_{\rm eff}$, $\log g$, M and $\tau_{\rm cool}$ values reported in Table 9.3 include these corrections.

9.4.2 DZs

Figure 9.6 shows examples of photometric and spectroscopic fits to three DZ white dwarfs that are part of our sample. The complete set of fits is available in the online journal, with the exception of LP 658−2, Ross 640, SDSS J080440.63+223948.6 and WD 2251−070 (PSO J055509.987−041037.276, PSO J162824.563+364623.925, PSO J080440.637+223945.828 and PSO J225355.149−064701.663), for which we directly use the values reported in Papers I and II and in Blouin et al. (2019a). As in Papers I, II and III, our models are in excellent agreement with the observations. Our solutions are consistent across all wavelengths and they properly reproduce the observed spectral lines. In particular, for the three examples shown in Figure 9.6, we obtain good fits to the resonance line of Ca I at 4226 Å and to the Ca II H & K doublet. This suggests that the pressure and temperature structure of our DZ models are accurate, since these profiles are sensitive to the physical conditions in the line-forming regions of the atmosphere (Allard & Alekseev, 2014).

9.4.3 DQs

In Figure 9.7, we show examples of photometric and spectroscopic fits to three DQs (the complete set of fits is available in the online journal). Clearly, our best solutions are in good agreement with the observations. Things get more complicated if we look at cooler carbon-polluted atmospheres. The cooling sequence of DQs stops at $T_{\rm eff} \approx 6000$ K (Dufour et al., 2005; Koester & Knist, 2006) to give way to DQpec white dwarfs. The spectra of those objects are vaguely similar to those of DQs : they show Swan-like absorption

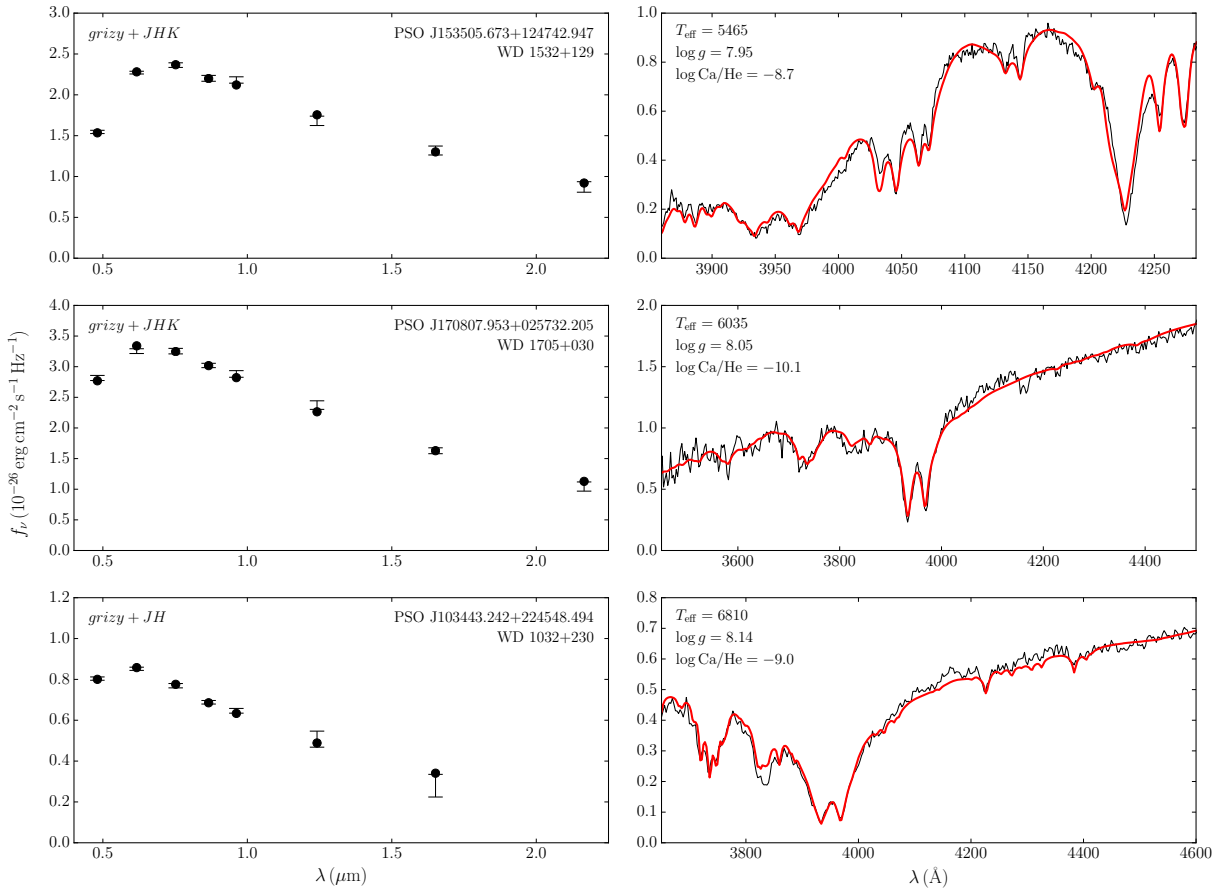

Figure 9.6 – Examples of photometric and spectroscopic fits for three DZ white dwarfs. Each row represents one object. For the spectroscopic fits, the observations are shown in black and the best fit is represented by the red spectrum. The complete set of fits (16 objects) is available in the online journal. (Voir aussi la Figure C.2 de l'Annexe C.)

bands that are blue-shifted by a few hundred angstroms (Bergeron et al., 1994; Schmidt et al., 1995; Hall & Maxwell, 2008). Using density functional theory (DFT) calculations, Kowalski (2010) has convincingly shown that the physical explanation for the DQ→DQpec transition is the pressure-driven distortion of the C_2 Swan bands. As a carbon-polluted white dwarf cools down, its atmosphere becomes denser. Near $T_{\rm eff} = 6000\,{\rm K}$, the helium density becomes high enough to affect the electronic levels of the C_2 molecule, which leads to an increase of the electronic transition energy T_e of the Swan bands. It is this increase that explains the shift of the C_2 Swan bands toward shorter wavelengths. According to the

ab initio calculations of Kowalski (2010), the shift of T_e is linear with respect to density,

$$\Delta T_e\,(\mathrm{eV}) \approx \alpha\,\rho\,(\mathrm{g\,cm^{-1}}), \tag{9.5}$$

with $\alpha = 1.6$. However, as pointed out by Kowalski (2010), such a shift overestimates the distortion of Swan bands in the spectra of DQpec white dwarfs. There are two ways to solve this problem : either we change the slope of Equation 9.5 or we find a way to decrease the photospheric density of DQpec models.

Kowalski (2010) proposed that the photospheric density of DQpec stars could be lowered if hydrogen is added to their atmospheres. In fact, in their analysis of LHS 290, they show a fit where they compensate for the strong $\Delta T_e = 1.6\rho$ shift by supposing an ad hoc log H/He $= -2.2$ hydrogen abundance. We are very skeptical that this is the correct way of reconciling the DFT calculations with the observations, since such a high amount of H would lead to the formation of a significant quantity of CH. We added the CH rovibrational bands to our code using the Kurucz line lists[11], which rely on data from Masseron et al. (2014). Figure 9.8 shows synthetic spectra computed for parameters very similar to those of LHS 290 ($T_{\mathrm{eff}} = 6000\,\mathrm{K}$ and log C/He $= -6.0$) and with different H/He abundance ratios. Clearly, a hydrogen abundance as low as log H/He $= -4.0$ is sufficient to produce an unmissable CH G band near 4300 Å and the log H/He $= -2.2$ value can be safely rejected. For the models of Figure 9.8, the pure helium and the log H/He $= -4.0$ models have photospheric densities of $0.20\,\mathrm{g\,cm^{-3}}$ and $0.16\,\mathrm{g\,cm^{-3}}$ (at $\tau_R = 2/3$), respectively. This slight reduction of the density is not sufficient to compensate for the too important shift implied by the $\alpha = 1.6$ parameter. Therefore, we conclude that adding ad hoc amounts of hydrogen in the atmospheres of DQpec stars is not the solution to the discrepancy between the DFT calculations and the observations.

9.4.3.1 Calibration of α

While we rejected the idea that an undetected amount of hydrogen could bring the density down to a level where the $\alpha = 1.6$ value is compatible with the observations, it is still possible that a missing piece of input physics in our models leads to an overestimation of the photospheric density in cool carbon-polluted white dwarfs. However, we believe that

[11] http://kurucz.harvard.edu

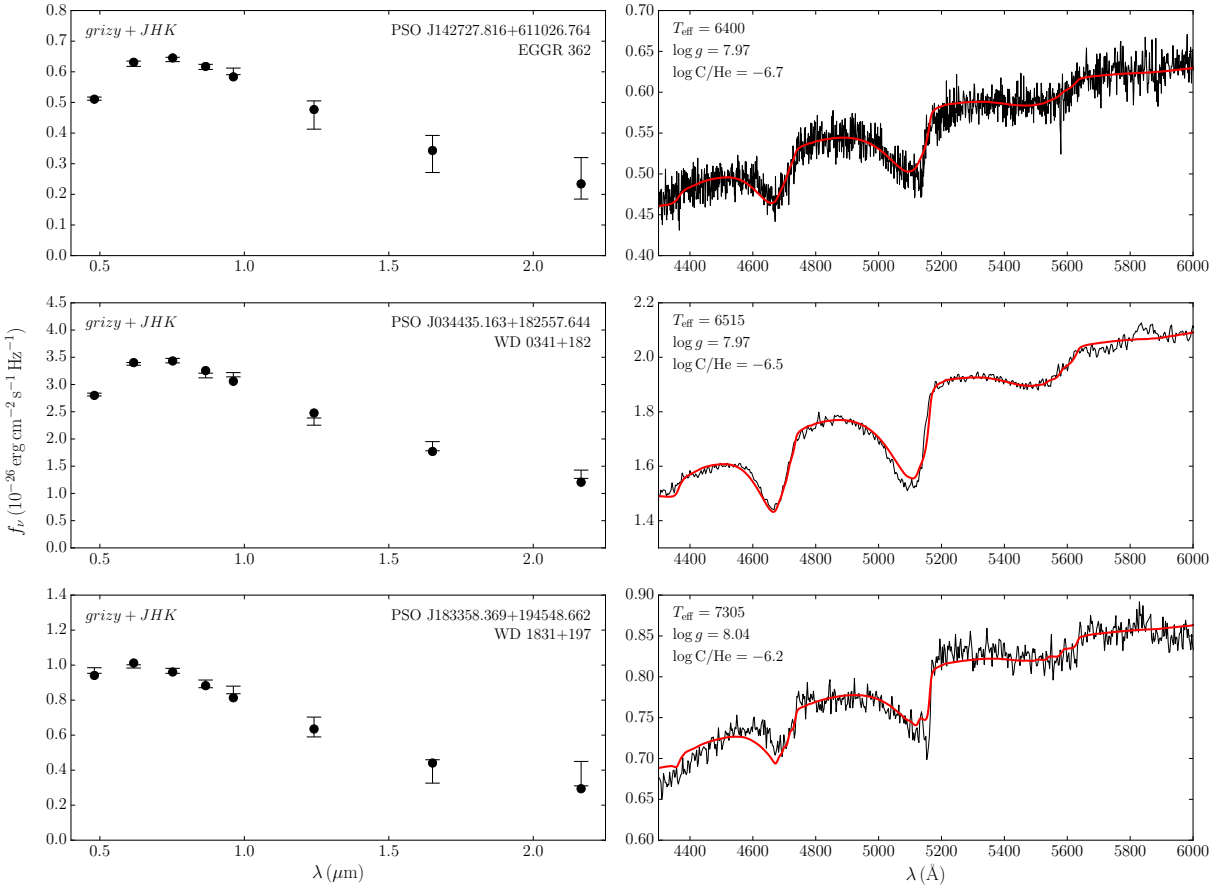

Figure 9.7 – Similar to Figure 9.6, but for DQ/DQpec white dwarfs. Note that a shift parameter of $\alpha = 0.2$ was assumed for the C_2 Swan bands (see Section 9.4.3.1). The complete set of fits (22 objects) is available in the online journal. (Voir aussi la Figure C.3 de l'Annexe C.)

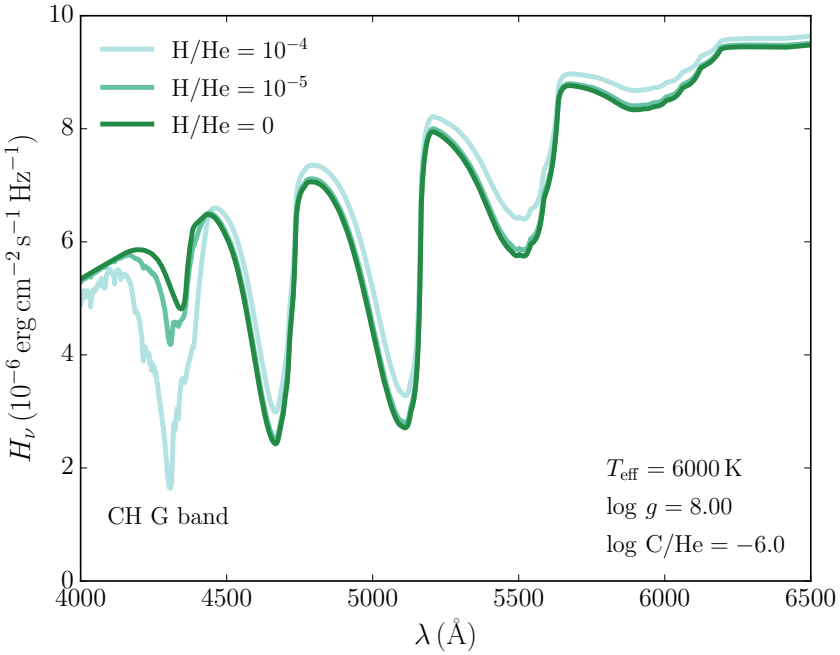

Figure 9.8 – Synthetic spectra computed with different H/He abundance ratios and for atmospheric parameters similar to those of LHS 290. Note that a shift parameter of $\alpha = 0.2$ was assumed for the C_2 Swan bands (see Section 9.4.3.1).

it is more likely that the current implementation of the shift of C_2 Swan bands is incorrect. In particular, we still use the standard Swan band spectrum, which we merely shift at every atmospheric layer with the ΔT_e value given by Equation 9.5. Until the absorption of C_2 in dense helium is modeled, which is a much more computationally intensive task than computing $\Delta T_e(\rho)$, this approximation will remain unjustified.

In the meantime, for the purpose of this paper, it is sufficient to resort to a more approximative way of fitting DQpec objects and we calibrate α using the observed spectra of distorted Swan bands. After testing several α parameters, we found that the value that leads—for most objects—to the best agreement between models and observations is $\alpha = 0.2$. This value is actually a compromise, since we found that no fixed α parameter could perfectly reproduce the distorted Swan bands of all DQpec white dwarfs. Nevertheless, as shown in Figure 9.9, the $\alpha = 0.2$ value allows a good fit to the Swan bands of carbon-polluted white dwarfs across a large temperature range. The most important disagreement is for WD 1008+290, where the bands could be more rounded. Note, however, that additional mechanisms might play a role, since WD 1008+290 has an intense

magnetic field ($B > 10\,\mathrm{MG}$, Schmidt et al., 1999) that could affect the position of the Swan bands (Liebert et al., 1978; Bues, 1991, 1999).

9.4.3.2 Problematic objects

In our analysis of DQ and DQpec objects, we encountered five cases for which a completely satisfying solution could not be found. Here, we detail the challenges posed by those objects and speculate about possible ways of resolving the discrepancies between models and observations.

GJ 1086 GJ 1086 (G 99−37) is one of the only two known white dwarfs to show a CH G band (the other one being BPM 27606). Using a hydrogen abundance of log H/He = −4.3, we are able to achieve a reasonable fit to the G band (Figure 9.10). However, our solution overestimates the distortion of the Swan bands (the C_2 bands of our fit are too rounded compared to the observations). This problem suggests that GJ 1086 contains more hydrogen than assumed, since adding hydrogen would reduce the distortion of the Swan bands by decreasing the photospheric density. However, the H/He ratio is already constrained by the strength of the CH G band, and thus we cannot find any solution that simultaneously fits all spectral features. One way to fix this problem would be to change the C_2 and/or CH dissociation equilibrium. After all, pressure effects are known to affect the H/H_2 ratio in dense hydrogen (Vorberger et al., 2007; Holst et al., 2008) and in dense helium-rich mediums (Kowalski, 2006b), so it is likely that something similar occurs with C_2 and CH in the dense atmospheres of cool carbon-polluted white dwarfs. If the nonideal effects on the dissociation equilibria are such that they reduce the CH/C_2 ratio, they could explain (at least in part) the discrepancy described above. Furthermore, it is also worth noting that GJ 1086 is a magnetic white dwarf (Angel & Landstreet, 1974), with $B \approx 7\,\mathrm{MG}$ (Berdyugina et al., 2007; Vornanen et al., 2010). As already stated, the impact of such strong fields on the opacities of carbon-polluted atmospheres remains unclear. Note also that convection might be suppressed (Tremblay et al., 2015; Gentile Fusillo et al., 2018), which would significantly affect the atmosphere structure.

WD 1235+422 WD 1235+422 is characterized by strong Swan bands that are very well represented by our models (Figure 9.10). However, our fit to the near-infrared photometry

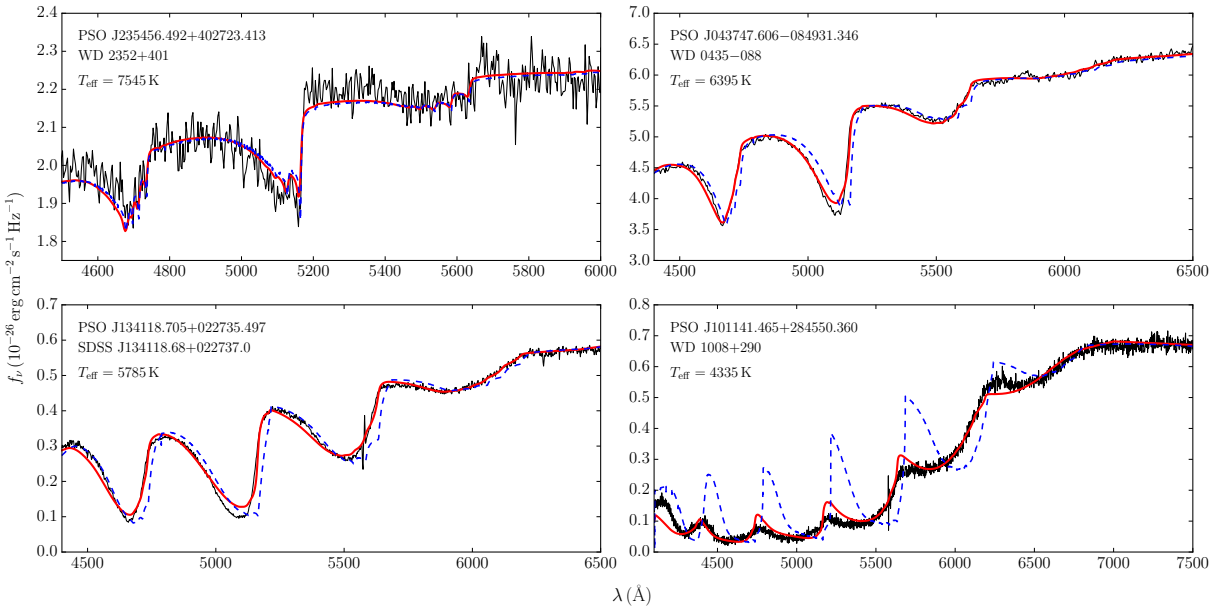

Figure 9.9 – Spectroscopic fits to the Swan bands of four DQ/DQpec stars. These four stars represent a sequence of decreasing temperature, which also corresponds to a sequence of increasing photospheric density and of increasing distortion of the Swan bands by high-pressure effects. The red spectra (solid lines) correspond to our best solutions assuming $\alpha = 0.2$ and the blue ones (dashed lines) correspond to the case where the Swan bands are not distorted by high-pressure effects (i.e., $\alpha = 0$). Note that the blue spectra were computed assuming the same atmospheric parameters as those found by fitting the observational data with a grid of $\alpha = 0.2$ models.

is less satisfying. While our overestimation of the flux in the J and H bands might be due to observational errors, it is also possible that we are missing an absorption source in the infrared. Given the effective temperature of WD 1235+422, H_2-He CIA cannot explain this flux depletion. In Section 9.4.3.3, we explore the possibility that the infrared flux depletion of WD 1235+422 is due to C_2-He CIA. It is also worth noting that WD 1235+422 is another magnetic white dwarf (Vornanen et al., 2013).

LHS 1126 Wickramasinghe et al. (1982) were the first to identify the strong near-infrared flux deficit that characterizes the SED of LHS 1126 (GJ 2012). Bergeron et al. (1994) and Giammichele et al. (2012) have explained this flux deficit as being due to H_2-He CIA (they find mixed H/He compositions of log H/He = 0.1 and −1.2, respectively). However, their solutions are not compatible with the ultraviolet observations of LHS 1126, since Wolff et al. (2002) found that Lyα is better reproduced with log H/He = −5.5. Ano-

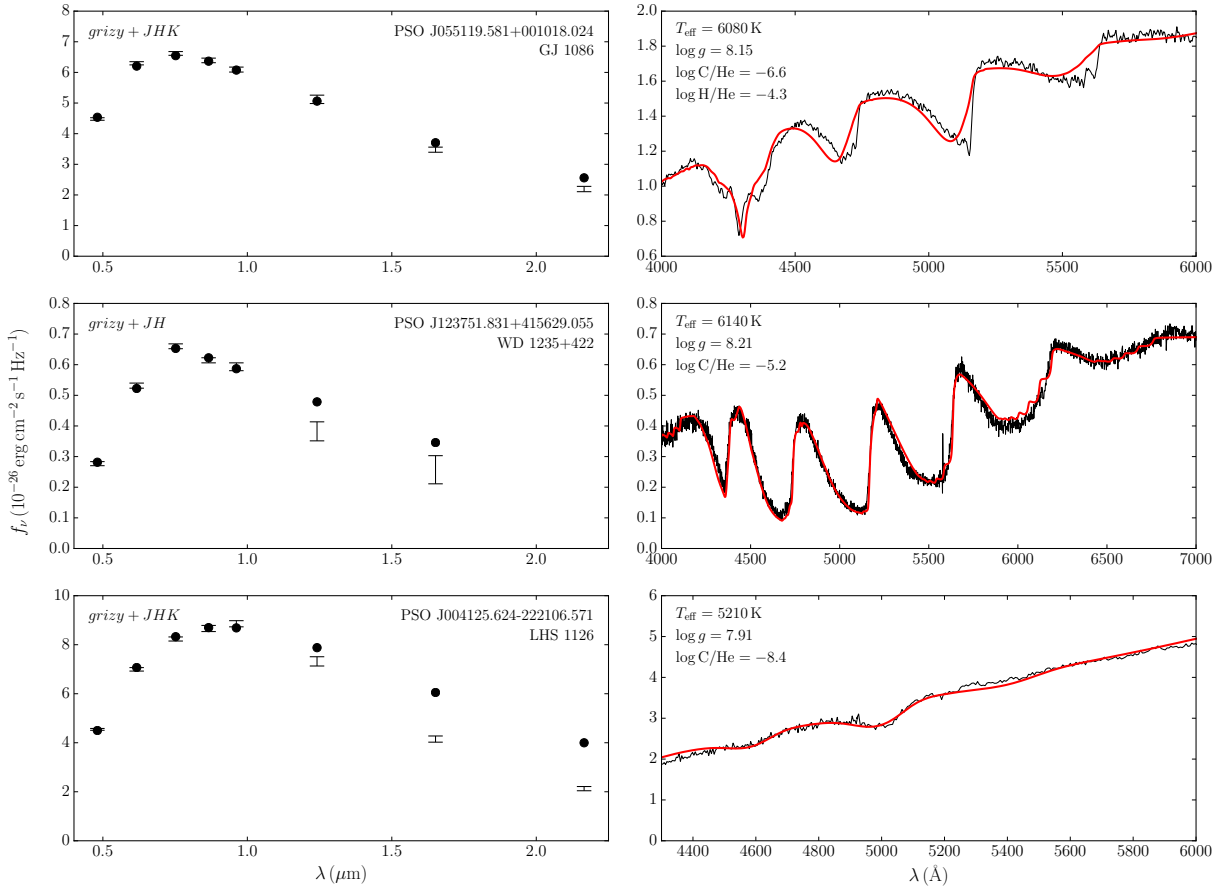

Figure 9.10 – Similar to Figure 9.7, but for three problematic carbon-polluted white dwarfs. Note that our fits of WD 1235+422 and LHS 1126 are based on hydrogen-free models (see text for details).

ther puzzling finding is that the near and mid-infrared energy distribution of LHS 1126 fits a Rayleigh–Jeans spectrum mimicking a $T_{\rm eff} > 10^5$ K blackbody (Kilic et al., 2006). As with GJ 1086 and WD 1235+422, we also have to worry about the usual suspect—magnetism—as spectropolarimetric measurements of LHS 1126 cannot rule out the presence of a $B < 3$ MG magnetic field (Schmidt et al., 1995).

As all previous analyses of LHS 1126, our fit is far from satisfactory. We interpreted the small depression at ≈ 5000 Å as being due to distorted Swan bands and, based on the depth of this feature, we concluded that log C/He = −8.4. Regarding our fit to the photometry, we find a hydrogen abundance of log H/He = −1.2 if we adjust the H/He ratio to the near-infrared photometry. As explained above, this solution must be rejected because of the Lyα analysis of Wolff et al. (2002). The origin of the infrared flux depletion remains

unknown and for this reason the solution displayed in Figure 9.10 was obtained assuming a hydrogen-free atmosphere and ignoring the JHK bands in our fit to the photometric data. Based on novel ab initio calculations, Kowalski (2014) proposed that He−He−He CIA might explain the infrared flux depletion of LHS 1126. This opacity source is included in our models, but fails to explain the SED of LHS 1126. As noted by Kowalski (2014), this failure may be due to our poor constraints on the ionization equilibrium of helium under high-pressure conditions (Fortov et al., 2003; Kowalski et al., 2007), which controls the photospheric density and therefore the intensity of He−He−He CIA. That being said, our sample contains many helium-rich objects that have denser photospheres than LHS 1126 (e.g., the 16 DC stars cooler than 5000 K for which we find a pure helium composition) and none of them shows a discrepancy similar to that observed here.

WD 1036−204 and WD 1008+290 These two objects —identified in Table 9.3 as PSO J103855.315−204049.761 and PSO J101141.465+284550.360—present a very similar problem. For both of them, our models were unable to properly match the photometric observations. In particular, we were forced to ignore the g and r bands in order to obtain an adequate fit to the other photometric bands. We do not know what explains this discrepancy, but we note that both objects have a very low effective temperature (4530 ± 215 K for WD 1036−204 and 4335 ± 165 K for WD 1008+290) and strong magnetic fields (Schmidt et al., 1999; Jordan & Friedrich, 2002) that might affect their structures and opacities.

9.4.3.3 C_2−He CIA

For some DQs in our sample, our fits to the infrared photometry are unsatisfactory (see for instance WD 1235+422 in Figure 9.10). A possible explanation for this mismatch is the omission of an important opacity source in our atmosphere models. Here, we investigate the possibility that C_2−He CIA affects the SED of cool carbon-polluted atmospheres. A priori, this hypothesis might seem unlikely since the peak of the C_2−He CIA spectrum is expected to be in the mid-infrared, beyond the JHK bandpasses considered here. In fact, the fundamental vibrational band of C_2 is located at $1855\,\mathrm{cm}^{-1}$ (Herzberg, 1950), which implies that absorption will be especially important near $5.4\,\mu$m. In contrast, H_2−He CIA,

which dominates the SED of the coolest mixed H/He white dwarfs (Bergeron & Leggett, 2002; Kilic et al., 2012; Gianninas et al., 2015), peaks near 2.3 μm where the fundamental vibrational band of H_2 is located. Nevertheless, it is possible that C_2 overtone bands, which are located at lower wavelengths, are important enough to affect the near-infrared SED of some cool DQpec stars.

To investigate this issue, we use the methodology presented in Blouin et al. (2017) for H_2-He CIA. More precisely, we use ab initio molecular dynamics (MD) to simulate the evolution of a C_2 molecule in a dense helium medium. In this framework, atoms move according to classical dynamics and DFT is used at each time step to compute the electronic charge density. As shown in Blouin et al. (2017), this methodology is accurate at both low and high densities, where many-body collisions become important.

The simulations were performed with the CPMD[12] plane-wave DFT code (Marx & Hutter, 2000; Hutter et al., 2008). The DFT calculations were carried out using the PBE exchange-correlation functional (Perdew et al., 1996) and ultrasoft pseudopotentials (Vanderbilt, 1990). Each simulation consisted of one C_2 molecule surrounded by 15, 31, or 63 He atoms in a cubic box whose length was adjusted to obtain the desired density. The density–temperature space was explored with 35 distinct simulations, ranging from $T = 4000$ to 8000 K and from $\rho = 0.08$ to 1.4 g cm^{-3}. For each simulation, we computed at every time step the dipole moment resulting from the total electronic charge density and the distribution of all nuclei (Silvestrelli et al., 1998; Berghold et al., 2000). At the end of the MD simulations, we obtained the absorption spectra $\alpha(\omega)$ using the Fourier transform of the dipole moment time autocorrelation function (Silvestrelli et al., 1997; Kowalski, 2014; Blouin et al., 2017).

We took precautions to make sure that the periodic boundary conditions of the simulation cell do not give rise to any artificial absorption features. To do so, we performed simulations with different box sizes while keeping the density constant by adjusting the number of helium atoms in each simulation. We found that absorption spectra obtained from MD simulations performed in a box of at least 10 au (5.3 Å) are virtually identical to those obtained from simulations performed in larger boxes. Therefore, finite-size effects are negligible as long as the simulation cell is at least 10 au large and all simulations presented

[12] http://cpmd.org

here satisfy this criterion. Note that we also verified that our simulations have converged with respect to the MD simulation time by comparing absorption spectra obtained for different trajectory lengths. We found that a 32 ps trajectory is usually sufficient to obtain a satisfactory convergence.

Figure 9.11 shows the results of our DFT-MD calculations for different densities representative of the photosphere of cool carbon-polluted white dwarfs. At low densities, the general shape of the C_2-He CIA spectrum is very similar to that of H_2-He CIA (for comparison, see Figure 3 of Abel et al., 2012), except that the rotational and vibrational bands are located at higher wavelengths. This is a direct consequence of the higher mass of the C_2 molecule. Also similar to H_2-He CIA is the evolution of the absorption spectrum with increasing density. In particular, the fundamental band becomes less and less important, while the rotational band becomes more prominent and shifts toward lower wavelengths (Blouin et al., 2017). For the purpose of this paper, the main result of our simulations is that the overtone bands of the C_2-He CIA are too weak to significantly affect the near-infrared flux of cool carbon-polluted white dwarfs. In fact, we implemented C_2-He CIA in our model atmosphere code—using analytical fits to our results—and we found that it only has an effect for cool ($T_{\rm eff} \leq 5000\,{\rm K}$), relatively carbon-rich ($\log {\rm C/He} \geq -5$) models and that this effect is limited to wavelengths beyond the K band.

9.5 The spectral evolution of cool white dwarfs

Now that we have determined the atmospheric composition of each of the 501 objects included in our sample (Table 9.3), we are ready to revisit the spectral evolution of cool white dwarfs. Before going to the results (Section 9.5.2), we discuss how we can account for selection biases in our sample (Section 9.5.1).

9.5.1 Correcting for biases

The quantity of interest for the study of the spectral evolution of white dwarfs is the fraction of stars that have a hydrogen-rich atmosphere in a volume-complete sample, $\rho_{\rm H}/\rho_{\rm tot} = \rho_{\rm H}/(\rho_{\rm H} + \rho_{\rm He})$.[13] Unfortunately, the sample considered in this paper is not volume-complete. We decided not to use a volume-complete sample as it would drastically

[13] In this work, an atmosphere with a H/He abundance ratio greater than 1 is considered hydrogen-rich.

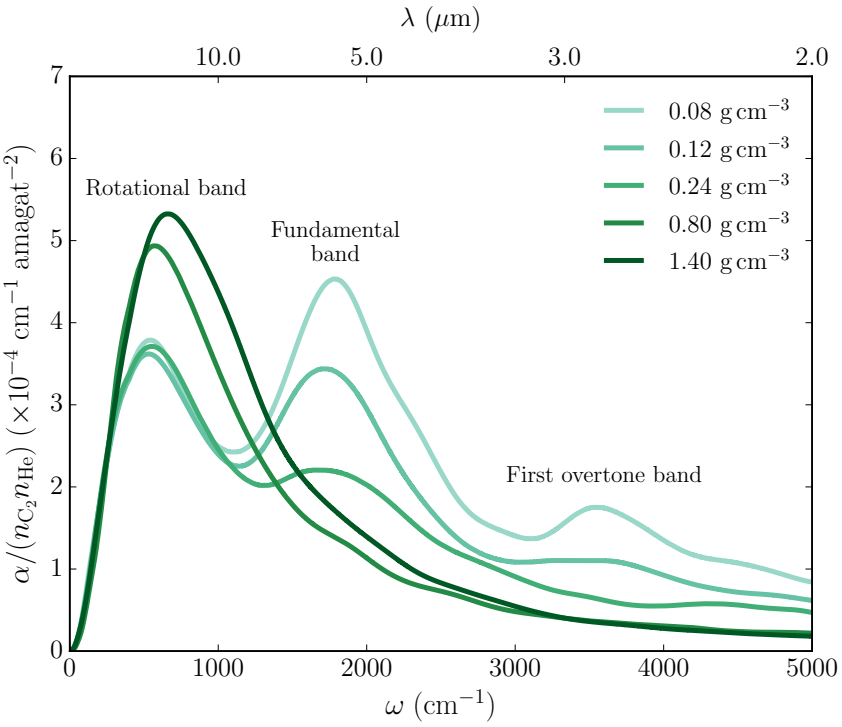

Figure 9.11 – C_2-He CIA spectra for different densities at $T = 4000\,K$. All spectra are divided by the number density of C_2 and He.

reduce the number of objects in our sample (the almost complete 20 pc sample contains 106 white dwarfs cooler than 8000 K, Hollands et al., 2018b) and significantly increase the statistical errors on ρ_H/ρ_{tot}.

Given the incompleteness of our sample, a correction must be applied to relate the number of white dwarfs in our sample (N_H^{sample} and N_{He}^{sample}) to the unbiased space density ratio. Remember that the four main selection criteria (Section 9.3.1) are that each star must have a parallax measurement from the *Gaia* DR2, *grizy* photometry from Pan-STARRS1, J photometry from 2MASS and a spectrum to allow an accurate spectral classification. By far, the two main limiting factors out of those four criteria are the need for J photometry from 2MASS and the need for spectroscopic observations. Below, we examine how each of these two criteria can induce a bias on $N_H^{sample}/N_{tot}^{sample}$ and how we can correct for those biases to obtain the unbiased space density ratio ρ_H/ρ_{tot}.

If we ignore for the moment the criterion on spectroscopic observations, our sample is effectively limited by the 2MASS J band, since Pan-STARRS and *Gaia* have much deeper

fields than 2MASS. Depending on the effective temperature, a hydrogen-rich white dwarf can be more or less luminous in the J band than a helium-rich object with the same effective temperature and surface gravity. This can induce a selection bias in favor of hydrogen-rich or helium-rich objects. To correct for this bias, we use the $V^{\max}$ correction (Schmidt, 1975), where $V^{\max}$ is the volume defined by the maximum distance at which a given object would still appear in our sample. More specifically, the quantity of interest is $V_{\rm H}^{\max}/V_{\rm He}^{\max}$, the ratio between the observed volume of hydrogen-rich objects and that of helium-rich objects. Using our model fluxes, we computed the ratio of the luminosities and, from there, we obtained $V_{\rm H}^{\max}/V_{\rm He}^{\max}$. The corresponding $V^{\max}$ ratios are given in Table 9.5. Note that we assumed $\log g = 8$ to compute $V_{\rm H}^{\max}/V_{\rm He}^{\max}$, which is justified by the very similar mass distributions of hydrogen-rich and helium-rich white dwarfs (Giammichele et al., 2012). The decrease of $V_{\rm H}^{\max}/V_{\rm He}^{\max}$ at low temperatures is a direct consequence of the onset of CIA, which significantly enhances the opacity in the J band for hydrogen-rich objects. With the data of Table 9.5, we can relate the number of hydrogen-rich and helium-rich white dwarfs in our sample to the space density ratio,

$$\frac{\rho_{\rm H}}{\rho_{\rm H}+\rho_{\rm He}} = \left(1+\frac{N_{\rm He}^{\rm sample}V_{\rm H}^{\max}}{N_{\rm H}^{\rm sample}V_{\rm He}^{\max}}\right)^{-1}. \tag{9.6}$$

Let us now turn to the bias induced by the requirement of having spectroscopic observations for every object in our sample. An appreciable fraction of our spectra (158 out of 501) are from the Sloan Digital Sky Survey (SDSS), which is plagued by numerous selection effects. The SDSS consists of first imaging the sky in five bandpasses and then using this photometry to select targets that deserve spectroscopic observations. This target selection process is based on many different selection criteria that overlap with one another (Harris et al., 2003; Eisenstein et al., 2006b). Hence, modeling the selection biases induced by the SDSS is an intractable task.

Fortunately, we do not need to worry about these selection effects for objects cooler than 6000 K, since for the vast majority of those cool objects we rely on spectroscopic observations from other sources (Figure 9.12).[14] However, above 6000 K, SDSS objects are

[14]For the most part, objects that are not in the SDSS are from the Limoges et al. (2015) sample. White dwarfs in that sample were selected from reduced proper motion diagrams (Limoges et al., 2013) and are therefore not subject to biases in favor of hydrogen-rich or helium-rich objects.

$T_{\rm eff}$ (K)	$V_{\rm H}^{\rm max}/V_{\rm He}^{\rm max}$
8500	1.15
8000	1.16
7500	1.17
7000	1.19
6500	1.21
6000	1.23
5500	1.22
5000	1.20
4750	1.18
4500	1.15
4250	1.09
4000	1.01
3750	0.82

Table 9.5 – $V^{\rm max}$ correction for the ratio of hydrogen-rich to helium-rich objects

much more abundant and we might be at the mercy of SDSS selection effects. To evaluate the severity of those selection effects, we computed the fraction of hydrogen-rich stars for objects of our sample that were spectroscopically observed by the SDSS and for those that were not. We found absolutely no difference for the 6000−8000 K temperature range as a whole (0.80 ± 0.04 for the SDSS objects and 0.82 ± 0.03 for the rest).[15] However, there are differences if we look at smaller temperature bins. For the 7000−8000 K bin, we found hydrogen-rich fractions of 0.91 ± 0.04 for the SDSS objects and 0.84 ± 0.05 for the rest, and, for the 6000−7000 K bin, we found 0.68 ± 0.06 and 0.80 ± 0.04. Strictly speaking, these differences between SDSS and non-SDSS objects are not statistically significant. The probability that, given the finite size of our samples, the fraction of hydrogen-rich objects is the same for stars observed by the SDSS and for those not observed by the SDSS (i.e., the p-value) is 0.26 for the 7000−8000 K bin and 0.11 for the 6000−7000 K bin. Nevertheless, it is worth keeping in mind that the SDSS might induce a small bias in favor of hydrogen-rich

[15]The uncertainties are due to the finite size of the samples and are estimated as $\sigma_f = \sqrt{f(1-f)/N}$, where N is the sample size and f is the fraction of objects that are hydrogen-rich. Note that $f \pm \sigma_f$ corresponds to a 68% confidence interval.

objects between 7000 and 8000 K and a small bias in favor of helium-rich objects between 6000 and 7000 K

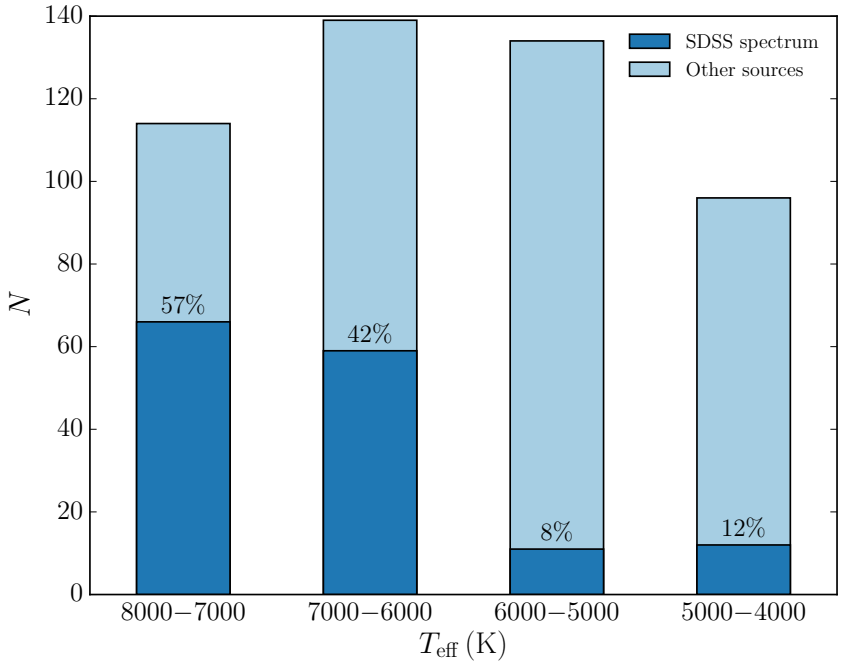

Figure 9.12 – The total length of each bar indicates the number of objects in our sample that fall in each effective temperature bin. The dark blue portion of each bar represents the fraction of those objects that were spectroscopically observed in the SDSS.

9.5.2 Results and discussion

Figure 9.13 shows the evolution of the $\rho_{\rm H}/\rho_{\rm tot}$ ratio as a function of decreasing effective temperature and compares our results to those of previous studies. Down to $T_{\rm eff} = 5000$ K, our results are in good agreement with previous studies—particularly with Limoges et al. (2015), whose results were based on a bigger sample than the six other studies shown in Figure 9.13. It is only below 5000 K that our results stand out from the rest. For the 4000−5000 K temperature bin, we find $\rho_{\rm H}/\rho_{\rm tot} = 0.69 \pm 0.05$, while other studies found either a much lower (≈ 0.4, Bergeron et al., 1997, 2001; Kilic et al., 2010b) or a much higher fraction ($\gtrsim 0.95$, Kowalski, 2006a; Kilic et al., 2009a; Limoges et al., 2015).

Two factors contribute to this difference. On the one hand, contrarily to Kowalski (2006a) and Kilic et al. (2009a,b), our sample includes metal-polluted white dwarfs. As

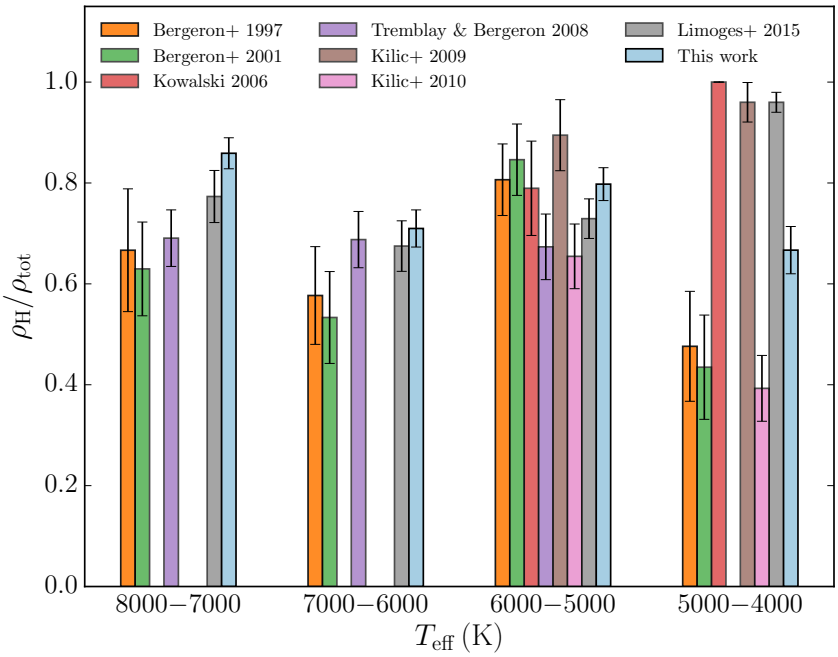

Figure 9.13 – Fraction of hydrogen-rich white dwarfs as a function of effective temperature for 1000 K bins. Different colors represent data taken from different studies (see legend). The error bars indicate the 1σ uncertainty associated with the finite number of objects in each bin. Note that the results of our sample were corrected using Equation 9.6 and the data of Table 9.5.

those objects are all helium-rich in the 4000−5000 K temperature bin, they contribute to give rise to a lower $\rho_{\rm H}/\rho_{\rm tot}$ ratio. On the other hand, our models (Paper I) include the nonideal input physics (in particular the improved Lyα opacities, Kowalski & Saumon, 2006) that led Kowalski (2006a), Kilic et al. (2009a,b) and Limoges et al. (2015) to conclude that the vast majority of cool DC white dwarfs are hydrogen-rich. This factor explains why we find a higher $\rho_{\rm H}/\rho_{\rm tot}$ ratio than Bergeron et al. (1997, 2001) and Kilic et al. (2010b), who did not include such high-density nonideal effects in their atmosphere models. Note, however, that our conclusions are less extreme than Kowalski (2006a), as we find that the SEDs of $\approx 25\%$ of DC white dwarfs cooler than 5000 K are better fitted with helium-rich models (Section 9.4.1). This is the expected result. We know many DZ white dwarfs cooler than $T_{\rm eff} = 5000$ K that must have a helium-rich atmosphere in order to explain their broad spectral lines (for examples, see Dufour et al. 2007, Hollands et al. 2017 and Paper III). As the pollution of a white dwarf by rocky debris is independent from the evolution of

the white dwarf itself, a significant number of nonpolluted counterparts (i.e., helium-rich DCs) must exist.

From Figure 9.13, the fraction of hydrogen-rich stars seems almost consistent with an evolution at a fixed $\rho_{\rm H}/\rho_{\rm tot}$ ratio. However, the picture looks quite different if we use smaller temperature bins. Figure 9.14 shows the same plot as Figure 9.13, but, this time, 500 K temperature bins were used. To make sure that no feature is missed by our arbitrary binning choice, we also added a continuous $\rho_{\rm H}/\rho_{\rm tot}$ vs $T_{\rm eff}$ curve to Figure 9.14 (in gray). This continuous curve was obtained by computing $\rho_{\rm H}/\rho_{\rm tot}$ within a 500 K moving bin, which eliminates the arbitrariness of the choice of the bin boundaries. Note also that the weight of each star in the calculation of $\rho_{\rm H}/\rho_{\rm tot}$ was computed using a Gaussian with a standard deviation given by the uncertainty on $T_{\rm eff}$.

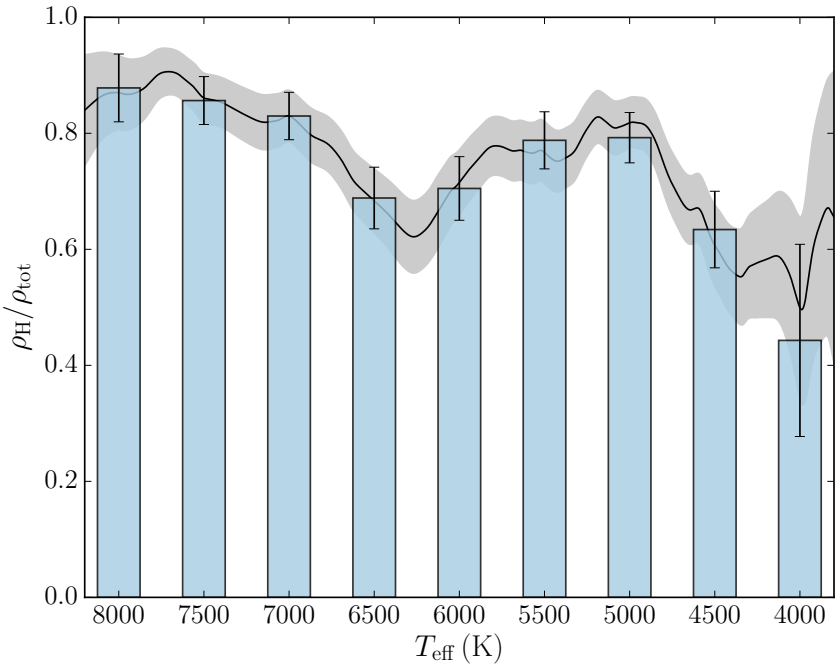

Figure 9.14 – Fraction of hydrogen-rich white dwarfs as a function of effective temperature for fixed 500 K bins (in blue) and for a 500 K moving bin (in gray, see text for details). As in Figure 9.13, the error bars indicate the 1σ uncertainty associated with the finite number of objects in each bin and the correction given by Equation 9.6 was applied.

Figure 9.14 reveals a much more complex picture than Figure 9.13. The hydrogen-rich fraction decreases from $T_{\rm eff} \approx 7500$ K until $T_{\rm eff} \approx 6250$ K, then increases until $T_{\rm eff} \approx 5000$ K, and decreases again below 5000 K. To confirm that these fluctuations of $\rho_{\rm H}/\rho_{\rm tot}$ are sta-

tistically significant, we compared the effective temperature distributions of hydrogen-rich and helium-rich stars in our sample (Figure 9.15). An Anderson–Darling test shows that hydrogen-rich and helium-rich white dwarfs do not follow the same temperature distribution, as the probability that both temperature distributions belong to the same population is 0.002.[16] Moreover, note that these conclusions remain unchanged if we take into account the $V_{\rm H}^{\rm max}/V_{\rm He}^{\rm max}$ corrections given in Table 9.5. If we randomly add or remove hydrogen-rich stars in each temperature bin (where the number of additions or withdrawals is determined by the $V_{\rm H}^{\rm max}/V_{\rm He}^{\rm max}$ ratio), we find that the probability that both the hydrogen-rich and helium-rich temperature distributions come from the same distribution is ≈ 0.004. Therefore, it is highly unlikely that the large increases and decreases of $\rho_{\rm H}/\rho_{\rm tot}$ with respect to $T_{\rm eff}$ (Figure 9.14) are due to random fluctuations associated with small number statistics.

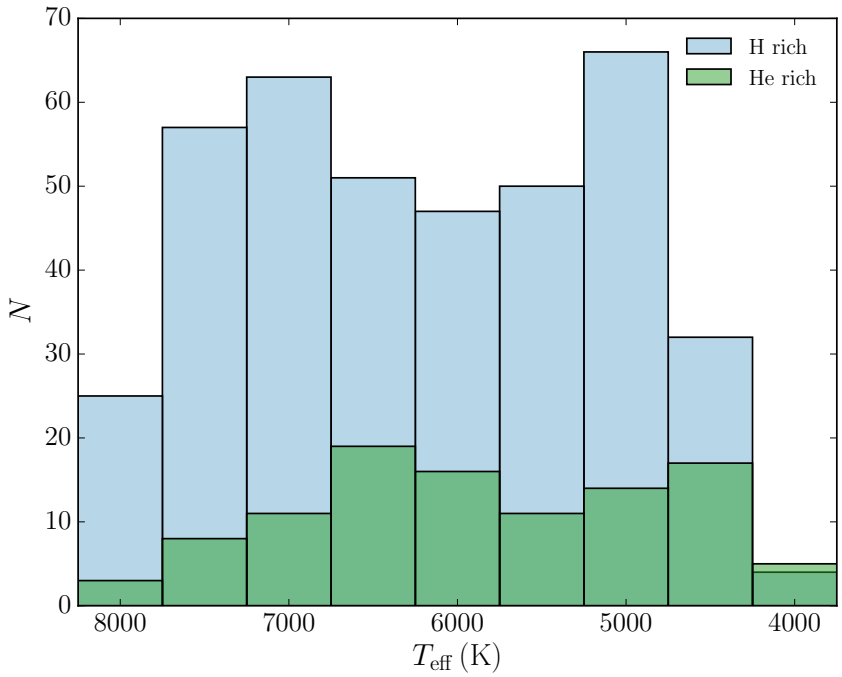

Figure 9.15 – Effective temperature distribution of hydrogen-rich and helium-rich stars in our sample. An Anderson–Darling test shows that the probability that both distributions belong to the same parent population is 0.002.

[16]The corresponding probability given by the more usual Kolmogorov–Smirnov test is significantly higher (0.013). However, the Anderson–Darling test is more appropriate, since it is more sensitive than the Kolmogorov–Smirnov test when the differences between both distributions are more important near their extremities (Feigelson & Babu, 2012), which is precisely the case here.

9.5.2.1 Behavior above 5000 K

As explained above, SDSS selection effects could lead to a bias in favor of hydrogen-rich objects between 7000 K and 8000 K and a bias in favor of helium-rich objects between 6000 K and 7000 K (Section 9.5.1). To check if the decrease of $\rho_{\rm H}/\rho_{\rm tot}$ between 7500 K and 6250 K is solely due to this bias, we compare the evolution of the hydrogen-rich fraction obtained using all stars in our sample to that obtained from a subsample that excludes all SDSS objects (Figure 9.16). Although both samples have different behaviors at high temperatures, they both show a clear decrease of $\rho_{\rm H}/\rho_{\rm tot}$ between 7000 K and 6250 K, suggesting that this feature is not due to SDSS biases.

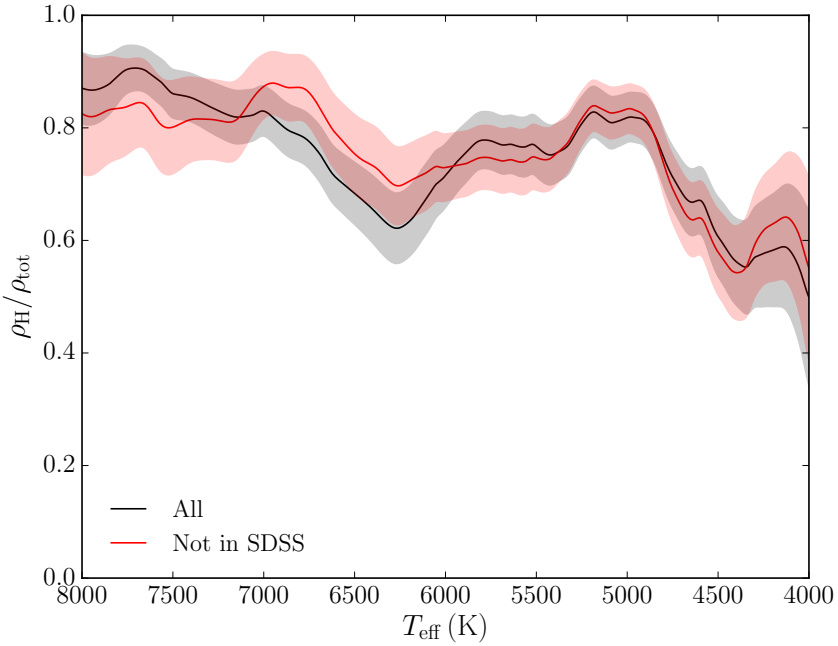

Figure 9.16 – Fraction of hydrogen-rich white dwarfs as a function of effective temperature for a 500 K moving bin. The results obtained using our whole sample are shown in gray and those obtained by excluding SDSS objects are show in red.

Another potential problem with our analysis of $\rho_{\rm H}/\rho_{\rm tot}$ is that it includes several objects with a very low mass (Figure 9.17). Since it is impossible for a star with a mass below $\approx 0.45\,M_{\odot}$ to become a white dwarf through single-star evolution within the age of the Universe, those objects are likely part of binary systems (Liebert et al., 2005; Rebassa-Mansergas et al., 2011). Figure 9.18 compares the hydrogen-rich fractions that we find if we include and if we exclude those low-mass objects. Clearly, the evolution of $\rho_{\rm H}/\rho_{\rm tot}$

above 5000 K is the same for both samples, so the contamination of our sample by binary systems cannot explain the decrease of $\rho_{\rm H}/\rho_{\rm tot}$ in the 7500−6250 K range and the increase in the 6250−5000 K range.

Another way to look at the evolution of the hydrogen-rich fraction is to look at $\rho_{\rm H}/\rho_{\rm tot}$ as a function of the cooling age (Figure 9.19). While the horizontal axis is distorted compared to Figure 9.14, the decrease of $\rho_{\rm H}/\rho_{\rm tot}$ before 6250 K and the increase down to 5000 K are still clearly visible.[17] This shows that the trends observed in the $\rho_{\rm H}/\rho_{\rm tot}$ vs $T_{\rm eff}$ plot (Figure 9.14) are representative of the temporal evolution of cool white dwarfs.

All things considered, the decrease of the hydrogen-rich fraction from $T_{\rm eff} \approx 7500$ K to $T_{\rm eff} \approx 6250$ K and the subsequent increase down to $T_{\rm eff} \approx 5000$ K appear to be real. The decrease of $\rho_{\rm H}/\rho_{\rm tot}$ is consistent with what we expect from convective mixing. The deepening of the convection zone with decreasing effective temperature mixes the superficial hydrogen layer with the more massive helium layer underneath, which can turn DAs into non-DAs (Tassoul et al., 1990; Bergeron et al., 1997; Rolland et al., 2018). However, the increase of $\rho_{\rm H}/\rho_{\rm tot}$ in the 6250−5000 K range is much more intriguing. This increase is similar to that observed at the blue edge of the non-DA gap (Bergeron et al., 1997, 2001), albeit located at slightly lower temperatures. No satisfactory physical explanation for this increase can be found in the literature (Hansen, 1999; Malo et al., 1999; Bergeron et al., 2001) and we do not have any new scenario to propose.

9.5.2.2 Behavior below 5000 K

Let us now examine the decrease of $\rho_{\rm H}/\rho_{\rm tot}$ below 5000 K. The first thing to note is that this feature cannot be affected by SDSS selection biases, since there are very few SDSS objects with $T_{\rm eff} < 5000$ K in our sample (see Figures 9.12 and 9.16). Secondly, we note that the decrease of the hydrogen-rich fraction becomes less obvious if we eliminate the low-mass objects from our sample. For the blue curve of Figure 9.18, the decline of $\rho_{\rm H}/\rho_{\rm tot}$ between 5000 K and 4000 K is barely significant. Thirdly, no significant counterpart for the decrease below 5000 K in the $\rho_{\rm H}/\rho_{\rm tot}$ vs $T_{\rm eff}$ figure is visible if we plot $\rho_{\rm H}/\rho_{\rm tot}$ as a function of the cooling age (Figure 9.19). Therefore, it is not clear that the decrease of $\rho_{\rm H}/\rho_{\rm tot}$ below 5000 K reflects the temporal evolution of cool white dwarfs. Instead, the

[17] A hydrogen-rich white dwarf with $\log g = 8$ has a cooling age of 2.0 Gyr when $T_{\rm eff} = 6250$ K and of 5.7 Gyr when $T_{\rm eff} = 5000$ K (Fontaine et al., 2001).

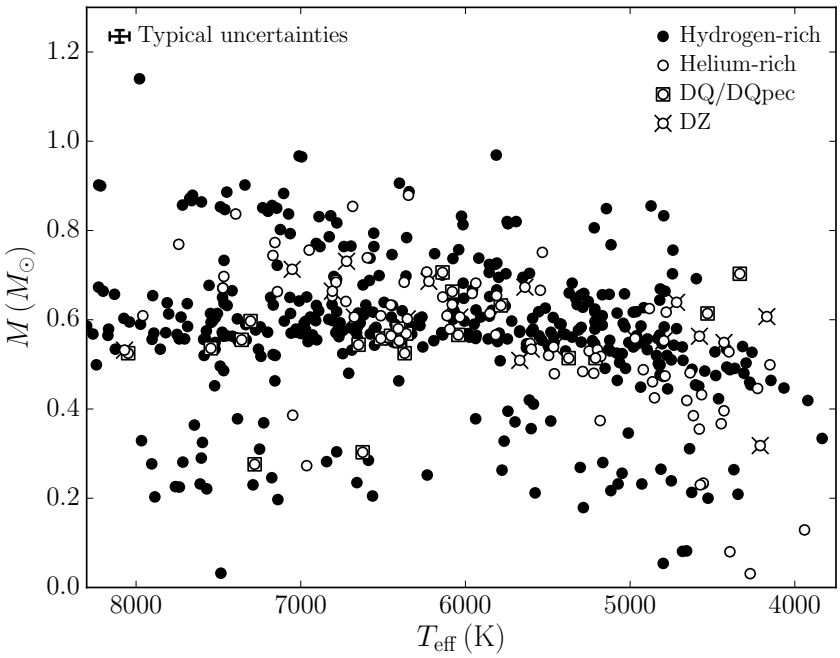

Figure 9.17 – Mass of white dwarfs in our sample as a function of their effective temperatures. Typical uncertainties on M and $T_{\rm eff}$ are shown in the top-left corner.

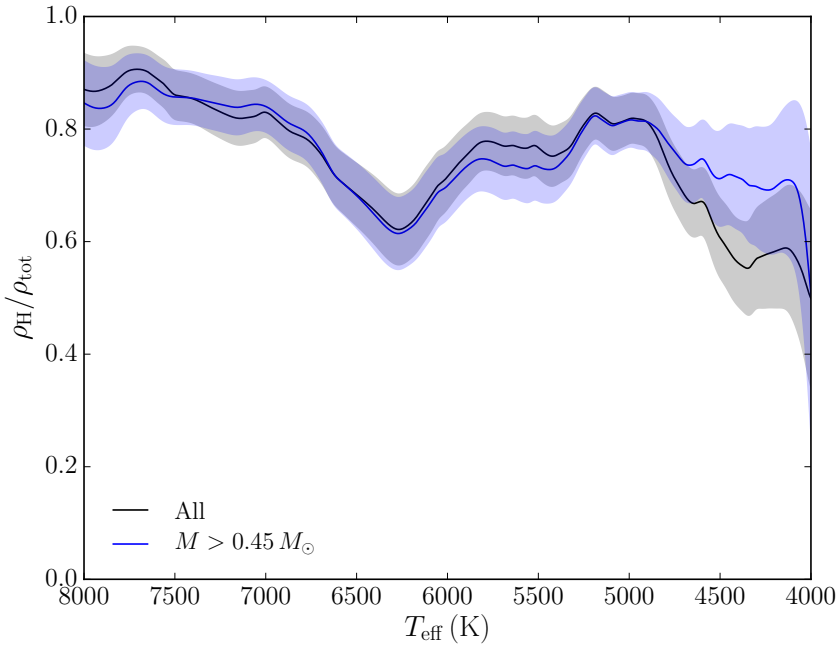

Figure 9.18 – Fraction of hydrogen-rich white dwarfs as a function of effective temperature for a 500 K moving bin. The results obtained using our whole sample are shown in gray and those obtained by excluding objects with $M \leq 0.45\,M_\odot$ are shown in blue.

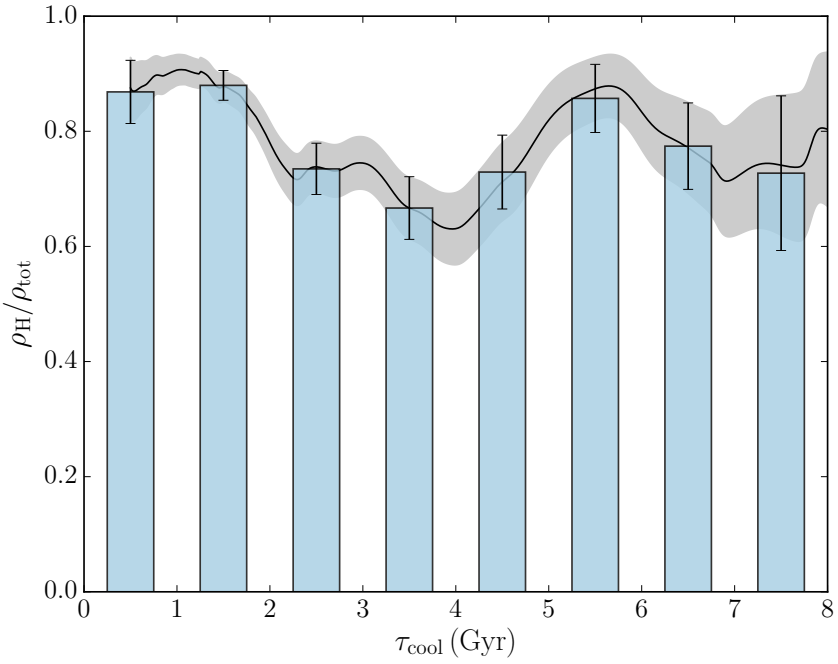

Figure 9.19 – Fraction of hydrogen-rich white dwarfs as a function of cooling age for a 1 Gyr moving bin (in gray) and for fixed 1 Gyr bins (in blue).

finding that helium-rich white dwarfs become more abundant below 5000 K may simply reflect the fact that they cool down faster than their hydrogen-rich counterparts.

In any case, our results rule out the possibility that cool white dwarfs all become hydrogen-rich as a result of hydrogen accretion from the interstellar medium. This scenario was already challenged by the fact that the accretion rate required for this conversion ($\approx 6 \times 10^{-17}\,M_{\odot}\,{\rm yr}^{-1}$, Kowalski, 2006a) is incompatible with the limits on the accretion rates of cool helium-rich DA/DZA white dwarfs (10^{-20} to $10^{-17}\,M_{\odot}\,{\rm yr}^{-1}$, Dufour et al., 2007; Rolland et al., 2018).

9.6 Conclusion

A detailed photometric and spectroscopic analysis of a homogeneous sample of 501 cool white dwarfs was presented. Our analysis was based on a state-of-the-art model atmosphere code that includes all of the nonideal input physics required to accurately model the dense atmospheres of cool white dwarfs. As our models are the first to successfully model the most challenging cool DZ white dwarfs (Paper I, II and III) and as our analysis makes use

of the largest homogeneous sample of cool white dwarfs studied to date, our results are on firmer grounds than previous attempts at constraining the spectral evolution of cool white dwarfs.

A satisfactory fit was found for all 501 white dwarfs studied in this work, except for a handful of carbon-polluted objects. We explored a few avenues to improve our fits to those stars, such as empirically adjusting the pressure shift of the distorted Swan bands and computing the absorption resulting from C_2-He collisions. We also revisited a peculiar class of DC stars (known as peculiar non-DAs) for which spectroscopic and photometric observations suggest conflicting chemical compositions. We reported evidence that is at odds with the interpretation according to which those objects form a real physical group.

We found that hydrogen-rich white dwarfs become less abundant when the effective temperature decreases from 7500 K to 6250 K, which is likely explained by convective mixing. From 6250 K to 5000 K, the trend is reversed and the fraction of white dwarfs with a hydrogen-rich atmosphere increases. So far, no physical scenario is available to explain this observation. Finally, at lower temperatures, we find that hydrogen-rich white dwarfs become rarer from 5000 K to 4000 K. This trend invalidates the scenario according to which accretion of hydrogen from the interstellar medium dominates the spectral evolution of cool white dwarfs.

Acknowledgments We wish to thank Pierre Bergeron for many enlightening discussions on the spectral evolution of white dwarfs. We are grateful to Mukremin Kilic for sharing with us his spectrum of SDSS J134118.68+022737.0. We also thank Adela Kawka and Stephane Vennes for allowing us to use their VLT/FORS2 spectra of NLTT 8733, NLTT 14553 and NLTT 57760.

This work was supported in part by the NSERC (Canada) and the Fund FRQNT (Québec). This work has made use of the Montreal White Dwarf Database (Dufour et al., 2017).

This work has made use of data from the European Space Agency (ESA) mission *Gaia* (https://www.cosmos.esa.int/gaia), processed by the *Gaia* Data Processing and Analysis Consortium (DPAC, https://www.cosmos.esa.int/web/gaia/dpac/consortium). Funding for the DPAC has been provided by national institutions, in particular the institutions participating in the *Gaia* Multilateral Agreement.

The Pan-STARRS1 Surveys (PS1) and the PS1 public science archive have been made possible through contributions by the Institute for Astronomy, the University of Hawaii, the Pan-STARRS Project Office, the Max-Planck Society and its participating institutes, the Max Planck Institute for Astronomy, Heidelberg and the Max Planck Institute for Extraterrestrial Physics, Garching, The Johns Hopkins University, Durham University, the University of Edinburgh, the Queen's University Belfast, the Harvard-Smithsonian Center for Astrophysics, the Las Cumbres Observatory Global Telescope Network Incorporated, the National Central University of Taiwan, the Space Telescope Science Institute, the National Aeronautics and Space Administration under Grant No. NNX08AR22G issued through the Planetary Science Division of the NASA Science Mission Directorate, the National Science Foundation Grant No. AST-1238877, the University of Maryland, Eotvos Lorand University (ELTE), the Los Alamos National Laboratory, and the Gordon and Betty Moore Foundation.

CHAPITRE 10

Conclusions

Dans cette thèse, une nouvelle génération de modèles d'atmosphère d'étoiles naines blanches froides a été développée. Ces nouveaux modèles comblent les lacunes qui freinaient jusqu'ici leur application aux plus vieilles naines blanches de notre Galaxie. D'une part, contrairement au code de modèles d'atmosphère précédemment utilisé par le groupe de Montréal (Bergeron et al., 1995; Dufour et al., 2005, 2007), les nouveaux modèles décrits dans cette thèse prennent en compte les effets non idéaux qui apparaissent à la photosphère des naines blanches froides riches en hélium. L'atmosphère de ces objets étant particulièrement transparente, leur photosphère atteint des densités assez élevées pour que les interactions entre particules ne soient plus négligeables. Dans de telles conditions, une bonne partie de la physique constitutive des modèles doit être révisée (opacités, équilibre chimique, équation d'état). D'autre part, contrairement aux modèles de Kowalski (2006a), les modèles présentés dans cette thèse ne sont pas limités aux atmosphères composées uniquement d'hydrogène ou d'hélium. Ils permettent une description adéquate des naines blanches froides polluées par des métaux. Non seulement est-ce un attribut important si l'on souhaite correctement décrire toutes les naines blanches froides, mais surtout, cela nous permet de tester nos modèles. Comme les naines blanches polluées par des métaux sont les seules naines blanches froides à présenter des raies spectrales, elles constituent notre meilleure opportunité de tester la précision de nos modèles d'atmosphère.

Pour mettre ce code d'atmosphère au point, une bonne partie du code de Dufour (2006) a dû être réécrit :

1. Il a fallu y intégrer une série d'effets non idéaux précédemment décrits dans la littérature, dont des corrections pour les opacités du continu (Iglesias et al., 2002; Rohrmann, 2018), les profils de la raie Lyα à haute densité (Kowalski & Saumon,

2006), l'équilibre d'ionisation non idéal de l'hélium (Kowalski et al., 2007) et une équation d'état réaliste (Becker et al., 2014).

2. Nous avons recalculé les profils d'opacité induite par les collisions entre l'hydrogène moléculaire et l'hélium neutre (Chapitre 4). Nos simulations de dynamique moléculaire ab initio montrent que—pour les conditions physiques qui règnent à la photosphère des plus froides naines blanches—les profils d'absorption sont fortement distordus par rapport aux profils traditionnellement utilisés.

3. Au moyen de la théorie de la fonctionnelle de la densité et de la théorie classique des fluides, nous avons calculé l'équilibre d'ionisation des métaux dans l'atmosphère des naines blanches froides (Chapitre 5). Pour toutes les espèces considérées, nous trouvons que l'ionisation est de plus en plus favorisée lorsque la densité augmente, ce qui est cohérent avec les observations.

4. Nous avons amélioré le calcul des profils d'absorption de plusieurs raies métalliques importantes pour la modélisation précise des naines blanches polluées par des métaux (voir par exemple Chapitre 5, Chapitre 8 et Allard et al. 2018). Dans tous les cas, ces nouveaux profils permettent d'améliorer l'accord entre modèles et observations.

Une fois ce code d'atmosphère développé, nous l'avons appliqué à quelques problèmes astrophysiques. D'une part, nous nous en sommes servi pour analyser les plus froides naines blanches polluées par des métaux. Nous sommes ainsi parvenus à obtenir un accord satisfaisant—sans ajustement ad hoc de la physique constitutive des modèles—avec les observations de plusieurs étoiles que les autres codes d'atmosphère peinent à modéliser correctement. Cela inclut entre autres Ross 640 et LP 658−2 (Chapitre 5) ; SDSS J0804+2239, la première naine blanche DZ qui montre de la CIA (Chapitre 6) ; et WD J2356−209 et WD 2251−070, les plus vieilles naines blanches DZ connues (Chapitres 7 et 8). Ces résultats positifs suggèrent que la physique constitutive de nos modèles est adéquate pour décrire la photosphère dense des naines blanches froides riches en hélium. En plus de présenter un beau défi pour nos modèles, certaines de ces étoiles se sont révélées très intéressantes d'un point de vue astrophysique. C'est en particulier le cas de WD J2356−209. Notre analyse a révélé que son atmosphère contient une abondance inédite de sodium, qui y a été

présumément déposée suite à l'accrétion d'un planétésimal riche en sodium dont la nature exacte demeure inconnue.

Après avoir appliqué nos modèles à quelques objets individuels d'intérêt, nous les avons également employés pour analyser le plus gros échantillon homogène de naines blanches froides étudié à ce jour (Chapitre 9). L'analyse détaillée de cet ensemble de 501 objets a permis de mettre en lumière trois tendances intéressantes. D'abord, entre $T_{\rm eff} \approx 7500\,{\rm K}$ et $\approx 6250\,{\rm K}$, on observe une diminution de la fraction de naines blanches qui ont une atmosphère riche en hydrogène, ce qui s'explique probablement par le phénomène de brassage convectif (Rolland et al., 2018). Ensuite, entre $\approx 6250\,{\rm K}$ et $\approx 5000\,{\rm K}$, on assiste à une remontée de cette même fraction. Il n'existe pour le moment aucune explication physique pour cette augmentation de la fraction d'étoiles riches en hydrogène, mais notons que nous ne sommes pas les premiers à identifier une telle tendance (Bergeron et al., 1997, 2001). Enfin, en bas de $T_{\rm eff} \approx 5000\,{\rm K}$, on observe une diminution de la fraction d'étoiles riches en hydrogène, qui est peut-être simplement due au refroidissement plus efficace des naines blanches riches en hélium. Cette tendance invalide complètement un scénario précédemment proposé dans la littérature selon lequel l'accrétion d'hydrogène du milieu interstellaire domine l'évolution chimique de l'atmosphère des naines blanches froides (Kowalski, 2006a).

Les résultats présentés dans cette thèse représentent un grand pas en avant dans notre compréhension des plus vieilles étoiles naines blanches. Pour la toute première fois, nous avons à notre disposition des modèles qui permettent d'extraire avec précision et exactitude les paramètres fondamentaux de naines blanches froides de tous les types spectraux (DA, DC, DQ et DZ). De pair avec des modèles évolutifs de naines blanches, ce code d'atmosphère trouvera plusieurs applications dans le vaste domaine de la cosmochronologie. Il pourra servir à retracer l'historique de formation stellaire du voisinage solaire et à contraindre beaucoup plus précisément l'âge des plus vieilles populations stellaires de la Voie lactée. De plus, tel que vu au Chapitre 7, le code d'atmosphère développé dans cette thèse nous permet de sonder l'évolution à long terme des systèmes exoplanétaires, des milliards d'années après que leur étoile hôte ait épuisé ses réserves de carburant nucléaire. Nous pouvons ainsi non seulement déterminer la composition chimique des planétésimaux composant ses systèmes planétaires, mais aussi contraindre leurs propriétés dynamiques. En déterminant l'âge de ces naines blanches et la quantité de débris rocheux qu'elles ont

accrétés, on peut établir des contraintes que doivent respecter les simulations dynamiques d'évolution des systèmes planétaires (Veras et al., 2013, 2016; Hollands et al., 2018a).

Avec les centaines de milliers de nouvelles naines blanches découvertes par le satellite *Gaia*, nous sommes certainement sur le point de vivre une révolution dans le domaine. Pour l'instant, en l'absence de données spectroscopiques sur ces nouveaux objets, les analyses que l'on peut réaliser demeurent limitées. Cette situation sera de courte durée, puisque de nombreux relevés spectroscopiques devraient combler ce manque d'ici quelques années. C'est entre autres le cas de WEAVE, un spectrographe multi-objets qui sera installé sur le télescope William–Herschel et qui devrait obtenir des spectres pour quelque 60 000 naines blanches ; de DESI, qui s'intéressera à l'énergie sombre, mais qui observera également près de 100 000 naines blanches à des fins de calibration ; et de 4MOST, qui comporte un sous-relevé dédié exclusivement aux naines blanches.

Immanquablement, ces nouvelles données permettront d'identifier de nombreux objets uniques qui, comme WD J2356−209, ne ressemblent à aucune autre naine blanche connue. Il y a donc de nombreux défis en vue pour nos modèles d'atmosphère. Le code développé dans cette thèse sera le mieux placé d'entre tous pour percer les mystères des objets les plus âgés parmi ces nouvelles découvertes. Par ailleurs, en combinant ces nouveaux relevés aux données *Gaia*, on sera en mesure d'agrandir considérablement la taille de notre échantillon de naines blanches complet en volume. Il sera alors possible d'établir des statistiques beaucoup plus robustes—sans avoir à considérer de biais observationnels—quant à l'évolution spectrale des naines blanches froides, ce qui permettra de raffiner l'analyse présentée au Chapitre 9.

Bien que le code d'atmosphère présenté dans cette thèse permette de modéliser correctement la quasi-totalité des naines blanches froides, rappelons que deux classes d'objets résistent encore à nos efforts de modélisation : les DQpec et les naines blanches ultra-froides. Dans le premier cas, il s'agit de naines blanches froides qui montrent dans leur spectre des bandes distordues et décalées de carbone moléculaire. Bien que l'on soit capable d'obtenir un accord satisfaisant entre observations et modèles, il est pour l'instant nécessaire d'ajuster sans justification physique l'intensité du décalage de ces bandes (Chapitre 9), ce qui est loin d'être satisfaisant. Plusieurs pistes devraient être explorées pour solutionner ce problème. Dans un premier temps, il faudrait se débarrasser de l'approxi-

mation consistant à simplement déplacer l'absorption des bandes moléculaires de carbone par une quantité correspondant au décalage des niveaux électroniques de la molécule de C_2. Il faudrait plutôt explicitement modéliser l'absorption du C_2 dans un milieu dense et riche en hélium, ce qui est une tâche beaucoup plus exigeante d'un point de vue computationnel. De plus, des efforts devraient être consacrés à mieux comprendre et à intégrer les effets du magnétisme aux modèles—rappelons qu'une grande fraction des DQpec sont fortement magnétiques. Il faudrait entre autres clarifier l'impact des champs magnétiques sur le flux convectif et comprendre comment les champs magnétiques peuvent modifier la forme des bandes moléculaires.

En ce qui a trait à la seconde classe d'objets mal modélisés—les naines blanches ultra-froides, il s'agit d'objets dont le flux infrarouge est très fortement réduit par la présence de CIA. Pour l'instant, les modèles peinent à reproduire la forme de la distribution d'énergie dans l'infrarouge. Les résultats présentés dans le Chapitre 4, qui montrent comment les profils de CIA H_2-He se comportent à haute densité, semblent pousser les modèles dans la bonne direction. Toutefois, la densité prédite par les modèles d'atmosphère n'est pas suffisamment élevée pour produire une distorsion des profils de CIA qui permettrait de reproduire les observations. Il semble donc subsister un problème avec la structure des modèles de naines blanches ultra-froides riches en hélium. Il est probable que ce problème soit relié à l'équilibre d'ionisation de l'hélium. Aux densités atteintes à la photosphère des naines blanches ultra-froides, on s'attend à ce qu'une bonne partie des atomes d'hélium soient ionisés par pression. Toutefois, les détails de ce processus d'ionisation demeurent incertains, puisque des différences persistent entre les prédictions théoriques et les mesures expérimentales disponibles (Kowalski et al., 2007). En particulier, il se peut que l'ionisation de l'hélium à la photosphère des naines blanches ultra-froides soit moins importante que prévue, ce qui augmenterait la densité photosphérique et la distorsion des profils de CIA H_2-He.

Une autre amélioration qui pourrait être apportée au code d'atmosphère serait d'y traiter davantage de raies spectrales dans le cadre du formalisme d'autocorrélation. Pour le moment, seule une douzaine de raies importantes sont incluses via ce formalisme : les profils d'absorption de toutes les autres sont calculés avec l'approximation d'impact. Idéalement, tous les profils de raies devraient être calculés avec le formalisme d'autocorrélation, ce qui

permettra peut-être de résoudre quelques petites imperfections quant à l'accord entre les modèles et les spectres de DZ froides (par exemple, la source d'absorption non identifiée près de 4500 Å dans le spectre de WD J2356−209). Une telle amélioration nécessiterait toutefois le calcul de centaines de potentiels d'interaction et de moments dipolaires de transition, ce qui représente pour l'instant une tâche irréalisable d'un point de vue computationnel.

Dans un autre ordre d'idées, il faudrait également réviser les temps de diffusion des éléments lourds dans l'atmosphère des naines blanches froides riches en hélium. Bien déterminer ces temps de diffusion est de première importance si l'on souhaite relier précisément les abondances de métaux mesurées à la photosphère des DZ froides à la composition des planétésimaux accrétés. Or, ces calculs ont été réalisés au moyen de modèles qui ne prennent pas en compte les effets non idéaux de manière aussi précise que ce qui a été fait dans cette thèse. En particulier, l'implémentation de l'ionisation par pression de l'hélium, qui affecte grandement l'opacité des atmosphères riches en hélium, serait à revoir.

La science est une entreprise incrémentielle. Cette thèse a commencé là où d'autres s'étaient arrêtés, solutionnant des problèmes laissés derrière. À son tour, ce travail soulève de nouvelles questions qui constitueront le point de départ de nouvelles recherches. Notre compréhension des étoiles naines blanches froides avance rapidement. Une nouvelle génération d'instruments astronomiques, des expériences en laboratoire plus précises et un accès répandu à des puissances de calcul récemment impensables devraient tous contribuer à repousser encore plus loin la frontière séparant le connu de l'inconnu.

BIBLIOGRAPHIE

Abel, M., & Frommhold, L. 2013, Can. J. Phys., 91, 857

Abel, M., Frommhold, L., Li, X., & Hunt, K. L. 2012, J. Chem. Phys., 136, 044319

Akaike, H. 1974, IEEE Transactions on Automatic Control, 19, 716

Alam, S., Albareti, F. D., Allende Prieto, C., et al. 2015, ApJS, 219, 12

Allard, N. F., & Alekseev, V. 2014, Adv. Space Res., 54, 1248

Allard, N. F., Allard, F., Hauschildt, P. H., Kielkopf, J. F., & Machin, L. 2003, A&A, 411, L473

Allard, N. F., Drira, I., Gerbaldi, M., Kielkopf, J., & Spielfiedel, A. 1998a, A&A, 335, 1124

Allard, N. F., Guillon, G., Alekseev, V., & Kielkopf, J. 2016a, A&A, 593, A13

Allard, N. F., Homeier, D., Guillon, G., Viel, A., & Kielkopf, J. 2014, J. Phys. Conf. Ser., 548, 012006

Allard, N. F., Kielkopf, J., & Feautrier, N. 1998b, A&A, 330, 782

Allard, N. F., Kielkopf, J. F., Blouin, S., et al. 2018, A&A, 619, A152

Allard, N. F., Kielkopf, J. F., & Loeillet, B. 2004, A&A, 424, 347

Allard, N. F., Leininger, T., Gadéa, F., Brousseau-Couture, V., & Dufour, P. 2016b, A&A, 588, A142

Allard, N. F., Nakayama, A., Spiegelman, F., Kielkopf, J. F., & Stienkemeier, F. 2013, Eur. Phys. J. D, 67, 52

Allard, N. F., Royer, A., Kielkopf, J., & Feautrier, N. 1999, Phys. Rev. A, 60, 1021

Anderson, P. W. 1952, Phys. Rev., 86, 809

Angel, J. R. P. 1978, Annu. Rev. Astron. Astrophys., 16, 487

Angel, J. R. P., Borra, E. F., & Landstreet, J. D. 1981, ApJS, 45, 457

Angel, J. R. P., Illing, R. M. E., & Landstreet, J. D. 1972, ApJL, 175, L85

Angel, J. R. P., & Landstreet, J. D. 1974, ApJ, 191, 457

Baranger, M. 1958a, Phys. Rev., 111, 481

—. 1958b, Phys. Rev., 111, 494

Bardyn, A., Baklouti, D., Cottin, H., et al. 2017, MNRAS, 469, S712

Baron, E., & Hauschildt, P. H. 1998, ApJ, 495, 370

Beauchamp, A. 1995, Thèse de doctorat, Université de Montréal, Montréal, QC

Becker, A., Lorenzen, W., Fortney, J. J., et al. 2014, ApJS, 215, 21

Bédard, A., Bergeron, P., & Fontaine, G. 2017, ApJ, 848, 11

Bedin, L. R., Salaris, M., Piotto, G., et al. 2009, ApJ, 697, 965

—. 2005, ApJL, 624, L45

Berdyugin, A. V., & Piirola, V. 1999, A&A, 352, 619

Berdyugina, S. V., Berdyugin, A. V., & Piirola, V. 2007, Phys. Rev. Lett., 99, 091101

Bergeron, P. 2003, ApJ, 586, 201

Bergeron, P., Dufour, P., Fontaine, G., et al. 2019, ApJ, 876, 67

Bergeron, P., & Leggett, S. 2002, ApJ, 580, 1070

Bergeron, P., Leggett, S., & Ruiz, M. T. 2001, ApJS, 133, 413

Bergeron, P., Ruiz, M., & Leggett, S. 1997, ApJS, 108, 339

Bergeron, P., Ruiz, M. T., Hamuy, M., et al. 2005, ApJ, 625, 838

Bergeron, P., Ruiz, M.-T., Leggett, S. K., Saumon, D., & Wesemael, F. 1994, ApJ, 423, 456

Bergeron, P., Saumon, D., & Wesemael, F. 1995, ApJ, 443, 764

Bergeron, P., Wesemael, F., & Fontaine, G. 1991, ApJ, 367, 253

Bergeron, P., Wesemael, F., Dufour, P., et al. 2011, ApJ, 737, 28

Berghold, G., Mundy, C. J., Romero, A. H., Hutter, J., & Parrinello, M. 2000, Phys. Rev. B, 61, 10040

Birnbaum, G. 1978, JQSRT, 19, 51

Birnbaum, G., Bachet, G., & Frommhold, L. 1987, Phys. Rev. A, 36, 3729

Birnbaum, G., Chu, S.-I., Dalgarno, A., Frommhold, L., & Wright, E. 1984, Phys. Rev. A, 29, 595

Blouin, S., Allard, N. F., Leininger, T., Gadéa, F. X., & Dufour, P. 2019a, ApJ, 875, 137

Blouin, S., Dufour, P., & Allard, N. F. 2018a, ApJ, 863, 184

Blouin, S., Dufour, P., Allard, N. F., & Kilic, M. 2018b, ApJ, 867, 161

Blouin, S., Dufour, P., Allard, N. F., et al. 2019b, ApJ, 872, 188

Blouin, S., Kowalski, P., & Dufour, P. 2017, ApJ, 848

Bondi, A. 1964, JPhCh, 68, 441

Born, M., & Oppenheimer, R. 1927, Annalen der Physik, 389, 457

Borysow, A. 1992, Icarus, 96, 169

—. 2002, A&A, 390, 779

Borysow, A., Borysow, J., & Fu, Y. 2000, Icarus, 145, 601

Borysow, A., Frommhold, L., & Moraldi, M. 1989, ApJ, 336, 495

Borysow, A., Jørgensen, U., & Zheng, C. 1997, A&A, 324, 185

Borysow, A., Jørgensen, U. G., & Fu, Y. 2001, JQSRT, 68, 235

Borysow, J., Frommhold, L., & Birnbaum, G. 1988, ApJ, 326, 509

Borysow, J., Trafton, L., Frommhold, L., & Birnbaum, G. 1985, ApJ, 296, 644

Bouanich, J., Brodbeck, C., Nguyen-Van-Thanh, & Drossart, P. 1990, JQSRT, 44, 393

Bowman, N. J., & Lewis, E. L. 1978, J. Phys. B, 11, 1703

Boys, S. F., & Bernardi, F. d. 1970, Mol. Phys., 19, 553

Brassard, P., Fontaine, G., Chayer, P., & Green, E. M. 2010, in American Institute of Physics Conference Series, Vol. 1273, American Institute of Physics Conference Series, ed. K. Werner & T. Rauch, 259–262

Brinkworth, C. S., Gänsicke, B. T., Girven, J. M., et al. 2012, ApJ, 750, 86

Brodbeck, C., Bouanich, J.-P., Frommhold, L., et al. 1995, Phys. Rev. A, 51, 1209

Broomall, J. R., Johnson, W. D., & Onn, D. G. 1976, Phys. Rev. B, 14, 2819

Bues, I. 1991, in NATO Advanced Science Institutes (ASI) Series C, Vol. 336, NATO Advanced Science Institutes (ASI) Series C, ed. G. Vauclair & E. Sion, 285

Bues, I. 1999, in Astronomical Society of the Pacific Conference Series, Vol. 169, 11th European Workshop on White Dwarfs, ed. S.-E. Solheim & E. G. Meistas, 240

Buontempo, U., Cunsolo, S., & Dore, P. 1975, J. Chem. Phys., 62, 4062

Burnham, K. P., & Anderson, D. R. 2002, Model Selection and Inference (New York : Springer)

Catalan, S., Isern, J., García-Berro, E., & Ribas, I. 2008, MNRAS, 387, 1693

Celliers, P. M., Loubeyre, P., Eggert, J. H., et al. 2010, Phys. Rev. Lett., 104, 184503

Ceperley, D. M., & Alder, B. 1980, Phys. Rev. Lett., 45, 566

Chabrier, G., & Potekhin, A. Y. 1998, Phys. Rev. E, 58, 4941

Chambers, K. C., Magnier, E. A., Metcalfe, N., et al. 2016, arXiv preprint, 1612.05560

Chandrasekhar, S. 1931, ApJ, 74, 81

—. 1935, MNRAS, 95, 207

Charpinet, S., Fontaine, G., & Brassard, P. 2009, Nature, 461, 501

Chayer, P., Fontaine, G., & Wesemael, F. 1995, ApJS, 99, 189

Chisholm, D., MacDonald, J., Crawford, M., & Welsh, H. 1952, Phys. Rev., 88, 957

Chisholm, D., & Welsh, H. 1954, Can. J. Phys., 32, 291

Čížek, J. 1966, J. Chem. Phys., 45, 4256

Cox, A. N. 2015, Allen's Astrophysical Quantities (Springer)

Crawford, M., Welsh, H., MacDonald, J., & Locke, J. 1950, Phys. Rev., 80, 469

Croll, B., Dalba, P. A., Vanderburg, A., et al. 2017, ApJ, 836, 82

Crowley, B. 2014, HEDP, 13, 84

Cummings, J. D., Kalirai, J. S., Tremblay, P.-E., Ramirez-Ruiz, E., & Choi, J. 2018, ApJ, 866, 21

Cunsolo, S., & Gush, H. 1972, Can. J. Phys., 50, 2058

Czuchaj, E., Rebentrost, F., Stoll, H., & Preuss, H. 1991, Chem. Phys. Lett., 182, 191

Czuchaj, E., Rebentrost, F., Stoll, H., & Preuss, H. 1996, Chem. Phys., 207, 51

Dalgarno, A. 1962, Spectral Reflectivity of the Earth's Atmosphere III : The Scattering of Light by Atomic Systems (Geophysical Corporation of America Rep.)

Dantona, F., & Mazzitelli, I. 1979, A&A, 74, 161

Debes, J. H., & Sigurdsson, S. 2002, ApJ, 572, 556

Dewaele, A., Eggert, J., Loubeyre, P., & Le Toullec, R. 2003, Phys. Rev. B, 67, 094112

Dickinson, A. S., & Gadéa, F. X. 2002, Phys. Rev. A, 65, 052506

Dorn, C., Khan, A., Heng, K., et al. 2015, A&A, 577, A83

Driver, R. D., & Snider, J. L. 1976, ApJ, 208, 518

Dufour, P. 2006, Thèse de doctorat, Université de Montréal, Montréal, QC

Dufour, P., Bergeron, P., & Fontaine, G. 2005, ApJ, 627, 404

Dufour, P., Bergeron, P., Schmidt, G. D., et al. 2006, ApJ, 651, 1112

Dufour, P., Blouin, S., Coutu, S., et al. 2017, in ASP Conf. Ser., Vol. 509, 20th European White Dwarf Workshop, ed. P.-E. Tremblay, B. Gaensicke, & T. Marsh, 3–8

Dufour, P., Kilic, M., Fontaine, G., et al. 2010, ApJ, 719, 803

Dufour, P., Kilic, M., Fontaine, G., et al. 2012, ApJ, 749, 6

Dufour, P., Liebert, J., Fontaine, G., & Behara, N. 2007, Nature, 450, 522

Dufour, P., Bergeron, P., Liebert, J., et al. 2007, ApJ, 663, 1291

Dunning, T. H. 1989, J. Chem. Phys, 90, 1007

Dupuis, J., Fontaine, G., Pelletier, C., & Wesemael, F. 1993, ApJS, 84, 73

Eggert, J., Brygoo, S., Loubeyre, P., et al. 2008, Phys. Rev. Lett., 100, 124503

Eisenstein, D. J., Liebert, J., Koester, D., et al. 2006a, AJ, 132, 676

Eisenstein, D. J., Liebert, J., Harris, H. C., et al. 2006b, ApJS, 167, 40

Farihi, J. 2016, New Astron. Rev., 71, 9

Farihi, J., Barstow, M. A., Redfield, S., Dufour, P., & Hambly, N. C. 2010, MNRAS, 404, 2123

Farihi, J., Dufour, P., Napiwotzki, R., & Koester, D. 2011, MNRAS, 413, 2559

Farihi, J., Gänsicke, B. T., & Koester, D. 2013, Science, 342, 218

Farihi, J., Jura, M., & Zuckerman, B. 2009, ApJ, 694, 805

Feautrier, P. 1964, Comptes Rendus de l'Académie des sciences, 258

Feigelson, E. D., & Babu, G. J. 2012, Modern Statistical Methods for Astronomy

Fermi, E. 1927, Rend. Accad. Naz. Lincei, 6, 32

Fernández, B., Hättig, C., Koch, H., & Rizzo, A. 1999, J. Chem. Phys, 110, 2872

Fock, V. 1930, Zeitschrift für Physik, 61, 126

Fontaine, G., & Brassard, P. 2008, PASP, 120, 1043

Fontaine, G., Brassard, P., & Bergeron, P. 2001, PASP, 113, 409

Fontaine, G., Graboske Jr, H., & Van Horn, H. 1977, ApJS, 35, 293

Fontaine, G., & Wesemael, F. 1987, in IAU Colloq. 95 : Second Conference on Faint Blue Stars, ed. A. G. D. Philip, D. S. Hayes, & J. W. Liebert, 319–326

Fortney, J. J., Baraffe, I., & Militzer, B. 2010, in Exoplanets, ed. S. Seager (University of Arizona Press), 397–418

Fortov, V., Ternovoi, V. Y., Zhernokletov, M., et al. 2003, JETP, 97, 259

Fowler, R. H. 1926, MNRAS, 87, 114

Frommhold, L. 1993, Collision-Induced Absorption in Gases (New York : Cambridge University Press)

Frost, A. A., & Musulin, B. 1954, J. Chem. Phys, 22, 1017

Fusillo, N. P. G., Tremblay, P.-E., Gänsicke, B. T., et al. 2018, arXiv preprint, 1807.03315

Gaia Collaboration. 2016, A&A, 595, A1

—. 2018, A&A, 616, A1

Gänsicke, B. T., Marsh, T. R., Southworth, J., & Rebassa-Mansergas, A. 2006, Science, 314, 1908

Gänsicke, B. T., Aungwerojwit, A., Marsh, T. R., et al. 2016, ApJL, 818, L7

García-Berro, E., Torres, S., Althaus, L. G., et al. 2010, Nature, 465, 194

Gentile Fusillo, N. P., Tremblay, P.-E., Jordan, S., et al. 2018, MNRAS, 473, 3693

GharibNezhad, E., Shayesteh, A., & Bernath, P. F. 2013, MNRAS, 432, 2043

Giammichele, N., Bergeron, P., & Dufour, P. 2012, ApJS, 199, 29

Giammichele, N., Charpinet, S., Fontaine, G., et al. 2018, Nature, 554, 73

Gianninas, A., Bergeron, P., & Ruiz, M. T. 2011, ApJ, 743, 138

Gianninas, A., Curd, B., Thorstensen, J. R., et al. 2015, MNRAS, 449, 3966

Giannozzi, P., Baroni, S., Bonini, N., et al. 2009, J. Phys. Condens. Matter, 21, 395502

Girven, J., Brinkworth, C. S., Farihi, J., et al. 2012, ApJ, 749, 154

Graham, J. R., Matthews, K., Neugebauer, G., & Soifer, B. T. 1990, ApJ, 357, 216

Guillot, B. 1991, J. Chem. Phys., 95, 1543

Gustafsson, M., & Frommhold, L. 2001, ApJ, 546, 1168

Hall, P. B., & Maxwell, A. J. 2008, ApJ, 678, 1292

Hammer, D., Frommhold, L., Meyer, W., et al. 1999, J. Chem. Phys., 111, 6283

Hansen, B. M. 1999, ApJ, 520, 680

Hansen, B. M., Brewer, J., Fahlman, G. G., et al. 2002, ApJL, 574, L155

Hansen, B. M., Richer, H. B., Fahlman, G. G., et al. 2004, ApJS, 155, 551

Hansen, B. M., Anderson, J., Brewer, J., et al. 2007, ApJ, 671, 380

Hansen, J.-P., & McDonald, I. R. 2013, Theory of Simple Liquids with Applications to Soft Matter, 4th edn. (Academic Press)

Hare, W., & Welsh, H. 1958, Can. J. Phys., 36, 88

Harris, H. C., Liebert, J., Kleinman, S. J., et al. 2003, AJ, 126, 1023

Harris, M., Lewis, E. L., McHugh, D., & Shannon, I. 1986, J. Phys. B, 19, 3207

Harrison, J. H. D., Bonsor, A., & Madhusudhan, N. 2018, MNRAS, 479, 3814

Hättig, C., Larsen, H., Olsen, J., et al. 1999, J. Chem. Phys, 111, 10099

Hauschildt, P. H., & Baron, E. 1999, J. Comput. Appl. Math., 109, 41

Hauschildt, P. H., Baron, E., & Allard, F. 1997, ApJ, 483, 390

Hernando, A., Barranco, M., Mayol, R., et al. 2010, J. Low Temp. Phys., 158, 105

Hernando, A., Barranco, M., Mayol, R., Pi, M., & Krośnicki, M. 2008, Phys. Rev. B, 77, 024513

Herzberg, G. 1950, Molecular spectra and molecular structure. Vol.1 : Spectra of diatomic molecules

Hill, G. J., Nicklas, H. E., MacQueen, P. J., et al. 1998, in Proc. SPIE, Vol. 3355, Optical Astronomical Instrumentation, ed. S. D'Odorico, 375–386

Hinde, R. J. 2003, J. Phys. B, 36, 3119

Hohenberg, P., & Kohn, W. 1964, Phys. Rev., 136, B864

Holberg, J., & Bergeron, P. 2006, ApJ, 132, 1221

Holberg, J. B., Sion, E. M., Oswalt, T., et al. 2008, AJ, 135, 1225

Hollands, M. A., Gänsicke, B. T., & Koester, D. 2018a, MNRAS, 477, 93

Hollands, M. A., Koester, D., Alekseev, V., Herbert, E. L., & Gänsicke, B. T. 2017, MNRAS, 467, 4970

Hollands, M. A., Tremblay, P.-E., Gänsicke, B. T., Gentile-Fusillo, N. P., & Toonen, S. 2018b, MNRAS, 480, 3942

Holst, B., Redmer, R., & Desjarlais, M. P. 2008, Phys. Rev. B, 77, 184201

Homeier, D., Allard, N., Allard, F., et al. 2005, in ASP Conf. Proc., Vol. 334, 14th European Workshop on White Dwarfs, ed. D. Koester & S. Moehler, 209

Homeier, D., Allard, N., Johnas, C. M. S., Hauschildt, P. H., & Allard, F. 2007, in ASP Conf. Proc., Vol. 372, 15th European Workshop on White Dwarfs, ed. R. Napiwotzki & M. R. Burleigh, 277

Hoover, W. G. 1985, Phys. Rev. A, 31, 1695

Hornkohl, J. O., Parigger, C. G., & Nemes, L. 2005, Appl. Opt., 44, 3686

Huber, K., & Herzberg, G. 1979, Molecular Spectra and Molecular Structure : IV. Constants of Diatomic Molecules (New York : Van Nostrand)

Hummer, D., & Mihalas, D. 1988, ApJ, 331, 794

Hurvich, C. M., & Tsai, C.-L. 1989, Biometrika, 76, 297

Hutter, J., Alavi, A., Deutsch, T., et al. 2008, CPMD : Car-Parinello Molecular Dynamics, 3.17.1, IBM Corp 1990-2008 and MPI für Festkörperforschung Stuttgart 1997-2001. www.cpmd.org

Ichimaru, S., Iyetomi, H., & Tanaka, S. 1987, Phys. Rev., 149, 91

Iftimie, R., & Tuckerman, M. E. 2005, J. Chem. Phys., 122, 214508

Iglesias, C. A., Rogers, F. J., & Saumon, D. 2002, ApJL, 569, L111

Jahn, S., & Kowalski, P. M. 2014, Reviews in Mineralogy and Geochemistry, 78, 691

Jessberger, E. K., Christoforidis, A., & Kissel, J. 1988, Nature, 332, 691

John, T. 1994, MNRAS, 269, 871

Jordan, S. 2007, in Astronomical Society of the Pacific Conference Series, Vol. 372, 15th European Workshop on White Dwarfs, ed. R. Napiwotzki & M. R. Burleigh, 139

Jordan, S., & Friedrich, S. 2002, A&A, 383, 519

Jørgensen, U., Hammer, D., Borysow, A., & Falkesgaard, J. 2000, A&A, 361, 283

Jura, M. 2003, ApJL, 584, L91

—. 2008, AJ, 135, 1785

Jura, M., Xu, S., Klein, B., Koester, D., & Zuckerman, B. 2012, ApJ, 750, 69

Jura, M., & Young, E. 2014, Annu. Rev. Earth Planet. Sci., 42, 45

Kalirai, J. S. 2012, Nature, 486, 90

Kapranidis, S. 1983, ApJ, 275, 342

Kapranidis, S., & Liebert, J. 1986, ApJ, 305, 863

Kawka, A., & Vennes, S. 2006, ApJ, 643, 402

—. 2012, MNRAS, 425, 1394

—. 2016, MNRAS, 458, 325

Kedziera, D., & Kaczmarek-Kedziera, A. 2016, Remarks on Wave Function Theory and Methods, ed. J. Leszczynski (Dordrecht : Springer Netherlands), 1–49

Kelley, J., & Bragg, S. 1984, Phys. Rev. A, 29, 1168

Kendall, R. A., Dunning, T. H., & Harrison, R. J. 1992, J. Chem. Phys, 96, 6796

Kepler, S. O., Koester, D., & Ourique, G. 2016a, Science, 352, 67

Kepler, S. O., Pelisoli, I., Koester, D., et al. 2015, MNRAS, 446, 4078

—. 2016b, MNRAS, 455, 3413

Kilic, M., Farihi, J., Nitta, A., & Leggett, S. K. 2008, AJ, 136, 111

Kilic, M., Kowalski, P. M., Reach, W. T., & Von Hippel, T. 2009a, ApJ, 696, 2094

Kilic, M., Kowalski, P. M., & Von Hippel, T. 2009b, ApJ, 138, 102

Kilic, M., Thorstensen, J. R., Kowalski, P., & Andrews, J. 2012, MNRAS, 423, L132

Kilic, M., von Hippel, T., Mullally, F., et al. 2006, ApJ, 642, 1051

Kilic, M., Munn, J. A., Harris, H. C., et al. 2006, AJ, 131, 582

Kilic, M., Munn, J. A., Williams, K. A., et al. 2010a, ApJL, 715, L21

Kilic, M., Leggett, S. K., Tremblay, P.-E., et al. 2010b, ApJS, 190, 77

Kiselyov, O. E., & Martynov, G. A. 1990, J. Chem. Phys., 93, 1942

Kissel, J., Altwegg, K., Clark, B. C., et al. 2007, Space Sci. Rev., 128, 823

Kittel, C. 1996, Introduction to Solid State Physics, 7th edn. (New York : Wiley)

Klein, B., Jura, M., Koester, D., Zuckerman, B., & Melis, C. 2010, ApJ, 709, 950

Kleinman, S. J., Kepler, S. O., Koester, D., et al. 2013, ApJS, 204, 5

Koester, D. 1976, A&A, 52, 415

Koester, D. 2009, A&A, 498, 517

Koester, D., & Chanmugam, G. 1990, Rep. Prog. Phys., 53, 837

Koester, D., Girven, J., Gänsicke, B. T., & Dufour, P. 2011, A&A, 530, A114

Koester, D., & Knist, S. 2006, A&A, 454, 951

Koester, D., & Wilken, D. 2006, A&A, 453, 1051

Koester, D., & Wolff, B. 2000, A&A, 357, 587

Kohn, W., & Sham, L. J. 1965, Phys. Rev., 140, A1133

Kollmar, C., & Neese, F. 2010, Mol. Phys., 108, 2449

Kołos, W., & Peek, J. 1976, Chem. Phys., 12, 381

Kongsted, J., Osted, A., Mikkelsen, K. V., & Christiansen, O. 2002, Chem. Phys. Lett., 364, 379

Kowalski, P. 2006a, Thèse de doctorat, Vanderbilt University, Nashville, TN

Kowalski, P., Mazevet, S., Saumon, D., & Challacombe, M. 2007, Phys. Rev. B, 76, 075112

Kowalski, P., & Saumon, D. 2006, ApJL, 651, L137

Kowalski, P. M. 2006b, ApJ, 641, 488

—. 2010, A&A, 519, L8

Kowalski, P. M. 2010, in AIP Conf. Proc., Vol. 1273, 18th European White Dwarf Workshop, ed. K. Werner & T. Rauch, 424–427

—. 2014, A&A, 566, L8

Kowalski, P. M., & Saumon, D. 2004, ApJ, 607, 970

Kowalski, P. M., Saumon, D., Holberg, J., & Leggett, S. 2013, in ASP Conf. Ser., Vol. 469, 18th European White Dwarf Workshop, 173

Kramida, A., Yu. Ralchenko, Reader, J., & NIST ASD Team. 2015, NIST Atomic Spectra Database, 5.3, National Institute of Standards and Technology, Gaithersburg, MD. http://physics.nist.gov/asd

Kwok, S. 2000, The Origin and Evolution of Planetary Nebulae (Cambridge University Press)

Lamb, D., & Van Horn, H. 1975, ApJ, 200, 306

Landau, L., & Lifchitz, E. 1980, Course of Theoretical Physics, 3rd edn., Vol. 5 (Oxford : Pergamon)

Latour, M., Fontaine, G., Green, E. M., & Brassard, P. 2015, A&A, 579, A39

Lawrence, A., Warren, S. J., Almaini, O., et al. 2007, MNRAS, 379, 1599

Leggett, S., Ruiz, M. T., & Bergeron, P. 1998, ApJ, 497, 294

Leggett, S. K., Bergeron, P., Subasavage, J. P., et al. 2018, ApJS, 239, 26

Lenzuni, P., Chernoff, D. F., & Salpeter, E. E. 1991, ApJS, 76, 759

Lenzuni, P., & Saumon, D. 1992, Revista Mexicana de Astronomia y Astrofisica, 23, 223

Lewis, J. 1976, Physica A, 82, 500

Lewis, J. 1980, in Intermolecular Spectroscopy and Dynamical Properties of Dense Systems - Course LXXV, ed. J. van Kranendonk (Societa Italiana di Fisica), 91–110

Lewis, J. 1985, in Phenomena Induced by Intermolecular Interactions, ed. G. Birnbaum (New York : Plenum Press), 215–257

Li, X., Mandal, A., Miliordos, E., & Hunt, K. L. 2012, J. Chem. Phys., 136, 044320

Liebert, J. 1986, in Astrophysics and Space Science Library, Vol. 128, IAU Colloq. 87 : Hydrogen Deficient Stars and Related Objects, ed. K. Hunger, D. Schoenberner, & N. Kameswara Rao, 367–381

Liebert, J., Angel, J. R. P., Stockman, H. S., & Beaver, E. A. 1978, ApJ, 225, 181

Liebert, J., Bergeron, P., & Holberg, J. B. 2005, ApJS, 156, 47

Liebert, J., Wesemael, F., Hansen, C. J., et al. 1986, ApJ, 309, 241

Limoges, M.-M., Bergeron, P., & Lépine, S. 2015, ApJS, 219, 19

Limoges, M.-M., Lépine, S., & Bergeron, P. 2013, AJ, 145, 136

Lodders, K. 2003, ApJ, 591, 1220

Lovallo, C. C., & Klobukowski, M. 2004, J. Chem. Phys, 120, 246

Lundqvist, S., & March, N. H. 2013, Theory of the Inhomogeneous Electron Gas (Springer Science & Business Media)

MacDonald, J., & Vennes, S. 1991, ApJ, 371, 719

Mactaggart, J. 1971, Thèse de doctorat, University of Toronto, Toronto, ON

Magni, G., & Mazzitelli, I. 1979, A&A, 72, 134

Malo, A., Wesemael, F., & Bergeron, P. 1999, ApJ, 517, 901

Maroulis, G. 2000, J. Phys. Chem. A, 104, 4772

Martyna, G. J., & Tuckerman, M. E. 1999, J. Chem. Phys, 110, 2810

Marx, D., & Hutter, J. 2000, Modern Methods and Algorithms of Quantum Chemistry, 1, 141

Masili, M., & Starace, A. F. 2003, Phys. Rev. A, 68, 012508

Masseron, T., Plez, B., Van Eck, S., et al. 2014, A&A, 571, A47

Mateo, D., Hernando, A., Barranco, M., Mayol, R., & Pi, M. 2011, Phys. Rev. B, 83, 174505

McCook, G. P., & Sion, E. M. 1999, ApJS, 121, 1

McKellar, A., Mactaggart, J., & Welsh, H. 1975, Can. J. Phys., 53, 2060

Melis, C., & Dufour, P. 2017, ApJ, 834, 1

Melis, C., Farihi, J., Dufour, P., et al. 2011, ApJ, 732, 90

Melis, C., Jura, M., Albert, L., Klein, B., & Zuckerman, B. 2010, ApJ, 722, 1078

Mestel, L. 1952, MNRAS, 112, 583

Meyer, W., & Frommhold, L. 1986, Phys. Rev. A, 34, 2771

Mihalas, D. 1978, Stellar Atmospheres, 2nd edn. (San Francisco : WH Freeman and Co.)

Mihalas, D., Dappen, W., & Hummer, D. 1988, ApJ, 331, 815

Militzer, B., & Hubbard, W. B. 2013, ApJ, 774, 148

Møller, C., & Plesset, M. S. 1934, Phys. Rev., 46, 618

Mould, J., & Liebert, J. 1978, ApJ, 226, L29

Muchmore, D. 1984, ApJ, 278, 769

Müller, W., Flesch, J., & Meyer, W. 1984, J. Chem. Phys., 80, 3297

Nakayama, A., & Yamashita, K. 2001, J. Chem. Phys., 114, 780

Neese, F. 2012, Wiley Interdisciplinary Reviews : Computational Molecular Science, 2, 73

Neese, F., Hansen, A., Wennmohs, F., & Grimme, S. 2009, Acc. Chem. Res., 42, 641

Nellis, W., Holmes, N., Mitchell, A., et al. 1984, Phys. Rev. Lett., 53, 1248

Nosé, S. 1984, J. Chem. Phys, 81, 511

Nägele, G. 2008, in Soft Matter : From Synthetic to Biological Materials, ed. J. Dhont, G. Gompper, G. Nägele, D. Richter, & R. G. Winkler (Forschungszentrum Jülich GmbH), B2.1–B2.47

Oke, J. B., Cohen, J. G., Carr, M., et al. 1995, PASP, 107, 375

Oppenheimer, B. R., Hambly, N. C., Digby, A. P., Hodgkin, S. T., & Saumon, D. 2001, Science, 292, 698

Oswalt, T. D., Smith, J. A., Wood, M. A., & Hintzen, P. 1996, Nature, 382, 692

Pachucki, K. 2012, Phys. Rev. A, 85, 042511

Pagliai, M., Cavazzoni, C., Cardini, G., et al. 2008, J. Chem. Phys., 128, 224514

Pagliai, M., Muniz-Miranda, F., Cardini, G., Righini, R., & Schettino, V. 2011, J. Mol. Struct., 993, 438

Paquette, C., Pelletier, C., Fontaine, G., & Michaud, G. 1986, ApJS, 61, 197

Partridge, H., Stallcop, J. R., & Levin, E. 2001, J. Chem. Phys, 115, 6471

Pätzold, M., Andert, T., Hahn, M., et al. 2016, Nature, 530, 63

Pelletier, C., Fontaine, G., Wesemael, F., Michaud, G., & Wegner, G. 1986, ApJ, 307, 242

Percus, J. K., & Yevick, G. J. 1958, Phys. Rev., 110, 1

Perdew, J. P., Burke, K., & Ernzerhof, M. 1996, Phys. Rev. Lett., 77, 3865

Perdew, J. P., Ruzsinszky, A., Tao, J., et al. 2005, J. Chem. Phys., 123, 062201

Piskunov, N., Kupka, F., Ryabchikova, T., Weiss, W., & Jeffery, C. 1995, ApJS, 112, 525

Plimpton, S. 1995, J. Comput. Phys., 117, 1

Putney, A. 1997, ApJS, 112, 527

Putney, A., & Jordan, S. 1995, ApJ, 449, 863

Raddi, R., Gänsicke, B. T., Koester, D., et al. 2015, MNRAS, 450, 2083

Raghavachari, K., Trucks, G. W., Pople, J. A., & Head-Gordon, M. 1989, Chem. Phys. Lett., 157, 479

Ramabhadran, R. O., & Raghavachari, K. 2013, J. Chem. Theory Comput., 9, 3986

Ramírez, R., Kumar, P. P., Marx, D., et al. 2004, J. Chem. Phys., 121, 3973

Rebassa-Mansergas, A., Nebot Gómez-Morán, A., Schreiber, M. R., Girven, J., & Gänsicke, B. T. 2011, MNRAS, 413, 1121

Renedo, I., Althaus, L. G., Bertolami, M. M., et al. 2010, ApJ, 717, 183

Richer, H. B., Fahlman, G. G., Rosvick, J., & Ibata, R. 1998, ApJL, 504, L91

Rocchetto, M., Farihi, J., Gänsicke, B. T., & Bergfors, C. 2015, MNRAS, 449, 574

Rohrmann, R. D. 2018, MNRAS, 473, 457

Rolland, B., Bergeron, P., & Fontaine, G. 2018, ApJ, 857, 56

Ross, M., & Young, D. A. 1986, Phys. Lett. A, 118, 463

Rumble, J. R. 2018, CRC Handbook of Chemistry and Physics, 99th edn. (Boca Raton, FL : CRC Press/Taylor & Francis)

Russell, C. T., Raymond, C. A., Coradini, A., et al. 2012, Science, 336, 684

Rybicki, G. 1971, JQSRT, 11, 589

Salim, S., Rich, R. M., Hansen, B. M., et al. 2004, ApJ, 601, 1075

Saumon, D., Bergeron, P., Lunine, J., Hubbard, W. B., & Burrows, A. 1994, ApJ, 424, 333

Saumon, D., & Chabrier, G. 1991, Phys. Rev. A, 44, 5122

—. 1992, Phys. Rev. A, 46, 2084

Saumon, D., Chabrier, G., & Van Horn, H. 1995, ApJS, 99, 713

Saumon, D., Holberg, J. B., & Kowalski, P. M. 2014, ApJ, 790, 50

Saumon, D., & Jacobson, S. 1998, ApJL, 511, L107

Sayres, C., Subasavage, J. P., Bergeron, P., et al. 2012, AJ, 143, 103

Schatzman, E. 1945, Annales d'Astrophysique, 8, 143

Schmidt, G. D., Bergeron, P., & Fegley, B. 1995, ApJ, 443, 274

Schmidt, G. D., Liebert, J., Harris, H. C., Dahn, C. C., & Leggett, S. K. 1999, ApJ, 512, 916

Schmidt, M. 1975, ApJ, 202, 22

Schröder, K.-P., & Smith, R. C. 2008, MNRAS, 386, 155

Seiff, A., Kirk, D. B., Knight, T. C., et al. 1998, J. Geophys. Res. : Planets, 103, 22857

Shayesteh, A., Ram, R. S., & Bernath, P. F. 2013, J. Mol. Spectrosc., 288, 46

Silvestrelli, P. L., Bernasconi, M., & Parrinello, M. 1997, Chem. Phys. Lett., 277, 478

Silvestrelli, P. L., Marzari, N., Vanderbilt, D., & Parrinello, M. 1998, Solid State Commun., 107, 7

Silvestrelli, P. L., & Parrinello, M. 1999, Phys. Rev. Lett., 82, 3308

Sion, E. M. 1984, ApJ, 282, 612

Sion, E. M., Greenstein, J. L., Landstreet, J. D., et al. 1983, ApJ, 269, 253

Slater, J. C. 1929, Phys. Rev., 34, 1293

Smith, G. 1972, J. Phys. B, 5, 2310

Soubiran, F., Mazevet, S., Winisdoerffer, C., & Chabrier, G. 2012, Phys. Rev. B, 86, 115102

Stienkemeier, F., Higgins, J., Callegari, C., et al. 1996, Zeitschrift für Physik D Atoms, Molecules and Clusters, 38, 253

Strout, D. L., & Scuseria, G. E. 1995, J. Chem. Phys., 102, 8448

Subasavage, J. P., Henry, T. J., Bergeron, P., Dufour, P., & Hambly, N. C. 2008, AJ, 136, 899

Subasavage, J. P., Henry, T. J., Bergeron, P., et al. 2007, AJ, 134, 252

Subasavage, J. P., Jao, W.-C., Henry, T. J., et al. 2009, AJ, 137, 4547

—. 2017, AJ, 154, 32

Tassoul, M., Fontaine, G., & Winget, D. E. 1990, ApJS, 72, 335

Tennyson, J., & Yurchenko, S. N. 2012, MNRAS, 425, 21

Tennyson, J., Yurchenko, S. N., Al-Refaie, A. F., et al. 2016, J. Mol. Spectrosc., 327, 73

Thomas, L. H. 1927, Proceedings of the Cambridge Philosophical Society, 23, 542

Tremblay, P.-E., & Bergeron, P. 2008, ApJ, 672, 1144

Tremblay, P.-E., & Bergeron, P. 2009, ApJ, 696, 1755

Tremblay, P.-E., Fontaine, G., Freytag, B., et al. 2015, ApJ, 812, 19

Tremblay, P.-E., Kalirai, J., Soderblom, D., Cignoni, M., & Cummings, J. 2014, ApJ, 791, 92

Tsuneda, T. 2014, Density Functional Theory in Quantum Chemistry (Springer)

van Kranendonk, J. 1957, Physica, 23, 825

—. 1968, Can. J. Phys., 46, 1173

van Kranendonk, J. 1980, in Intermolecular Spectroscopy and Dynamical Properties of Dense Systems - Course LXXV, ed. J. van Kranendonk (Societa Italiana di Fisica), 77–90

Vanderbilt, D. 1990, Phys. Rev. B, 41, 7892

Vanderburg, A., Johnson, J. A., Rappaport, S., et al. 2015, Nature, 526, 546

Vauclair, G., & Reisse, C. 1977, A&A, 61, 415

Veras, D., Mustill, A. J., Bonsor, A., & Wyatt, M. C. 2013, MNRAS, 431, 1686

Veras, D., Mustill, A. J., Gänsicke, B. T., et al. 2016, MNRAS, 458, 3942

Verlet, L. 1967, Phys. Rev., 159, 98

von Hippel, T., & Gilmore, G. 2000, AJ, 120, 1384

Vorberger, J., Tamblyn, I., Militzer, B., & Bonev, S. A. 2007, Phys. Rev. B, 75, 024206

Vornanen, T., Berdyugina, S. V., & Berdyugin, A. 2013, A&A, 557, A38

Vornanen, T., Berdyugina, S. V., Berdyugin, A. V., & Piirola, V. 2010, ApJL, 720, L52

Walkup, R., Stewart, B., & Pritchard, D. 1984, Phys. Rev. A, 29, 169

Wang, H. S., Lineweaver, C. H., & Ireland, T. R. 2018, Icarus, 299, 460

Weck, P. F., Stancil, P. C., & Kirby, K. 2003, J. Chem. Phys., 118, 9997

Weissman, P. R. 2007, in IAU Symposium, Vol. 236, Near Earth Objects, our Celestial Neighbors : Opportunity and Risk, ed. G. B. Valsecchi, D. Vokrouhlický, & A. Milani, 441–450

Werner, H.-J., Knowles, P. J., Knizia, G., Manby, F. R., & Schütz, M. 2012, Wiley Interdisciplinary Reviews : Computational Molecular Science, 2, 242

Wickramasinghe, D. T., Allen, D. A., & Bessell, M. S. 1982, MNRAS, 198, 473

Wigner, E. 1932, Phys. Rev., 40, 749

Wilson, D. J., Gänsicke, B. T., Koester, D., et al. 2015, MNRAS, 451, 3237

Winget, D., & Kepler, S. 2008, ARA&A, 46, 157

Winget, D. E., Hansen, C., Liebert, J., et al. 1987, ApJ, 315, L77

Winisdoerffer, C., & Chabrier, G. 2005, Phys. Rev. E, 71, 026402

Wolff, B., Koester, D., & Liebert, J. 2002, A&A, 385, 995

Wood, M. 1990, Thèse de doctorat, University of Texas at Austin, Austin, TX

Wood, M. A. 1995, in Lecture Notes in Physics, Berlin Springer Verlag, Vol. 443, White Dwarfs, ed. D. Koester & K. Werner, 41

Woon, D. E., & Dunning, T. H. 1993, J. Chem. Phys, 98, 1358

Woon, D. E., & Dunning, T. H. 1994, J. Chem. Phys., 100, 2975

Wright, E. L., Eisenhardt, P. R. M., Mainzer, A. K., et al. 2010, AJ, 140, 1868

Xu, S., Zuckerman, B., Dufour, P., et al. 2017, ApJL, 836, L7

Zaghloul, M. R. 2009, ApJ, 699, 885

Zeidler-K.T., E. M., & Koester, D. 1982, A&A, 113, 173

Zeidler-K.T., E. M., Weidemann, V., & Koester, D. 1986, A&A, 155, 356

Zuckerman, B., & Becklin, E. E. 1987, Nature, 330, 138

Zuckerman, B., Koester, D., Dufour, P., et al. 2011, ApJ, 739, 101

Zuckerman, B., Koester, D., Melis, C., Hansen, B. M., & Jura, M. 2007, ApJ, 671, 872

Annexe A

The Montreal White Dwarf Database : A Tool for the Community

Parallèlement à mon projet de doctorat, j'ai conçu la *Montreal White Dwarf Database*. Il s'agit d'une base de données qui rassemble en un seul endroit tout ce que nous connaissons des quelque 50 000 naines blanches identifiées à ce jour. Cette base de données est accessible en ligne via une interface intuitive qui permet de visualiser l'information souhaitée sous forme de tableaux ou de graphiques. Il s'agit désormais d'un outil incontournable, utilisé par l'ensemble de la communauté. Cette annexe est une adaptation d'un compte-rendu de conférence—intitulé «The Montreal White Dwarf Database : A Tool for the Community»[1]—qui détaille les fonctionnalités de la *Montreal White Dwarf Database*.

A.1 Abstract

We present the Montreal White Dwarf Database[2] (MWDD), an accessible database with sortable/filterable tables and interactive plots that will, when fully completed, allow the community to explore the physical properties of all white dwarfs ever analyzed by the Montreal group, as well as display data and analyses from the literature. We present its current capability and show how it will continuously be updated to instantly reflect improvements made on both the theoretical and observational fronts.

A.2 Introduction

The last decade or so has seen a dramatic increase in the number of spectroscopically identified white dwarf stars, going from about 2500 at the beginning of the millennium to around 30 000 at the time of this writing. For many years, one of the most important places to look for information about white dwarf stars has been the George P. McCook and Edward M. Sion White Dwarf Catalog[3]. However, this catalog currently contains

[1] Dufour, P., Blouin, S., Coutu, S., Fortin-Archambault, M., Thibeault, C., Bergeron, P., & Fontaine, G. 2017, in ASP Conf. Ser., Vol. 509, 20th European White Dwarf Workshop, ed. P.-E. Tremblay, B. Gaensicke, & T. Marsh, 3.

[2] http://montrealwhitedwarfdatabase.org/

[3] http://www.astronomy.villanova.edu/WDCatalog/

"only" 14 294 objects (it was last updated in 2013), leaving many new SDSS white dwarfs behind. Moreover, this invaluable resource contains very little information on the physical parameters published in the literature.

As a result of the huge amount of data and analyses now available, keeping an eye on the big picture has become increasingly difficult. Many basic questions now require a tremendous amount of work just to get updated and obtain accurate answers. Questions such as : How complete is the census of white dwarfs within a given distance of the Sun ? How many have metals, are magnetic, are in binary systems, or are helium-rich ? What fraction of these are there as a function of effective temperature ? What are the properties of any given population ? What are their mass distributions, luminosity functions, etc. ? To answer those questions, one usually needs to compile all the information from the literature, double check it, look out for updates, and assess how recent data/models change the picture. This is a very time-consuming task that has to be repeated again and again as time moves forward. Even the most comprehensive efforts are practically out-of-date very soon after they are published (for the local sample, Holberg et al., 2008; Giammichele et al., 2012, come to mind).

A tool that would allow to easily get answers to those basic questions would certainly be useful to all of us. This is why we decided to make good use of the little surplus money from our organization of the previous workshop in Montreal and give it back to the community by creating this database. In what follows we present the main characteristics of MWDD as well as our vision of it in the near future.

A.3 Database description

The Montreal White Dwarf Database aims to gather in one place all the information and available data about the spectroscopically identified white dwarfs that have been discovered to this day. Interactive tables and tools to easily generate plots and display data have also been implemented (see below). The structure and philosophy behind MWDD were inspired by other databases available to the exoplanets community, such as the Open Exoplanet Catalogue[4] and the Exoplanet Orbit Database[5].

[4] http://www.openexoplanetcatalogue.com/
[5] http://exoplanets.org/

We constructed a compilation of known white dwarf stars by simply copying in spreadsheets (one .csv file per paper/source) all the information (names, magnitudes, effective temperature, surface gravity, abundances, etc.) contained in the tables of well-known papers that analyzed large samples (we also included compilations from a few review papers and websites). Since a star can be published under many different names, each star is assigned a unique identifier via SIMBAD. This allows us to automatically merge together as one entry in the database objects entered under different names in different papers. MWDD currently includes data compiled from 120 papers for a total approaching 30 000 white dwarfs. As more papers are linked to the database its degree of completeness will improve.

A.3.1 Search filters

We implemented numerous filtering options to allow anyone to quickly isolate certain types of white dwarfs of interest or do some statistics. It is currently possible to filter by numerous parameters such as coordinates, effective temperature, mass, distance and magnitude, as well as some important white dwarf characteristics such as their spectral type, surface composition, variability or magnetism. Plots, histograms, statistics and the table (see below) are automatically updated to reflect the choices made in the search filter section.

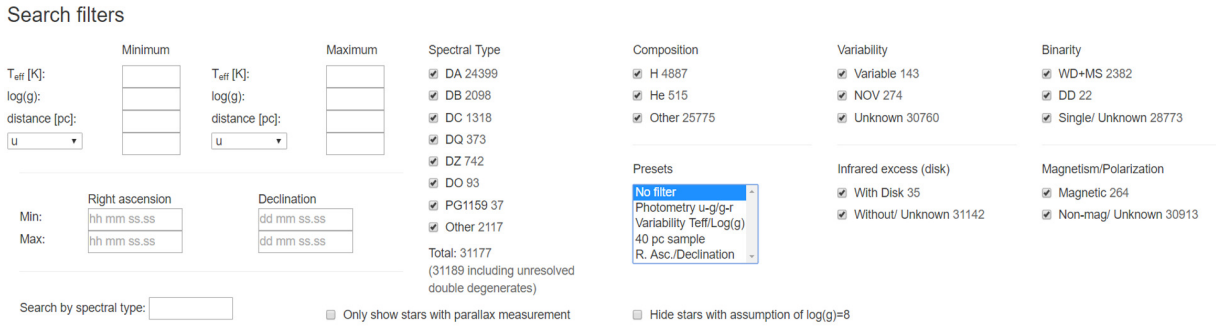

Figure A.1 – Filter interface in MWDD.

A.3.2 Table

All the properties compiled in the database can be selected and viewed via the “Table” tab. Table columns are dragable and sortable. Clicking on “Options” allow the user to

select among a long list of available parameters. One can also search by name, or enter a list of names. It is also possible to export the data of all objects that pass the filters.

The values presented in the table are the last published ones (except for a few sources which have been given lower priority). In the future, a quality flag to use what we consider the best values will be implemented. Meanwhile, we encourage users to go on the individual white dwarf page in order to view the various literature values included in the database and assess themselves which parameters are to be trusted most.

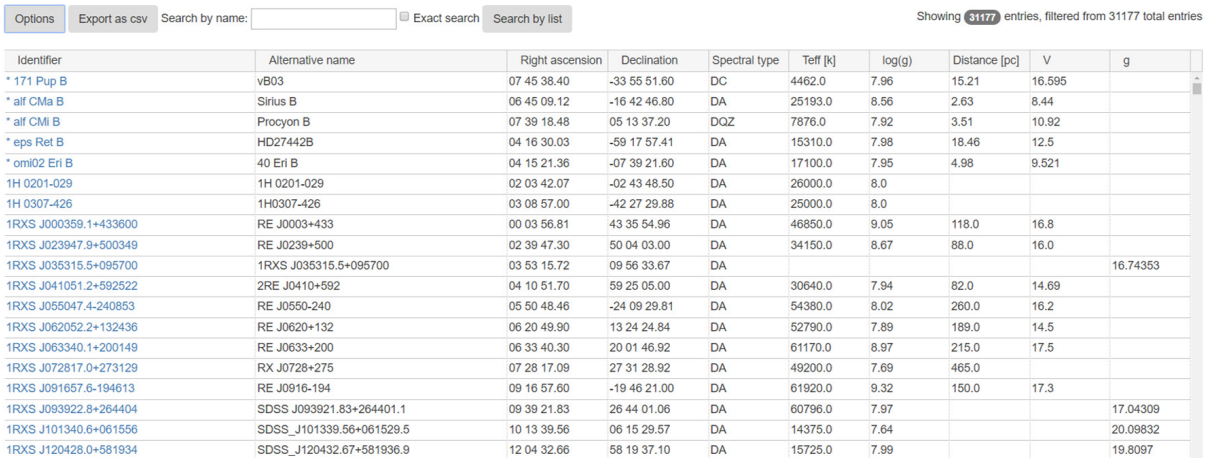
Options | Export as csv | Search by name: | Exact search | Search by list | Showing 31177 entries, filtered from 31177 total entries

Identifier	Alternative name	Right ascension	Declination	Spectral type	Teff [k]	log(g)	Distance [pc]	V	g
* 171 Pup B	vB03	07 45 38.40	-33 55 51.60	DC	4462.0	7.96	15.21	16.595	
* alf CMa B	Sirius B	06 45 09.12	-16 42 46.80	DA	25193.0	8.56	2.63	8.44	
* alf CMi B	Procyon B	07 39 18.48	05 13 37.20	DQZ	7876.0	7.92	3.51	10.92	
* eps Ret B	HD27442B	04 16 30.03	-59 17 57.41	DA	15310.0	7.98	18.46	12.5	
* omi02 Eri B	40 Eri B	04 15 21.36	-07 39 21.60	DA	17100.0	7.95	4.98	9.521	
1H 0201-029	1H 0201-029	02 03 42.07	-02 43 48.50	DA	26000.0	8.0			
1H 0307-426	1H0307-426	03 08 57.00	-42 27 29.88	DA	25000.0	8.0			
1RXS J000359.1+433600	RE J0003+433	00 03 56.81	43 35 54.96	DA	46850.0	9.05	118.0	16.8	
1RXS J023947.9+500349	RE J0239+500	02 39 47.30	50 04 03.00	DA	34150.0	8.67	88.0	16.0	
1RXS J035315.5+095700	1RXS J035315.5+095700	03 53 15.72	09 56 33.67	DA					16.74353
1RXS J041051.2+592522	2RE J0410+592	04 10 51.70	59 25 05.00	DA	30640.0	7.94	82.0	14.69	
1RXS J055047.4-240853	RE J0550-240	05 50 48.46	-24 09 29.81	DA	54380.0	8.02	260.0	16.2	
1RXS J062052.2+132436	RE J0620+132	06 20 49.90	13 24 24.84	DA	52790.0	7.89	189.0	14.5	
1RXS J063340.1+200149	RE J0633+200	06 33 40.30	20 01 46.92	DA	61170.0	8.97	215.0	17.5	
1RXS J072817.0+273129	RX J0728+275	07 28 17.09	27 31 28.92	DA	49200.0	7.69	465.0		
1RXS J091657.6-194613	RE J0916-194	09 16 57.60	-19 46 21.00	DA	61920.0	9.32	150.0	17.3	
1RXS J093922.8+264404	SDSS J093921.83+264401.1	09 39 21.83	26 44 01.06	DA	60796.0	7.97			17.04309
1RXS J101340.6+061556	SDSS_J101339.56+061529.5	10 13 39.56	06 15 29.57	DA	14375.0	7.64			20.09832
1RXS J120428.0+581934	SDSS_J120432.67+581936.9	12 04 32.66	58 19 37.10	DA	15725.0	7.99			19.8097

Figure A.2 – An example of the table interface.

A.3.3 Plots, histograms and statistics

JavaScript is used to make the numerous interactive plots and histograms in the user interface. The "Scatter Plot" tab allows to plot any physical quantity as a function of another. Only stars passing the selected filters will appear. Moving the mouse on an object highlights its basic atmospheric properties and clicking on it opens an individual white dwarf page (see below). It is possible to export the data of stars present in a plot in order to make your own plot by selecting "Show only stars visible in Scatter Plot" in the "Table" tab.

The "Histogram" tab allows, for example, to quickly get the mass distribution of selected objects or distribution of any other variable of interest. One can also easily get a measure of the current status of our census of white dwarfs within a given distance from the Sun in the "Cumulative Number" tab (see Holberg et al., 2008). For example, by clicking on "40 pc

sample" in the "Presets" options, one can see that we estimate a 50.0% completeness within that distance. These numbers are automatically updated as new papers are published and included in the database, allowing the community to get an instant picture of our neighborhood.

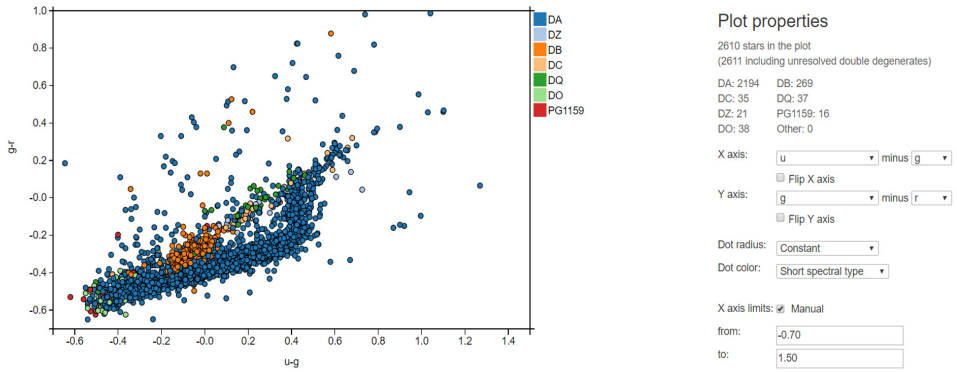

Figure A.3 – $u-g$ vs $g-r$ diagram for white dwarfs brighter than $g = 17.75$.

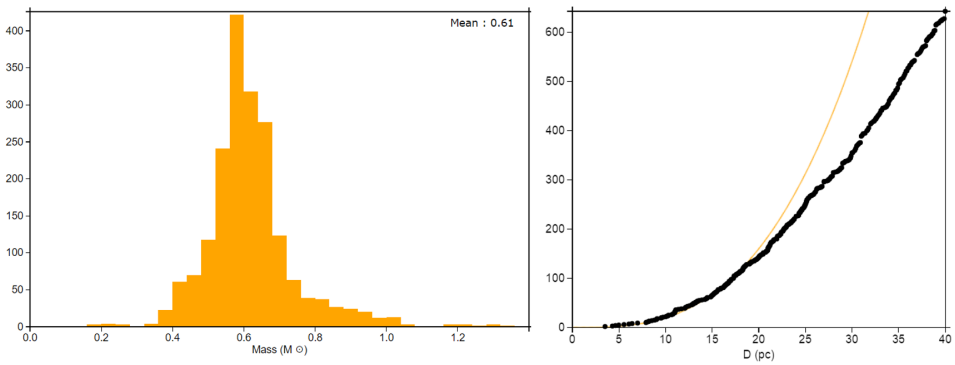

Figure A.4 – Mass distribution of DA white dwarfs (left) and cumulative number as a function of distance for all white dwarfs within 40 pc (right). The straight line represents the expected number of white dwarfs for a uniform space density of $4.8\times10^{-3}\,\mathrm{pc}^{-3}$.

A.3.4 Individual white dwarf pages

Each object in the database has an individual page (accessible via the "Table" tab, or by clicking on an object in the "Scatter Plot" tab). All the references included in the database that contain that object are listed for an easy comparison between parameters from different sources. Spectroscopic data, when available, can also be visualized interactively. This includes all SDSS spectra, IUE archive data, and many of the spectra secured

by the Montreal group over the last three decades. Optical spectra for more than 97% of the stars included in the database can currently be viewed and downloaded. We hope MWDD eventually becomes a standard repository of spectra for everyone to use. If you are in possession of worthy data and wish to share them with the community, we will be glad to link them to the database.

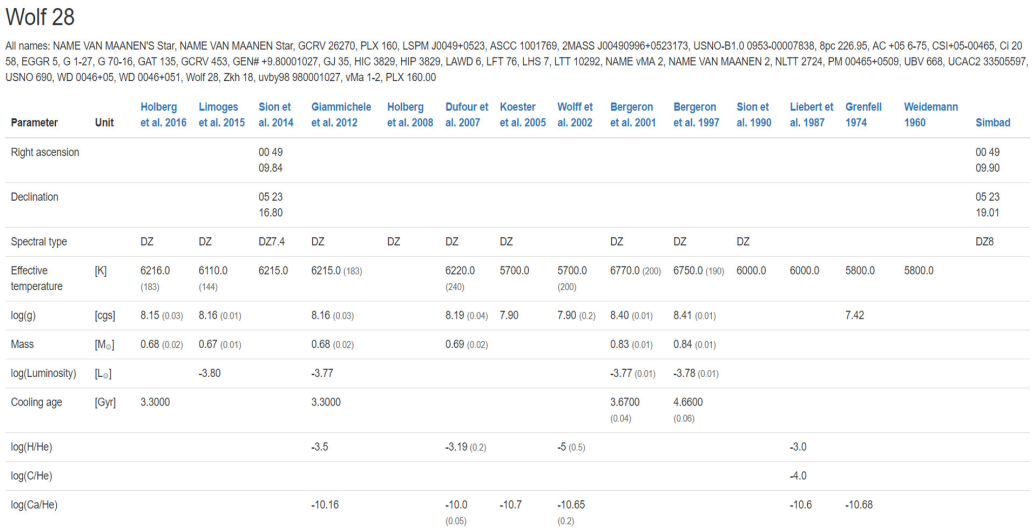

Wolf 28

All names: NAME VAN MAANEN'S Star, NAME VAN MAANEN Star, GCRV 26270, PLX 160, LSPM J0049+0523, ASCC 1001769, 2MASS J00490996+0523173, USNO-B1.0 0953-00007838, 8pc 226.95, AC +05 6-75, CSI+05-00465, Ci 20 58, EGGR 5, G 1-27, G 70-16, GAT 135, GCRV 453, GEN# +9.80001027, GJ 35, HIC 3829, HIP 3829, LAWD 6, LFT 76, LHS 7, LTT 10292, NAME vMA 2, NAME VAN MAANEN 2, NLTT 2724, PM 00465+0509, UBV 668, UCAC2 33505597, USNO 690, WD 0046+05, WD 0046+051, Wolf 28, Zkh 18, uvby98 980001027, vMa 1-2, PLX 160.00

Parameter	Unit	Holberg et al. 2016	Limoges et al. 2015	Sion et al. 2014	Giammichele et al. 2012	Holberg et al. 2008	Dufour et al. 2007	Koester et al. 2005	Wolff et al. 2002	Bergeron et al. 2001	Bergeron et al. 1997	Sion et al. 1990	Liebert et al. 1987	Grenfell 1974	Weidemann 1960	Simbad
Right ascension				00 49 09.84												00 49 09.90
Declination				05 23 16.80												05 23 19.01
Spectral type		DZ	DZ	DZ7.4	DZ	DZ	DZ	DZ		DZ	DZ	DZ				DZ8
Effective temperature	[K]	6216.0 (183)	6110.0 (144)	6215.0	6215.0 (183)		6220.0 (240)	5700.0	5700.0 (200)	6770.0 (200)	6750.0 (190)	6000.0	6000.0	5800.0	5800.0	
log(g)	[cgs]	8.15 (0.03)	8.16 (0.01)		8.16 (0.03)		8.19 (0.04)	7.90	7.90 (0.2)	8.40 (0.01)	8.41 (0.01)			7.42		
Mass	[$M_\odot$]	0.68 (0.02)	0.67 (0.01)		0.68 (0.02)		0.69 (0.02)			0.83 (0.01)	0.84 (0.01)					
log(Luminosity)	[$L_\odot$]		-3.80		-3.77					-3.77 (0.01)	-3.78 (0.01)					
Cooling age	[Gyr]	3.3000			3.3000					3.6700 (0.04)	4.6600 (0.06)					
log(H/He)					-3.5		-3.19 (0.2)		-5 (0.5)				-3.0			
log(C/He)													-4.0			
log(Ca/He)					-10.16		-10.0 (0.05)	-10.7	-10.65 (0.2)				-10.6	-10.68		

Figure A.5 – An example of an individual white dwarf page (van Maanen 2).

A.3.5 Evolutionary models and diffusion timescales

One of the most frequent requests we routinely receive concerns the white dwarf properties (mass, radius, cooling age, etc.) for a given surface gravity, temperature and composition. These numbers can now be easily accessed directly on the MWDD webpage. For pedagogical purposes, a cartoon of the white dwarf size relative to Earth also automatically appears when the user enters $\log g$ and $T_{\rm eff}$. Another frequent request concerns the diffusion timescale of heavy elements at the surface of white dwarf stars. Some 25 years after Paquette et al. (1986), we improved significantly on their calculations of diffusion coefficients by (1) using a much more accurate numerical scheme for estimating the so-called collision integrals, and (2) introducing a more physical prescription of the screening length used as the independent variable in the evaluation of these coefficients. Details of these improved calculations will be provided elsewhere. An interpolation routine allows the user

to enter $\log g$ and $T_{\rm eff}$ and obtain the settling timescales for all 27 elements from Li to Cu in the periodic table (also downloadable as a plain text file).

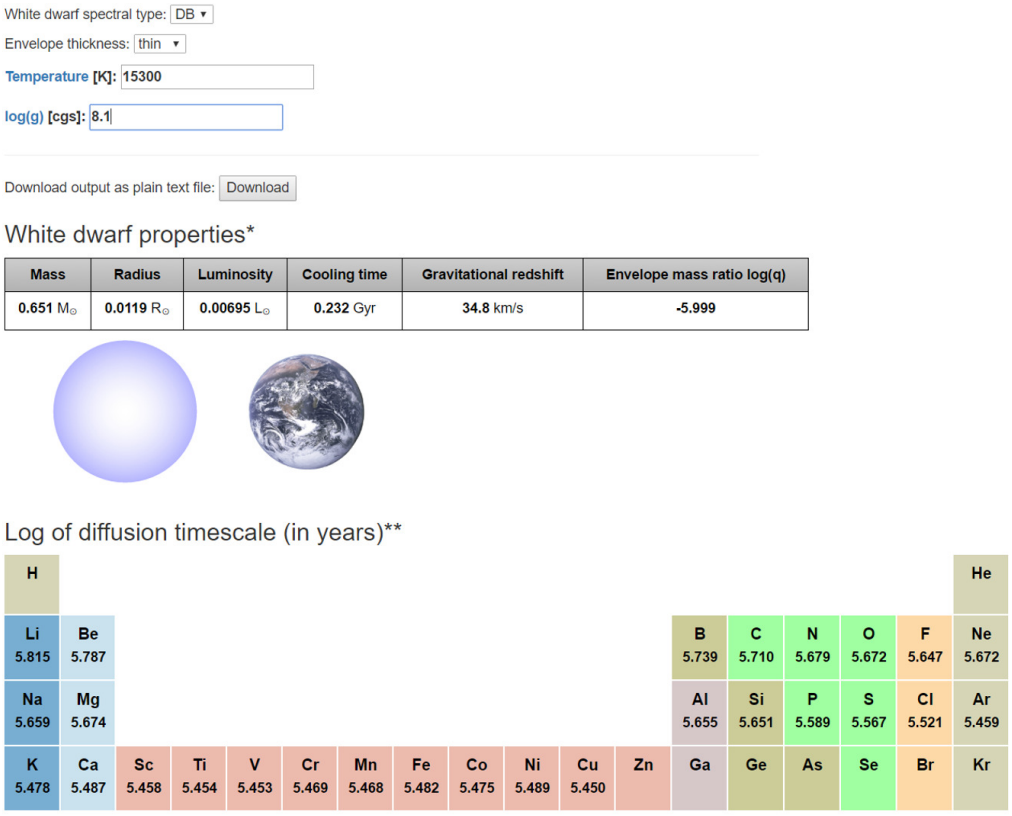

Figure A.6 – White dwarf properties and diffusion timescales.

A.3.6 What's next ?

The next step, among other things, to improve the usefulness of the database to the community will be to add the possibility to make luminosity functions and filter with the S/N ratio, wavelength range coverage and resolution of the spectroscopic observations. A comment section to discuss individual objects or general topics will also be implemented. We also plan to include our own results from model atmosphere fitting. In the near future, we will include photometric/spectroscopic fits and distance estimates for every simple object present in the database (i.e., stars that can easily be fitted with a standard grid such as single DA, DB, DC and DQ stars). The homogeneity of the analysis should allow a much clearer view of the properties of white dwarf stars in general. Moreover, once all

the data from the database will be directly linked with our fitting routines, it will be much easier to update the parameters whenever new data or new grids become available. For example, when *Gaia* parallaxes become available, it will be possible to provide instantly to the community the mass distribution of cool white dwarfs by simply adding one single file to the database (white dwarf names + parallaxes) and then running our fitting routines (which typically takes a few seconds per object). More complicated stars that stand out will then be treated accordingly and included once we are satisfied with the results.

We should stress that the database is not complete (it only includes data found in a few selected papers) and should not replace in any way a thorough search through the literature. It is nevertheless a good place to start to quickly get information about any given star. While we will periodically link data from new papers to the database, it is our hope that the members of the community will participate in our efforts to make the database as complete as possible by submitting .csv files (templates are available) for their own work or interesting papers not yet included. We welcome contributions and corrections from all professional astronomers and white dwarf aficionados.

If using MWDD was useful for your research, please cite this manuscript and include an appropriate acknowledgment, a very simple action that will help us tremendously in getting the funding necessary to maintain/improve MWDD in the future.

Acknowledgments This work was supported in part by the NSERC (Canada) and by the Fund FRQNT (Québec).

Annexe B

Données sur l'échantillon du Chapitre 9

Tableau B.1 – Données astrométriques

PSO	MWDD object ID	Gaia object Id	R.A. (J2015.5)	Decl. (J2015.5)	π (mas)
J000224.474+635745.512	2MASS J00022257+6357443	431635455820288128	0.6033724	63.9627281	38.080(0.079)
J000410.478−034008.751	PHL 2595	2447889401738675072	1.0439384	−3.6691769	21.076(0.100)
J000720.831+123018.402	WD 0004+122	2766234439302571904	1.8371872	12.5048777	57.308(0.114)
J000728.917+340342.227	NLTT 301	2875903332533220992	1.8705266	34.0618834	29.336(0.099)
J000754.487+394731.294	LP 240−30	383108338321272448	1.9774884	39.7919426	29.038(0.064)
J000935.139+310840.332	EGGR 1	2861792754354276352	2.3959624	31.1440912	18.638(0.077)
J001122.399+424038.082	GD 5	384636109728592768	2.8432990	42.6770566	42.714(0.045)
J001214.188+502514.381	GJ 1004	395234439752169344	3.0583199	50.4200515	91.983(0.029)
J001412.352−131109.057	GJ 3016	2418116963320446720	3.5508822	−13.1867135	53.812(0.070)
J001737.914−051650.624	LP 644−81	2443826805441462656	4.4082578	−5.2812190	21.405(0.153)
J002147.235+264032.448	LP 349−1	2855790657816672000	5.4467303	26.6753550	30.682(0.133)
J002214.960+423638.540	GJ 3031	385105360675267840	5.5622012	42.6105420	29.318(0.060)
J002645.591+002532.159	LBQS 0024−0042	2543511282306520832	6.6900280	−0.4256509	7.959(0.123)
J002736.859+054159.737	NLTT 1450	2555215995900584448	6.9037873	5.6997308	46.091(0.078)
J003325.772+250616.063	LP 349−41	2807462655009880320	8.3576247	25.1045070	25.962(0.089)
J003426.931+151758.962	WD 0031+150	2780524585769652736	8.6122529	15.2995149	22.341(0.099)
J004056.278−080913.497	WD 0038−084	2522401586766106624	10.2345940	−8.1540579	26.902(0.122)
J004125.624−222106.571	GJ 2012	2349916559152267008	10.3562895	−22.3522805	109.879(0.029)
J004506.415−060826.910	PHL 6585	2523840155996531456	11.2768905	−6.1417281	33.336(0.163)
J005111.307−202800.918	LHS 1158	2356519298275043200	12.7978825	−20.4674786	37.249(0.096)
J005313.605+392704.586	NLTT 2934	368075574827351168	13.3064695	39.4511147	20.903(0.079)
J005550.264−112726.361	GJ 3064	2472557872820632320	13.9593830	−11.4568671	44.573(0.037)
J005559.021+594801.879	MASTER OT J005559.13+594802.1	426122397136335872	13.9967877	59.8004595	43.781(0.070)
J005729.321+005347.980	WIRED J005729.27−005348.3	2535960553705265024	14.3722783	−0.8966980	9.747(0.165)
J010350.186+050433.459	EGGR 7	2552121179905893888	15.9594194	5.0761553	44.864(0.119)
J010456.255+211952.899	EGGR 462	2790494850219788160	16.2405193	21.3363189	30.972(0.135)
J010457.741+212011.454	EGGR 463	2790494850219788160	16.2405193	21.3363189	30.972(0.135)
J010543.124−092055.331	WD 0103−096	2473296504116465408	16.4296737	−9.3487203	14.360(0.101)
J010850.626+760018.502	LSPM J0108+7600	563004280465719040	17.2115022	76.0051610	19.490(0.086)
J011505.153−013315.894	LHS 1219	2533575369771883648	18.7719225	−1.5544325	29.394(0.113)
J011931.957−141533.389	LHS 1233	2456160271800004096	19.8829887	−14.2599527	39.416(0.102)
J012137.654+344043.058	2MASS J01213782+3440431	320029150076023808	20.4067506	34.6786361	25.693(0.117)
J012314.892−020926.687	WD 0120−024	2485211533668928640	20.8123035	−2.1574026	23.078(0.155)
J012422.339+402356.511	EGGR 517	372119985092019840	21.0937879	40.3989187	36.972(0.078)
J012524.681−260051.250	GJ 1039	5037084872486444928	21.3530733	−26.0146055	60.401(0.032)
J014545.034+291823.982	LHS 5040	302388929117252736	26.4383324	29.3066578	24.479(0.188)
J014743.832−271140.530	G 274−95	5025127443016406144	26.9325603	−27.1948318	28.314(0.057)
J014840.441+361528.181	LP 244−8	318528007466920192	27.1685082	36.2576111	28.484(0.092)
J015252.137+255341.393	WD 0150+256	297470774951165568	28.2174389	25.8948156	28.701(0.058)
J015329.141+355729.048	LSPM J0153+3557	342283089327885184	28.3715470	35.9580319	22.933(0.208)
J015441.879+140305.490	WD 0151+138	77986298173874176	28.6746909	14.0512697	16.213(0.174)
J020141.494−265037.976	LP 884−82	5024591705975610752	30.4231851	−26.8439153	21.890(0.098)
J020512.364−051749.608	WD J0205−053	2490975272405858048	31.3025313	−5.2967255	30.901(0.210)
J020615.382+183625.432	LHS 1341	92597914738232448	31.5647020	18.6071035	27.353(0.180)
J021121.900+395515.688	GJ 1042	333010327952701696	32.8426172	39.9204890	58.230(0.035)
J021148.605+711911.081	NLTT 7194	522115156720215040	32.9529482	71.3195881	36.995(0.062)
J021458.074+774555.006	2MASS J02145697+7746000	561231932144411008	33.7430491	77.7650019	25.197(0.153)
J021720.077−065628.431	LP 649−83	2486955560973911424	34.3340481	−6.9412478	22.553(0.162)
J022300.401+554426.370	2MASS J02230030+5544272	457474219590579328	35.7518491	55.7405569	25.976(0.068)
J022348.968+205548.480	PM J02238+2055	87648226538760064	35.9540579	20.9295811	26.293(0.215)
J022552.460+422800.625	WD 0222+422	339492017717622016	36.4688128	42.4667542	19.820(0.157)
J022633.136+645925.124	LHS 1405	515289392829738624	36.6390921	64.9900158	32.370(0.124)
J023141.297+270952.353	EGGR 411	127366331745660288	37.9226166	27.1647394	35.537(0.101)
J023237.925−141159.716	GJ 3162	5146358426863612160	38.1580992	−14.2006488	59.993(0.055)
J023339.034+212510.652	LP 410−52	88996326578456192	38.4127084	21.4193997	35.177(0.101)

Tableau B.1 – Données astrométriques (suite)

PSO	MWDD object ID	Gaia object Id	R.A. (J2015.5)	Decl. (J2015.5)	π (mas)
J023521.704−240053.976	WD 0233−242	5125186299678747008	38.8403052	−24.0157037	54.068(0.049)
J023521.711−225121.625	LP 830−13	5125500927507946880	38.8405974	−22.8561996	21.527(0.095)
J023759.111+163809.334	LP 410−67	81606375784491520	39.4962863	16.6355892	31.245(0.119)
J023919.953+260955.585	WD 0236+259	126342377182577408	39.8335451	26.1652149	47.952(0.063)
J024050.276+314255.267	GD 32	133116227803380224	40.2093798	31.7152680	30.226(0.071)
J024213.914+165520.195	LP 410−80	81957772828837888	40.5580862	16.9213277	23.706(0.088)
J024532.297−195133.920	LP 771−7	5128633195616949120	41.3852255	−19.8593907	31.126(0.145)
J024630.966−022729.142	GJ 1052	2495751967528809216	41.6292974	−2.4586278	46.602(0.109)
J024835.828+542317.614	GJ 3182	453562088496088320	42.1486562	54.3879146	92.034(0.041)
J024944.380+330729.037	2MASS J02494417+3307251	139623068897753856	42.4350958	33.1249170	27.999(0.085)
J025304.815+001342.702	WD 0250+000	2498159515741377152	43.2701175	0.2283601	14.682(0.165)
J025545.823+210620.174	LP 411−22	109247788869176448	43.9411311	21.1054425	20.029(0.129)
J025617.236+495439.572	LP 154−64	439494077735062144	44.0718543	49.9108250	26.566(0.094)
J025959.483+081155.692	EGGR 476	8578256576520320	44.9985298	8.1986833	33.909(0.061)
J030059.741+543235.525	2MASS J03005951+5432377	447366340472109440	45.2491849	54.5430413	20.681(0.066)
J030520.838+260310.841	LP 355−20	115409280235239296	46.3366695	26.0528851	21.359(0.214)
J030713.734−071512.018	WD 0304−074	5179920984941553408	46.8070878	−7.2536754	32.856(0.145)
J030924.869+002524.299	2MASS J03092486+0025256	3266873724451739776	47.3536426	0.4233160	23.273(0.172)
J031058.979+663357.325	2MASS J03105758+6634022	492442090962517376	47.7474241	66.5655232	26.114(0.125)
J031243.033+221825.918	LP 355−39	62311183668001664	48.1794679	22.3070507	15.742(0.105)
J031938.376+363029.887	PM J03196+3630	234469931207274112	49.9100292	36.5083068	31.202(0.107)
J032020.354+233327.088	LP 355−59	62884540326096896	50.0848802	23.5572323	25.478(0.186)
J032511.232−014926.027	GJ 3223	3261591090771914240	51.2970472	−1.8245875	59.119(0.118)
J032515.708−172231.463	LP 772−61	5105681684956745728	51.3156542	−17.3755619	18.014(0.108)
J033634.295−221526.866	LP 832−30	5088251195844051328	54.1431345	−22.2576462	26.020(0.102)
J034038.848+002946.688	2MASS J03403873−0029447	3263484003117848832	55.1619853	−0.4964177	19.622(0.130)
J034323.178+195815.625	2MASS J03432310+1958133	63126196662620416	55.8466840	19.9711414	48.140(0.062)
J034435.163+182557.644	Wolf 219	44901791432527232	56.1470694	18.4311970	53.002(0.049)
J034707.030+013842.218	WD 0344+014	3270079526697712768	56.7794475	1.6448107	49.620(0.069)
J035456.254+004410.986	WD 0352−008	3256598792586547584	58.7345117	−0.7364686	20.343(0.088)
J040026.399+081402.559	GJ 3259	3301319572621418368	60.1096019	8.2335605	53.754(0.055)
J040101.957+513120.939	2MASS J04010150+5131304	250862824946594816	60.2588489	51.5215665	39.878(0.095)
J040647.378−064436.467	WD 0404−068	3197019139399144320	61.6974834	−6.7434747	13.721(0.162)
J041017.736+195422.560	EGGR 417	48829075167625472	62.5744341	19.9058974	34.215(0.160)
J041226.558−111747.822	G 160−51	3189621320226676736	63.1109362	−11.2966267	28.493(0.051)
J041805.483+421059.576	NLTT 12934	229143725086190336	64.5228253	42.1830315	33.717(0.097)
J041920.974−093430.470	LP 714−52	3191738120628213760	64.8372974	−9.5752147	27.477(0.113)
J042553.649+121145.519	GJ 3285	3307009304776119936	66.4734625	12.1957510	62.385(0.044)
J042621.232+043223.564	GJ 3288	3283853143218651264	66.5889728	4.5393842	46.984(0.101)
J042926.378+494551.608	LSPM J0429+4945	258761510321879424	67.3599808	49.7641617	18.472(0.068)
J043200.394−192053.212	LP 775−28	2978374522004181888	68.0016698	−19.3483104	29.416(0.067)
J043329.882+041441.948	2MASS J04332980+0414477	3282093301842469376	68.3745667	4.2446700	41.157(0.086)
J043333.917−275324.912	LP 890−39	4891567154251463680	68.3918945	−27.8902661	43.008(0.062)
J043420.495+305418.826	NLTT 13519	159277625222514048	68.5853501	30.9049822	29.373(0.170)
J043645.095+270949.840	HD 283750B	151650935831913216	69.1881672	27.1636731	57.488(0.059)
J043747.606−084931.346	GJ 3306	3186021141200137472	69.4485689	−8.8263006	106.270(0.023)
J044028.432+092337.323	EGGR 419	3292685210887016192	70.1184612	9.3932519	30.774(0.083)
J044105.119−151901.469	LP 775−37	3173236054352419072	70.2714528	−15.3169699	27.060(0.071)
J045551.655+384050.251	2MASS J04555136+3840505	199060743352070528	73.9654392	38.6805723	30.873(0.171)
J050048.072−062440.883	WD 0458−064	3211353408067754368	75.2004041	−6.4115394	21.361(0.073)
J050532.333−173140.783	LP 776−52	2976789094955826560	76.3846573	−17.5282616	25.936(0.087)
J050552.605−172234.909	GJ 3329	2982808337003815040	76.4693472	−17.3758876	51.675(0.042)
J050819.108−145030.118	LP 717−1	2986577153625081344	77.0798046	−14.8420793	28.834(0.084)
J050836.610−152305.031	LP 777−3	2986473765172532864	77.1527343	−15.3842798	26.664(0.101)
J051403.315+080011.533	GJ 3339	3242153305741855744	78.5136362	8.0028866	46.630(0.059)
J051553.703+283915.520	2MASS J05155350+2839169	3422405214775411840	78.9739419	28.6542286	33.310(0.084)
J052656.411+443534.141	2MASS J05265609+4435395	208021900557436800	81.7353223	44.5924963	25.793(0.161)
J053525.054+571526.134	NLTT 15285	269226279739467904	83.8475319	57.2647436	24.340(0.152)
J053620.060+412956.109	GD 69	194394347281717504	84.0834369	41.4989386	30.993(0.039)
J054104.259+395940.128	LSR J0541+3959	190998058945380608	85.2679839	39.9942353	27.501(0.117)
J054307.203+363700.592	LSPM J0543+3637	3455921181049073280	85.7798662	36.6167596	45.006(0.043)
J054615.507+111556.787	LSPM J0546+1115	3337021260634868224	86.5645000	11.2656359	27.275(0.152)
J055119.581+001018.024	GJ 1086	3218697767783768320	87.8316594	−0.1715533	89.169(0.032)
J055509.987−041037.276	LP 658−2	3022956969731332096	88.7920210	−4.1786053	155.250(0.029)

Tableau B.1 – Données astrométriques (suite)

PSO	MWDD object ID	Gaia object Id	R.A. (J2015.5)	Decl. (J2015.5)	π (mas)
J055543.054+465041.451	WD 0551+468	1980272668510708 48	88.9293928	46.8445119	33.423(0.096)
J055900.939−041430.272	LP 659−7	3024247796382652800	89.7539219	−4.2418955	26.227(0.096)
J060231.360+155303.114	WD 0559+15	3348678699526809600	90.6309062	15.8840771	26.507(0.085)
J060236.792+090420.669	2MASS J06023672+0904237	3329569015639064192	90.6534073	9.0721644	26.876(0.098)
J060715.723+733151.212	EGGR 421	1114054838014073984	91.8150936	73.5307117	31.062(0.082)
J062048.218+064516.963	GJ 3392	3324181683539044224	95.2013053	6.7546980	41.473(0.103)
J063229.248+223002.761	2MASS J06322939+2230050	3382277296672027136	98.1217020	22.5006056	26.767(0.120)
J063629.892+405425.331	WD 0632+40	957295438016687616	99.1244886	40.9068720	25.213(0.078)
J064430.034+273110.880	2MASS J06443019+2731115	3386162214851684864	101.1250085	27.5196379	26.013(0.089)
J064721.800+023109.211	GJ 3410	3126453655659835136	101.8405195	2.5192500	55.252(0.047)
J065036.647+165751.533	2MASS J06503681+1657538	3358418684623972864	102.6525332	16.9641445	34.295(0.113)
J065326.433+640337.279	EGGR 342	1100655330324351616	103.3598675	64.0599643	35.803(0.057)
J065350.180+635553.354	G 250−27	1100267237077449728	103.4588146	63.9310771	35.956(0.057)
J070052.037+315735.908	GJ 3420	890661253803216896	105.2170615	31.9596108	50.972(0.066)
J070154.779−062757.770	GJ 261	3052844272764398208	105.4782023	−6.4666638	48.305(0.037)
J071014.089+374015.920	GJ 3431 B	946030529073021440	107.5585255	37.6708844	41.003(0.047)
J072704.270+143438.991	WD 0724+146	3166841329084630784	111.7679330	14.5773864	32.013(0.099)
J073330.974+640924.003	GJ 1098	1089400763661597440	113.3790853	64.1565119	49.974(0.047)
J074730.157+110732.567	SDSS J074730.12+110733.8	3151407827963355136	116.8757298	11.1255210	36.168(0.085)
J075026.326+174028.947	SDSS J075026.29+174029.7	668317840636534912	117.6097456	17.6745509	18.931(0.119)
J075313.399+422957.271	WD 0749+426	925532265076649472	118.3059689	42.4987692	36.469(0.170)
J075327.128+522928.170	EGGR 344	984190381489031424	118.3629592	52.4909753	45.817(0.049)
J075356.365−252359.103	2MASS J07535663−2524016	5602379190877207936	118.4844901	−25.3995219	56.123(0.080)
J075525.879+362150.851	EGGR 345	906771229452899584	118.8576701	36.3636308	24.567(0.053)
J075631.106+413945.958	WD 0753+417	922434906461782272	119.1296289	41.6626491	30.537(0.081)
J080440.637+223945.828	WD 0801+228	680099824985004288	121.1693079	22.6624052	25.278(0.139)
J080527.499+073530.748	NLTT 18922	3145802036649641472	121.3645604	7.5916004	29.062(0.135)
J080557.060+383338.445	WD 0802+387	908962109449446656	121.4868677	38.5600349	48.459(0.090)
J080648.040+221549.419	LSPM J0806+2215	677060225090183552	121.7001511	22.2635683	20.243(0.180)
J080756.012+485417.245	2MASS J08075600+4854195	934555334235313664	121.9833620	48.9046450	14.446(0.207)
J080812.648+185420.003	LP 424−13	669444943132791424	122.0525850	18.9054057	19.280(0.141)
J080940.284+111226.130	NLTT 19026	649672906567630976	122.4180409	11.2072531	19.040(0.144)
J080946.320+292031.390	GD 262	876571935709366272	122.4431754	29.3419709	30.931(0.065)
J080951.067+225053.892	2MASS J08095109+2250541	677196843705878272	122.4627521	22.8482781	18.059(0.157)
J081411.267+484526.630	WD 0810+489	931573222477949696	123.5469584	48.7571883	58.483(0.040)
J081516.954+163315.695	NLTT 19193	655808799925588992	123.8209329	16.5542376	13.978(0.211)
J081641.958+213731.315	EGGR 531	676031052142751488	124.1746854	21.6249252	25.389(0.094)
J082001.138+383432.316	EGGR 58	908364559240386944	125.0045619	38.5754316	22.406(0.087)
J082036.942+431004.142	2MASS J08203701+4310048	916276228300814976	125.1538224	43.1676928	10.866(0.138)
J082219.257+202324.964	2MASS J08221922+2023264	664021842547278592	125.5802652	20.3901335	23.299(0.110)
J083039.333+324141.361	GJ 1112	710766750855439360	127.6636659	32.6941835	44.721(0.058)
J083254.459+313902.462	LSPM J0832+3139	710452358868303232	128.2269921	31.6504783	19.533(0.147)
J083644.400+415410.862	US 1321	914985504729181568	129.1849721	41.9029925	8.437(0.126)
J084248.231−134713.555	WD 0840−136	5734737438536674432	130.7007575	−13.7871096	67.548(0.044)
J084257.516+240930.231	WD 0840+243	690287663506579328	130.7395406	24.1583478	26.182(0.105)
J084524.718+380154.023	GD 94	910341618586847232	131.3531447	38.0314800	24.801(0.073)
J084901.422+443934.262	2MASS J08490170+4439355	914211487199415680	132.2556500	44.6593981	22.111(0.329)
J084909.341+342947.937	Ton 953	716504796716020352	132.2888375	34.4966260	32.374(0.055)
J084948.563+331924.777	SDSS J084948.61+331924.9	716112442863454464	132.4523214	33.3235127	21.901(0.086)
J085140.169+162452.740	LP 426−17	611645983387812992	132.9168773	16.4144506	32.390(0.076)
J085458.584+275225.052	WD 0851+280	692904776058392064	133.7439910	27.8735436	15.195(0.183)
J085550.006+370015.667	2MASS J08554980+3700171	718682620012682112	133.9585107	37.0042787	19.093(0.132)
J085749.645+180802.235	WD 0855+183	612262122214240512	134.4568671	18.1338913	19.073(0.152)
J085830.771+412631.472	WD 0855+416	912718071240545152	134.6280896	41.4416419	26.134(0.092)
J085913.053+005844.420	LP 606−32	5764485618978306176	134.8044886	−0.9790874	54.727(0.065)
J090240.325+153555.388	LP 426−51	610411820238973056	135.6677006	15.5984705	20.820(0.234)
J090318.540+201244.329	LB 9169	636651837034002944	135.8272534	20.2121120	17.932(0.116)
J090531.867+731448.572	GJ 3529	1123700235048742016	136.3821769	73.2465610	38.886(0.073)
J091037.423+215613.422	WD 0907+221	685295640197734528	137.6560905	21.9368925	19.963(0.135)
J091244.972+195153.321	WD 0909+200	636732410620758016	138.1872713	19.8645798	29.405(0.179)
J091247.877+225153.618	LP 369−19	686867284694206336	138.1993559	22.8647516	22.160(0.247)
J091356.663+404734.285	WD 0910+410	815429197896495104	138.4858665	40.7928264	17.980(0.124)
J091554.370+532508.067	EGGR 250	1022780838737369216	138.9758064	53.4184663	97.290(0.039)
J091601.736+225947.182	2MASS J09160189+2259476	638935758908460288	139.0070733	22.9964123	18.463(0.268)

Tableau B.1 – Données astrométriques (suite)

PSO	MWDD object ID	Gaia object Id	R.A. (J2015.5)	Decl. (J2015.5)	π (mas)
J092430.651+312028.766	WD 0921+315	700531568527365376	141.1275585	31.3410381	26.392(0.282)
J092840.368+184112.020	WD 0925+189	633911196927706880	142.1683227	18.6864212	27.623(0.107)
J093340.911+291121.177	EGGR 324	696261653777188864	143.4202592	29.1890471	33.932(0.074)
J093931.267+495148.240	LSPM J0939+4951	826275295988399232	144.8796321	49.8633548	29.226(0.108)
J094316.755+513438.235	NLTT 22401	1020076452450631296	145.8200027	51.5770274	21.585(0.177)
J094346.583−070353.564	GJ 3565	3820383996887145088	145.9440002	−7.0653951	34.770(0.070)
J094534.421+015438.872	WD 0942+021	3846557660732848384	146.3934796	1.9107819	18.530(0.144)
J094621.500+325127.762	WD 0943+33	793575201703625984	146.5896735	32.8575862	22.684(0.098)
J094806.002+202315.455	LP 428−41	639665392247496576	147.0247869	20.3876214	27.237(0.191)
J094850.155+131926.151	2MASS J09485008+1319275	614379236149119360	147.2090408	13.3238235	18.246(0.211)
J095016.774+531514.490	EGGR 251	1020653077580086784	147.5695339	53.2539687	36.308(0.048)
J095021.748+150906.037	NLTT 22727	616396182856185728	147.5905408	15.1513600	25.942(0.260)
J095120.241+190009.463	WD 0948+192	627240597321087488	147.8345658	19.0023556	20.262(0.228)
J100119.459+465647.156	SDSS J100119.48+465650.6	822352371643412352	150.3310758	46.9461154	24.300(0.271)
J100204.130+432644.466	SDSS J100204.11+432645.7	808030648576069760	150.5171954	43.4456071	28.478(0.195)
J100720.864+154133.780	SDSS J100720.93+154133.6	621824987157964544	151.8368606	15.6926804	13.906(0.214)
J101141.465+284550.360	LP 315−42	740483560857296768	152.9226264	28.7633376	67.787(0.078)
J101201.471−184333.327	WD 1009−184	5669427512997660800	153.0054253	−18.7259648	55.275(0.061)
J101414.305+040137.831	2MASS J10141450+0401369	3860751256335185408	153.5594083	4.0271634	19.499(0.169)
J101436.119+422620.980	2MASS J10143597+4226228	805470233890349440	153.6506349	42.4390169	32.023(0.068)
J101501.500+080613.272	WD 1012+083B	3875651975353757440	153.7560070	8.1038054	33.546(0.311)
J101502.390+080637.662	EGGR 183	3875652014008894720	153.7596199	8.1106228	33.763(0.119)
J101535.340+185020.708	LP 429−65	624921521139276800	153.8971510	18.8389022	14.825(0.248)
J101704.973+761901.473	LP 18−535	1127701323501940224	154.2714256	76.3170013	22.000(0.059)
J101833.069−044228.789	LP 669−73	3780210350269115776	154.6376591	−4.7080193	16.550(0.154)
J101959.412+521406.822	WD 1016+524	848290091460808448	154.9976311	52.2350187	20.075(0.140)
J102210.384+461247.763	2MASS J10221035+4612491	833470465721350784	155.5432176	46.2131842	30.342(0.067)
J102234.759+460058.953	GD 117	833452873535333760	155.6445529	46.0163536	14.409(0.077)
J102251.304+390412.599	LP 212−60	755877620910173696	155.7132144	39.0699468	25.739(0.142)
J102309.572+632744.105	GJ 1133	1052520154368111872	155.7906528	63.4624807	62.729(0.024)
J102747.464+192823.959	WD 1025+197	624510170646474112	156.9473213	19.4732076	22.300(0.136)
J102907.775+112715.911	GJ 2080	3882611201058534400	157.2827855	11.4540347	29.653(0.072)
J103443.242+224548.494	WD 1032+230	721648380828681984	158.6798920	22.7634426	24.518(0.104)
J103532.475+212602.541	LSPM J1035+2126	721244821406496640	158.8850196	21.4337880	18.873(0.113)
J103658.049+711053.356	WD 1033+714	1076941716370493696	159.2355217	71.1809797	56.697(0.058)
J103855.315−204049.761	GJ 3614	3553682127126319360	159.7302162	−20.6800800	70.763(0.075)
J103954.941+380037.844	NLTT 24978	752057981939651584	159.9786771	38.0105573	12.878(0.145)
J104019.619+100359.316	PM J10403+1004	3870354528331257984	160.0816449	10.0663739	26.897(0.140)
J104153.917+141545.969	V* CY Leo	3884899559633556224	160.4748598	14.2624720	26.532(0.093)
J104447.915+194309.977	2MASS J10444792+1943108	3986646093630282112	161.1996529	19.7193714	7.784(0.136)
J104718.292+000717.423	WD 1044+003	3806529291383459456	161.8262073	0.1214514	11.854(0.179)
J104801.365+633447.084	2MASS J10480182+6334487	1055313016981775488	162.0051442	63.5796177	29.124(0.095)
J105211.523+405002.027	LP 213−79	776762672481353984	163.0478290	40.8336923	29.446(0.084)
J105349.342+242531.813	LP 373−23	3996172640334271872	163.4550922	24.4253865	23.425(0.180)
J105544.832+211104.132	LSPM J1055+2111	3988212592756945152	163.9366034	21.1843593	21.057(0.151)
J105629.925+233615.998	WD 1053+238	3989883777417007232	164.1245076	23.6042543	22.534(0.175)
J105638.557−225251.802	WD 1054−226	3549471753507182592	164.1605953	−22.8809618	27.621(0.068)
J105734.525−073122.157	LAWD 34	3763445409285757824	164.3928444	−7.5227116	81.463(0.040)
J110616.348+451854.994	2MASS J11061649+4518556	782378320745502336	166.5680205	45.3152060	24.616(0.155)
J110709.497+144655.668	WD 1104+150	3968635204109066880	166.7893193	14.7822706	26.027(0.076)
J110844.207+080137.334	PG 1106+083	3818473629793533312	167.1842984	8.0268029	26.413(0.064)
J110941.418+551226.486	2MASS J11094130+5512289	843807902246527232	167.4226853	55.2071875	27.947(0.079)
J111007.301+011043.437	WD 1107+014	3810416820902223616	167.5300303	1.1788804	20.988(0.109)
J111058.542+202606.418	WD 1108+207	3990494251184010496	167.7434672	20.4350704	35.990(0.201)
J111316.386+285903.381	WD 1110+292	3999033225988190720	168.3180415	28.9839299	19.884(0.482)
J111536.983+003313.724	2MASS J11153694+0033171	3810099989754827136	168.9041251	0.5536649	25.218(0.144)
J111640.112+062702.381	WD 1114+06	3817262208497857024	169.1667659	6.4506349	26.652(0.084)
J111930.819−103811.799	WD 1116−103	3566494186369726720	169.8783364	−10.6365350	12.892(0.115)
J112146.030+155325.732	2MASS J11214601+1553256	3967492742808436864	170.4417938	15.8904899	12.619(0.279)
J112215.702+283941.904	WD 1119+289	4022081429247669632	170.5651110	28.6615619	21.862(0.183)
J112331.433+070120.130	WD 1120+073	3817534337625985280	170.8750681	7.0247038	31.235(0.808)
J112521.167+211111.240	LP 374−46	3978862277154958592	171.3379276	21.1861479	26.161(0.092)
J113109.007+064306.428	2MASS J11310905+0643061	3910338303034941824	172.7874274	6.7184688	14.539(0.145)
J113215.317+280934.445	WD 1129+284	4018868591847502208	173.0637112	28.1595623	19.613(0.108)

Tableau B.1 – Données astrométriques (suite)

PSO	MWDD object ID	Gaia object Id	R.A. (J2015.5)	Decl. (J2015.5)	π (mas)
J113534.369+572450.561	GD 311	845973046799769984	173.8929746	57.4139342	17.103(0.047)
J113728.135+204109.010	WD 1134+209	3979070527235441792	174.3668141	20.6856741	13.255(0.161)
J114544.189+630554.734	EGGR 353	863131372427958912	176.4337685	63.0982799	41.641(0.049)
J114604.299+051401.648	WD 1143+055	3897015868534544000	176.5177655	5.2338154	15.957(0.102)
J114626.080−013642.070	WD 1143−013	3794567429507510528	176.6088934	−1.6121242	30.456(0.078)
J114735.229+300921.087	WD 1145+304	4020794214664565120	176.8966801	30.1558749	16.563(0.135)
J114904.718−292149.352	WD 1146−291	3480776843983381632	177.2698144	−29.3635458	32.230(0.110)
J114935.585+235320.393	LP 375−44	4004175916749342592	177.3980840	23.8890163	22.907(0.245)
J115038.627+034259.007	NLTT 28735	3895853993981558400	177.6608364	3.7161440	21.181(0.229)
J115052.411+683115.592	2MASS J11505233+6831161	1058284412796260480	177.7183290	68.5209264	58.513(0.026)
J115135.911−273220.489	WD 1149−272	3487220772397809536	177.8993753	−27.5389996	39.754(0.053)
J115643.568+182219.804	EGGR 85	3926968661219149184	179.1811537	18.3721244	37.450(0.072)
J115814.502+000500.689	SDSS J115814.51+000458.2	3795052348495488896	179.5603913	0.0837193	29.032(0.170)
J115916.225+484238.185	LP 170−33	786717135370412800	179.8172907	48.7105420	23.229(0.100)
J115933.001+130031.870	WD 1156+132	3919950955240152832	179.8873783	13.0088797	16.104(0.225)
J115939.211+353801.753	WD 1157+359	4031471636506212352	179.9131048	35.6336630	21.543(0.120)
J120003.043+433541.267	WD 1157+438	1537794524729363712	180.0123190	43.5947438	26.762(0.049)
J120635.803+082310.491	2MASS J12063596+0823090	3904993787466857472	181.6489501	8.3863707	16.044(0.089)
J120843.248+542945.781	SDSS J120843.31+542946.9	1573121554156399872	182.1801477	54.4959567	15.169(0.091)
J121118.777+072445.566	WD 1208+076	3904628406009296896	182.8281241	7.4123974	39.492(0.084)
J121130.013+572411.970	GJ 3710	1575357587146077056	182.8752794	57.4032008	50.103(0.034)
J121135.169+205340.438	SDSS J121135.18+205340.8	3951770649948609920	182.8964897	20.8945390	10.038(0.165)
J121235.829−062221.312	LP 674−29	3596192953212776704	183.1489794	−6.3729224	23.013(0.149)
J121432.328+782253.364	LP 20−214	1717341818608187648	183.6352163	78.3812365	30.597(0.097)
J121531.435+463014.334	PSO J183.8810+46.5039	1545050717357814272	183.8804833	46.5040214	21.962(0.100)
J122121.000+330635.639	2MASS J12212103+3306350	4016670251491467520	185.3374877	33.1099130	10.859(0.133)
J122422.760+001819.365	WIRED J122422.94−001819.5	3696633688303809664	186.0946431	−0.3054008	20.564(0.108)
J122619.639+183634.295	WD 1223+188	3947104533054775168	186.5816794	18.6094758	27.950(0.090)
J122634.852+351309.788	LHS 2559	1518943638389520384	186.6447256	35.2194111	28.700(0.113)
J122724.369+315021.737	WD 1224+321	4015547856277853824	186.8515423	31.8392058	25.818(0.090)
J122801.626+330034.312	NLTT 30811	4015951102167164032	187.0067589	33.0093155	19.188(0.192)
J122830.251+125635.668	LBQS 1225+1313	3907977484067188096	187.1260463	12.9432946	19.334(0.094)
J123150.339+145204.739	WD 1229+151	3933031020441648384	187.9598338	14.8678626	22.156(0.218)
J123448.747+054719.416	NLTT 31172	3708366954839619328	188.7029078	5.7887856	19.841(0.117)
J123512.389+231828.183	LSPM J1235+2318	3958889751516035200	188.8016789	23.3076175	14.593(0.150)
J123743.069+602322.024	2MASS J12374322+6023203	1580009552123749888	189.4293006	60.3895942	21.532(0.129)
J123751.831+415629.055	WD 1235+422	1534384148897669248	189.4656093	41.9416888	27.659(0.088)
J123913.860+452506.791	WD 1239+454	1541286711100812160	189.8072924	45.4182831	37.208(0.066)
J124023.476−231753.913	WD 1237−230	3501922067493606272	190.0971691	−23.2989038	23.849(0.075)
J124029.901+180727.367	WD 1238+183	3935942939548822272	190.1243753	18.1242321	25.385(0.136)
J124258.203+654218.514	LSPM J1242+6542	1680452683804651520	190.7422563	65.7050010	17.675(0.088)
J124452.382−105109.608	PG 1242−106	3530399693530713344	191.2179248	−10.8527352	24.805(0.043)
J124748.960−011112.138	WD 1245−009	3683627840135415808	191.9540674	−1.1869346	21.338(0.084)
J125007.330+544650.211	EGGR 536	1570514066627694336	192.5301528	54.7796517	42.051(0.107)
J125245.331+194310.385	LSPM J1252+1943	3942041105914664832	193.1887418	19.7194217	11.895(0.358)
J125411.085+362057.994	LP 267−311	1517239773324267904	193.5457658	36.3494699	35.020(0.089)
J125733.603+542850.633	WD J1257+5428	1570271658673389568	194.3898887	54.4807298	8.374(0.064)
J125804.287+501445.665	GD 321	1555883930548870400	194.5175910	50.2459930	19.964(0.059)
J130008.706+032830.355	Wolf 457	3704392873140270336	195.0358708	3.4743447	60.796(0.199)
J130020.930+013047.370	2MASS J13002125+0130453	3690395231125833600	195.0869803	1.5132333	27.716(0.118)
J130121.441+671307.704	GD 484	1679365202380970880	195.3396153	67.2188260	32.461(0.048)
J130144.036+260041.437	WD 1259+262	1460293317343353344	195.4335343	26.0114084	15.390(0.130)
J130317.094+260314.916	WD 1300+263	1459546263999675264	195.8204638	26.0542141	26.304(0.196)
J130446.151−052837.530	LP 676−58	3629758603668233728	196.1919814	−5.4771241	34.691(0.140)
J130842.398+013445.854	WD 1306+018	3691158803295816192	197.1765561	1.5793838	8.897(0.136)
J130843.338+850225.050	GJ 3768	1726678630833373824	197.1823244	85.0400767	60.723(0.036)
J131023.745+140418.781	WD 1307+143	3743905507112335616	197.5988948	14.0717393	17.922(0.064)
J131312.582+022644.647	2MASS J13131314+0226457	3691685882071367936	198.3015285	2.4455792	32.303(0.189)
J131618.994−200731.461	LHS 2710	3506567328028533120	199.0786551	−20.1254038	43.075(0.126)
J131748.947+215710.064	LSPM J1317+2157	3943650619138622848	199.4539174	21.9525764	31.507(0.074)
J131924.739−214800.750	WD 1316−215	3506061587037686144	199.8530673	−21.8005586	50.480(0.102)
J132011.397+471221.248	PB 153	1551402252435630592	200.0475247	47.2058238	12.592(0.099)
J132436.951+085752.240	WD 1322+092	3731853549706103680	201.1540493	8.9643232	17.211(0.085)
J132741.571+575508.731	EGGR 358	1566012013187728768	201.9226460	57.9192601	24.637(0.053)

Tableau B.1 – Données astrométriques (suite)

PSO	MWDD object ID	Gaia object Id	R.A. (J2015.5)	Decl. (J2015.5)	π (mas)
J132937.161−013433.029	WD 1327−013	3638457669084084224	202.4048301	−1.5760423	18.534(0.125)
J133038.022+544524.110	SDSS J133038.05+544524.4	1565012935076040832	202.6583017	54.7566116	20.708(0.049)
J133058.968+302952.520	EGGR 391	1468213546275054208	202.7451867	30.4977935	39.146(0.047)
J133250.742+011703.162	EGGR 437	3711214067185666560	203.2114315	1.2839129	24.101(0.096)
J133546.712−054256.602	WD 1333−054	3633287421812873600	203.9443710	−5.7157490	22.347(0.066)
J133630.389+362346.851	WD 1334+366	1472029470098019072	204.1262770	36.3961929	28.182(0.055)
J133651.973+372720.163	SDSS J133652.05+372720.8	1472500473391093120	204.2164325	37.4555229	23.252(0.073)
J134118.705+022735.497	SDSS J134118.68+022737.0	3713218786120541824	205.3279624	2.4597096	24.878(0.131)
J134121.453+050046.122	WD 1336+052	3714914271705535360	205.3389684	5.0128174	68.198(0.068)
J134532.753+420045.327	2MASS J13453297+4200437	1500607765872799616	206.3862496	42.0126792	26.684(0.067)
J134701.200+255256.047	NLTT 35224	1444528416543875456	206.7547443	25.8821711	15.444(0.095)
J134723.647+102136.240	EGGR 360	3725570772761744384	206.8476068	10.3599537	48.079(0.042)
J134801.746+233447.805	GJ 1179 B	1251824057289839744	207.0055637	23.5801061	84.269(0.035)
J134902.454+115506.917	WD 1346+121	3728074738695246336	207.2603003	11.9181562	35.444(0.193)
J134944.359+275522.603	G 150−43	1451566149955227520	207.4346142	27.9230085	33.329(0.053)
J135201.997+005420.119	2MASS J13520197−0054195	3659054987910568320	208.0082857	−0.9056740	14.637(0.130)
J135211.598+105349.561	NLTT 35504	3727155340815968256	208.0480455	10.8969221	28.236(0.108)
J135334.809+292857.538	SDSS J135334.86+292857.6	1452337006389928960	208.3949092	29.4826459	16.951(0.101)
J135347.019−273856.388	LP 912−27	6177179298350278016	208.4457365	−27.6491772	18.294(0.098)
J140343.526+520648.866	GD 330	1512752769450543488	210.9311138	52.1135053	23.603(0.053)
J140346.138+064442.067	WD 1401+069	3672656947473710592	210.9422910	6.7448567	20.437(0.133)
J140617.154+181247.113	LSPM J1406+1812	1245468295966061952	211.5712564	18.2128790	22.725(0.109)
J140625.514+160827.545	WD 1404+163	1231446224176456064	211.6061499	16.1409389	17.871(0.121)
J140644.407+313025.074	LP 324−69	1454347089739329152	211.6848030	31.5071528	25.358(0.181)
J141039.948+024510.269	WD 1408+029	3667514634669861120	212.6664218	2.7525846	36.086(0.101)
J141143.197+220644.803	WD 1409+223	1253353890280943104	212.9298595	22.1124131	19.016(0.123)
J141454.587+433656.944	LSPM J1414+4336	1504443450842002176	213.7270944	43.6156826	20.226(0.078)
J141558.925+433715.275	2MASS J14155889+4337160	1504453896202493568	213.9955312	43.6208422	14.706(0.112)
J141843.593+145258.108	SDSS J141843.58+145258.3	1228760220348642304	214.6815722	14.8826951	14.782(0.752)
J142006.434+532233.120	2MASS J14200627+5322351	1608061254844374784	215.0268461	53.3757245	15.757(0.053)
J142054.438−090509.261	WD 1418−088	6329136310728635776	215.2263222	−9.0859669	26.988(0.135)
J142336.667+303740.042	NLTT 37197	1284932139108595712	215.9028101	30.6276039	14.585(0.120)
J142727.816+611026.764	EGGR 362	1666378698746614528	216.8654069	61.1740659	23.283(0.060)
J142747.971+053230.563	WD 1425+057	3669936102871625600	216.9496884	5.5416466	23.928(0.091)
J142833.880+440343.831	WD 1426+442	1494157691363079168	217.1413464	44.0619752	22.277(0.064)
J143047.929+043838.453	WD 1428+048	3669065354086975872	217.6997205	4.6439877	16.295(0.122)
J143358.119+190736.216	NLTT 37753	1239213243034520192	218.4920723	19.1265675	20.236(0.201)
J143642.449+433241.327	WD 1434+437	1493367245581725184	219.1766081	43.5451188	36.856(0.072)
J144045.262+080727.089	NLTT 38058	1172780578685760512	220.1887729	8.1240184	23.572(0.193)
J144147.102+581656.252	2MASS J14414721+5816565	1616879612977156352	220.4460439	58.2822633	15.499(0.102)
J144722.038−303525.947	LP 914−20	6217739938701063808	221.8416643	−30.5906355	17.889(0.100)
J144724.377−174220.078	GJ 3866	6282457918962299776	221.8506220	−17.7058531	75.172(0.068)
J145011.700−191407.545	WD 1447−190	6281218357040987136	222.5485235	−19.2353822	20.520(0.054)
J145806.627+293722.103	EGGR 298	1281989124439286912	224.5277390	29.6222890	35.013(0.034)
J150549.155−071441.102	GD 175	6332763530870415488	226.4545730	−7.2447902	37.037(0.069)
J151625.008+280320.782	SDSS J151625.07+280320.9	1271649969930799872	229.1040763	28.0557507	21.248(0.057)
J152038.306+390351.208	LSPM J1520+3903	1388493176528426752	230.1594186	39.0643482	10.571(0.062)
J152542.833+562906.754	EGGR 489	1602197696772907648	231.4283818	56.4850960	30.922(0.054)
J152621.138+293624.753	NLTT 40234	1273685372108354176	231.5881722	29.6070417	43.128(0.051)
J153035.370+023537.655	WD 1528+027	4421098773108860928	232.6473593	2.5937482	18.560(0.084)
J153417.410+021847.134	WD 1531+024	4424031479858305408	233.5724187	2.3130068	29.583(0.085)
J153450.542+464951.710	LHS 3088	1401010605309570816	233.7102386	46.8311614	32.409(0.105)
J153505.673+124742.947	WD 1532+12	1193520666521113344	233.7734767	12.7951150	51.902(0.059)
J153553.942+212509.304	NLTT 40657	1211378350265079808	233.9746289	21.4193994	21.395(0.102)
J153904.039+581116.586	2MASS J15390421+5811158	1602106536090424832	234.7666349	58.1879723	14.017(0.095)
J154234.676+232936.602	WD 1540+236	1218051664291152000	235.6445268	23.4931195	36.023(0.067)
J154927.312+480227.403	WD 1547+481	1401366366041668224	237.3639616	48.0408194	23.847(0.068)
J155214.453+185226.905	SDSS J155214.46+185226.8	1203637376090060928	238.0601972	18.8740825	14.712(0.061)
J155533.929+502547.684	GD 353	1403348682426861568	238.8909468	50.4299047	32.701(0.046)
J155857.666+041704.388	PM J15589+0417	4425632987265111680	239.7402391	4.2844506	44.467(0.085)
J155937.372+252908.504	2MASS J15593735+2529090	1220062430539961344	239.9057222	25.4855768	18.531(0.055)
J160112.509+531703.077	WD 1559+534	1404831472640252928	240.3018558	53.2844601	26.536(0.044)
J160453.120+005512.673	EGGR 492	4411572123331402880	241.2205618	0.9200914	30.885(0.134)
J160520.416+555648.009	PSO J241.3352+55.9465	1621523537776065280	241.3346459	55.9468235	11.119(0.072)

Tableau B.1 – Données astrométriques (suite)

PSO	MWDD object ID	Gaia object Id	R.A. (J2015.5)	Decl. (J2015.5)	π (mas)
J160714.202+342343.655	WD 1605+345	1323922779935068160	241.8092256	34.3951859	29.115(0.059)
J161424.609+090559.583	LSPM J1614+0906	4452997701376633728	243.6025383	9.0994368	35.795(0.093)
J162626.179+193841.981	NLTT 42805	1201036206454896000	246.6089256	19.6451778	36.295(0.058)
J162632.170+135555.760	2MASS J16263203+1355547	4463681655863346816	246.6341116	13.9322227	17.662(0.088)
J162753.421+091210.805	GJ 1201	4452521234885949184	246.9724494	9.2024248	39.879(0.049)
J162824.563+364623.925	Ross 640	1331106782752978688	247.1015230	36.7742836	62.915(0.022)
J162838.600+705315.999	NLTT 42988	1653044367185115264	247.1608278	70.8873927	30.401(0.098)
J163233.374+085119.813	WD 1630+089	1058284412796260480	177.7183290	68.5209264	58.513(0.026)
J163332.333+523147.315	SDSS J163332.24+523149.3	1424245175791207936	248.3849247	52.5295432	19.057(0.073)
J163419.735+571024.918	WD 1633+572	1431176943768691328	248.5809770	57.1742944	67.322(0.023)
J163501.681+431733.032	PG 1633+434	1405343643196929536	248.7572925	43.2921302	68.970(0.017)
J163729.220+011000.455	SDSS J163729.22+011000.8	4384056565671592576	249.3717449	1.1667226	14.909(0.118)
J163740.613+134033.370	EGGR 259	4461228611063376128	249.4191610	13.6757448	21.913(0.070)
J163920.319+403042.216	2MASS J16392030+4030413	1355979969155873792	249.8346444	40.5117551	15.980(0.073)
J164031.981+222927.177	2MASS J16403197+2229289	1299314816353108992	250.1332725	22.4907814	14.188(0.098)
J164056.980+534107.114	GD 356	1425909733315616000	250.2372506	53.6851015	49.651(0.030)
J164136.626+151230.835	EGGR 196	4462612140287443840	250.4026189	15.2076479	31.476(0.109)
J165445.708+382932.684	WD 1653+385	1351956512512484480	253.6904627	38.4921007	36.583(0.051)
J165847.290−061710.343	WD 1656−062	4340322876499078400	254.6973976	−6.2863715	31.509(0.117)
J165935.575+442540.414	WD 1658+445	1358325021299899136	254.8978941	44.4276753	35.059(0.048)
J165939.800+320317.653	WD 1657+321	1313405848136604672	254.9155305	32.0546394	26.701(0.081)
J170246.328+102244.288	NLTT 44063	4444590625015876864	255.6930704	10.3791420	34.011(0.131)
J170401.508+200701.791	WIRED J170401.50+200700.9	4561641991506408448	256.0062775	20.1172217	19.116(0.077)
J170447.882+360845.357	WD 1703+362	1339274053906752896	256.1996730	36.1457812	23.280(0.117)
J170513.263+042343.184	2MASS J17051325+0423452	4391500847801807104	256.3052925	4.3951358	21.786(0.059)
J170807.953+025732.205	GJ 1211	4388138816124225792	257.0331369	2.9585877	55.973(0.034)
J171450.782+391839.916	WD 1713+393	1341543072245722752	258.7115992	39.3112596	25.256(0.042)
J172349.645+045845.730	PM J17238+0458	4390134326651497728	260.9568265	4.9792520	15.048(0.087)
J172818.445+021107.752	2MASS J17281847+0211101	4376680324417193472	262.0768208	2.1852763	23.003(0.074)
J173336.090+794915.945	NLTT 45205	1706631093589103872	263.4023334	79.8210531	37.239(0.081)
J174146.220+240145.262	NLTT 45288	4581383928942599296	265.4425636	24.0289209	31.668(0.058)
J174248.474+433806.596	WD 1741+436	1349256249394224128	265.7019375	43.6349758	31.826(0.068)
J174300.542+170142.511	LP 448−24	4549622027311531904	265.7519906	17.0281536	29.910(0.142)
J174707.557+285910.684	2MASS J17470830+2859098	4596322473734130304	266.7839878	28.9853712	27.354(0.082)
J174941.331+824704.308	GJ 699.1	1711005951573009792	267.4097664	82.7881794	61.159(0.016)
J175704.476+405253.312	WD 1755+408	4611543459874840832	269.2686924	40.8817978	32.300(0.073)
J175822.216+141731.058	WD 1756+143	4499839473701254400	269.5917775	14.2914031	46.959(0.055)
J180127.345+505001.780	NLTT 45830	2123432247756223488	270.3637920	50.8340005	32.334(0.076)
J180151.415+084609.344	LSPM J1801+0846	4476287041283507840	270.4643261	8.7693520	19.292(0.134)
J181331.031+324829.110	EGGR 373	4592910074976281472	273.3790807	32.8079332	22.623(0.049)
J181335.270+324841.621	EGGR 330	4592910105037219072	273.3967541	32.8114116	22.505(0.073)
J181527.531+315851.639	LP 334−22	4592623171160970112	273.8648369	31.9811337	21.805(0.102)
J181608.846+245438.131	WD 1814+24	4578913738632417920	274.0368477	24.9103126	26.564(0.061)
J181706.119+132811.013	WD 1814+134	4497414466452138496	274.2751394	13.4688057	66.070(0.051)
J181959.432+173920.273	2MASS J18195921+1739190	4523585076572785408	274.9978115	17.6556804	29.313(0.108)
J182120.071+610059.413	GJ 4054	2158285185808357504	275.3339439	61.0157101	72.919(0.027)
J183358.369+194548.662	WD 1831+19	4525569007873380736	278.4932578	19.7630165	25.427(0.052)
J185106.731+773836.627	NLTT 47202	2292861388958880640	282.7790529	77.6434640	32.896(0.068)
J185713.929+202625.343	2MASS J18571395+2026292	4518917168694695168	284.3080106	20.4399290	30.774(0.071)
J185739.691+533032.692	WD 1856+534	2146576589564898688	284.4156750	53.5090244	40.398(0.070)
J191316.499+294932.083	2MASS J19131653+2949275	2039140284770609152	288.3186969	29.8257587	26.930(0.068)
J191435.901+142820.697	GJ 2145	4320303621677848832	288.6495289	14.4721554	25.496(0.064)
J191647.498+804432.340	LSPM J1916+8044	2295446546953958272	289.1982177	80.7423968	28.226(0.121)
J191858.653+384318.615	GJ 1234	2052891361294411520	289.7444338	38.7215495	84.212(0.023)
J194002.218+834852.743	2MASS J19400895+8348579	2301882675705225472	295.0025683	83.8143006	27.940(0.153)
J194529.731+465009.911	LSR J1945+4650A	2080526555267050496	296.3736255	46.8359023	34.731(0.061)
J200535.745−105655.436	GJ 4133	4190813690536580608	301.3999688	−10.9488049	57.762(0.080)
J200655.192+614308.342	NLTT 48779	2237893023118101504	301.7302133	61.7188206	29.844(0.089)
J201355.464+064237.635	V* V1412 Aql	4249667902270614272	303.4808902	6.7099446	43.618(0.047)
J202220.821+833357.324	NLTT 49358	2302010356492847744	305.5856954	83.5661363	25.981(0.084)
J203109.399−165841.014	LP 815−31	6862687522250677376	307.7890135	−16.9780328	43.792(0.064)
J205020.293+263037.327	GJ 4166	1844125748497557632	312.5840575	26.5100277	52.346(0.050)
J205100.086−245206.115	WD 2048−250	6805808514433280000	312.7506028	−24.8685383	37.313(0.053)
J205648.322−045041.820	VB 11	6913810483611035776	314.2024568	−4.8452766	61.752(0.068)

Tableau B.1 – Données astrométriques (suite)

PSO	MWDD object ID	Gaia object Id	R.A. (J2015.5)	Decl. (J2015.5)	π (mas)
J205906.010+003348.099	2MASS J20590586−0033476	6917473674103954560	314.7751840	−0.5634312	13.092(0.131)
J205945.315+551735.433	LSPM J2059+5517	2188860027203347968	314.9391333	55.2934727	44.070(0.075)
J210202.556+191253.722	EGGR 377	1789361097242243584	315.5105493	19.2147098	30.392(0.066)
J210212.316+245739.102	WD 2059+247	1841254644460354688	315.5516784	24.9611140	35.759(0.062)
J210745.033+074042.876	PM J21077+0740	1737167215848315264	316.9376246	7.6784843	26.056(0.091)
J211050.100−212929.023	EGGR 581	6831993452567326592	317.7088466	−21.4919922	31.438(0.098)
J211329.157+072705.563	GJ 2152	1739921801713625600	318.3719130	7.4516693	34.092(0.065)
J211640.387−072455.126	WD 2114−076	6898521877506794880	319.1683645	−7.4155249	24.682(0.139)
J212042.160+581921.738	GD 548	2191146977029443584	320.1756884	58.3225563	25.757(0.037)
J212147.719−013035.307	WD 2119−017	2685959542034846464	320.4487265	−1.5100277	28.575(0.087)
J212212.288+041351.975	WD 2119+040	2693095097621419648	320.5511167	4.2306558	41.333(0.078)
J213424.400+365518.543	GD 395	1951870157081161216	323.6015331	36.9217036	25.343(0.049)
J214208.829+132843.106	EGGR 551	1767494804558717824	325.5369995	13.4785722	21.290(0.074)
J214632.643+155040.799	WD 2144+156	1772407315138035584	326.6362251	15.8447247	13.448(0.292)
J214913.617+041547.631	NLTT 52166	2696628687474414208	327.3067694	4.2630399	28.437(0.092)
J215500.756−275036.006	WD 2152−280	6617996741403360128	328.7533835	−27.8432258	42.489(0.108)
J220947.316+142950.134	EGGR 302	2735175263041913088	332.4473942	14.4975014	36.859(0.045)
J221034.377+453235.823	2MASS J22103453+4532401	1962707287281651712	332.6430628	45.5429139	27.759(0.088)
J221408.663+372708.893	EGGR 584	1955134710179436672	333.5355115	37.4518797	34.293(0.078)
J221748.096+370752.142	WD 2215+368	1907041590544054656	334.4508903	37.1312021	49.133(0.079)
J221851.326+483928.522	GD 402	1999615350008375552	334.7140389	48.6578659	25.202(0.042)
J221928.867+212222.995	BD+20 5125B	1778836056545324160	334.8707343	21.3732680	18.614(0.177)
J222740.527+175320.338	WD 2225+176	2737921155893258496	336.9190292	17.8889024	24.009(0.109)
J222802.026+120732.876	2MASS J22280206+1207334	2730508416002618752	337.0084248	12.1257386	29.471(0.086)
J222934.149+232739.619	WD 2227+232	1875613386395668864	337.3925565	23.4607666	27.360(0.209)
J223037.292+125621.531	2MASS J22303724+1256212	2730989658498251776	337.6554574	12.9392861	23.578(0.129)
J223049.491−094509.568	2MASS J22304953−0945090	2609067704606647680	337.7061799	−9.7527402	14.498(0.127)
J223056.031+152356.162	WD 2228+151	2736054627915080448	337.7339336	15.3991052	26.312(0.177)
J223402.331+554327.087	LSPM J2234+5543	2006489634151514112	338.5100577	55.7242595	18.217(0.076)
J223858.645+131303.550	2MASS J22385855+1313039	2731772377633104128	339.7444404	13.2175504	15.722(0.118)
J224104.814+364639.407	LSPM J2241+3646	1904585689586580736	340.2702408	36.7776236	19.185(0.088)
J224157.680+133234.281	2MASS J22415762+1332390	2731866347221858432	340.4903890	13.5425022	28.056(0.166)
J224946.766+362321.573	LP 289−7	1903614958258305536	342.4452813	36.3891242	22.951(0.140)
J225124.135+293946.047	GJ 1275	1884744525522874880	342.8521248	29.6629400	51.468(0.136)
J225339.217+813041.465	WD 2253+812	2286958798223194624	343.4147282	81.5115994	26.702(0.127)
J225355.149−064701.663	GJ 1276	2611561706216413696	343.4832164	−6.7847356	117.151(0.048)
J225549.954−075002.977	HD 216777B	2610488514148351360	343.9585223	−7.8341989	27.784(0.105)
J225555.991+054519.616	GJ 4305 B	2711324446359728384	343.9836486	5.7551359	40.416(0.138)
J230244.708+431247.175	2MASS J23024490+4312478	1931838292168404480	345.6860605	43.2130311	19.078(0.067)
J230538.921+433401.116	2MASS J23053906+4334038	1931870929622075008	346.4120034	43.5667145	21.203(0.149)
J230812.905+241424.726	WD 2305+239	2842462137347560320	347.0540524	24.2401036	25.209(0.151)
J231205.986+131054.970	WD 2309+129	2812250821990695936	348.0248151	13.1817015	31.403(0.115)
J231424.920−063249.681	GJ 893.1	2631876970245863552	348.6034525	−6.5473655	38.676(0.063)
J231519.254−020938.450	EGGR 554	2638553754605793408	348.8309134	−2.1605123	33.631(0.062)
J231612.797+172045.536	LP 462−12	2818727009902345600	349.0535756	17.3459279	15.232(0.141)
J231909.035−061309.035	EGGR 555	2631967439437024384	349.7870347	−6.2207237	27.613(0.284)
J231935.449−022904.088	LP 702−67	2637741490390750080	349.8977705	−2.4846637	24.096(0.097)
J232328.410+725507.872	PM J23234+7255	2228616684031896192	350.8685541	72.9188914	20.238(0.050)
J232418.827+283553.370	PM J23243+2835	2869130517001766400	351.0784050	28.5979942	25.519(0.065)
J232520.161+140341.102	WD 2322+137	2813020961166816512	351.3343144	14.0614946	42.339(0.126)
J232557.991+255219.244	EGGR 380	2841348430852439680	351.4918567	25.8716971	21.543(0.096)
J233856.534+210120.429	NLTT 57507	2826254713186397440	354.7359198	21.0225095	25.357(0.133)
J233901.088+531600.768	2MASS J23390042+5316000	1993289138054372480	354.7552676	53.2668974	23.009(0.081)
J234245.734−100122.294	WD 2340−102	2435433202010203264	355.6905655	−10.0229533	20.308(0.216)
J234314.753−165943.917	LP 823−44	2394366515727615104	355.8112715	−16.9957334	40.322(0.159)
J234612.394+115849.053	PM J23462+1158	2763719512612656000	356.5515538	11.9801887	27.546(0.104)
J234735.257+030434.827	NLTT 57978	2742789930821144320	356.8971172	3.0765152	39.739(0.077)
J234753.583+022339.475	NLTT 57996	2646617809106367360	356.9731170	2.3941352	14.379(0.274)
J234858.098+430036.913	LP 239−54	1922778419431649280	357.2422698	43.0099983	18.933(0.150)
J234954.980+293358.408	GJ 4365	2867032958053059200	357.4790099	29.5656246	47.741(0.050)
J235313.281+205115.352	WD 2350+205	2823398800448735104	358.3054531	20.8540714	17.488(0.079)
J235456.492+402723.413	EGGR 507	1921351390779081600	358.7356794	40.4559229	45.216(0.031)

Tableau B.2 – Données photométriques

PSO	Type spectral	g	r	i	z	y	J	H	K
J000224.474+635745.512	DC	17.63	16.99	16.73	16.63	16.57	15.80	15.57	15.51
J000410.478−034008.751	DA	16.91	16.75	16.73	16.76	16.79	16.12	15.89	15.44
J000720.831+123018.402	DC	16.77	16.25	16.02	15.93	15.92	15.08	15.10	14.90
J000728.917+340342.227	DC	17.61	17.23	17.12	17.05	17.08	16.39	16.25	15.83
J000754.487+394731.294	DC	17.25	16.53	16.23	16.12	16.06	15.18	14.85	14.65
J000935.139+310840.332	DC	16.81	16.74	16.85	16.94	17.01	16.45	16.19	–
J001122.399+424038.082	DA	15.42	15.27	15.23	15.28	15.31	14.54	14.35	14.39
J001214.188+502514.381	DAH	14.52	14.27	14.20	14.21	14.22	13.49	13.25	13.19
J001412.352−131109.057	DAH	16.12	15.76	15.62	15.59	15.60	14.81	14.55	14.63
J001737.914−051650.624	DA	17.91	17.52	17.35	17.32	17.27	16.48	16.35	–
J002147.235+264032.448	DC	18.09	17.44	17.18	17.09	17.02	16.18	15.91	–
J002214.960+423638.540	DA	16.75	16.35	16.21	16.17	16.18	15.34	15.12	14.94
J002645.591+002532.159	DA	17.44	17.39	17.41	17.49	17.53	16.85	16.61	–
J002736.859+054159.737	DA	16.37	15.95	15.79	15.74	15.72	14.97	14.67	14.57
J003325.772+250616.063	DA	17.10	16.81	16.70	16.70	16.71	15.96	15.71	–
J003426.931+151758.962	DA	16.98	16.81	16.77	16.80	16.82	16.08	15.94	15.52
J004056.278−080913.497	DA	17.53	17.22	17.09	17.09	17.09	16.39	16.29	–
J004125.624−222106.571	DQP	14.76	14.29	14.11	14.06	14.03	13.34	13.48	13.74
J004506.415−060826.910	DC	18.60	17.95	17.66	17.59	17.57	16.69	16.63	15.68
J005111.307−202800.918	DA	17.61	16.97	16.70	16.64	16.55	15.75	15.38	15.22
J005313.605+392704.586	DA	16.66	16.56	16.56	16.62	16.68	16.03	15.84	15.40
J005550.264−112726.361	DA	15.35	15.17	15.16	15.19	15.19	14.51	14.35	14.29
J005559.021+594801.879	DC	17.54	16.79	16.48	16.37	16.30	15.44	15.21	15.04
J005729.321+005347.980	DA	17.74	17.52	17.46	17.48	17.50	16.59	–	–
J010350.186+050433.459	DA	14.06	14.01	14.05	14.12	14.18	13.50	13.40	13.42
J010456.255+211952.899	DA	18.21	17.66	17.46	17.38	17.34	16.52	16.50	–
J010457.741+212011.454	DC	18.45	17.76	17.47	17.36	17.32	16.73	16.27	15.59
J010543.124−092055.331	DA	17.23	17.18	17.22	17.31	17.37	16.62	–	–
J010850.626+760018.502	DA	17.86	17.52	17.42	17.40	17.37	16.61	16.40	–
J011505.153−013315.894	DA	17.90	17.35	17.15	17.07	17.05	16.29	15.76	15.97
J011931.957−141533.389	DA	17.27	16.68	16.42	16.36	16.31	15.56	15.13	15.19
J012137.654+344043.058	DZ	16.75	16.65	16.67	16.75	16.80	16.13	16.15	–
J012314.892−020926.687	DA	17.69	17.31	17.15	17.13	17.12	16.46	16.30	15.57
J012422.339+402356.511	DA	17.41	16.88	16.67	16.61	16.57	15.86	15.51	15.28
J012524.681−260051.250	DC	15.13	15.01	15.00	15.06	15.13	14.44	14.31	14.33
J014545.034+291823.982	DC	18.49	17.92	17.70	17.62	17.60	16.56	16.09	–
J014743.832−271140.530	DA	16.50	16.31	16.26	16.29	16.34	15.60	15.39	15.25
J014840.441+361528.181	DA	17.08	16.75	16.66	16.65	16.66	15.86	15.48	15.42
J015252.137+255341.393	DA	15.79	15.68	15.68	15.76	15.81	15.07	15.07	15.15
J015329.141+355729.048	DA	17.20	17.06	17.04	17.10	17.11	16.53	16.01	15.74
J015441.879+140305.490	DQ	17.86	17.64	17.62	17.67	17.68	16.72	–	–
J020141.494−265037.976	DA	17.16	17.08	17.10	17.15	17.24	16.53	–	–
J020512.364−051749.608	DC	19.08	18.10	17.65	17.48	17.40	16.68	16.14	–
J020615.382+183625.432	DC	19.00	18.11	17.73	17.59	17.49	16.50	16.38	–
J021121.900+395515.688	DAZ	14.59	14.46	14.48	14.49	14.53	13.83	13.67	13.60
J021148.605+711911.081	DC	17.50	16.94	16.69	16.64	16.59	15.78	15.42	15.32
J021458.074+774555.006	DC	18.97	18.32	18.00	17.88	17.82	16.48	–	–
J021720.077−065628.431	DAZ	18.25	17.76	17.55	17.48	17.48	16.64	16.18	15.67
J022300.401+554426.370	DA	17.08	16.91	16.86	16.90	16.91	16.07	15.78	15.68
J022348.968+205548.480	DC	18.98	18.13	17.77	17.66	17.59	16.77	–	–
J022552.460+422800.625	DA	17.61	17.32	17.21	17.23	17.22	16.50	16.26	16.17
J022633.136+645925.124	DC	18.80	17.87	17.48	17.33	17.24	16.22	15.78	15.58
J023141.297+270952.353	DA	17.74	17.06	16.79	16.69	16.63	15.84	15.44	15.31
J023237.925−141159.716	DA	16.02	15.56	15.37	15.34	15.29	14.49	14.26	14.16
J023339.034+212510.652	DC	17.90	17.17	16.91	16.80	16.74	15.95	15.39	15.74
J023521.704−240053.976	DC	16.29	15.66	15.38	15.29	15.22	14.45	14.34	14.12
J023521.711−225121.625	DA	17.32	17.08	16.99	17.01	17.03	16.19	15.83	15.78
J023759.111+163809.334	DC	17.46	17.03	16.86	16.80	16.79	15.97	15.83	–
J023919.953+260955.585	DA	16.35	15.95	15.78	15.73	15.71	14.91	14.61	14.47
J024050.276+314255.267	DA	16.19	16.05	16.04	16.08	16.12	15.49	15.22	14.90
J024213.914+165520.195	DQ	17.17	16.91	16.91	16.93	16.99	16.29	16.46	–
J024532.297−195133.920	DC	18.71	17.81	17.46	17.31	17.21	16.50	16.36	–
J024630.966−022729.142	DAZ	15.63	15.43	15.40	15.42	15.45	14.68	14.59	14.48
J024835.828+542317.614	DAZ	15.72	15.10	14.87	14.74	14.69	13.87	13.54	13.47

Tableau B.2 – Données photométriques (suite)

PSO	Type spectral	g	r	i	z	y	J	H	K
J024944.380+330729.037	DA	17.37	16.98	16.82	16.78	16.78	16.01	15.49	15.39
J025304.815+001342.702	DA	17.34	17.28	17.27	17.35	17.41	17.04	16.72	–
J025545.823+210620.174	DA	17.66	17.37	17.27	17.26	17.27	16.48	16.04	16.05
J025617.236+495439.572	DA	17.43	17.10	16.97	16.96	16.96	16.17	15.79	–
J025959.483+081155.692	DAH	16.06	15.78	15.73	15.80	15.79	14.97	14.75	14.85
J030059.741+543235.525	DA	16.75	16.64	16.66	16.74	16.76	16.07	15.92	15.75
J030520.838+260310.841	DA	18.43	17.90	17.67	17.61	17.59	16.76	16.30	–
J030713.734−071512.018	DA	17.57	17.17	17.03	17.00	16.97	15.82	15.95	–
J030924.869+002524.299	DC	18.16	17.71	17.53	17.48	17.48	16.74	16.63	–
J031058.979+663357.325	DC	18.67	17.85	17.55	17.45	17.38	16.55	16.30	–
J031243.033+221825.918	DA	17.19	16.92	16.83	16.82	16.83	16.13	15.86	15.88
J031938.376+363029.887	DZ	16.46	16.32	16.38	16.48	16.53	15.84	15.84	15.38
J032020.354+233327.088	DC	18.37	17.53	17.16	17.01	16.94	16.21	15.65	15.76
J032511.232−014926.027	DAZH	16.40	15.87	15.66	15.59	15.59	14.76	14.44	14.38
J032515.708−172231.463	DA	17.30	17.13	17.09	17.13	17.12	16.67	16.11	–
J033634.295−221526.866	DAZ	17.31	16.96	16.83	16.81	16.79	16.04	15.57	–
J034038.848+002946.688	DA	17.23	17.08	17.05	17.10	17.15	16.46	16.23	–
J034323.178+195815.625	DA	15.81	15.66	15.64	15.68	15.73	14.95	14.96	15.04
J034435.163+182557.644	DQ	15.28	15.08	15.06	15.15	15.14	14.59	14.35	14.23
J034707.030+013842.218	DC	16.86	16.24	15.98	15.90	15.87	15.00	14.87	14.70
J035456.254+004410.986	DA	17.32	17.01	16.87	16.85	16.85	16.11	15.92	15.67
J040026.399+081402.559	DA	16.13	15.69	15.49	15.44	15.43	14.56	14.34	14.12
J040101.957+513120.939	DC	17.67	17.08	16.85	16.79	16.76	15.93	15.74	–
J040647.378−064436.467	DA	17.96	17.59	17.45	17.44	17.42	16.53	16.41	–
J041017.736+195422.560	DC	18.02	17.45	17.23	17.14	17.12	16.13	15.96	–
J041226.558−111747.822	DAP	15.55	15.42	15.43	15.49	15.55	14.81	14.72	14.68
J041805.483+421059.576	DA	17.54	16.95	16.72	16.63	16.60	15.70	15.36	15.61
J041920.974−093430.470	DAP	17.64	17.31	17.19	17.22	17.19	16.30	15.80	–
J042553.649+121145.519	DC	15.57	15.29	15.19	15.20	15.22	14.48	14.35	14.25
J042621.232+043223.564	DA	17.51	16.83	16.55	16.46	16.42	15.47	15.18	15.17
J042926.378+494551.608	DA	16.53	16.50	16.55	16.66	16.74	15.97	15.75	–
J043200.394−192053.212	DA	17.27	16.89	16.73	16.70	16.70	16.00	15.62	15.72
J043329.882+041441.948	DA	17.50	16.87	16.62	16.54	16.49	15.54	15.26	15.18
J043333.917−275324.912	DC	17.11	16.55	16.33	16.27	16.23	15.37	15.11	14.92
J043420.495+305418.826	DC	18.47	17.80	17.52	17.41	17.39	16.49	16.35	15.83
J043645.095+270949.840	DA	16.04	15.61	15.44	15.38	15.38	14.60	14.23	14.14
J043747.606−084931.346	DQ	13.86	13.62	13.58	13.66	13.67	13.01	12.91	12.76
J044028.432+092337.323	DA	17.09	16.81	16.71	16.71	16.73	15.94	15.58	15.58
J044105.119−151901.469	DA	17.19	16.86	16.75	16.73	16.71	15.98	15.90	15.41
J045551.655+384050.251	DA	17.95	17.38	17.14	17.06	17.03	16.14	15.85	15.32
J050048.072−062440.883	DA	16.70	16.61	16.61	16.68	16.72	16.01	15.99	15.39
J050532.333−173140.783	DA	17.39	17.11	17.00	16.99	16.98	16.32	16.00	15.75
J050552.605−172234.909	DAH	16.25	15.78	15.57	15.51	15.50	14.74	14.41	14.40
J050819.108−145030.118	DQ	17.55	17.04	16.88	16.86	16.83	16.20	16.11	–
J050836.610−152305.031	DA	18.12	17.59	17.36	17.32	17.23	16.47	16.06	–
J051403.315+080011.533	DA	16.02	15.80	15.72	15.74	15.75	15.11	14.92	14.86
J051553.703+283915.520	DAH	16.68	16.41	16.34	16.34	16.36	15.66	15.31	15.27
J052656.411+443534.141	DC	18.66	17.93	17.64	17.52	17.45	16.50	16.43	15.85
J053525.054+571526.134	DC	17.96	17.38	17.11	16.97	16.90	16.46	–	–
J053620.060+412956.109	DA	14.82	14.70	14.71	14.75	14.79	14.09	13.94	13.82
J054104.259+395940.128	DA	17.63	17.25	17.12	17.11	17.09	16.35	16.20	15.73
J054307.203+363700.592	DAZ	15.83	15.58	15.50	15.51	15.51	14.78	14.60	14.51
J054615.507+111556.787	DC :	18.26	17.66	17.39	17.30	17.25	16.33	16.08	15.63
J055119.581+001018.024	DQ	14.77	14.40	14.35	14.39	14.44	13.73	13.68	13.71
J055509.987−041037.276	DZ	14.85	14.22	13.96	13.86	13.84	13.05	12.86	12.78
J055543.054+465041.451	DA	17.53	16.98	16.75	16.68	16.62	15.71	15.46	15.51
J055900.939−041430.272	DA	17.30	16.99	16.88	16.87	16.88	16.11	15.95	–
J060231.360+155303.114	DA	16.95	16.78	16.75	16.78	16.80	16.06	15.93	15.85
J060236.792+090420.669	DA	17.17	16.84	16.72	16.69	16.70	15.95	15.54	–
J060715.723+733151.212	DA	17.28	17.05	16.96	16.98	16.98	16.20	16.16	–
J062048.218+064516.963	DA	16.60	16.23	16.09	16.06	16.05	15.38	15.02	14.96
J063229.248+223002.761	DA	17.67	17.23	17.05	17.00	16.98	16.12	15.81	–
J063629.892+405425.331	DA	16.80	16.71	16.75	16.82	16.88	16.06	16.11	15.76
J064430.034+273110.880	DA	17.15	16.98	16.94	16.96	17.03	16.23	16.75	–

Tableau B.2 – Données photométriques (suite)

PSO	Type spectral	g	r	i	z	y	J	H	K
J064721.800+023109.211	DA	15.78	15.64	15.61	15.65	15.66	14.87	14.76	14.58
J065036.647+165751.533	DA	17.70	17.14	16.93	16.86	16.83	16.14	15.73	15.31
J065326.433+640337.279	DA	16.84	16.48	16.35	16.33	16.32	15.53	15.41	15.33
J065350.180+635553.354	DA	16.60	16.27	16.15	16.14	16.13	15.28	15.10	14.91
J070052.037+315735.908	DA	16.97	16.32	16.03	15.93	15.90	15.03	14.67	14.66
J070154.779−062757.770	DA	15.57	15.33	15.26	15.25	15.27	14.54	14.22	14.36
J071014.089+374015.920	DQ	15.71	15.54	15.54	15.59	15.65	15.06	14.78	14.83
J072704.270+143438.991	DA	17.09	16.69	16.53	16.50	16.50	15.71	15.27	15.18
J073330.974+640924.003	DAP	16.54	15.97	15.75	15.68	15.64	14.81	14.52	14.38
J074730.157+110732.567	DA	16.74	16.69	16.72	16.82	16.86	16.10	15.77	15.64
J075026.326+174028.947	DA	17.29	17.12	17.10	17.11	17.15	16.84	16.32	15.74
J075313.399+422957.271	DC	17.98	17.19	16.88	16.78	16.71	15.72	15.80	–
J075327.128+522928.170	DC	15.66	15.58	15.60	15.69	15.76	15.08	15.25	15.08
J075356.365−252359.103	DA	16.64	16.02	15.76	15.68	15.62	14.75	14.47	14.30
J075525.879+362150.851	DA	16.15	16.07	16.10	16.15	16.21	15.58	15.44	15.88
J075631.106+413945.958	DA	16.85	16.68	16.63	16.66	16.67	15.99	15.84	15.89
J080440.637+223945.828	DZ	18.16	17.61	17.41	17.36	17.28	16.88	–	–
J080527.499+073530.748	DA	17.83	17.34	17.14	17.10	17.07	16.24	15.96	15.59
J080557.060+383338.445	DA	17.22	16.58	16.31	16.22	16.18	15.34	15.19	14.90
J080648.040+221549.419	DA	18.13	17.75	17.60	17.57	17.57	16.73	16.56	–
J080756.012+485417.245	DA	18.25	18.03	17.95	17.98	17.98	16.66	–	–
J080812.648+185420.003	DA	18.17	17.76	17.60	17.56	17.55	16.82	16.36	–
J080940.284+111226.130	DZ	17.71	17.54	17.54	17.58	17.63	16.74	–	–
J080946.320+292031.390	DA	16.26	16.10	16.07	16.11	16.15	15.41	15.39	15.34
J080951.067+225053.892	DA	17.82	17.59	17.54	17.56	17.59	16.53	–	–
J081411.267+484526.630	DC	15.16	14.97	14.94	14.98	15.01	14.32	14.13	14.06
J081516.954+163315.695	DC	18.87	18.15	17.85	17.75	17.66	16.78	16.14	15.67
J081641.958+213731.315	DA	17.14	16.86	16.74	16.74	16.73	15.94	15.84	15.96
J082001.138+383432.316	DA	16.58	16.48	16.49	16.56	16.60	16.07	15.83	15.58
J082036.942+431004.142	DA	17.66	17.47	17.45	17.48	17.49	16.66	–	–
J082219.257+202324.964	DC	16.27	16.14	16.16	16.22	16.29	15.62	15.48	15.38
J083039.333+324141.361	DA	15.81	15.69	15.67	15.71	15.76	14.98	14.96	14.87
J083254.459+313902.462	DA	17.99	17.71	17.55	17.53	17.55	16.77	–	–
J083644.400+415410.862	DA	17.45	17.36	17.39	17.45	17.48	16.84	16.57	–
J084248.231−134713.555	DZ	16.00	15.54	15.42	15.40	15.41	14.62	14.41	14.54
J084257.516+240930.231	DA	17.39	17.03	16.88	16.86	16.85	15.99	15.92	15.60
J084524.718+380154.023	DA	16.05	16.00	16.02	16.12	16.16	15.49	15.45	15.43
J084901.422+443934.262	DC	17.93	17.63	17.52	17.51	17.50	16.28	–	–
J084909.341+342947.937	DA	15.73	15.62	15.61	15.69	15.73	15.04	14.83	14.90
J084948.563+331924.777	DA	16.58	16.48	16.50	16.56	16.60	15.88	15.85	15.75
J085140.169+162452.740	DC	16.92	16.59	16.48	16.49	16.50	15.75	15.69	15.70
J085458.584+275225.052	DA	17.70	17.52	17.46	17.48	17.53	16.50	–	–
J085550.006+370015.667	DA	17.92	17.48	17.29	17.25	17.23	16.51	16.18	15.85
J085749.645+180802.235	DA	17.35	17.14	17.09	17.14	17.12	16.42	16.08	–
J085830.771+412631.472	DAH	17.03	16.87	16.87	16.93	16.96	16.16	–	15.73
J085913.053+005844.420	DC	16.68	16.08	15.83	15.74	15.71	14.83	14.58	14.69
J090240.325+153555.388	DC	18.40	17.66	17.34	17.24	17.18	16.23	16.09	–
J090318.540+201244.329	DA	17.07	16.92	16.91	16.97	16.98	16.27	16.19	15.86
J090531.867+731448.572	DC	17.28	16.73	16.51	16.43	16.40	15.56	15.27	15.13
J091037.423+215613.422	DA	17.61	17.24	17.07	17.05	17.02	16.31	16.11	16.03
J091244.972+195153.321	DA	18.06	17.46	17.23	17.15	17.13	16.06	15.90	15.80
J091247.877+225153.618	DC	18.70	18.09	17.83	17.74	17.67	16.75	16.55	15.99
J091356.663+404734.285	DA	17.40	17.18	17.14	17.18	17.20	16.40	16.11	–
J091554.370+532508.067	DCP	13.94	13.86	13.87	13.92	14.00	13.31	13.21	13.13
J091601.736+225947.182	DAH	18.50	18.11	17.96	17.95	17.92	16.91	–	–
J092430.651+312028.766	DC	18.62	17.93	17.65	17.55	17.50	16.47	15.97	–
J092840.368+184112.020	DA	16.66	16.58	16.59	16.68	16.72	15.99	16.27	15.68
J093340.911+291121.177	DA	16.02	15.97	16.02	16.12	16.19	15.59	15.40	15.28
J093931.267+495148.240	DA	17.54	17.22	17.10	17.11	17.09	16.20	16.28	–
J094316.755+513438.235	DC	18.80	18.11	17.83	17.73	17.69	16.68	16.60	–
J094346.583−070353.564	DA	16.59	16.26	16.14	16.13	16.12	15.37	15.02	14.99
J094534.421+015438.872	DA	17.41	17.24	17.21	17.24	17.28	16.56	16.12	–
J094621.500+325127.762	DA	17.27	17.06	17.00	17.03	17.04	16.39	15.97	15.85
J094806.002+202315.455	DC	18.43	17.76	17.49	17.38	17.34	16.62	16.26	15.74

Tableau B.2 – Données photométriques (suite)

PSO	Type spectral	g	r	i	z	y	J	H	K
J094850.155+131926.151	DA	17.48	17.27	17.22	17.25	17.27	16.47	16.09	–
J095016.774+531514.490	DQ	15.18	15.18	15.27	15.40	15.48	14.91	14.89	14.92
J095021.748+150906.037	DC	17.85	17.39	17.20	17.15	17.12	16.16	15.95	–
J095120.241+190009.463	DC	18.06	17.68	17.53	17.49	17.51	16.70	16.36	–
J100119.459+465647.156	DC	19.13	18.30	17.94	17.84	17.75	16.73	16.23	–
J100204.130+432644.466	DC	18.45	17.72	17.45	17.35	17.27	16.38	–	–
J100720.864+154133.780	DA	17.68	17.56	17.54	17.61	17.64	16.64	–	–
J101141.465+284550.360	DQPH	18.26	16.40	15.97	16.00	16.01	15.12	14.72	14.54
J101201.471−184333.327	DZ	15.56	15.33	15.29	15.34	15.39	14.68	14.52	14.31
J101414.305+040137.831	DA	16.81	16.73	16.71	16.78	16.86	15.91	15.76	15.53
J101436.119+422620.980	DA	16.36	16.27	16.28	16.36	16.41	15.67	15.50	15.28
J101501.500+080613.272	DC	18.21	17.43	17.12	17.01	16.95	16.06	15.98	15.22
J101502.390+080637.662	DA	16.14	15.93	15.88	15.89	15.92	15.25	15.13	14.96
J101535.340+185020.708	DC	19.24	18.47	18.15	18.02	17.93	16.73	–	–
J101704.973+761901.473	DA	16.87	16.68	16.67	16.72	16.76	16.09	15.65	–
J101833.069−044228.789	DAZ	17.15	17.07	17.10	17.18	17.25	16.54	16.36	–
J101959.412+521406.822	DA	18.42	17.94	17.75	17.68	17.65	16.81	16.69	–
J102210.384+461247.763	DA	16.39	16.26	16.24	16.29	16.32	15.55	15.46	15.56
J102234.759+460058.953	DA	16.73	16.62	16.65	16.73	16.78	16.12	16.14	15.77
J102251.304+390412.599	DZ	17.53	17.28	17.25	17.28	17.32	16.70	–	–
J102309.572+632744.105	DA	14.83	14.62	14.57	14.62	14.65	13.87	13.73	13.69
J102747.464+192823.959	DA	17.38	17.23	17.23	17.26	17.27	16.42	16.45	–
J102907.775+112715.911	DAH	16.72	16.53	16.50	16.55	16.58	15.90	15.55	–
J103443.242+224548.494	DZ	16.64	16.57	16.68	16.81	16.87	16.24	16.41	–
J103532.475+212602.541	DAH	17.38	17.22	17.18	17.24	17.26	16.50	16.83	–
J103658.049+711053.356	DC	17.28	16.56	16.27	16.19	16.12	15.19	14.84	14.98
J103855.315−204049.761	DQP	16.62	15.75	15.72	15.71	15.65	14.63	14.35	14.04
J103954.941+380037.844	DA	17.99	17.83	17.81	17.86	17.88	16.92	–	–
J104019.619+100359.316	DC	17.39	17.08	16.98	16.98	16.99	16.01	16.34	–
J104153.917+141545.969	DC	16.59	16.48	16.49	16.57	16.63	15.82	15.75	15.68
J104447.915+194309.977	DA	17.58	17.51	17.52	17.57	17.64	16.86	16.75	–
J104718.292+000717.423	DC	17.43	17.30	17.31	17.37	17.40	16.61	16.40	–
J104801.365+633447.084	DA	17.83	17.29	17.08	17.02	16.96	16.13	15.80	15.50
J105211.523+405002.027	DC	16.96	16.69	16.64	16.61	16.67	16.11	15.53	–
J105349.342+242531.813	DA	17.96	17.59	17.46	17.43	17.43	16.76	16.34	–
J105544.832+211104.132	DAH	17.80	17.49	17.39	17.38	17.39	16.62	–	–
J105629.925+233615.998	DA	18.31	17.78	17.57	17.50	17.46	16.52	16.57	–
J105638.557−225251.802	DA	16.09	16.02	16.01	16.09	16.14	15.52	15.40	15.94
J105734.525−073122.157	DC	14.39	14.29	14.31	14.38	14.45	13.77	13.68	13.48
J110616.348+451854.994	DA	16.97	16.86	16.87	16.95	17.00	16.24	15.96	15.86
J110709.497+144655.668	DA	16.75	16.54	16.47	16.49	16.53	15.75	15.47	15.42
J110844.207+080137.334	DA	16.18	16.09	16.10	16.15	16.21	15.63	15.36	15.24
J110941.418+551226.486	DA	17.27	17.11	17.07	17.14	17.16	16.25	16.40	–
J111007.301+011043.437	DC	17.63	17.42	17.41	17.45	17.51	16.60	–	–
J111058.542+202606.418	DC	18.03	17.33	17.05	16.90	16.85	15.98	15.53	15.56
J111316.386+285903.381	DA	18.40	17.72	17.45	17.37	17.31	16.33	15.81	–
J111536.983+003313.724	DA	17.84	17.25	17.02	16.91	16.84	15.80	15.65	15.59
J111640.112+062702.381	DA	16.89	16.63	16.55	16.57	16.56	15.70	15.60	15.52
J111930.819−103811.799	DA	16.65	16.51	16.50	16.55	16.59	15.90	15.76	15.41
J112146.030+155325.732	DA	17.80	17.68	17.69	17.75	17.79	16.63	–	–
J112215.702+283941.904	DA	18.20	17.81	17.63	17.61	17.59	16.52	–	–
J112331.433+070120.130	DC	18.07	17.24	16.86	16.74	16.62	15.96	15.55	–
J112521.167+211111.240	DC	17.17	16.89	16.82	16.84	16.86	16.24	16.18	15.65
J113109.007+064306.428	DA	17.34	17.23	17.25	17.32	17.36	16.71	16.19	–
J113215.317+280934.445	DAH	17.01	16.91	16.92	16.98	17.05	16.46	16.12	–
J113534.369+572450.561	DQ	16.48	16.40	16.47	16.55	16.62	16.02	15.89	15.89
J113728.135+204109.010	DA	17.47	17.37	17.38	17.46	17.52	16.55	16.43	–
J114544.189+630554.734	DA	16.62	16.17	16.01	15.95	15.91	15.12	14.85	14.68
J114604.299+051401.648	DA	17.02	16.81	16.74	16.77	16.80	16.02	16.01	–
J114626.080−013642.070	DA	16.48	16.28	16.24	16.22	16.25	15.54	15.38	15.18
J114735.229+300921.087	DC	17.81	17.64	17.64	17.69	17.74	16.82	–	–
J114904.718−292149.352	DA	17.56	17.17	17.03	17.00	17.00	16.04	15.74	–
J114935.585+235320.393	DC	18.55	17.95	17.69	17.62	17.59	16.43	15.99	–
J115038.627+034259.007	DA	17.93	17.58	17.42	17.40	17.42	16.50	–	–

Tableau B.2 – Données photométriques (suite)

PSO	Type spectral	g	r	i	z	y	J	H	K
J115052.411+683115.592	DA	15.37	15.15	15.11	15.13	15.15	14.46	14.22	14.22
J115135.911−273220.489	DQ	15.95	15.73	15.73	15.77	15.80	15.17	14.92	14.77
J115643.568+182219.804	DC	15.67	15.60	15.63	15.72	15.80	15.10	15.22	15.09
J115814.502+000500.689	DC	18.72	17.86	17.52	17.40	17.34	16.72	15.99	–
J115916.225+484238.185	DA	17.68	17.32	17.19	17.17	17.17	16.47	15.96	16.08
J115933.001+130031.870	DQP	18.18	17.76	17.70	17.80	17.91	16.95	–	–
J115939.211+353801.753	DA	17.45	17.35	17.34	17.41	17.43	16.55	–	–
J120003.043+433541.267	DA	15.82	15.76	15.80	15.86	15.93	15.20	15.20	15.32
J120635.803+082310.491	DA	16.99	16.95	16.99	17.07	17.15	16.59	15.88	–
J120843.248+542945.781	DA	17.27	17.21	17.23	17.31	17.38	16.63	16.55	–
J121118.777+072445.566	DA	17.07	16.54	16.31	16.26	16.23	15.37	15.09	15.10
J121130.013+572411.970	DA	15.97	15.60	15.48	15.48	15.46	14.68	14.36	14.46
J121135.169+205340.438	DA	17.75	17.55	17.48	17.53	17.53	16.74	–	15.88
J121235.829−062221.312	DA	17.20	16.92	16.83	16.84	16.88	16.02	15.68	15.50
J121432.328+782253.364	DZ	18.05	17.38	17.12	17.03	17.00	16.18	15.65	15.64
J121531.435+463014.334	DA	17.25	17.03	16.98	17.01	17.01	16.18	–	–
J122121.000+330635.639	DA	17.99	17.89	17.91	17.99	18.03	16.71	–	–
J122422.760+001819.365	DA	17.51	17.27	17.19	17.21	17.23	16.57	16.35	15.51
J122619.639+183634.295	DC	16.36	16.29	16.33	16.40	16.50	15.83	15.46	15.68
J122634.852+351309.788	DA	17.78	17.20	16.95	16.91	16.85	15.86	16.15	–
J122724.369+315021.737	DA	16.83	16.59	16.52	16.53	16.55	15.89	15.50	15.49
J122801.626+330034.312	DC	18.78	17.97	17.65	17.53	17.49	16.70	16.16	16.01
J122830.251+125635.668	DA	17.00	16.86	16.87	16.92	16.95	16.29	16.15	15.88
J123150.339+145204.739	DA	18.36	17.99	17.84	17.81	17.77	16.92	–	–
J123448.747+054719.416	DA	17.44	17.32	17.34	17.40	17.45	16.60	16.23	15.34
J123512.389+231828.183	DA	17.36	17.26	17.28	17.34	17.41	16.85	16.50	15.91
J123743.069+602322.024	DA	18.40	17.88	17.68	17.62	17.62	16.65	15.99	–
J123751.831+415629.055	DQ	17.79	17.09	16.85	16.93	16.97	16.55	16.50	–
J123913.860+452506.791	DA	16.63	16.37	16.30	16.31	16.31	15.60	15.20	–
J124023.476−231753.913	DA	16.76	16.35	16.18	16.12	16.11	15.35	15.08	14.94
J124029.901+180727.367	DA	17.89	17.43	17.24	17.20	17.15	16.59	15.93	15.79
J124258.203+654218.514	DA	17.65	17.43	17.37	17.39	17.40	16.55	–	–
J124452.382−105109.608	DA	14.77	14.71	14.74	14.83	14.89	14.23	14.07	14.08
J124748.960−011112.138	DA	16.97	16.81	16.77	16.83	16.86	16.06	15.96	15.74
J125007.330+544650.211	DC	18.34	17.30	16.84	16.68	16.62	15.79	15.66	15.40
J125245.331+194310.385	DQ	17.77	17.63	17.62	17.67	17.72	16.78	–	–
J125411.085+362057.994	DC	17.82	17.12	16.84	16.74	16.78	15.90	15.72	15.40
J125733.603+542850.633	DA	16.83	16.74	16.76	16.80	16.83	16.30	15.73	–
J125804.287+501445.665	DA	16.60	16.57	16.62	16.71	16.78	16.37	16.12	15.62
J130008.706+032830.355	DA	16.05	15.63	15.47	15.42	15.43	14.65	14.32	14.22
J130020.930+013047.370	DA	17.77	17.25	17.05	17.00	16.97	16.23	15.97	–
J130121.441+671307.704	DA	16.66	16.44	16.38	16.41	16.42	15.62	15.32	15.34
J130144.036+260041.437	DA	17.75	17.56	17.52	17.54	17.56	16.93	16.18	–
J130317.094+260314.916	DC	19.24	18.35	17.98	17.83	17.76	16.80	16.40	–
J130446.151−052837.530	DA	17.49	16.95	16.73	16.67	16.63	15.83	15.55	15.48
J130842.398+013445.854	DA	17.20	17.15	17.15	17.24	17.31	16.60	–	–
J130843.338+850225.050	DAP	16.31	15.76	15.58	15.52	15.49	14.69	14.46	14.34
J131023.745+140418.781	DA	16.41	16.36	16.43	16.53	16.61	15.84	15.89	–
J131312.582+022644.647	DC	18.72	17.83	17.44	17.28	17.25	16.30	16.01	–
J131618.994−200731.461	DZ	17.47	16.93	16.77	16.71	16.68	15.88	15.61	15.55
J131748.947+215710.064	DC	16.94	16.69	16.63	16.66	16.69	16.03	15.79	–
J131924.739−214800.750	DA	16.90	16.54	16.39	16.36	16.34	15.56	15.33	15.09
J132011.397+471221.248	DA	17.58	17.50	17.52	17.61	17.66	16.78	–	–
J132436.951+085752.240	DA	16.64	16.60	16.64	16.74	16.82	16.18	16.17	15.81
J132741.571+575508.731	DA	16.78	16.61	16.55	16.60	16.58	15.95	15.70	15.72
J132937.161−013433.029	DA	17.20	17.08	17.04	17.09	17.13	16.43	16.20	–
J133038.022+544524.110	DA	16.87	16.77	16.77	16.84	16.89	16.16	15.91	15.44
J133058.968+302952.520	DZH	16.21	15.89	15.94	16.08	16.12	15.40	15.28	15.41
J133250.742+011703.162	DAH	17.12	16.96	16.94	16.98	17.03	16.40	16.30	–
J133546.712−054256.602	DA	16.35	16.27	16.30	16.38	16.45	15.61	15.48	15.35
J133630.389+362346.851	DA	16.47	16.29	16.25	16.27	16.29	15.55	15.34	15.31
J133651.973+372720.163	DA	17.07	16.97	16.99	17.07	17.12	16.51	16.33	–
J134118.705+022735.497	DQ	17.93	17.32	17.17	17.18	17.18	16.50	–	–
J134121.453+050046.122	DC	17.26	16.30	15.88	15.72	15.64	14.70	14.59	14.48

Tableau B.2 – Données photométriques (suite)

PSO	Type spectral	g	r	i	z	y	J	H	K
J134532.753+420045.327	DC	17.74	17.01	16.69	16.59	16.54	15.61	15.43	–
J134701.200+255256.047	DA	17.61	17.46	17.43	17.47	17.51	16.72	16.30	–
J134723.647+102136.240	DAH	15.21	15.06	15.03	15.07	15.09	14.41	14.14	14.23
J134801.746+233447.805	DA	16.06	15.31	14.99	14.88	14.81	13.92	13.67	13.62
J134902.454+115506.917	DC	18.54	17.82	17.44	17.26	17.21	16.46	16.19	–
J134944.359+275522.603	DA	16.45	16.33	16.30	16.35	16.40	15.74	15.68	15.60
J135201.997+005420.119	DA	17.74	17.56	17.54	17.58	17.61	16.76	16.82	–
J135211.598+105349.561	DA	17.08	16.75	16.63	16.61	16.60	15.74	15.59	–
J135334.809+292857.538	DA	17.50	17.40	17.40	17.47	17.51	16.62	–	–
J135347.019−273856.388	DA	16.93	16.84	16.84	16.91	16.94	16.14	16.07	15.90
J140343.526+520648.866	DA	16.52	16.41	16.42	16.49	16.48	15.71	15.67	–
J140346.138+064442.067	DC	17.44	17.27	17.27	17.32	17.38	16.59	16.62	–
J140617.154+181247.113	DA	17.28	17.14	17.12	17.19	17.23	16.72	16.41	–
J140625.514+160827.545	DA	17.61	17.39	17.34	17.34	17.35	16.60	16.31	–
J140644.407+313025.074	DC	18.60	17.92	17.65	17.53	17.48	16.61	–	16.12
J141039.948+024510.269	DAZ	16.93	16.50	16.34	16.30	16.27	15.47	15.14	15.02
J141143.197+220644.803	DC	17.58	17.43	17.41	17.46	17.52	16.86	16.26	–
J141454.587+433656.944	DA	17.53	17.26	17.18	17.20	17.21	16.46	–	–
J141558.925+433715.275	DA	17.98	17.80	17.76	17.79	17.83	16.80	16.75	–
J141843.593+145258.108	DA	16.80	16.71	16.71	16.72	16.77	16.00	15.66	15.53
J142006.434+532233.120	DA	16.96	16.85	16.87	16.93	16.99	16.40	15.87	–
J142054.438−090509.261	DA	15.46	15.38	15.39	15.47	15.52	14.76	14.73	14.76
J142336.667+303740.042	DA	18.08	17.57	17.37	17.31	17.28	16.44	16.18	15.67
J142727.816+611026.764	DQ	17.13	16.91	16.88	16.93	16.95	16.35	16.23	16.05
J142747.971+053230.563	DC	17.02	16.87	16.84	16.90	16.94	16.30	16.03	15.93
J142833.880+440343.831	DZ	17.01	16.88	16.95	17.07	17.14	16.32	15.96	–
J143047.929+043838.453	DA	17.15	17.06	17.09	17.16	17.24	16.52	16.49	–
J143358.119+190736.216	DA	18.67	18.09	17.85	17.79	17.77	16.88	–	–
J143642.449+433241.327	DC	17.89	17.17	16.88	16.78	16.74	15.83	15.62	15.60
J144045.262+080727.089	DA	17.94	17.50	17.31	17.26	17.23	16.54	15.94	–
J144147.102+581656.252	DA	18.00	17.78	17.72	17.75	17.74	16.77	–	–
J144722.038−303525.947	DA	17.41	17.24	17.22	17.26	17.26	16.56	16.35	–
J144724.377−174220.078	DC	16.85	16.14	15.87	15.79	15.72	14.95	14.64	14.72
J145011.700−191407.545	DA	15.87	15.75	15.74	15.79	15.83	15.06	14.87	14.78
J145806.627+293722.103	DA	15.67	15.54	15.55	15.61	15.65	14.97	14.61	14.74
J150549.155−071441.102	DAH	16.00	15.79	15.73	15.76	15.78	15.08	14.99	14.85
J151625.008+280320.782	DAH	16.60	16.53	16.55	16.64	16.74	15.98	16.26	15.70
J152038.306+390351.208	DA	17.02	16.96	17.00	17.08	17.15	16.35	–	–
J152542.833+562906.754	DC	17.18	16.72	16.55	16.50	16.49	15.51	15.21	15.10
J152621.138+293624.753	DA	17.03	16.47	16.24	16.16	16.14	15.30	14.96	14.80
J153035.370+023537.655	DA	16.84	16.75	16.76	16.81	16.88	16.11	16.03	–
J153417.410+021847.134	DA	16.31	16.28	16.33	16.40	16.48	15.78	15.79	–
J153450.542+464951.710	DC	18.61	17.74	17.38	17.23	17.21	16.45	16.14	–
J153505.673+124742.947	DZ	15.93	15.51	15.47	15.54	15.55	14.94	14.73	14.71
J153553.942+212509.304	DA	17.50	17.23	17.14	17.14	17.17	16.29	16.08	–
J153904.039+581116.586	DA	17.86	17.68	17.65	17.70	17.75	16.75	–	–
J154234.676+232936.602	DA	16.95	16.60	16.46	16.43	16.43	15.76	15.48	15.76
J154927.312+480227.403	DC	17.38	17.17	17.11	17.14	17.18	16.63	–	–
J155214.453+185226.905	DA	16.53	16.45	16.47	16.53	16.59	15.88	15.72	15.45
J155533.929+502547.684	DA	16.72	16.42	16.30	16.30	16.32	15.51	15.04	15.03
J155857.666+041704.388	DC	16.22	15.99	15.99	16.07	16.21	15.46	15.27	14.82
J155937.372+252908.504	DA	16.57	16.53	16.57	16.69	16.74	16.18	15.93	15.60
J160112.509+531703.077	DA	16.69	16.48	16.43	16.45	16.49	15.66	15.59	15.35
J160453.120+005512.673	DC	18.05	17.38	17.10	16.99	16.95	16.08	15.97	15.53
J160520.416+555648.009	DA	17.74	17.55	17.50	17.55	17.57	16.77	16.10	15.88
J160714.202+342343.655	DA	17.40	16.96	16.80	16.75	16.74	15.87	15.73	15.63
J161424.609+090559.583	DC	17.84	17.14	16.85	16.75	16.72	15.87	15.77	15.40
J162626.179+193841.981	DA	16.80	16.50	16.38	16.38	16.38	15.64	15.33	15.41
J162632.170+135555.760	DA	17.45	17.28	17.23	17.25	17.28	16.49	16.16	–
J162753.421+091210.805	DA	16.25	16.05	16.05	16.04	16.08	15.25	15.19	15.04
J162824.563+364623.925	DZA	13.85	13.91	14.00	14.13	14.25	13.64	13.65	13.57
J162838.600+705315.999	DA	18.10	17.50	17.22	17.14	17.08	16.10	15.85	–
J163233.374+085119.813	DA	15.32	14.90	14.72	14.69	14.67	13.85	13.61	13.49
J163332.333+523147.315	DA	17.48	17.25	17.17	17.18	17.22	16.37	16.19	–

Tableau B.2 – Données photométriques (suite)

PSO	Type spectral	g	r	i	z	y	J	H	K
J163419.735+571024.918	DQP	15.15	14.84	14.76	14.78	14.81	14.11	14.08	14.13
J163501.681+431733.032	DAZ	14.97	14.75	14.68	14.69	14.72	13.99	13.77	13.61
J163729.220+011000.455	DA	17.68	17.53	17.50	17.53	17.58	16.83	–	–
J163740.613+134033.370	DA	17.02	16.84	16.80	16.82	16.85	15.93	15.67	15.73
J163920.319+403042.216	DA	17.07	17.05	17.09	17.18	17.27	16.51	–	–
J164031.981+222927.177	DA	17.67	17.55	17.56	17.62	17.70	16.83	16.43	–
J164056.980+534107.114	DAH	15.12	15.00	15.04	15.12	15.19	14.49	14.48	14.37
J164136.626+151230.835	DA	15.78	15.66	15.65	15.67	15.75	15.07	14.98	15.06
J165445.708+382932.684	DAZ	16.94	16.59	16.44	16.40	16.41	15.53	15.35	15.27
J165847.290−061710.343	DA	17.40	16.97	16.79	16.73	16.74	15.81	15.57	15.43
J165935.575+442540.414	DA	16.99	16.56	16.38	16.34	16.32	15.43	15.19	15.01
J165939.800+320317.653	DA	17.61	17.36	17.27	17.27	17.29	16.46	–	15.73
J170246.328+102244.288	DA	18.19	17.63	17.40	17.33	17.30	16.41	16.05	–
J170401.508+200701.791	DA	17.72	17.46	17.36	17.37	17.38	16.70	16.46	–
J170447.882+360845.357	DC	18.61	17.95	17.65	17.57	17.50	16.55	–	–
J170513.263+042343.184	DA	16.18	16.15	16.19	16.28	16.37	15.70	15.65	15.40
J170807.953+025732.205	DZ	15.28	15.12	15.12	15.20	15.25	14.56	14.50	14.51
J171450.782+391839.916	DAP	16.52	16.31	16.26	16.30	16.34	15.63	15.38	15.41
J172349.645+045845.730	DA	16.94	16.92	16.98	17.07	17.13	16.40	16.05	–
J172818.445+021107.752	DA	16.31	16.26	16.31	16.40	16.47	15.67	15.95	15.94
J173336.090+794915.945	DC	17.29	16.92	16.76	16.75	16.77	16.06	16.05	–
J174146.220+240145.262	DA	16.61	16.47	16.46	16.50	16.54	15.99	15.57	15.71
J174248.474+433806.596	DA	17.37	16.91	16.71	16.66	16.64	15.80	15.67	–
J174300.542+170142.511	DC	18.90	18.04	17.68	17.54	17.47	16.34	–	15.78
J174707.557+285910.684	DC	17.48	17.10	16.96	16.91	16.88	16.23	16.17	–
J174941.331+824704.308	DA	14.40	14.25	14.25	14.28	14.32	13.63	13.47	13.43
J175704.476+405253.312	DC	17.44	16.99	16.79	16.75	16.75	15.92	15.88	15.82
J175822.216+141731.058	DA	16.54	16.08	15.88	15.81	15.80	14.93	14.66	14.66
J180127.345+505001.780	DC	18.03	17.34	17.05	16.96	16.90	16.00	16.20	–
J180151.415+084609.344	DA	17.88	17.47	17.30	17.26	17.24	16.38	16.01	–
J181331.031+324829.110	DA	16.45	16.36	16.37	16.43	16.49	15.72	15.68	15.76
J181335.270+324841.621	DA	17.19	16.95	16.87	16.88	16.88	16.21	15.95	15.81
J181527.531+315851.639	DA	18.50	17.91	17.66	17.58	17.54	16.70	16.31	–
J181608.846+245438.131	DAP	17.05	16.85	16.81	16.83	16.86	16.08	16.11	15.51
J181706.119+132811.013	DA	16.24	15.59	15.32	15.24	15.18	14.38	14.10	14.07
J181959.432+173920.273	DC	18.31	17.63	17.36	17.27	17.18	16.39	–	15.96
J182120.071+610059.413	DAH	16.03	15.37	15.09	14.99	14.94	14.07	13.81	13.80
J183358.369+194548.662	DQ	16.43	16.41	16.44	16.52	16.57	15.98	16.04	15.61
J185106.731+773836.627	DC	17.55	17.01	16.79	16.71	16.67	15.93	15.80	–
J185713.929+202625.343	DA	16.85	16.63	16.55	16.59	16.62	15.87	15.61	–
J185739.691+533032.692	DC	17.60	16.91	16.62	16.52	16.47	15.68	15.43	15.55
J191316.499+294932.083	DA	17.26	16.97	16.85	16.83	16.84	16.12	15.67	–
J191435.901+142820.697	DA	16.94	16.76	16.71	16.73	16.78	15.84	15.24	15.03
J191647.498+804432.340	DA	17.89	17.38	17.19	17.14	17.10	16.28	16.07	–
J191858.653+384318.615	DC	14.75	14.50	14.43	14.44	14.46	13.78	13.67	13.52
J194002.218+834852.743	DC	18.93	18.25	17.93	17.86	17.80	16.65	–	–
J194529.731+465009.911	DA	17.45	16.96	16.76	16.70	16.67	15.88	15.56	15.47
J200535.745−105655.436	DC	17.41	16.63	16.31	16.21	16.18	15.28	14.99	14.75
J200655.192+614308.342	DA	16.84	16.34	16.14	16.09	16.05	15.17	14.90	14.68
J201355.464+064237.635	DC	15.90	15.69	15.65	15.68	15.73	15.02	–	–
J202220.821+833357.324	DC	17.53	17.18	17.05	17.04	17.04	16.16	16.40	–
J203109.399−165841.014	DAZ	16.52	16.08	15.90	15.85	15.82	14.98	14.79	14.79
J205020.293+263037.327	DA	16.00	15.39	15.12	15.02	14.98	14.10	13.91	–
J205100.086−245206.115	DA	15.57	15.46	15.46	15.54	15.59	14.90	14.70	14.60
J205648.322−045041.820	DC	17.17	16.32	15.95	15.82	15.75	14.73	14.56	14.33
J205906.010+003348.099	DA	17.69	17.58	17.58	17.63	17.70	16.72	–	–
J205945.315+551735.433	DC	17.86	17.04	16.69	16.57	16.52	15.66	15.45	15.49
J210202.556+191253.722	DA	16.47	16.27	16.21	16.22	16.25	15.64	15.56	15.40
J210212.316+245739.102	DA	16.76	16.45	16.33	16.32	16.32	15.52	15.21	15.06
J210745.033+074042.876	DA	16.54	16.38	16.36	16.41	16.44	15.77	15.79	–
J211050.100−212929.023	DA	16.98	16.65	16.52	16.50	16.50	15.69	15.48	15.70
J211329.157+072705.563	DA	16.30	16.05	15.99	15.98	16.00	15.21	14.95	14.81
J211640.387−072455.126	DC	18.33	17.59	17.28	17.17	17.11	16.34	16.26	15.52
J212042.160+581921.738	DA	16.02	15.95	15.97	16.07	16.12	15.39	15.26	–

Tableau B.2 – Données photométriques (suite)

PSO	Type spectral	g	r	i	z	y	J	H	K
J212147.719−013035.307	DA	16.73	16.49	16.42	16.43	16.46	15.65	15.65	15.43
J212212.288+041351.975	DA	17.14	16.51	16.25	16.16	16.12	15.24	15.01	14.88
J213424.400+365518.543	DA	16.50	16.38	16.39	16.46	16.50	15.81	15.93	15.45
J214208.829+132843.106	DA	16.64	16.55	16.53	16.59	16.64	16.02	15.73	15.49
J214632.643+155040.799	DA	16.61	16.55	16.57	16.65	16.71	15.93	15.72	–
J214913.617+041547.631	DA	17.16	16.63	16.40	16.33	16.29	15.38	15.21	15.10
J215500.756−275036.006	DC	16.71	16.27	16.08	16.05	16.03	15.19	15.11	14.96
J220947.316+142950.134	DA	15.67	15.56	15.57	15.64	15.69	14.97	14.78	14.77
J221034.377+453235.823	DC	17.57	17.14	16.98	16.94	16.91	16.20	15.97	–
J221408.663+372708.893	DC	17.10	16.82	16.78	16.84	16.89	16.25	16.06	15.62
J221748.096+370752.142	DC	17.57	16.77	16.43	16.31	16.23	15.40	15.20	14.97
J221851.326+483928.522	DA	16.19	16.04	16.03	16.08	16.11	15.48	15.30	15.32
J221928.867+212222.995	DC	18.42	17.71	17.43	17.32	17.28	16.45	–	16.02
J222740.527+175320.338	DAZ	16.89	16.66	16.62	16.62	16.64	15.85	15.57	15.47
J222802.026+120732.876	DZ	16.32	16.22	16.28	16.36	16.44	15.87	15.76	15.95
J222934.149+232739.619	DA	18.36	17.79	17.53	17.44	17.42	16.36	16.03	–
J223037.292+125621.531	DA	17.16	17.07	17.06	17.12	17.16	16.52	16.25	15.68
J223049.491−094509.568	DA	17.50	17.36	17.36	17.42	17.48	16.68	–	–
J223056.031+152356.162	DA	18.11	17.61	17.44	17.36	17.36	16.34	16.01	–
J223402.331+554327.087	DA	17.43	17.26	17.23	17.26	17.31	16.57	–	–
J223858.645+131303.550	DA	17.06	17.00	17.04	17.12	17.18	16.63	16.42	–
J224104.814+364639.407	DA	17.20	17.07	17.05	17.11	17.16	16.38	16.17	–
J224157.680+133234.281	DA	17.50	17.17	17.03	17.02	17.00	16.17	–	–
J224946.766+362321.573	DA	18.60	17.99	17.75	17.67	17.65	16.58	16.22	–
J225124.135+293946.047	DA	15.75	15.35	15.17	15.13	15.12	14.32	13.98	13.94
J225339.217+813041.465	DC :	18.27	17.66	17.26	17.05	16.99	15.69	–	–
J225355.149−064701.663	DZ	16.30	15.33	15.02	14.90	14.87	14.01	13.69	13.55
J225549.954−075002.977	DA	16.55	16.37	16.32	16.31	16.37	15.63	15.28	15.20
J225555.991+054519.616	DA	16.39	16.04	15.91	15.85	15.81	15.18	14.89	15.02
J230244.708+431247.175	DA	16.59	16.52	16.57	16.64	16.70	15.96	15.97	–
J230538.921+433401.116	DC	18.81	18.11	17.83	17.74	17.67	16.77	–	–
J230812.905+241424.726	DC	18.49	17.80	17.54	17.44	17.39	16.55	–	–
J231205.986+131054.970	DA	17.67	17.11	16.88	16.80	16.78	15.91	15.47	15.27
J231424.920−063249.681	DQ	15.44	15.37	15.43	15.52	15.61	14.95	14.94	14.73
J231519.254−020938.450	DZ	16.43	16.23	16.22	16.25	16.29	15.49	15.75	–
J231612.797+172045.536	DC	18.42	17.75	17.48	17.37	17.32	16.52	16.57	15.57
J231909.035−061309.035	DC	18.62	17.82	17.48	17.34	17.27	16.31	15.84	–
J231935.449−022904.088	DA	17.48	16.91	16.67	16.59	16.55	15.77	15.30	15.36
J232328.410+725507.872	DA	16.53	16.43	16.43	16.49	16.55	15.83	15.77	–
J232418.827+283553.370	DA	16.47	16.32	16.32	16.35	16.38	15.60	15.24	15.41
J232520.161+140341.102	DA	16.38	15.80	15.56	15.46	15.42	14.51	14.37	14.36
J232557.991+255219.244	DA	17.23	16.86	16.71	16.70	16.68	15.84	15.43	15.46
J233856.534+210120.429	DA	18.14	17.65	17.45	17.36	17.28	16.32	16.18	–
J233901.088+531600.768	DA	17.29	17.02	16.93	16.93	16.97	16.10	–	15.63
J234245.734−100122.294	DA	18.81	18.23	17.96	17.88	17.82	16.84	16.58	–
J234314.753−165943.917	DZ	17.66	17.09	16.88	16.80	16.79	15.80	16.00	–
J234612.394+115849.053	DC	17.41	17.13	17.04	17.04	17.04	16.33	–	15.62
J234735.257+030434.827	DC	17.16	16.52	16.28	16.21	16.18	15.62	15.60	–
J234753.583+022339.475	DA	18.49	17.91	17.71	17.63	17.58	16.44	16.28	–
J234858.098+430036.913	DC	18.52	17.82	17.50	17.41	17.39	16.67	15.95	15.74
J234954.980+293358.408	DA	15.95	15.59	15.44	15.41	15.42	14.57	14.35	14.16
J235313.281+205115.352	DA	16.67	16.54	16.53	16.58	16.63	15.92	15.85	15.58
J235456.492+402723.413	DQ	14.97	14.90	14.97	15.10	15.16	14.58	14.45	14.51

Tableau B.3 – Paramètres atmosphériques

PSO	$T_{\rm eff}$ (K)	$\log g$	M ($M_\odot$)	$\tau_{\rm cool}$(Gyr)[1]	log H/He[2]	log C/He	log Ca/He
J000224.474+635745.512	4565(50)	7.758(0.024)	0.432(0.013)	4.45	He	–	–
J000410.478−034008.751	6955(60)	7.931(0.023)	0.551(0.013)	1.40	H	–	–
J000720.831+123018.402	4885(45)	8.090(0.021)	0.625(0.014)	6.45	He	–	–
J000728.917+340342.227	5545(50)	8.153(0.021)	0.666(0.013)	5.02	He	–	–
J000754.487+394731.294	4680(25)	6.768(0.039)	0.081(0.016)	1.40	H	–	–
J000935.139+310840.332	7960(290)	8.053(0.100)	0.609(0.062)	1.21	He	–	–
J001122.399+424038.082	6990(50)	7.975(0.017)	0.577(0.010)	1.47	H	–	–
J001214.188+502514.381	6445(40)	8.247(0.012)	0.746(0.008)	3.24	H	–	–
J001412.352−131109.057	5855(35)	8.217(0.016)	0.724(0.010)	4.10	H	–	–
J001737.914−051650.624	5630(40)	7.918(0.026)	0.537(0.015)	2.40	H	–	–
J002147.235+264032.448	4895(35)	7.963(0.024)	0.557(0.014)	5.75	H	–	–
J002214.960+423638.540	5700(25)	7.586(0.017)	0.371(0.007)	1.49	H	–	–
J002645.591+002532.159	7735(115)	7.096(0.044)	0.225(0.010)	0.51	H	–	–
J002736.859+054159.737	5600(35)	7.979(0.019)	0.573(0.011)	2.75	H	–	–
J003325.772+250616.063	6140(45)	7.970(0.021)	0.571(0.013)	2.00	H	–	–
J003426.931+151758.962	6830(65)	8.016(0.024)	0.601(0.014)	1.66	H	–	–
J004056.278−080913.497	6040(40)	8.266(0.018)	0.757(0.012)	4.05	H	–	–
J004125.624−222106.571	5210(60)	7.907(0.038)	0.514(0.023)	4.21	He	−8.4	–
J004506.415−060826.910	4875(40)	8.419(0.023)	0.855(0.016)	8.94	H	–	–
J005111.307−202800.918	4895(30)	7.923(0.025)	0.533(0.015)	5.28	H	–	–
J005313.605+392704.586	7450(80)	7.951(0.025)	0.564(0.015)	1.21	H	–	–
J005550.264−112726.361	6970(50)	7.977(0.018)	0.578(0.010)	1.49	H	–	–
J005559.021+594801.879	4625(25)	7.848(0.021)	0.489(0.011)	5.54	H	–	–
J005729.321+005347.980	6565(60)	7.048(0.040)	0.205(0.010)	0.74	H	–	–
J010350.186+050433.459	7965(60)	7.452(0.017)	0.329(0.006)	0.61	H	–	–
J010456.255+211952.899	5220(35)	8.346(0.020)	0.806(0.013)	7.62	H	–	–
J010457.741+212011.454	4790(30)	8.135(0.021)	0.664(0.014)	7.85	H	–	–
J010543.124−092055.331	8040(85)	8.001(0.027)	0.595(0.016)	1.06	H	–	–
J010850.626+760018.502	5985(90)	7.969(0.037)	0.569(0.022)	2.14	H	–	–
J011505.153−013315.894	5215(30)	8.059(0.021)	0.618(0.013)	5.31	H	–	–
J011931.957−141533.389	5050(30)	7.905(0.020)	0.524(0.011)	4.26	H	–	–
J012137.654+344043.058	7050(85)	8.219(0.027)	0.713(0.017)	2.35	He	–	−10.9
J012314.892−020926.687	5745(45)	7.951(0.024)	0.557(0.014)	2.35	H	–	–
J012422.339+402356.511	5255(25)	8.095(0.017)	0.641(0.011)	5.50	H	–	–
J012524.681−260051.250	6950(155)	8.284(0.050)	0.756(0.034)	2.86	He	–	–
J014545.034+291823.982	5125(40)	8.122(0.027)	0.657(0.017)	6.42	H	–	–
J014743.832−271140.530	6760(50)	8.003(0.019)	0.593(0.011)	1.67	H	–	–
J014840.441+361528.181	6070(40)	8.052(0.018)	0.620(0.011)	2.44	H	–	–
J015252.137+255341.393	7490(65)	7.828(0.021)	0.496(0.011)	1.00	H	–	–
J015329.141+355729.048	7125(70)	8.329(0.024)	0.802(0.016)	2.86	H	–	–
J015441.879+140305.490	6370(90)	7.918(0.039)	0.525(0.022)	1.78	He	−7.0	–
J020141.494−265037.976	7665(75)	8.426(0.021)	0.867(0.014)	2.77	H	–	–
J020512.364−051749.608	3920(45)	7.720(0.033)	0.419(0.017)	6.62	H	–	–
J020615.382+183625.432	4270(35)	7.786(0.032)	0.454(0.017)	6.08	H	–	–
J021121.900+395515.688	7200(60)	7.966(0.018)	0.572(0.010)	1.35	H	–	–
J021148.605+711911.081	4790(45)	7.838(0.025)	0.474(0.014)	4.68	He	–	–
J021458.074+774555.006	4400(65)	7.934(0.035)	0.528(0.021)	6.37	He	–	–
J021720.077−065628.431	5315(30)	7.991(0.024)	0.577(0.014)	3.95	H	–	–
J022300.401+554426.370	6825(60)	8.305(0.020)	0.786(0.013)	3.08	H	–	–
J022348.968+205548.480	4395(40)	7.847(0.031)	0.488(0.017)	6.32	H	–	–
J022552.460+422800.625	6190(65)	7.940(0.030)	0.553(0.017)	1.87	H	–	–
J022633.136+645925.124	4145(40)	7.805(0.028)	0.464(0.015)	6.70	H	–	–
J023141.297+270952.353	4830(25)	7.869(0.021)	0.502(0.012)	4.97	H	–	–
J023237.925−141159.716	5465(30)	8.034(0.017)	0.605(0.010)	3.59	H	–	–
J023339.034+212510.652	4750(30)	7.884(0.022)	0.510(0.012)	5.48	H	–	–
J023521.704−240053.976	4555(50)	7.267(0.022)	0.234(0.007)	2.33	He	–	–
J023521.711−225121.625	6395(40)	7.982(0.019)	0.579(0.011)	1.85	H	–	–
J023759.111+163809.334	5250(55)	7.935(0.027)	0.530(0.015)	4.28	He	–	–
J023919.953+260955.585	5590(30)	8.029(0.017)	0.603(0.010)	3.11	H	–	–
J024050.276+314255.267	7165(60)	8.068(0.019)	0.633(0.012)	1.56	H	–	–

[1] $\tau_{\rm cool}$ n'inclut pas le temps d'évolution précédant la phase naine blanche.
[2] Les abondances sont calculées en comparant le nombre d'atomes de chaque espèce chimique.

Tableau B.3 – Paramètres atmosphériques (suite)

PSO	$T_{\rm eff}$ (K)	$\log g$	M ($M_\odot$)	$\tau_{\rm cool}$(Gyr)	log H/He	log C/He	log Ca/He
J024213.914+165520.195	6360(60)	7.993(0.022)	0.569(0.013)	1.97	He	−6.5	–
J024532.297−195133.920	4275(30)	7.797(0.026)	0.460(0.014)	6.18	H	–	–
J024630.966−022729.142	6780(40)	8.161(0.015)	0.691(0.009)	2.21	H	–	–
J024835.828+542317.614	4980(25)	8.060(0.017)	0.617(0.010)	6.48	H	–	–
J024944.380+330729.037	5670(35)	7.977(0.018)	0.572(0.011)	2.60	H	–	–
J025304.815+001342.702	7685(85)	7.986(0.032)	0.585(0.019)	1.17	H	–	–
J025545.823+210620.174	6145(45)	7.970(0.022)	0.571(0.013)	2.00	H	–	–
J025617.236+495439.572	5955(40)	8.128(0.018)	0.667(0.011)	3.15	H	–	–
J025959.483+081155.692	6405(40)	7.772(0.019)	0.463(0.010)	1.39	H	–	–
J030059.741+543235.525	7520(60)	8.020(0.021)	0.605(0.013)	1.30	H	–	–
J030520.838+260310.841	5215(40)	7.941(0.029)	0.546(0.017)	3.86	H	–	–
J030713.734−071512.018	5690(40)	8.362(0.019)	0.820(0.013)	5.47	H	–	–
J030924.869+002524.299	5200(65)	7.940(0.032)	0.533(0.019)	4.51	He	–	–
J031058.979+663357.325	4585(35)	7.778(0.029)	0.451(0.015)	4.82	H	–	–
J031243.033+221825.918	6230(50)	7.237(0.025)	0.252(0.007)	0.94	H	–	–
J031938.376+363029.887	6080(80)	8.099(0.031)	0.634(0.019)	3.07	He	–	−9.2
J032020.354+233327.088	4345(25)	7.171(0.029)	0.209(0.009)	2.44	H	–	–
J032511.232−014926.027	5280(25)	8.123(0.016)	0.659(0.010)	5.63	H	–	–
J032515.708−172231.463	6905(65)	7.938(0.026)	0.555(0.015)	1.44	H	–	–
J033634.295−221526.866	5860(35)	7.949(0.019)	0.557(0.011)	2.19	H	–	–
J034038.848+002946.688	7065(60)	8.095(0.023)	0.650(0.014)	1.69	H	–	–
J034323.178+195815.625	7105(55)	8.451(0.015)	0.883(0.010)	3.50	H	–	–
J034435.163+182557.644	6515(60)	7.974(0.025)	0.558(0.015)	1.79	He	−6.5	–
J034707.030+013842.218	4615(50)	7.661(0.024)	0.385(0.012)	3.58	He	–	–
J035456.254+004410.986	5940(45)	7.598(0.024)	0.378(0.010)	1.37	H	–	–
J040026.399+081402.559	5460(25)	7.941(0.016)	0.549(0.009)	2.87	H	–	–
J040101.957+513120.939	4780(40)	8.077(0.020)	0.617(0.013)	6.57	He	–	–
J040647.378−064436.467	5780(35)	7.288(0.030)	0.263(0.009)	1.16	H	–	–
J041017.736+195422.560	5115(35)	8.290(0.021)	0.768(0.014)	7.73	H	–	–
J041226.558−111747.822	7385(65)	7.582(0.023)	0.378(0.010)	0.81	H	–	–
J041805.483+421059.576	5065(25)	7.869(0.020)	0.504(0.011)	3.81	H	–	–
J041920.974−093430.470	6015(40)	8.350(0.018)	0.813(0.012)	4.58	H	–	–
J042553.649+121145.519	5960(75)	8.140(0.027)	0.659(0.018)	3.71	He	–	–
J042621.232+043223.564	4815(25)	8.143(0.017)	0.669(0.011)	7.82	H	–	–
J042926.378+494551.608	8300(90)	7.984(0.025)	0.586(0.015)	0.95	H	–	–
J043200.394−192053.212	5720(55)	8.018(0.026)	0.597(0.016)	2.73	H	–	–
J043329.882+041441.948	4965(30)	8.063(0.020)	0.618(0.012)	6.58	H	–	–
J043333.917−275324.912	5170(30)	8.046(0.019)	0.609(0.012)	5.41	H	–	–
J043420.495+305418.826	4820(25)	8.103(0.020)	0.644(0.013)	7.48	H	–	–
J043645.095+270949.840	5555(30)	8.054(0.017)	0.618(0.010)	3.43	H	–	–
J043747.606−084931.346	6395(30)	7.966(0.013)	0.552(0.008)	1.86	He	−6.3	–
J044028.432+092337.323	6185(60)	8.252(0.022)	0.748(0.015)	3.70	H	–	–
J044105.119−151901.469	6005(35)	8.015(0.017)	0.597(0.011)	2.30	H	–	–
J045551.655+384050.251	5080(30)	8.055(0.021)	0.615(0.013)	5.98	H	–	–
J050048.072−062440.883	7505(60)	8.035(0.021)	0.614(0.013)	1.33	H	–	–
J050532.333−173140.783	6140(45)	8.179(0.019)	0.700(0.012)	3.27	H	–	–
J050552.605−172234.909	5390(25)	7.909(0.017)	0.530(0.010)	2.85	H	–	–
J050819.108−145030.118	5375(20)	7.906(0.014)	0.514(0.008)	3.60	He	−7.4	–
J050836.610−152305.031	5215(40)	8.068(0.024)	0.624(0.015)	5.42	H	–	–
J051403.315+080011.533	6555(45)	8.318(0.015)	0.794(0.010)	3.54	H	–	–
J051553.703+283915.520	6360(45)	8.174(0.017)	0.698(0.011)	2.88	H	–	–
J052656.411+443534.141	4680(35)	7.883(0.027)	0.509(0.015)	5.75	H	–	–
J053525.054+571526.134	4575(65)	7.252(0.036)	0.230(0.011)	2.28	He	–	–
J053620.060+412956.109	7290(50)	7.129(0.017)	0.230(0.004)	0.60	H	–	–
J054104.259+395940.128	5810(40)	8.223(0.022)	0.727(0.014)	4.25	H	–	–
J054307.203+363700.592	6385(40)	8.050(0.015)	0.620(0.009)	2.12	H	–	–
J054615.507+111556.787	4960(30)	7.974(0.022)	0.564(0.013)	5.55	H	–	–
J055119.581+001018.024	6080(45)	8.146(0.019)	0.663(0.012)	3.43	−4.3	−6.6	–
J055509.987−041037.276	4430(40)	7.967(0.022)	0.549(0.014)	6.96	He	–	−11.4
J055543.054+465041.451	5130(25)	7.922(0.020)	0.534(0.011)	4.04	H	–	–
J055900.939−041430.272	6070(40)	8.086(0.018)	0.641(0.011)	2.66	H	–	–
J060231.360+155303.114	6885(55)	8.272(0.018)	0.764(0.012)	2.77	H	–	–
J060236.792+090420.669	5940(40)	7.950(0.020)	0.558(0.012)	2.12	H	–	–
J060715.723+733151.212	6400(60)	8.488(0.019)	0.906(0.013)	4.53	H	–	–

Tableau B.3 – Paramètres atmosphériques (suite)

PSO	$T_{\rm eff}$ (K)	$\log g$	M ($M_\odot$)	$\tau_{\rm cool}$(Gyr)	log H/He	log C/He	log Ca/He
J062048.218+064516.963	5810(25)	8.129(0.014)	0.667(0.009)	3.43	H	–	–
J063229.248+223002.761	5480(40)	7.979(0.023)	0.572(0.013)	3.08	H	–	–
J063629.892+405425.331	7720(80)	8.411(0.021)	0.857(0.014)	2.64	H	–	–
J064430.034+273110.880	6890(60)	8.374(0.019)	0.831(0.013)	3.42	H	–	–
J064721.800+023109.211	6995(60)	8.577(0.015)	0.965(0.009)	4.03	H	–	–
J065036.647+165751.533	5170(30)	8.120(0.019)	0.656(0.012)	6.19	H	–	–
J065326.433+640337.279	5855(35)	8.105(0.018)	0.652(0.011)	3.13	H	–	–
J065350.180+635553.354	5945(50)	8.003(0.022)	0.590(0.013)	2.31	H	–	–
J070052.037+315735.908	4840(25)	7.901(0.019)	0.520(0.011)	5.28	H	–	–
J070154.779−062757.770	6430(40)	8.000(0.015)	0.590(0.009)	1.88	H	–	–
J071014.089+374015.920	6650(50)	7.951(0.018)	0.544(0.011)	1.65	He	−6.4	–
J072704.270+143438.991	5670(35)	7.982(0.020)	0.575(0.012)	2.62	H	–	–
J073330.974+640924.003	5150(25)	7.844(0.017)	0.491(0.009)	3.19	H	–	–
J074730.157+110732.567	7980(90)	8.880(0.017)	1.140(0.008)	3.50	H	–	–
J075026.326+174028.947	6940(65)	8.024(0.024)	0.606(0.014)	1.61	H	–	–
J075313.399+422957.271	4480(60)	7.824(0.024)	0.475(0.013)	5.74	0.0	–	–
J075327.128+522928.170	7395(190)	8.404(0.054)	0.837(0.037)	2.95	He	–	–
J075356.365−252359.103	4975(25)	7.937(0.017)	0.542(0.010)	5.04	H	–	–
J075525.879+362150.851	7705(60)	7.937(0.021)	0.557(0.012)	1.09	H	–	–
J075631.106+413945.958	6820(50)	8.377(0.016)	0.833(0.011)	3.52	H	–	–
J080440.637+223945.828	4970(100)	7.980(0.050)	0.558(0.031)	5.87	−1.6	–	−10.0
J080527.499+073530.748	5370(35)	8.124(0.020)	0.660(0.012)	5.11	H	–	–
J080557.060+383338.445	4915(25)	8.076(0.018)	0.627(0.011)	6.90	H	–	–
J080648.040+221549.419	5760(35)	8.073(0.024)	0.631(0.015)	3.05	H	–	–
J080756.012+485417.245	6495(60)	8.081(0.032)	0.639(0.020)	2.15	H	–	–
J080812.648+185420.003	5630(45)	7.934(0.026)	0.546(0.015)	2.47	H	–	–
J080940.284+111226.130	6720(80)	8.247(0.029)	0.731(0.019)	2.94	He	–	−11.7
J080946.320+292031.390	7010(50)	8.082(0.018)	0.642(0.011)	1.70	H	–	–
J080951.067+225053.892	6585(50)	8.157(0.022)	0.688(0.014)	2.45	H	–	–
J081411.267+484526.630	6515(120)	8.058(0.045)	0.609(0.029)	2.08	He	–	–
J081516.954+163315.695	4655(35)	6.772(0.076)	0.082(0.031)	1.43	H	–	–
J081641.958+213731.315	6140(45)	7.962(0.021)	0.566(0.012)	1.98	H	–	–
J082001.138+383432.316	7550(65)	8.034(0.021)	0.614(0.013)	1.31	H	–	–
J082036.942+431004.142	6845(55)	7.329(0.031)	0.282(0.009)	0.80	H	–	–
J082219.257+202324.964	7050(215)	7.640(0.103)	0.386(0.048)	0.99	He	–	–
J083039.333+324141.361	7200(50)	8.394(0.014)	0.846(0.009)	3.14	H	–	–
J083254.459+313902.462	6010(40)	8.098(0.023)	0.648(0.015)	2.83	H	–	–
J083644.400+415410.862	7610(75)	7.129(0.035)	0.232(0.009)	0.54	H	–	–
J084248.231−134713.555	4795(120)	7.972(0.052)	0.553(0.031)	6.21	He	–	−10.0
J084257.516+240930.231	5795(35)	7.972(0.020)	0.570(0.012)	2.36	H	–	–
J084524.718+380154.023	7890(100)	7.958(0.028)	0.570(0.016)	1.05	H	–	–
J084901.422+443934.262	5810(65)	8.133(0.035)	0.654(0.022)	4.08	He	–	–
J084909.341+342947.937	7415(70)	7.949(0.021)	0.563(0.012)	1.22	H	–	–
J084948.563+331924.777	7545(65)	8.001(0.023)	0.594(0.014)	1.25	H	–	–
J085140.169+162452.740	5815(75)	7.990(0.031)	0.566(0.020)	2.96	He	–	–
J085458.584+275225.052	6745(65)	7.884(0.031)	0.524(0.017)	1.41	H	–	–
J085550.006+370015.667	5480(35)	7.597(0.026)	0.373(0.011)	1.67	H	–	–
J085749.645+180802.235	6655(45)	7.944(0.022)	0.558(0.013)	1.58	H	–	–
J085830.771+412631.472	7145(60)	8.401(0.018)	0.850(0.012)	3.24	H	–	–
J085913.053+005844.420	4655(45)	7.733(0.020)	0.419(0.010)	3.99	He	–	–
J090240.325+153555.388	4625(30)	7.179(0.040)	0.213(0.012)	2.13	H	–	–
J090318.540+201244.329	7155(65)	7.875(0.025)	0.520(0.014)	1.20	H	–	–
J090531.867+731448.572	5170(25)	8.012(0.018)	0.588(0.011)	4.98	H	–	–
J091037.423+215613.422	5740(50)	7.640(0.030)	0.395(0.014)	1.55	H	–	–
J091244.972+195153.321	5040(25)	8.020(0.020)	0.592(0.012)	5.74	H	–	–
J091247.877+225153.618	4940(35)	7.948(0.030)	0.548(0.018)	5.34	H	–	–
J091356.663+404734.285	6690(65)	7.899(0.026)	0.532(0.014)	1.47	H	–	–
J091554.370+532508.067	7170(155)	8.265(0.051)	0.744(0.035)	2.48	He	–	–
J091601.736+225947.182	5755(35)	8.186(0.027)	0.703(0.017)	4.09	H	–	–
J092430.651+312028.766	4795(25)	8.008(0.027)	0.584(0.016)	6.66	H	–	–
J092840.368+184112.020	7675(75)	8.434(0.019)	0.872(0.013)	2.80	H	–	–
J093340.911+291121.177	8225(90)	8.477(0.020)	0.902(0.013)	2.49	H	–	–
J093931.267+495148.240	6025(45)	8.378(0.018)	0.832(0.012)	4.70	H	–	–
J094316.755+513438.235	4800(25)	7.818(0.026)	0.473(0.014)	4.54	H	–	–

Tableau B.3 – Paramètres atmosphériques (suite)

PSO	$T_{\rm eff}$ (K)	$\log g$	M ($M_\odot$)	$\tau_{\rm cool}$(Gyr)	log H/He	log C/He	log Ca/He
J094346.583−070353.564	5975(40)	7.955(0.019)	0.561(0.011)	2.10	H	–	–
J094534.421+015438.872	6905(60)	8.066(0.023)	0.632(0.015)	1.74	H	–	–
J094621.500+325127.762	6620(60)	8.141(0.022)	0.678(0.014)	2.31	H	–	–
J094806.002+202315.455	4835(30)	7.966(0.024)	0.558(0.014)	6.05	H	–	–
J094850.155+131926.151	6670(65)	7.973(0.031)	0.575(0.018)	1.64	H	–	–
J095016.774+531514.490	8050(35)	7.912(0.010)	0.525(0.006)	0.98	He	−5.5	–
J095021.748+150906.037	5420(35)	8.010(0.026)	0.590(0.016)	3.60	H	–	–
J095120.241+190009.463	5460(75)	7.843(0.041)	0.479(0.022)	2.91	He	–	–
J100119.459+465647.156	4415(45)	7.858(0.038)	0.494(0.021)	6.38	H	–	–
J100204.130+432644.466	4735(35)	7.942(0.025)	0.543(0.015)	6.18	H	–	–
J100720.864+154133.780	7275(75)	7.974(0.034)	0.577(0.020)	1.33	H	–	–
J101141.465+284550.360	4335(165)	8.211(0.085)	0.703(0.057)	7.89	He	−6.8	–
J101201.471−184333.327	5600(65)	7.937(0.032)	0.534(0.019)	3.09	He	–	−10.4
J101414.305+040137.831	7475(70)	7.965(0.025)	0.572(0.015)	1.22	H	–	–
J101436.119+422620.980	7605(75)	8.421(0.019)	0.864(0.013)	2.81	H	–	–
J101501.500+080613.272	4545(20)	7.842(0.025)	0.485(0.014)	5.72	H	–	–
J101502.390+080637.662	6660(55)	7.965(0.020)	0.570(0.012)	1.63	H	–	–
J101535.340+185020.708	4525(25)	7.135(0.048)	0.200(0.014)	2.17	H	–	–
J101704.973+761901.473	6985(70)	7.969(0.023)	0.573(0.014)	1.46	H	–	–
J101833.069−044228.789	7810(85)	8.073(0.028)	0.638(0.017)	1.26	H	–	–
J101959.412+521406.822	5350(35)	7.964(0.025)	0.561(0.015)	3.48	H	–	–
J102210.384+461247.763	7145(60)	8.208(0.019)	0.722(0.012)	2.05	H	–	–
J102234.759+460058.953	7595(65)	7.445(0.024)	0.325(0.009)	0.68	H	–	–
J102251.304+390412.599	5640(60)	8.162(0.028)	0.673(0.018)	4.78	He	–	−10.4
J102309.572+632744.105	6780(50)	8.045(0.017)	0.618(0.010)	1.77	H	–	–
J102747.464+192823.959	7075(65)	8.381(0.022)	0.837(0.015)	3.23	H	–	–
J102907.775+112715.911	6905(60)	8.282(0.018)	0.771(0.012)	2.81	H	–	–
J103443.242+224548.494	6810(75)	8.144(0.024)	0.664(0.015)	2.30	He	–	−9.0
J103532.475+212602.541	6965(75)	8.097(0.028)	0.651(0.018)	1.78	H	–	–
J103658.049+711053.356	4745(40)	8.195(0.022)	0.703(0.015)	8.42	H	–	–
J103855.315−204049.761	4530(215)	8.074(0.124)	0.614(0.078)	7.04	He	−7.2	–
J103954.941+380037.844	7025(70)	7.966(0.032)	0.572(0.018)	1.44	H	–	–
J104019.619+100359.316	5850(70)	8.070(0.029)	0.614(0.019)	3.44	He	–	–
J104153.917+141545.969	7140(205)	8.142(0.073)	0.663(0.047)	1.89	He	–	–
J104447.915+194309.977	7570(65)	7.083(0.037)	0.221(0.009)	0.53	H	–	–
J104718.292+000717.423	6965(225)	7.346(0.128)	0.273(0.042)	0.82	He	–	–
J104801.365+633447.084	5215(30)	7.995(0.021)	0.579(0.013)	4.53	H	–	–
J105211.523+405002.027	6110(95)	8.061(0.037)	0.609(0.024)	2.68	He	–	–
J105349.342+242531.813	5820(40)	8.217(0.022)	0.724(0.014)	4.18	H	–	–
J105544.832+211104.132	6090(45)	8.117(0.022)	0.660(0.014)	2.86	H	–	–
J105629.925+233615.998	5230(35)	7.951(0.026)	0.553(0.015)	3.92	H	–	–
J105638.557−225251.802	7690(70)	8.070(0.022)	0.636(0.014)	1.31	H	–	–
J105734.525−073122.157	7155(155)	8.308(0.050)	0.773(0.034)	2.74	He	–	–
J110616.348+451854.994	7490(85)	8.406(0.022)	0.853(0.014)	2.86	H	–	–
J110709.497+144655.668	6580(45)	7.963(0.019)	0.568(0.011)	1.67	H	–	–
J110844.207+080137.334	7535(70)	8.006(0.022)	0.597(0.013)	1.27	H	–	–
J110941.418+551226.486	7010(50)	8.580(0.015)	0.967(0.010)	4.03	H	–	–
J111007.301+011043.437	6595(140)	8.259(0.049)	0.739(0.032)	3.23	He	–	–
J111058.542+202606.418	4720(35)	8.004(0.024)	0.580(0.015)	6.88	H	–	–
J111316.386+285903.381	4815(25)	7.340(0.052)	0.265(0.017)	2.16	H	–	–
J111536.983+003313.724	5010(20)	7.549(0.021)	0.346(0.009)	2.27	H	–	–
J111640.112+062702.381	6325(45)	7.965(0.019)	0.568(0.011)	1.84	H	–	–
J111930.819−103811.799	7140(60)	6.995(0.028)	0.197(0.007)	0.58	H	–	–
J112146.030+155325.732	7330(85)	7.935(0.044)	0.555(0.025)	1.23	H	–	–
J112215.702+283941.904	5650(45)	8.174(0.026)	0.695(0.017)	4.27	H	–	–
J112331.433+070120.130	4370(30)	7.348(0.057)	0.264(0.019)	2.83	H	–	–
J112521.167+211111.240	6095(95)	8.011(0.037)	0.579(0.023)	2.43	He	–	–
J113109.007+064306.428	7520(65)	7.897(0.027)	0.534(0.015)	1.09	H	–	–
J113215.317+280934.445	7555(70)	8.136(0.023)	0.677(0.014)	1.51	H	–	–
J113534.369+572450.561	7280(20)	7.356(0.009)	0.276(0.003)	0.74	He	−6.5	–
J113728.135+204109.010	7585(85)	7.871(0.034)	0.520(0.018)	1.03	H	–	–
J114544.189+630554.734	5490(35)	7.915(0.019)	0.534(0.011)	2.64	H	–	–
J114604.299+051401.648	6590(60)	7.343(0.026)	0.285(0.008)	0.89	H	–	–
J114626.080−013642.070	6615(40)	8.034(0.018)	0.611(0.011)	1.85	H	–	–

Tableau B.3 – Paramètres atmosphériques (suite)

PSO	$T_{\rm eff}$ (K)	$\log g$	M ($M_\odot$)	$\tau_{\rm cool}$(Gyr)	log H/He	log C/He	log Ca/He
J114735.229+300921.087	6810(165)	8.128(0.062)	0.653(0.041)	2.15	He	–	–
J114904.718−292149.352	5745(50)	8.363(0.021)	0.820(0.014)	5.29	H	–	–
J114935.585+235320.393	5010(30)	7.949(0.028)	0.549(0.016)	5.00	H	–	–
J115038.627+034259.007	5840(35)	8.056(0.024)	0.621(0.015)	2.77	H	–	–
J115052.411+683115.592	6695(40)	8.275(0.014)	0.765(0.009)	3.05	H	–	–
J115135.911−273220.489	6450(50)	7.985(0.019)	0.564(0.011)	1.86	He	−6.8	–
J115643.568+182219.804	7475(220)	8.154(0.075)	0.671(0.049)	1.68	He	–	–
J115814.502+000500.689	4225(65)	7.787(0.031)	0.446(0.016)	5.64	−0.1	–	–
J115916.225+484238.185	5855(35)	8.034(0.018)	0.608(0.011)	2.59	H	–	–
J115933.001+130031.870	6410(60)	8.011(0.034)	0.580(0.021)	1.98	He	−5.7	–
J115939.211+353801.753	7340(75)	8.479(0.020)	0.902(0.013)	3.35	H	–	–
J120003.043+433541.267	7855(75)	7.895(0.023)	0.534(0.013)	0.97	H	–	–
J120635.803+082310.491	8075(95)	8.014(0.029)	0.603(0.017)	1.07	H	–	–
J120843.248+542945.781	7800(105)	8.032(0.031)	0.613(0.019)	1.20	H	–	–
J121118.777+072445.566	5220(30)	7.930(0.018)	0.540(0.011)	3.70	H	–	–
J121130.013+572411.970	5910(40)	8.030(0.018)	0.606(0.011)	2.49	H	–	–
J121135.169+205340.438	6660(60)	7.164(0.036)	0.235(0.009)	0.77	H	–	–
J121235.829−062221.312	6260(45)	7.915(0.023)	0.539(0.013)	1.76	H	–	–
J121432.328+782253.364	4210(20)	7.511(0.022)	0.318(0.009)	3.55	He	–	−11.2
J121531.435+463014.334	6605(50)	8.069(0.020)	0.633(0.012)	2.00	H	–	–
J122121.000+330635.639	7590(100)	7.936(0.037)	0.556(0.021)	1.13	H	–	–
J122422.760+001819.365	6445(60)	8.069(0.024)	0.632(0.015)	2.15	H	–	–
J122619.639+183634.295	7465(225)	8.193(0.075)	0.697(0.050)	1.82	He	–	–
J122634.852+351309.788	5080(35)	7.797(0.025)	0.464(0.013)	3.17	H	–	–
J122724.369+315021.737	6440(50)	7.933(0.020)	0.550(0.011)	1.69	H	–	–
J122801.626+330034.312	4560(30)	7.241(0.035)	0.232(0.011)	2.35	H	–	–
J122830.251+125635.668	7245(60)	7.986(0.022)	0.584(0.013)	1.37	H	–	–
J123150.339+145204.739	5740(50)	8.354(0.025)	0.815(0.017)	5.26	H	–	–
J123448.747+054719.416	7460(85)	8.396(0.023)	0.847(0.015)	2.85	H	–	–
J123512.389+231828.183	7580(75)	7.940(0.029)	0.558(0.017)	1.14	H	–	–
J123743.069+602322.024	5295(30)	8.001(0.023)	0.583(0.014)	4.16	H	–	–
J123751.831+415629.055	6140(45)	8.211(0.018)	0.706(0.012)	3.80	He	−5.2	–
J123913.860+452506.791	6355(40)	8.305(0.014)	0.784(0.009)	3.75	H	–	–
J124023.476−231753.913	5575(35)	7.115(0.023)	0.212(0.006)	1.13	H	–	–
J124029.901+180727.367	5430(40)	8.012(0.025)	0.591(0.015)	3.57	H	–	–
J124258.203+654218.514	6545(50)	7.989(0.022)	0.583(0.013)	1.76	H	–	–
J124452.382−105109.608	7885(50)	6.996(0.016)	0.203(0.004)	0.45	H	–	–
J124748.960−011112.138	6980(55)	8.001(0.020)	0.592(0.012)	1.53	H	–	–
J125007.330+544650.211	3835(35)	7.537(0.028)	0.334(0.012)	4.86	H	–	–
J125245.331+194310.385	6625(65)	7.444(0.062)	0.303(0.022)	0.95	He	−6.8	–
J125411.085+362057.994	4445(65)	7.624(0.032)	0.367(0.014)	3.78	He	–	–
J125733.603+542850.633	7485(85)	6.441(0.068)	0.032(0.030)	0.35	H	–	–
J125804.287+501445.665	8230(75)	8.127(0.021)	0.673(0.013)	1.21	H	–	–
J130008.706+032830.355	5610(35)	8.188(0.018)	0.704(0.012)	4.54	H	–	–
J130020.930+013047.370	5295(25)	7.945(0.018)	0.550(0.011)	3.53	H	–	–
J130121.441+671307.704	6580(50)	8.234(0.017)	0.738(0.011)	2.94	H	–	–
J130144.036+260041.437	6770(55)	7.951(0.024)	0.562(0.014)	1.53	H	–	–
J130317.094+260314.916	4260(30)	7.917(0.027)	0.527(0.016)	7.51	H	–	–
J130446.151−052837.530	5215(30)	8.024(0.020)	0.596(0.012)	4.90	H	–	–
J130842.398+013445.854	7760(75)	7.100(0.035)	0.226(0.008)	0.50	H	–	–
J130843.338+850225.050	5300(25)	8.117(0.015)	0.655(0.010)	5.46	H	–	–
J131023.745+140418.781	8240(75)	7.828(0.023)	0.499(0.012)	0.79	H	–	–
J131312.582+022644.647	4295(55)	7.875(0.037)	0.503(0.021)	6.95	H	–	–
J131618.994−200731.461	4720(25)	8.110(0.017)	0.639(0.011)	7.31	He	–	−10.7
J131748.947+215710.064	6235(95)	8.212(0.033)	0.707(0.023)	3.61	He	–	–
J131924.739−214800.750	5815(35)	8.588(0.014)	0.969(0.009)	5.95	H	–	–
J132011.397+471221.248	7740(75)	7.936(0.026)	0.557(0.015)	1.07	H	–	–
J132436.951+085752.240	8125(70)	7.894(0.023)	0.534(0.013)	0.89	H	–	–
J132741.571+575508.731	6805(60)	8.011(0.022)	0.598(0.013)	1.66	H	–	–
J132937.161−013433.029	7100(60)	8.009(0.023)	0.597(0.014)	1.48	H	–	–
J133038.022+544524.110	7475(65)	8.094(0.020)	0.650(0.013)	1.45	H	–	–
J133058.968+302952.520	6220(45)	8.180(0.019)	0.686(0.012)	3.41	−3.0	–	−8.1
J133250.742+011703.162	7065(55)	8.315(0.018)	0.793(0.012)	2.85	H	–	–
J133546.712−054256.602	7750(70)	7.954(0.022)	0.567(0.012)	1.09	H	–	–

Tableau B.3 – Paramètres atmosphériques (suite)

PSO	$T_{\rm eff}$ (K)	$\log g$	M ($M_\odot$)	$\tau_{\rm cool}$(Gyr)	log H/He	log C/He	log Ca/He
J133630.389+362346.851	6770(55)	7.982(0.019)	0.580(0.011)	1.61	H	–	–
J133651.973+372720.163	7655(75)	8.444(0.020)	0.879(0.013)	2.87	H	–	–
J134118.705+022735.497	5785(20)	8.098(0.013)	0.632(0.008)	3.88	He	−6.0	–
J134121.453+050046.122	4065(20)	7.774(0.017)	0.447(0.009)	6.66	H	–	–
J134532.753+420045.327	4270(75)	6.688(0.086)	0.031(0.040)	1.35	He	–	–
J134701.200+255256.047	7030(55)	7.978(0.022)	0.579(0.013)	1.46	H	–	–
J134723.647+102136.240	6970(65)	8.007(0.020)	0.596(0.012)	1.55	H	–	–
J134801.746+233447.805	4605(20)	7.783(0.017)	0.454(0.009)	4.81	H	–	–
J134902.454+115506.917	4150(125)	7.884(0.073)	0.499(0.042)	6.58	He	–	–
J134944.359+275522.603	7230(55)	8.403(0.016)	0.851(0.010)	3.15	H	–	–
J135201.997+005420.119	6945(70)	7.946(0.028)	0.560(0.016)	1.43	H	–	–
J135211.598+105349.561	5935(40)	7.962(0.019)	0.565(0.011)	2.16	H	–	–
J135334.809+292857.538	7465(110)	8.223(0.030)	0.733(0.019)	1.88	H	–	–
J135347.019−273856.388	7470(105)	7.948(0.033)	0.563(0.019)	1.20	H	–	–
J140343.526+520648.866	7385(75)	8.015(0.024)	0.602(0.015)	1.35	H	–	–
J140346.138+064442.067	6785(155)	8.183(0.054)	0.689(0.036)	2.48	He	–	–
J140617.154+181247.113	7200(80)	8.390(0.023)	0.843(0.015)	3.12	H	–	–
J140625.514+160827.545	6555(55)	7.981(0.024)	0.579(0.014)	1.74	H	–	–
J140644.407+313025.074	4805(35)	7.947(0.028)	0.546(0.016)	5.95	H	–	–
J141039.948+024510.269	5590(30)	7.990(0.018)	0.579(0.011)	2.85	H	–	–
J141143.197+220644.803	6785(165)	8.175(0.059)	0.684(0.039)	2.44	He	–	–
J141454.587+433656.944	6325(55)	7.993(0.023)	0.585(0.013)	1.93	H	–	–
J141558.925+433715.275	6810(60)	8.071(0.024)	0.634(0.015)	1.83	H	–	–
J141843.593+145258.108	7250(90)	7.406(0.092)	0.310(0.032)	0.74	H	–	–
J142006.434+532233.120	7525(70)	7.741(0.026)	0.452(0.013)	0.90	H	–	–
J142054.438−090509.261	7645(60)	7.547(0.023)	0.364(0.009)	0.73	H	–	–
J142336.667+303740.042	5285(30)	7.017(0.030)	0.179(0.008)	1.21	H	–	–
J142727.816+611026.764	6400(30)	7.966(0.012)	0.553(0.007)	1.86	He	−6.7	–
J142747.971+053230.563	6725(155)	8.109(0.057)	0.641(0.037)	2.13	He	–	–
J142833.880+440343.831	6355(95)	8.045(0.034)	0.602(0.021)	2.33	He	–	−9.3
J143047.929+043838.453	7725(75)	8.020(0.025)	0.606(0.015)	1.21	H	–	–
J143358.119+190736.216	5080(35)	7.907(0.033)	0.525(0.019)	4.12	H	–	–
J143642.449+433241.327	4685(40)	7.934(0.024)	0.539(0.014)	6.30	0.4	–	–
J144045.262+080727.089	5465(35)	7.961(0.025)	0.561(0.014)	3.00	H	–	–
J144147.102+581656.252	6560(60)	8.045(0.024)	0.617(0.015)	1.94	H	–	–
J144722.038−303525.947	6910(70)	8.011(0.025)	0.598(0.015)	1.60	H	–	–
J144724.377−174220.078	4795(30)	8.387(0.015)	0.833(0.010)	9.06	0.3	–	–
J145011.700−191407.545	7175(50)	7.195(0.019)	0.246(0.005)	0.66	H	–	–
J145806.627+293722.103	7335(60)	7.993(0.020)	0.589(0.012)	1.34	H	–	–
J150549.155−071441.102	6640(45)	8.005(0.016)	0.593(0.010)	1.75	H	–	–
J151625.008+280320.782	7900(90)	8.099(0.025)	0.654(0.015)	1.28	H	–	–
J152038.306+390351.208	7905(80)	7.293(0.026)	0.277(0.008)	0.55	H	–	–
J152542.833+562906.754	5180(75)	7.636(0.041)	0.374(0.019)	2.53	He	–	–
J152621.138+293624.753	5125(25)	7.955(0.017)	0.554(0.010)	4.47	H	–	–
J153035.370+023537.655	7520(65)	7.924(0.024)	0.549(0.013)	1.14	H	–	–
J153417.410+021847.134	8215(85)	8.475(0.019)	0.900(0.013)	2.50	H	–	–
J153450.542+464951.710	4310(25)	7.833(0.022)	0.480(0.012)	6.45	H	–	–
J153505.673+124742.947	5465(30)	7.948(0.017)	0.539(0.010)	3.62	He	–	−8.7
J153553.942+212509.304	6265(35)	8.028(0.018)	0.606(0.011)	2.12	H	–	–
J153904.039+581116.586	6930(80)	7.957(0.030)	0.566(0.017)	1.47	H	–	–
J154234.676+232936.602	5855(40)	8.190(0.019)	0.706(0.012)	3.89	H	–	–
J154927.312+480227.403	6370(120)	8.177(0.043)	0.684(0.029)	3.06	He	–	–
J155214.453+185226.905	7605(70)	7.342(0.024)	0.290(0.008)	0.63	H	–	–
J155533.929+502547.684	6075(35)	8.022(0.016)	0.601(0.010)	2.27	H	–	–
J155857.666+041704.388	6685(120)	8.430(0.035)	0.854(0.023)	3.88	He	–	–
J155937.372+252908.504	8165(85)	7.973(0.024)	0.579(0.014)	0.98	H	–	–
J160112.509+531703.077	6655(40)	7.988(0.016)	0.584(0.010)	1.69	H	–	–
J160453.120+005512.673	4820(25)	7.864(0.021)	0.499(0.012)	4.97	H	–	–
J160520.416+555648.009	6780(60)	7.397(0.028)	0.304(0.010)	0.86	H	–	–
J160714.202+342343.655	5555(30)	7.964(0.018)	0.564(0.011)	2.78	H	–	–
J161424.609+090559.583	4775(20)	7.902(0.019)	0.520(0.011)	5.57	H	–	–
J162626.179+193841.981	6075(35)	8.236(0.016)	0.737(0.010)	3.79	H	–	–
J162632.170+135555.760	6785(65)	7.967(0.025)	0.571(0.015)	1.56	H	–	–
J162753.421+091210.805	6780(60)	8.353(0.018)	0.817(0.012)	3.44	H	–	–

Tableau B.3 – Paramètres atmosphériques (suite)

PSO	$T_{\rm eff}$ (K)	$\log g$	M ($M_\odot$)	$\tau_{\rm cool}$(Gyr)	log H/He	log C/He	log Ca/He
J162824.563+364623.925	8070(140)	7.923(0.008)	0.532(0.005)	1.01	−3.5	–	−9.1
J162838.600+705315.999	4935(45)	8.010(0.030)	0.586(0.018)	6.12	H	–	–
J163233.374+085119.813	5600(25)	7.555(0.016)	0.356(0.007)	1.51	H	–	–
J163332.333+523147.315	6480(55)	7.945(0.022)	0.558(0.013)	1.69	H	–	–
J163419.735+571024.918	6045(50)	7.991(0.025)	0.566(0.015)	2.43	He	−7.2	–
J163501.681+431733.032	6525(35)	8.174(0.013)	0.699(0.009)	2.63	H	–	–
J163729.220+011000.455	7000(65)	7.961(0.026)	0.569(0.015)	1.44	H	–	–
J163740.613+134033.370	6745(60)	7.974(0.022)	0.576(0.013)	1.60	H	–	–
J163920.319+403042.216	8200(95)	8.113(0.025)	0.664(0.016)	1.19	H	–	–
J164031.981+222927.177	7445(95)	8.064(0.029)	0.632(0.018)	1.41	H	–	–
J164056.980+534107.114	7740(60)	8.277(0.016)	0.769(0.011)	1.93	He	–	–
J164136.626+151230.835	7240(50)	7.870(0.017)	0.518(0.010)	1.16	H	–	–
J165445.708+382932.684	5800(35)	8.173(0.016)	0.695(0.011)	3.87	H	–	–
J165847.290−061710.343	5515(30)	8.067(0.017)	0.626(0.011)	3.70	H	–	–
J165935.575+442540.414	5535(30)	7.949(0.017)	0.554(0.010)	2.73	H	–	–
J165939.800+320317.653	6340(45)	8.459(0.016)	0.887(0.011)	4.52	H	–	–
J170246.328+102244.288	5145(35)	8.410(0.019)	0.849(0.013)	8.17	H	–	–
J170401.508+200701.791	6280(50)	8.021(0.022)	0.602(0.013)	2.07	H	–	–
J170447.882+360845.357	4820(30)	7.825(0.026)	0.477(0.014)	4.54	H	–	–
J170513.263+042343.184	8170(70)	7.948(0.022)	0.565(0.012)	0.94	H	–	–
J170807.953+025732.205	6035(85)	8.052(0.140)	0.606(0.086)	2.81	He	–	−10.1
J171450.782+391839.916	6710(50)	7.803(0.020)	0.480(0.010)	1.29	H	–	–
J172349.645+045845.730	8260(90)	7.953(0.027)	0.568(0.016)	0.92	H	–	–
J172818.445+021107.752	8130(80)	8.102(0.022)	0.657(0.014)	1.19	H	–	–
J173336.090+794915.945	5535(55)	8.280(0.023)	0.751(0.015)	5.72	He	–	–
J174146.220+240145.262	7175(60)	8.411(0.017)	0.856(0.011)	3.25	H	–	–
J174248.474+433806.596	5405(30)	7.975(0.017)	0.569(0.010)	3.33	H	–	–
J174300.542+170142.511	4315(30)	7.939(0.025)	0.540(0.015)	7.56	H	–	–
J174707.557+285910.684	5495(60)	7.916(0.028)	0.520(0.016)	3.25	He	–	–
J174941.331+824704.308	7170(45)	7.878(0.015)	0.522(0.008)	1.20	H	–	–
J175704.476+405253.312	5180(60)	7.913(0.029)	0.518(0.017)	4.37	He	–	–
J175822.216+141731.058	5395(30)	7.972(0.017)	0.567(0.010)	3.37	H	–	–
J180127.345+505001.780	4635(60)	7.850(0.024)	0.481(0.013)	5.12	−0.3	–	–
J180151.415+084609.344	5585(30)	7.677(0.023)	0.411(0.011)	1.73	H	–	–
J181331.031+324829.110	7575(55)	7.969(0.019)	0.575(0.011)	1.19	H	–	–
J181335.270+324841.621	6415(45)	7.967(0.020)	0.570(0.012)	1.79	H	–	–
J181527.531+315851.639	5030(25)	7.847(0.020)	0.491(0.011)	3.78	H	–	–
J181608.846+245438.131	6740(55)	8.273(0.017)	0.764(0.012)	2.97	H	–	–
J181706.119+132811.013	4920(25)	7.842(0.019)	0.488(0.010)	4.27	He	–	–
J181959.432+173920.273	4820(30)	7.979(0.023)	0.566(0.014)	6.25	H	–	–
J182120.071+610059.413	4865(20)	7.793(0.017)	0.461(0.009)	4.04	He	–	–
J183358.369+194548.662	7305(140)	8.040(0.043)	0.597(0.027)	1.47	He	−6.2	–
J185106.731+773836.627	4850(60)	7.743(0.030)	0.425(0.016)	3.63	He	–	–
J185713.929+202625.343	6555(45)	8.273(0.017)	0.764(0.012)	3.24	H	–	–
J185739.691+533032.692	4430(60)	7.686(0.030)	0.396(0.015)	4.25	He	–	–
J191316.499+294932.083	6085(35)	8.109(0.017)	0.655(0.011)	2.81	H	–	–
J191435.901+142820.697	6800(50)	8.171(0.018)	0.697(0.012)	2.24	H	–	–
J191647.498+804432.340	5320(30)	8.084(0.021)	0.634(0.013)	4.96	H	–	–
J191858.653+384318.615	6140(85)	8.127(0.029)	0.651(0.019)	3.12	He	–	–
J194002.218+834852.743	4740(35)	8.274(0.022)	0.756(0.015)	8.85	H	–	–
J194529.731+465009.911	5330(30)	8.105(0.018)	0.648(0.012)	5.14	H	–	–
J200535.745−105655.436	4600(20)	8.179(0.015)	0.692(0.010)	8.75	H	–	–
J200655.192+614308.342	5305(25)	7.328(0.018)	0.269(0.006)	1.45	H	–	–
J201355.464+064237.635	6455(115)	8.098(0.042)	0.633(0.027)	2.36	He	–	–
J202220.821+833357.324	5605(85)	7.961(0.038)	0.547(0.023)	3.28	He	–	–
J203109.399−165841.014	5500(35)	7.928(0.019)	0.542(0.011)	2.70	H	–	–
J205020.293+263037.327	4930(25)	7.227(0.020)	0.232(0.006)	1.78	H	–	–
J205100.086−245206.115	7465(70)	8.073(0.020)	0.637(0.012)	1.42	H	–	–
J205648.322−045041.820	4365(35)	7.854(0.024)	0.491(0.013)	6.50	H	–	–
J205906.010+003348.099	7380(70)	7.932(0.027)	0.553(0.016)	1.21	H	–	–
J205945.315+551735.433	4415(35)	7.929(0.021)	0.534(0.013)	7.15	0.6	–	–
J210202.556+191253.722	6650(45)	8.040(0.017)	0.615(0.010)	1.85	H	–	–
J210212.316+245739.102	6015(35)	8.151(0.015)	0.682(0.010)	3.26	H	–	–
J210745.033+074042.876	7060(55)	8.036(0.020)	0.614(0.012)	1.56	H	–	–

Tableau B.3 – Paramètres atmosphériques (suite)

PSO	$T_{\rm eff}$ (K)	$\log g$	M ($M_\odot$)	$\tau_{\rm cool}$(Gyr)	log H/He	log C/He	log Ca/He
J211050.100−212929.023	5935(35)	8.057(0.017)	0.622(0.011)	2.63	H	–	–
J211329.157+072705.563	6395(50)	7.965(0.020)	0.569(0.012)	1.80	H	–	–
J211640.387−072455.126	4640(25)	7.474(0.024)	0.311(0.009)	2.80	H	–	–
J212042.160+581921.738	7820(95)	7.961(0.028)	0.571(0.016)	1.08	H	–	–
J212147.719−013035.307	6450(45)	8.027(0.018)	0.606(0.011)	1.96	H	–	–
J212212.288+041351.975	4935(25)	7.770(0.019)	0.449(0.010)	3.56	H	–	–
J213424.400+365518.543	7415(70)	8.118(0.020)	0.665(0.013)	1.54	H	–	–
J214208.829+132843.106	7390(70)	7.942(0.022)	0.559(0.013)	1.22	H	–	–
J214632.643+155040.799	7715(90)	7.310(0.046)	0.281(0.014)	0.59	H	–	–
J214913.617+041547.631	5165(25)	7.368(0.020)	0.280(0.007)	1.63	H	–	–
J215500.756−275036.006	5220(55)	7.846(0.026)	0.480(0.014)	3.68	He	–	–
J220947.316+142950.134	7475(65)	8.126(0.018)	0.671(0.012)	1.53	H	–	–
J221034.377+453235.823	5290(55)	7.854(0.028)	0.484(0.017)	3.52	He	–	–
J221408.663+372708.893	6345(95)	8.469(0.028)	0.879(0.019)	4.56	He	–	–
J221748.096+370752.142	4485(35)	7.917(0.023)	0.528(0.014)	6.80	H	–	–
J221851.326+483928.522	7155(55)	7.767(0.020)	0.463(0.010)	1.05	H	–	–
J221928.867+212222.995	4395(90)	6.795(0.097)	0.080(0.038)	1.61	He	–	–
J222740.527+175320.338	6550(50)	7.919(0.022)	0.543(0.012)	1.58	H	–	–
J222802.026+120732.876	6675(90)	8.049(0.032)	0.606(0.019)	2.04	He	–	−9.9
J222934.149+232739.619	5035(25)	8.123(0.021)	0.658(0.014)	6.86	H	–	–
J223037.292+125621.531	7450(80)	8.454(0.021)	0.886(0.014)	3.13	H	–	–
J223049.491−094509.568	7255(70)	7.900(0.027)	0.534(0.015)	1.20	H	–	–
J223056.031+152356.162	5350(30)	8.158(0.019)	0.682(0.013)	5.58	H	–	–
J223402.331+554327.087	6890(55)	8.048(0.020)	0.620(0.012)	1.70	H	–	–
J223858.645+131303.550	7975(90)	7.993(0.028)	0.590(0.016)	1.07	H	–	–
J224104.814+364639.407	7185(60)	8.094(0.020)	0.650(0.013)	1.61	H	–	–
J224157.680+133234.281	5920(50)	8.237(0.022)	0.738(0.014)	4.11	H	–	–
J224946.766+362321.573	5030(25)	8.006(0.021)	0.584(0.013)	5.61	H	–	–
J225124.135+293946.047	5610(25)	7.696(0.017)	0.420(0.008)	1.75	H	–	–
J225339.217+813041.465	3940(35)	6.932(0.056)	0.129(0.019)	2.39	He	–	–
J225355.149−064701.663	4170(90)	8.060(0.080)	0.607(0.050)	8.36	He	–	−9.8
J225549.954−075002.977	6690(55)	7.983(0.021)	0.581(0.013)	1.66	H	–	–
J225555.991+054519.616	5805(35)	7.939(0.020)	0.551(0.011)	2.23	H	–	–
J230244.708+431247.175	7905(80)	7.933(0.023)	0.556(0.013)	1.01	H	–	–
J230538.921+433401.116	4770(20)	7.764(0.023)	0.445(0.012)	4.08	H	–	–
J230812.905+241424.726	4825(25)	7.863(0.024)	0.498(0.013)	4.94	H	–	–
J231205.986+131054.970	5120(30)	7.914(0.021)	0.530(0.012)	4.00	H	–	–
J231424.920−063249.681	7360(40)	7.966(0.013)	0.555(0.008)	1.31	He	−6.0	–
J231519.254−020938.450	5670(140)	7.895(0.072)	0.509(0.041)	2.65	He	–	−10.1
J231612.797+172045.536	4800(20)	6.697(0.054)	0.054(0.024)	1.21	H	–	–
J231909.035−061309.035	4465(40)	7.725(0.034)	0.423(0.017)	4.69	H	–	–
J231935.449−022904.088	5075(25)	7.221(0.022)	0.232(0.007)	1.57	H	–	–
J232328.410+725507.872	7470(75)	7.808(0.024)	0.486(0.012)	0.99	H	–	–
J232418.827+283553.370	7060(55)	7.962(0.021)	0.570(0.012)	1.41	H	–	–
J232520.161+140341.102	5050(20)	7.300(0.018)	0.256(0.006)	1.70	H	–	–
J232557.991+255219.244	5765(35)	7.482(0.022)	0.328(0.009)	1.33	H	–	–
J233856.534+210120.429	5285(35)	8.074(0.022)	0.628(0.014)	5.07	H	–	–
J233901.088+531600.768	6275(50)	7.997(0.022)	0.587(0.013)	1.99	H	–	–
J234245.734−100122.294	4980(45)	7.932(0.034)	0.539(0.020)	4.94	H	–	–
J234314.753−165943.917	4580(30)	7.990(0.036)	0.563(0.022)	6.88	He	–	−10.5
J234612.394+115849.053	5935(75)	8.175(0.029)	0.682(0.019)	4.06	He	–	–
J234735.257+030434.827	4580(50)	7.597(0.032)	0.355(0.014)	3.31	−1.2	–	–
J234753.583+022339.475	5115(40)	7.163(0.049)	0.217(0.014)	1.46	H	–	–
J234858.098+430036.913	4750(20)	7.258(0.028)	0.239(0.009)	2.11	H	–	–
J234954.980+293358.408	5790(25)	7.864(0.015)	0.508(0.008)	2.02	H	–	–
J235313.281+205115.352	7225(60)	7.563(0.024)	0.369(0.010)	0.84	H	–	–
J235456.492+402723.413	7545(55)	7.933(0.018)	0.536(0.010)	1.14	He	−5.9	–

Annexe C

Ajustements photométriques des étoiles de l'échantillon du Chapitre 9

Figure C.1 – Ajustements photométriques des étoiles DA et DC

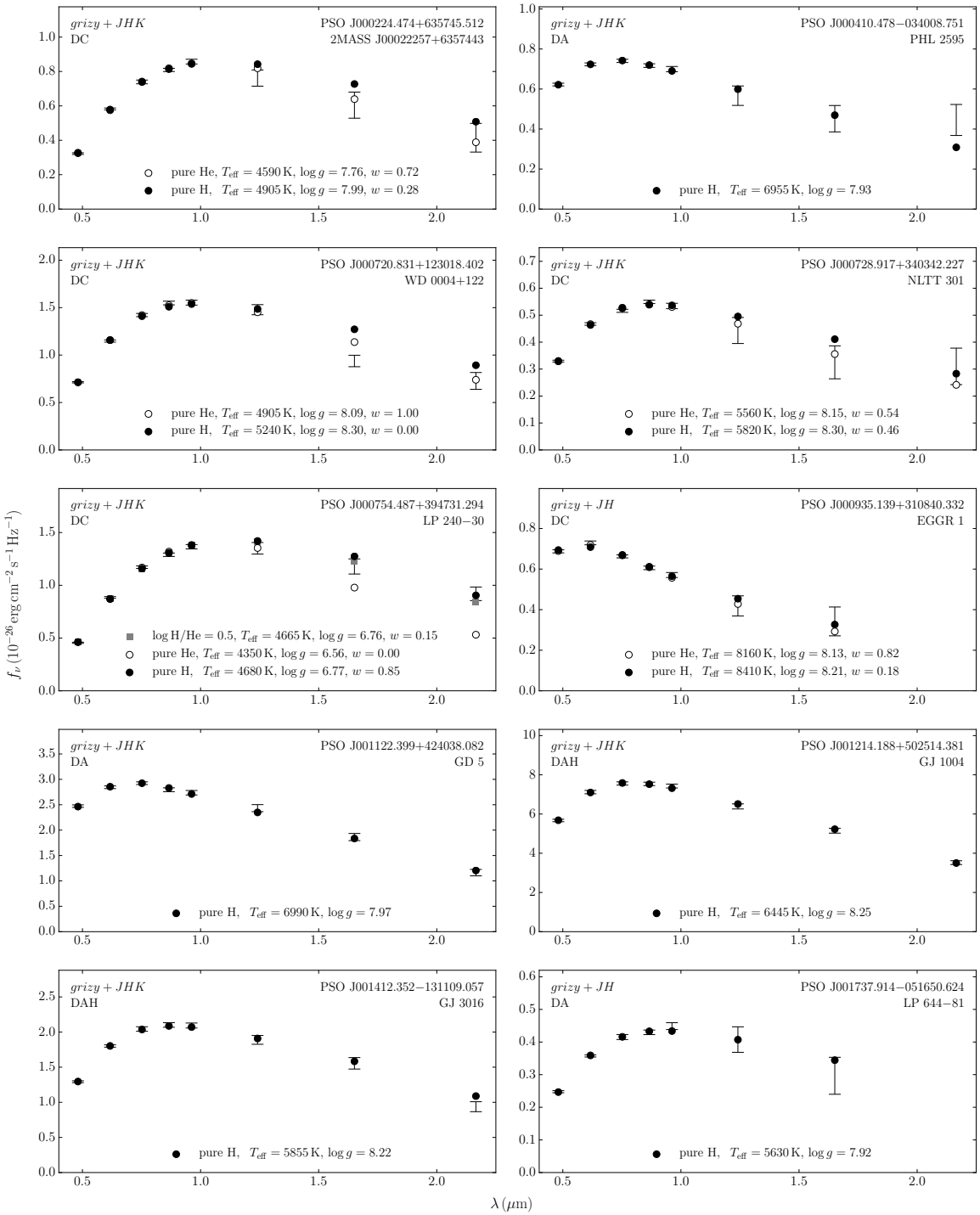

Figure C.1 – Ajustements photométriques des étoiles DA et DC (suite)

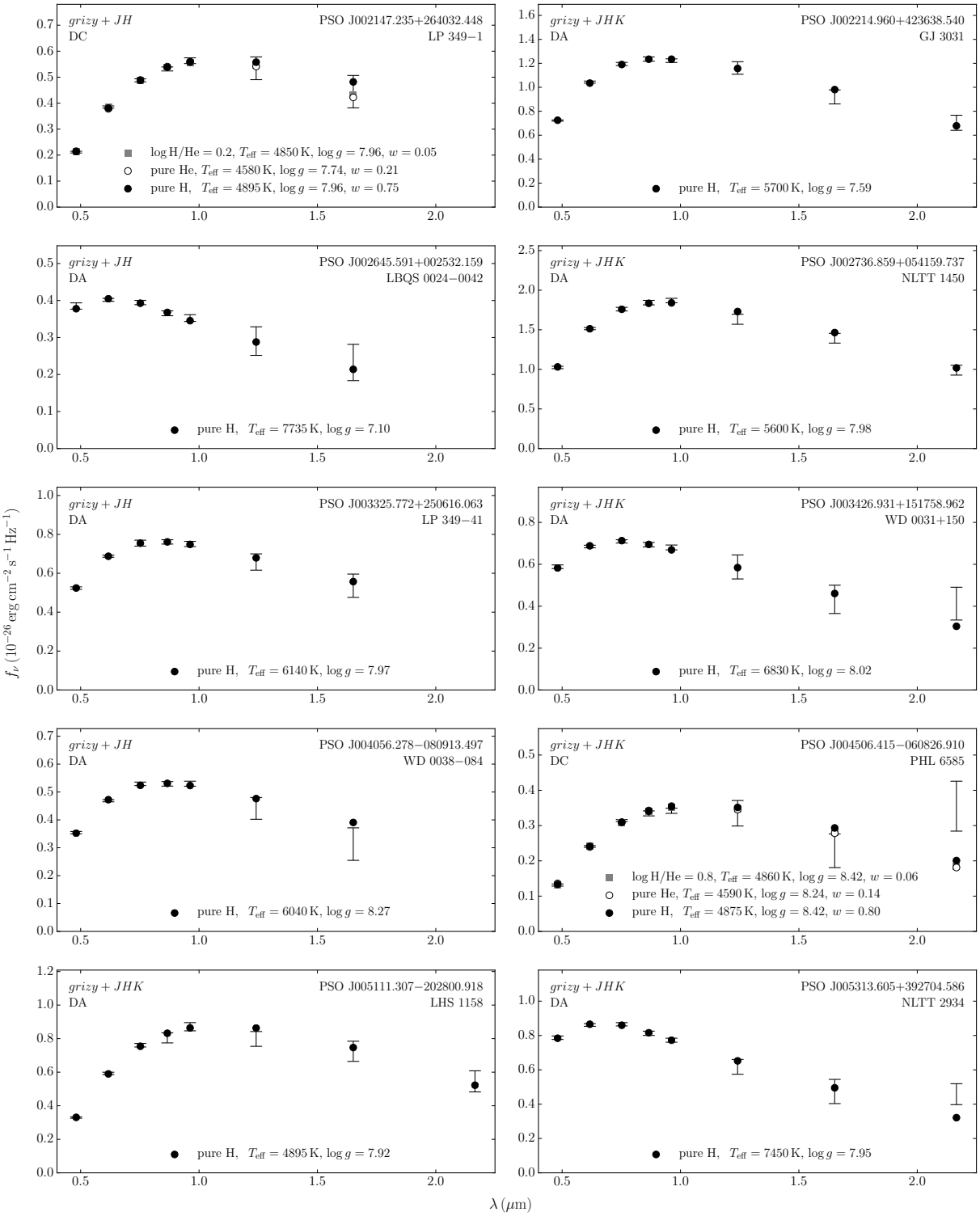

Figure C.1 – Ajustements photométriques des étoiles DA et DC (suite)

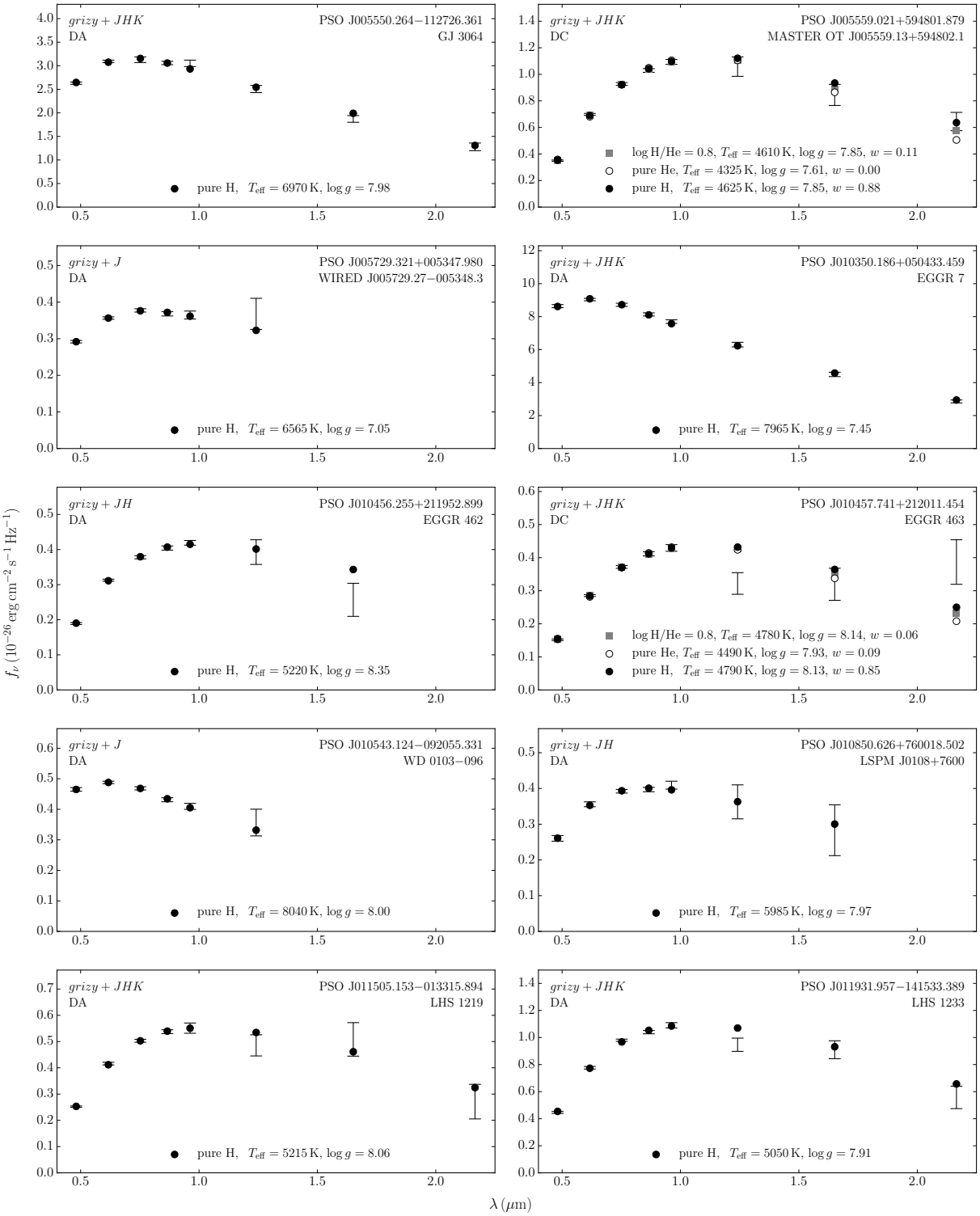

Figure C.1 – Ajustements photométriques des étoiles DA et DC (suite)

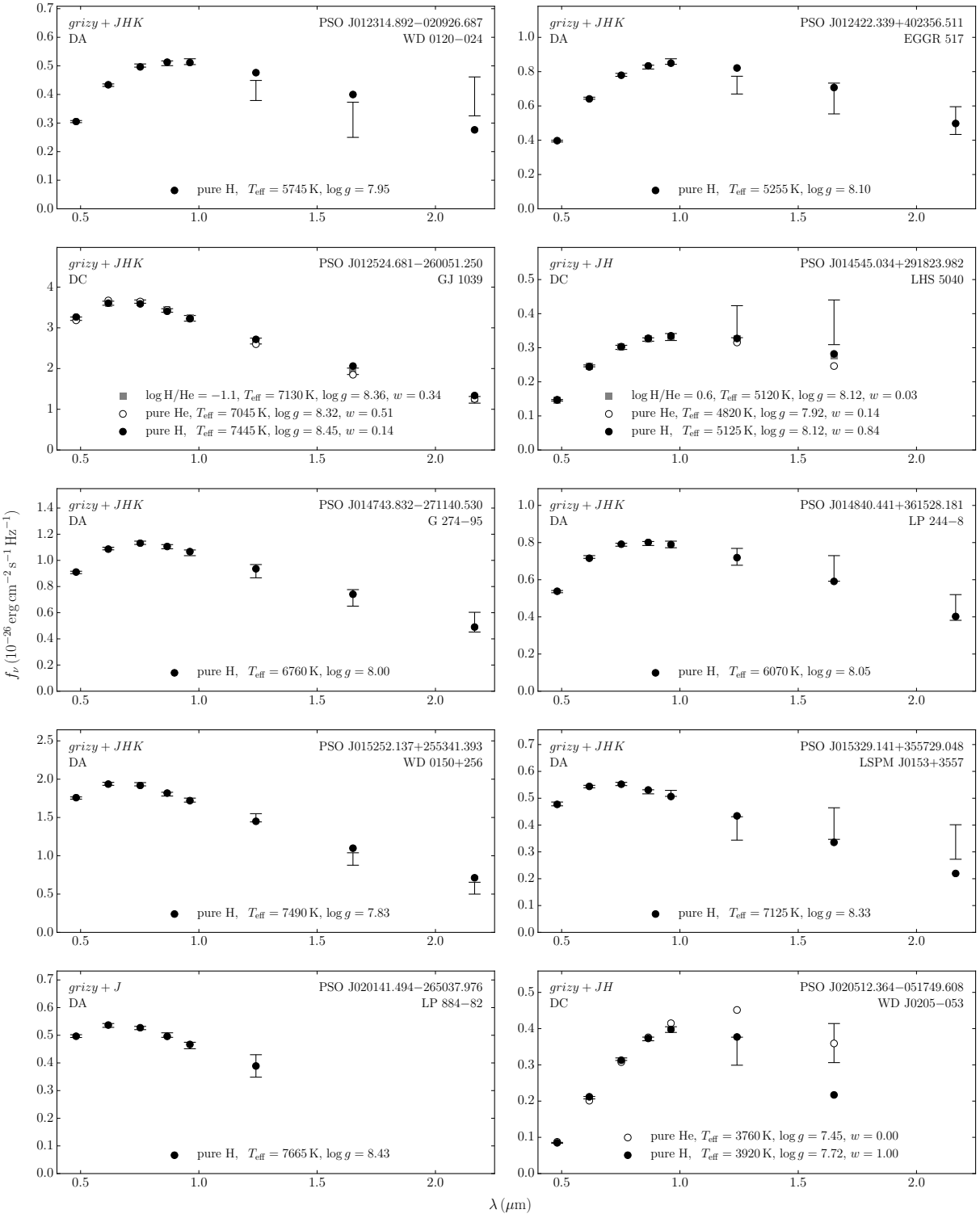

Figure C.1 – Ajustements photométriques des étoiles DA et DC (suite)

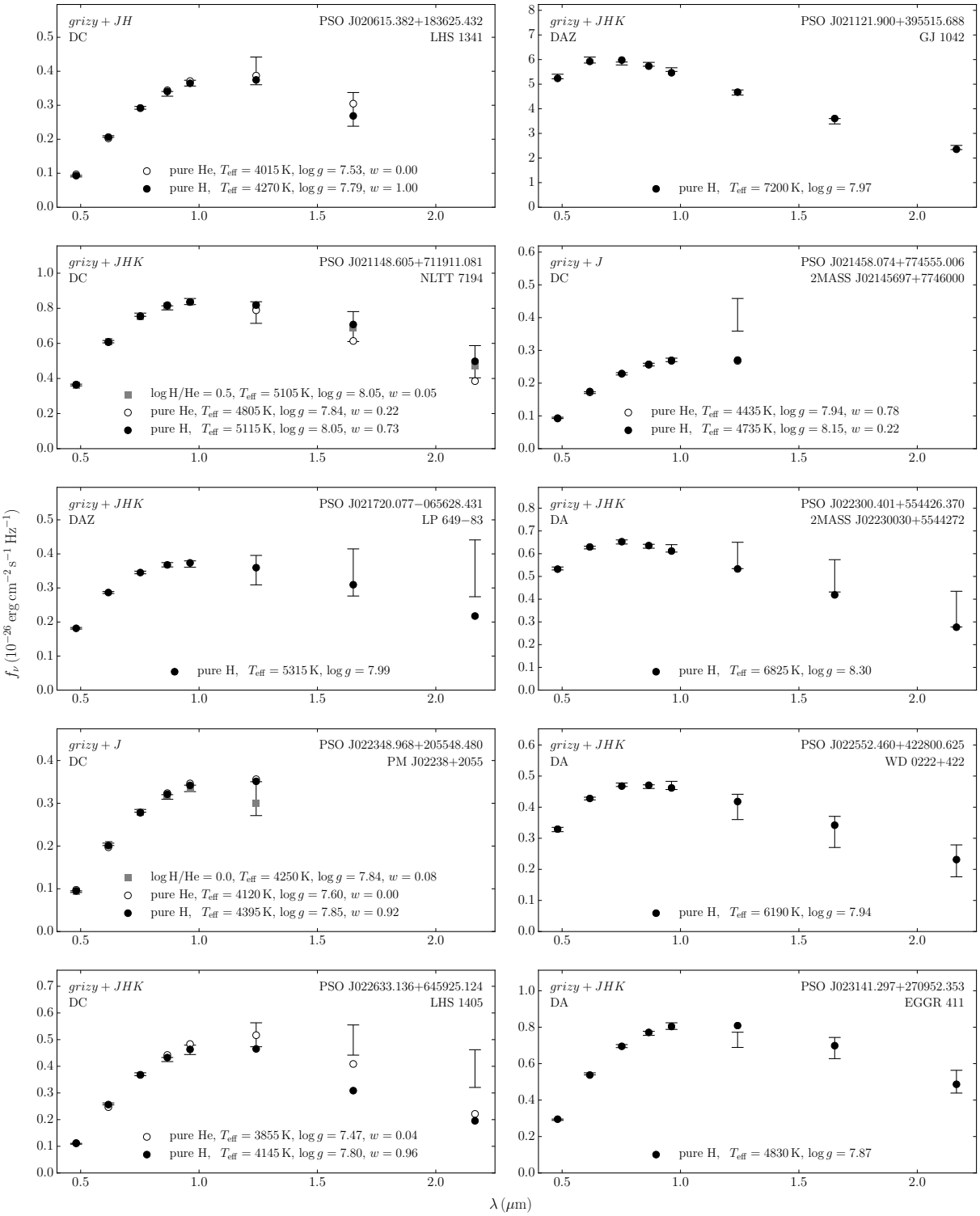

Figure C.1 – Ajustements photométriques des étoiles DA et DC (suite)

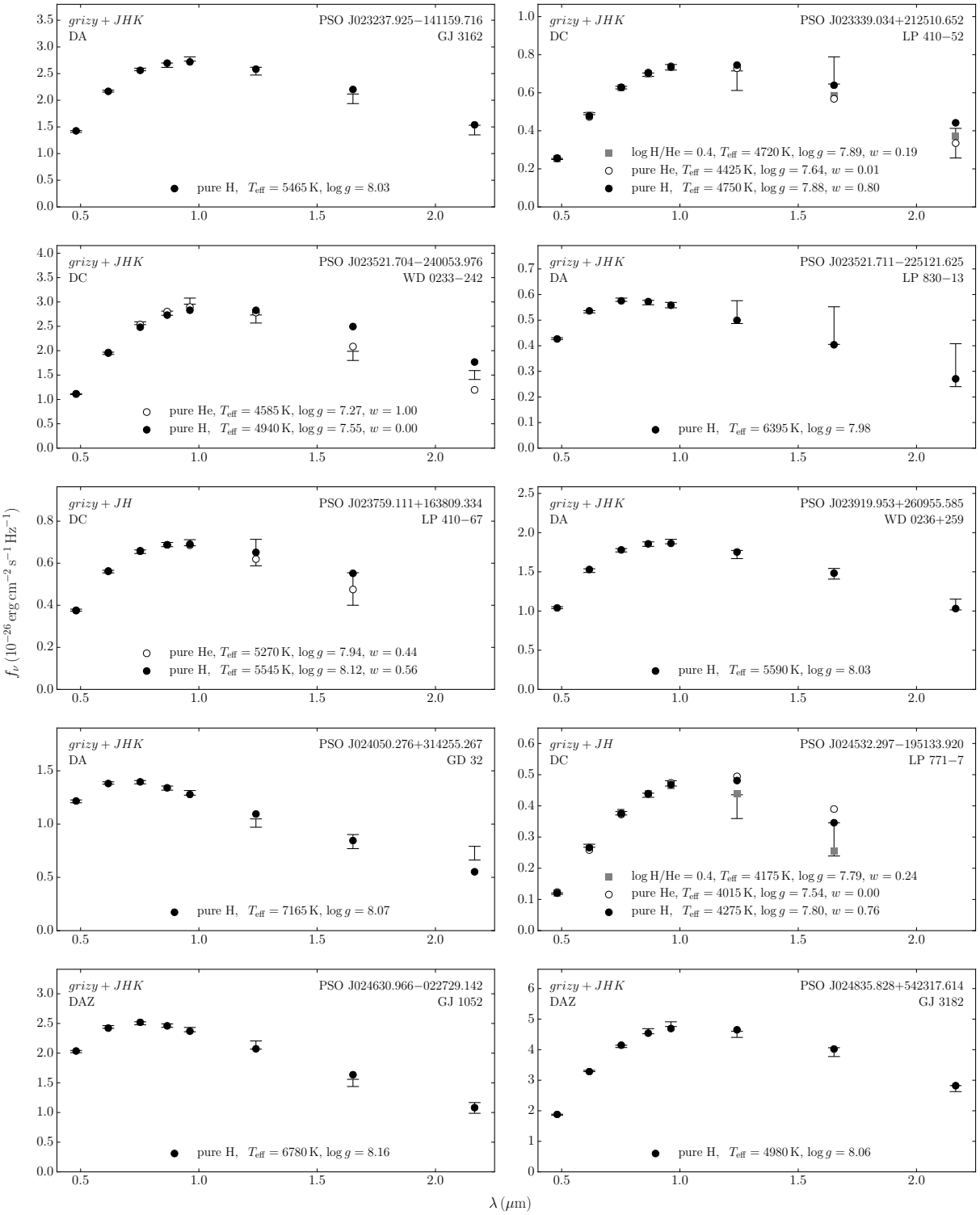

Figure C.1 – Ajustements photométriques des étoiles DA et DC (suite)

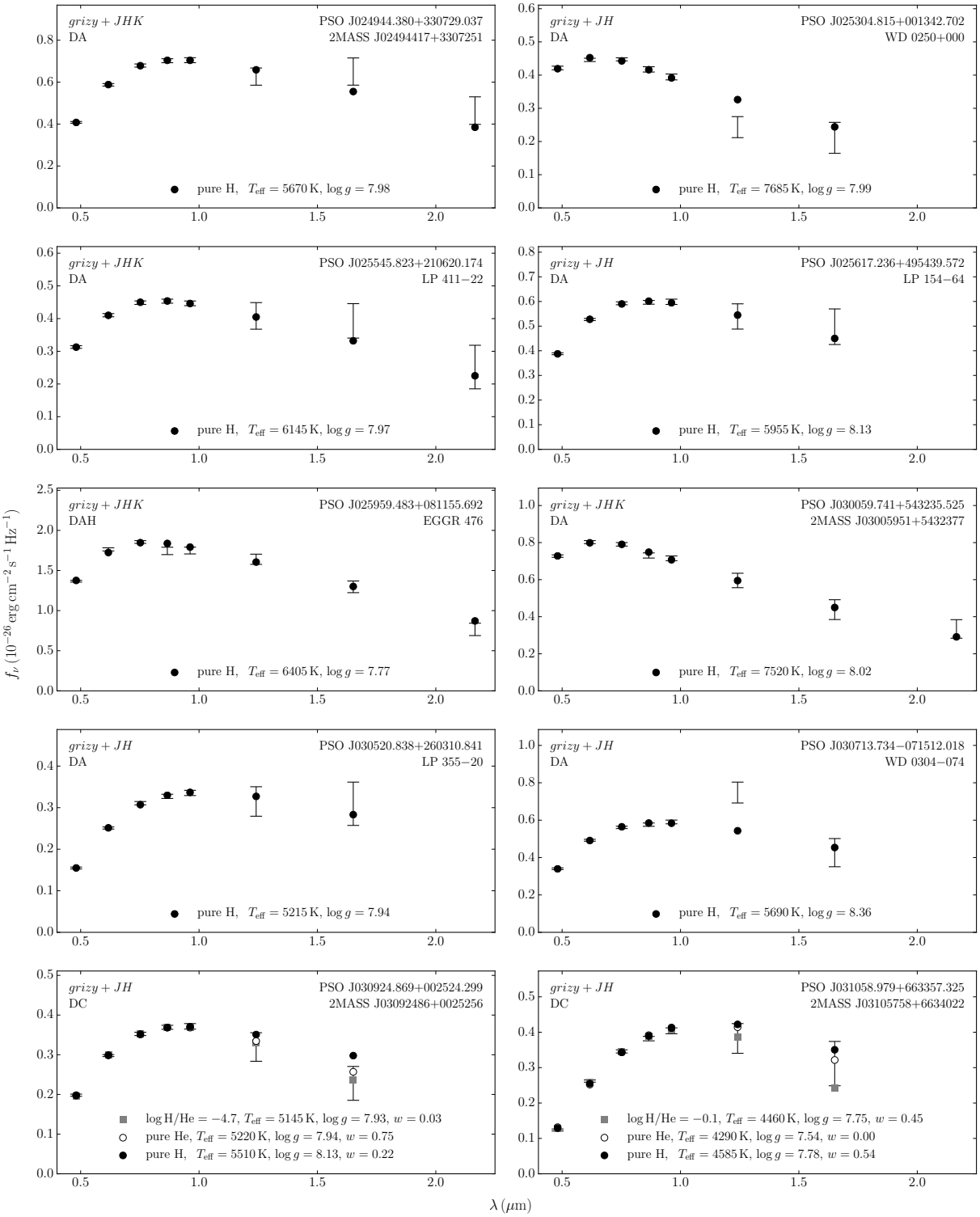

Figure C.1 – Ajustements photométriques des étoiles DA et DC (suite)

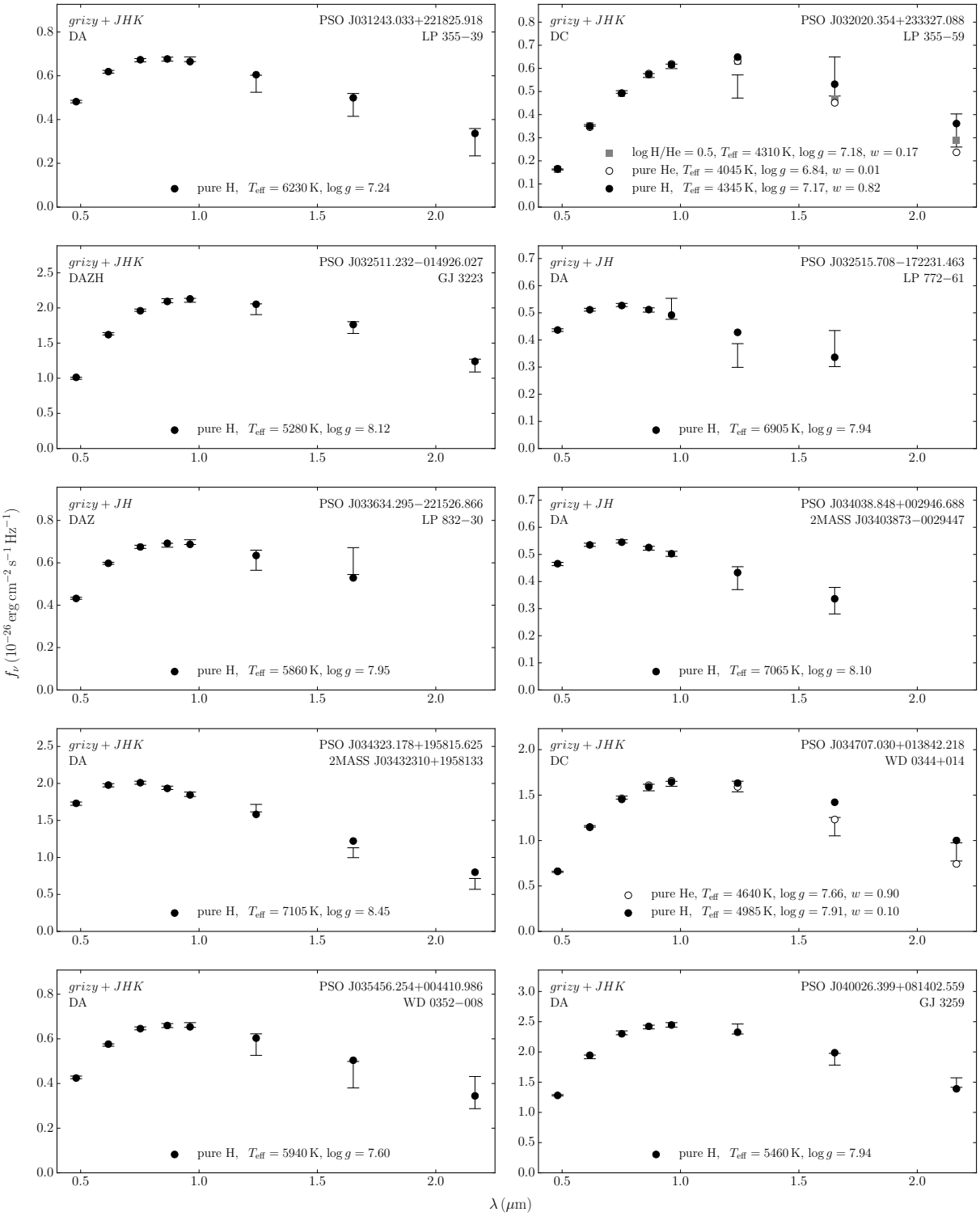

Figure C.1 – Ajustements photométriques des étoiles DA et DC (suite)

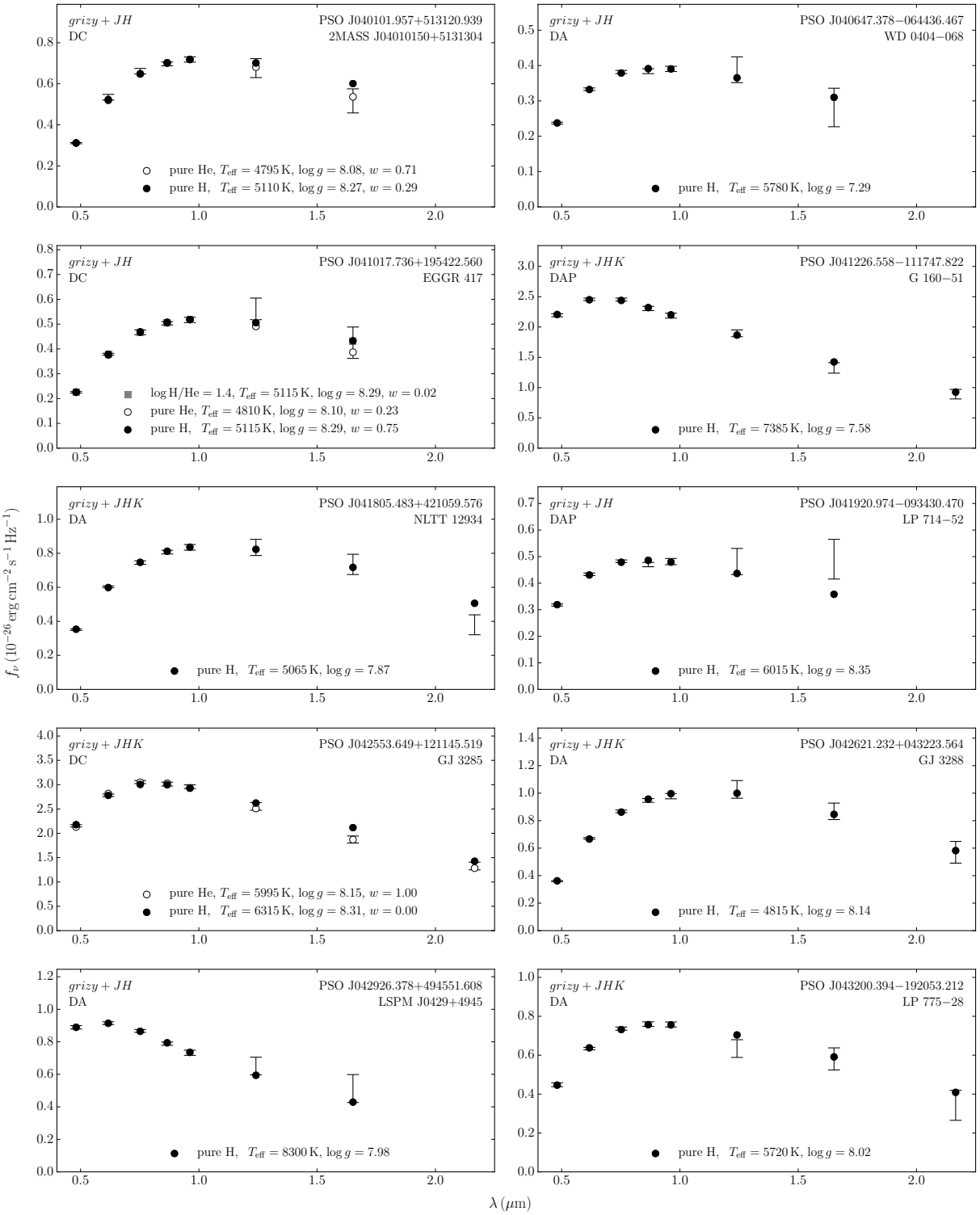

Figure C.1 – Ajustements photométriques des étoiles DA et DC (suite)

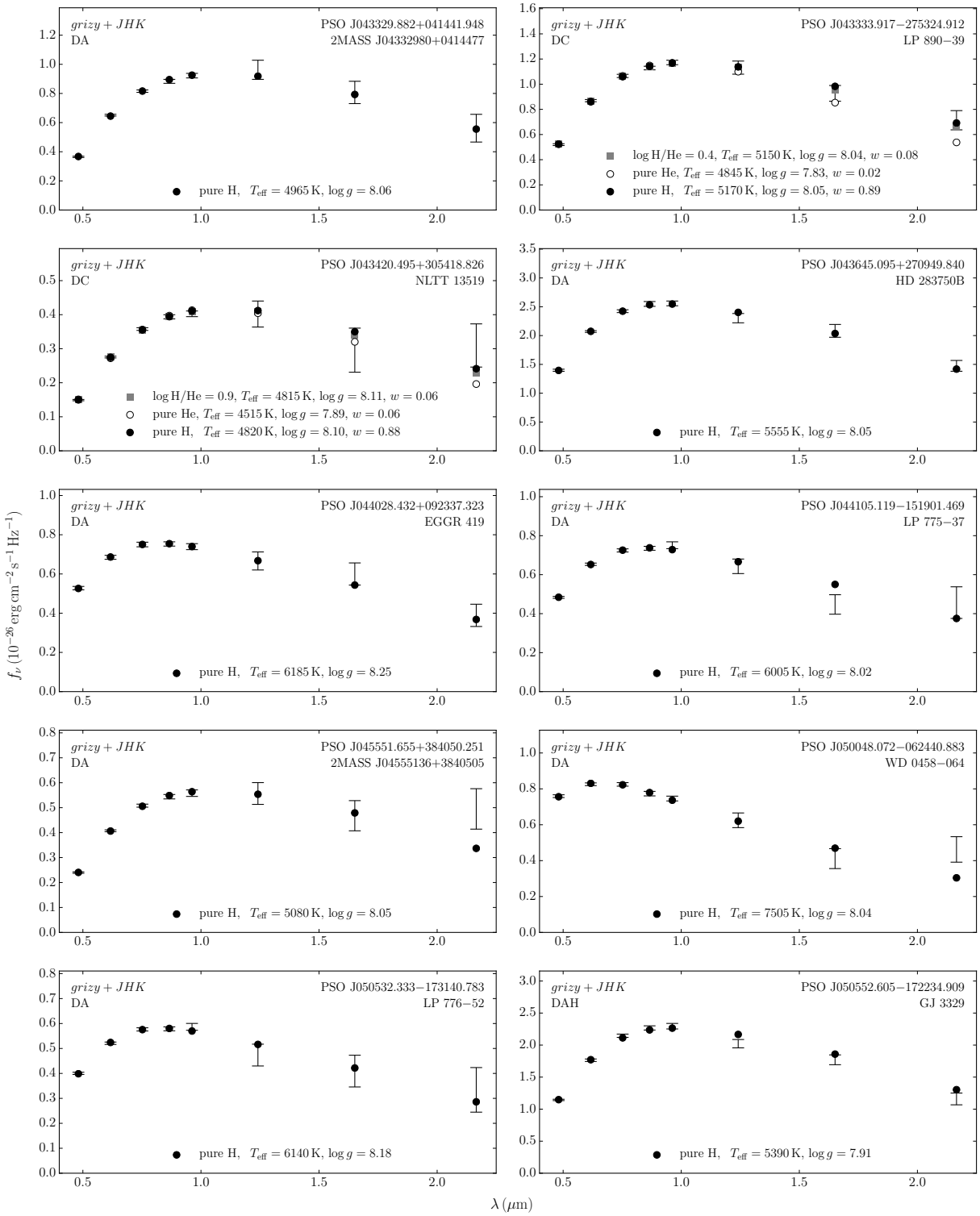

Figure C.1 – Ajustements photométriques des étoiles DA et DC (suite)

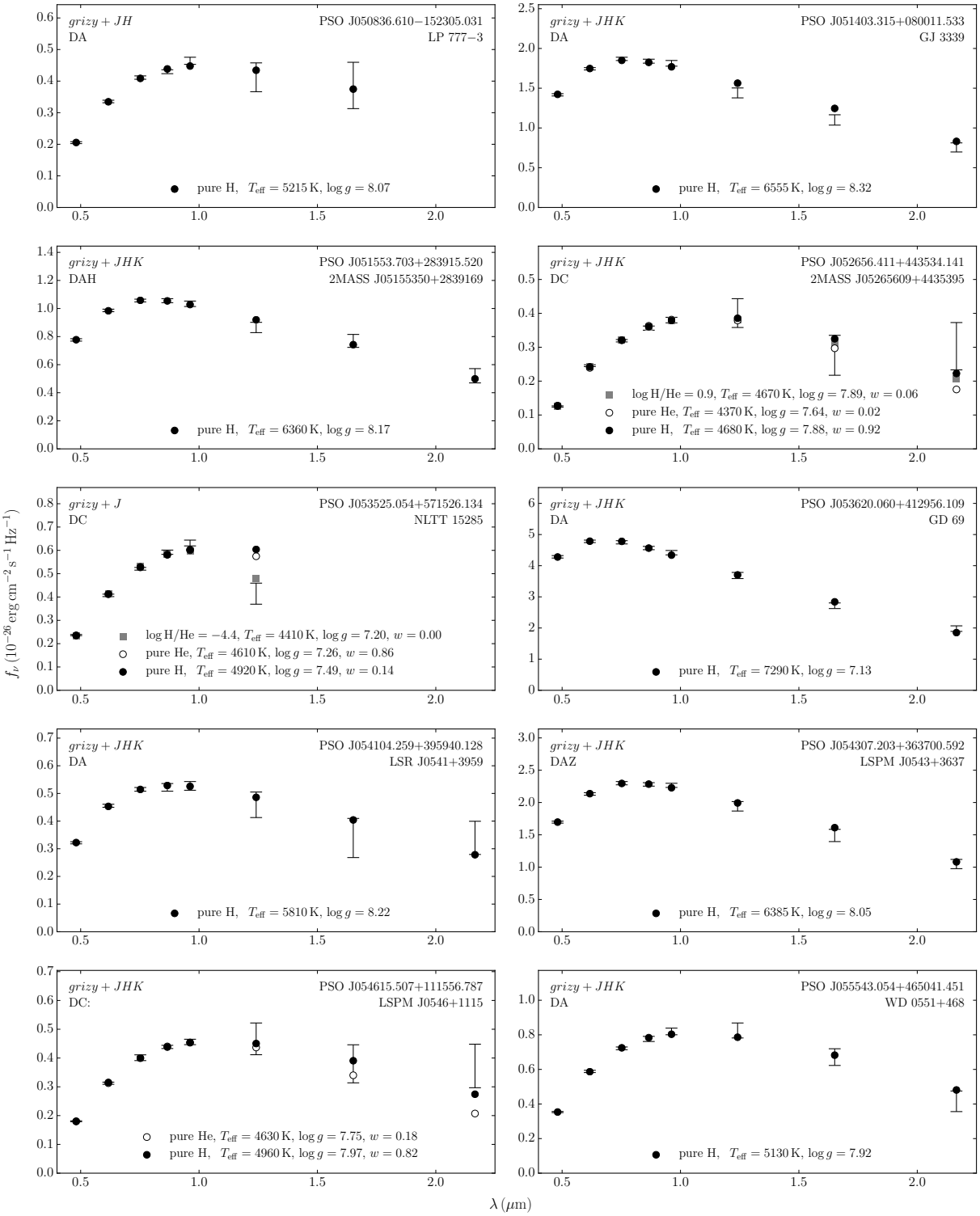

Figure C.1 – Ajustements photométriques des étoiles DA et DC (suite)

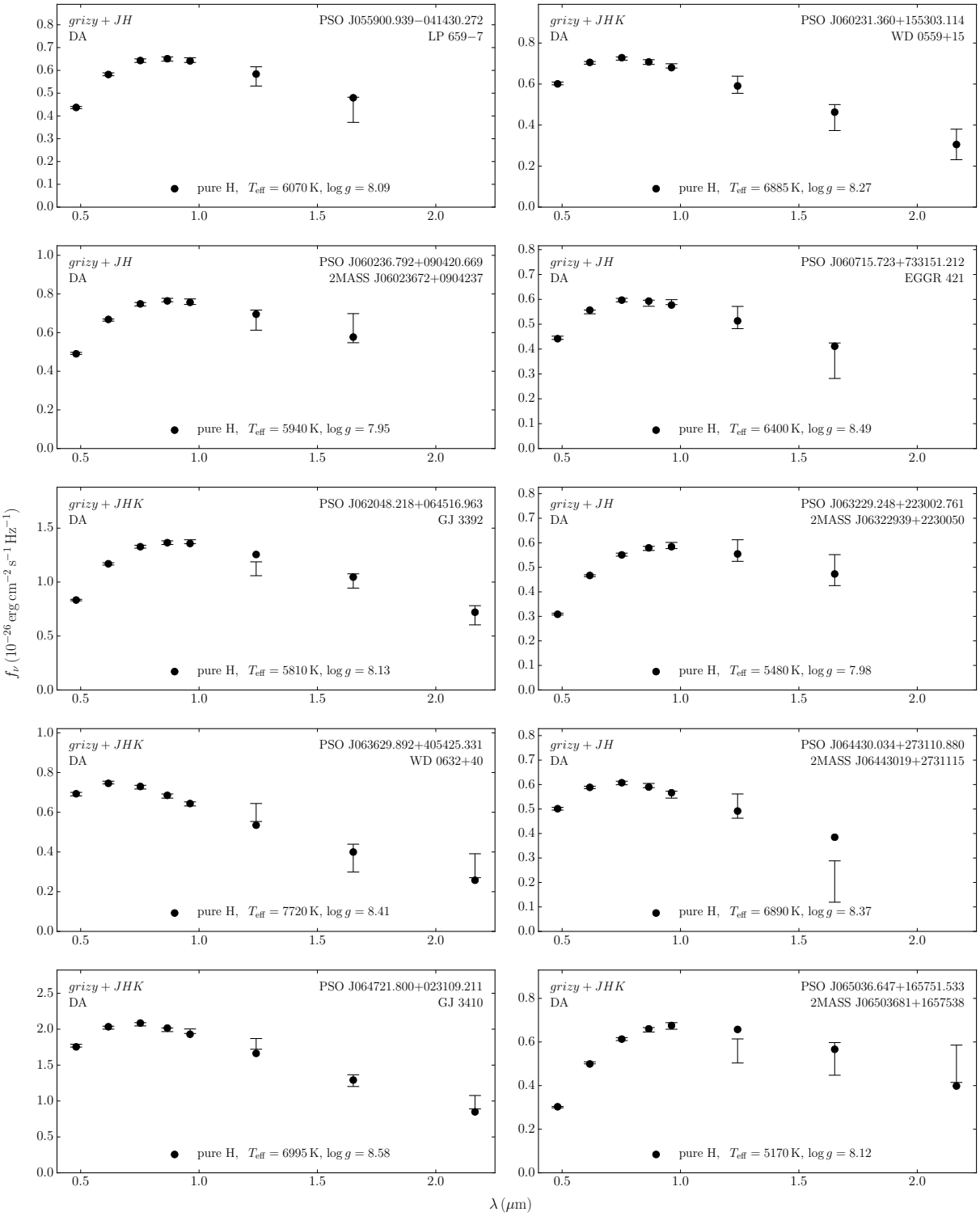

Figure C.1 – Ajustements photométriques des étoiles DA et DC (suite)

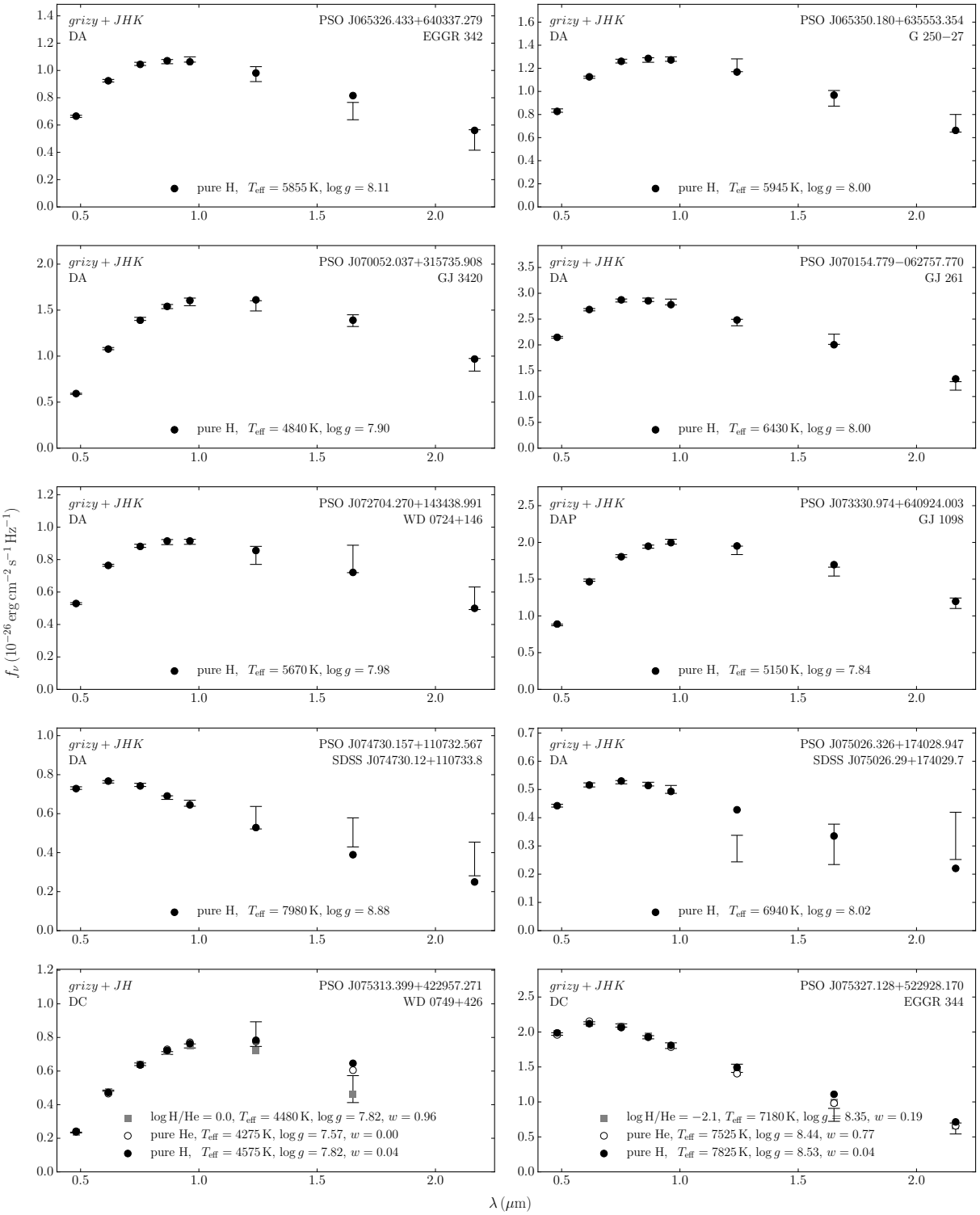

Figure C.1 – Ajustements photométriques des étoiles DA et DC (suite)

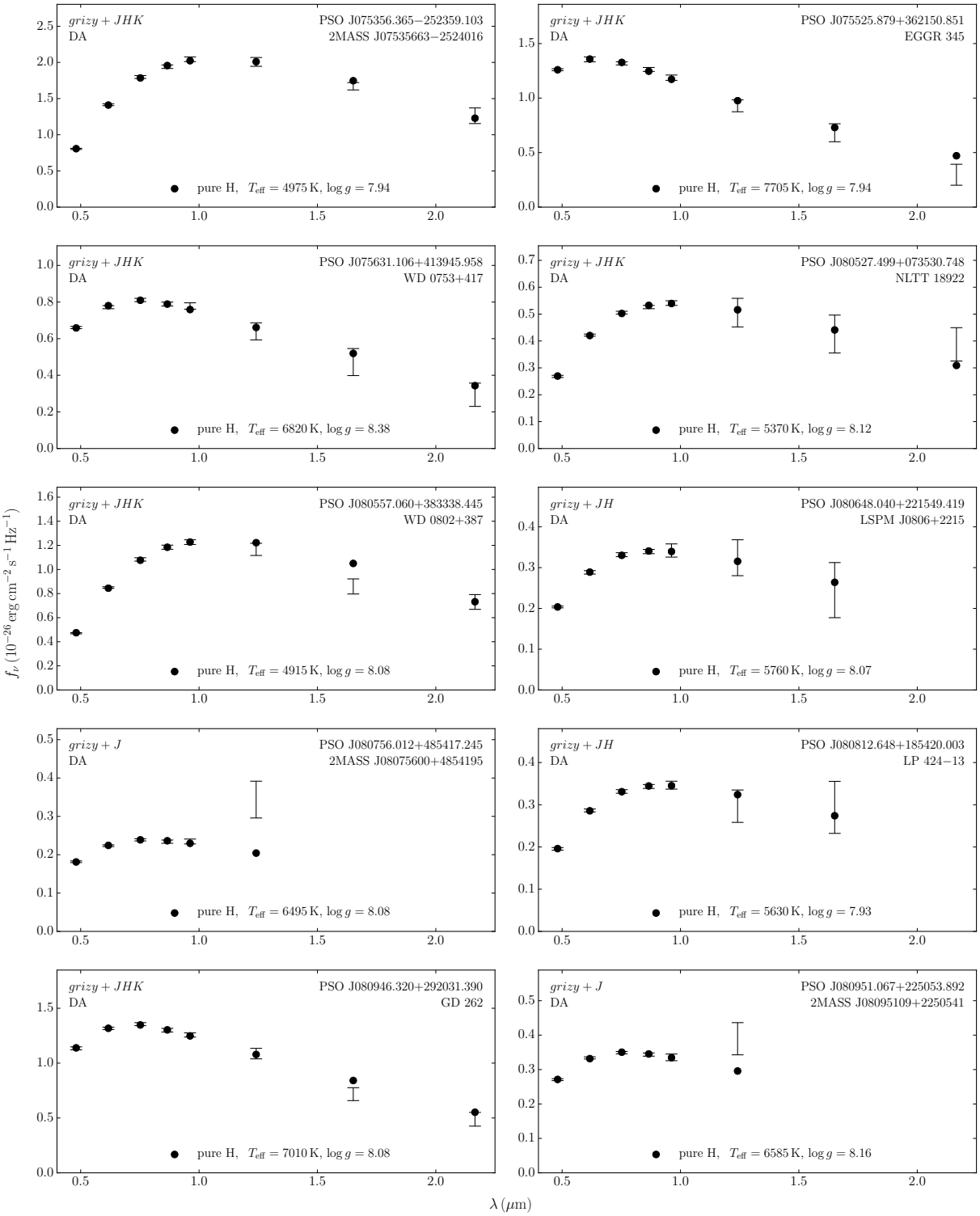

Figure C.1 – Ajustements photométriques des étoiles DA et DC (suite)

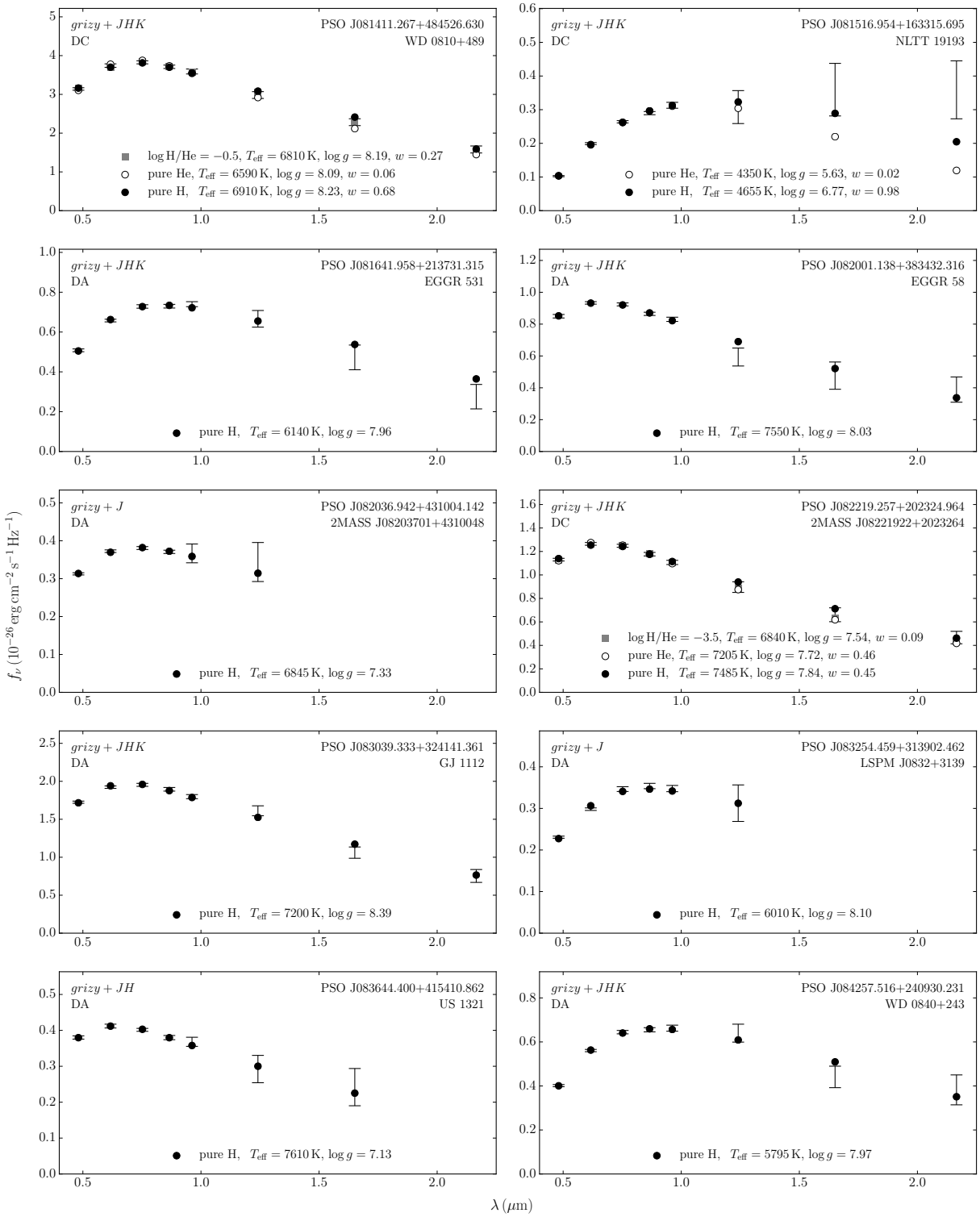

Figure C.1 – Ajustements photométriques des étoiles DA et DC (suite)

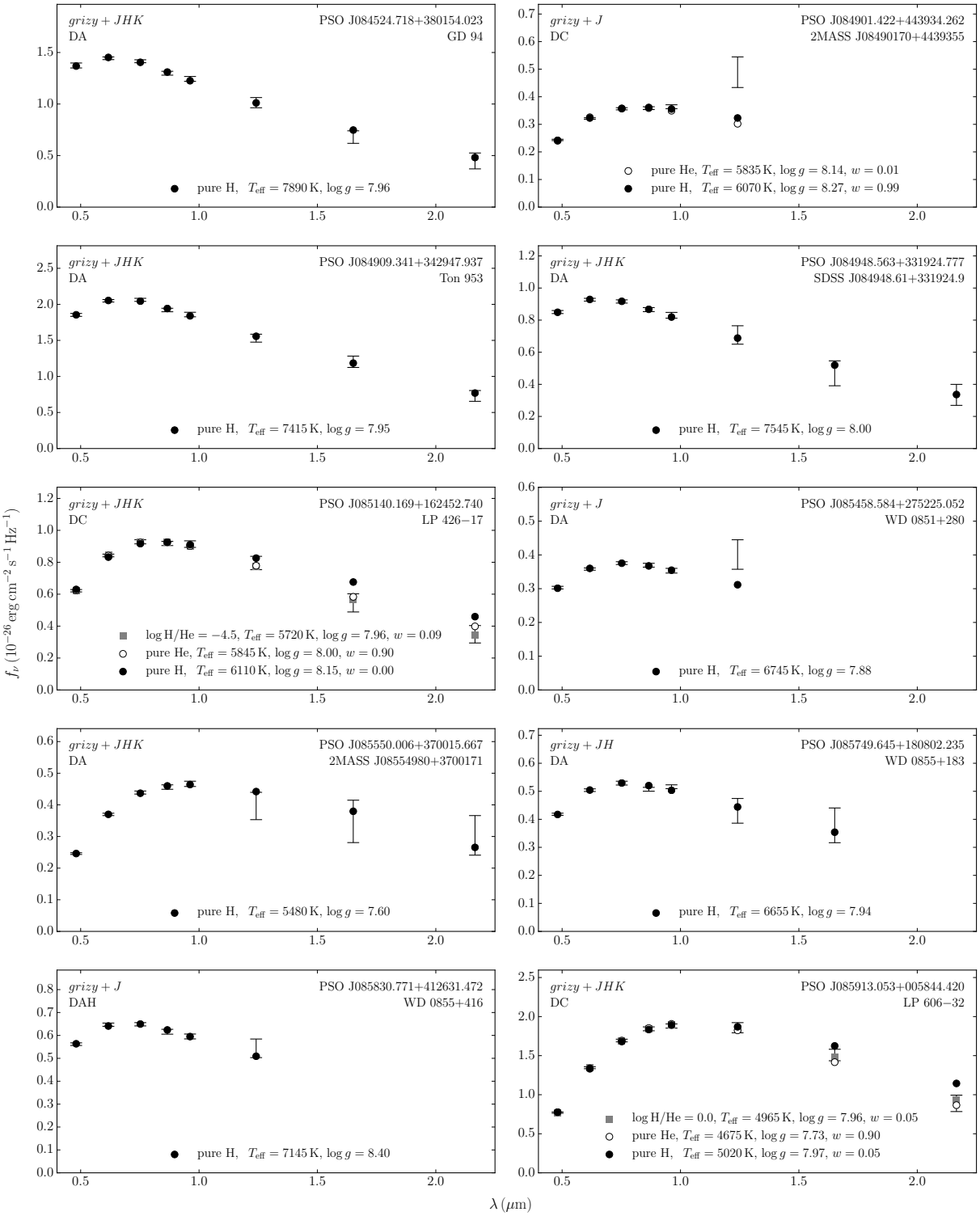

Figure C.1 – Ajustements photométriques des étoiles DA et DC (suite)

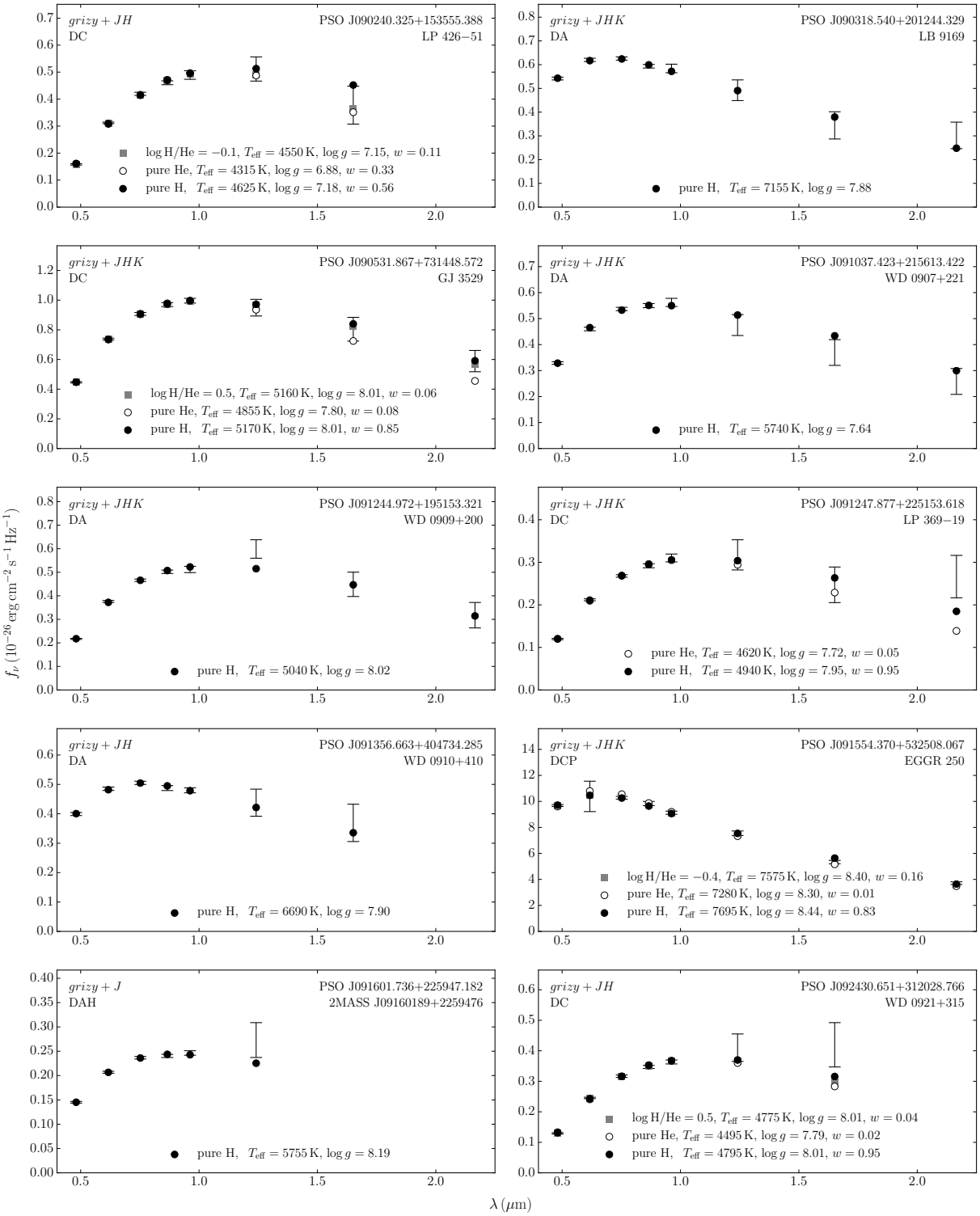

Figure C.1 – Ajustements photométriques des étoiles DA et DC (suite)

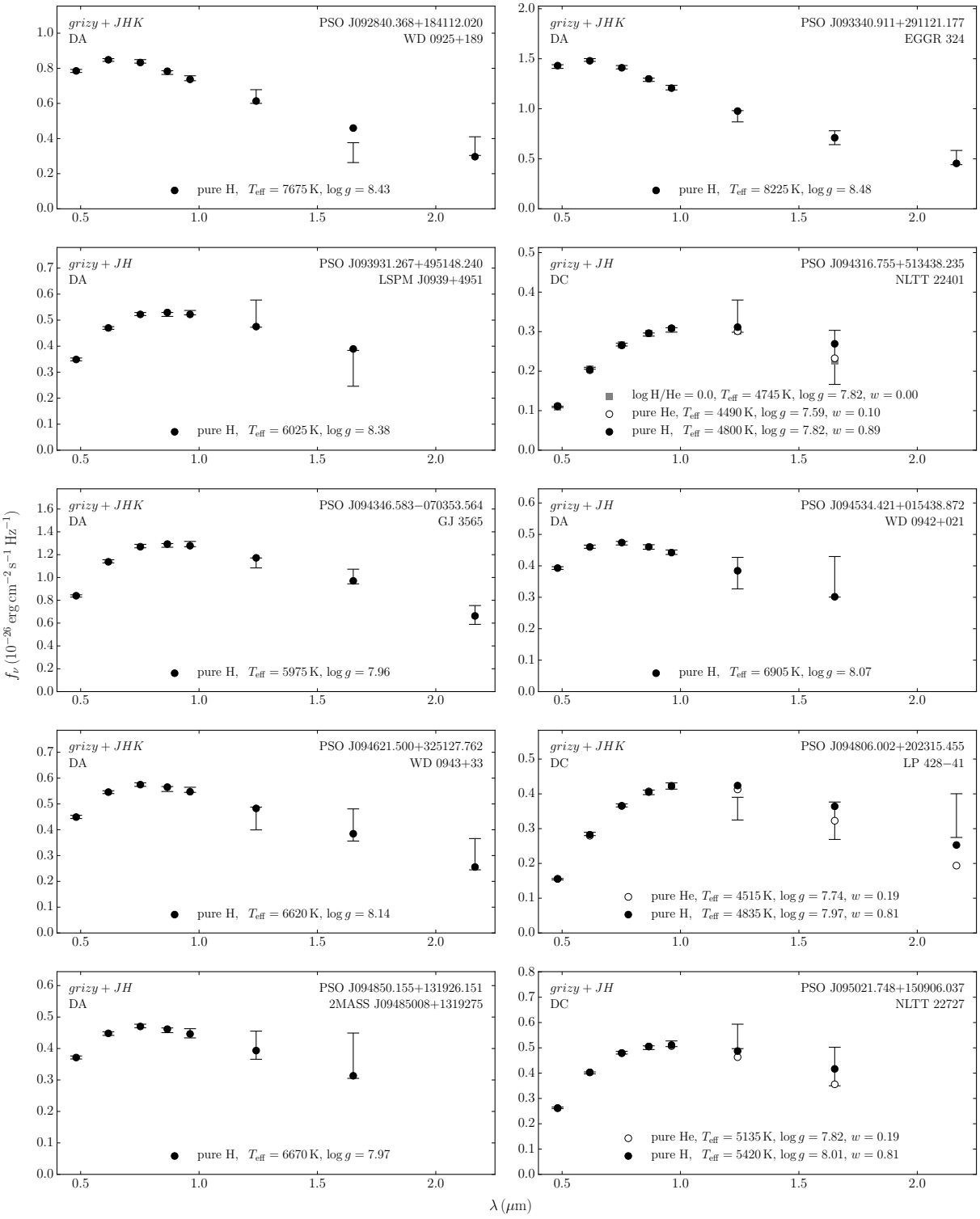

Figure C.1 – Ajustements photométriques des étoiles DA et DC (suite)

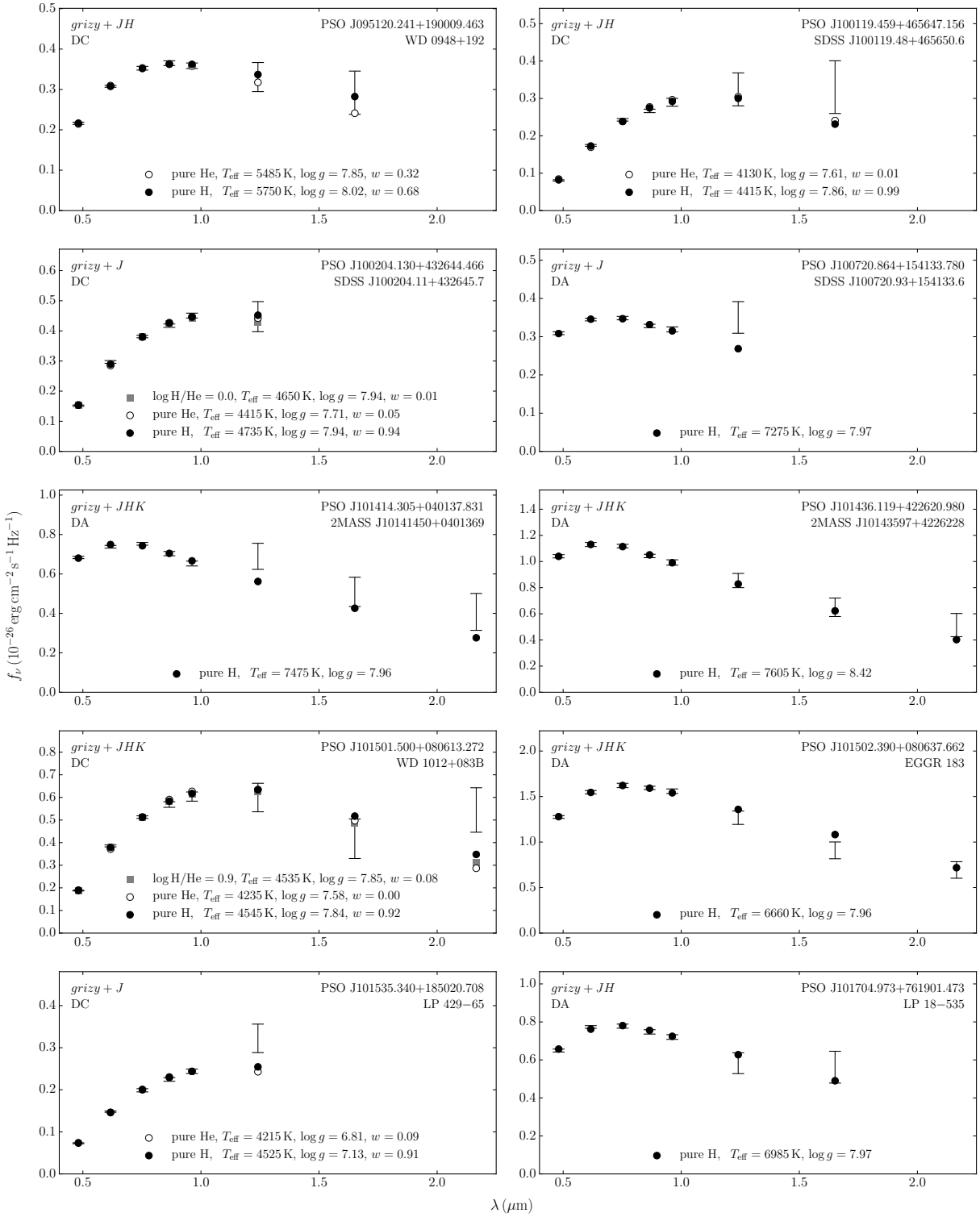

Figure C.1 – Ajustements photométriques des étoiles DA et DC (suite)

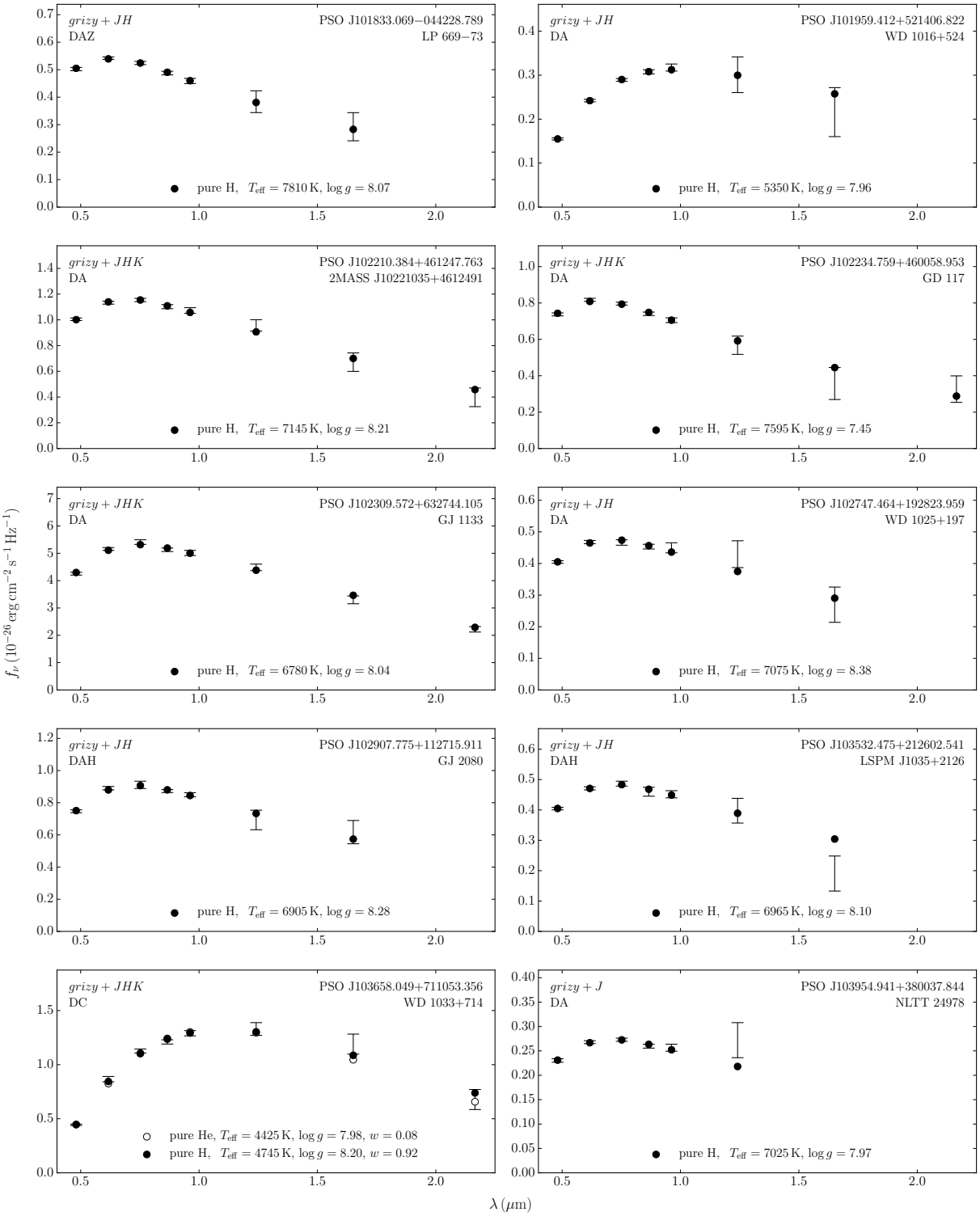

Figure C.1 – Ajustements photométriques des étoiles DA et DC (suite)

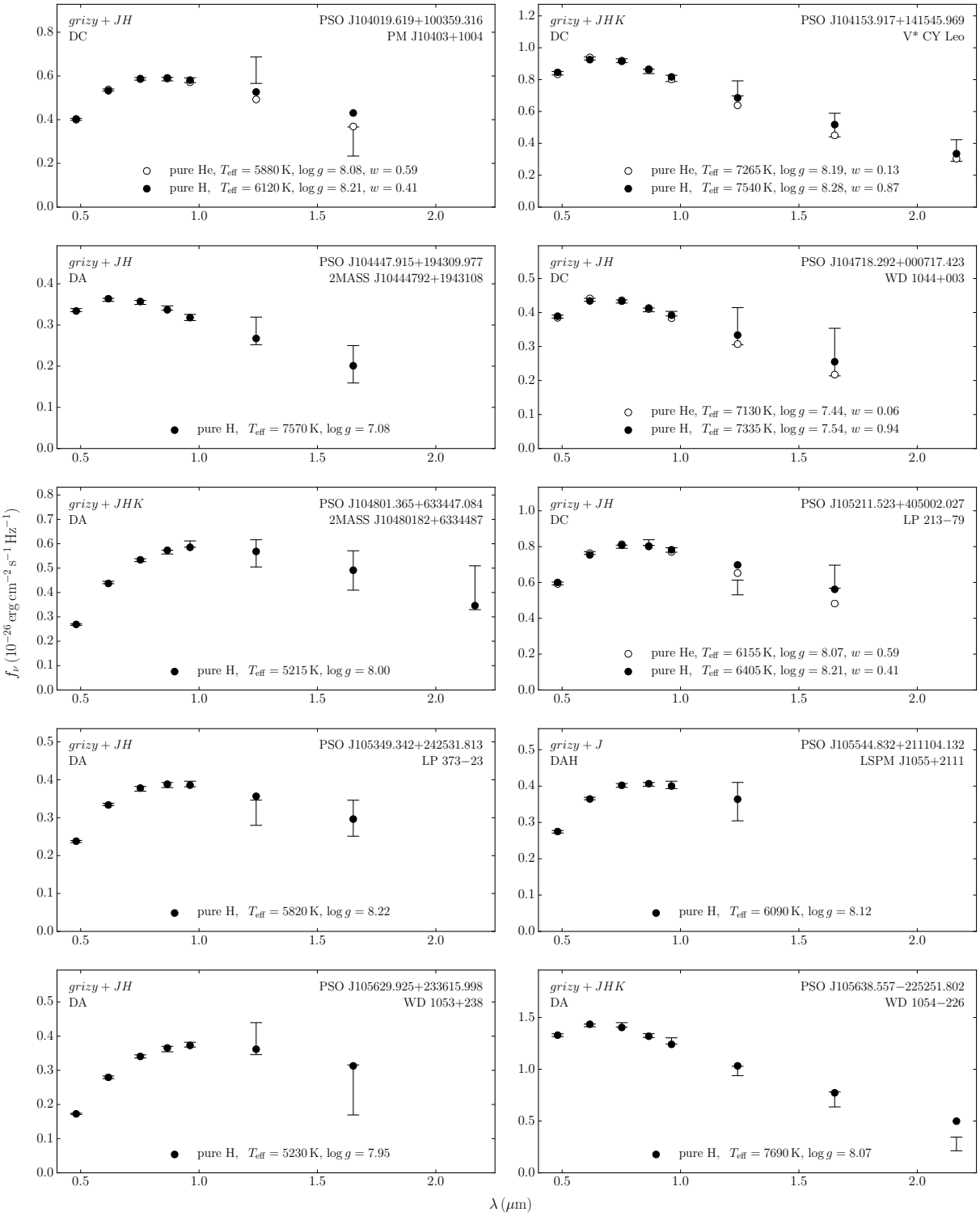

Figure C.1 – Ajustements photométriques des étoiles DA et DC (suite)

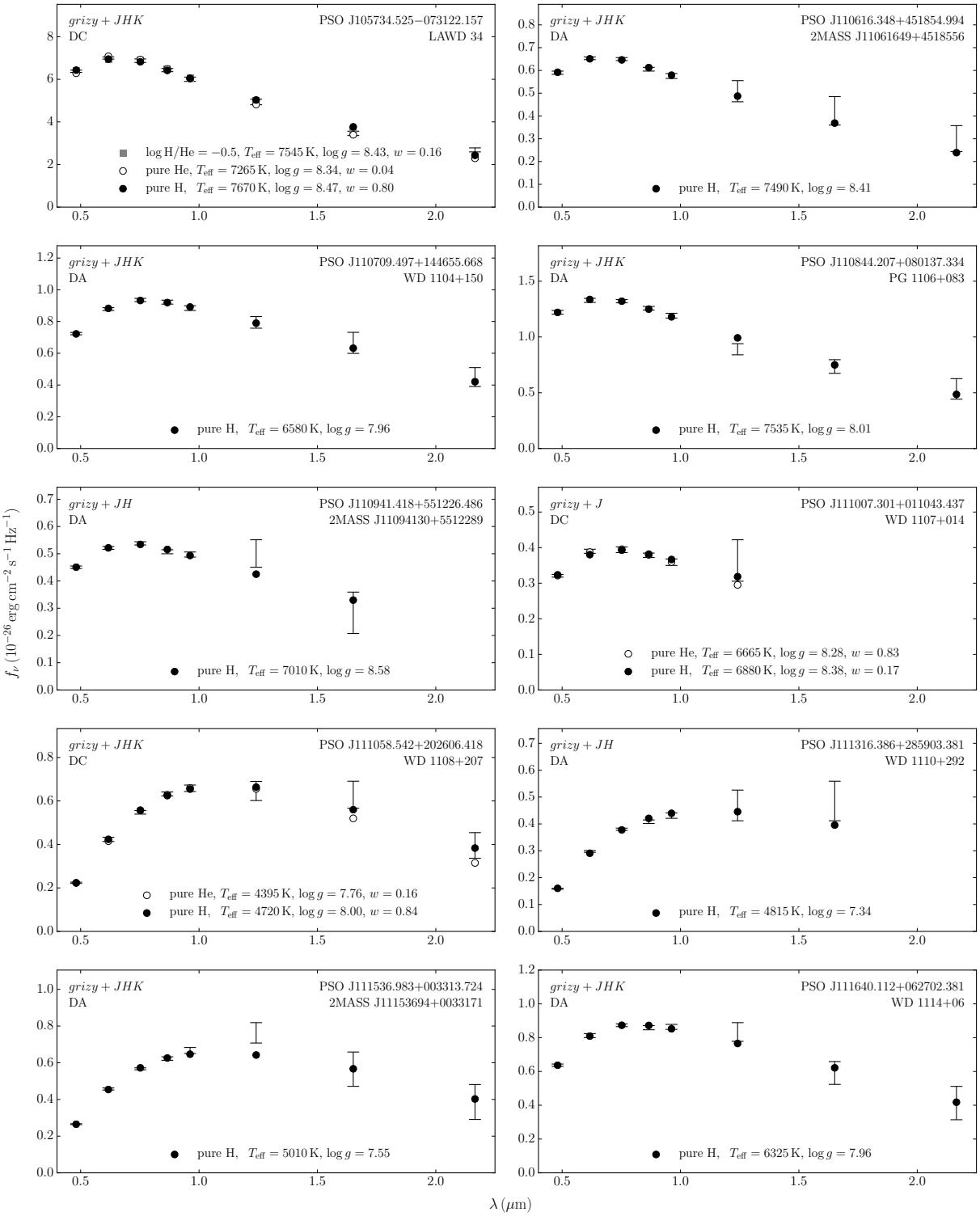

Figure C.1 – Ajustements photométriques des étoiles DA et DC (suite)

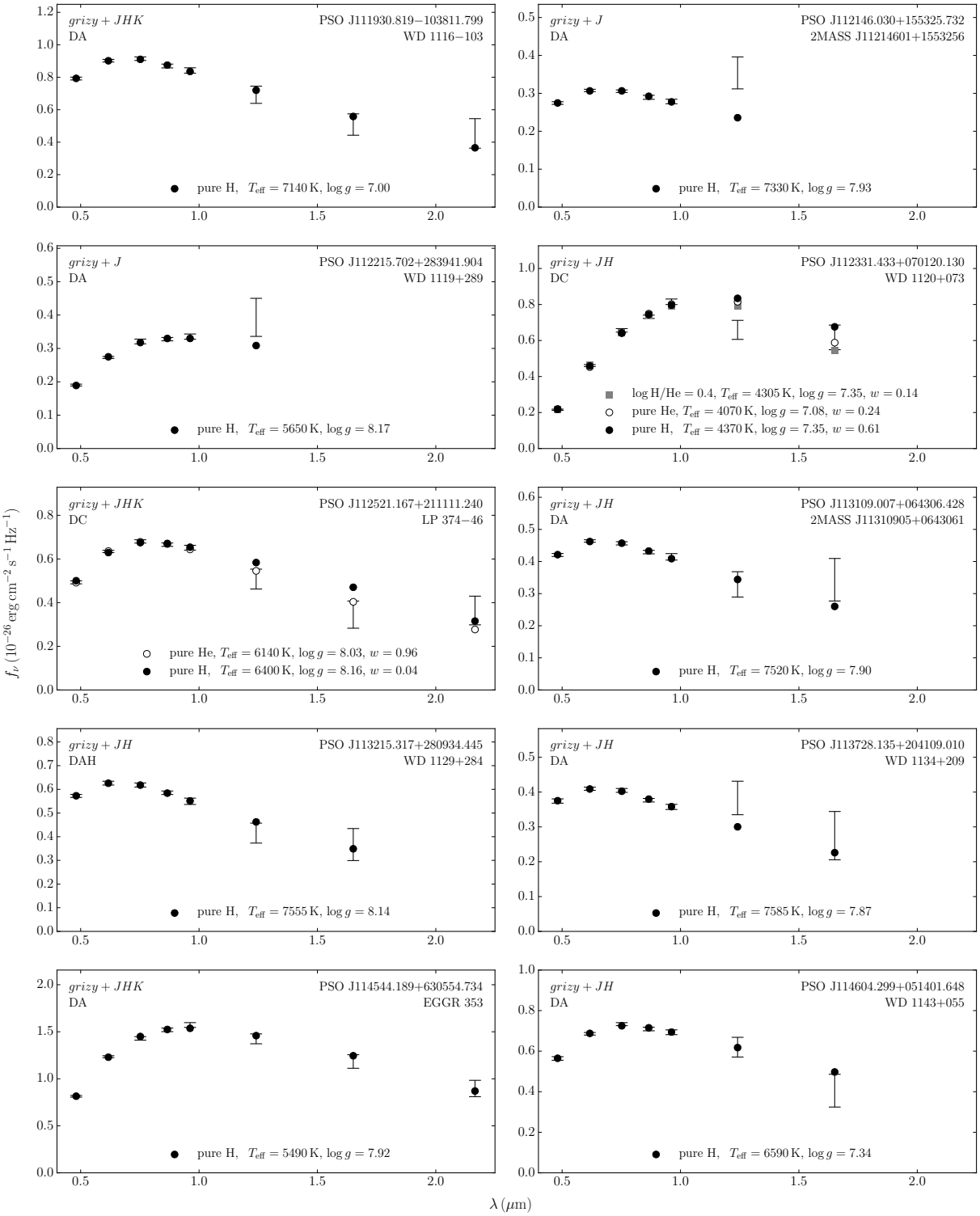

Figure C.1 – Ajustements photométriques des étoiles DA et DC (suite)

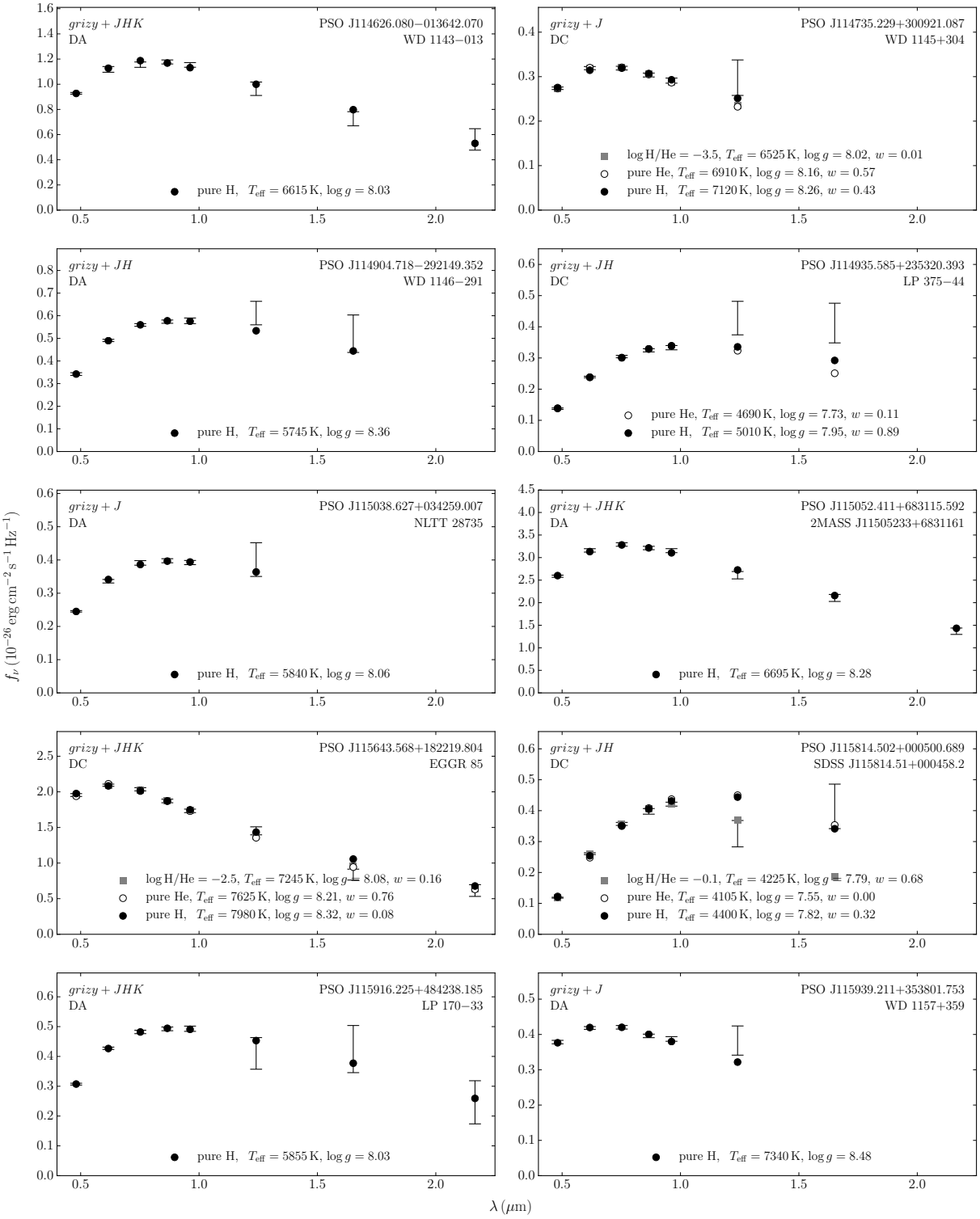

Figure C.1 – Ajustements photométriques des étoiles DA et DC (suite)

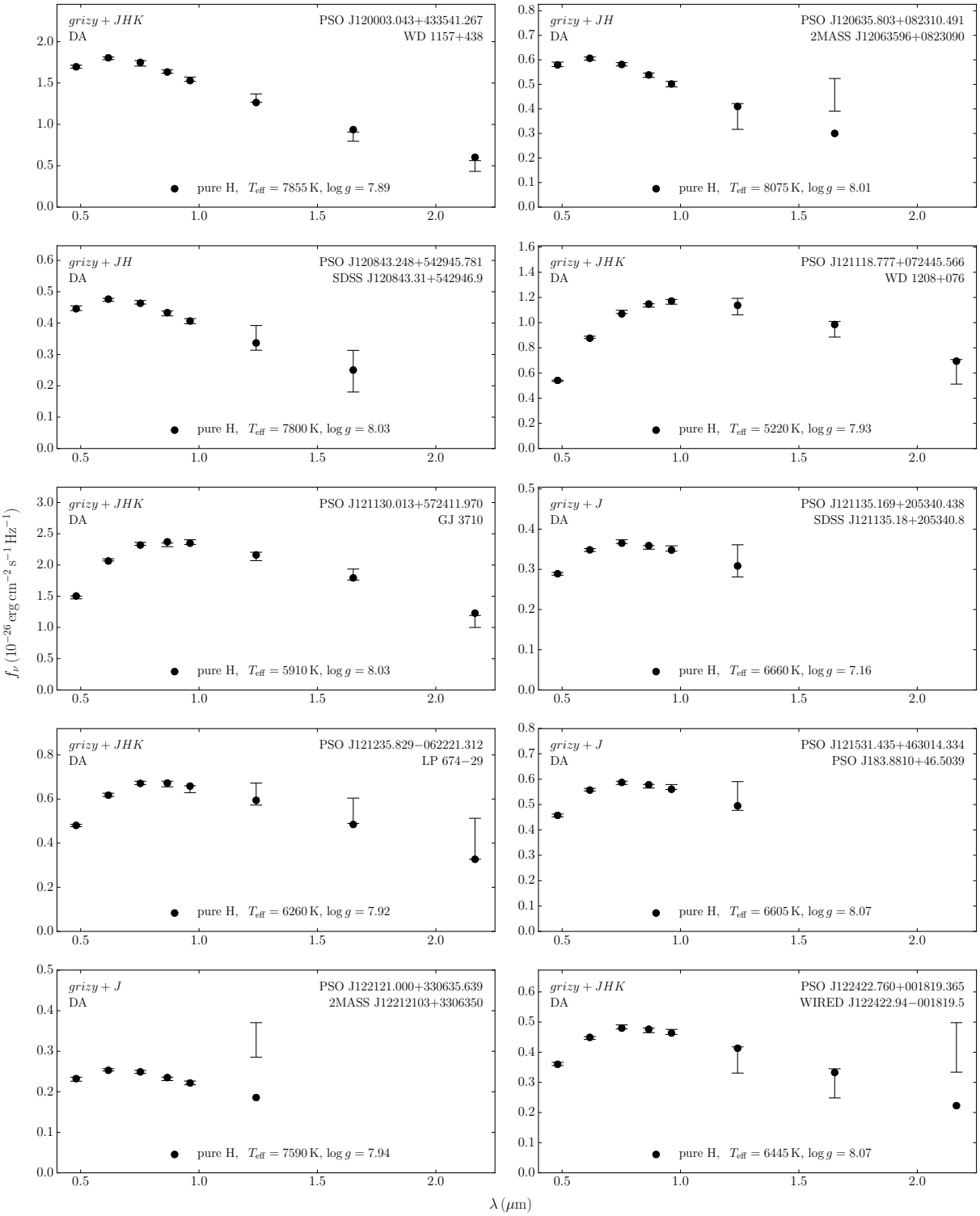

Figure C.1 – Ajustements photométriques des étoiles DA et DC (suite)

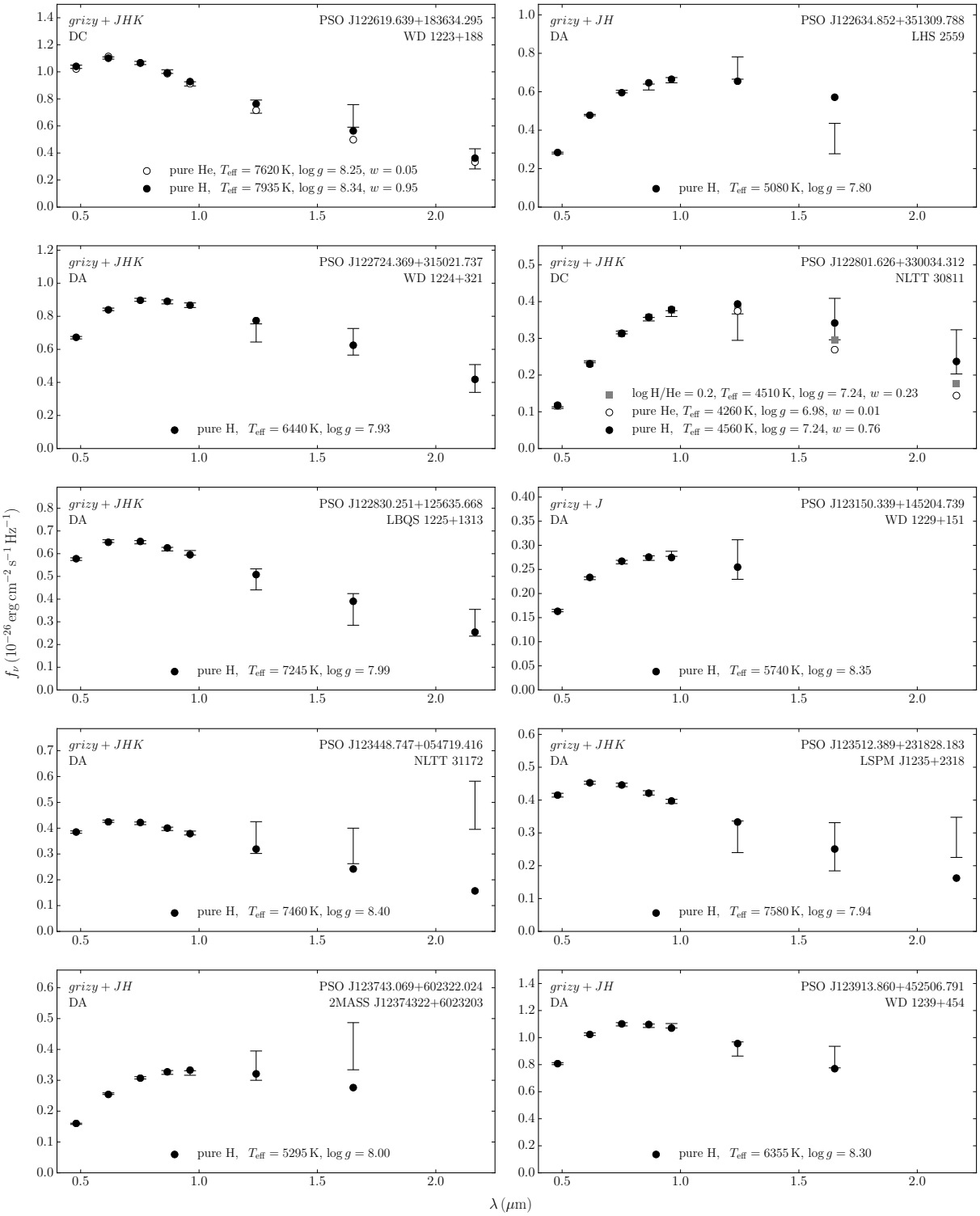

Figure C.1 – Ajustements photométriques des étoiles DA et DC (suite)

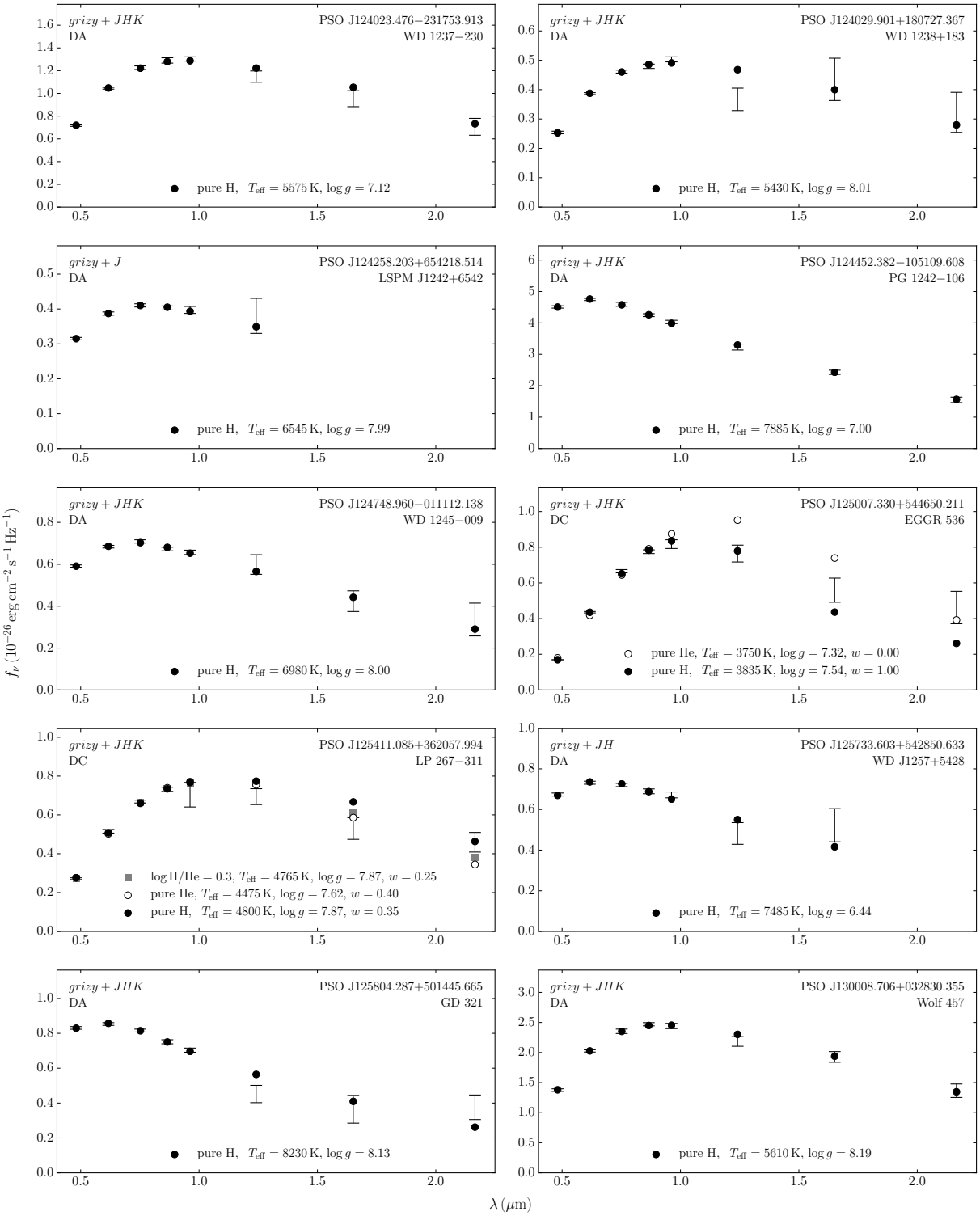

Figure C.1 – Ajustements photométriques des étoiles DA et DC (suite)

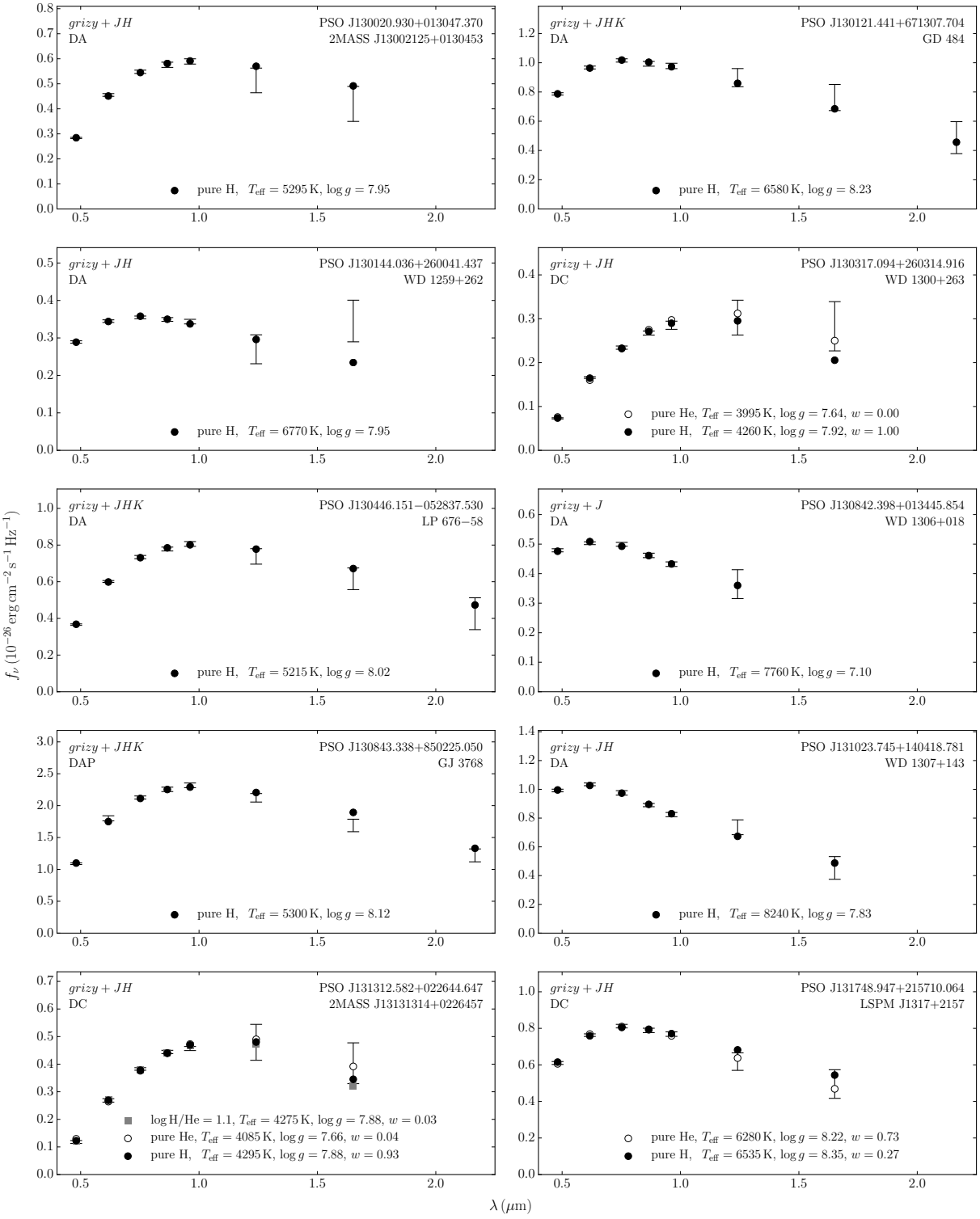

Figure C.1 – Ajustements photométriques des étoiles DA et DC (suite)

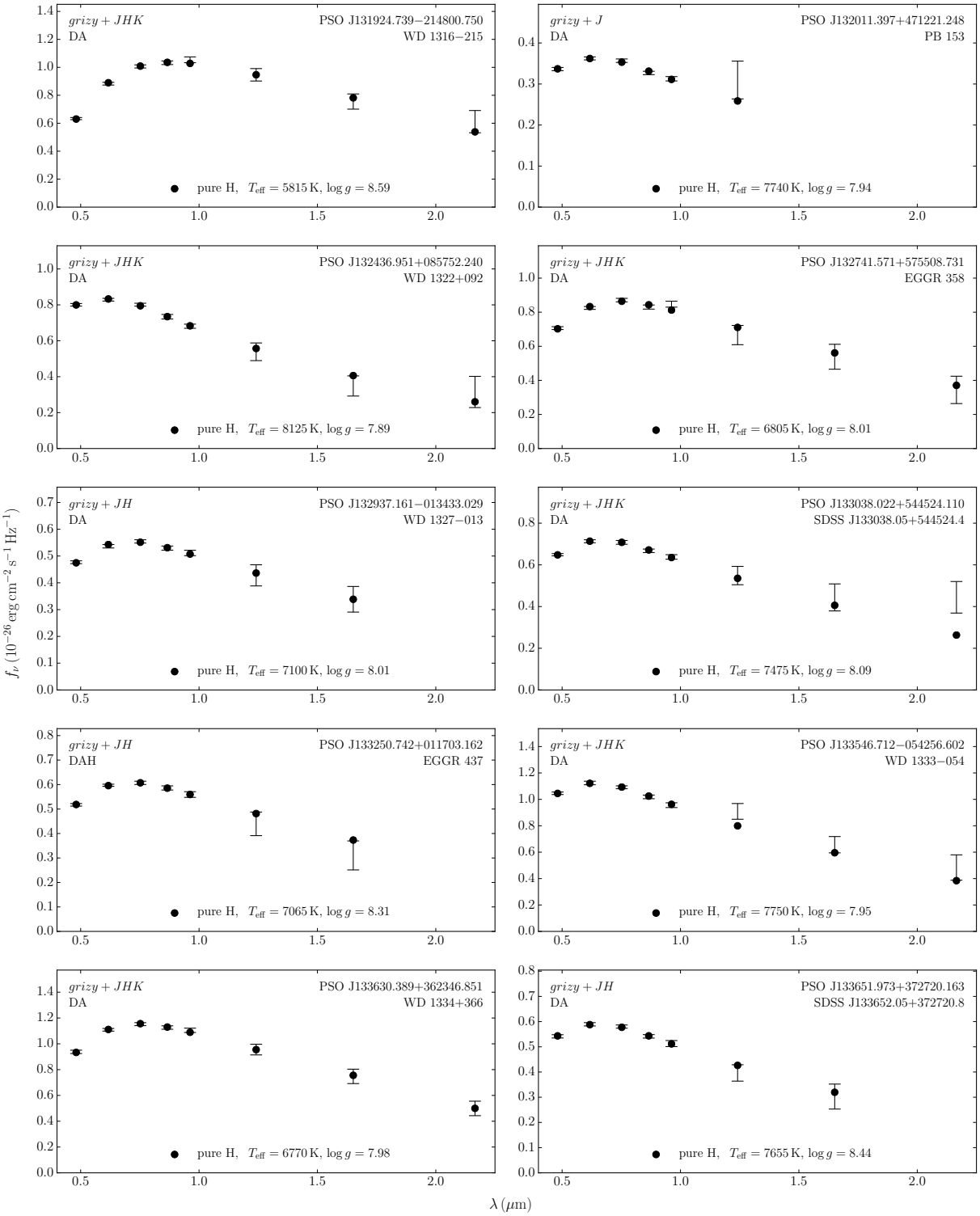

Figure C.1 – Ajustements photométriques des étoiles DA et DC (suite)

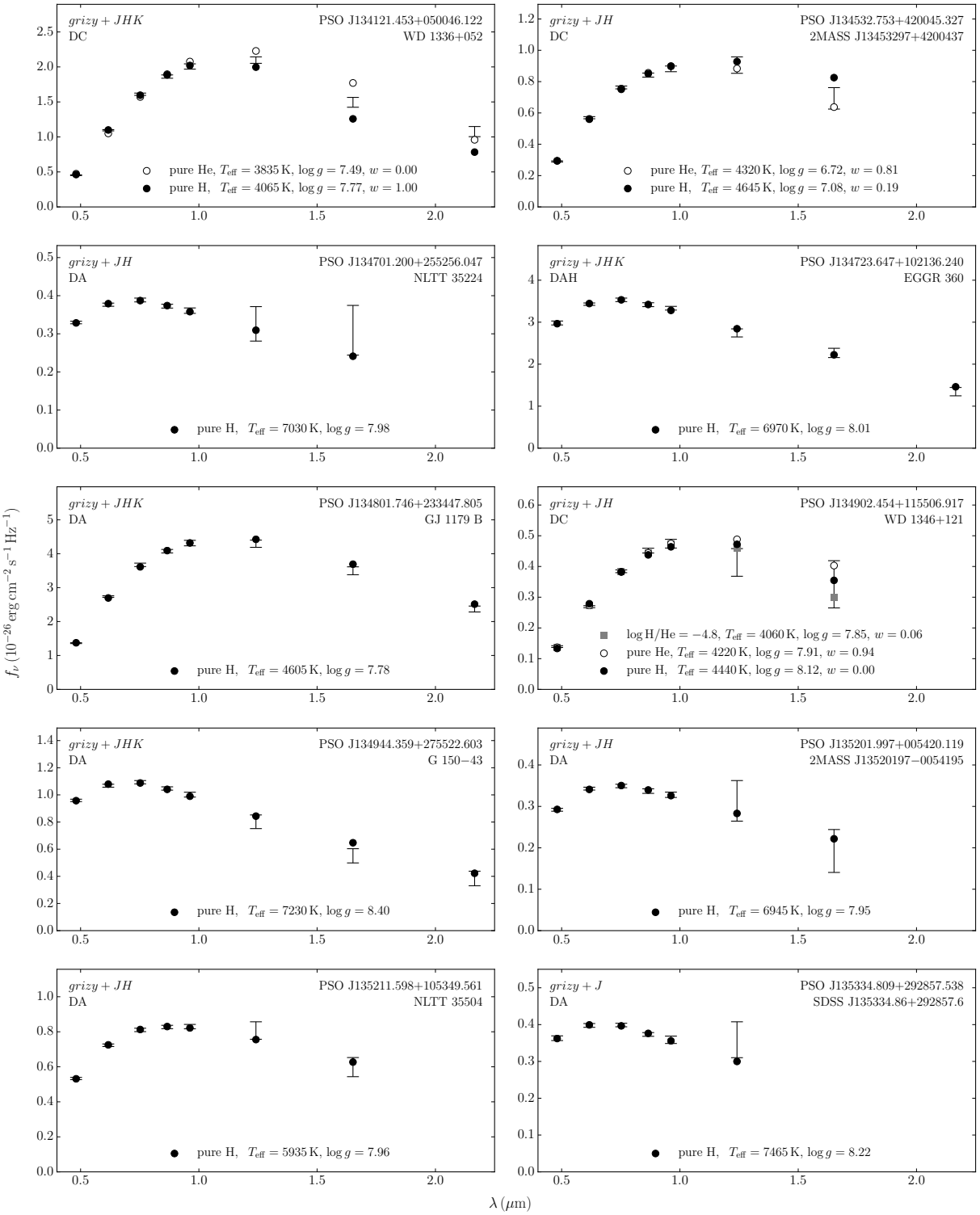

Figure C.1 – Ajustements photométriques des étoiles DA et DC (suite)

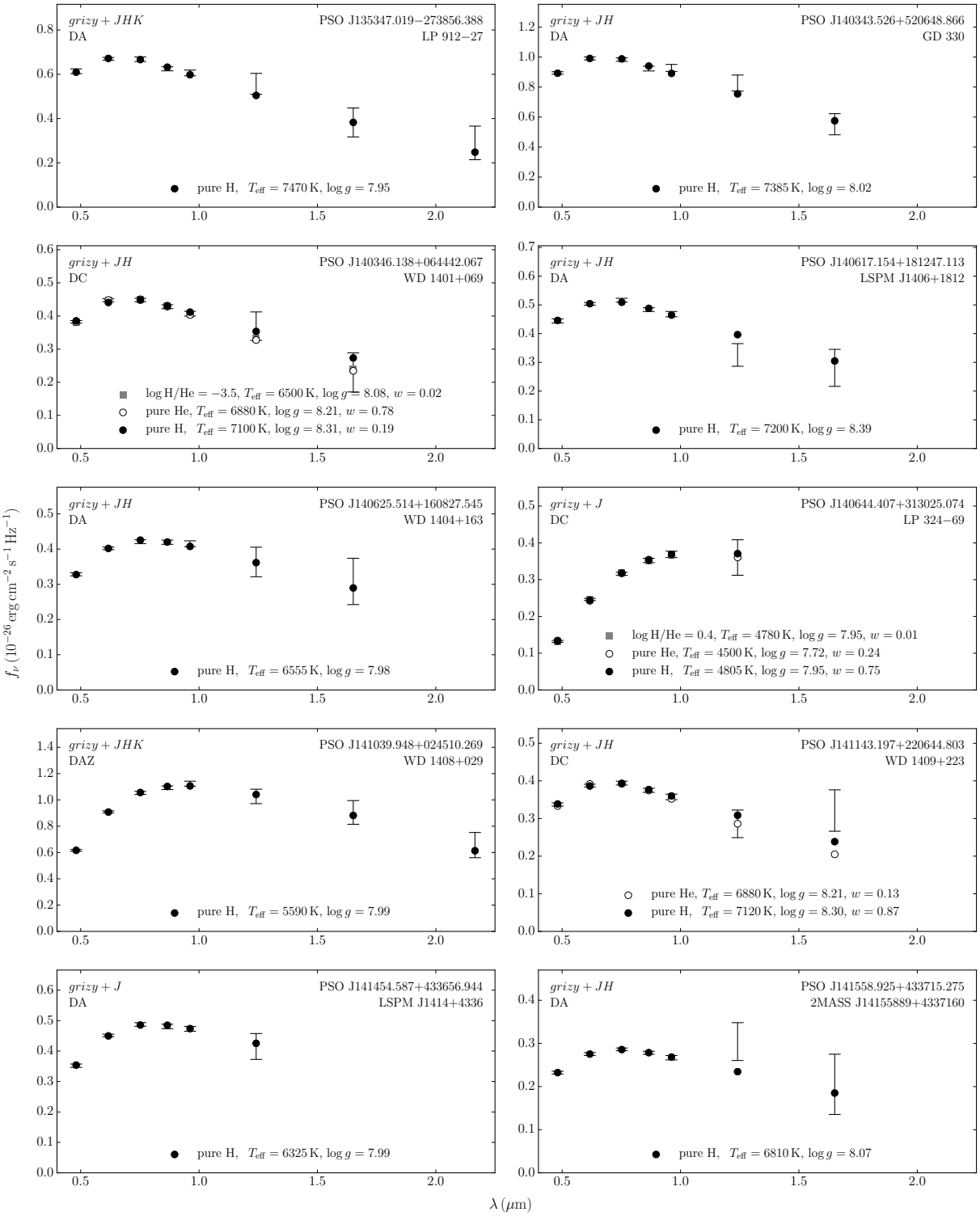

Figure C.1 – Ajustements photométriques des étoiles DA et DC (suite)

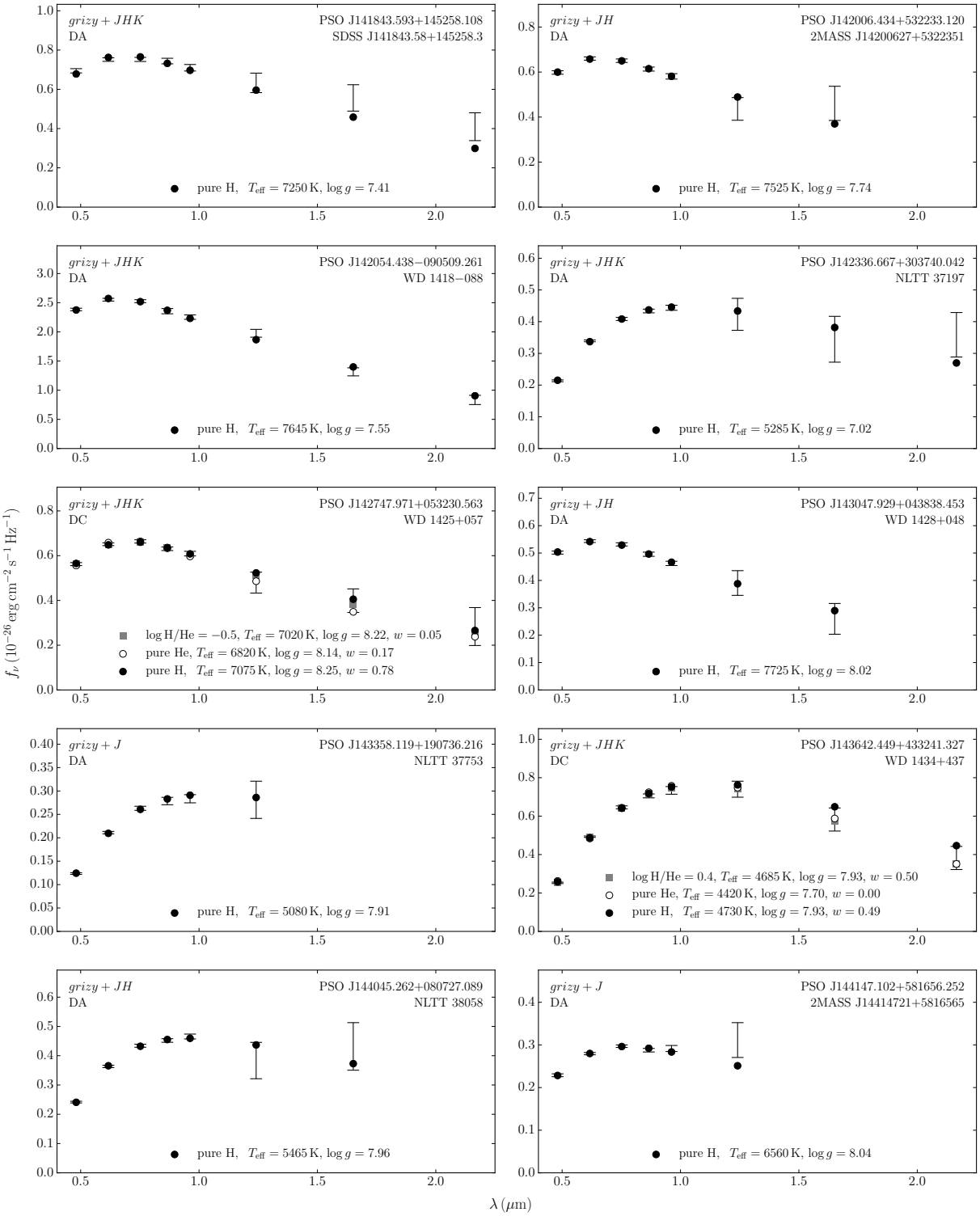

Figure C.1 – Ajustements photométriques des étoiles DA et DC (suite)

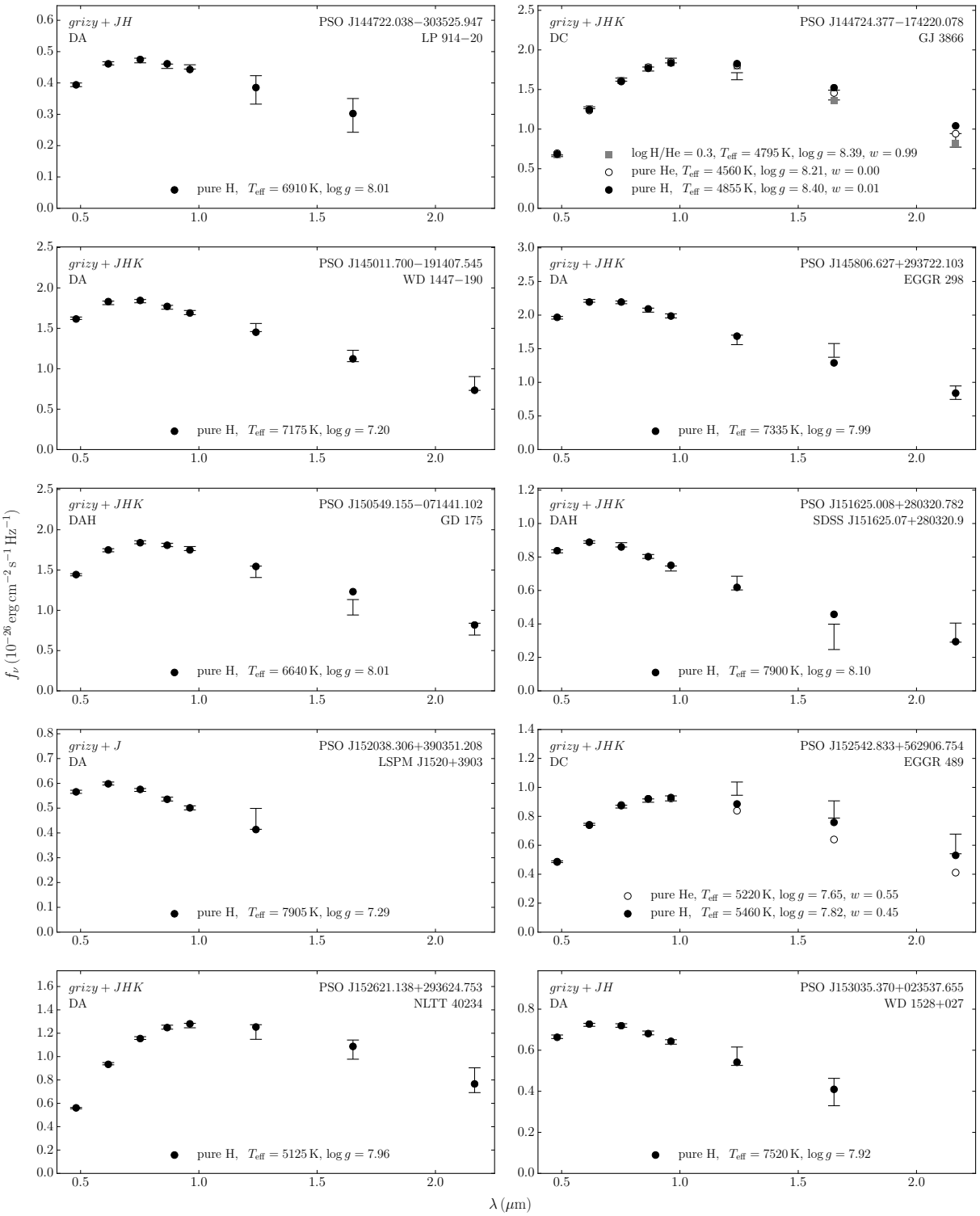

Figure C.1 – Ajustements photométriques des étoiles DA et DC (suite)

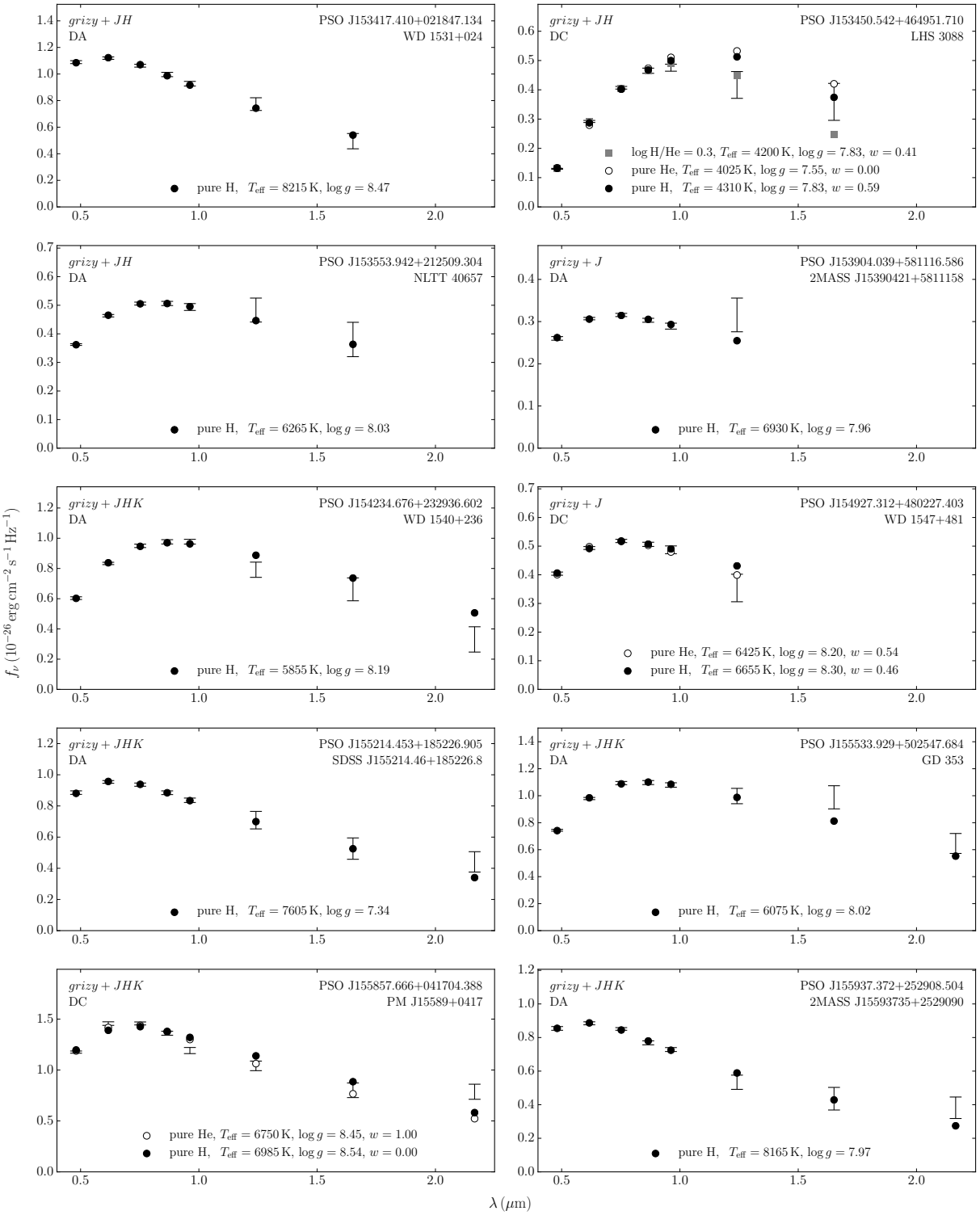

Figure C.1 – Ajustements photométriques des étoiles DA et DC (suite)

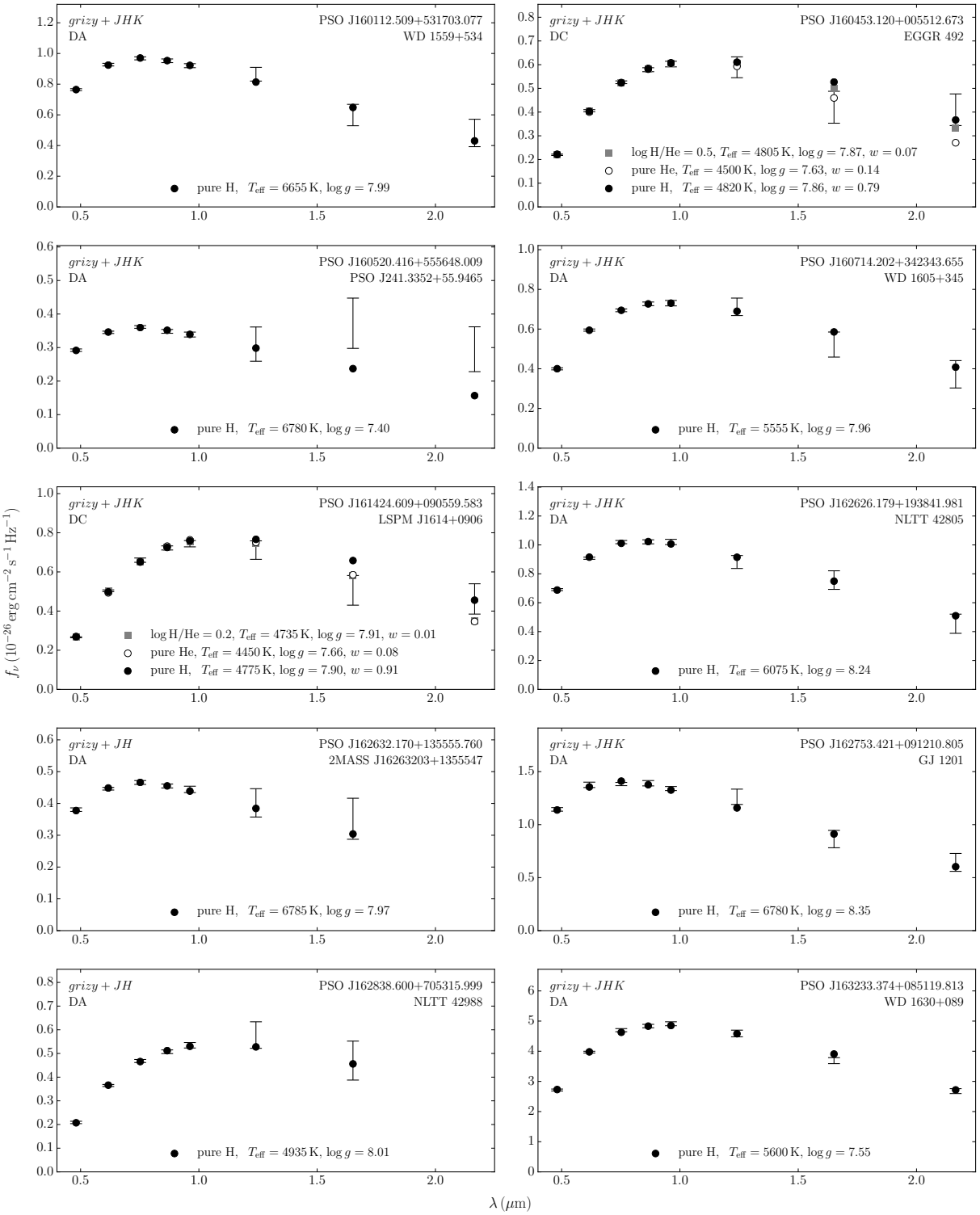

Figure C.1 – Ajustements photométriques des étoiles DA et DC (suite)

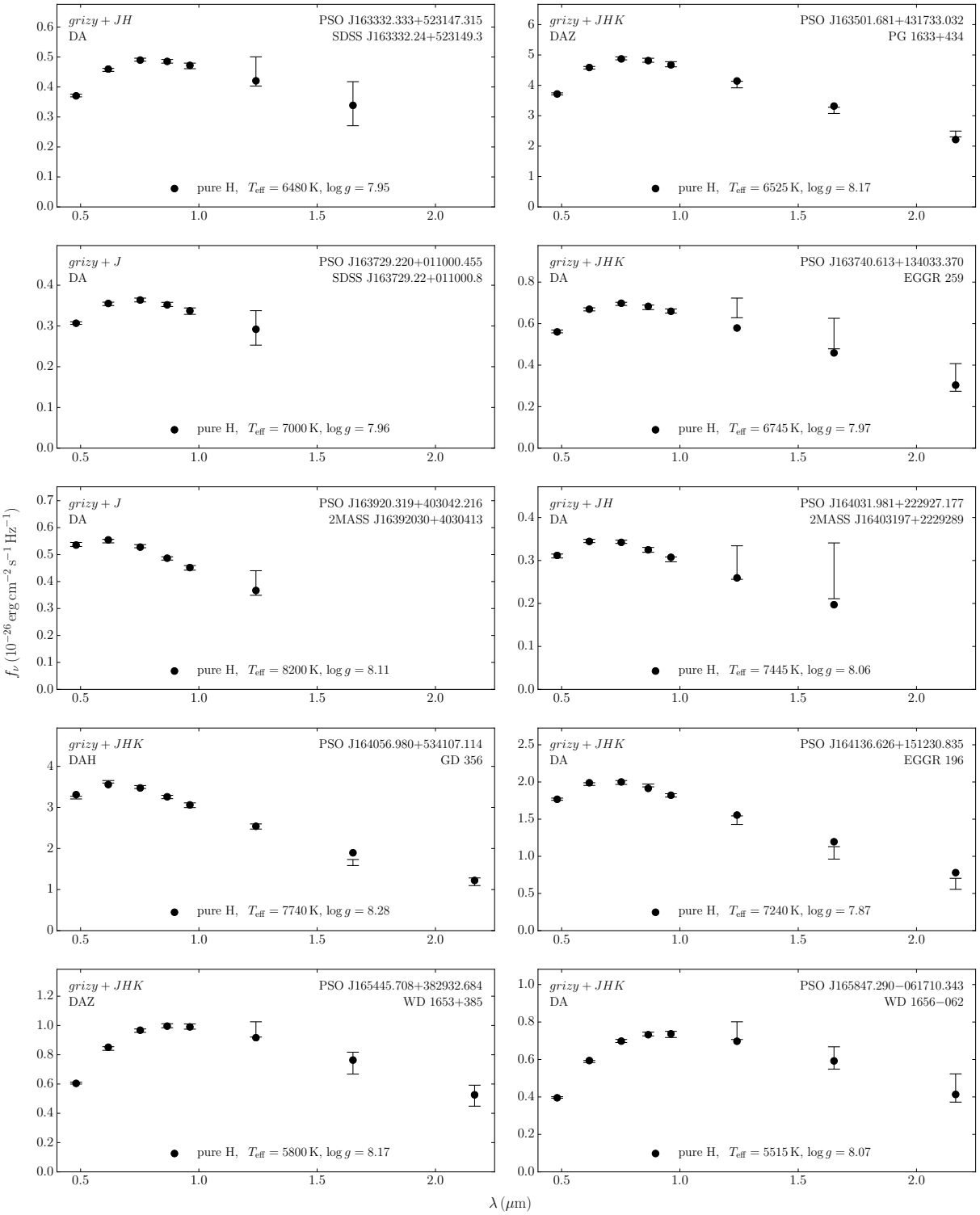

Figure C.1 – Ajustements photométriques des étoiles DA et DC (suite)

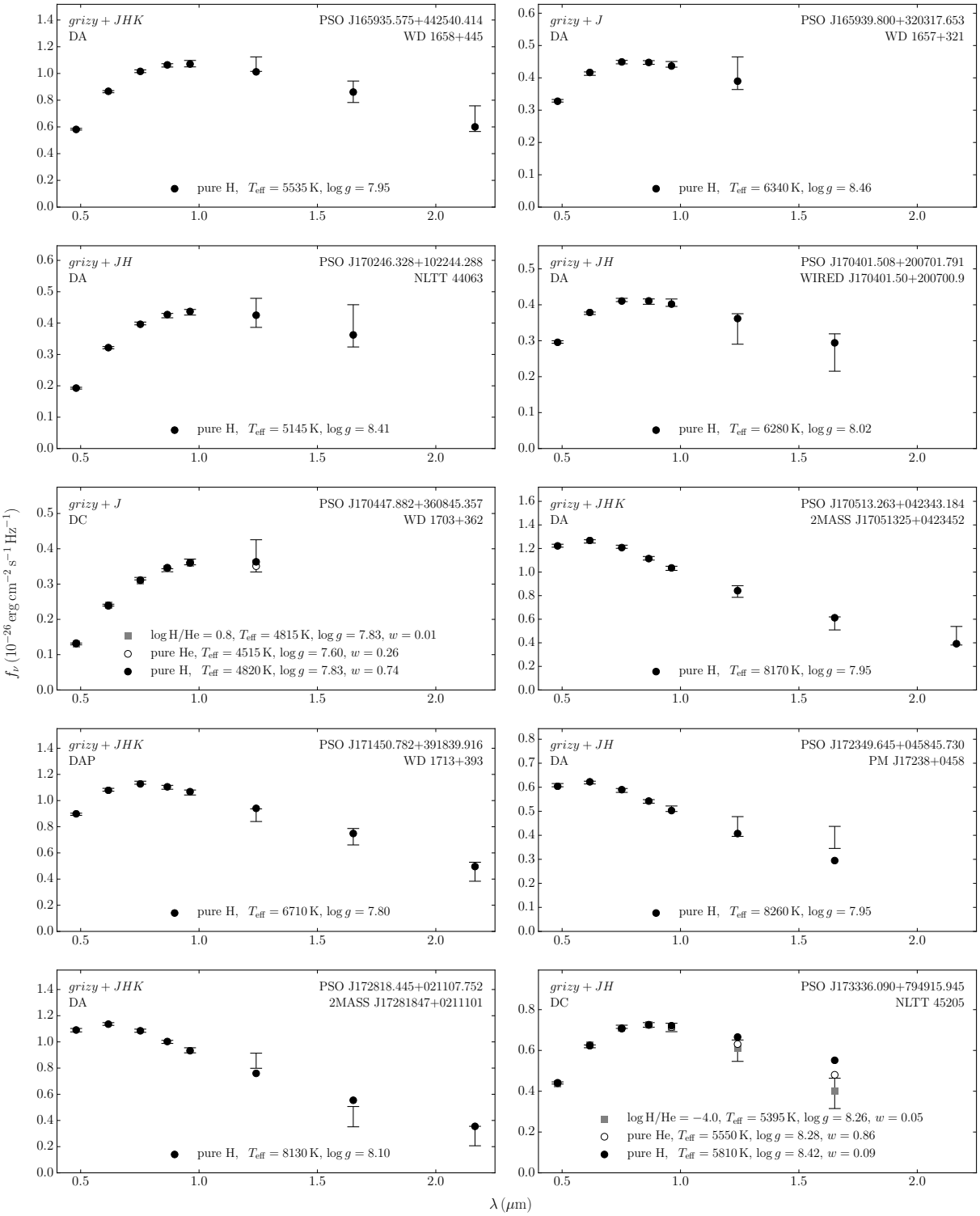

Figure C.1 – Ajustements photométriques des étoiles DA et DC (suite)

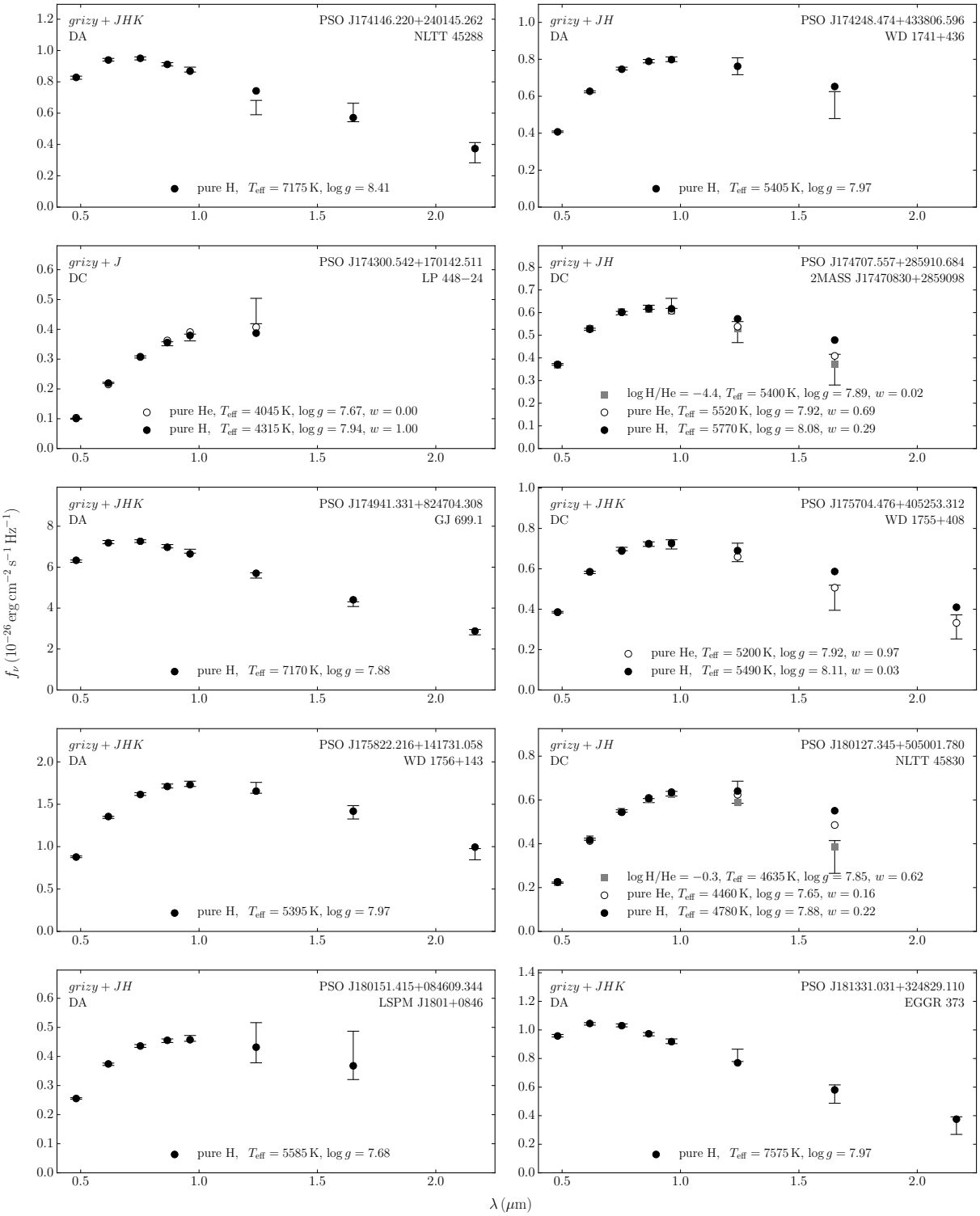

Figure C.1 – Ajustements photométriques des étoiles DA et DC (suite)

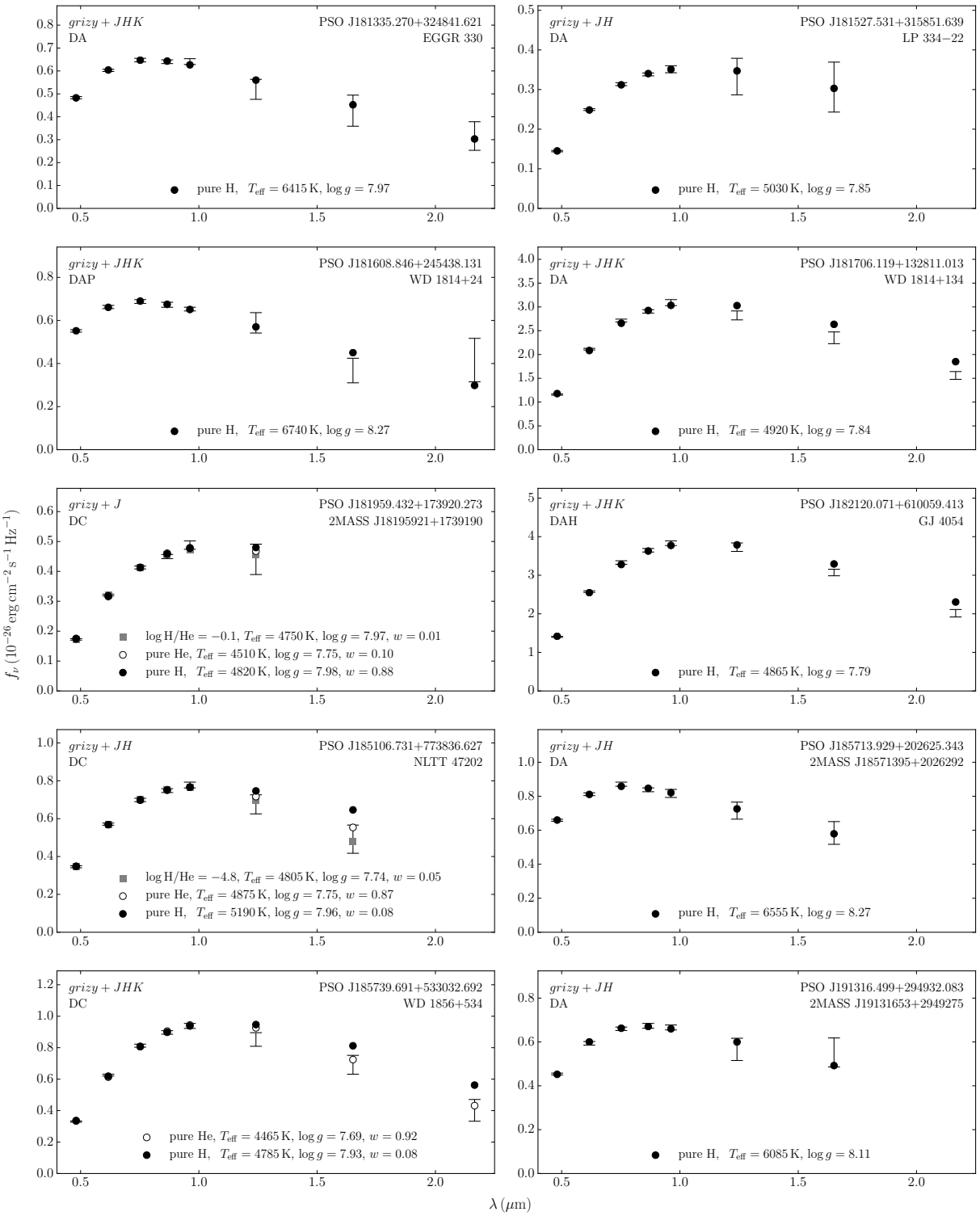

Figure C.1 – Ajustements photométriques des étoiles DA et DC (suite)

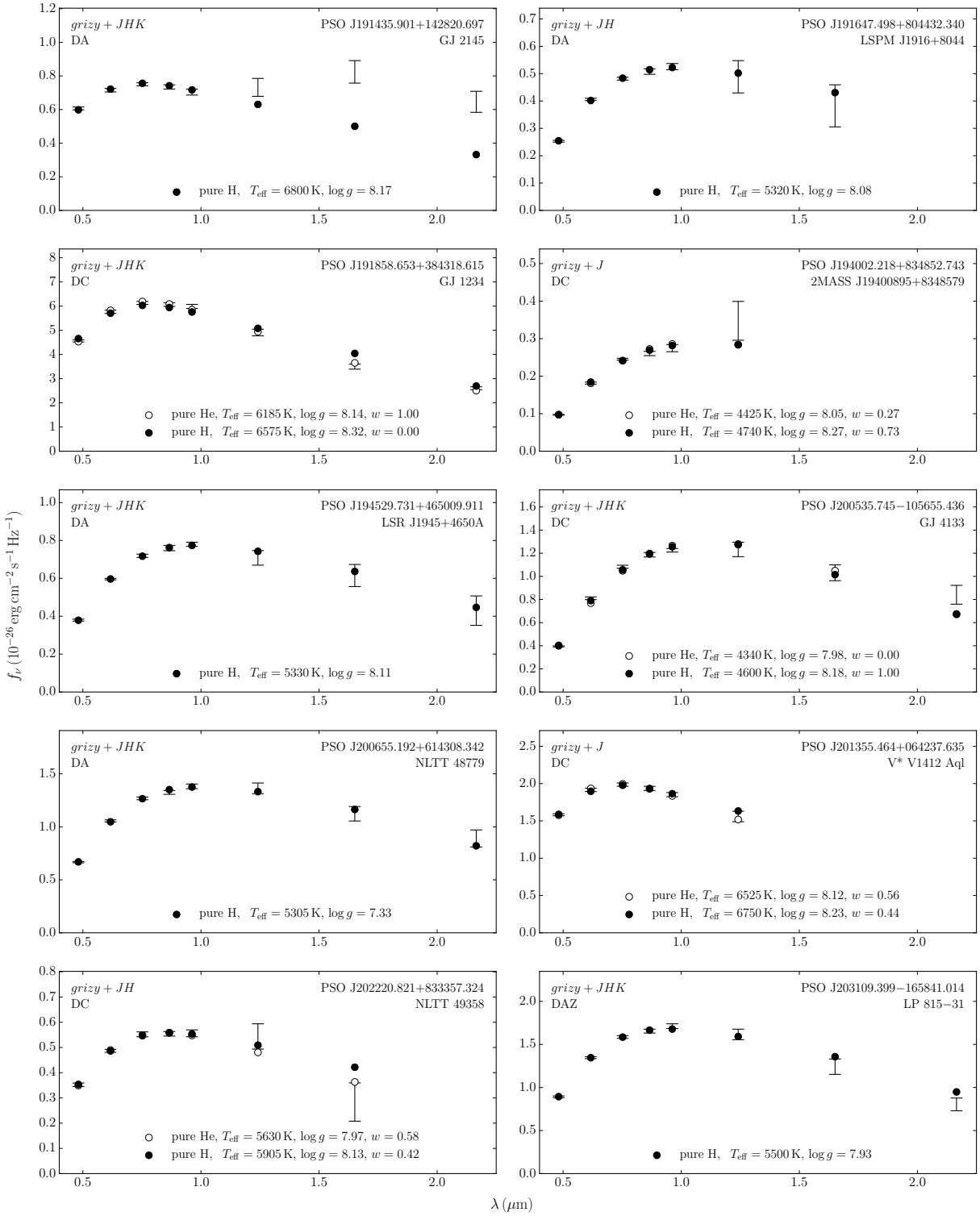

Figure C.1 – Ajustements photométriques des étoiles DA et DC (suite)

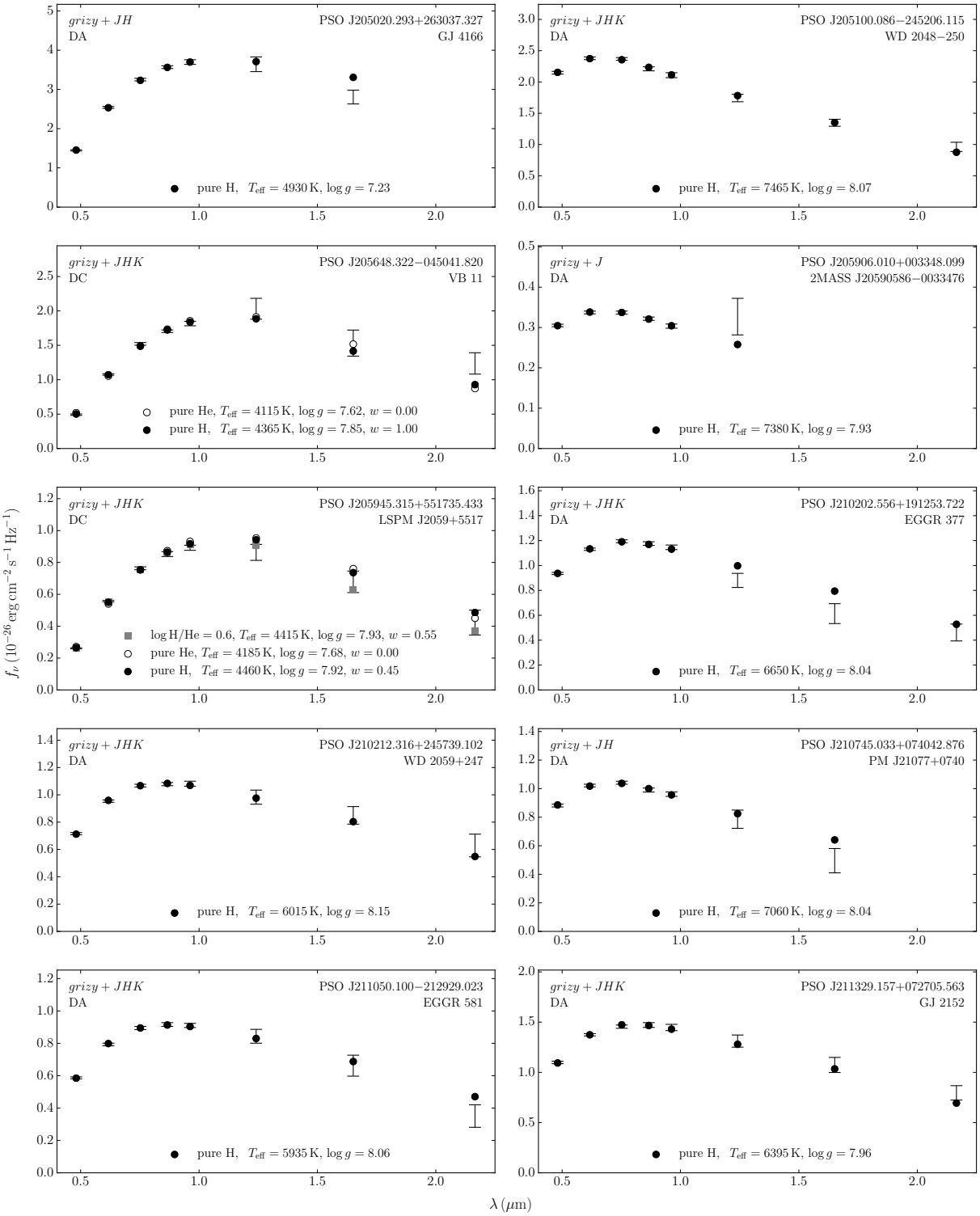

Figure C.1 – Ajustements photométriques des étoiles DA et DC (suite)

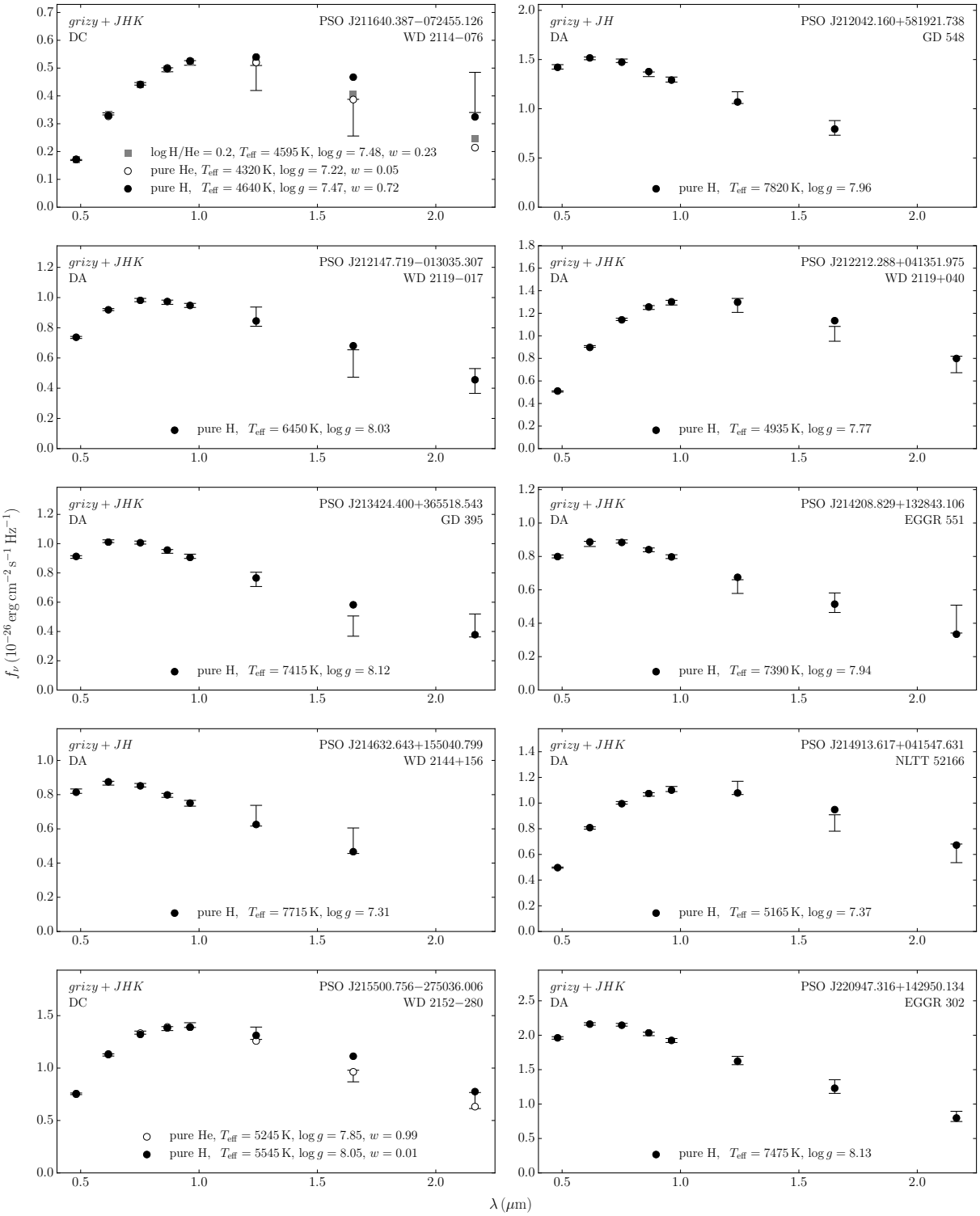

Figure C.1 – Ajustements photométriques des étoiles DA et DC (suite)

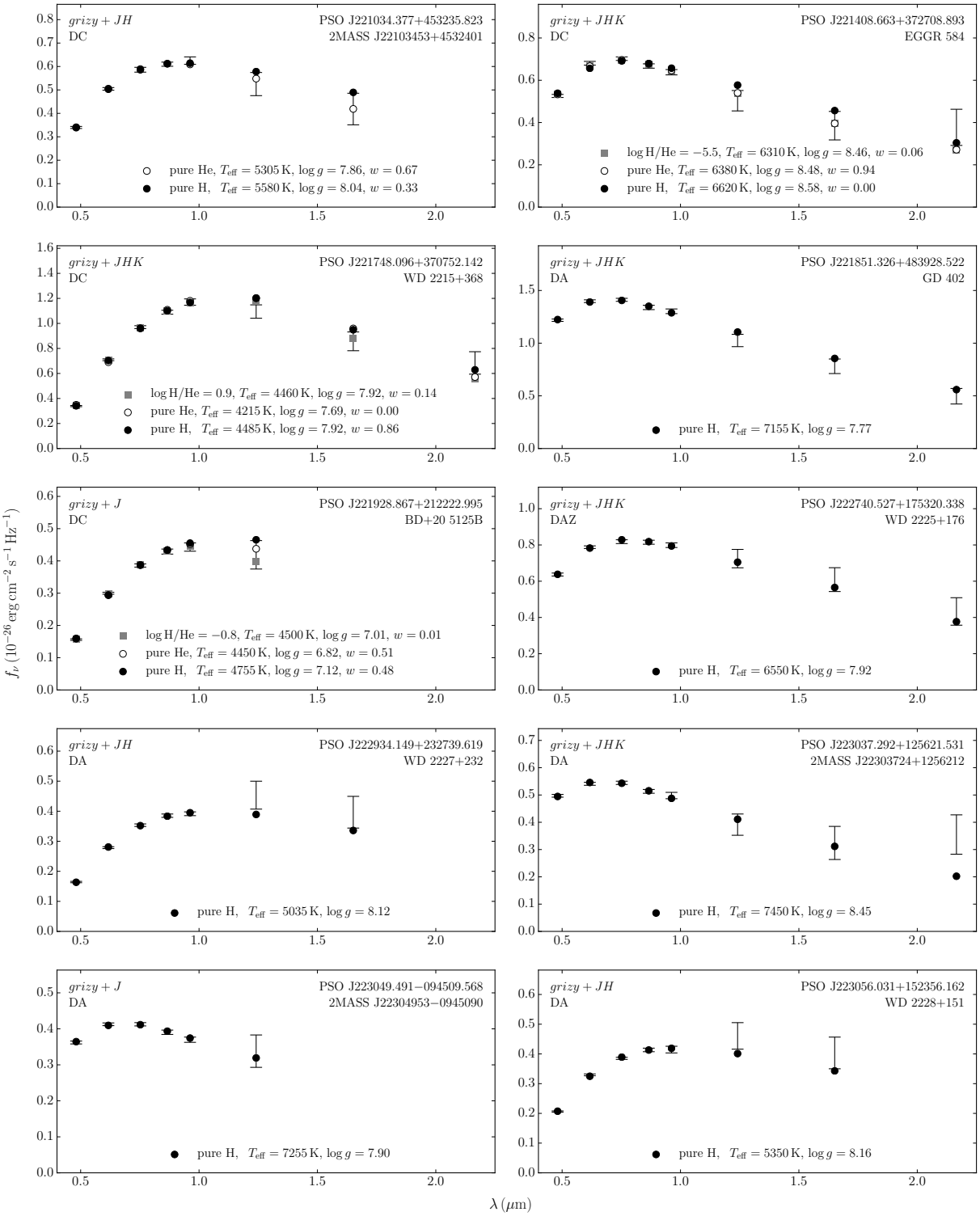

Figure C.1 – Ajustements photométriques des étoiles DA et DC (suite)

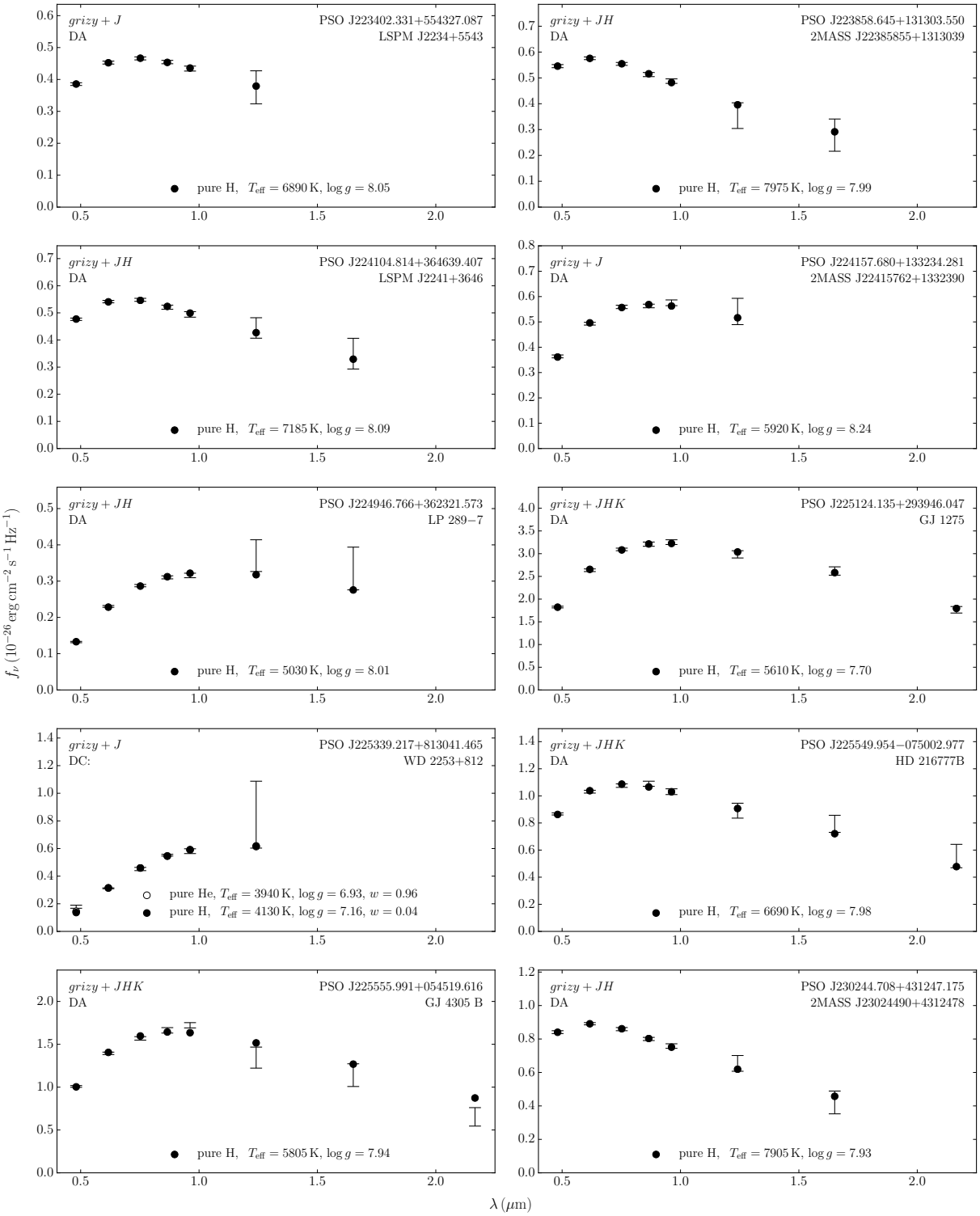

Figure C.1 – Ajustements photométriques des étoiles DA et DC (suite)

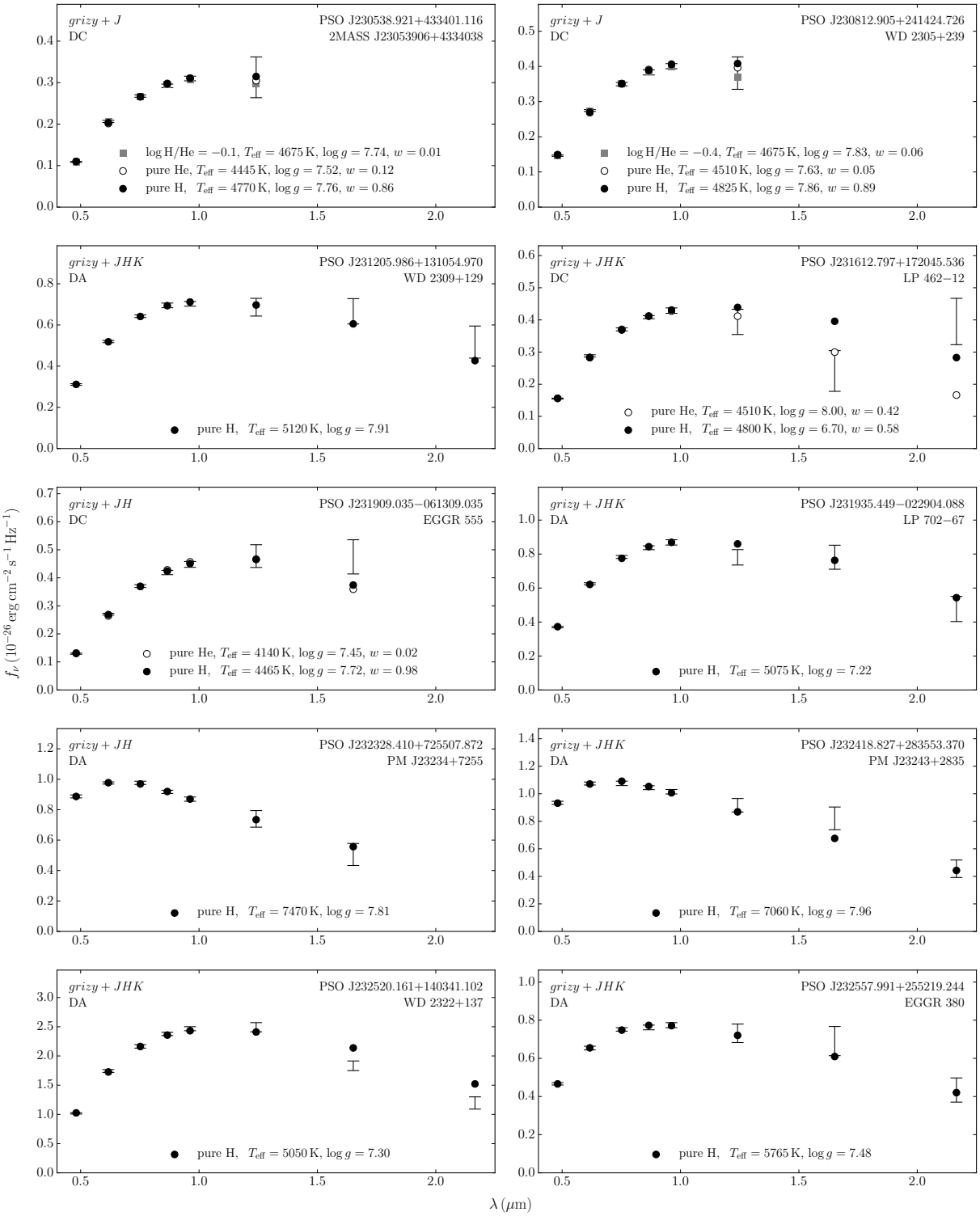

Figure C.1 – Ajustements photométriques des étoiles DA et DC (suite)

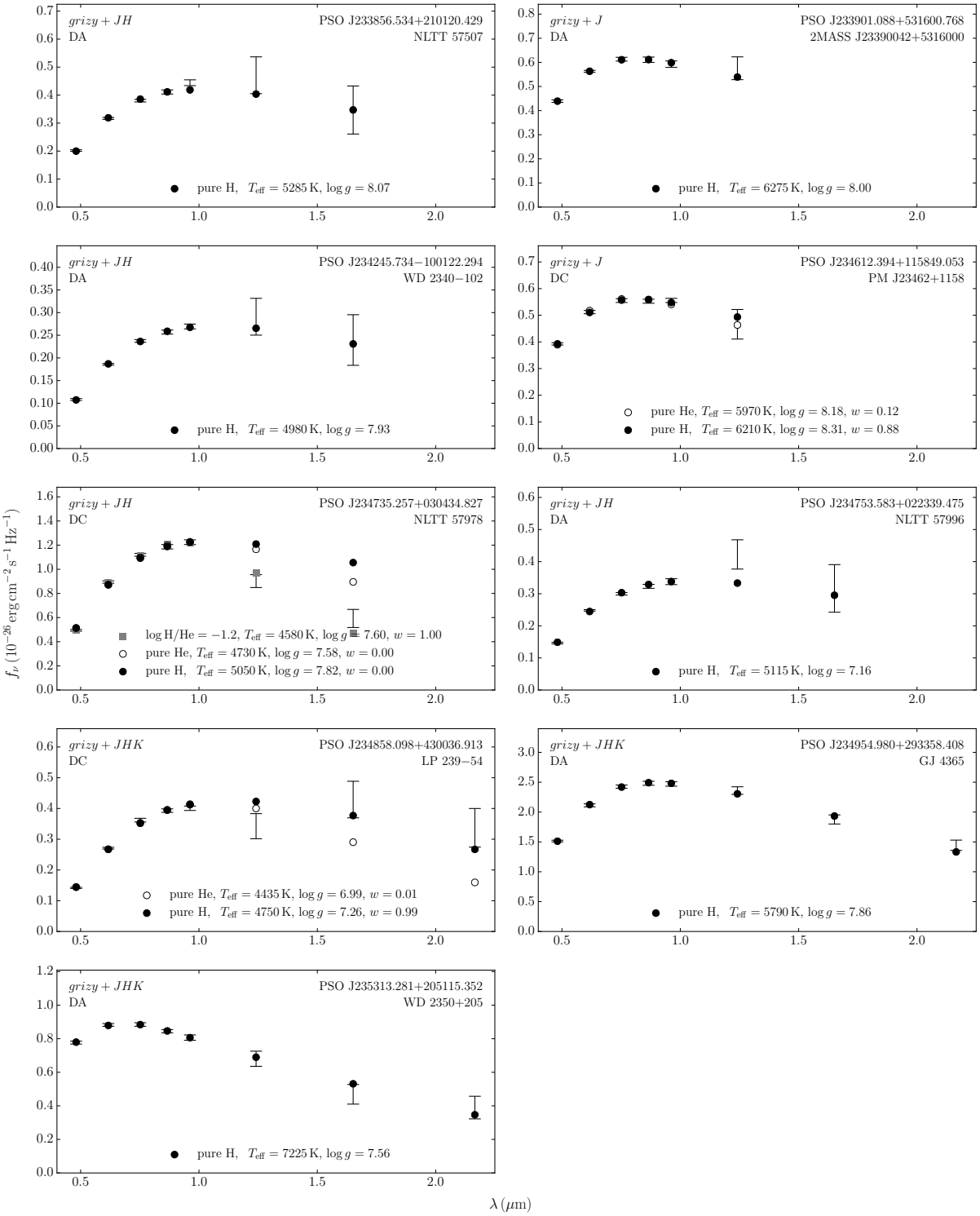

Figure C.2 – Ajustements photométriques et spectroscopiques des étoiles DZ

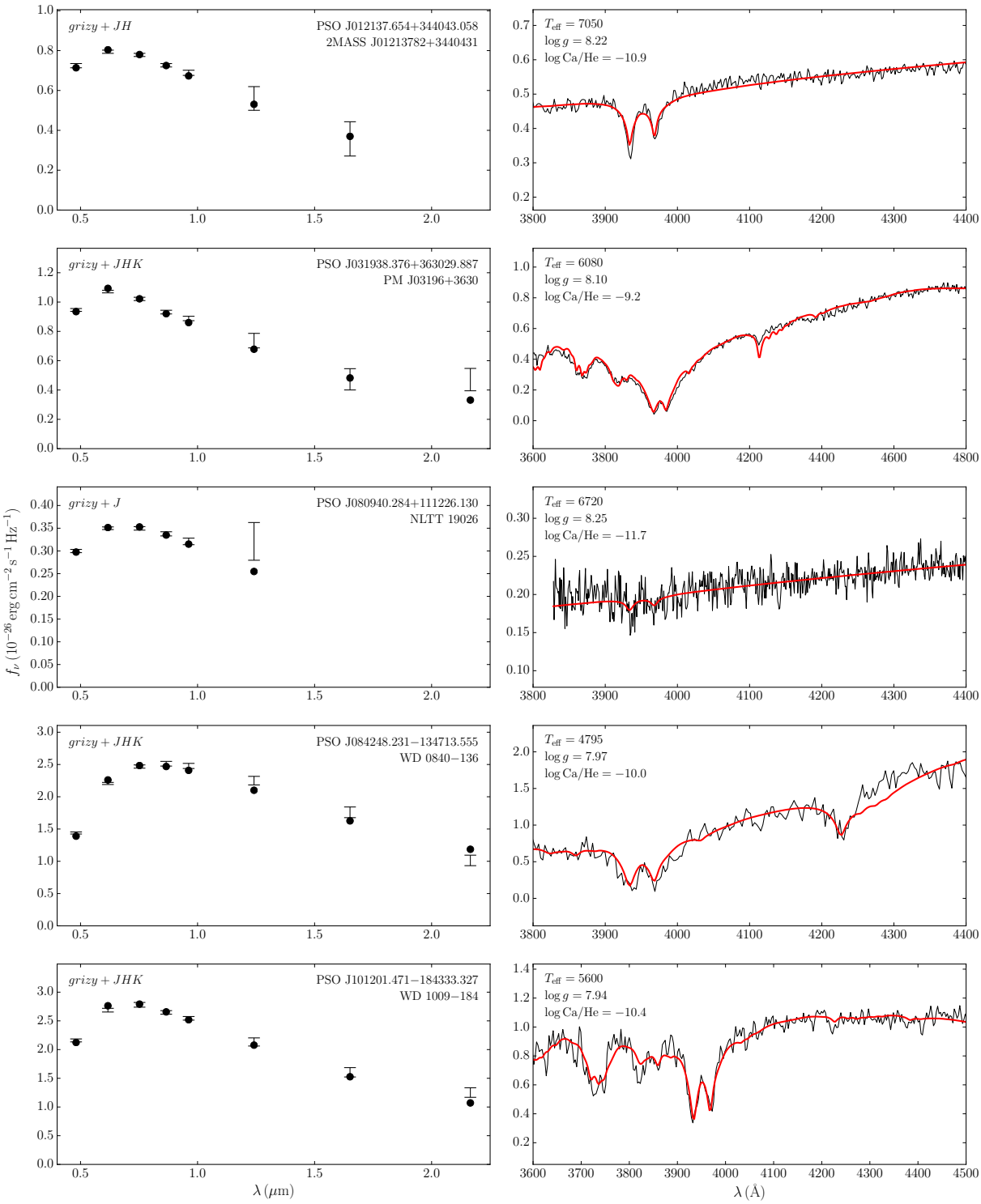

Figure C.2 – Ajustements photométriques et spectroscopiques des étoiles DZ (suite)

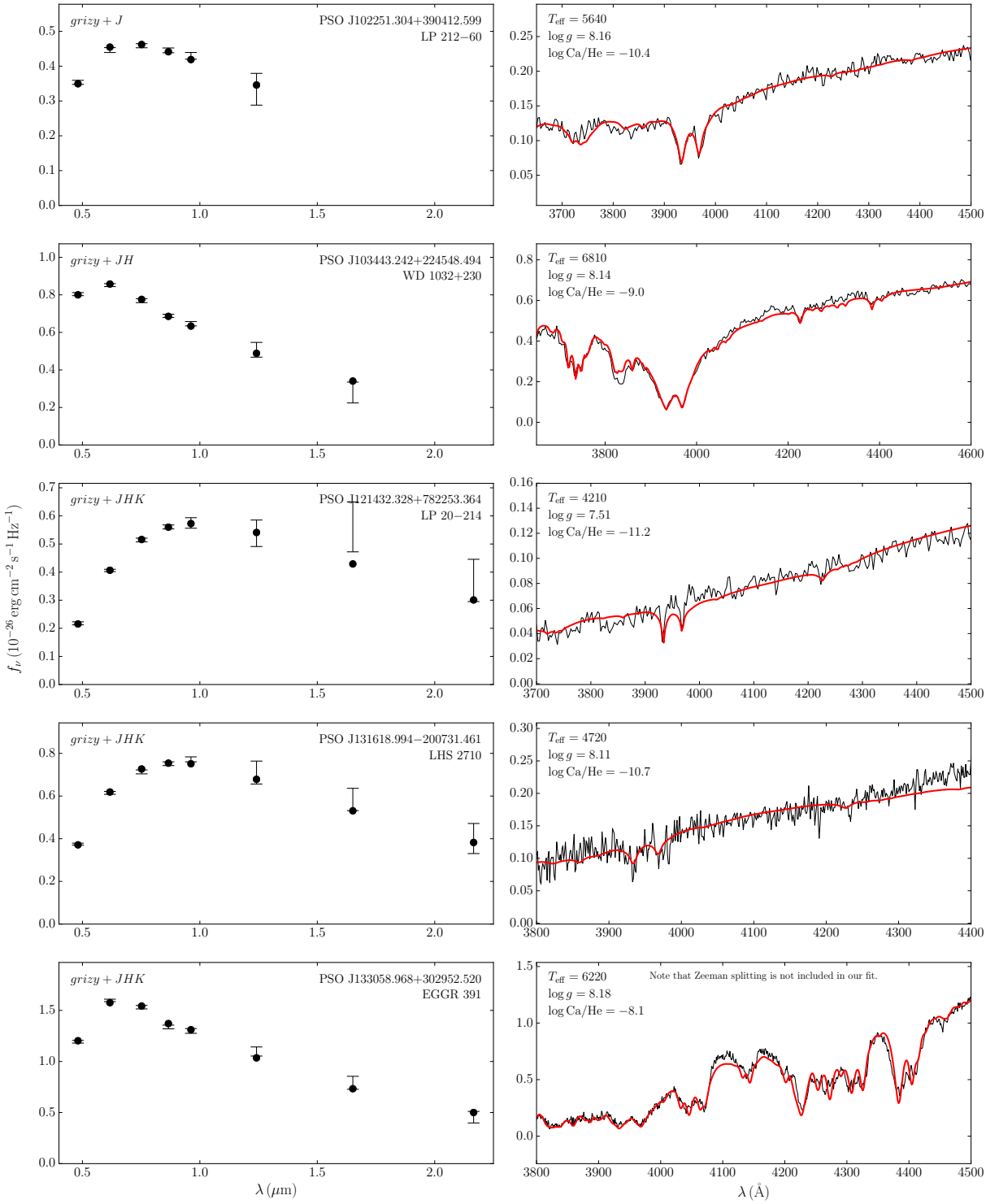

Figure C.2 – Ajustements photométriques et spectroscopiques des étoiles DZ (suite)

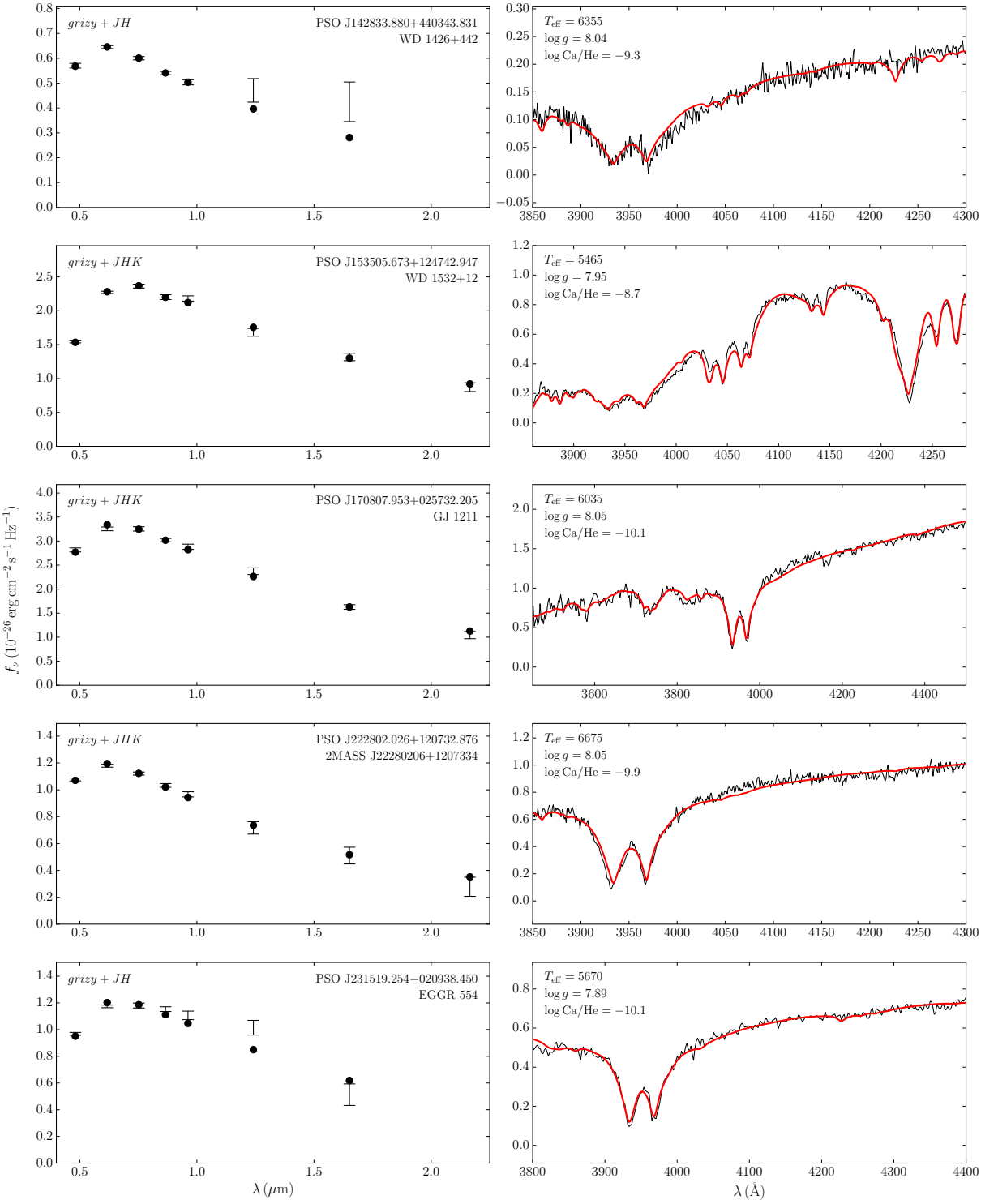

Figure C.2 – Ajustements photométriques et spectroscopiques des étoiles DZ (suite)

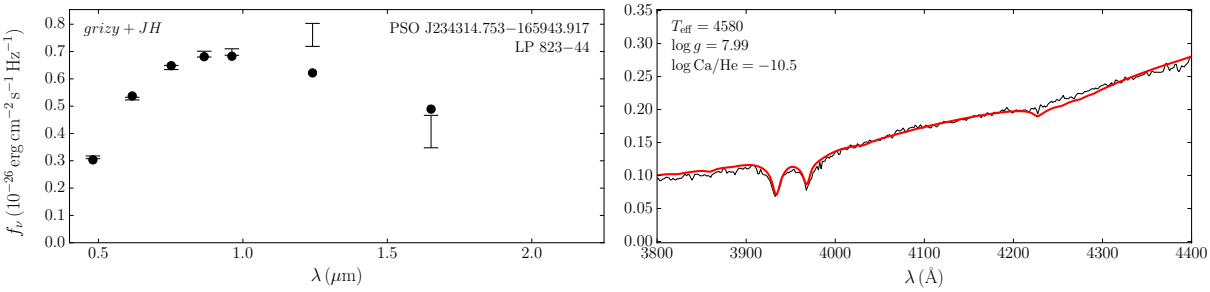

Figure C.3 – Ajustements photométriques et spectroscopiques des étoiles DQ/DQpec

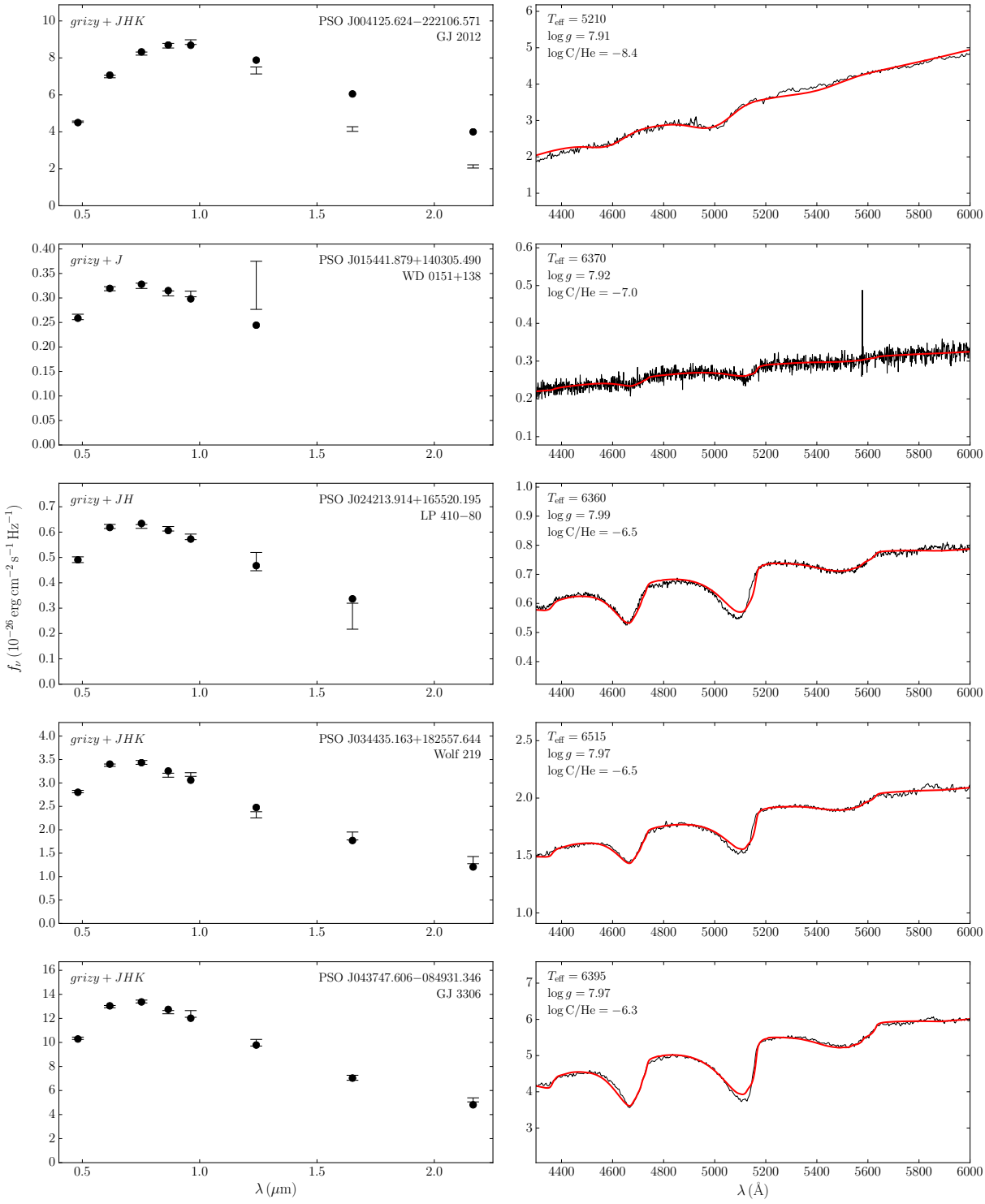

Figure C.3 – Ajustements photométriques et spectroscopiques des étoiles DQ/DQpec (suite)

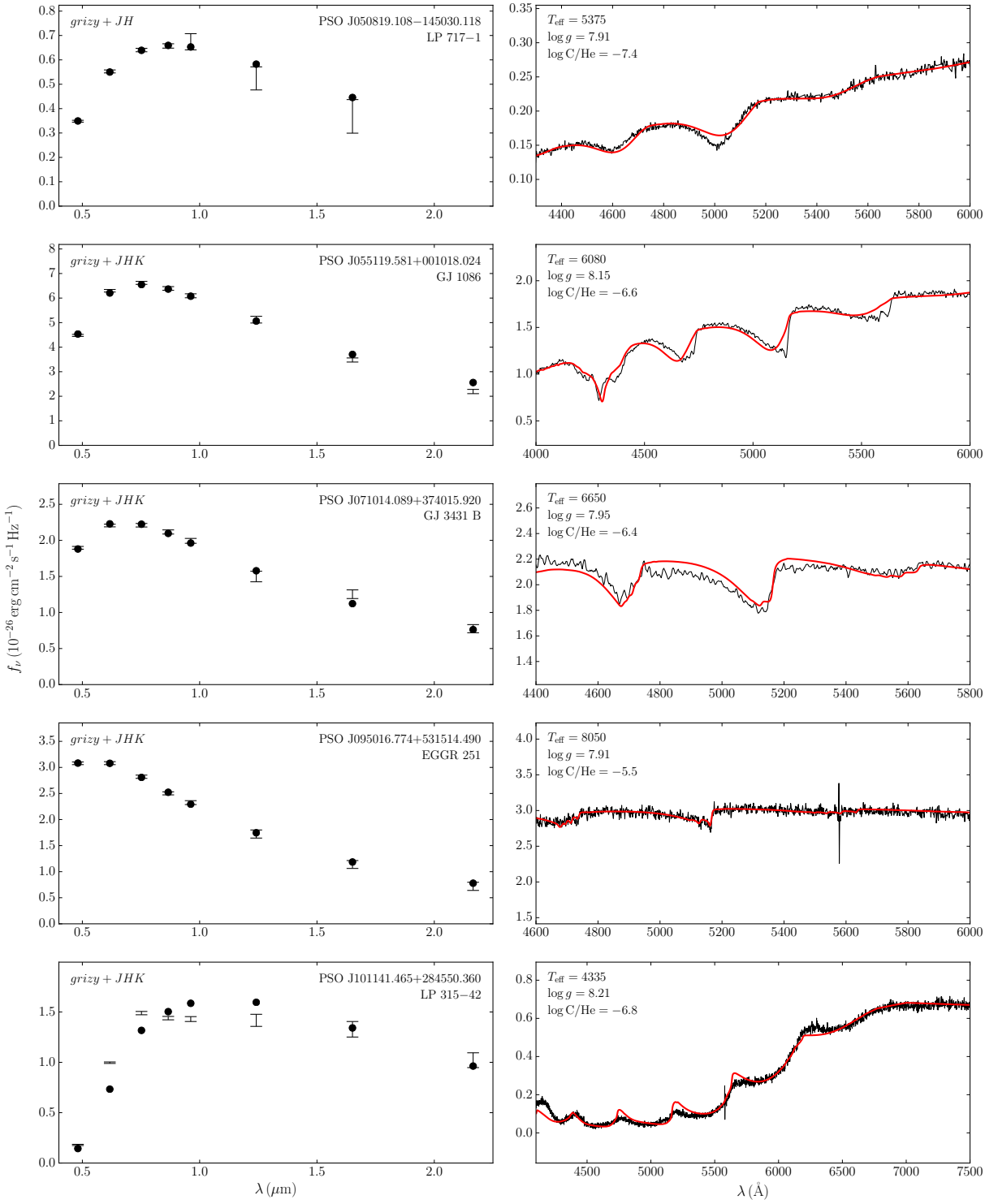

Figure C.3 – Ajustements photométriques et spectroscopiques des étoiles DQ/DQpec (suite)

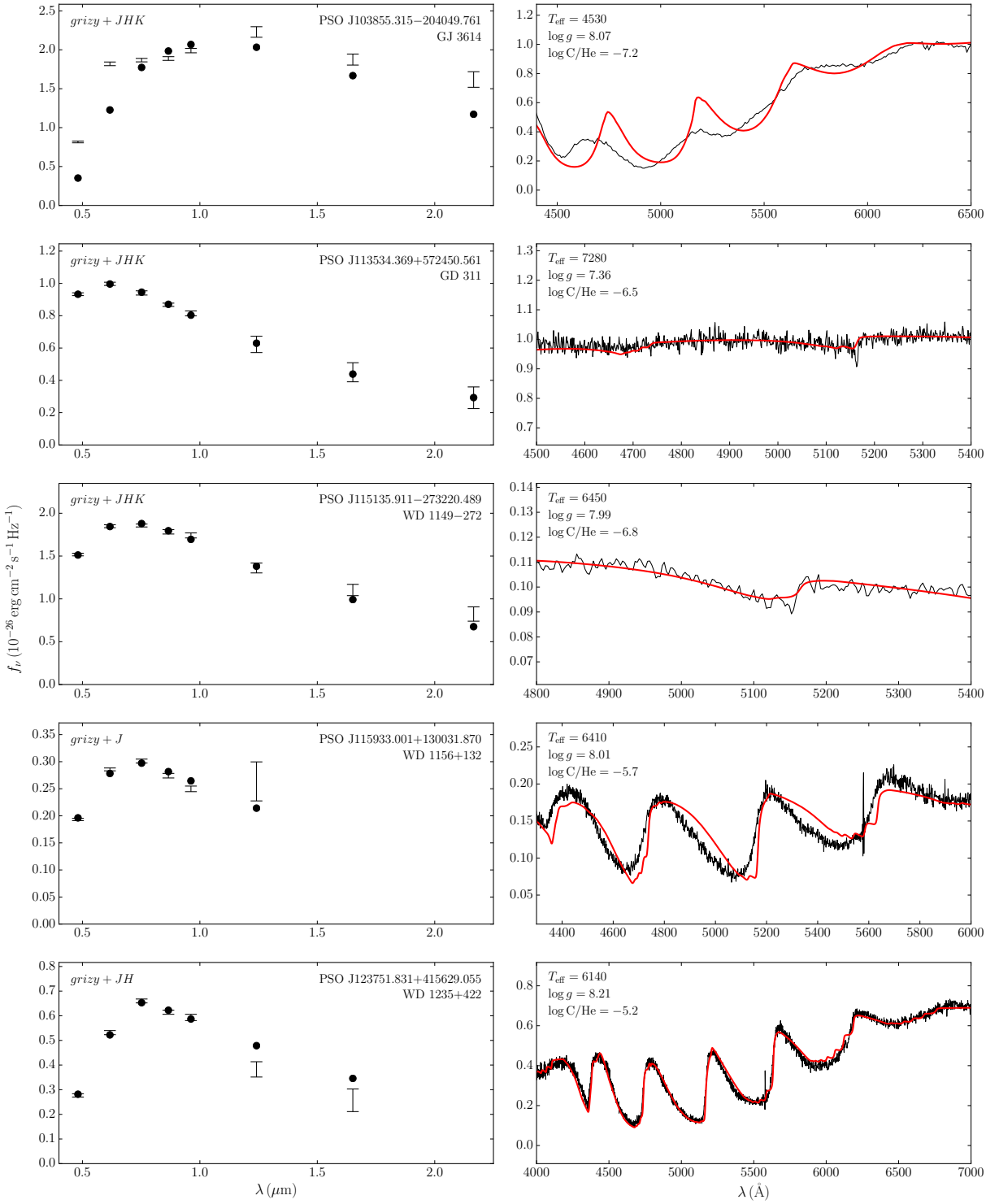

Figure C.3 – Ajustements photométriques et spectroscopiques des étoiles DQ/DQpec (suite)

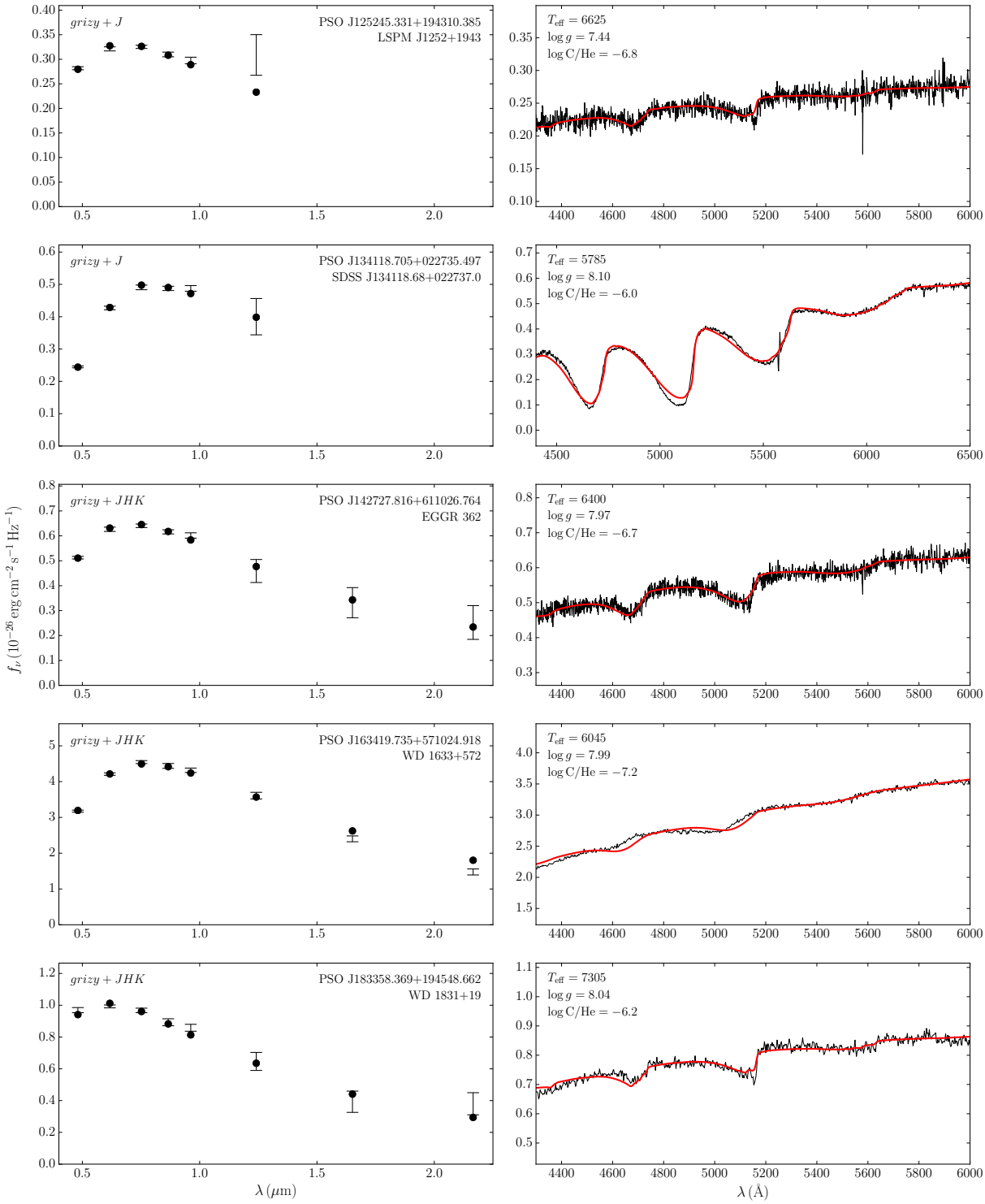

Figure C.3 – Ajustements photométriques et spectroscopiques des étoiles DQ/DQpec (suite)